

# JOURNAL OF THE ELECTROCHEMICAL SOCIETY

ELECTROCHEMICAL  
SCIENCE AND TECHNOLOGY

SOLID-STATE  
SCIENCE AND TECHNOLOGY

REVIEWS AND NEWS



VOL. 119, NO. 6

JUNE 1972

# FUTURE MEETINGS

## Of The Electrochemical Society



### MIAMI BEACH, FLORIDA—OCTOBER 8, 9, 10, 11, 12 & 13, 1972

Headquarters at the Fontainebleau Hotel

Planned symposia for the Miami Beach Meeting include the following Divisions and subjects:

**Battery**—Load Leveling and Standby Power, General Sessions; **Corrosion**—Effects of Metallurgical Substrates on Fundamental Corrosion Processes, General Session; **Dielectrics and Insulation**—Electrets Charge Storage and Transport in Dielectrics, Oxide-Electrolyte Interfaces, General Session; **Electrodeposition**—General Session; **Electrodeposition and Electronics**—Electrodeposition Processes in the Electronics Industry; **Electronics**—Semiconductor General Session, Chemistry and Physics of Compound Semiconductor Surfaces, General Electronics (Molecular Beam Epitaxy); **Electro-Organic**—General Session; **Electrothermics and Metallurgy**—Trace Elements; **New Technology Committee with the Battery, Corrosion, Electro-Organic, and Electrothermics and Metallurgy Divisions**—Marine Electrochemistry.

---

### CHICAGO, ILLINOIS—MAY 13, 14, 15, 16, 17 & 18, 1973

Headquarters at the Sheraton-Chicago Hotel

The following Divisions are planning symposia:

Dielectrics and Insulation; Electronics (Semiconductor, General, Luminescence); Electro-Organic; Electrothermics and Metallurgy; Industrial Electrolytic; Physical Electrochemistry; New Technology Committee—Electrochemical Aspects of Bio-Engineering.

---

### BOSTON, MASSACHUSETTS—OCTOBER 7, 8, 9, 10, 11 & 12, 1973

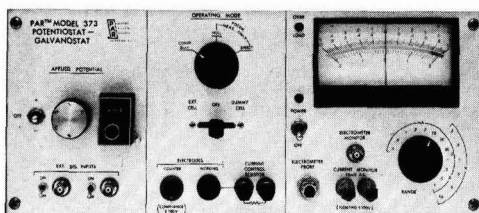
Headquarters at the Sheraton-Boston Hotel

The following divisions are planning symposia:

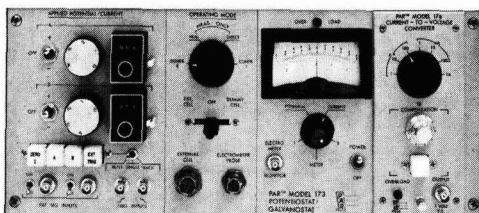
Battery; Corrosion; Dielectrics and Insulation; Electrodeposition; Electronics; Electrothermics and Metallurgy; New Technology Committee—Electrochemical Control of the Environment.



# THE RIGHT POTENTIOSTAT FOR THE RIGHT JOB ... FROM P.A.R.



**M-173 \$2475**



**M-373 \$1895**

**M-371 \$1995**

No matter what your potentiostatic or galvanostatic control requirements are, there's a P.A.R. instrument to fill your needs. Our 100V, 1A Model 173 offers the ultimate in versatility and convenience with two electronically-switchable, independent potential sources and a choice of plug-in current readout modules. Our 100V, 1A Model 373 is a low cost version of the 173 offering equivalent control specifications. Our Model 371 has full 20V, 7A capability. **All** instruments feature 1  $\mu$ s rise time and are, of course, all solid state. Each comes complete with our unique Model 178 electrometer probe. Write or call for our new brochure. Princeton Applied Research Corporation, P.O. Box 2565, Princeton, New Jersey 08540. (609) 452-2111. Telex: 84-3409.

**204**

## EDITOR

Norman Hackerman

## DIVISIONAL EDITORS

## BATTERY

R. J. Brodd  
Elton J. Cairns  
F. P. Malaspina

L. W. Niedrach  
G. F. Nordblom  
J. L. Weininger

## CORROSION

Theodore R. Beck  
J. W. Faust, Jr.  
Z. A. Foroulis  
Jerome Kruger

Ken Nobe  
Earl S. Snively, Jr.  
J. Bruce Wagner

## DIELECTRICS AND INSULATION

Robert S. Alwitt  
Newton Schwartz

Donald M. Smyth  
Lawrence Young

## ELECTRODEPOSITION

Seymour Senderoff

## ELECTRONICS

Ephraim Banks  
Charles M. Chapman  
George R. Cronin  
Simon Larach  
I. Arnold Lesk  
Ernest Paskell

Jerome Prener  
Bertram Schwartz  
Alan J. Strauss  
P. Wang  
J. M. Woodall

## ELECTRO-ORGANIC

Manuel M. Baizer  
Stanley Wawzonek

## ELECTROTHERMICS AND METALLURGY

Joan B. Berkowitz  
J. M. Blocher, Jr.

W. E. Kuhn  
W. W. Smeltzer

## INDUSTRIAL ELECTROLYTIC

P. A. Dana  
Scott Lynn

## PHYSICAL ELECTROCHEMISTRY

Allen J. Bard  
M. W. Breiter  
A. J. de Bethune

R. M. Hurd  
Royce J. Murray  
C. W. Tobias

## EDITORIAL STAFF

Nancy Gay Stewart, Assistant to the Editor  
Julius Klerer, Book Review Editor

## PUBLICATION STAFF

Sarah A. Kilfoyle, Publication Editor  
Beverly M. Bruns, Assistant Publication Editor

## PUBLICATION COMMITTEE

Newton Schwartz, Chairman  
Elton Cairns  
Robert T. Foley  
Norman Hackerman  
Earl S. Snively, Jr.  
Fred Strieter  
Dennis R. Turner  
Jack H. Westbrook

## ADVERTISING OFFICE

P.O. Box 2071  
Princeton, N. J. 08540



JUNE 1972

## ELECTROCHEMICAL SCIENCE AND TECHNOLOGY

## TECHNICAL PAPERS

T. R. Crompton  
G. Uitenbroek  
... 655

Removal of Surface Antimony from Antimony Lead Alloys by Sulfuric Acid-Hydrogen Peroxide Pickling

G. D. McDonald  
E. Y. Weissman  
T. S. Roemer  
... 660

Lead-Fluoroboric Acid Battery

T. Smith  
F. Mansfeld  
... 663

An Ellipsometric-Electrochemical Cell: Initial Films on Titanium in Water and Methanol Solutions

N. Feldstein  
J. A. Weiner  
... 668

Contact Angle Measurements of Tin Sensitizing Solutions

D. M. MacArthur  
... 672

A Study of Gold Reduction and Oxidation in Aqueous Solutions

G. Neubert  
E. Gorman  
R. Van Reet  
K. B. Prater  
... 677

Current Distribution at the Rotating Ring-Disk Electrode

A. K. Vijh  
... 679

Electrode Kinetic Studies on Electro-Organic Syntheses Involving Carbonium Ions  
I. Anodic Oxidation of Acetate Ions to Methyl Acetate

G. J. Barnes  
A. W. Aldag  
R. C. Jerner  
... 684

Surface Concentration of Molybdenum in Types 316 and 304 Stainless Steel by Auger Electron Spectroscopy

S. E. Forman  
W. J. Rhines  
... 686

Vibration Characteristics of Crystal Slicing ID Saw Blades

L. Nanis  
T. K. G. Nambodhiri  
... 691

Mathematics of the Electrochemical Extraction of Hydrogen from Iron

R. N. Roy  
W. Vernon  
A. Bothwell  
J. Gibbons  
... 694

Standard Potentials of Ag-AgCl Electrode and Related Thermodynamic Quantities in Dimethyl Sulfide-Water Mixtures from 5° to 45°C

C. R. Ito  
S. Asakura  
K. Nobe  
... 698

Diffusion Kinetics at Microelectrodes

# ELECTROCHEMICAL SOCIETY

Vol. 119 • No. 6

J. R. Lloyd  
E. M. Sparrow  
E. R. G. Eckert  
... 702

Local Natural Convection Mass Transfer Measurements

D. Landolt  
... 708

Throwing Power Measurements during High Rate Nickel Dissolution under Active and Transpassive Conditions

## TECHNICAL NOTES

R. S. Perkins  
... 713

Gallium Oxidation in Alkaline Solution

P. L. Wallace  
J. C. Walden  
J. W. Magana  
... 715

A Rapid and Complete Method to Remove Plutonium Contamination from Aluminum

N. Q. Lam  
S. J. Rothman  
L. J. Norwicki  
... 715

An Electrochemical Technique for Microsectioning Silver

## BRIEF COMMUNICATION

R. Greif  
R. Kappesser  
I. Cornet  
... 717

Transport in Non-Newtonian Flow

## DISCUSSION SECTION

... 719

## SOLID-STATE SCIENCE AND TECHNOLOGY

### TECHNICAL PAPERS

J. W. Lindsay  
K. Terada  
M. A. Thompson  
... 726

Oxidation of Beta-Phase Plutonium

J. L. Stakebake  
L. M. Steward  
... 730

Plutonium Oxidation in Moist Oxygen-Nitrogen Mixtures

E. T. Fitzgibbons  
K. J. Sladek  
W. H. Hartwig  
... 735

TiO<sub>2</sub> Film Properties as a Function of Processing Temperature

R. J. R. S. B. Bhalla  
E. W. White  
... 740

Cathodoluminescence Characteristics of Mn<sup>2+</sup>-Activated Willemite (Zn<sub>2</sub>SiO<sub>4</sub>) Single Crystals

## DIVISION OFFICERS

### Battery Division

Alvin J. Salkind, Chairman  
Ralph J. Brodd, Vice-Chairman  
Howard R. Karas, Secretary-Treasurer  
General Battery Corp.  
P. O. Box 1262  
Reading, Pa. 19603

### Corrosion Division

Z. A. Foroulis, Chairman  
J. P. Pemsler, Vice-Chairman  
Roger Staehle, Secretary-Treasurer  
Ohio State University  
Dept. of Metallurgical Engineering  
116 West 19th Avenue  
Columbus, Ohio 43210

### Dielectrics and Insulation Division

Lawrence Gregor, Chairman  
Lyon Mandelcorn, Vice-Chairman  
Benjamin Vroman, Treasurer  
Frederick Vratny, Secretary  
Bell Telephone Laboratories  
Murray Hill, New Jersey 07974

### Electrodeposition Division

Rolf Weil, Chairman  
John L. Griffin, Vice-Chairman  
Vladimir Hospadaruk, Secretary-Treasurer  
1412 Plainfield Avenue  
Dearborn Heights, Michigan 48129

### Electronics Division

Erik Pell, Chairman  
I. Arnold Lesk, Vice-Chairman (Semiconductors)  
William A. McAllister, Vice-Chairman (Luminescence)  
Ian M. Croll, Vice-Chairman (General)  
Jerry M. Woodall, Secretary-Treasurer  
Thomas J. Watson Research Center  
IBM Corporation  
Yorktown Heights, New York 10598

### Electro-Organic Division

Allen J. Bard, Chairman  
Manuel M. Baizer, Vice-Chairman  
Charles K. Mann, Secretary-Treasurer  
Department of Chemistry  
Florida State University  
Tallahassee, Florida 32306

### Electrothermics and Metallurgy Division

Joan B. Berkowitz, Chairman  
Walter W. Smeltzer, Senior Vice-Chairman  
Robert Bakish, Junior Vice-Chairman  
John M. Blocher, Jr., Secretary-Treasurer  
Battelle Memorial Institute  
Columbus, Ohio 43200

### Industrial Electrolytic Division

Nolan E. Richards, Chairman  
D. N. Goens, Vice-Chairman  
Thomas C. Jeffery, Secretary-Treasurer  
816 Ardmore  
Lake Charles, Louisiana 70602

### Physical Electrochemistry Division

Robert E. Meredith, Chairman  
Manfred W. Breiter, Vice-Chairman  
James D. E. McIntyre, Secretary-Treasurer  
Bell Telephone Laboratories, Inc.  
IE-439  
Murray Hill, New Jersey 07974

## SOCIETY OFFICERS AND STAFF

**Theodore D. McKinley**, President  
E. I. du Pont de Nemours & Co., Inc.  
Pigments Department  
Experimental Station  
Wilmington, Del. 19898

**N. Bruce Hannay**, Vice-President  
Bell Telephone Laboratories, Inc.  
Murray Hill, N. J. 07971

**David A. Vermilyea**, Vice-President  
General Electric Research Laboratories  
Building K01, Room 3A45  
Schenectady, N. Y. 12301

**Theodore R. Beck**, Vice-President  
10035 31 Avenue, N.E.  
Seattle, Wash. 98125

**Dennis R. Turner**, Secretary  
Bell Telephone Laboratories, Inc.  
Room 1E-245  
Murray Hill, N. J. 07971

**R. Homer Cherry**, Treasurer  
2350 Huntingdon Road  
Huntingdon Valley, Pa. 19006

**Ernest G. Enck**, Executive Secretary  
The Electrochemical Society, Inc.  
P.O. Box 2071  
Princeton, N. J. 08540

**V. H. Brannock**, Assistant Executive Secretary  
The Electrochemical Society, Inc.  
P.O. Box 2071  
Princeton, N. J. 08540

**Marie Fallon**, Financial Secretary  
The Electrochemical Society, Inc.  
P.O. Box 2071  
Princeton, N. J. 08540

Manuscripts submitted to the Journal should be sent, in triplicate, to the Editorial Office at P. O. Box 2071, Princeton, N. J. 08540. They should conform to the revised "Instructions to Authors" available from Society Headquarters. Manuscripts so submitted, as well as papers presented before a National technical meeting, become the property of the Society and may not be published elsewhere in whole or in part without written permission of the Society. Address such requests to the Editor.

The Electrochemical Society does not maintain a supply of reprints of papers appearing in its Journal. A photoprint copy of any particular paper may be obtained from University Microfilms, 300 North Zeeb Road, Ann Arbor, Michigan 48106.

Inquiries regarding positive microfilm copies of volumes should be addressed to University Microfilms, Inc., 300 N. Zeeb St., Ann Arbor, Mich. 48106.

Walter J. Johnson, Inc., 111 Fifth Ave., New York, N. Y., 10003, have reprint rights to out-of-print volumes of the Journal, and also have available for sale back volumes and single issues, with the exception of the current calendar year. Anyone interested in securing back copies should correspond directly with them.

Published monthly by The Electrochemical Society, Inc., at 215 Canal St., Manchester, N. H.; Executive Offices, Editorial Office, and Circulation Dept., and Advertising Office at P. O. Box 2071, Princeton, N. J. 08540, combining the JOURNAL and TRANSACTIONS OF THE ELECTROCHEMICAL SOCIETY. Statements and Opinions given in articles and papers in the JOURNAL OF THE ELECTROCHEMICAL SOCIETY are those of the contributors, and The Electrochemical Society assumes no responsibility for them.

Claims for missing numbers will not be allowed if received more than 60 days from date of mailing plus time normally required for postal delivery of JOURNAL and claim. No claims allowed because of failure to notify the Circulation Dept., The Electrochemical Society, P. O. Box 2071, Princeton, N. J., 08540, of a change of address, or because copy is "missing from files." Subscription to members as part of membership service; subscription to non-members \$40.00 plus \$3.00 for postage outside U.S. and Canada. Single copies \$2.50 to members, \$4.00 to nonmembers. © 1972 by The Electrochemical Society, Inc. Second Class Postage Paid at Princeton, New Jersey, and at additional mailing offices. Printed in U.S.A.

## SOLID STATE SCIENCE (Cont.)

**R. E. Enstrom**  
**J. J. Hanak**  
**J. R. Appert**  
**K. Strater**  
... 743

Effect of Impurity Gas Additions on the Superconducting Critical Current of Vapor-Deposited Nb<sub>3</sub>Sn

**R. S. Ronen**  
**P. H. Robinson**  
... 747

Hydrogen Chloride and Chlorine Gettering: An Effective Technique for Improving Performance of Silicon Devices

**R. R. Mehta**  
**S. F. Vogel**  
... 752

Sputtered Cadmium Oxide and Indium Oxide/Tin Oxide Films as Transparent Electrodes to Cadmium Sulfide

**M. Kowalchik**  
**A. S. Jordan**  
**M. H. Read**  
... 756

Coprecipitation of Ga<sub>2</sub>O<sub>3</sub> in the Liquid-Phase Epitaxial Growth of GaP

**V. S. Ban**  
... 761

Mass Spectrometric Studies of Vapor-Phase Crystal Growth  
II. GaN

**L. M. Foster**  
**J. E. Scardefield**  
**J. F. Woods**  
... 765

Thermodynamic Analysis of the III-V Alloy Semiconductor Phase Diagrams  
III. The Solidus Boundary in the Ga<sub>1-x</sub>Al<sub>x</sub>As Pseudobinary System

**C. F. Gibbon**  
**E. I. Povelonis**  
**D. R. Ketchow**  
... 767

The Effect of Mask Edges on Dopant Diffusion into Semiconductors

**R. C. Henderson**  
... 772

Silicon Cleaning with Hydrogen Peroxide Solutions: A High Energy Electron Diffraction and Auger Electron Spectroscopy Study

**V. J. Silvestri**  
... 775

Thermodynamic Calculations of the Ge-H-Cl System

**T. Yashiro**  
... 780

Some Properties of Vapor Deposited Ge<sub>3</sub>N<sub>4</sub> Films and the Ge<sub>3</sub>N<sub>4</sub>-Ge Interface

**G. Dionne**  
**J. C. Woolley**  
... 784

Crystal Growth and Isothermal Annealing of Pb<sub>1-x</sub>Sn<sub>x</sub>Te Alloys

## TECHNICAL NOTES

**R. C. Taylor**  
**V. Sadagopan**  
... 788

Preparation and Properties of Hexaferrite Films

**H. G. Maguire**  
**P. D. Augustus**  
... 791

The Detection of Silicon-Oxynitride Layers on the Surfaces of Silicon-Nitride Films by Auger Electron Emission


## DISCUSSION SECTION

... 793

## REVIEWS AND NEWS

### NEWS

... 165C



**No matter where  
your battery goes,  
we can make it  
go better.**

From tiny tasks to titanic projects, batteries must perform powerful and precise functions. And whatever the job to be done, battery performance gets a boost when you use Webril® nonwoven fabrics for separators and absorbers. For a number of very good reasons.

If primary and secondary battery systems are to perform much more reliably, they must inhibit dendrite growth and passage. Permit free ionic passage. Remain unaffected by acid or alkali. Loss of active plate material must be minimized. And electrolyte

contact with plates must be assured. Webril nonwoven fabrics can do all this.

They have been performance-tested for over millions of hours in mercury-zinc, zinc-air, lead-acid, cuprous chloride, and nickel-cadmium systems. The unusually broad line of fine Webril products gives you greater design flexibility. You can choose from polypropylene, Dynel\*, nylon, highly purified cotton, modified cellulose, and other fibers.

Find out more today. Write Mr. P.N. Dangel, Electrical Specialties Department.



The Kendall Company, Fiber Products Division, Walpole, Mass. 02081

\*Union Carbide Corp. trademark for its modacrylic fiber.



# THE ELECTROCHEMICAL SOCIETY, INC.

The Electrochemical Society is an international organization of individuals and companies concerned with or interested in electrochemistry and allied subjects.

## OBJECTIVES

1. The advancement of the theory and practice of electrochemistry, electrometallurgy, electrothermics, electronics, solid state and allied subjects.
2. To encourage research and the reporting of such research for the dissemination of knowledge in the field of electrochemistry and solid state.
3. To insure the availability of adequate training in the field of electrochemistry for chemists, engineers, metallurgists, physicists, and solid state investigators.

## BENEFITS OF MEMBERSHIP

1. Assurance of keeping abreast of the latest scientific developments in your particular fields of interest.
2. Enjoyment of personal association with fellow scientists and engineers in the professions.
3. Opportunity to contribute to the advancement of the science and application of electrochemistry and solid state in your areas of interest.
4. Stimulation of interdisciplinary exchanges.

## DIVISIONS

The activities of the Society are carried on by its nine divisions as follows:

Battery	Electronics
Corrosion	(Including Semiconductors and Luminescence)
Dielectrics and Insulation	Electro-Organic
Electrodeposition	Electrothermics and Metallurgy
	Industrial Electrolytic
	Physical Electrochemistry

## SECTIONS

Local Sections of the Society have been organized in the following cities and regions:

Boston	Niagara Falls
Chicago	North Texas
Cleveland	Ontario-Quebec
Columbus	Pacific Northwest
Detroit	Philadelphia
Indianapolis	Pittsburgh
Midland (Michigan)	San Francisco
Metropolitan New York	Southern California-Nevada
National Capital Area	South Texas



## Removal of Surface Antimony from Antimony Lead Alloys by Sulfuric Acid-Hydrogen Peroxide Pickling

T. R. Crompton and G. Uitenbroek\*

Oldham & Son Limited, Denton, Manchester, England

### ABSTRACT

It has been shown that treatment of cast antimonial lead alloys with mixtures of hydrogen peroxide and sulfuric acid at 20°C dissolves surface antimony at an appreciably greater rate than occurs with sulfuric acid alone, even at elevated temperatures. Optimum hydrogen peroxide-sulfuric acid reagent compositions have been established for the maximum solution of antimony from the alloy. A correlation exists between the quantity of antimony removed by this treatment and the quantity of antimony that is subsequently released from the alloy into sulfuric acid electrolyte when it is set up as an anode against pure lead cathodes. Batteries made using positive grids which have been pickled in hydrogen peroxide-sulfuric acid mixtures, then brightened by dipping in a 10% aqueous solution of diethylene triamine have been shown to have a greater life on charge/discharge cycles than batteries made using standard unpickled grids.

Antimony is added as an alloying constituent to impart increased hardness to lead used in the manufacture of grids for lead-acid batteries. Alloy grids are much less liable to distortion during battery manufacturing operations. However, positive battery plates used in lead-acid battery manufacture, made from such castings, will, during plate formation, release a large proportion of their surface antimony, which will migrate towards the negative plate, thereby contaminating the formation electrolyte, the negative active material, and the positive active material. Similarly, in battery operation, antimony contamination of plates will occur. Both forms of antimony contamination have adverse effects on battery performance such as increases in positive plate corrosion (i.e., shorter life) and in self-discharge rates; also it prevents the positive plate from reaching its true potential. For these reasons research has been undertaken to study removal of antimony from such grids.

Burbank and Simon (1) have shown the manner in which the anodic corrosion of lead and its hypoeutectic antimony alloys takes place in sulfuric acid and how such corrosion is related to the microstructure of these alloys. Pure lead and alloys containing up to 0.5% antimony corrode intergranularly (i.e., grain boundary attack). At higher concentrations a combination of intergranular and interdendritic penetration occurs, but up to 6% antimony the attack remains preferentially intergranular. At higher antimony concentration (6-12%) the corrosion is more evenly distributed between intergranular attack and attack along the interdendritic network of segregated antimony. Burbank and Simon also revealed by x-ray diffraction that the surface of castings containing 6% or more antimony is richer in antimony than within the bulk of the castings, i.e., an antimony-rich surface layer is present.

A search brought to light one patent, by Bosch (2), which involves a pickling treatment for removing con-

centrations of antimony on the surface of cast lead-antimony alloys used in lead acid battery manufacture. This process involves dipping the as-cast metal in sulfuric acid of 1.75 sp gr. This treatment it is claimed will remove antimony from a surface layer of at least  $10^{-6}$  mm thickness of alloy.

The work described below for removing surface antimony from antimonial lead differs from that described by Bosch in that it incorporates a sulfuric acid-hydrogen peroxide reagent which has been shown to be much more effective than sulfuric acid alone in removing surface antimony from antimonial lead.

### Experimental

**Pickling in sulfuric acid.**—Experiments were first carried out to establish the extent to which pickling in aqueous sulfuric acid dissolved antimony from 7% antimonial lead. One kilogram of metal was immersed in 2 liters of sulfuric acid of known specific gravity and maintained at a constant temperature. In the work described in this paper the lead was in the form of cast grids of the type used in the manufacture of lead acid batteries. After various time intervals portions of the acid were removed and dissolved antimony determined by a procedure which is sensitive enough to detect down to 0.2 mg antimony in a liter of test solution.

**Pickling in sulfuric acid-hydrogen peroxide mixture.**—A range of solutions were prepared such that the final mixtures had a known specific gravity with respect to sulfuric acid (between 1.03 and 1.60 sp gr at 20°C) and contained a known concentration of hydrogen peroxide (between 2 volume and 5 volume concentration).<sup>1</sup> In all cases the solutions were prepared immediately prior to use. The pickling experiments were then carried out as discussed above.

**Determination of antimony in sulfuric acid-hydrogen peroxide mixtures.**—**Reagents.**—Standard antimony so-

<sup>1</sup> One volume concentration  $H_2O_2$  is that concentration (0.3g  $H_2O_2$ /liter) which upon decomposition produces 1 ml oxygen at STP per milliliter of the peroxide solution.

\* Electrochemical Society Active Member.

Key words: battery, lead-acid, alloys, antimony, battery grids, pickling.

lution, prepared from potassium antimonyl tartrate "ANALAR" to contain 0.1 mg antimony per milliliter.

Ascorbic acid/potassium iodide reagent was prepared by dissolving 70g potassium iodide "ANALAR" and 5g ascorbic acid in deionized water and making up to 500 ml. This solution must be prepared freshly as required.

Sulfuric acid was 1.2 sp gr, aqueous.

Potassium permanganate (1N) aqueous, was prepared from "ANALAR" solid.

**Calibration curve.**—Into seven 100 ml volumetric flasks, pipette 0.0, 0.1, 0.2, 0.3, 0.5, 0.7, and 1.0 ml of standard antimony solution (e.g., 0.0 to 0.1 mg Sb) then add 10 ml of 1.2 gravity sulfuric acid. Add 25 ml potassium iodide/ascorbic acid reagent to each flask then make up to 100 ml with 1.2 sp gr sulfuric acid.

Fill two 10 mm glass spectrophotometer cells, respectively with the solution which is free from antimony (control) and the solution containing 0.1 ml standard antimony solution.

Place the two cells in spectrophotometer and measure the optical density at 425 m $\mu$  of the sample solution relative to the control (antimony free) solution in the reference beam. Repeat with each of the standard antimony solutions.

Plot a curve of milligrams antimony in the original 100 ml test solution vs. the corresponding optical densities obtained.

**Analysis of pickling solutions.**—Transfer a suitable volume (maximum 100 ml) of pickling solution into a 100 ml volumetric flask. If the specific gravity of the sulfuric acid in the pickling solution is less than 1.2 then add a calculated volume of 1.6 sp gr sulfuric acid to adjust the gravity in the final mixture to 1.2. If the specific gravity of the pickling solution exceeds 1.2 then add a calculated volume of deionized water sufficient to adjust the gravity of the final mixture to 1.2. Add sufficient 1.2 sp gr sulfuric acid to make the volume up to 10 ml. To a second control 100 ml volumetric flask add 10 ml 1.2 sp gr sulfuric acid. To both solutions add dropwise from a burette, potassium permanganate solution until a faint pink color is produced which persists for 5 min, indicating complete neutralization of hydrogen peroxide. Add 25 ml potassium iodide/ascorbic acid reagent and make up to 100 ml with 1.2 sp gr sulfuric acid. Refer the optical density to the calibration curve to obtain the weight of antimony present in the original 100 ml of diluted pickling solution.

If it is found that the concentration of antimony in the original pickling solutions is too high, then this solution should be diluted by a known amount with sulfuric acid of the same specific gravity and the above analysis repeated.

**Measurement of the release of antimony from alloys under electrochemical conditions.**—Pickled and unpickled castings (150g) in 4.5, 7, and 10% antimonial lead were set up as anodes, against pure lead cathodes in cells containing a liter of 1.25 sp gr sulfuric acid. A 2A current was passed through the castings and the antimony content of the electrolyte determined at intervals.

**Construction of test batteries.**—The test batteries used in the study were Miners Caplamps batteries constructed with two cells, each containing a tubular positive plate and two negative plates and a standard separator system.

A low antimonial alloy (4.5% antimony) was used throughout; only the positive grids were pickled.

Pickling was conducted for 8 hr at 15°–20°C in a solution consisting of 4 volume strength hydrogen peroxide in 1.200 sp gr sulfuric acid. The solution was contained in a glass or polyethylene tank and the lead grids were suspended, without touching in this solution at a ratio of 1 kg of lead to 2 liters of solution.

In some experiments the grids were then rinsed in cold running water to remove acid and were then allowed to dry. Such grids had on the surface a very

thin whitish layer, presumably of lead sulfate. In other experiments, pickled grids were immediately dipped in a 10% aqueous solution of diethylene triamine for a few minutes until lead sulfate had been completely removed and the metal was bright. The plates were then quickly rinsed in water and left to air dry.

Batches of batteries containing unpickled, pickled and water washed, and pickled and amine washed positive grids were then assembled by standard manufacturing methods.

The batteries were then continuously cycled according to the following schedule: charge: constant voltage charge at 4.90 to 2.45V per cell (about 15 hr); discharge: for 9 hr through a 1A calibrated bulb recording the time taken to reach 1.85V per cell. Cycling tests were discontinued when the discharge time dropped below 7 hr, i.e., end of battery life.

## Results

**Sulfuric acid pickling.**—Antimony extraction was extremely low at acid gravities of 1.2 and 1.4 even at operating temperatures up to 80°C. At 1.6 gravity and 80°C, 72 mg of antimony was dissolved from the alloy in 300 hr from 1 kilo of alloy, i.e., only 0.1% of the antimony content of the original alloy (7%) was dissolved into the pickling solution. At 80°C in 1.4 gravity acid, a small amount of white precipitate was noted in the acid, presumably lead sulfate. At 80°C in 1.6 gravity acid, a small amount of a brown orange precipitate was noted in suspension in the solution and as a coating on the metal. This solid contained about 4% antimony and, presumably by its color, contained antimony sulfide. The solution itself had a deep brown discoloration. In the same experiment, a bubbler containing 10% aqueous silver nitrate solution was connected to the sealed vessel in which the pickling was carried out and it was observed that during the experiment, a black precipitate formed in the silver nitrate solution. This was presumably, silver stibide and/or silver sulfide produced by reaction of silver ions with stibine and/or hydrogen sulfide produced during pickling. These observations fit in with the reactions known to occur between antimony and hot sulfuric acid solutions of specific gravity greater than 1.55. Decomposition products of this type were not observed in pickling experiments conducted in acid gravities below 1.4

**Sulfuric acid-hydrogen peroxide pickling.**—Figure 1 compares the rate of extraction of antimony from 7% antimonial lead by strong sulfuric acid at 80°C and by various acid-hydrogen peroxide mixtures at normal ambient temperatures. The dramatic increase in antimony extraction resulting upon incorporation of hydrogen peroxide is immediately evident.

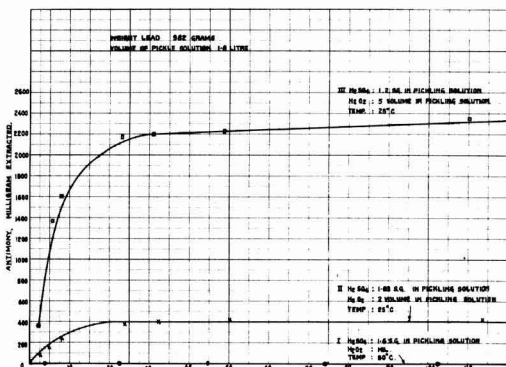


Fig. 1. Comparison of pickling rates of 7% antimonial lead in sulfuric acid and hydrogen peroxide/sulfuric acid.

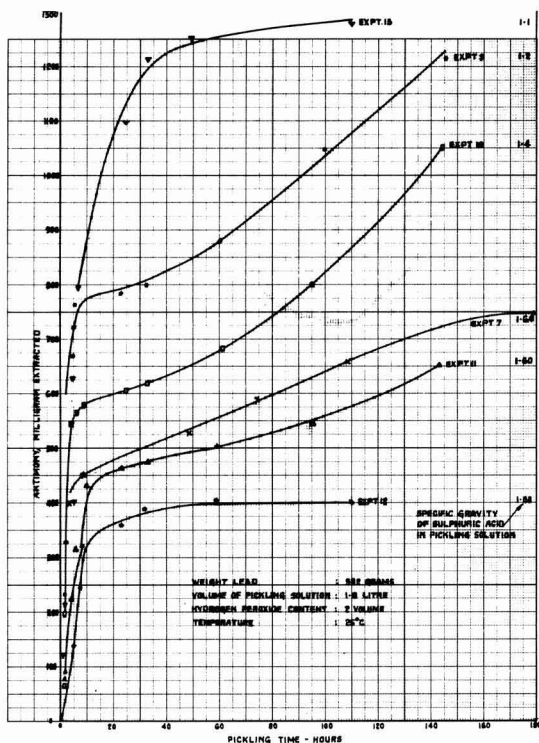


Fig. 2. Influence of sulfuric acid concentration on pickling rate of 7% antimonial lead.

Increase in the concentrations of acid and peroxide leads to higher antimony extractions (compare curves II and III, Fig. 1).

**Effect of sulfuric acid concentration.**—The curves in Fig. 2 plot the course of antimony extraction occurring from 7% antimonial lead during pickling times of up to 180 hr at 25°C in a reagent consisting of hydrogen peroxide (2 volume) and sulfuric acid (between 1.03 and 1.60 sp gr). Experimental replication is satisfactory (compare curves 7 and 11). At acid gravities of under 1.1, antimony extraction ceased after 40-50 hr, reaching 70-80% of this value in 10 hr. At acid gravities higher than 1.1 antimony extraction from the grid still continued after 180 hr with no evidence of leveling out. The highest antimony extraction recorded was obtained with 1.1 to 1.2 gravity acid. Also, at acid gravities in this range, antimony extraction following a 5 hr pickling was about half that obtained during a 140 hr pickle. After pickling, the metal became eventually gray or white colored and, at certain acid concentrations a turbidity or precipitate, presumably of lead sulfate, formed in the solution. At acid concentrations of 1.2-1.3 sp gr and pickling times up to 30 hr no insoluble matter was evident in the solution.

**Effect of hydrogen peroxide concentration.**—The results in Fig. 2 show that extension of the pickling time above 10-20 hr is not a very efficient method of increasing the antimony extraction rate in the case of a reagent consisting of 2 volume hydrogen peroxide and sulfuric acid in the 1.1-1.2 sp gr range. Next, a comparison was made between antimony extraction obtained for 7% antimonial lead using 2 volume and 5 volume hydrogen peroxide, both with 1.2 gravity acid at 25°C. After 10 hr the antimony extraction increased almost *pro rata* with increase of hydrogen peroxide concentration, and, in fact, the solution containing 5 volume hydrogen peroxide removed as much antimony in 5-10 hr as did the weaker reagent in 140 hr. The

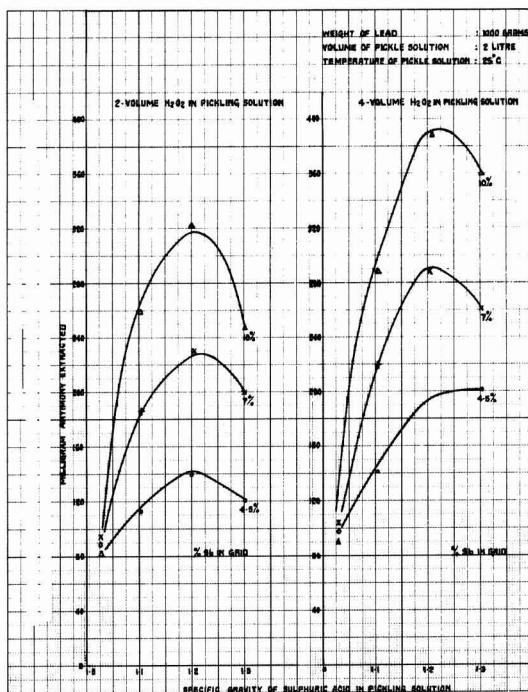


Fig. 3. Influence of acid gravity and hydrogen peroxide concentration on antimony extraction in 8 hr pickle of 4.5, 7, and 10% antimonial lead.

quantities of antimony dissolved from approximately 1 kilo of lead in a 140 hr pickle using the two and five volume hydrogen peroxide were respectively 1.3g and 2.4g. Thus, increasing the concentration of peroxide in the reagent is a more effective method of increasing antimony extraction than extension of pickling time.

Figure 3 shows the effect of sulfuric acid and hydrogen peroxide concentration on antimony extraction during an 8 hr pickle at 25°C for freshly cast lead alloys containing 4.5, 7.0, and 10% antimony. For each alloy, antimony extraction was highest at an acid gravity of 1.2 and at the higher peroxide concentration. A repeat experiment on these alloys three weeks after casting gave an identical set of curves. A plot of weight of antimony extracted during an 8 hr pickle against the antimony content of the alloy showed a linear relationship for each of the eight reagent systems quoted in Fig. 3.

Tables I and II show the effect of reagent composition and pickling time on the percentage of the original

Table I. Percentage dissolution of antimony from 7% antimonial lead (thin section 1/16 in.)

Sulfuric acid gravity	Per cent of original antimony content of alloy extracted into pickling solution		
	10 hr	Pickling time 20 hr	Extended*
1.6 (nil hydrogen peroxide) at 80°C	<0.001	0.001	0.1 (300.I)
1.03 (2 vol. H <sub>2</sub> O <sub>2</sub> ) at 25°C	0.45	0.5	0.6 (40.M)
1.1 (2 vol. H <sub>2</sub> O <sub>2</sub> ) at 25°C	1.2	1.5	1.9 (70.M)
1.2 (2 vol. H <sub>2</sub> O <sub>2</sub> ) at 25°C	1.0	1.1	1.7 (140.I)
1.2 (5 vol. H <sub>2</sub> O <sub>2</sub> ) at 25°C	2.6	3.0	3.3 (70.M)
1.4 (2 vol. H <sub>2</sub> O <sub>2</sub> ) at 25°C	0.8	0.9	1.4 (145.I)
1.6 (2 vol. H <sub>2</sub> O <sub>2</sub> ) at 25°C	0.6	0.65	1.0 (160-180.I)

\* Numerals in brackets indicate prolonged pickling time in hours. I indicates that antimony concentration of solution is still increasing at end of test period. M indicates that it had reached a maximum at end of test period.

Table II. Percentage dissolution of antimony from various antimonial lead (thicker section  $\frac{1}{8}$ - $\frac{1}{4}$  in.)

Sulfuric acid gravity	$\frac{1}{8}$ hr	Per cent of original content of alloy extracted into pickling solution			7% antimonial lead pickling time $\frac{1}{8}$ hr	10% antimonial lead pickling time $\frac{1}{8}$ hr
		4.5% antimonial lead pickling time	4.5% antimonial lead pickling time	Extended*		
		10 hr	20 hr			
1.03 (2 vol. $H_2O_2$ ) at 25°C	0.2	0.3	0.4	0.5 (50)	0.1	0.1
1.03 (4 vol. $H_2O_2$ ) at 25°C	0.2	—	—	—	0.15	0.1
1.1 (2 vol. $H_2O_2$ ) at 25°C	0.25	0.5	0.6	0.7 (50)	0.3	0.25
1.1 (4 vol. $H_2O_2$ ) at 25°C	0.3	—	—	—	0.3	0.3
1.2 (2 vol. $H_2O_2$ ) at 25°C	0.3	0.9	0.9	—	0.3	0.3
1.2 (4 vol. $H_2O_2$ ) at 25°C	0.4	0.75	—	—	0.4	0.4
1.3 (2 vol. $H_2O_2$ ) at 25°C	0.3	—	—	—	0.3	0.25
1.3 (4 vol. $H_2O_2$ ) at 25°C	0.4	—	—	—	0.4	0.4

\* Numerals in brackets indicate pickling time in hours, antimony extraction had reached a maximum within these times.

antimony content of the alloy which is removed by pickling. Comparison of these results show that with similar reagents the percentage of the original antimony content of the alloy which is extracted from thinner section moldings is higher than with thicker section moldings, due, presumably to the higher area to volume ratio of the former with its consequent increased surface area per unit weight of lead available for antimony dissolution. The inefficiency of pickling with strong sulfuric acid without peroxide at 80°C is clearly evident in Table I, which shows that only 0.001% of the original antimony content of the alloy has been extracted. Contrasted with this and confirming the earlier experiments, 3% antimony extraction occurs when pickling is carried out at 25°C in 1.2 gravity acid containing 5 volume peroxide. Clearly, this antimony removal must occur principally at the metal surface (or in the region near to the surface). If, with an as-cast alloy there is no enrichment of antimony at the surface above the normal level this result implies that, on the average, the pickling reagent penetrates only to a depth of between 0.001 and 3% of the average thickness of the metal. If, on the other hand, as had been postulated, antimonial lead castings have a very thin surface layer of appreciably higher antimony content than the bulk of the alloy, then the average depth of reagent penetration into the grid to produce the observed antimony extractions would be less than those quoted above.

**Hydrogen peroxide decomposition.**—It was observed that gas bubbles were continuously formed on the surface of grids during pickling at 25°C. The gas is produced by a gradual decomposition of hydrogen peroxide to oxygen and water and is presumably catalytically induced by lead or by impurities therein. Peroxide decomposition was monitored during pickling by analyzing timed samples by titration with standard potassium permanganate.

Figure 4, shows, for 7% antimonial grids during a 40 hr pickle, the influence of acid gravity on antimony extraction and the parallel decomposition of hydrogen peroxide. It is seen that hydrogen peroxide decomposi-

tion is highest under those conditions under which antimony extractions are highest.

**Effect of pickling on subsequent release of antimony from alloys under electrochemical conditions.**—Obviously, the more efficient the removal of antimony by pickling then the lower will be the equilibrium antimony content of the electrolyte in an electrolysis experiment, compared to the equilibrium antimony content obtained by electrolysis of unpickled control alloys. This procedure therefore offers a method of ascertaining the influence of chemical pickling in acid hydrogen peroxide on the subsequent rate of removal of antimony from the alloy under conditions where a current flows.

Figure 5 plots the relationship between the antimony content of the original alloy and the weight of antimony removed from 150g of three lead alloys during a 25 hr electrolysis. It is seen that less antimony is removed by electrolysis of alloys which have been previously pickled compared to the unpickled controls. The effect of chemical pickling upon subsequent antimony removal occurring upon electrolysis, is greatest

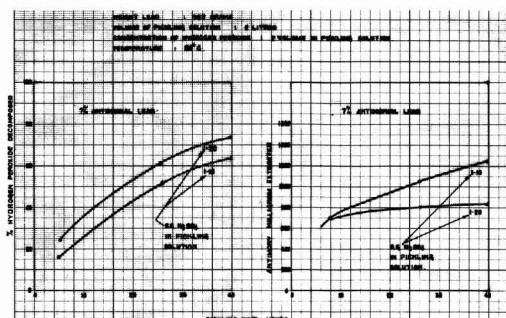


Fig. 4. Relation between pickling time, antimony extraction, and hydrogen peroxide decomposition.

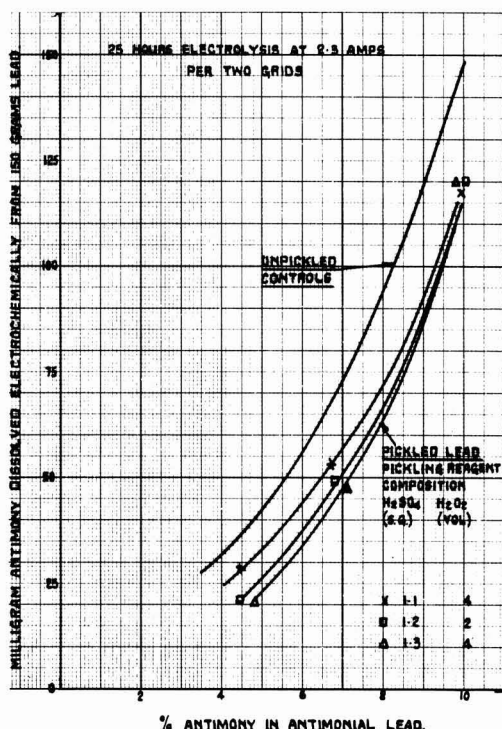


Fig. 5. Electrochemical removal of antimony from pickled and unpickled lead as a function of original antimony content of alloy.



in the case of the 4.5% antimonial alloy in which antimony removal upon electrolysis is about half the value obtained for the unpickled control. Smaller effects of pickling on antimony removal during electrolysis were noted in the case of the two higher antimonial alloys.

It was attempted to ascertain whether a relationship existed between antimony removal from the grid during chemical pickling and the amount of antimony which is subsequently removed from the grid upon electrolysis.

If, during electrolysis of an unpickled metal casting, the concentration of antimony that builds up in the electrolyte in time  $T$  is denoted by  $X$  mg Sb/g alloy and if, during the same time interval, the concentration of antimony that builds up in the electrolyte in contact with pickled alloy at the same initial antimony content is denoted by  $Y$  mg Sb/g alloy, then  $(X - Y)$  is a measure of the efficiency of the chemical pickling process in removing surface antimony from the alloys. If the weight of antimony removed from the alloy during pickling is denoted by  $Z$  mg/g alloy, then it follows that for an alloy of a particular composition, an increase in the value of  $Z$  should be accompanied by a decrease in the value of  $Y$ , i.e., an increase in the value of  $(X - Y)$  for each of the three alloys examined. That this is so is confirmed by examination of Table III.

It follows from the previous discussion that  $(X - Y) 100/X$  represents the percentage reduction in extractable antimony that occurs as a result of chemical pickling of alloys compared to unpickled controls in the same antimonial alloy. This quantity is a direct measure of the reduced amount of electroextraction of antimony from alloys that occurs under standard electrochemical conditions as a result of various chemical pickling treatments of the alloys. It is interesting to examine, therefore, the influence of increasing the antimony removal from alloys, i.e., increasing  $Z$  during pickling (by using different pickling reagents) on  $(X - Y) 100/X$ . This is shown in Fig. 6 which plots  $Z$  against  $(X - Y) 100/X$ . It is seen that three groups of results are obtained corresponding to the 4.5, 7, and 10% antimonial alloys. At each alloy composition, as expected, an increase in antimony removal ( $Z$ ) during pickling is accompanied by an increase in the percentage reduction of electroextractable antimony  $(X - Y) 100/X$ . The latter is greater in the case of the 4.5% antimonial alloy (viz. 40-50%) and least in the case of the 10% alloy (viz. about 20%).

**Mining caplamp battery cycling tests.**—The results in Table IV give distinct evidence that batteries made up with 4.5% antimonial lead positive grids which have been pickled and amine washed have a longer cycle life than batteries made using either unpickled grids of the same antimony content or grids which have been pickled but not amine washed.

Table III. Influence of pickling the alloy on subsequent solution of antimony by electrolysis

Alloy composition w/w % Sb	Pickling reagent composition		Z	Y* (25 hr electrolysis)	(X - Y)* (25 hr electrolysis)
	H <sub>2</sub> SO <sub>4</sub> sp gr	H <sub>2</sub> O <sub>2</sub> vol.			
4.5	1.03	2	13	32	4
	1.1	4	22	28	8
	1.2	2	21.5	21	15
	1.3	4	31	22	14
7.0	1.03	2	14	66	6
	1.1	4	34	66	17
	1.2	2	35	52	20
	1.3	4	40	52	20
10.0	1.03	2	13	138	10
	1.1	4	44	120	28
	1.2	2	50	120	28
	1.3	4	55.5	120	28

\* For explanation of terms see text.

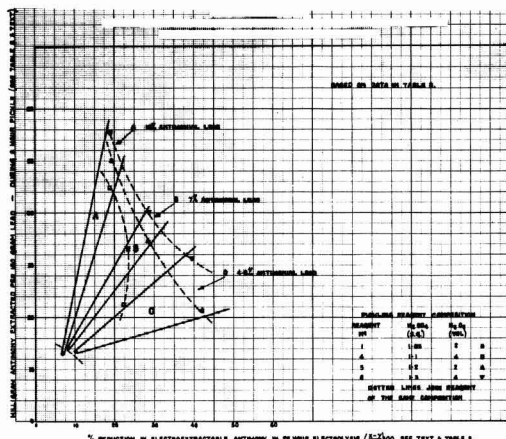


Fig. 6. Effect of efficiency of antimony removal during pickling on per cent reduction in electroextractable antimony from lead.

## Discussion

Pickling of antimonial lead at ambient temperature in mixtures of hydrogen peroxide and sulfuric acid is a considerably more efficient method of stripping off the surface rich antimony layer that has been postulated to exist on these alloys than is achieved by pickling in sulfuric acid alone, even at elevated temperatures. For alloys in the composition range studied up to 10% antimony, antimony extraction is highest at a sulfuric acid concentration in the pickling solution corresponding to  $1.20 \pm 0.10$  sp gr.

This applies at all hydrogen peroxide concentrations between the extremes of the range studied (2-5 volume strength). At any particular hydrogen peroxide concentration in the reagent, the extraction of antimony during a standard pickling time decreases as the sulfuric acid concentration is decreased below or is increased above the acid gravity of  $1.20 \pm 0.10$ . At a particular acid concentration and pickling time, antimony extraction increases with increase in hydrogen peroxide concentration. Increase of the concentration of hydrogen peroxide in the pickling solution is usually a more efficient method of antimony removal than extension of the pickling time.

Depending on various factors viz. reagent composition, pickling time, surface area/volume ratio of lead, antimony content of alloy, between 0.1 and 3.3% of the original total antimony content of the alloy is extracted during pickling processes (Tables I and II). Also, as indicated in Table III, the greater the amount of antimony that is removed from the surface of the lead by pickling prior to electrolysis then the smaller the amount of surface antimony that is left on the grid. This indicates that both pickling and electrolysis

Table IV. Effect of grid pickling on cyclic life tests of mining caplamp cells

Positive spine pickling	No. pickle	Grid pickled then water washed	Grid pickled then amine washed
Cycles to end of life (when discharge to 3.70V decreases to less than 7 hr			
Battery No.			
1	360	80	500
2	480	360	540
3	340	340	440
4	360	360	420
5	300	400	440
6	340	500	540
7	400	400	440
8		360	420
9		380	540
10		400	500
11		340	560
12		420	440
13		240	480
14		400	520
Average	368	377	484

remove antimony from the surface, only, of the lead. Obviously, the higher the extraction of surface antimony during pickling the less are adverse effects to be expected by antimony in subsequent battery operation. Data in Fig. 5 and 6 indicate that positive 4.5% antimonial lead grids that have been pickled for 8 hr in a 1.2-1.3 gravity sulfuric acid/2-4 volume hydrogen peroxide pickling solution would be expected under electrochemical conditions to release only approximately 50% of the amount of antimony obtained from an unpickled 4.5% antimonial alloy. The corresponding figure for pickled 10% antimonial alloy is 80% of the amount of extracted antimony that would be obtained for the unpickled alloy. Thus the beneficial effects of pickling on subsequent battery performance would be expected to be greater in the case of lower antimonial alloys.

The data in Table IV indicate that an 8 hr pickling of 4.5% antimonial positive grids in a reagent comprising sulfuric acid (1.20 sp gr) and hydrogen peroxide (4 volume) followed by amine treatment to remove surface deposits leads to an approximately 30% increase in cyclic life of the particular type of battery studied. Examination of the data in Table II shows that extension of the pickling time with this reagent to times greater than 8 hr would have removed considerably more antimony (perhaps 2-3 times as much) than was in fact removed during 8 hr. Possibly, positive grids which had been given an extended pickling time would lead to further improvements in

cyclic life to that obtained in the experiments described above. Additionally, it is possible that negative grid pickling would have further beneficial effects.

It is clear that, to obtain maximum benefits from grid pickling, a careful study should first be conducted of the effect of pickling reagent composition, pickling time and other factors on antimony removal occurring during pickling for the types of plates it is intended to use in each particular type of battery.

### Acknowledgments

Acknowledgments are made to Mr. D. Andrew and Mr. D. Butterworth who assisted in the experimental work and to the Directors of Oldham & Son Limited for their permission to publish the work.

The work described in this paper is the subject of the following British patent application: No. 18551/70 filed April 17, 1970 entitled "Improvements in Methods of Treating Grids for Electric Storage Battery plates."

Manuscript submitted Aug. 9, 1971; revised manuscript received ca. Feb. 2, 1972.

Any discussion of this paper will appear in a Discussion Section to be published in the December 1972 JOURNAL.

### REFERENCES

1. J. B. Burbank and A. C. Simon, *This Journal*, **100**, 11 (1953).
2. Robert Bosch, G.m.B.H. Germany, Brit. Pat. 837,969 (1960).

## Lead-Fluoroboric Acid Battery

G. D. McDonald,\* E. Y. Weissman,\* and T. S. Roemer

Globe-Union, Inc., Milwaukee, Wisconsin 53201

### ABSTRACT

A reserve battery is described that can operate over a wide temperature range, including temperatures as low as  $-60^{\circ}\text{C}$  at coulombic efficiencies of 16% or better. The battery is based on the system: lead/fluoroboric acid/lead dioxide and utilizes a bonded lead dioxide cathode. The system is discussed based on data such as: capacities, current-voltage relationships, and coulombic efficiencies, as a function of temperature; self-discharge characteristics; specific energy; and cost considerations.

The lead/fluoroboric acid/lead dioxide battery has typically been used for applications requiring an inexpensive reserve-type power supply capable of high discharge rates over a wide temperature range. An example of such an application is the proximity fuze battery (1, 2). The characteristics of a typical Pb/HBF<sub>4</sub>/PbO<sub>2</sub> battery are summarized in Table I, where the listed specifications have been all exceeded to a significant degree (e.g., 50 sec of 0.040A discharge, above 18V at  $+60^{\circ}\text{C}$ ; 90 sec of 30 mA discharge, above 15V, at  $-40^{\circ}\text{C}$ ).

\* Electrochemical Society Active Member.

Key words: fluoroboric acid battery, lead dioxide electrode, bonded lead dioxide electrode, lead-fluoroboric acid battery.

Table I. Characteristics of a fluoroboric acid proximity fuze battery

Number of cells:	14
Minimum voltage:	15V
Current:	0.030A
Discharge duration:	20 sec
Temperature range:	$-40^{\circ}$ to $+60^{\circ}\text{C}$
Activation time:	$<0.4$ sec
Battery volume:	2.5 cc
Battery weight:	approx. 4g
Special features:	a) shelf life of up to 20 yr b) low cost of raw materials (lead at 45¢/kg; fluoroboric acid at 55¢/kg)

Fluoroboric acid is particularly well suited for such types of reserve batteries because of its wide liquidus range, good conductivity, and ready availability (used in the electroplating industry). Table II summarizes its properties as well as the over-all electrochemical reaction in which it participates. The boric acid is present in order to suppress hydrolysis in which the fluorine atoms attached to the boron are stepwise replaced by hydroxyl groups, with the other hydrolysis product being hydrofluoric acid.

An important feature of this electrochemical system is the solubility of lead fluoroborate, the reaction product formed at each electrode (approximately 380g per liter). Because of this property, dense, nonporous,

Table II. The fluoroboric acid electrolyte

Over-all reaction	
$\text{Pb} + \text{PbO}_2 + 4\text{HBF}_4 \rightarrow 2\text{Pb}(\text{BF}_4)_2 + 2\text{H}_2\text{O}$	
$E = 1.86$ at $25^{\circ}\text{C}$	
Electrolyte characteristics	
Available as 48% aq. solution (with $\sim 2.5\%$ H <sub>2</sub> BO <sub>3</sub> )	
Freezing point:	$-78^{\circ}\text{C}$
Decomposition point:	$+130^{\circ}\text{C}$
Conductivity	
at room temp.:	0.61 ohm <sup>-1</sup> cm <sup>-1</sup>
at $-60^{\circ}\text{C}$ :	0.06 ohm <sup>-1</sup> cm <sup>-1</sup>

and structurally stable electrodes can effectively be used with a resultant savings in required battery volume. At the same time, fluoroboric acid attacks most other metals and metal oxides to give soluble reaction products. While we have found that neither lead nor lead dioxide are attacked in the absence of oxygen, the generally corrosive nature of this electrolyte requires a careful selection of the battery materials of construction.

At the present time, lead-fluoroboric acid type batteries use bipolar electroplated electrodes consisting of nickel-plated steel shim stock with lead plated on one side and layers of  $\alpha$ - and  $\beta$ -lead dioxide on the other. Capacity densities of the order of 7 A-sec per  $\text{cm}^2$  of geometric electrode area are attainable. Attempts to increase this capacity by heavier plating have proved fruitless owing to adhesion or active material brittleness problems. The only successful attempts to increase cell capacity have resulted from increases in electrode plate area (3).

Lately, some work (4) has been carried out in the area of development of bonded lead dioxide electrodes possessing higher capacities and improved mechanical properties. The present paper summarizes results obtained along similar lines, based primarily on the use of electrode hot-pressing techniques.

### Experimental

The raw materials were: commercially available lead dioxide powder (Fisher Scientific; particle size range: 90-100 $\mu$ ); lead sheet (99% pure, 0.52 mm thickness); and 48% fluoroboric acid (Harshaw Chemical). All materials were used without preliminary purification or processing steps. The lead dioxide particles were solvent-coated with suitable thermoplastic binders and the resulting mix was comminuted and then hot-pressed onto expanded metal (e.g., nickel) current collector grids.<sup>1</sup> The test cells were constructed using lead sheet counterelectrodes, a "back-to-back" configuration (lead dioxide cathode sandwiched between two lead anodes), and microporous polyvinyl chloride separators.

When using 2.5 by 3.8 cm electrodes with 1.5 ml of electrolyte the cells weighed about 10g each, had a volume of 2  $\text{cm}^3$ , and a theoretical capacity of approximately 0.5 A-hr. They were evaluated by force-discharging at constant current and recording voltage vs. time. Linear voltage sweeps were carried out with a Wenking Model 121 potentiostat and a Wenking SMP 66 function generator. Internal resistance measurements were based on a modification of a previously reported technique (5), using 20  $\mu\text{sec}$  interruptions.

Self-discharge tests were also carried out, by maintaining a test cell at open-circuit at various temperatures for predetermined time intervals and then discharging it at the given temperature and/or at room temperature. A Conrad environmental chamber was used for all tests taking place at other than room temperature.

### Results and Discussion

Figure 1 shows typical discharge curves of a fluoroboric acid test cell at various temperatures; they all exhibit well defined voltage end points and no apparent activation transients. Figure 2 exhibits the effect of discharge rate on the coulombic efficiency (i.e., available capacity) of the lead dioxide electrode. For the types of electrodes evaluated there appears to be essentially no change in attainable capacity up to about 50  $\text{mA}/\text{cm}^2$ . Higher discharge currents result in lower capacities.

It is interesting to note that 200  $\text{mA}/\text{cm}^2$  corresponds to approximately the 1 min rate, at which

<sup>1</sup> The oxidizing characteristics of lead dioxide would seem to present a potential hazard. However, no difficulties were encountered in this work and DTA tests of the plastic-coated lead dioxide have exhibited initiation temperatures for a redox reaction which are about 30°C higher than the hot-pressing temperatures required for electrode preparation. Nevertheless, this aspect will warrant further attention prior to any development of large scale manufacturing processes.

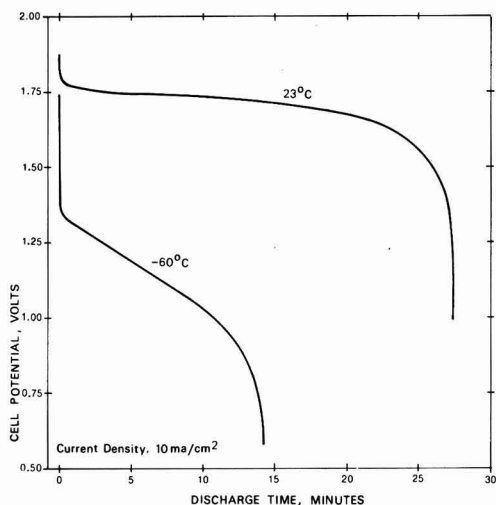


Fig. 1. Typical discharge curves for a Pb/HBF<sub>4</sub>/PbO<sub>2</sub> test cell

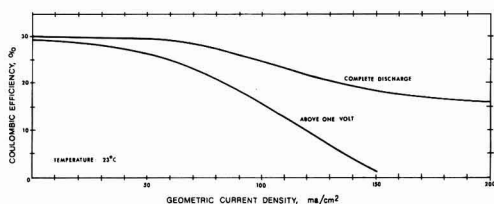


Fig. 2. Coulombic efficiency characteristics of the lead dioxide electrode in fluoroboric acid.

point the efficiency is still 16%. Furthermore, we have evidence to indicate that pulse current densities of 300  $\text{mA}/\text{cm}^2$  are also possible.

Figure 3 shows the effect of temperature on the coulombic efficiency of the system. At low temperatures the internal resistance accounts for the lower capacity, whereas at the higher temperatures, capacity is limited by self-discharge. Indeed, as far as this latter aspect is concerned, we note that commercially available electroplated bipolar electrodes have an activated stand capability of less than 6 min at room temperature. As opposed to that, state-of-the-art, high rate, bonded lead dioxide electrodes do not self-discharge appreciably for the first 48 hr at room temperature (Fig. 4). At a temperature of -50°C, corresponding to a variety of applications (e.g., weather balloons), no significant self-discharge has been observed after 4 months of activated stand.

Figure 5 summarizes our findings regarding the activated stand capability of a bonded, high rate, lead dioxide electrode at the upper temperature extreme of 80°C. The capacity loss is rapid, about 1.33% per min, corresponding to complete self-discharge after 75 min. Similar studies were conducted at 40° and 60°C. The

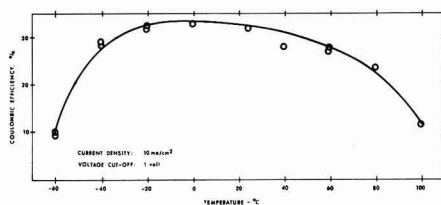


Fig. 3. Coulombic efficiency characteristics of the lead dioxide electrode in fluoroboric acid.

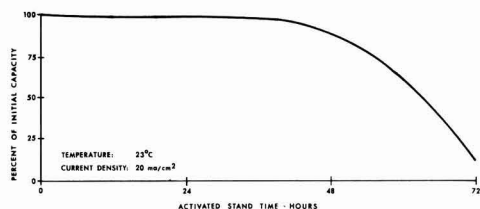


Fig. 4. Self-discharge characteristics of high rate, bonded, lead dioxide electrode in fluoroboric acid.

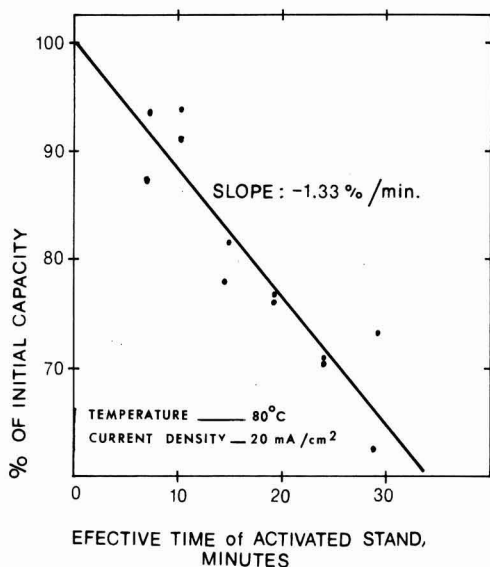


Fig. 5. Self-discharge characteristics of high rate, bonded, lead dioxide electrode in fluoroboric acid.

absolute temperature was found to be logarithmically related to the self-discharge rate with an intercept of 375 (correlation coefficient of 0.9994).

As expected, most of the loss in capacity is due to grid-active material interactions. Recent test results, based on the use of modified, low rate electrodes, not containing metallic current collector grids, have shown some promise for long activated stand lives under difficult conditions. An example in point is a 79 hr steady current discharge of  $155 \mu\text{A}$  per  $\text{cm}^2$  (which happens to be a discharge rate required by some

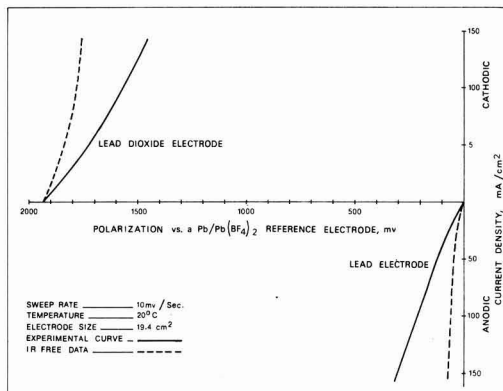


Fig. 6. Linear voltage scans for the system  $\text{Pb}/\text{HBF}_4/\text{PbO}_2$

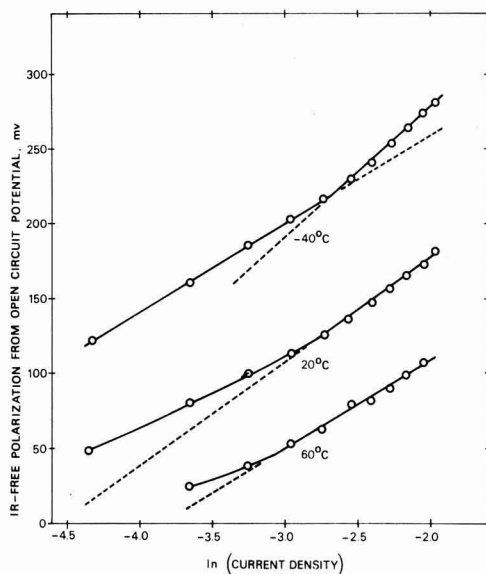


Fig. 7. Tafel plots for the lead dioxide electrode in fluoroboric acid.

applications) at  $50^\circ\text{C}$ , recently demonstrated in our laboratory.

A general operation aspect, noteworthy from a design standpoint, is the complete lack of gassing in this type of battery, either due to self-discharge or any other reason.

Figure 6 presents some typical linear voltage sweep data. Single electrode potentials are expressed vs. a

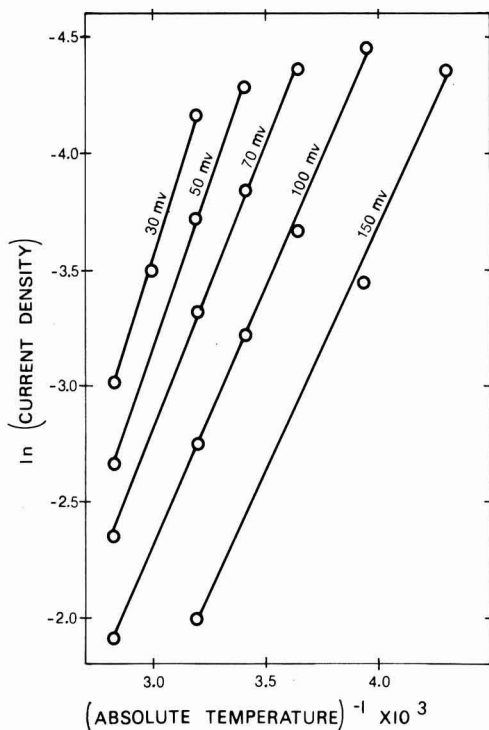


Fig. 8. Arrhenius plots for the lead dioxide electrode in fluoroboric acid.

lead-lead fluoroborate reference electrode. The scans were terminated at 3A owing to equipment limitations. Figure 7 is a Tafel plot of these data. At high temperatures essentially ideal behavior is exhibited, while at the lower temperatures, the curve is suggestive of a dissolution process (6). The Tafel slope, based on these lines, exhibits the theoretical linear temperature dependence with a slope corresponding to  $R/F$ . The calculated exchange current at 20°C is approximately  $10^{-5}$  A/cm<sup>2</sup>.

Figure 8 is an Arrhenius plot of the data yielding an activation energy of 1.1 kcal/gmole at 100 mV polarization for the linear portions of the curves (i.e., the lower current regions). This very low value, together with the Tafel information, would indicate diffusion control of the reaction. However, an examination of Fig. 8 shows that the activation energy is dependent on electrode polarization. This suggests that chemical polarization also plays a role (7). The low activation energy, however, would seem to indicate that the electrode reaction proceeds with little impedance and that constructional parameters affecting the internal resistance of a cell will be the limiting factor for this system.

### Conclusions

The improvements already demonstrated for the fluoroboric acid battery by the use of high capacity bonded lead dioxide electrodes of both the high rate (metallic current collector) and low rate variety are likely to increase the utility of this system for low specific energy ( $\leq 45$  whr/kg) applications, requiring wide temperature range capabilities at low cost. One feature representing a completely new aspect of this

technology is the significantly longer activated stand life demonstrated for the present state-of-the-art lead-fluoroboric acid system.

It is therefore possible that this type of reserve battery may provide sufficiently attractive design-related characteristics to be considered as an alternative to some of the costlier systems presently in use.

### Acknowledgments

The authors would like to acknowledge the able experimental assistance of John Slater who effectively contributed to the concluding portion of this work.

Manuscript submitted Nov. 3, 1971; revised manuscript received Jan. 25, 1972. This was Paper 21 presented at the Cleveland, Ohio, Meeting of the Society, Oct. 3-7, 1971.

Any discussion of this paper will appear in a Discussion Section to be published in the December 1972 JOURNAL.

### REFERENCES

1. M. A. Barron, "Proc. 23rd Annual Power Sources Conf.," May 20-22, 1969, pp. 134-136.
2. F. G. Turrill and W. C. Kirchberger, "Proc. 24th Annual Power Sources Conf.," May 19-21, 1970, pp. 36-39.
3. J. P. Schrodt, W. J. Otting, J. O. Schoegler, and D. N. Craig, *Trans. Electrochem. Soc.*, **90**, 405 (1946).
4. T. J. Kilduff and E. F. Horsey, "Proc. 24th Annual Power Sources Conf.," May 19-21, 1970, pp. 30-35.
5. L. Reid, D. Cole, and I. Trachtenberg, *This Journal*, **113**, 954 (1966).
6. J. O'M. Bockris and E. C. Potter, *ibid.*, **99**, 169 (1952).
7. S. V. Gorbachev, "Soviet Electrochemistry" (Proceedings of the Fourth Conf. on Electrochemistry), Vol. 1, pp. 63-71, Consultants Bureau, N. Y. (1961).

## An Ellipsometric-Electrochemical Cell: Initial Films on Titanium in Water and Methanol Solutions

Tennyson Smith\* and Florian Mansfeld\*

North American Rockwell Science Center, Thousand Oaks, California 91360

### ABSTRACT

An ellipsometric-electrochemical cell is described for simultaneous ellipsometric and electrochemical measurements of metal samples. The unique feature of this cell is the ability to prepare in one cavity with an appropriate etch-polishing solution surfaces which within the experimental error of ellipsometric measurements approach an atomically clean state. The reaction product and etchant are washed away in a second cavity and *in situ* measurements of changes on the surface are made in a third cavity without exposing the sample to the atmosphere. It is demonstrated that Ti surfaces, which have the same optical constants as observed after ion bombardment cleaning and annealing in an ultra high vacuum system ( $\sim 10^{-10}$  Torr), can be prepared in the cell. Results are reported for the initial film growth on clean Ti in aqueous HF, aqueous NaCl, aqueous methanol-HCl, and anhydrous methanol-HCl solutions as a function of applied electrochemical potential.

It is well known that obtaining and studying atomically clean metal surfaces requires a means for removing surface films in an ultra high vacuum (UHV) system (e.g., ion bombardment, cleaving, scraping). The UHV system must operate in the  $10^{-9}$ - $10^{-10}$  Torr range in order to maintain a clean surface for periods of minutes to hours. It would be desirable to study metal surfaces which approach cleanliness obtainable in a UHV system, but immersed in an electrolyte in an electrochemical cell. This can in some instances be accomplished in an ordinary electrochemical cell if the

metal surface contamination can be removed electrochemically and the electrolyte does not contain surface active contamination. However, for many metals (e.g., Ti) air-formed oxide films cannot be removed electrochemically.

The purpose of this paper is to report our attempts to introduce atomically clean Ti surfaces to the electrolyte of interest and observe surface reactions *in situ* via ellipsometry as well as potential and current measurements. The technique involves cleaning of the surface by a suitable process (etching, electropolishing, etc.), followed by exposing this freshly cleaned surface to the electrolyte without exposing it to another environment (such as air).

\* Electrochemical Society Active Member.

Key words: aqueous and anhydrous solutions, HF contamination, optical constants, polarization, ultra high vacuum.



### Experimental Techniques

**Materials.**—The cell was constructed of glass reinforced Teflon, the electrolyte reservoirs were of glass, the etchant reservoir tanks were of Teflon, as were the tubes connecting the reservoirs with the cell. Consequently, the etchant (20%  $\text{H}_2\text{SO}_4$ , 20%  $\text{HF}$ , 30%  $\text{HNO}_3$  by volume) was exposed only to Teflon, while the electrolyte was exposed only to Teflon, glass, paraffin (used for sealing), the platinum counterelectrode, and the sample.

The Ti samples were cut from Ti-75A as cylinders having a slight taper. The surface to be studied was polished to a mirror finish with 600 silicon carbide paper and etched to remove surface damage. The final polishing solution consisted of  $1\mu$  alumina in a solution of 1 part ammonium hydroxide, 1 part distilled water, and 1 part 3% hydrogen peroxide. The hydrogen peroxide was added last and was fresh.

**Electrolytes.**—The electrolytes were prepared from reagent grade materials and bidistilled water.

**The cell.**—A photograph of the assembled cell is shown in Fig. 1. Figure 2 shows a side view of the Teflon cell, which contains three cavities (A, B, and C) and a Teflon slider S that holds the metal sample. When the sample is positioned at cavity A, etchant (20%  $\text{H}_2\text{SO}_4$ , 20%  $\text{HF}$ , 30%  $\text{HNO}_3$  by volume) can be made to flow through the cavity from its reservoir, past the sample and into the collector reservoir. After exposing the sample to the etchant for a predetermined length of time, the sample is positioned at cavity B. At cavity B the electrolyte is forced past the sample to remove etchant carried from cavity A, and is then collected in another reservoir. After thus washing the sample in cavity B for a predetermined period, it is positioned at cavity C through which the test solution is flowing for observation by ellipsometry with or without a potential applied to the specimen. The window W in Fig. 2 is used for visual inspection of the sample in cavity C. The slider S in Fig. 2 consists of a rectangular plate of Teflon  $S_1$  bolted to a steel plate  $S_2$ . The sample is forced into a cylindrical well (slightly smaller than the large diameter of the tapered sample) with attached bolt and nut, such that the metal surface is about 0.004 in. below the surface of the Teflon slider. This is to ensure that the metal sample will not scratch the cell surface as the sample is sliding up and down and thus cause leaks between cavities. In order to prevent leakage between cavities, the slider surface must be pressed against the cell surface with considerable pressure. To accomplish this, a plate P is

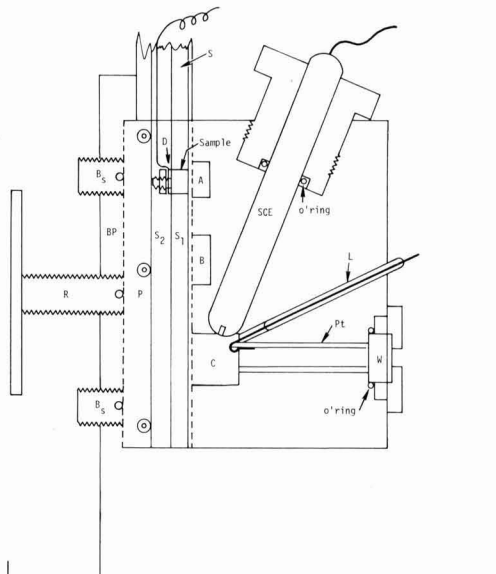


Fig. 2. Sketch of ellipsometric-electrochemical cell

spring loaded against the back plate BP, with the spring load bolts B and a wrench R. To reduce the friction between plates P and  $S_2$ , bearings are placed in plate P or  $S_2$  to roll on. The slider is pulled up and down with a lever and can be positioned by a notched side arm such that the sample is at the center of cavity A, B, or C.

**Electrodes.**—The counterelectrode consists of a platinum cylinder in the channel leading to window W. This Pt counterelectrode is spot welded to a Pt wire which had been sealed into a glass tube and inserted into the cell, as shown in Fig. 2 as L. A saturated calomel reference electrode (SCE) is inserted as shown in Fig. 2. The O-rings in the windows and around the SCE were coated with paraffin before use. For electrical connections to the sample, an insulated copper wire is spot welded to a copper washer that is placed on the sample bolt under the nut as shown at D (Fig. 2). Entrance and exit channels for the etchant, washing solution, and electrolyte are placed such that the entrance to each cavity is at the bottom of the cavity and the exit at the top. This eliminates collection of gas bubbles in the cavities. The channels for the light beam are placed such that the beam has an angle of incidence of  $70^\circ$ .

**Ellipsometry.**—A good description of ellipsometry can be found in Ref. (1). The cell was constructed to be mounted on a Rudolph ellipsometer (sensitivity  $0.01^\circ$ ). Filters were used to isolate the 5461Å light from a mercury lamp or the 6328Å light from a He-Ne laser. The polarizer and compensator were placed before the reflecting surface and the analyzer and detector after the reflecting surface. The ellipsometer parameters  $\Delta$  and  $\psi$  refer to the phase shift of the normal and parallel component of the polarized light and the arctan of the amplitude ratio of these components, respectively. The polarizer angle  $p$  and analyzer angle  $a$  are related to  $\Delta$  and  $\psi$  (in zone I) by  $\Delta = 2p + \pi/2$  and  $\psi = a$ .  $p$  and  $a$  values were averaged for the four zones to minimize alignment errors (1).

To correct for the birefringence of the windows, it would be desirable to measure  $p$  and  $a$  values with and without the windows. However, since measurement with electrolyte in the cell but without windows cannot be made, it was necessary to first measure the correction due to the windows in an unstressed state, i.e.,

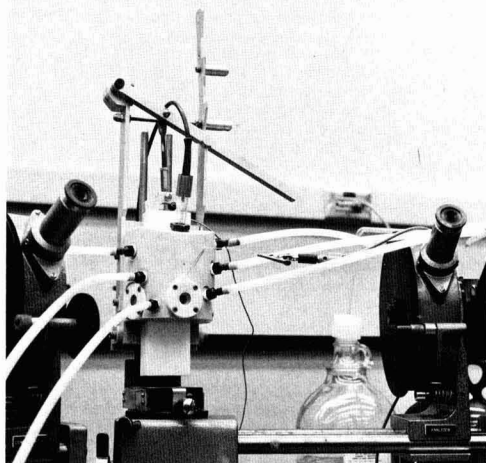


Fig. 1. Photograph of cell

Table I. Measurements to obtain window corrections

Test condition	Zone	p	a
Windows off	1	11.52	29.63
	1	11.65	29.70
	1	11.52	29.67
	1	11.63	29.57
Average value		$11.58 \pm 0.06$	$29.64 \pm 0.04$
	3	10.77	30.34
	2	10.65	29.39
	4	11.50	30.70
Average of 4 zones		$11.25 \pm 0.41$	$30.02 \pm 0.50$
Windows, no pressure			
(Average 4 zones)	9.15	30.48	
Correction for loose windows	2.10	-0.46	
CH <sub>3</sub> OH flowing, windows leaking			
(Average 4 zones)	5.08	28.93	
CH <sub>3</sub> OH flowing, leak tight			
(Average 4 zones)	4.37	28.02	
Correction for window pressure	0.71	0.91	
Correction for loose windows	2.10	-0.46	
Total window correction	2.81	0.45	

measurement of  $p$  and  $a$  with and without the windows but with air in the cell. The results in Table I indicate that for unstressed windows a correction of  $11.25^\circ - 9.15^\circ = 2.10^\circ$  must be made. A second correction is necessary for the stress induced in the windows when sufficient pressure is applied to prevent leakage of electrolyte from the cell. To obtain this correction, measurements of  $p$  and  $a$  were made with electrolyte in the cell and the windows held loosely in position (electrolyte leaking) and with enough pressure to prevent leakage. The results in Table I indicate this correction to be  $5.08^\circ - 4.37^\circ = 0.71^\circ$ . The total window correction is then  $2.10^\circ + 0.71^\circ = 2.81^\circ$  for  $p$ . A similar calculation yields a total correction of  $0.45^\circ$  for  $a$ . Measurement of  $p$  and  $a$  without windows (air in cell) show that measurements can be repeated with an average deviation of about  $\pm 0.05^\circ$  (see Table I).

**HF contamination.**—Care must be taken to be sure that none of the HF in the etching-polishing solution is carried into the working cavity (C of Fig. 2). This can occur if scratches exist in the Teflon slider or mating cell surface, or if insufficient pressure is used between these parts. A check for such leakage was made by using distilled water in the washing and working cavities and monitoring the pH of the water leaving the working cell. To show the drastic effect of small HF contamination in the electrolyte in the working cell, a series of experiments was performed with varying concentrations of HF added to distilled H<sub>2</sub>O as test electrolyte. The resultant changes in  $p$  and  $a$  are shown as a function of time in Fig. 3a. Tests with small additions of H<sub>2</sub>SO<sub>4</sub>, HCl, or HNO<sub>3</sub> of similar concentration gave virtually no changes in  $p$  and  $a$  readings. The effect of HF must result from the strong complexing action of the F<sup>-</sup> ion resulting in thick films of corrosion products. Accelerated corrosion of Ti in sulfuric acid containing fluoride ions has been reported recently (7).

Since there are only two experimental ellipsometric parameters  $p$  and  $a$  and there are three unknowns, film thickness  $d$ , index of refraction  $n_f$ , and absorption coefficient  $\kappa_f$ , a unique solution for  $d$ ,  $n_f$ , and  $\kappa_f$  is not possible. It becomes necessary, therefore, to interpret  $p$  and  $a$  in terms of  $d$  and  $n_f$  for reasonable ranges of  $\kappa_f$ . A discussion of the problems inherent in the interpretation of the ellipsometric results in terms of thickness  $d$  and film index of refraction is given in Appendix A. A computer program (2) is used to calculate solutions for  $d$  and index of refraction of the film  $n_f$  while assuming various values of the absorption coefficient  $\kappa_f$  (i.e.,  $\kappa_f = 0, 1, 2$ , and 3). In the case of films formed in pure water, solutions for  $n_f$  and  $d$  were not found except for  $\kappa_f \rightarrow 0$ . In the case of films formed in the presence of HF, solutions were found for  $\kappa_f \approx 0$  and 1, but for  $\kappa_f = 0$  the values of  $n_f$  were too small and  $d$  too large to be realistic. It is concluded that films formed in solutions containing HF as contamination are absorbing with  $\kappa_f \sim 1$ , whereas films formed in pure water are transparent with  $\kappa_f \sim 0$ .

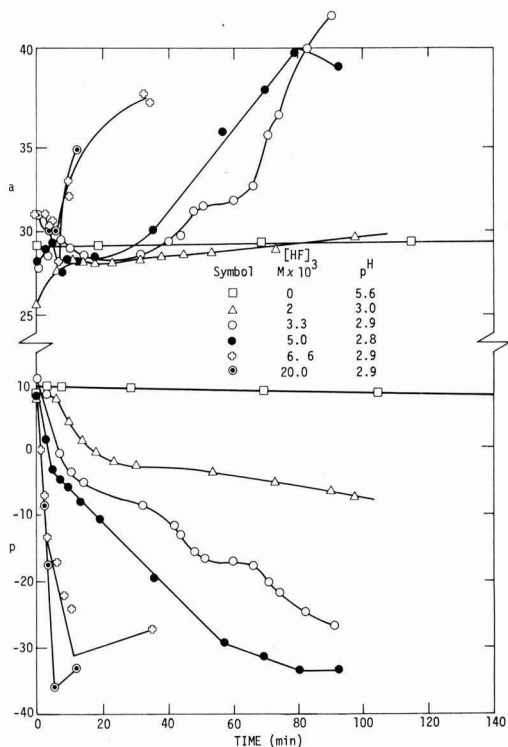
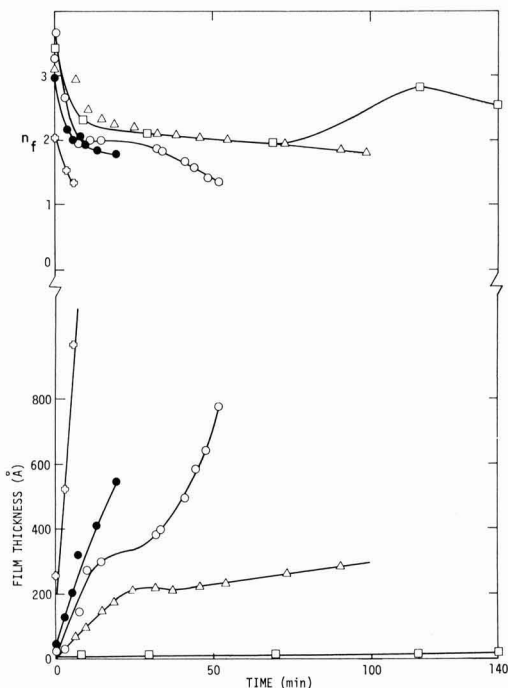
Fig. 3(a). Effect of HF contamination in distilled H<sub>2</sub>O on ellipsometric readings ( $p, a$ ).Fig. 3(b). Film thickness and index of refraction,  $n_f$ 

Figure 3b shows the calculated values of film thickness  $d$ , and index of refraction  $n_f$  which corresponds to Fig. 3a, with  $\kappa_f = 0$  for pure water and  $\kappa_f = 1$  for HF

solutions. In distilled water, without HF addition, a film of about 14 Å is formed in 100 min. The addition of HF causes very thick films to grow. The initial growth rate of these films is second order with respect to HF concentration. In every case  $n_f$  decreases and levels off as the films grow.

### Experimental Results

**Optical constants of cleaned surfaces.**—A test of the surface cleanliness was made by comparing the optical constants obtained in the ellipsometric-electrochemical cell immediately after etching and washing, with the optical constants obtained after cleaning by ion bombardment and annealing in an ultra high vacuum (UHV) system (3). Auger spectroscopy in the UHV was used to determine the presence of contamination in the first atom layers of the Ti substrate. It was possible to prepare surfaces with less than 0.1 monolayers of Cl and S which were the only contaminants after ion bombardment and annealing at about 550°C. Zone refined polycrystalline Ti was used in the UHV system, while polycrystalline Ti-75A was used in the ellipsometric-electrochemical cell. It would be expected that the optical constants of these materials are the same. In experiments in the cell the Ti surface was cleaned by passing the etching-polishing solution<sup>1</sup> through cavity A for 10 sec. The specimen was then washed in cavity B for 10 sec with the test electrolyte and moved to cavity C, through which the test electrolyte was slowly flowing. The ellipsometer readings  $\Delta$  and  $\psi$  were recorded as a function of time. Using the computer program (2) mentioned above the optical constants were then calculated. The initial values for various electrolytes are compared with those obtained in the UHV system in Table II. The average values of the optical constants for a freshly cleaned surface  $n_s = 3.05 \pm 0.05$  and  $\kappa_s = 1.20 \pm 0.06$  are close to the values obtained in the UHV system,  $n_s = 3.09 \pm 0.01$  and  $\kappa_s = 1.11 \pm 0.01$  for  $\lambda = 5461 \text{ Å}$ . Similar agreement is found for  $\lambda = 6328 \text{ Å}$ . This indicates that etching the Ti-75A sample in cavity A for 10 sec and washing in cavity B for 10 sec provides a surface which is approaching an atomically clean state (within the uncertainty of  $n_s$  and  $\kappa_s$ ). The uncertainty of  $n_s$  and  $\kappa_s$  for experiments in the cell is about 0.05 units which corresponds to an uncertainty with respect to surface cleanliness of about 3 Å effective thickness for  $\text{TiO}_2$  as the contamination.

**Electrochemical studies.**—The primary purpose of the cell was to make possible simultaneous ellipsometric and electrochemical studies. Solutions used were 3.5% NaCl,  $\text{CH}_3\text{OH}$ -1N HCl "aqueous" and  $\text{CH}_3\text{OH}$ -1N HCl "anhydrous." The "aqueous" solutions were prepared by adding concentrated (37%) HCl to methanol, while the "anhydrous" solutions were prepared by

saturation  $\text{CH}_3\text{OH}$  with HCl gas and then diluting with  $\text{CH}_3\text{OH}$  until the solution was 1N in HCl. For further details, see Ref. (4). These solutions were used since it had been shown earlier by potentiostatic polarization curves (4), that Ti is covered with a passive film in the aqueous solutions, but no such film can form in anhydrous solutions. Figure 4 shows a typical plot of the change in polarizer and analyzer readings as a function of time for potentiostatic anodic polarization of Ti-75A in aqueous 3.5% NaCl. The bars at the end of the curves at 1500 mV indicate the range of the scatter of the data. The data at each potential were obtained for a freshly cleaned and polished surface. Most of the curves increase rapidly with time, level off after about 100 sec, then slowly increase with time. Pitting occurred in aqueous  $\text{CH}_3\text{OH}$ -HCl solutions (4) when a potential of +200 mV was exceeded as indicated by a continuous rise of the anodic current. Within the scatter of the data  $p$  and  $a$  values were close to those measured in aqueous NaCl solutions where no pitting was observed. Figure 5 shows average values of the change in  $p$  (Fig. 5a) and  $a$  (Fig. 5b) after 100 sec as a function of the applied potential. Curve 1 in Fig. 5a is for Ti in 3.5% NaCl, curve 2 is for Ti in aqueous  $\text{CH}_3\text{OH}$ -1N HCl, and curve 3 is for Ti in anhydrous  $\text{CH}_3\text{OH}$ -1N HCl.

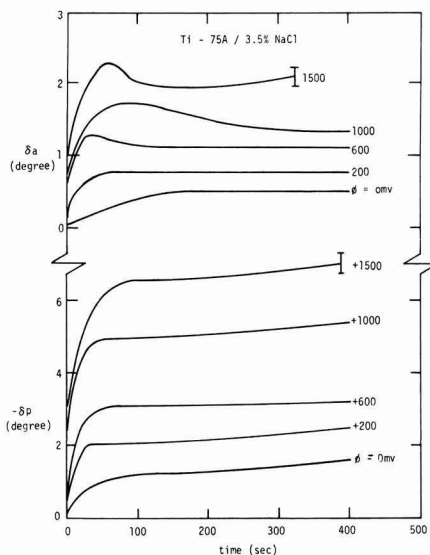


Fig. 4. Changes of ellipsometric values as a function of time and potential (vs. SCE). Ti-75A, aqueous 3.5% NaCl.

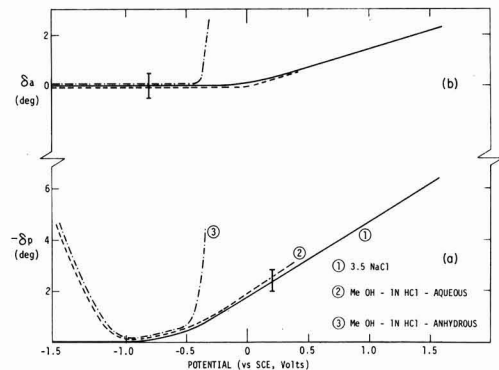


Fig. 5. Ellipsometric values after 100 sec and film thickness as a function of potential. — 3.5% NaCl, - - -  $\text{CH}_3\text{OH}$ -1N HCl-aqueous, ····  $\text{CH}_3\text{OH}$ -1N HCl-anhydrous.

<sup>1</sup> The mixture of  $\text{HF}$ - $\text{HNO}_3$ - $\text{H}_2\text{SO}_4$ - $\text{H}_2\text{O}$  removes oxide films on Ti, but also chemically polishes the surface. Effects of surface roughness on ellipsometric data are therefore not to be expected.

Table II. Optical constants of polycrystalline Ti 75A in various electrolytes compared to zone refined Ti in the ultra high vacuum (UHV)

N = number of experiments

Electrolyte	$\lambda$ (Å)	Optical constants $n_s$	$\kappa_s$	N
<b>I. Ellipsometric-electrochemical cell</b>				
$\text{CH}_3\text{OH}$	5461	$3.03 \pm 0.01$	$1.20 \pm 0.01$	5
$\text{CH}_3\text{OH}$ -0.01N NaCl	5461	$3.06 \pm 0.18$	$1.30 \pm 0.06$	4
-0.3% $\text{H}_2\text{O}$				
$\text{H}_2\text{O}$	5461	$2.96 \pm 0.01$	$1.23 \pm 0.03$	8
6N HCl	5461	$3.15 \pm 0.01$	$1.08 \pm 0.01$	4
		$3.05 \pm 0.05$	$1.20 \pm 0.06$	
$\text{CH}_3\text{OH}$	6328	$3.28$	$1.11$	2
$\text{CH}_3\text{OH}$ -1N HCl aq.	6328	$3.31 \pm 0.05$	$1.01 \pm 0.02$	20
$\text{CH}_3\text{OH}$ -1N HCl anh.	6328	$3.30 \pm 0.05$	$1.05 \pm 0.02$	18
$\text{H}_2\text{O}$	6328	$3.27 \pm 0.06$	$1.14 \pm 0.05$	12
3.5% NaCl	6328	$3.25 \pm 0.03$	$1.12 \pm 0.005$	13
		$3.26 \pm 0.03$	$1.11 \pm 0.02$	
<b>II. UHV</b>				
$5 \times 10^{-10}$ Torr	5461	$3.09 \pm 0.01$	$1.11 \pm 0.01$	5
$5 \times 10^{-10}$ Torr	6328	$3.16 \pm 0.01$	$1.12 \pm 0.01$	5

The results in Fig. 5 show that the changes of the ellipsometric parameters with potential in 3.5% NaCl are essentially the same as in aqueous  $\text{CH}_3\text{OH}$ -1N HCl for potentials noble to the rest potential which for a freshly cleaned specimen was  $\sim -0.8\text{V}$ . However, for Ti in anhydrous  $\text{CH}_3\text{OH}$ -1N HCl very thick films form at potentials more positive than  $-0.4\text{V}$ . For potentials cathodic to the rest potential ( $< -0.8\text{V}$ ) no film is formed in 3.5% NaCl. The films that form more negative than  $-0.8\text{V}$  in the methanol solutions are essentially the same in aqueous and anhydrous solutions.

### Discussion

It has been shown (Table II) that it is possible to prepare by proper etching and washing in our ellipsometric-electrochemical cell Ti surfaces the cleanliness of which approaches cleanliness obtained in UHV after ion bombardment. The finding that it is possible to produce a clean surface in an environment like water is not contradicted by the results of Beck and co-workers (8), who showed that the anodic current on a freshly broken Ti surface in an electrolyte decreases to a very small value in a few milliseconds. While this can be called repassivation, it does not have to mean that the whole surface is being covered by an oxide film, but might result from blockage of the most active sites on the freshly broken surface by adsorbed oxygen as demonstrated by Frankenthal for passivation of Fe-Cr (9). Depending on the applied potential and the electrolyte, different films are formed: it was observed, however, that at least for the first 100 sec after the electrode was immersed in the electrolyte (cavity C) film growth was very slow at potentials close to the rest-potential. Our results in 3.5% NaCl at potentials noble to the rest-potential are similar to those obtained by Green and Sedricks (5) for Ti-7.76% Al who found a linear increase of the ellipsometric parameter  $\Delta$  with potential. The film thickening at potentials active to  $-1.0\text{V}$ , reported by these authors based on some indirect evidence but not shown by ellipsometric results, was not detected in our studies.

The different behavior of Ti-75A at potentials noble to the rest-potential in anhydrous and aqueous solutions of  $\text{CH}_3\text{OH}$ -HCl can be explained based on the result obtained in a study of the effect of water on passivity and pitting of Ti (4). In aqueous  $\text{CH}_3\text{OH}$ -1N HCl enough water is present to produce a passive film, which is destroyed by pitting when the applied potential exceeds the critical pitting potential. Consequently, it was found in the present study that thin films grow in aqueous solutions at about 40 A/V for the first 100 sec, when an anodic potential was applied. In anhydrous  $\text{CH}_3\text{OH}$ -1N HCl no passive film can be formed; thus, anodic polarization results in accelerated dissolution under charge transfer control (4). The rapid change of ellipsometric parameters in this solution is then due to accumulation of corrosion products on the surface of the test specimen.

Films formed on Ti-75A at potentials negative to the rest potential seem to be identical for aqueous and anhydrous solutions of  $\text{CH}_3\text{OH}$ -HCl. They therefore do not require water molecules for their formation. While hydride formation might take place, more experiments have to be carried out to determine the nature of these films. Potentiostatic polarization experiments in  $\text{CH}_3\text{OH}$ -HCl solutions have shown (6), that at potentials more negative than  $-1.2\text{V}$  the current continuously increases at constant potential with an ever increasing rate of gas evolution. Potentiokinetic measurements show a change in slope at this potential and a marked hysteresis when the potential is decreased to more noble potentials leading to a more noble rest-potential.

Due to the difficulties mentioned above and described in Appendix A, unique values of the complex index of refraction of the films formed and their thickness cannot be obtained. However, certain conclusions

can be drawn concerning these physical parameters from the ellipsometric data in Fig. 5. In the anodic region ( $\phi > -0.8\text{V}$ ) for films formed in NaCl or aqueous methanolic solutions (curves 1 and 2) experimental values for  $p$  and  $a$  are consistent with those calculated with a complex refractive index of  $n_f \sim 2.5$  and  $\kappa_f \sim 0$ . These values are consistent with  $\text{TiO}_2$  films as reported in the literature (10-13). The anodic oxide film forms at about 40 A/V in the first 100 sec between  $-0.5$  and  $1.5\text{V}$ . This is estimated from the slopes of the curves in Fig. 5 between  $-0.5$  and  $+1.5\text{V}$  and the slopes of the curves for  $n_f = 2.5$ ,  $\kappa_f = 0$  in Fig. A-1a. This is about twice the value reported (13,14) for much larger potentials (0-200V).

In the cathodic region ( $\phi < -0.8\text{V}$ ) the lack of a change in  $p$  and  $a$  indicates that films are not formed on Ti in the NaCl solutions. Very peculiar films are formed in aqueous and anhydrous methanol solutions in the cathodic region. The peculiarity lies in the fact that for these films the polarizer azimuth  $p$  changes dramatically but within experimental error no change in the analyzer azimuth  $a$  occurs. Figure A-1a of the appendix indicates that for transparent films (i.e.,  $\kappa_f = 0$ )  $\delta a$  remains unchanged or becomes negative only for  $n_f$  slightly greater than 1 or less. However, for these values of  $n_f$ ,  $\delta p$  is positive. Therefore, the cathodic films formed in  $\text{CH}_3\text{OH}$ -HCl cannot be transparent (nonabsorbing). Figure A-1c and d indicate that for  $\kappa_f > 2$ ,  $\delta a$  is always positive, therefore cathodic films formed in  $\text{CH}_3\text{OH}$ -HCl are limited to the range of  $n_f$  and  $\kappa_f$  found in Fig. A-1b and in particular to values of about  $n_f \sim 1-3$ ,  $\kappa_f \sim 1$ . The large absorption coefficient  $\kappa_f \sim 1$  corresponds to films of metallic character (e.g., for Ti  $n \approx 3$ ,  $\kappa \approx 1$ ). The cathodic films formed in  $\text{CH}_3\text{OH}$ -HCl may be titanium hydride or colloidal particles of metallic Ti with some electrolyte between the particles. Further experimental data are needed to elucidate this point.

Our results also have shown that care has to be taken to avoid the presence of  $\text{F}^-$  ions which even in very small amounts leads to severe corrosion and film formation on Ti.

### Acknowledgment

We would like to acknowledge the help of A. J. Lewin and N. G. Taylor in the design of the cell.

Manuscript submitted Nov. 15, 1971; revised manuscript received Feb. 14, 1972.

Any discussion of this paper will appear in a Discussion Section to be published in the December 1972 JOURNAL.

### APPENDIX A

Since there are only two experimental ellipsometric parameters  $p$  and  $a$  and there are three unknowns, film thickness  $d$ , index of refraction  $n_f$ , and absorption coefficient  $\kappa_f$ , a unique solution for  $d$ ,  $n_f$ , and  $\kappa_f$  is not possible. It becomes necessary, therefore, to interpret  $p$  and  $a$  in terms of  $d$  and  $n_f$  for reasonable ranges of  $\kappa_f$ . To aid this interpretation, values of  $p$  and  $a$  were computed for various values of  $d$ ,  $n_f$ , and  $\kappa_f$  for Ti in distilled water for very thin films with  $\lambda = 6328\text{\AA}$  and an angle of incidence of  $70^\circ$ . Figure A-1 shows plots of  $p$  and  $a$  vs.  $d$  for the values of  $n_f$  (first number) and  $\kappa_f$  (second number) reported in brackets on each curve. From Fig. A-1 and a knowledge of the range of values expected for  $n_f$  and  $\kappa_f$ , it is possible to anticipate the relative increase or decrease of  $p$  and  $a$  as the film

Table A-1. Comparison of optical constants of Ti and W to show the effect of surface contamination

Metal	Preparation	$n$	$\kappa$	Ref.
W	Ion bombard. $10^{-10}$ Torr, annealed	3.75	0.800	(13)
W	Heat treatment. $10^{-5}$ to $5 \times 10^{-10}$ Torr	3.40	0.88	(15)
Ti	Ion bombard. $10^{-10}$ Torr, annealed	3.09	1.11	(13)
Ti	Polished in air	2.0	1.5	(16)

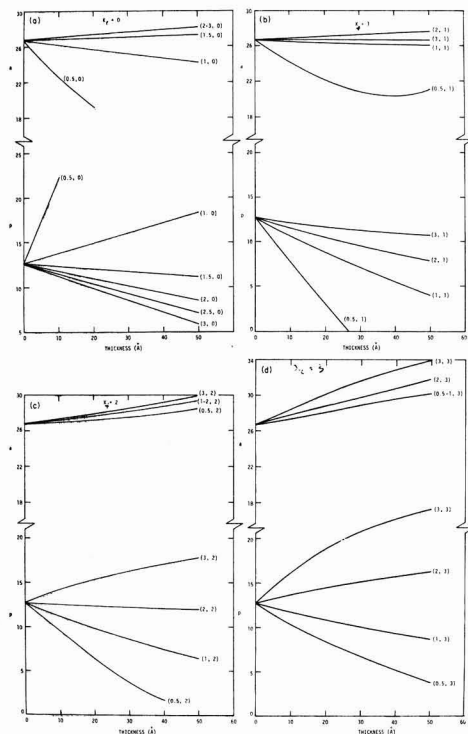


Fig. A-1. Computed values of  $p$  and  $a$  vs. film thickness  $d$  for  $\text{TiO}_2/\text{Ti}$  in water at  $6328\text{\AA}$ , for various values of the absorption coefficient of the film  $\kappa_f$  and refractive index of the film  $n_f$ .

grows. For example, more metallic films are expected to have lower values of  $n_f$  and higher values of  $\kappa_f$ . The opposite is expected for insulating films. Consequently, insulating films will always cause  $p$  to decrease and  $a$  to increase as  $d$  increases.  $a$  only decreases for very small values of  $n_f$  and  $\kappa_f$ , and  $p$  only increases for very small or very large values of  $n_f$  and  $\kappa_f$ .

It should be noted that accurate values for optical constants are difficult to obtain due to surface contamination. For example, Table A-I gives reported values for Ti and W for different preparation of the samples. Computer calculations using the exact Drude relations indicate that contamination tends to decrease  $n$  and increase  $\kappa$  if the ambient is gas or vacuum. Therefore, it is believed that the lower values reported for W and Ti in Table A-I resulted from surface contamination.

#### REFERENCES

1. F. L. McCrackin et al., *J. Res. Nat. Bur. Std., A*, **67**, 363 (1963).
2. F. L. McCrackin, *Nat. Bur. Std. Tech. Notes* 474, April 1969.
3. T. Smith, *J. Opt. Soc. Am.*, To be published.
4. F. Mansfeld, *This Journal*, **118**, 1412 (1971).
5. J. A. S. Green and A. J. Sedriks, *Met. Trans.*, **2**, 1807 (1971).
6. F. Mansfeld, Unpublished results.
7. M. J. Maudry and G. Rosenblatt, *This Journal*, **119**, 29 (1972).
8. T. R. Beck, M. J. Blackburn, and W. H. Smyrl, Quarterly Report No. 20, Contract NAS7-489, also Quarterly Report No. 14.
9. R. P. Frankenthal, *This Journal*, **116**, 580, 1646 (1969).
10. R. C. Menard, *J. Opt. Soc. Am.*, **52**, 427 (1962).
11. G. Hass, *Vacuum*, **11**, 331 (1952).
12. M. Kayama, *Chem. Abstracts* 62: 12572e; *Rika Gaku Kenkyusho Hokoku*, **39**, 121 (1963).
13. T. Smith, Unpublished data.
14. M. E. Sibert, *This Journal*, **110**, 65 (1963).
15. D. W. Juenker, L. J. LeBlanc, and C. R. Martin, *J. Opt. Soc.*, **58**, 164 (1968).
16. M. M. Kirillova and B. A. Charikov, *Phys. Metals Metallurg.*, **15**, 138 (1963).

## Contact Angle Measurements of Tin Sensitizing Solutions

N. Feldstein\* and J. A. Weiner

RCA Corporation, David Sarnoff Research Center, Princeton, New Jersey 08540

#### ABSTRACT

A study of tin sensitizing solutions was made by contact angle measurements. Through the control of solution composition, i.e., stannous and stannic concentrations, major improvements in the effectiveness of such sensitizers on hydrophobic surfaces have resulted. The incorporation of excess sodium chloride was found to further improve the performance of such sensitizing solutions. The presence of the stannic ions facilitates the adsorption of the stannous ions necessary for the reduction of palladium.

In the plating of dielectric substrates, a pretreatment of the substrate is essential in order to effectively deposit metals by the electroless plating technique. One of the more prevalent procedures in commercial use is the two-step immersion sequence of acidic stannous chloride solution followed by an acidic palladium chloride solution. In general, the first bath is referred to as the sensitizer solution while the second solution is the activator. The net result of this sequence is the formation of finely divided palladium nuclei which initiate the autocatalytic plating process (1,2). The

formation of the palladium metal nuclei is believed to be due to a redox reaction taking place between the adsorbed stannous ions on the surface and the palladium ions in the activating solution.

In spite of the wide commercial application of plated plastic parts, very little work has been reported regarding the chemistry of sensitizing and activating solutions. A review of this technology has been summarized by Goldie (3). Pearlstein (4) has observed variations in plating due to compositional changes of either the sensitizer or activator solutions. More recently, Cohen et al. (5,6), investigated the solution chemistry of the tin chloride sensitizing process. This study was based upon the Mossbauer spectroscopy of

\* Electrochemical Society Active Member.  
Key words: sensitizing solutions, electroless plating, contact angle measurements.



tin. Their proposed model invokes a colloidal formation based on the stannic ion with stannous ions bound onto this colloid.

Although the sensitizer compositions described in the literature are most effective for a wide variety of substrates, such solutions possess a major shortcoming whenever hydrophobic substrates are employed. Based upon work in this laboratory, it has been demonstrated that the performance of conventional-type sensitizers ( $\text{SnCl}_2 \cdot n\text{HCl}$  plus colloidal  $\text{Sn(IV)}$ ) (5, 6) may be greatly improved for use with hydrophobic substrates. This is achieved primarily through the proper control of the stannous-stannic concentrations.

In this investigation, a study of tin sensitizing solutions was undertaken employing contact angle measurements. Such an approach was believed to be useful since adsorption of thin films can potentially alter the resulting contact angle. Such an approach may lead to a more quantitative way by which the effectiveness of sensitizers may be evaluated. A later publication (7) will propose a mechanism for the sensitization of hydrophobic and hydrophilic substrates by tin-type solutions.

### Experimental Procedures

**Chemicals and solutions.**—All chemicals used throughout were Baker Reagent grade; the hydrochloric acid used was Mallinckrodt electronic grade. The water used was deionized and then distilled. The following solution was used throughout this investigation

Concentrate 2.6M  $\text{SnCl}_2 \cdot 2\text{H}_2\text{O}$  in concentrated HCl (37%) (Final HCl is 9.4M)

Working sensitizer solutions of different compositions were made from this concentrate.

**Substrate preparation.**—Cover glass plates,  $2 \times 2$  in. (E. Leitz, Inc., New York, Cat. No. 19821), which were cleaned in a mild soap solution, rinsed and spin dried, served as substrates. These substrates were coated with commercially available photoresists to form hydrophobic surfaces for testing. A positive resist, AZ-1350 (distributed by Shipley Company, Newton, Massachusetts) was spin coated onto the glass at 5000 rpm for 60 sec. To remove solvent(s) and polymerize the resist film, a baking procedure of  $200^\circ\text{C}$  for 3 min was employed. For a typical negative resist, KTFR (Eastman Kodak Company) was used. The resist composition was mixed in accordance with the manufacturer's specification. This resist was spin coated at 8000 rpm for 30 sec. A baking procedure of 7 min at  $200^\circ\text{C}$  was employed. Teflon<sup>1</sup> (FEP) Type A film was also used in conjunction with this study. The film thickness chosen was 20 mils. Prior to the contact angle measurements on the Teflon, a mild soap cleanup was employed.

**Substrate treatment.**—Two basic procedures were employed prior to the contact angle measurements. In the first procedure (procedure "a"), drops of varied sensitizer composition were placed on the photoresist surface, and the contact angle was measured. An alternate procedure was developed (procedure "b") which resulted in a greater sensitivity in the measurements. This adopted procedure consisted of

1. Immersion of substrate into various sensitizer compositions for 1.0 min.
2. Substrates were dipped (about 2 sec) in D.I. water of 1 liter volume.
3. Substrates were rinsed in D.I. water in an overflow rinse tank (volume = 1.2 liter) with a flow rate about 4 liters/min.
4. Substrates were spin dried in air.
5. Drops of D.I. water (or palladium chloride solution consisting of 1 g/liter  $\text{PdCl}_2$  and 1 cc/liter concentrated HCl) were placed on the photoresist surface

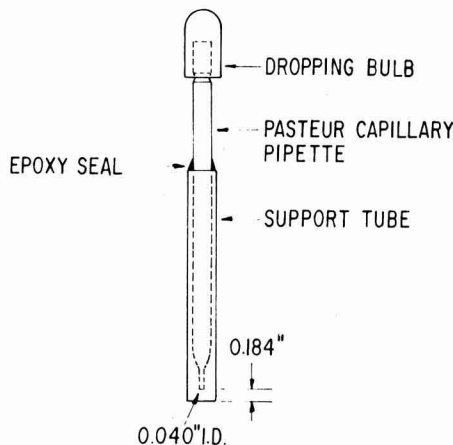


Fig. 1. Dispensing device for contact angle measurements

using a Pasteur pipette from a controlled height of 0.184 in. (See Fig. 1).

### 6. Contact angle was measured.

**Contact angle measurements.**—All measurements were made using a contact angle goniometer Model A-100 (Ramé-Hart, Inc., 43 Bloomfield Avenue, Mountain Lakes, New Jersey 07046). Due to the spreading effect, contact angles were measured as a function of time and extrapolated to time zero. A time interval of 10 min was chosen for convenience, however, no changes in the extrapolated values were noted in measurements greater than 10 min. Figure 2 shows the contact angle of sessile drops as employed in procedures "a" and "b," respectively. A least square calculation was used to derive the extrapolated values at zero time. All reported angles are the extrapolated values, and these values were found to be reproducible within  $\pm 2^\circ$ , except for the case of Teflon, which resulted in variations of  $\pm 5^\circ$ .

**Surface tension measurements.**—Surface tension measurements were made using a Fisher Surface Tensiometer Model 20. A 6 cm Pt-Ir ring was used for making measurements.

### Results and Discussion

In the first stage of this investigation, a procedure was attempted in which the contact angle was measured by placing sensitizer drops onto the organic surface. Typical results employing this procedure showed little change upon the addition of stannic ions. Surface tension measurements of sensitizing solutions, with and without added stannic ions, resulted in variations of a few per cent. Specifically, the addition of  $2.5 \times 10^{-2}\text{M}$  stannic chloride to a solution composed of 0.13M  $\text{SnCl}_2$  and 0.47M HCl, resulted in surface tensions ranging from 68 dynes/cm to 70 dynes/cm. These minor alterations in the surface tension of the sensitizer solutions are consistent with the minor variations of contact angle. It is concluded that a different mechanism takes place, other than surface tension modification, which accounts for the variations in the effectiveness of the present sensitizers on hydrophobic-type substrates. Therefore, this approach was not further pursued.

Examination of the contact angle following the sensitization step showed a greater degree of sensitivity in comparison to the results of procedure "a". Hence, all reported angles are based upon the modified procedure (Fig. 2, procedure "b"). In the modified procedure, it was found that results within experimental error were obtained by using drops of either water or palladium chloride solutions. For convenience, the use of water drops was adopted for most of the experimental work.

<sup>1</sup> Teflon (fluorocarbon film)—Trademark of E. I. du Pont de Nemours & Co.

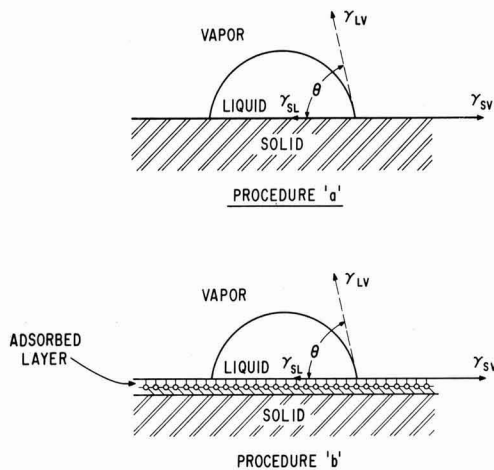


Fig. 2. Contact angle of sessile drops

In a recent study, the role of the stannic ions in conventional-type sensitizers was described. As pointed out (6), typical reagent grade stannous chloride contains approximately 5 mole per cent (m/o) stannic ions, and upon dissolution in aerated water, further oxidation yields a total of about 6 m/o of stannic ions. A model based upon the formation of colloidal stannic compound(s) has been invoked to account for the mechanism of sensitization. The stannous ions are bound onto these colloids and are presumably retained on the surface by both an adsorption- and absorption-type mechanism. Table I shows the resulting contact angle measurements of different sensitizer compositions. It is quite evident that for sensitizers 1 through 4, the contact angle is nearly the same and thus seems to be independent of composition ( $\text{SnCl}_2/\text{nHCl}$  ratio) as well as the manner by which the sensitizer was prepared. It should be recalled (6) that sensitizers A, B, and C were proposed as a means for controlling the colloid present in the stannous solutions. By contrast, the incorporation of the stannic chloride solution as made in this laboratory (Table I, No. 5) shows clearly the modifications associated with such combinations, further suggesting that other mechanism(s) may take place during the sensitization process which are especially important in the case of the hydrophobic-type substrates.

Figures 3 and 4 show the variations of the contact angle due to the compositional modification of the sen-

Table I. Contact angle<sup>(a)</sup> for typical stannous sensitizers/activators

Sensitizer/activator system	Contact angle (degrees)
1 Bell Telephone Laboratories "A" <sup>(b)</sup>	66
2 Bell Telephone Laboratories "B" <sup>(c)</sup>	65
3 Bell Telephone Laboratories "C" <sup>(d)</sup>	67
4 RCA <sup>(e)</sup>	66
5 RCA <sup>(f)</sup>	53
6 Catalyst 9F and Accelerator 19 <sup>(g)</sup>	71

<sup>(a)</sup> AZ-1350 resist was used.

<sup>(b)</sup> Solution prepared by dissolving 20.0g  $\text{SnCl}_2 \cdot 2\text{H}_2\text{O}$  in water, adding 10.0 ml concentrated HCl and then diluting up to 1 liter with water.

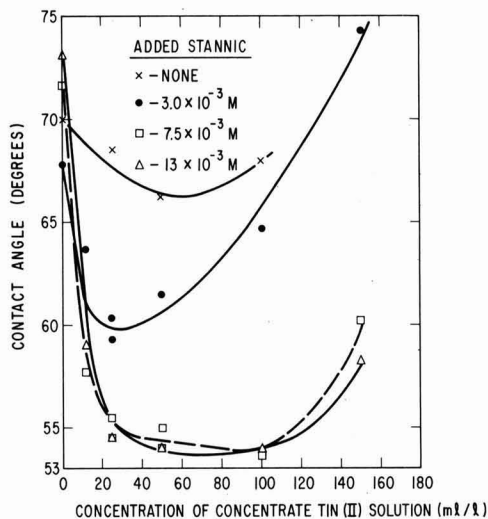
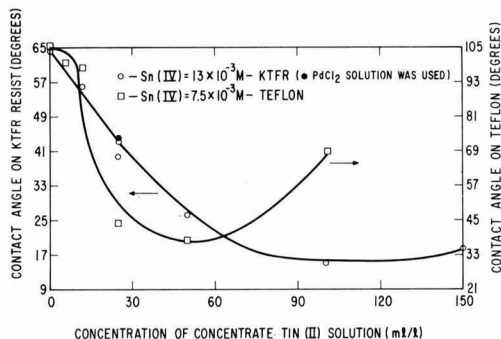
<sup>(c)</sup> Solution prepared by dissolving 20.0g  $\text{SnCl}_2 \cdot 2\text{H}_2\text{O}$  in 10.0 ml HCl and then diluting to 1 liter with water.

<sup>(d)</sup> Solution prepared by dissolving 10.0 ml HCl in nearly 1 liter water, adding and dissolving 20.0g  $\text{SnCl}_2 \cdot 2\text{H}_2\text{O}$  and then diluting to 1 liter with water.

<sup>(e)</sup> Solution composed of 0.13M  $\text{SnCl}_2$  in 0.47M HCl.

<sup>(f)</sup> Same as Footnote (e) plus  $7.5 \times 10^{-3}\text{M}$   $\text{SnCl}_4$ .

<sup>(g)</sup> Shipley Company, Inc., Newton, Mass., Catalyst 9F was mixed with 2 parts water and 1 part HCl as suggested by supplier. Accelerator was mixed with 4 parts of water. Immersion in the above two was for 3 min each; a sufficient DI rinse was carried out between the catalyst and accelerator.

Fig. 3. Contact angle variations vs. compositional changes on AZ-1350 resist. Concentrate tin(II)—2.6M  $\text{SnCl}_2$ , 9.4M HCl.Fig. 4. Contact angle variations vs. compositional changes. Concentrate tin(II)—2.6M  $\text{SnCl}_2$ , 9.4M HCl.

sitizer solution. The choice of substrate materials in these figures was made because of the good reproducibility obtained in their preparation. For a constant added  $\text{Sn(IV)}$ , a sharp drop in the measured contact angle takes place upon increasing the  $\text{Sn}^{+2}/\text{Sn}^{+4}$  ratio. A minimum in the contact angle is found, after which further increase in the  $\text{Sn}^{+2}/\text{Sn}^{+4}$  ratio results in an increase in the contact angle. Increasing the tin (IV) concentration results in displacing the minimum towards lower values. However, a convergence is found at the higher tin (IV) concentrations. The increasing portion of the curves with excess addition of  $\text{SnCl}_2/\text{nHCl}$  is due to a combination of factors: (i) increasing the hydrogen ion concentration tends to increase the measured contact angle and (ii) the large excess of stannous ions relative to the stannic ions prevents the surface adsorption of the latter ions. These factors were qualitatively tested and verified. A full account concerning the shape of these curves will be covered in a later publication.

Figure 4 shows the variations in the measured contact angle on KTFR resist and Teflon. The general trend for these cases is similar to that demonstrated in Fig. 3. Of the various materials examined, the Teflon shows the most dramatic change in contact angle with variations in the stannous/stannic ratio.

Figure 5 shows the effect(s) of added sodium chloride on the resulting contact angle. As seen from Fig. 5, the addition of this salt to a conventional-type sensitizer (0.13M  $\text{SnCl}_2$  and 0.47M HCl) results in no appreciable effect on the measured contact angle. At the

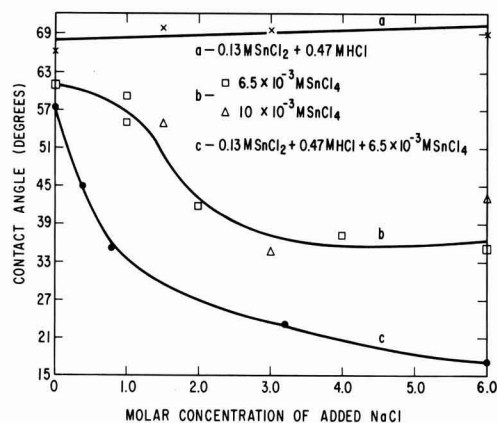


Fig. 5. Contact angle variations vs. sodium chloride concentration on AZ-1350 resist.

same time, the addition of sodium chloride to solutions containing the stannic ions alone shows a substantial decrease in the measured contact angle. Excess addition of sodium chloride to this media ( $6.5 \times 10^{-3}$  or  $1 \times 10^{-2}$  M SnCl<sub>4</sub>) results in a leveling effect. In curve c, the effect of added sodium chloride to a solution containing both the stannous and stannic ions is demonstrated. The concentrations of the stannous, stannic, and hydrochloric acid are the combined concentrations of those concentrations used for curves a and b. Although there is a general resemblance between curves b and c, the effect of sodium chloride is more pronounced in a system which combines the stannous and the stannic ions. These results are thus suggestive that an interaction exists whereby the degree of surface modification due to sensitization is altered to a greater extent. Substitution of bromide ion for the chloride resulted in the same general characteristics.

Table II provides a summary of the contact angle measurements resulting at each of the steps along the sensitization and activation sequence. As seen, the major surface modifications take place after the sensitization step. Once the surface is suitably "sensitized," very little change is noted at the conclusion of the activation step. In an alternative sequence, the process of sensitization and activation was divided into

Table II. Contact angle measurements during the different stages of pretreatment

Two-step sequence		Three-step sequence	
Contact angle (degrees)		Contact angle (degrees)	
AZ-1350 resist, as prepared	70	AZ-1350 resist as prepared	70
After sensitization <sup>(a)</sup>	53	After stannic <sup>(b)</sup>	59
After activation	51	After stannous <sup>(c)</sup>	53 <sup>(d)</sup>
		After activation	56

<sup>(a)</sup> Sensitizer used composed of 0.13M SnCl<sub>2</sub>,  $7.5 \times 10^{-3}$  M SnCl<sub>4</sub> and 0.47M HCl.

<sup>(b)</sup> Solution composed of  $7.5 \times 10^{-3}$  M SnCl<sub>4</sub> plus 1M NaCl to compensate for the chloride content present in a combined solution.

<sup>(c)</sup> Solution composed of 0.13M SnCl<sub>2</sub> and 0.47M HCl.

<sup>(d)</sup> Deletion of the stannic immersion step gives a contact angle of 67°.

three distinct steps: (i) immersion in stannic, (ii) immersion in stannous, and (iii) immersion in palladium chloride activator solution. As seen from Table II, the major change in the contact angle is observed following the stannic immersion step with a slight change in the subsequent steps (immersion in stannous and palladium, respectively). It is interesting to note that a contact angle of 53° has resulted prior to the activation step independent of the path taken. Furthermore, upon deletion of the stannic ions, following immersion in stannous type solution, the observed contact angle is about 67°. It is thus concluded that the presence of the stannic ions provides a new mechanism (7) by which the active stannous ions are adsorbed onto the substrate. The stannic ion may be incorporated along with a conventional-type stannous sensitizer solution or used as a separate immersion step prior to conventional-type sensitization. In a subsequent publication (7), a mechanism accounting for the different modes of sensitization will be given.

### Conclusion

In the plating of dielectric substrates, a pretreatment step of sensitization and activation is generally employed. Following this sequence, a catalytic layer is present which is capable of initiating electroless plating baths. In general, it is desired to have a continuous conductive metallic layer prior to an electrolytic build-up of the metallic films. There are, however, materials which do not yield a uniform metallic film. These materials are generally hydrophobic. Of the various steps prior to the electroless plating, the sensitization process controls whether the final metallic film is uniform.

In the current investigation, it has been demonstrated that contact angle measurements can quantitatively demonstrate the effectiveness of sensitizing solutions. Furthermore, controlled additions of stannic ions with or without sodium chloride provide a simple and effective way of modifying conventional sensitizers for the uniform plating of hydrophobic substrates. The role of the added stannic ions is to provide a path for the adsorption of the stannous ions. The stannous ions adsorbed on the substrate were not necessarily bound to any stannic ions in bulk solution, and, in fact, separate solutions may be used effectively, thus separating the stannous from the stannic ions.

### Acknowledgments

The authors wish to thank G. L. Schnable for useful discussions and for the reviewing of this paper.

Manuscript submitted Sept. 24, 1971; revised manuscript received ca. Dec. 6, 1971.

Any discussion of this paper will appear in a Discussion Section to be published in the December 1972 JOURNAL.

### REFERENCES

1. J. P. Morton and M. Schlesinger, *This Journal*, **115**, 16 (1968).
2. R. Sard, *ibid.*, **117**, 864 (1970).
3. W. Goldie, "Metallic Coatings of Plastics," Vol. I, Chap. 5, Electrochemical Publications Limited, Hatch End, Middlesex, England (1968).
4. F. Pearlstein, *Metal Finishing*, **53**, 59 (1955).
5. R. L. Cohen, J. F. D'Amico, and K. W. West, *This Journal*, **118**, 2042, (1971).
6. R. L. Cohen and K. W. West, *ibid.*, **119**, 433 (1972).
7. N. Feldstein, Unpublished results.

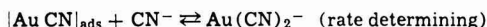
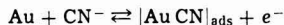
# A Study of Gold Reduction and Oxidation in Aqueous Solutions

D. M. Mac Arthur\*

Bell Telephone Laboratories, Incorporated, Murray Hill, New Jersey 07974

## ABSTRACT

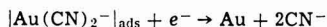
The electrochemical behavior of gold in alkaline cyanide, citrate, and phosphate buffered solutions has been studied using cyclic voltammetry and galvanostatic transients. Two reaction paths were observed. At low overvoltage the reaction goes through an adsorbed intermediate.



At larger overvoltages a direct transfer between the gold complex in solution and the metal atom was found on reduction. The reduction reaction was the same in all the solutions but in the phosphate and citrate baths the gold did not oxidize to a soluble species.

The electrodeposition of gold on various electronic devices is in widespread practice because the metal has good corrosion resistance, electrical conductivity, and bonding properties. A complete understanding of the reaction mechanism for electrodeposition would be of considerable value to the technology of gold plating but has not been achieved. The work described here was undertaken to add to our knowledge of the reaction mechanism for gold reduction and oxidation in practical gold-plating baths.

Maja (1) has reported on the alkaline gold cyanide bath which contains an excess of free cyanide and on the basis of thermodynamics and kinetic measurements concluded that reduction from alkaline solution occurs as follows<sup>1</sup>



He also found that the oxidation reaction is



Cathro and Koch (2) used potentiostatic and galvanostatic measurements on gold oxidation in alkaline cyanide electrolytes. They concluded that gold was oxidized to  $|\text{AuCN}|_{\text{ads}}$  at potentials less than  $-0.6\text{V}$  (SCE reference) and became passive in the potential range  $-0.6$  to  $-0.3\text{V}$  through the formation of a gold oxide or basic cyanide. A second active region was found at approximately  $+0.1\text{V}$  which, it was proposed, was the conversion of an adsorbed  $\text{Au}(\text{I})$  basic cyanide to an adsorbed  $\text{Au}(\text{III})$  basic cyanide. A third active region at  $+0.4\text{V}$  was found and was passivated by the formation of  $\text{Au}_2\text{O}_3$ . Thermodynamically the formation of gold oxides is expected to occur at potentials considerably more positive than  $-0.3\text{V}$ . Basic gold cyanides are not known to exist in alkaline cyanide solutions. It is difficult to accept therefore that a gold oxide or basic cyanide can form at a potential of  $-0.3\text{V}$ . It is also difficult to accept that an  $\text{Au}(\text{III})$  salt can exist in contact with an aqueous cyanide solution since  $\text{Au}(\text{CN})_4^-$  is known to be unstable with respect to  $\text{Au}(\text{CN})_2^-$  and cyanogen in these solutions, or that steady-state currents in the range of  $1\text{--}2\text{ mA/cm}^2$  can be observed for the oxidation of one adsorbed species to another. We believe, therefore, that the proposed passivation mechanisms at  $-0.3$  and  $+0.1\text{V}$  may be in error.

Taran and co-workers (3) have proposed that solutions with a low pH have a more easily discharged gold complex in solution and that the citrate solution, in particular, has adsorbed citrate on the gold metal surface.

These authors have proposed various reaction mechanisms. Although the solutions vary, it is difficult to accept that the reactions can be so different since the initial and final gold species are the same. In this work cyclic voltammetry and galvanostatic transient techniques are used to provide additional information on the reaction mechanisms.

## Experimental

Three gold plating solutions were used in this work as follows:

Alkaline cyanide; 15.0g  $\text{KAu}(\text{CN})_2$ , 55.0g  $\text{KCN}$ , 5.0g  $\text{KOH}$  per liter of solution pH 12.2

Citrate; 50.0g dibasic ammonium citrate, 20.0g  $\text{KAu}(\text{CN})_2$  per liter of solution pH 5.0.

Phosphate; 18.2g  $\text{KAu}(\text{CN})_2$ ; 36.4g dibasic potassium phosphate; 9.1g monobasic potassium phosphate pH 7.0.

Reagent grade chemicals were used throughout. Deionized water that had been passed through both cation and anion exchangers was used to prepare solutions.

Wire electrodes 0.025 in. in diameter and held in a gold-plated pin vise were used as working electrodes. These wires were about 1 in. in length and were immersed 0.5 in. into the solutions. It would be preferable to use an immersed electrode with defined area, but the problem of leakage around edges, particularly in cyclic potentiometry experiments led to the adoption of this technique. The counterelectrode was either a platinum- or gold-plated platinum wire. A saturated calomel reference electrode was used and all potentials are referred to this electrode. In the galvanostatic transient experiments, a gold wire reference electrode in the same solution was used, and its potential frequently checked against the calomel reference.

A standard potentiostatic circuit incorporating an X-Y recorder, potentiostat, and triangular wave function generator was used in the potential scan experiments. The galvanostatic transient experiments used a 24V battery supply for the cathodic transient with a potentiometer for current control and a Western Electric 276B mercury-wetted relay to switch the current. Another 3V battery was used to apply a small anodic current preceding the cathodic transient. Potentials were fed through a high impedance voltage follower and displayed on an oscilloscope which was triggered by the switching circuit.

Solutions (100 ml) were contained in a double-walled Pyrex flask with circulating water for tempera-

\* Electrochemical Society Active Member.

Key words: electrodeposition, gold plating, cyclic voltammetry.

<sup>1</sup> The solutions of commercial significance in gold plating all contain gold predominately as the  $\text{Au}(\text{CN})_2^-$  complex.

ture control. The temperature was  $61^{\circ} \pm 1^{\circ}\text{C}$ . The flask had a machined Teflon lid. All solutions were deoxygenated by bubbling  $\text{N}_2$  through them.

## Results

### Cyclic Voltammetry Experiments

**The alkaline cyanide bath.**—Figure 1 shows a scan of the bath using a gold wire electrode. (In this preliminary scan a 0.020 in. diameter wire was used.) Two reduction regions A and B may be observed and two oxidation regions C and F are also evident. The oxidation peaks C and F were observed as distinct peaks in all scans moving in the anodic direction, but only in the first two scans were they separate when moving in the cathodic direction. As scanning was continued, peak F disappeared and the peak in the C region became complex as shown in the figure. Peaks A and B were only observed when moving from the anodic to cathodic potentials in all scans.

The areas under peaks C and F on the anodic scan were approximately 105 and 150 millicoulombs as determined by geometric integration of the curves. The double layer charging current was about  $1\ \mu\text{A}$  and negligible. Oxidation of a monolayer of Au would require only about 0.05 millicoulombs (using the area of the electrode as  $0.20\ \text{cm}^2$ , assuming  $\text{Au(I)}$  was formed and taking the radius of the Au atom as  $1.5\text{\AA}$ ). The peaks correspond to oxidation of 2000-3000 monolayers. This is too large to represent a thin adsorbed layer nor can it be the formation of an insoluble film since there is no corresponding large reduction peak and the peaks do not change upon continued scanning. It will be shown that peak C is an oxidation reaction that proceeds through a surface film to a soluble product and that peak F is an oxidation reaction passivated by the formation of an oxide on the electrode. The area under peak B on the other hand is approximately 1 millicoulomb, a quantity that could correspond to an adsorbed species. Peak A will be shown to correspond to reduction of  $\text{Au(CN)}_2^-$  from solution.

Some of the details of the gold reaction are obscured in the standard solution because of the high free cyanide level (approximately 0.85M). Figure 2 shows a potential scan of a gold wire (0.025 in. diameter) in a solution of 0.2M KCN and 0.2M KOH. This solution is about one quarter the concentration in  $\text{CN}^-$  and twice the concentration  $\text{OH}^-$  of the standard bath. In Fig. 2 the solution does not contain  $\text{Au(CN)}_2^-$  to an appreciable extent. Peak A is not present, but there is some evidence of peak B at  $-1.0\text{V}$ . It is not as large as in solutions containing relatively large amounts of  $\text{Au(CN)}_2^-$ , and therefore it appears to be related to the presence of  $\text{Au(CN)}_2^-$  in solution. Peaks C and F are evident scanning in both directions and peak F shows further evidence of being complex. In addition a broad peak E on the side of the oxygen wave and a reduction peak D located just anodic to the oxidation peak F when scanning in the cathodic direction, are

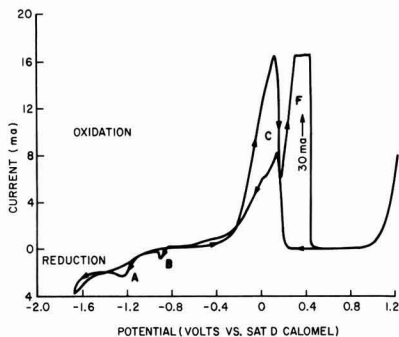


Fig. 1. Potential scan of a Au wire in the alkaline cyanide gold bath. Velocity  $0.040\ \text{V/sec}$ .

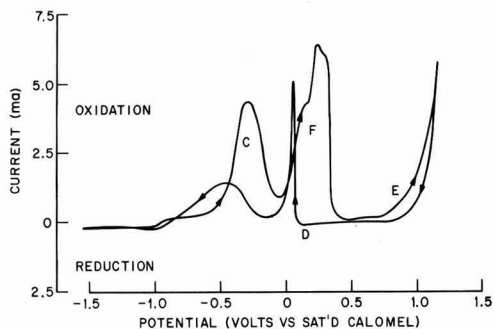


Fig. 2. Potential scan of a Au wire in 0.2M KCN and 0.2M KOH. Velocity  $0.042\ \text{V/sec}$ .

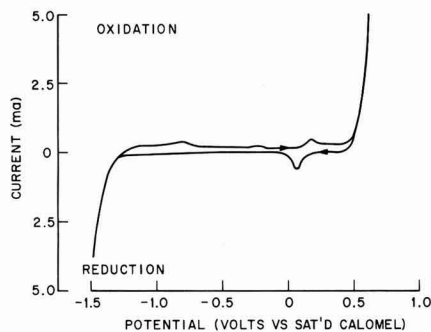


Fig. 3. Potential scan of a Au wire in 0.2M KOH

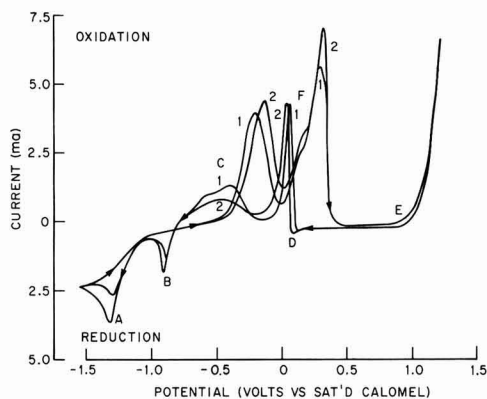


Fig. 4. Potential scans of a Au wire in 0.2M KCN, 0.2M KOH and  $0.035\text{M}\ \text{KAu(CN)}_2$ . Curve 1,  $0.041\ \text{V/sec}$ ; curve 2,  $0.099\ \text{V/sec}$ .

observed. Peak D may be seen more clearly in Fig. 4. In order to identify peak D comparison may be made to Fig. 3 which is a scan of a gold wire in 0.2M KOH only. The rest potential of the  $\text{Au/Au}_2\text{O}_3$  electrode in KOH solutions has been reported (4) as about 1.1V on the hydrogen electrode scale. For the 0.2M KOH solution this would be about 0.1V on the SCE scale. The oxidation peak and the reduction peak which are close to this value in the figure may reasonably be assigned to the formation and reduction of gold oxide. By analogy it then appears reasonable to correlate peak D in the alkaline cyanide solutions with reduction of gold oxide on the electrode. Peak E is assumed to be a thickening of the gold oxide layer which is first formed at potentials closer to 0.1V.

Figure 4 shows two scans at different velocities of the same 0.2M KCN, 0.2M KOH solution to which



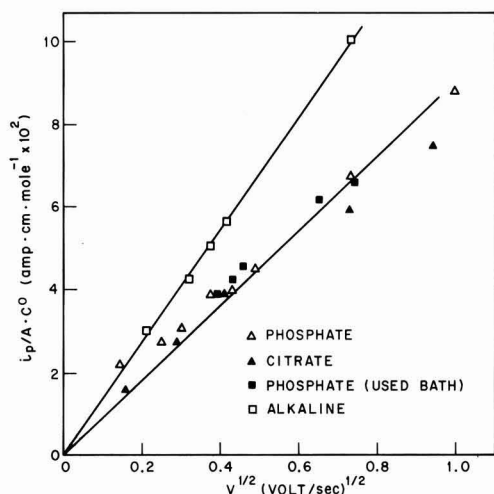


Fig. 5. Peak height as a function of the square root of the scan rate for reduction peak A.

$\text{KAu}(\text{CN})_2$  has been added to make the  $\text{Au}(\text{CN})_2^-$  concentration 0.035M. The behavior of peaks A, B, C, and F as the scan rate is varied will now be discussed. At high scan rates the cylindrical geometry of the wire electrode may be approximated by planar geometry. This approximation is valid for rates determined by the inequality (5)

$$\frac{1}{r} \left( \frac{D}{nV} \right)^{1/2} < 0.2$$

which, for the wires used in this work requires that the scan rate be greater than 0.45 V/sec.<sup>2</sup> Although the effect of cylindrical geometry may be found in the shape of the recorded curves it turns out (5) that the peak height is only slightly altered, and the peak current is a linear function of the square root of the scan rate for velocities as low as 0.1 V/sec. At 61°C this function is

$$i_p = 2.57 \times 10^5 n^{3/2} A D^{1/2} C^\circ V^{1/2}$$

A plot of  $i_p/A \cdot C^\circ$  as a function of  $V^{1/2}$  is shown in Fig. 5 for peak A. A linear relationship was observed indicating a diffusion limited reaction which must be the reduction of the  $\text{Au}(\text{CN})_2^-$  from solution. The true area of the gold wire was estimated from the peak height vs.  $V^{1/2}$  plot for the oxidation of  $\text{Fe}(\text{CN})_6^{4-}$  and its known diffusion coefficient in dilute chloride solution at room temperature. A roughness factor of 1.3 was determined. Using this true area of the gold wire the diffusion coefficient of  $\text{Au}(\text{CN})_2^-$  in the 0.2M KOH, 0.2M KCN solution was found to be  $1.8 \times 10^{-5} \text{ cm}^2 \text{ sec}^{-1}$  at 61°C. Literature sources (6) give the value of  $1.60 \times 10^{-5} \text{ cm}^2 \text{ sec}^{-1}$  which is satisfactory agreement.

Peak B was found to have a constant capacity of about 1 millicoulomb in the two different alkaline cyanide solutions and for the various scan rates used. This would correspond to about 15-30 molecular layers depending on how tightly packed the atoms were. The reduction reaction would appear to have two possible paths; one through an adsorbed state (peak B) and one by direct charge transfer (peak A).

The number of coulombs passed in area C increased as the scan rate decreased. This was evident not only in the cathodic to anodic scan but in the reverse direction also. In addition the current did not increase without limit when moving in the anodic direction as would be expected for a charge transfer reaction forming directly a soluble species from a metal electrode.

These observations then are consistent with a reaction mechanism in which charge transfer forms an intermediate on the electrode and the intermediate species is solubilized in a following chemical reaction.

Cathro and Koch (2) concluded that the peak in area C was passivated by the formation of an adsorbed basic gold cyanide. The shape of the peak is not consistent with a passivation type reaction which causes an abrupt decrease in current (compare the shape of peak F and C). It is consistent with the charge transfer followed by chemical reaction mechanism in which the chemical reaction is rate limiting and the surface intermediate interferes with the charge transfer reaction.

Peak F has the characteristic shape of a passivated reaction which is depassivated upon reduction of a surface film at D. As mentioned earlier, this reduction potential corresponds to that for gold oxide which, therefore, is the passivating film. Cathro and Koch (2) observed two peaks in this area and indeed peak F does give evidence of being composed of two overlapping peaks. The number of coulombs passed in this region is much too large for the reaction to be the formation of an adsorbed layer. In addition, the observation that the number of coulombs passed does not increase with decreasing scan rate (except to a small and sometimes variable extent) suggests that the reaction is direct oxidation to a soluble species complicated by the presence of gold oxide which eventually passivates the electrode. This phenomenon has also been observed (7) for gold oxidation in acid chloride solutions and the same explanation for passivation was proposed.

**The citrate bath.**—Gold-plated Kovar (Fe, Ni, Co alloy) wires were used for some of the experiments in the citrate and phosphate baths. The gold was electro-deposited at about 1 mA (approximately 4 mA/cm<sup>2</sup>) from the solution before commencing the scans. In the citrate and phosphate solutions the gold is not oxidized to a soluble species because of the absence of excess  $\text{CN}^-$  or other complexing agents and the electrocoated wires were not observed to differ from the solid gold wires.

Figure 6 shows scans at three different speeds of a gold-plated Kovar wire in the citrate bath. The peak numbering scheme used in describing the results of the alkaline bath is retained here and also for the phosphate bath to be described next. A plot of  $i_p/A \cdot C^\circ$  (peak A) as a function of  $V^{1/2}$  is included in Fig. 5. A linear relationship was observed but the calculated diffusion coefficient was  $0.88 \times 10^{-5} \text{ cm}^2 \text{ sec}^{-1}$  not in agreement with the literature value (6) of  $1.67 \times 10^{-5} \text{ cm}^2 \text{ sec}^{-1}$ . This lack of agreement indicates that peak A is not a simple charge transfer reaction involving reduction of a soluble species. The absence of a clearly

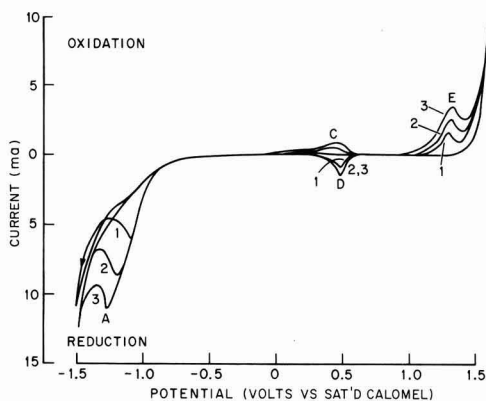


Fig. 6. Potential scans of Au plated wire in the citrate bath. Curve 1, 0.17 V/sec; curve 2, 0.52 V/sec; curve 3, 0.85 V/sec.

\* A list of symbols used is included at the end of the paper.

defined peak B which is assumed to be reduction of an adsorbed intermediate suggests that this reduction path is also occurring in the potential range of peak A resulting in the low calculated value for the diffusion coefficient. More evidence to establish that this is the case was obtained from the galvanostatic transients which will be described later.

Peak C was observed to have a capacity in the range of 0.1–0.3 millicoulombs—that expected for the formation of an insoluble surface layer. From a comparison of this figure with the preceding figures, it is concluded that this is oxidation of gold to the adsorbed intermediate observed in the alkaline bath but in this case the following chemical step to a solubilized product does not occur because of the absence of excess  $\text{CN}^-$ . Peaks D and E are reduction of gold oxide and oxidation of gold, respectively.

**The phosphate bath.**—Figure 7 shows scans of a gold wire in the phosphate bath. The current in peak A is plotted in Fig. 5. The calculated  $D$  is  $0.88 \times 10^{-5} \text{ cm}^2 \text{ sec}^{-1}$  the same as that for the citrate bath and not in agreement with the literature value (4) of  $1.63 \times 10^{-5} \text{ cm}^2 \text{ sec}^{-1}$ . In this bath it is also concluded that reduction through the adsorbed intermediate is occurring in the same potential range as the direct charge transfer to  $\text{Au}(\text{CN})_2^-$  although evidence for peak B may be seen on the edge of the reduction wave. Peak C was observed to have capacities ranging from 0.2 to 1.1 millicoulombs indicating that in this bath oxidation proceeds to the intermediate surface state which is not solubilized.

#### Galvanostatic Transient Experiments

**Oxidation.**—Galvanostatic transients for a gold wire during oxidation in a 0.2M KOH, 0.2M KCN, and  $3.58 \times 10^{-2}\text{M}$   $\text{KAu}(\text{CN})_2$  solution were obtained in the range of 18 to 48  $\text{mA/cm}^2$ . A potential of 0.3 to 0.45V (peak F) was observed for the oxidation followed by a sharp potential rise to oxygen evolution at potentials greater than 1V [Fig. 8(a)]. The transition time was taken as the commencement of the sharp potential rise. For the lower current densities another plateau at about 0.1V was observed with a capacity of about 1.7 millicoulombs/ $\text{cm}^2$  before the potential plateau at 0.3–0.45V. The transition times include this plateau because the surface intermediate is later chemically dissolved. Figure 9 is a plot of  $i\tau$  and  $i\tau^{1/2}$  determined from these oxidation experiments as a function of current density. The linear  $i\tau^{1/2}$  relationship is an indication that the predominate oxidation reaction is the formation of a soluble species. (If the reaction were predominately the formation of a surface film a linear  $i\tau$  relationship would be observed.) For a metal oxidation reaction into solution the concentration of the metal ion at the surface is

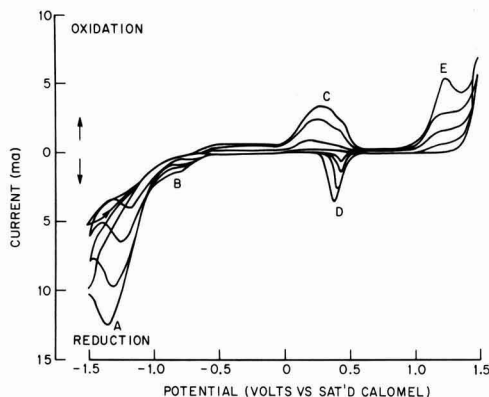


Fig. 7. Potential scans of a Au wire in the phosphate bath. Scan rates were 0.060, 0.24, 0.55, and 1.0 V/sec.

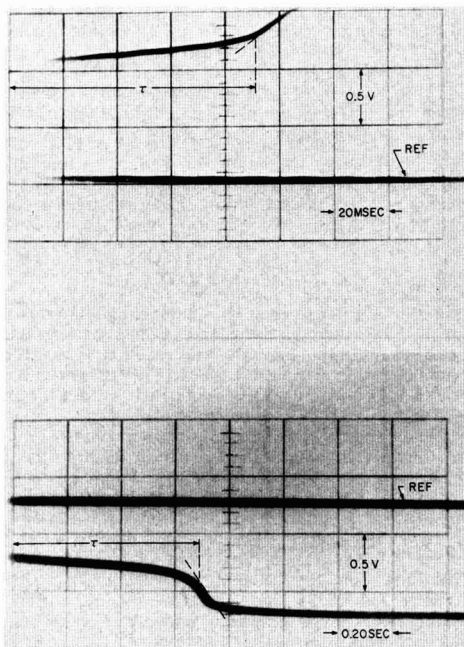


Fig. 8. (a) Upper curve, a typical potential-time transient for gold oxidation in 0.2M KOH, 0.2M KCN solution at 61°C. Current density 38  $\text{mA/cm}^2$ . (b) Lower curve, a typical potential-time transient for gold reduction. Wire electrode, alkaline cyanide solution 0.035M in  $\text{Au}(\text{CN})_2^-$ , current density 21  $\text{mA/cm}^2$ .

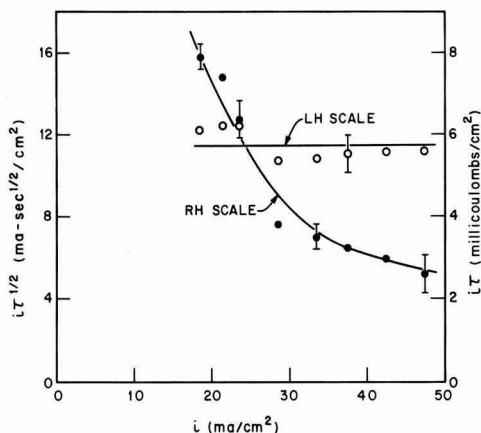


Fig. 9. Transition time curves for gold oxidation in 0.2M KOH, 0.2M KCN, and 0.2M  $\text{KAu}(\text{CN})_2$ .

$$C_0 = \frac{2i}{nFD^{1/2}} \sqrt{t/\pi}$$

If the electrode follows Nernst behavior then the potential of the electrode increases as the logarithm of the square root of time without abrupt transition. When a passivating reaction can occur, however, as it does in this case then the potential rises to the value where passivation occurs and then increases abruptly. The concentration of the metal ion when this occurs may be designated  $C_0^*$  and is given by

$$C_0^* = \frac{2i}{nFD^{1/2}} \sqrt{t/\pi}$$

Substitution of the value  $11.5 \times 10^{-3}$  (Fig. 9) for  $i_{r^{1/2}}$  into this equation gives a value of  $3.5 \times 10^{-2}$  mole/l for  $\text{Co}^*$ . This value is less than the saturation value for  $\text{Au}(\text{CN})_2^-$  suggesting that passivation occurs not from precipitation of gold cyanide but as a result of another reaction beginning at a potential of about 0.45V and this is the formation of gold oxide.

**Reduction.**—The transition time during reduction occurs when the reaction, under mass transport limited kinetics, reaches the condition that the surface concentration of the reacting species is zero. The transition time is given by

$$i_{r^{1/2}} = \frac{1}{2} \pi^{1/2} n F C^0 D^{1/2}$$

If the reaction is preceded by a slow chemical reaction then the  $i_{r^{1/2}}$  product is not constant but decreases with increasing current density. If the reaction is preceded by an adsorption step then the product  $i_{r^{1/2}}$  becomes constant at sufficiently high current densities and the  $i_{r^{1/2}}$  product increases. A convenient means of distinguishing these reaction mechanisms is thus available. Peters and Lingane (8) have modified transition time theory for planar electrodes to include cylindrical geometry. In the worst case considered here the correction is less than 10% for the cylindrical geometry so the unmodified theory is used throughout. A typical potential-time curve for gold reduction is given in Fig. 8(b).

The data from transition time experiments are displayed in Fig. 10. In these experiments four different solutions and three different geometries were used. Considering this, the scatter in the  $i_{r^{1/2}}/C^0$  values is not excessive. One set of data (the open circles) indicates a preceding adsorption step. These measurements were taken with the electrode "floating" without an applied potential before the imposition of the cathodic current. All the other data in the figure were obtained with an anodic current of from 50 to 200  $\mu\text{A}$  applied to the electrode before switching to the cathodic current. In these latter experiments the formation of an oxide on the surface prevented adsorption of the intermediate reduced in peak B (Fig. 2). On reduction the thin oxide layer was rapidly reduced and then  $\text{Au}(\text{CN})_2^-$  was reduced from solution. The oxide layer was thin (about 1 millicoulomb/cm<sup>2</sup>), reacted rapidly and at a potential about 0.5V anodic to the gold reduction wave so that it did not interfere in the measurements.

Experiments using the  $\frac{1}{2}$  in. diameter rod consistently gave transition times less than those using the  $\frac{1}{4}$  in. rod, and the wire, and with less scatter. This could be the result of a better geometry. In any event examining all the data there does not appear to be any

difference in the reduction mechanism from the three solutions and the diffusion coefficient of the reacting species is the same within the experimental error. This is expected to be the case since the reacting species is the same in all the solutions and the diffusion coefficient will vary only slightly with the activity of the ion in the solutions of different ionic strength. The average value from all the experiments with the exception of the "free floating" one provides a diffusion coefficient of  $1.8 \times 10^{-5} \text{ cm}^2 \text{ sec}^{-1}$ . The scatter in the data, however, place a possible error of  $\pm 0.35 \times 10^{-5} \text{ cm}^2 \text{ sec}^{-1}$  on this value.

There is sufficient agreement between this value for  $D$  and the literature values (6) for the diffusion coefficient of  $\text{Au}(\text{CN})_2^-$  in alkaline cyanide, citrate, and phosphate solutions to conclude that  $\text{Au}(\text{CN})_2^-$  is the reacting species and that the reason for the low  $D$  values found from the cyclic voltammetry experiment was the interference of the adsorbed intermediate in the citrate and phosphate solutions.

### Summary

**Oxidation of gold.**—The oxidation of gold in alkaline cyanide solutions is seen to be complex. It is concluded that at low overvoltages oxidation proceeds through a surface intermediate probably  $[\text{Au CN}]_{\text{ads}}$  and that the oxidation of gold in the region  $-0.6$  to  $-0.3\text{V}$  is limited by the dissolution of the surface intermediate. When the surface is completely covered the rate of reaction is controlled by the rate of chemical dissolution of the intermediate. In this work no true passive region was observed when the gold electrode was potentiostated at potentials less than  $+0.45\text{V}$  in the alkaline cyanide bath at temperatures higher than  $40^\circ\text{C}$ . The chemical dissolution reaction logically must be



At higher overvoltages a complex oxidation peak (F) was observed. In agreement with Cathro and Koch (2) it is concluded that this active region is passivated by the formation of oxide on the gold surface. The capacity of the peak does not allow assignment to the oxidation of a surface film. The results indicate that in this region gold is oxidized to a soluble species. The reaction is too complex to analyze fully at this time, but two possibilities are the direct oxidation of gold to  $\text{Au}(\text{CN})_2^-$  without the formation of an intermediate and the oxidation of gold to an  $\text{Au}(\text{III})$  complex which presumably would react with  $\text{CN}^-$  oxidizing this and being in itself reduced to  $\text{Au}(\text{CN})_2^-$ .

**Reduction of gold.**—Two reduction paths were observed. In the alkaline cyanide bath these were evident in the cyclic voltammetry curves but in the citrate and phosphate baths they were not. One reduction path was through an adsorbed intermediate and on the basis of the oxidation results this is presumed to be  $[\text{Au CN}]_{\text{ads}}$ . The other reduction path was a direct charge transfer to the soluble  $\text{Au}(\text{CN})_2^-$ . The two reduction paths may be expected to lead to electrodeposits differing in physical character.

Manuscript submitted April 30, 1971; revised manuscript received ca. July 29, 1971.

Any discussion of this paper will appear in a Discussion Section to be published in the December 1972 JOURNAL.

### LIST OF SYMBOLS

$r$	radius (cm)
$D$	diffusion coefficient ( $\text{cm}^2 \text{ sec}^{-1}$ )
$n$	number of electrons
$V$	scan rate of velocity (volts $\text{sec}^{-1}$ )
$i_p$	maximum current in a peak (A)
$A$	area of electrode ( $\text{cm}^2$ )
$C^0$	initial concentration (moles $\text{cm}^{-3}$ )
$C_s$	surface concentration (moles $\text{cm}^{-3}$ )
$t$	time (sec)
$\tau$	transition time (sec)

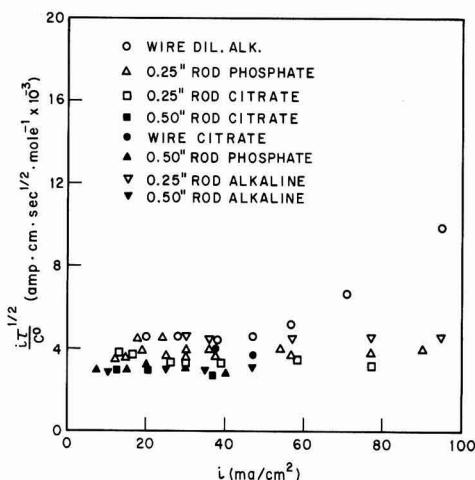


Fig. 10. Transition time plot for various Au electrodes in the citrate, phosphate, and alkaline Au plating solutions.

## REFERENCES

1. M. Maja, *Atti Accad. Sci. Torino: Classe Sci. Fis. Mat. Nat.*, **99**, 1111 (1965).
2. K. J. Cathro and D. F. A. Koch, *This Journal*, **111**, 1416 (1964).
3. L. A. Taran, S. I. Berezina, and G. S. Vozdvizhenskii, *Tr Kazan Khim in-ta*, **36**, 591 (1967). Foreign Language Center Trans. #3792.
4. R. Thacker and J. P. Hoar, *Electrochem. Technol.*, **2**, 61 (1964).
5. P. Delahay, "New Instrumental Methods in Electrochemistry," p. 122, Interscience (1954).
6. H. Y. Cheh, *This Journal*, **118**, 551 (1971).
7. J. N. Gaur and G. M. Schmid, *J. Electroanal. Chem.*, **24**, 279 (1970).
8. D. G. Peters and J. J. Lingane, *ibid.*, **2**, 1 (1961).

## Current Distribution at the Rotating Ring-Disk Electrode

G. Neubert, E. Gorman, R. Van Reet, and K. B. Prater\*

Department of Chemistry, University of Texas at El Paso, El Paso, Texas 79968

### ABSTRACT

The digital simulation method is used to calculate the current densities at both the ring and disk surfaces of a ring-disk electrode when the two surfaces are at the same potential. Simulated and experimental results show that the current density at the ring is nonuniform and measurably different from that at the disk electrode, even if the current density at the disk is assumed to be uniform. In addition, a technique is presented which allows the determination of the simulation representations of the electrode radii from experimental data.

Most treatments (1-3) of rotating disk and ring-disk electrodes have assumed that the disk is a uniformly accessible surface—that is, that the current density is uniform across the entire surface of the disk electrode. Newman (4) concluded that the current density should in fact be nonuniform at applied potentials below the limiting current. Alberly and Ulstrup (5) presented results of experiments at the ring-disk electrode in which observed collection efficiencies for the Br-Br<sub>2</sub> system deviated from those predicted by a theory based upon the assumption of uniform accessibility. This deviation was attributed to nonuniform accessibility by the authors. Marathe and Newman (6) then pointed out that the deviation observed by Alberly and Ulstrup was in the wrong direction to be attributable to nonuniform current density at the disk. It seemed to us that a more reasonable explanation for the observed deviation would be that the current efficiency at the disk was less than 100%. This has recently been confirmed by Alberly and Hitchman (7). In the same chapter (7) Alberly and Hitchman also present new ring-disk electrode data which are in agreement with Newman's treatment. These data and the data obtained by Marathe and Newman (6) and Bruckenstein and Miller (8) leave no doubt that under certain conditions nonuniform current density prevails at the disk electrode.

In response to the Alberly and Ulstrup paper (5), Marathe and Newman (6) suggested that the ring-disk electrode could be used for a quantitative study of nonuniform current distributions by applying the same potential to the disk and ring electrodes. They suggested that observed differences in the current densities at the ring and disk electrodes would be a direct measure of the nonuniformity of the current density at the disk electrode. The purpose of this paper is to present the results of digital simulation and experimental work which show that, due to the presence of the insulating gap between the ring and disk and the different boundary condition which holds there, even if the current density were uniform at the disk, a nonuniform and measurable different current density would be observed at the ring. Only in the limit as the width

of the gap approaches zero will the two current densities approach one another.

### Digital Simulation

The technique for the digital simulation of the rotating ring-disk electrode has been presented previously (3). For the purposes of this study two quantities in addition to the collection efficiency (3),  $N$ , were simulated for the reversible reaction



In order to accurately model the electrodes, it was necessary to simulate the limiting current at the ring when the disk was held at open circuit potential. This was done simply by applying the boundary condition which is used for the gap to the disk as well, and applying the usual disk boundary condition to the ring. The second simulation was that of the limiting currents and current densities at the disk and the ring when the two electrodes are shorted together and the potential is such that the limiting current is passed at the disk. In the nomenclature of Ref. (3), the boundary conditions were

$$\begin{aligned} F_A(1,1) &= F_A(1,K_R) = 0.0 \\ F_B(1,1) &= F_B(1,K_R) = 1.0 \end{aligned} \quad [2]$$

The dimensionless disk current parameter,  $ZD$ , which is calculated by this technique is

$$ZD = i_d / (0.51)^{1/3} n F A_d C^{\circ} A D_A^{2/3} \omega^{1/2} \nu^{-1/6} \quad [3]$$

where  $i_d$  is the limiting current at the disk,  $n$  is the number of electrons transferred per molecule,  $F$  is the Faraday,  $A_d$  is the area of the disk,  $C^{\circ} A$  is the bulk concentration of species  $A$ ,  $D_A$  is the diffusion coefficient of  $A$ ,  $\omega$  is the rotation rate, and  $\nu$  is the kinematic viscosity. Notes that  $ZD$  is proportional to the current density at the disk.

The dimensionless ring current parameter,  $ZR$ , which is calculated by this technique (3) is

$$ZR = i_r / (0.51)^{1/3} n F A_d C^{\circ} A D_A^{2/3} \omega^{1/2} \nu^{-1/6} \quad [4]$$

where  $i_r$  is the limiting ring current. When  $ZR$  is multiplied by the ratio of the area of the disk to the area of the ring,  $A_r$ , a new parameter,  $ZRN$ , is generated

\* Electrochemical Society Active Member.

Key words: ring-disk electrode, current distribution, uniform current density.

Table I. Dependence of current density ratio on width of gap

Width of gap <sup>(a)</sup>	CDR <sup>(b)</sup>
40	1.54
20	1.34
10	1.20
1	1.03

<sup>(a)</sup> Arbitrary units.

<sup>(b)</sup> Current density ratio— $(i_r/A_r)/(i_d/A_d)$ .

which is proportional to the average ring current density.

$$ZRN = i_r / (0.51)^{1/3} n F A_r C^{\circ} A_d^{2/3} \omega^{1/2} \nu^{-1/6} \quad [5]$$

Note that the ratio of ZRN to ZD is the ratio of average current density at the ring to the current density at the disk when the two are shorted together. That is

$$CDR = ZRN/ZD = (i_r/A_r)/(i_d/A_d) \quad [6]$$

Thus for a given electrode, three experimentally measurable parameters were calculated (i) the ratio of the limiting ring current with the disk inactive to the limiting disk current, (ii) the collection efficiency (3), and (iii) the ratio of the average current density at the ring to the current density at the disk when the two electrodes are shorted.

### Simulation Results

The simulated ratio of the average current density at the ring to the current density at the disk when the two electrodes are shorted together is presented in Table I for a series of electrodes differing only in the width of the gap. For these calculations, the radius of the disk was, in each case, 99.5 units, the width of the ring was 25 units, and the width of the gap was varied as shown in Table I. The current densities were calculated using the same boundary conditions at the ring and disk and assuming uniform current density at the disk.

As might be expected, the average ring current density approaches the disk current density as the thick-

ness of the gap approaches zero. As the gap is made wider, the average current density gets larger and would be expected to approach that for a ring electrode alone.

The current density profile for each of the electrodes is presented in Fig. 1. Again the results are as might be expected with a uniform current density being approached only as the width of the gap approaches zero.

### Experimental

All chemicals were reagent grade and used without further purification. The potentiostat which was used for limiting current measurements was a Werking Model 66TS10 and the recorder was a Hewlett Packard 7004A X-Y with 17171A d-c preamp plug-ins. For collection efficiency measurements, a constant current source with a floating power supply and utilizing Analog Devices operational amplifiers was used to supply the disk current. The platinum ring-disk electrodes were obtained from Pine Instruments, Grove City, Pennsylvania, and were rotated with a Motomatic E-550 motor with feedback controller modified to operate up to 10,000 rpm which was obtained from Electro Craft, Hopkins, Minnesota. All experiments were carried out at room temperature.

Before each run, the electrodes were pretreated by rotating them in an acid dichromate solution for 60 sec, rinsing with distilled water and drying. With this procedure, limiting currents could be reproduced within  $\pm 0.5\%$ . Measurements of the collection efficiency were made by applying a constant current to the disk electrode and determining the limiting current at the ring.

### Results and Discussion

Measurements were made on two electrodes. One, electrode A, had a relatively thin gap while the other, electrode B, had a much wider gap. The collection efficiencies of these electrodes were determined for solutions which were  $1 \times 10^{-3}M$  in  $K_3Fe(CN)_6$  and  $2M$  in KCl. The results are presented in Table II. In all runs, the current applied to the disk was less than the limiting current.

Next, the limiting disk current,  $i_{d0}$ , limiting ring current with the disk at open circuit,  $i_{r0}$ , and the limiting current with the disk and ring shorted together,  $i_{rth}$ , were measured in succession in the same solution. This procedure was repeated at rotation rates varying from 100 to 5000 rpm.

The ratio of  $i_{r0}$  to  $i_{d0}$  and the collection efficiency were used to determine the radius of the outer edge of the gap,  $r_2$ , and the radius of the outer edge of the ring,  $r_3$ , relative to the radius of the disk,  $r_1$ . This was done by simulating these two parameters for various values of the simulation representation of these radii, IR1, IR2, and IR3. A value of IR1 was selected and the parameters IR2 and IR3 were adjusted until the simulated values of  $i_{r0}/i_{d0}$  and the collection efficiency were in satisfactory agreement with the experimental values. Since (3)

$$IR1 - 0.5 = r_1 \Delta r \quad [7]$$

and

$$IR2 - 0.5 = r_2 \Delta r \quad [8]$$

$$(IR2 - 0.5)/(IR1 - 0.5) = r_2/r_1 \quad [9]$$

Table II. Experimental collection efficiencies

$\omega$ (a)	Electrode A		Electrode B	
	N	Runs	N	Runs
500	0.569 $\pm$ 0.005	15	0.452 $\pm$ 0.003	17
1000	0.569 $\pm$ 0.004	31	0.449 $\pm$ 0.002	9
2000	0.570 $\pm$ 0.004	14	0.450 $\pm$ 0.003	11
3000	0.563 $\pm$ 0.005	14	0.450 $\pm$ 0.002	10
4000	0.563 $\pm$ 0.004	14	0.450 $\pm$ 0.003	8
5000	0.561 $\pm$ 0.004	23	0.448 $\pm$ 0.002	20
Avg.	0.566 $\pm$ 0.005		0.450 $\pm$ 0.003	

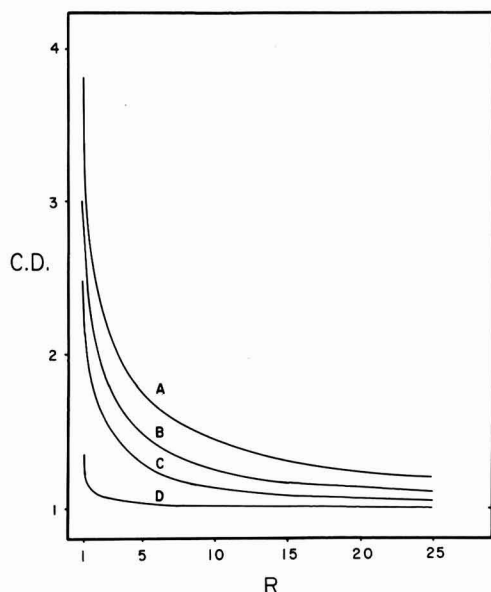
<sup>(a)</sup> Rotation rate, rpm.


Fig. 1. Ring current density profile for electrodes in Table I. Ring and disk are shorted together. R is the distance from the inner edge of the ring. C.D. is the ring current density at each point normalized by the disk current density. The width of the gaps are: A = 40, B = 20, C = 10, D = 1.



Table III. Experimental and simulated collection efficiencies and limiting current ratios

	Electrode A N $i_{ro}/i_d$		Electrode B N $i_{ro}/i_d$	
Experimental	0.566 ± 0.005	3.21 ± 0.04	0.450 ± 0.003	2.56 ± 0.03
Simulated	0.566	3.20	0.448	2.56

IR1 = 83, IR2 = 92, IR3 = 159      IR1 = 83, IR2 = 104, IR3 = 151

and similarly

$$(IR3 - 0.5)/(IR1 - 0.5) = r_3/r_1 \quad [10]$$

In a similar manner, it is found that the ratio of the area of the ring to the area of the disk,  $A_r/A_d$  is given by

$$A_r/A_d = [(IR3 - 0.5)^2 - (IR2 - 0.5)^2]/(IR1 - 0.5)^2 \quad [11]$$

Note that in order to determine  $r_2$  and  $r_3$  explicitly,  $r_1$  would have to be determined independently. This is not necessary for this work. The experimental results and best fit simulation results are presented in Table III.

With satisfactory values of IR1, IR2, and IR3 determined, it was then possible to calculate the expected values of the ratio of the average current density at the ring,  $i_{rs}/A_r$ , to the current density at the disk,  $i_d/A_d$ , when the ring and disk are shorted together for each of the two electrodes for which data were available. The experimental values of  $i_{rs}$  were obtained by subtracting the measured  $i_d$  from  $i_{rd}$ , the total ring and disk current. The ratio  $i_{rs}/i_d$  when multiplied by  $A_d/A_r$ , the reciprocal of Eq. [11], yields the experimental ratio of the current densities, CDR. The agreement between the experimental and simulated current density ratios is shown in Table IV.

### Conclusion

It has been shown that the current density at the ring electrode when shorted to the disk electrode is nonuniform even if the current density at the disk is uniform as it is at the limiting current. The digital simulation technique has been shown to accurately

Table IV. Experimental and simulated current density ratios

	Electrode A	Electrode B
Experimental	1.07 ± 0.01	1.21 ± 0.02
Simulated	1.07	1.20

calculate the average current density at the ring when the current density at the disk is uniform. It is expected that a nonuniform current density at the disk would give rise to measurably different average current densities at the ring under these conditions and that such a technique should be valuable in measuring such nonuniformity. The digital simulation of this case is now being undertaken.

### Acknowledgments

The authors wish to thank the Research Corporation and the University Research Institute of the University of Texas at El Paso for financial support of this work.

Manuscript submitted Nov. 3, 1971; revised manuscript received ca. Nov. 22, 1971.

Any discussion of this paper will appear in a Discussion Section to be published in the December 1972 JOURNAL.

NOTE ADDED IN PROOF: Newman has recently obtained similar results with an essentially analytical solution. See *This Journal*, 119, 212 (1972).

### REFERENCES

1. V. G. Levich, "Physicochemical Hydrodynamics," Prentice-Hall, Inc., Englewood Cliffs, N. J. (1962).
2. W. J. Albery and S. Bruckenstein, *Trans. Faraday Soc.*, **62**, 1920 (1966).
3. K. B. Prater and A. J. Bard, *This Journal*, **117**, 207 (1970).
4. J. Newman, *ibid.*, **113**, 1235 (1966).
5. W. J. Albery and J. Ulstrup, *Electrochem. Acta*, **13**, 281 (1968).
6. V. Marathe and J. Newman, *This Journal*, **116**, 1704 (1969).
7. W. J. Albery and M. L. Hitchman, "Ring-Disc Electrodes," Oxford University Press, London (1971).
8. S. Bruckenstein and B. Miller, *This Journal*, **117**, 1044 (1970).

## Electrode Kinetic Studies on Electro-Organic Syntheses Involving Carbonium Ions

### I. Anodic Oxidation of Acetate Ions to Methyl Acetate

Ashok K. Vijh\*

Hydro-Quebec Institute of Research, Varennes, P. Q., Canada

### ABSTRACT

Anodic electrosynthesis of methyl acetate on graphite electrodes in aqueous acetate solutions is known to proceed via intermediate formation of carbonium ions. Kinetic-mechanistic aspects of this reaction have not been examined previously and an attempt has been made in the present investigation to elucidate these aspects by carrying out electrode kinetic studies. Potentiostatic Tafel plots, potentiodynamic profiles, anodic charging curves, open-circuit potential decay measurements, capacity-potential relationships, apparent heats of activation, and reaction order derivatives are reported for this system. On the basis of an analysis of these data, it has been suggested that initial discharge step is the rate-determining step (r.d.s.) in the over-all reaction. Possible explanation for the occurrence of a carbonium ion pathway, in preference to a radical one as observed for the Kolbe reaction, in the present case is also put forward.

An interesting aspect of modern work in synthetic organic chemistry is the elucidation of the role of radicals and radical ions in various syntheses. This

problem also arises in some electro-organic syntheses in which it has been observed that radicals (1) or carbonium ions (2) can play an important role as reactive intermediates. If one considers the anodic oxidation of acetate ions in aqueous solutions on a platinum

\* Electrochemical Society Active Member.

Key words: carbonium ions, electro-organic synthesis, electrode kinetics, anodic oxidation, acetate ions.

electrode, one observes that ethane and carbon dioxide are formed in the over-all reaction



This reaction, called the Kolbe reaction, is known to proceed in several steps and is believed (1, 2) to occur by intermediate formation of radicals. When one conducts the anodic electrolysis of the aqueous acetate solutions on a graphite electrode, however, one does not obtain the usual Kolbe products but instead, methyl acetate is formed as the major product with a yield (2) of ca. 82%. The over-all reaction in this case is



Several investigators, notably Corey and co-workers (3, 4) and Koehl (5) have presented a great deal of evidence to show that the over-all reaction in Eq. [2] involves intermediate formation of carbonium ions. In several other related anodic electrosyntheses, Ross and co-workers (2) have postulated the intermediate formation and participation of carbonium ions.

Despite a great deal of synthetic work (2-5) on electro-organic syntheses involving carbonium ions, no electrode kinetic studies seem to have been carried out. The purpose of the present series of studies is to examine the electrode kinetic features of electro-organic syntheses involving carbonium ions, on the basis of general approaches applied earlier to the Kolbe reaction (1). The aim would be to present new electrochemical evidence and an associated kinetic analysis that will seek to examine the nature of various elementary steps involved in the over-all reaction as well as the identity of the rate determining step (r.d.s.) in a likely reaction pathway. An attempt will also be made to establish the nature and role of any adsorbed reaction intermediates that might be involved in the over-all reaction. It is believed that such electrode kinetic studies will provide vital information, supplementary to the previous synthetic work (2-5), needed to formulate a kinetic-mechanistic picture of electro-syntheses involving carbonium ions. It is hoped that a somewhat better understanding of the various aspects of these electrode processes thus developed will perhaps aid in the further explorations of electro-organic syntheses involving carbonium ions.

### Experimental Section

The instruments and the cell employed as well as the details on electrodes, gas purification, preparation of conductivity water, cell cleaning, etc. have been described recently (6). The general electrode kinetic approaches used in the present work were reviewed previously (1).

All electrode potentials expressed here are against a hydrogen reference electrode in the same solution. No pre-electrolysis was conducted in the present work since it was noted previously (1) that in electro-organic work pre-electrolysis tends to produce rather than remove traces of impurities.

All solutions were made from potassium acetate (Fisher, A.C.S. certified, mol. wt. 98.15), acetic acid (Fisher reagent, 99.7%), and conductivity water.

### Results

**Steady-state current-potential relationships.**—In Fig. 1, steady-state (point-by-point) potentiostatic current-potential relationships for the anodic oxidation of acetate ions on graphite electrodes in aqueous acidic solutions have been presented. An hysteresis between the ascending and descending curves is observed which is not entirely unexpected for anodic reactions (7). A Tafel slope of ca.  $2.3 \times 2RT/F$  is observed at higher anodic potentials, whereas Tafel lines showing higher slopes are indicated below 1.8V. Some rudimentary inhibition inflections, of the type discussed by Gilroy and Conway (8) may also be noted, around 0.5V on the ascending curve and around 1.3V on the descending

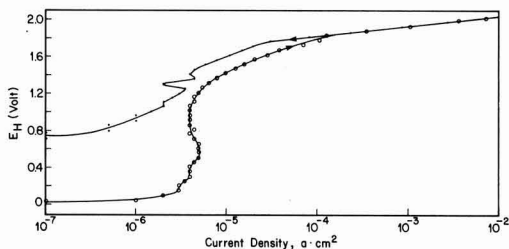


Fig. 1. Potentiostatic, steady-state (point-by-point) Tafel relationships on a graphite electrode in aqueous acetate solutions, both in the ascending and descending direction of potentials. The

Tafel slope at the high anodic potentials is ca.  $2.3 \times \frac{2RT}{F}$ . Solution is 5N  $\text{CH}_3\text{COOK} + 1\text{N } \text{CH}_3\text{COOH}$  in water. Room temperature. Time of polarization at every point is 2 min.

curve. The change in Tafel slopes around 1.8 would indicate two parallel mechanisms (7).

**Temperature effects on the rate.**—In Fig. 2 (a) and 2 (b), effect of temperature on the ascending and descending, respectively, Tafel plots has been represented. Only the linear Tafel regions have been shown. It is seen that the potential at which the two Tafel lines with different slopes intersect depends on the temperature, i.e., at higher temperature the change in the slope of the Tafel line, and the associated shift over to an alternative parallel mechanism, tends to occur at lower electrode potentials. This is not at all unexpected since temperature and potential both drive

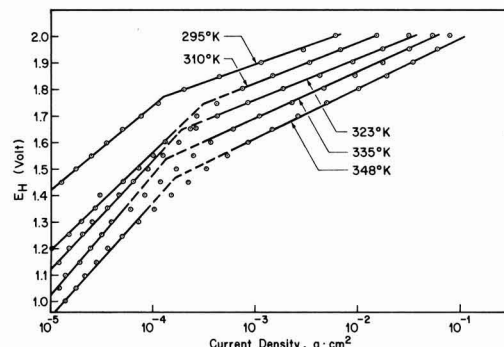


Fig. 2 (a). Tafel plots at the shown temperatures taken in the ascending direction of potentials. Graphite anode in 2N  $\text{CH}_3\text{COOK} + 1\text{N } \text{CH}_3\text{COOH}$ . Time of polarization at every potential is 2 min.

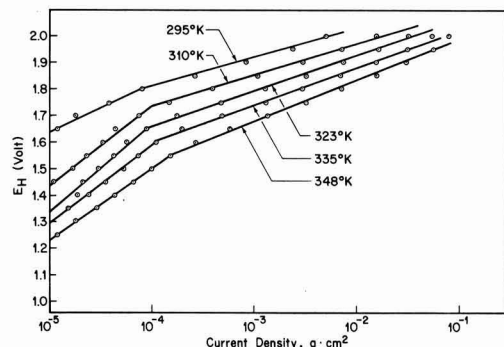


Fig. 2 (b). Same as Fig. 2 (a) but now taken in the descending direction of electrode potentials.

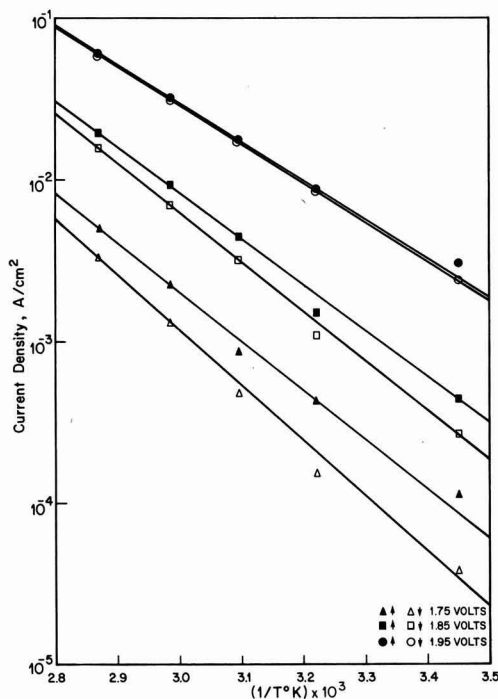


Fig. 3. The current density vs.  $1/T$  (where  $T$  is the absolute temperature) plots adopted from Fig. 2 (a) and 2 (b) in order to determine the apparent heat of activation. The  $\Delta H^*$  values lie between ca. 10 and 16.5 kcal depending on the electrode potential.

the reaction in the same direction, i.e., higher rates at higher values of potential or temperature.

The electrochemical Arrhenius plots at some typical electrode potentials, as derived from Fig. 2 (a) and 2 (b) have been presented in Fig. 3. It is seen that the apparent heat of activation as given by the differential,  $\left(\frac{\delta \log i}{\delta (1/T)}\right)_{\eta, \psi, T, \dots}$ , lies between ca. 10.6 and 16.6 kcal depending on the electrode potential.

**Reaction orders.**—An important parameter in the modern electrode kinetic analysis is recognized to be the electrochemical reaction order (7, 9). In the present work, the potentiostatic current-potential curves were studied at various acetate concentrations, both in the ascending [Fig. 4 (a)] and the descending [Fig. 4 (b)]

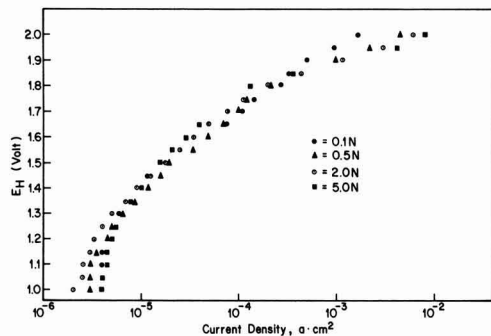


Fig. 4 (a). Tafel plots taken in the ascending direction of potentials in the following solutions: ● 0.1N  $\text{CH}_3\text{COOK} + 1\text{N}$   $\text{CH}_3\text{COOH}$ ; ▲ 0.5N  $\text{CH}_3\text{COOK} + 1\text{N}$   $\text{CH}_3\text{COOH}$ ; ○ 2.0N  $\text{CH}_3\text{COOK} + 1\text{N}$   $\text{CH}_3\text{COOH}$ ; ■ 5.0N  $\text{CH}_3\text{COOK} + 1\text{N}$   $\text{CH}_3\text{COOH}$ .

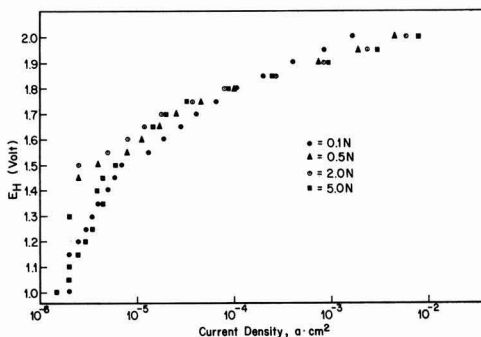


Fig. 4. (b). Same as Fig. 4 (a) but now taken in the descending direction of electrode potentials.

directions of the electrode potential. An attempt was made to deduce the reaction order derivative,  $\left(\frac{\delta \log i}{\delta \log C_{\text{CH}_3\text{COO}}}\right)_{\eta, \psi, T, \dots}$ , from these plots [Fig. 4 (a) and (b)] and the results are presented in Fig. 5. At lower potentials, the reaction order tends to be zero whereas at 2.0V, it is observed that

$$\left(\frac{\delta \log i}{\delta \log C_{\text{CH}_3\text{COO}}}\right)_{\eta, \psi, T, \dots} \approx 0.4$$

**Potentiodynamic profiles.**—No peaks were observed in the potentiodynamic profiles taken over a wide range of sweep rates. A typical potentiodynamic profile (1, 7) is shown in Fig. 6. Absence of peaks would preliminarily suggest absence of significant change in the electrode coverage in the potential range scanned as well as absence of diffusion-controlled oxidation-reduction of redox type species in the solution.

**Open-circuit decays.**—Open-circuit decay profiles triggered from various initial steady-state potentials show absence of any arrests. Typical results are given in Fig. 7. This would tend to confirm the conclusions deduced from the potentiodynamic profiles, namely,

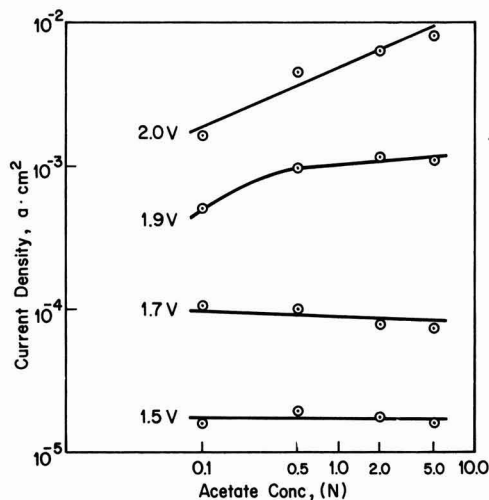


Fig. 5. Log [current density] vs. log. [acetate ion concentration] plot adopted from Fig. 4 (a). The  $\left(\frac{\delta \log i}{\delta \log C}\right)$  value at 2.0V is ca. 0.4 whereas at lower potentials these values approach zero. Essentially similar results are obtained when one constructs this plot from Fig. 4 (b).

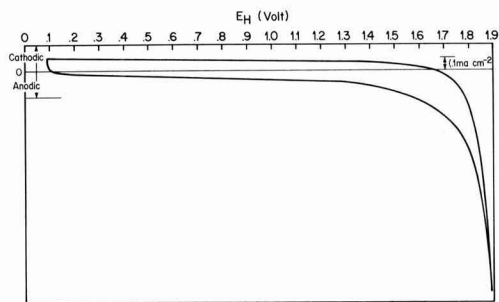


Fig. 6. A typical potentiodynamic profile on graphite in 2N  $\text{CH}_3\text{COOK} + 1\text{N CH}_3\text{COOH}$ . Sweep speed,  $5 \text{ mV sec}^{-1}$ . Absence of peaks may be noted. No peaks are observed even when one changes the sweep rate by several orders of magnitude.

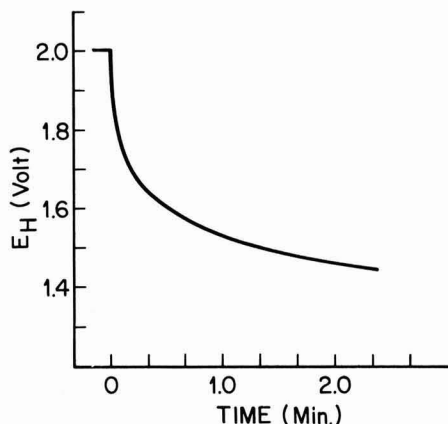


Fig. 7. A typical open-circuit potential decay profile for a graphite anode in 2N  $\text{CH}_3\text{COOK} + 1\text{N CH}_3\text{COOH}$ . Absence of arrests may be noted.

absence of significant electrode coverage by electroactive species in the steady state.

**Charging curves.**—In order to examine the possibility of coverage by adsorbed intermediates further, anodic charging curves were recorded at various current densities. Clear-cut arrests were again not observed although at low charging current densities, some incipient changes of slope in the charging curve were observed (Fig. 8). An electrode capacity-potential profile calculated from a typical charging curve (Fig. 8) is presented in Fig. 9 in which no clear-cut capacity maxima or minima, possibly diagnostic of changes of the electrode coverage during the transient, are observed. The maximum values of the differential capacity in this Fig. 9 would suggest the presence of some adsorption pseudocapacitance even when one takes into account the fact that the graphite electrodes have a very large ratio of real to geometric area (this ratio being unknown) and that such electrodes can uptake significant amounts of adsorption (6). The values of differential capacity in Fig. 9, however, cannot perhaps be taken as a sufficient evidence for the presence of significant amounts of adsorbed intermediates in the steady state. A consideration of the peculiarities of the graphite electrode (6) as well as the evidence in Fig. 6-8 would tend to indicate rather strongly that the anodic formation of methyl acetate in the present study probably proceeds without involving significant coverage by the adsorbed intermediates during the steady-state electrolysis.

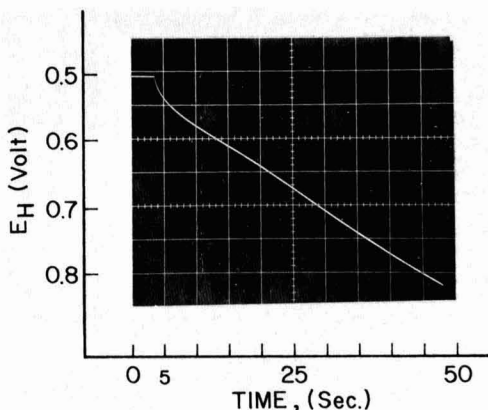


Fig. 8. An anodic charging curve (charging current density =  $27.6 \mu\text{A cm}^{-2}$ ) triggered from the rest potential (0.5V). Graphite in 2N  $\text{CH}_3\text{COOK} + 1\text{N CH}_3\text{COOH}$ . Although an incipient arrest is indicated, significant coverage of the electrode during steady-state electrolysis is not concluded on the basis of discussion in the text. This incipient arrest does not become more pronounced, but rather tends to disappear, when one changes the charging current density.

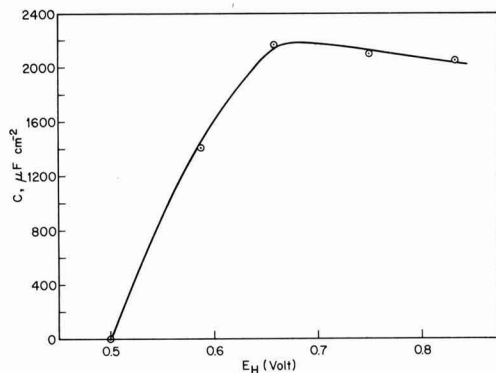
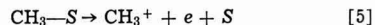
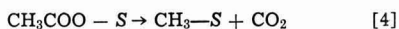


Fig. 9. A capacity-potential profile constructed from Fig. 8

## Discussion

The anodic formation of methyl acetate by an over-all two-electron reaction (i.e., Eq. [2]), which is known to proceed via intermediate formation of carbonium ions (2-5) may be assumed to involve the following elementary steps



Here, S, denotes the graphite electrode surface on which the reaction occurs.

A value of Tafel slope equal to  $2.3 \times 2RT/F$  and absence of a significant amount of electrode coverage in the steady state, as observed in this investigation, would indicate rather unambiguously that the initial discharge step (i.e., Eq. [3]) is the likely rate-determining step (r.d.s.) in the over-all reaction (1, 7), at least above 1.8V. The rate equation for this case in concentrated solutions ( $\psi \rightarrow 0$ ) may be written as

$$i = k(1 - \theta) \text{C}_{\text{CH}_3\text{COO}^-} e^{e\eta F/RT} \quad [7]$$

Where  $i$  is the current;  $\theta$ , the electrode coverage;  $k$ , a combination of constants;  $\text{C}_{\text{CH}_3\text{COO}^-}$ , the concentration

of acetate ions;  $\beta$ , the charge transfer symmetry factor;  $\eta$ , the anodic over potential;  $F$ , the Faraday;  $R$ , the gas constant; and,  $T$ , the absolute temperature. Since the coverage,  $\theta$ , is observed to approach zero, one may write Eq. [7] as

$$i = k C_{\text{CH}_3\text{COO}^-} e^{\beta n F / RT} \quad [8]$$

$$\text{or } \left( \frac{\delta \eta}{\delta \log i} \right) = 2.3 \times \frac{2RT}{F} = \text{Tafel slope}$$

The reaction order expected would be

$$\left( \frac{\delta \log i}{\delta \log C_{\text{CH}_3\text{COO}^-}} \right) = 1$$

This predicted reaction order, however, is not in agreement with the observed value ( $\approx 0.4$  at high anodic potentials) and the source of this discrepancy is not clear, although some tentative explanations can be put forward (see below).

The heats of activation observed (Fig. 2, 3) are quite high ( $> 10$  kcal mole $^{-1}$ ), which would qualitatively tend to support the mechanism suggested here, by analogy with the case of hydrogen evolution reaction.

On the basis of reaction order evidence (Fig. 4, 5) alone, it would appear attractive to suggest that a step subsequent to the initial discharge is perhaps the r.d.s. However, other evidence such as the Tafel slopes, lack of appreciable coverage as deduced from the transient studies, and rather high heat of activation would tend to support quite strongly the mechanistic proposal put forward here, namely, initial discharge as the r.d.s.

It appears interesting to speculate here on the possible reasons for the formation of carbonium ions, and thence methyl acetate, on graphite electrodes in contrast to the occurrence of the Kolbe reaction on platinum electrodes in the electrolysis system investigated here. Since the strength of  $\text{Pt}-\text{CH}_3$  and  $\text{C}-\text{CH}_3$  bonds, as estimated by the Pauling equation, is nearly identical (10), the explanation would seem to lie elsewhere. It has been pointed out by Ross (10) that the graphite electrodes possess paramagnetic centers on which the methyl radicals are probably bound ultra-strongly. If this suggestion is assumed to be correct, it is easy to see that the second electron transfer from

the adsorbed methyl radical, to give the carbonium ion, is more facile than the alternative path demanding desorptive coupling of the methyl radicals.

Although a clear-cut interpretation of the observed reaction orders seems difficult, a possible explanation may be mentioned. Fractional reaction orders of this magnitude would be expected if one invokes the presence of competing reactions, a situation consistent with the present case in which the efficiency of formation of methyl acetate is substantially less than 100%. This suggestion is particularly emphasized by the direction of the abrupt changes in slopes of the Tafel lines [Fig. 1, 2 (a) and 2 (b)], so characteristic of a change over to a parallel reaction or a parallel rate-determining step within the same reaction (7).

### Acknowledgments

The author is grateful to Mr. R. Jacques for carrying out the experimental work. Dr. G. Bélanger is thanked for some discussions during the progress of the work. Thanks are also due to Dr. P. Lenfant for his interest and encouragement.

Manuscript submitted Nov. 22, 1971; revised manuscript received Dec. 28, 1971.

Any discussion of this paper will appear in a Discussion Section to be published in the December 1972 JOURNAL.

### REFERENCES

1. A. K. Vijh and B. E. Conway, *Chem. Rev.*, **67**, 623 (1967).
2. S. D. Ross, *Trans. N. Y. Acad. Sci.*, **30**, 901 (1968).
3. E. J. Corey, N. L. Bauld, R. T. LaLonde, J. Casanova, Jr., and E. J. Kaiser, *J. Am. Chem. Soc.*, **82**, 2645 (1960).
4. E. J. Corey and J. Casanova, Jr., *ibid.*, **85**, 165 (1963).
5. W. J. Koehl, Jr., *ibid.*, **86**, 4684 (1964).
6. A. Bélanger, G. Bélanger, and A. K. Vijh, *This Journal*, **118**, 1543 (1971).
7. B. E. Conway "Theory and Principles of Electrode Processes," Ronald Press Co., New York (1965).
8. D. Gilroy and B. E. Conway, *J. Phys. Chem.*, **69**, 1259 (1965).
9. K. V. Vetter, "Electrochemical Kinetics," Academic Press, New York (1967).
10. S. D. Ross and M. Finkelstein, *J. Org. Chem.*, **34**, 2923 (1969).



# Surface Concentration of Molybdenum in Types 316 and 304 Stainless Steel by Auger Electron Spectroscopy

G. J. Barnes, A. W. Aldag, and R. C. Jerner

School of Chemical Engineering and Materials Science, University of Oklahoma, Norman, Oklahoma 73069

## ABSTRACT

Auger electron spectroscopy has been used to determine surface concentrations of Mo in Types 304 and 316 stainless steel. The technique involved was  $\text{Ar}^+$  bombardment removal of the stainless surface with alternate monitoring of the height of the 190 eV Mo peak. Surface concentrations of 14% were observed in mill-finished Type 316 containing 1.95% bulk Mo. Surface segregation of Mo was also observed in Type 304 containing 0.45% Mo impurity.

The effect of minor Mo additions on the corrosion resistance of 18-8 Type stainless steels is well established (1) and has led to increased utilization of molybdenum-bearing (2-4% Mo) stainless steels, especially in saline environments. The role of Mo in enhancing corrosion resistance has not been established because of a lack of information about the surface composition. Indeed, due to diffusion from the bulk, concentrations in the surface phase may be quite distinct from that in the bulk. Using Auger electron spectroscopy (AES), Harris (2), Haas (3), and Sickafus (4) have shown that certain thermal treatments can be used to concentrate bulk impurities at a free surface. In the case of 3340 steel, sulfur was observed (2) to concentrate at the surface after a short time at 330°C.

In the present studies, AES has been used to determine the concentration of Mo from the surface into the bulk of Types 316 and 304 stainless steel. Surface concentration of 14% was observed in mill-finished Type 316 containing 1.95% Mo. Surface segregation was also observed in Type 304 containing 0.45% Mo impurity.

## Review of Auger Spectroscopy

The technique of auger electron spectroscopy is not new (5) although its application to surface studies is relatively recent (6). The Auger electron emission process is analogous to x-ray emission from an excited atom and, in fact, the processes often occur simultaneously in a given experiment. When an inner core vacancy of an atom is neutralized by absorption of an electron from one of the outer shells either an x-ray or an Auger electron with a precise energy will be emitted from the sample (Fig. 1).

In applying AES to surface studies, the initial inner core vacancy is created by electron bombardment of the surface with 1-3 keV electrons. The secondary Auger electrons have energies typically between 0 and 1000 eV, and only those electrons coming from within a few monolayers of the surface escape with a well-defined energy (7). The Auger energy levels of many of the metals and typical surface contaminants are known and the values agree quite well with the x-ray values tabulated by Hill *et al.* (8).

The interest in Auger spectroscopy as applied to surface studies evolved from the early low energy electron diffraction (LEED) experiments of Lander (9). In analyzing the energy distribution for secondary electrons emitted by a solid surface, he attributed the small peaks to Auger transitions in the solid and suggested that the characteristic energies of these peaks could be used for qualitative surface chemical analysis. The peaks were, however, small and difficult to detect

within the broad, rather uniform background distribution. Harris (6) subsequently suggested that since the background was indeed relatively uniform, detection of Auger peaks could be greatly enhanced by electronically differentiating the energy distribution. This technique brought AES into its current prominence as a valuable tool for surface studies. Subsequent refinements were made by Palmberg (10) who demonstrated that the sensitivity for atoms at the surface could be enhanced by using a grazing incidence primary beam and that the energy resolution could be improved by replacing the old 3-grid LEED optics by a 4-grid system. Palmberg also confirmed experimentally that the low energy (<200 eV) Auger electron escape depth was of the order of 4-8 Å. The minimum sensitivity for surface impurities has been estimated to be a few per cent of a monolayer (11).

More recently AES experiments are being performed independent of LEED studies. In principle, since the Auger process involves inelastic collisions with the surface, a well-defined crystal geometry as required by LEED is not a prerequisite for AES. A new cylindrical mirror analyzer (12) with a coaxial electron gun provides a simple electron optics system with precise energy discrimination. This system can be adapted to most conventional ultrahigh vacuum chambers and AES experiments performed in conjunction with other types of surface studies. An example of the Auger spectra obtained from a stainless steel surface using PEL Cylindrical Analyzer is shown in Fig. 2. The various surface components are noted on the trace.

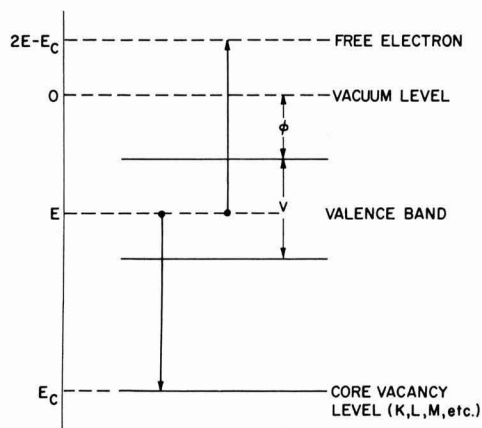


Fig. 1. Auger electron emission from an excited atom.  $\Phi$ , work function,  $V$ , width of the valence band,  $E_c$ , energy of the core electron level,  $E$ , original energy of the emitted electron.

Key words: segregation, corrosion, concentration gradient.

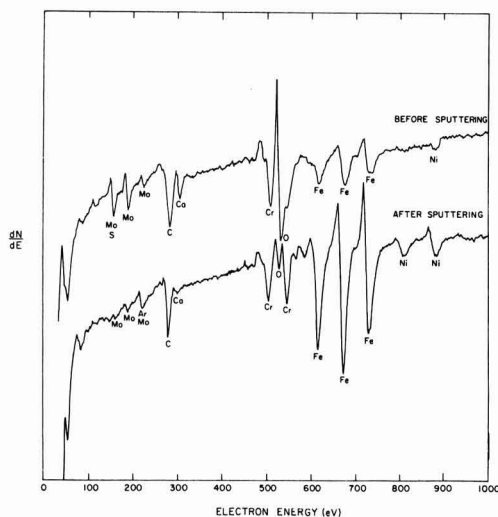


Fig. 2. (Upper) Auger electron spectrum of stainless steel before sputtering,  $V_B = 2000$  eV. (Lower) Auger electron spectrum of stainless steel after sputtering,  $V_B = 2000$  eV.

### Experimental Procedure

Types 304 and 316 mill-finished stainless steel sheet 0.050 in. thick, was used in this investigation. Specimens were washed with detergent, rinsed in distilled water, acetone, trichloroethylene, and acetone, and then dried with a lintfree cloth. The samples were then placed in an ion and titanium sublimation-pumped vacuum chamber, which was evacuated and then baked at 250°C for 6 hr. The system was rough-pumped, oil-free, using zeolite-filled cryosorption pumps. Pressure, as indicated by a nude ionization gauge, was in the low  $10^{-9}$  Torr range. An initial Auger spectrum was recorded and is shown in Fig. 2 (upper). This spectrum is representative of a surface cleaned in the manner described above but prior to electron or  $Ar^+$  bombardment. The ion pump was then deactivated and Ar was admitted to a sputtering pressure of  $1 \times 10^{-4}$  Torr. Titanium sublimation pumps were activated during the entire sputtering sequence in order to maintain Ar purity. After sputtering for a predetermined time, usually 15 sec, the ion pump was again activated, resulting in a rapid pressure reduction into the  $10^{-9}$  Torr range. The sample was then repositioned, by simple rotation, in front of the cylindrical mirror analyzer for Auger analysis. A spectrum was recorded next, and the sample was repositioned for additional sputtering. This sequence was repeated until the Auger spectra remained unchanged with additional sputtering. A spectrum taken after long-term sputtering is also shown in Fig. 2 (lower). It should be noted that the 190 eV Mo peak has been significantly reduced by sputtering from that in Fig. 2 (upper). The repetitive nature of several Auger spectra after long sputtering times demonstrates that the procedures used to reposition the sample were reproducible, and the spectra obtained are representative of the bulk composition (13).

### Results

The Auger spectrum for pure Mo is shown in Fig. 3. The major 190 eV Mo peak (14), corresponding to a  $M_5N_5$  (15) transition, was used to monitor the molybdenum concentration on the stainless steel surface as a function of sputter time. Assuming a unity removal coefficient (16), sputtering times were converted to atom layers removed. The resulting concentration gradients are shown in Fig. 4. As mentioned before, the values of the Mo concentration were obtained from stainless steel spectra after various sputter-

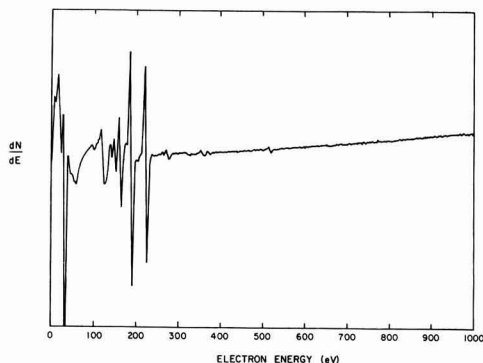


Fig. 3. Auger electron spectrum of pure molybdenum,  $V_B = 2000$  eV.

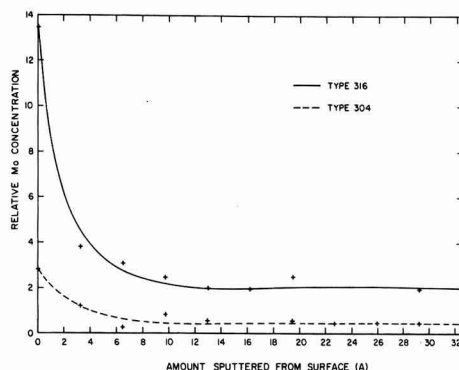


Fig. 4. Relative molybdenum concentration vs. amount of material removed in Types 304 and 316 stainless steel.

ing times. It is also assumed that the Auger spectrum obtained after long sputtering time is representative of the bulk concentration. If the Auger peak height is taken to be directly proportional to the concentration of atoms present (17), the minimum surface concentration can be estimated. These assumptions result in a surface concentration of 14-15% and 3-4% for Types 316 and 304, respectively. The initial 190 eV peak height is undoubtedly obtained from a surface which contains a carbonaceous deposit resulting from the pre-treatment and cleaning steps (18). Thus, the observed initial Mo concentration may be somewhat less than the actual values due to this overlayer.

The results shown in Fig. 4 indicate that Mo concentrates at the surface of mill-processed stainless. Surface segregation is observed even in Type 304 where Mo is present as an impurity. As the surface is removed by  $Ar^+$  bombardment, the major Mo Auger peak decreases in height to a value representative of the bulk concentration.

### Conclusions

It has been found that mill processing tends to concentrate Mo at the surface of Types 304 and 316 stainless steel. This surface segregation has been brought about in some manner by mill processing. Subsequent thermal or mechanical processing would disturb this surface concentration and in all probability result in the surface concentration of Mo being dependent on treatment. Thus any property, such as corrosion resistance, that is dependent on the presence of Mo might be altered significantly. Much of the scatter observed in corrosion tests on Types 304 and 316 stainless might be attributable to differences in molybdenum surface concentrations brought about by variations in thermal-

mechanical processing as well as other metallurgical factors.

### Acknowledgment

This investigation was conducted with funds provided by National Science Foundation Grant GY 8964.

Manuscript submitted Sept. 8, 1971; revised manuscript received Dec. 17, 1971.

Any discussion of this paper will appear in a Discussion Section to be published in the December 1972 JOURNAL.

### REFERENCES

1. M. G. Fontana and N. D. Greene, "Corrosion Engineering," p. 57, McGraw-Hill, New York (1967).
2. L. A. Harris, *J. Appl. Phys.*, **39**, 1428 (1968).
3. T. W. Haas and G. J. Dooley, III, *J. Metals*, **22**, 17 (1970).
4. E. N. Sickafus, *Surface Sci.*, **19**, No. 1, 181 (1970).
5. P. J. Auger, *J. Phys. Radium*, **6**, 205 (1925).
6. L. A. Harris, *J. Appl. Phys.*, **39**, 1419 (1968).
7. P. W. Palmberg and T. N. Rhodin, *ibid.*, **39**, 2425 (1968).
8. R. D. Hill, E. L. Church, and J. W. Mihelich, *Rev. Sci. Instr.*, **23**, 523 (1952).
9. J. J. Lander, *Phys. Rev.*, **91**, 1382 (1953).
10. P. W. Palmberg, *Appl. Phys. Letters*, **13**, 183 (1968).
11. R. E. Weber and W. T. Peria, *J. Appl. Phys.*, **38**, 4355 (1967).
12. P. W. Palmberg, G. K. Bohm, and J. C. Tracy, *Appl. Phys. Letters*, **13**, 254 (1969).
13. P. W. Palmberg and H. L. Marcus, *Trans. Am. Soc. Metals*, **62**, 1016 (1969).
14. D. F. Stein, R. E. Weber, and P. W. Palmberg, *J. Metals*, Feb., **39** (1971).
15. T. W. Haas, J. T. Grant, and G. J. Dooley, *Phys. Rev. B*, **1**, 1449 (1970).
16. N. Laegreid and G. K. Wehner, *J. Appl. Phys.*, **32**, 365 (1961).
17. R. E. Weber, and A. L. Johnson, *ibid.*, **40**, 1, 314-318 (1968).
18. H. Poppa and A. G. Elliot, *Surface Sci.*, **24**, 149 (1971).

## Vibration Characteristics of Crystal Slicing ID Saw Blades

S. E. Forman and W. J. Rhines

Bell Telephone Laboratories, Incorporated, Whippany, New Jersey 07981

### ABSTRACT

The natural frequencies and associated mode shapes have been determined for the transverse vibration of three ID saw blades commonly used for crystal wafering. The purpose of the investigation was to determine what frequencies of excitation could excite blade natural frequencies, since excessive blade transverse motion can be a cause of severe crystal and blade damage. The fundamental frequencies for the 4 in. ID-10% in. OD, the 4 in. ID-12 in. OD, and the 6 in. ID-16% in. OD blades, based on a maximum cutting edge hoop stress of 130,000 psi were found to be 780, 640, and 465 Hz, respectively. Experimental measurements have confirmed that cutting edge transverse motion exists with amplitudes up to 0.001 in. but at a frequency equal to the spinning speed, which is always an order of magnitude less than the computed natural frequency.

At the present time the most widely used method of slicing cylindrical crystal ingots into thin wafers is ID sawing. Unlike the more conventional OD saw, the ID saw is extremely thin, is clamped at its outer edge, and has diamond abrasive grit on its inner edge where the cutting is performed. In order to achieve the stiffness necessary to slice crystal ingots, the clamped blade must be placed in a highly tensioned state by one of several available tensioning devices. The basic ingot-blade-wafer system characteristic of the ID sawing process is shown in Fig. 1.

The most important functions of crystal wafering are to provide wafers with flat, parallel sides and to induce a minimum of damage to each side. In order to better understand the interaction of the blade with the ingot it is useful to determine the vibration characteristics of the blade. This allows the determination of excitation frequencies needed to cause resonance of the blade and hence large transverse displacements which could severely damage one or more of the elements in the ingot-blade-wafer system.

There is a great deal of published literature concerning the vibration characteristics of rotating disks. However, in almost every case treated the disk is clamped at its center and free around its outside edge (standard OD saw geometry). Mote presents an excellent listing of many of the theoretical and experimental investigations of vibration characteristics of these disks under various environmental conditions

(1). Rhines (2) has made a simplified calculation of the lowest natural frequency of an ID blade as a function of blade tension and blade dimensions. His results were obtained by Rayleigh's method using a one-term approximation for the fundamental mode shape.

In this paper, highly accurate approximations of the fundamental frequency and several higher frequencies are obtained using Lagrange's equations coupled with multiterm series approximations of the associated mode shapes. The calculations are made for the three blade sizes most widely used in the semiconductor industry. In addition, experimental measurements of actual blade transverse motion and its frequency of occurrence are presented.

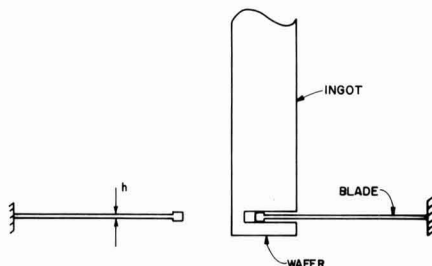


Fig. 1. Blade-ingot-wafer system

Key words: crystal wafering, ID sawing blade vibration.

Table I. Dimensions and properties of blades

Blade type	Blade dimensions 2a	2b	h
1	4	10%	0.004
2	4	12	0.004
3	6	16%	0.004

## Blade properties

Material: AISI 301 stainless steel  
 Density,  $\rho = 0.725 \times 10^{-3}$  lb-sec<sup>2</sup>/in.<sup>4</sup>  
 Young's modulus,  $E = 27.6 \times 10^6$  psi  
 0.2% Offset yield stress: 153,000 psi

## Analysis

**In-plane stress state.**—Physically the blade is a thin annular stainless steel plate of inner radius  $a$ , outer radius  $b$ , thickness  $h$ , density  $\rho$ , and Young's modulus  $E$ . Material properties and typical dimensions of ID blades are given in Table I. It is assumed that the stiffness given to the blade by the tensioning device is analogous to applying a uniform radial load  $\sigma_0$  to the blade's outer periphery as shown in Fig. 2. At the tensioning stress levels normally used, the contribution to the blade stiffness by the bending rigidity of the blade is negligible and the blade can be treated as an annular membrane.

The in-plane state of stress in the blade is a biaxial one consisting of the radial stress  $\sigma_r$  and the hoop stress  $\sigma_\theta$ . Each of these stresses is made up of contributions from tensioning and spinning. The tensioning stresses are given by the well-known formulas (3)

$$\begin{aligned}\sigma_r &= \frac{\sigma_0(1 - a^2/r^2)}{1 - a^2/b^2} \\ \sigma_\theta &= \frac{\sigma_0(1 + a^2/r^2)}{1 - a^2/b^2}\end{aligned}\quad [1]$$

The maximum value of stress due to tensioning is the hoop stress on the cutting edge (at  $r = a$ ), and its magnitude is

$$\sigma_{\max} = \frac{2\sigma_0}{1 - \frac{a^2}{b^2}}\quad [2]$$

The allowable value of  $\sigma_{\max}$  should be sufficiently below the 0.2% offset yield stress of the blade material in order to avoid large amounts of plastic deformation. Strain gauge experiments have shown (4) that for the 4 in. ID-10% in. OD blade the current fully tensioned value of  $\sigma_{\max}$  ranges from 100,000 to 130,000 psi and in what follows the value of 130,000 psi will be used for all geometries. At this tensioning stress level the con-

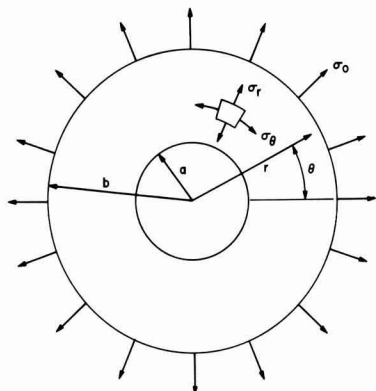


Fig. 2. Model of ID blade used for vibration analysis

tribution of spinning to the stress state is negligible for the current range of speeds used and will be ignored.

**Mode shapes and associated natural frequencies.**—The differential equation which governs the transverse vibration of the tensioned annular membrane described previously is (5)

$$\rho W_{,tt} - \sigma_r W_{,rr} - \sigma_\theta \left( \frac{1}{r} W_{,r} + \frac{1}{r^2} W_{,\theta\theta} \right) = 0 \quad [3]$$

where  $W$  is the transverse displacement of the membrane and partial derivatives are defined using comma notation, i.e.,  $W_{,r} = \partial W / \partial r$ . The geometric boundary conditions are taken to be

$$W = 0 \text{ at } r = b \quad [4]$$

and

$$W = \text{finite at } r = a$$

Because of the form of the in-plane stresses  $\sigma_r$  and  $\sigma_\theta$  given by Eq. [1] an exact solution to the previously described boundary value problem cannot be achieved and an approximate technique will be used.

The authors have found it convenient to use Lagrange's equations of motion coupled with a multiterm series representation of the transverse displacement. The displacement is assumed to be of the form

$$W(r, \theta, t) = \left[ \sum_{j=1}^J A_j(t) \sin \frac{j\pi(b-r)}{2(b-a)} \right] \cos n\theta \quad [5]$$

where  $n$  is the number of nodal diameters,  $j$  is the number of nodal circles, and  $A_j(t)$  is the set of generalized coefficients which are to be determined from Lagrange's equations of motion.

Lagrange's equations of motion for the case of free vibration are (6)

$$\frac{d}{dt} \left( \frac{\partial L}{\partial \dot{A}_i} \right) - \frac{\partial L}{\partial A_i} = 0 \quad (i = 1 \dots J) \quad [6]$$

where  $\dot{A}_i = \partial A_i / \partial t$  and  $L$  is the Lagrangian  $T - V$  where  $T$  is the kinetic energy and  $V$  is the potential energy of the blade. The kinetic energy is given by the formula

$$T = \frac{1}{2} \rho h \int_0^{2\pi} \int_a^b (W_{,t})^2 r dr d\theta \quad [7]$$

and the potential energy is given by

$$V = \frac{1}{2} h \int_0^{2\pi} \int_a^b \left( \sigma_r (W_{,r})^2 + \frac{\sigma_\theta}{r^2} (W_{,\theta})^2 \right) r dr d\theta \quad [8]$$

where  $\sigma_r$  and  $\sigma_\theta$  are given by Eq. [1] (1).

Substituting Eq. [5], [7], and [8] into Eq. [6] and performing the indicated differentiations and integrations gives rise to the following equations of motion

$$\begin{aligned} \sum_{j=1}^J \left\{ \rho h \pi \ddot{A}_j \int_a^b r \sin \frac{j\pi(b-r)}{2(b-a)} \sin \frac{i\pi(b-r)}{2(b-a)} dr \right. \\ + \frac{\sigma_0 h \pi A_j}{1 - \frac{a^2}{b^2}} \left\{ \frac{\pi^2 i j}{4(b-a)^2} \int_a^b \left( r - \frac{a^2}{r} \right) \cos \frac{j\pi(b-r)}{2(b-a)} \right. \\ \left. \cos \frac{i\pi(b-r)}{2(b-a)} dr + n^2 \int_a^b \left( \frac{1}{r} + \frac{a^2}{r^3} \right) \sin \frac{j\pi(b-r)}{2(b-a)} \right. \\ \left. \left. \sin \frac{i\pi(b-r)}{2(b-a)} dr \right\} \right\} = 0 \quad i = 1, 2, \dots, J \quad [9] \end{aligned}$$

To determine the blade natural frequencies  $A_i(t)$  is written in the form

$$A_i(t) = \tilde{A}_j \sin \omega t \quad [10]$$

where  $\omega$  is the natural frequency of the particular mode being considered. Substituting Eq. [10] into Eq.

[9] results in an eigenvalue problem which can be written in the following matrix notation

$$[K_{ij} - \lambda M_{ij}][\tilde{A}_j] = 0 \quad \begin{matrix} i = 1, \dots, J \\ j = 1, \dots, J \end{matrix} \quad [11]$$

where

$$\lambda = \frac{\rho(b^2 - a^2)}{\sigma_0} \omega^2 \quad [12]$$

$$M_{ij} = \int_a^b \frac{r}{b^2} \sin \frac{j\pi(b-r)}{2(b-a)} \sin \frac{i\pi(b-r)}{2(b-a)} dr \quad [13]$$

$$K_{ij} = \frac{\pi^2 a^2 j}{4(b-a)^2} \int_a^b \left( r - \frac{a^2}{r} \right) \cos \frac{j\pi(b-r)}{2(b-a)} \cos \frac{i\pi(b-r)}{2(b-a)} dr + n^2 \int_a^b \left( \frac{1}{r} + \frac{a^2}{r^3} \right) \sin \frac{j\pi(b-r)}{2(b-a)} \sin \frac{i\pi(b-r)}{2(b-a)} dr \quad [14]$$

Equation [11] can now be solved using a straightforward eigenvalue-eigenvector computer package. The individual integrals of  $M_{ij}$  and  $K_{ij}$  are also obtained numerically by a Romberg integration computer routine (7).

For each value of  $n$  the value of  $J$  is increased (starting at  $J = 2$ ) until less than a 1% error exists between consecutive values of  $\lambda$  for the cases of one to six nodal circles. When this occurs the transverse deflection of a radial cross section associated with the final value of  $\lambda$  is graphically compared with that associated with the previous value of  $\lambda$ . If there appear to be no serious deviations between the two shapes then the last value of  $\lambda$  is taken as the correct eigenvalue. However, if there are deviations on the order of 5% or more at any point of the cross section,  $J$  is increased until the deviations are less than 5%. It was in general found that the values of  $\lambda$  converged more rapidly as  $J$  increased than did the deviations between mode shapes.

### Results and Discussion

The values of the eigenvalue  $\lambda$  associated with several different mode shapes are given in Table II. Calculations have been made for the three blade geometries of Table I. The natural frequency in cycles per second is easily attained from the value of  $\lambda$  by the relation

$$f = \frac{1}{2\pi} \sqrt{\frac{\sigma_{\max} \lambda}{2b^2 \rho}} \quad [15]$$

where  $\sigma_{\max}$  is given by Eq. [2].

The values of the natural frequencies and sketches showing the nodal circles and nodal diameters of the associated mode shapes are given in Fig. 3, 4, and 5 for the three blade geometries. All calculations have been

Table II. Values of eigenvalue  $\lambda$  for various blade sizes

Nodal diam	1	2	3	Nodal circles	4	5	6
1. 4 in. ID-10% in. OD							
0	6.88	36.3	89.2	166	265	387	
1	12.2	41.9	94.6	171	271	393	
2	25.7	59.7	111	187	287	409	
3	42.9	88.3	142	215	314	437	
4	62.6	122	185	258	354	476	
2. 4 in. ID-12 in. OD							
0	6.51	34.3	84.2	156	251	368	
1	12.6	41.3	91.0	163	257	374	
2	26.3	77.7	112	183	277	394	
3	42.8	92.6	150	220	312	427	
4	61.7	125	197	275	365	478	
3. 6 in. ID-16% in. OD							
0	6.65	35.0	86.1	160	256	375	
1	12.4	41.4	92.2	166	262	381	
2	26.1	61.3	112	184	280	400	
3	42.9	91.0	146	217	312	430	
4	62	124	193	267	358	471	

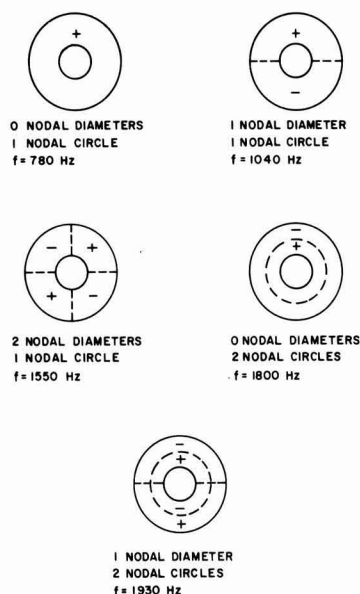


Fig. 3. Computed natural frequencies and associated mode shapes of 4 in. ID-10% in. OD blade ( $\sigma_{\max} = 130,000$  psi).

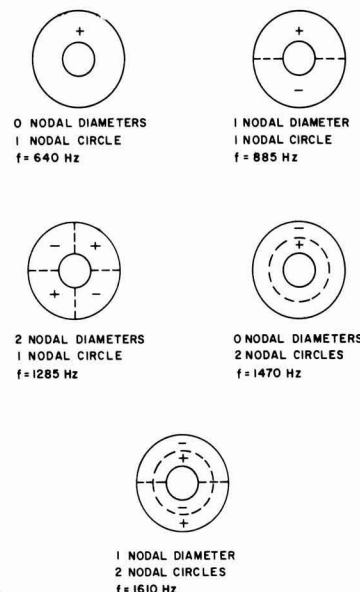


Fig. 4. Computed natural frequencies and associated mode shapes of 4 in. ID-12 in. OD blade ( $\sigma_{\max} = 130,000$  psi).

based on a maximum hoop stress of 130,000 psi. As indicated in (4), the frequencies associated with the fundamental and 2 nodal diameter-1 nodal circle modes of the 4 in. ID-10% in. OD blade have been verified experimentally to within 10%.

For the particular case of the fundamental mode, the natural frequency decreases from 780 Hz for the smallest blade size (4 in. ID-10% in. OD) to 465 Hz for the largest blade size (6 in. ID-16% in. OD). The usual spinning speeds utilized with the three blade geometries range from 30-40 Hz for the large blade and 50-70 Hz for the other two. Thus, it appears that, for



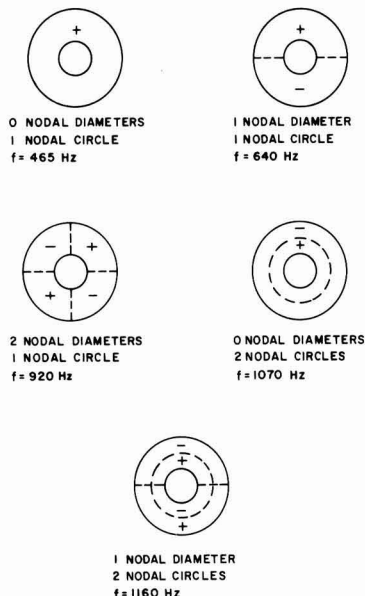


Fig. 5. Computed natural frequencies and associated mode shapes of 6 in. ID-16 in. OD blade ( $\sigma_{\max} = 130,000$  psi).

the range of  $\sigma_{\max}$  mentioned earlier, spindle speed is unlikely to be a source of excitation near the fundamental mode unless its magnitude is increased at least ten times.

Typical profiles of the transverse displacement of the radial cross section of a blade are presented for several mode shapes in Fig. 6-10. The number of nodal diameters is listed on each figure and the number of nodal circles is listed on each profile. In each case the displacement has been normalized with respect to the maximum value that occurs between the inner and outer radius. The curves shown are all obtained using  $J = 6$  in the series representation of the displacement for the 4 in. ID-10 in. OD blade.

For small numbers of nodal diameters the maximum value of transverse displacement always seems to occur at the cutting edge regardless of the number of nodal circles. This is due to the zero radial stress con-

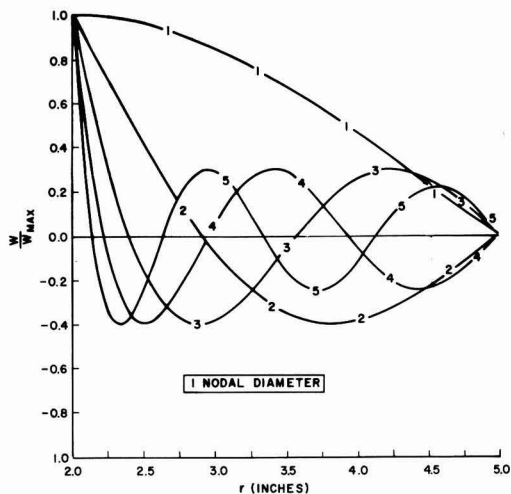


Fig. 7. Radial profiles of 4 in. ID-10 in. OD blade

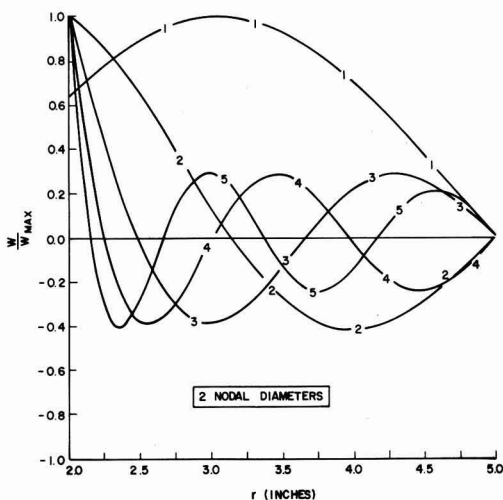


Fig. 8. Radial profiles of 4 in. ID-10 in. OD blade

dition at the inner edge. However as the number of nodal diameters increases, the maximum displacements start occurring away from the cutting edge.

**Experimental measurements.**—In order to determine the amplitude and frequency of cutting edge transverse motion, a displacement-measuring technique described by Yakunin and Khasdan (8) was used on a current ID slicing machine. They used an "inductive differential detector with a variable air gap." As the air gap between the detector and blade changed, the amplitude and frequency of any transverse displacements from the initial position could be recorded. A device such as this, with a sensitivity that enables it to measure deflections as small as  $0.1 \pm 0.02$  mils (1 mil = 0.001 in.) was used to make the measurements described here (4).

Hand rotation of the blade gave rise to transverse deflections of 0.6-0.7 mils. Spinning the blade without cutting (idling) gave rise to deflections ranging from 0.45 to 0.80 mils depending on the spinning speed. For both hand rotation and idling, the peak to peak displacement occurs once per blade revolution. During the cutting cycle, the transverse displacement spectrum still occurs once per revolution but the amplitude is

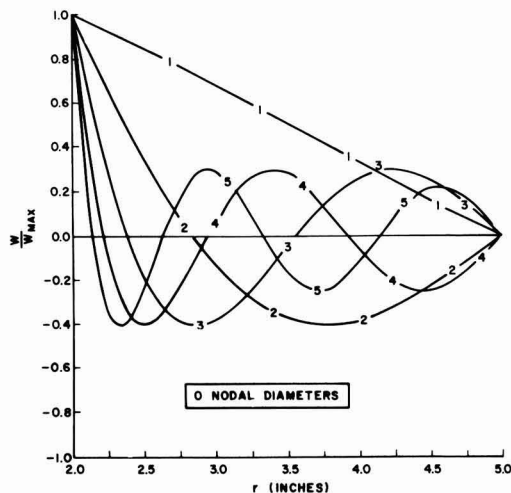


Fig. 6. Radial profiles of 4 in. ID-10 in. OD blade

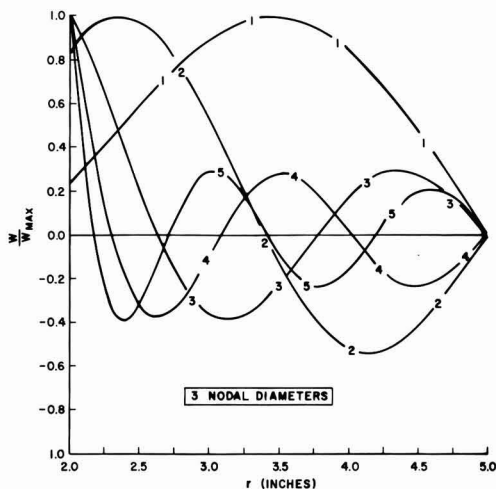


Fig. 9. Radial profiles of 4 in. ID-10 1/8 in. OD blade

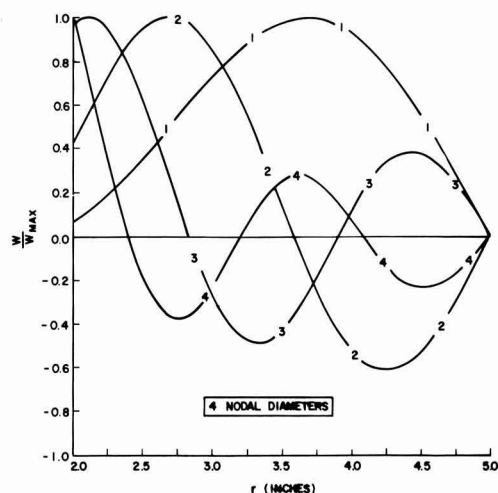


Fig. 10. Radial profiles of 4 in. ID-10 1/8 in. OD blade

altered. For a given spinning speed, the amplitude of the idling deflection decreases by 50-60% during feed and by 30-40% during retraction. It is believed that

this transverse motion is the cause of the periodic score marks often observed on wafers.

### Conclusions

The natural frequencies and associated mode shapes have been determined for the transverse vibration of three ID saw blades widely used in the semiconductor industry. The purpose of the investigation was to determine what excitation frequencies need to exist in order to excite natural frequencies of the blade.

It was found that for all three blades the spinning speeds used are an order of magnitude less than the lowest natural frequency. Since the frequency is directly proportional to the square root of the maximum hoop stress, the range of current maximum hoop stresses (100,000-130,000 psi) would have to be reduced by two orders of magnitude in order for the natural frequency to be on the same order as the spinning speed. The frequency also decreased as a function of the blade surface area, but for the current blade sizes being used the natural frequency is always an order of magnitude greater than the spinning speed. In conclusion, experimental measurements indicate that under present operating conditions, cutting edge transverse motion occurs at a frequency equal to the spinning speed. There is no indication of any blade excitation which occurs at frequencies near the natural frequency.

Manuscript submitted Nov. 3, 1971; revised manuscript received ca. Feb. 1, 1972.

Any discussion of this paper will appear in a Discussion Section to be published in the December 1972 JOURNAL.

### REFERENCES

1. C. D. Mote, Jr., "Effect of In-Plane Stresses on the Vibration Characteristics of Clamped-Free Discs," PhD Thesis, Univ. California, Berkeley, 1963.
2. W. J. Rhines, "Preliminary Investigation of the Vibration Characteristics of Crystal Slicing Circular Saw Blades," Internal Memorandum, Bell Telephone Laboratories, Inc.
3. C. T. Wang, "Applied Elasticity," McGraw-Hill Book Co., New York (1953).
4. S. E. Forman, "Mechanics of Crystal Wafering as Performed on ID Saws," Internal Memorandum, Bell Telephone Laboratories, Inc.
5. V. V. Bolotin, "The Dynamic Stability of Elastic Systems," Holden-Day, Inc., San Francisco (1964).
6. F. B. Hildebrand, "Methods of Applied Mathematics," 2nd ed., Prentice-Hall, Inc., Englewood Cliffs, N. J. (1965).
7. B. Carnahan, H. A. Luther, and J. O. Wilkes, "Applied Numerical Methods," John Wiley & Sons, Inc., New York (1969).
8. Y. K. Yakunin and S. M. Khasdan, *Woodworking Industry (USSR)*, Vol. 6, No. 8 and 9 (1957), CSIRO Translation No. 4065.

# Mathematics of the Electrochemical Extraction of Hydrogen from Iron

Leonard Nanis\* and T. K. Govindan Nambodhiri

The School of Chemical Engineering, University of Pennsylvania, Philadelphia, Pennsylvania 19104

## ABSTRACT

The transient current of hydrogen removal from iron following steady-state permeation is analyzed theoretically for two limiting conditions at the input side. For the fastest possible removal ( $C = 0$  at  $X = 0$  and at  $X = L$ ), the amount extracted at the potentiostated side ( $X = L$ ) is one third of the total present at steady-state permeation described by  $C_{(X)} = C_0(1 - X/L)$ . Comparison of the integrated total flux and the amount given by the integral of  $C_{(X)}$  indicates possible concentration dependence of hydrogen diffusivity in iron.

The study of diffusion of hydrogen through metals has attracted much interest because of its relation to the problem of hydrogen embrittlement. The electrochemical permeation technique (1) for measurement of diffusion of hydrogen in metals has been extensively employed recently (2, 3). The mathematical basis of this method was developed by McBreen *et al.* (4). This paper presents some results and conclusions concerning permeation in Armco iron based on an extension of the theory and application of permeation technique to provide additional information regarding hydrogen entry and extraction from metals.

**The permeation method.**—In the electrochemical permeation method, a thin membrane of the material is cathodically charged with hydrogen on one side, while the hydrogen diffusing out at the opposite side is oxidized by maintaining anodic conditions. Mathematically, this procedure provides the boundary condition

$$C = 0, \quad X = L, \quad t \geq 0 \quad [1]$$

The current needed to maintain the constant anodic potential is a direct measure of the rate at which hydrogen is diffusing out.

McBreen *et al.* (4) solved the diffusion equation (Fick's second law)

$$\frac{\partial^2 C}{\partial X^2} - \frac{1}{D} \frac{\partial C}{\partial t} = 0 \quad [2]$$

applying the pertinent initial condition

$$C = C_0(1 - X/L) \quad [3]$$

and boundary conditions to get expressions for the decay of permeation current from the steady state when the charging is stopped.

Two limiting decay transients were considered. For the fastest possible extraction, the concentration at the input side is considered to drop instantaneously to zero upon input current interruption, i.e.,

$$C = 0, \quad X = 0, \quad t > 0 \quad [4]$$

where time is reckoned from the instant of interruption. Slowest possible extraction through the potentiostated side Eq. [1] is based on the assumption of zero flux at the input side, i.e., after current interruption, the input side ( $X = 0$ ) becomes impermeable to hydrogen, described as

$$\frac{\partial C}{\partial X} = 0, \quad X = 0, \quad t > 0 \quad [5]$$

Using Laplace transform methods, McBreen *et al.* (4) obtained for the slowest possible decay (Eq. [5], [1],

[3], and [2]), the flux in terms of the previous steady-state value ( $J_s$ ) as

$$\frac{J_\tau}{J_s} = 1 - 2 \sum_{n=0}^{\infty} (-1)^n \operatorname{erfc} \frac{2n+1}{2\tau^{1/2}} \quad [6]$$

where  $\tau = Dt/L^2$ , a dimensionless time parameter.

Solving Eq. [2] with Eq. [1], [3], and [4], the fastest possible extraction gives

$$\frac{J_\tau}{J_s} = 1 - 2 \sum_{n=0}^{\infty} \frac{1}{\pi^{1/2}} \frac{1}{\tau^{1/2}} e^{-\frac{(2n+1)^2}{4\tau}} \quad [7]$$

It should be noted that Eq. [7] is a corrected version of a previous result (4).

The decay part of the permeation technique has been mostly neglected by previous workers. However, the decay transient is a source of additional information regarding the diffusivity and solubility of hydrogen in the membrane and of the nature of the reaction at the input metal-electrolyte interface. In particular, the time integral of flux from  $X = L$  reflects the total amount of hydrogen extracted at this side and is equal to the total hydrogen in the membrane if the input side is impermeable according to Eq. [5]. The total amount at steady state ( $t = 0$ ) is readily obtained from the product of average concentration (integral of Eq. [3]) and the volume of the permeated region of the membrane. Thus, integration of experimental decay curves of current *vs.* time should permit evaluation of the number of mols of hydrogen extracted for comparison with the prediction according to Eq. [3] using the value of  $C_0$ , which, in turn, is obtained from the steady-state permeation current density and the diffusivity derived from the build-up transient.

When the boundary conditions are such that the decay follows Eq. [7], i.e., fast decay, the amount of hydrogen extracted at the potentiostated side ( $X = L$ ) is only a fraction of the total amount in the membrane at steady-state permeation. The remaining part of the hydrogen diffuses out through the input side ( $X = 0$ ) in order to satisfy the boundary condition given by Eq. [4]. Hence, in order to calculate the hydrogen concentration of the membrane at steady-state permeation, it is essential to have an estimate of the relative amounts of hydrogen diffusing out at both sides of the membrane ( $X = 0$  and  $X = L$ ). The following mathematical analysis was performed to get these values.

**Mathematics of fast decay.**—Consider a membrane of thickness  $L$  which is charged from the side  $X = 0$  and potentiostated at  $X = L$  in order to maintain a zero concentration of hydrogen. During charging, a hydrogen concentration  $C_0$  is maintained at  $X = 0$ . The steady-state concentration profile obtained by charging is described by Eq. [3]. This profile becomes the initial

\* Electrochemical Society Active Member.

Key words: hydrogen dissolution in iron, hydrogen extraction, hydrogen diffusion, concentration-dependent diffusivity, permeation.

condition used together with the boundary conditions Eq. [1] and [4] to solve Eq. [2], with time measured from the instant of input current interruption. The solution sequence is to (i) obtain concentration of hydrogen as a function of time and position in the region  $0 < X < L$ ; (ii) obtain the gradient of concentration at  $X = 0$ ,  $X = L$  to determine flux; and (iii) integrate each flux with respect to time over the entire range  $0 < t < \infty$ . Both separation of variables and Laplace transform methods were used.

*Solution by the method of separation of variables.*—The concentration of hydrogen within the membrane during the fast decay was obtained as

$$C = \frac{2C_0}{\pi} \sum_{n=1}^{\infty} \frac{1}{n} \sin \frac{n\pi X}{L} e^{-\frac{n^2\pi^2 Dt}{L^2}} \quad [8]$$

Differentiating Eq. [8] with respect to  $X$  gives

$$\frac{\partial C}{\partial X} = \frac{2C_0}{L} \sum_{n=1}^{\infty} \cos \frac{n\pi X}{L} e^{-\frac{n^2\pi^2 Dt}{L^2}} \quad [9]$$

Substituting  $X = 0$  in Eq. [9], the gradient at the input surface is

$$\left. \frac{\partial C}{\partial X} \right|_{X=0} = \frac{2C_0}{L} \sum_{n=1}^{\infty} e^{-\frac{n^2\pi^2 Dt}{L^2}} \quad [10]$$

and for  $X = L$ , Eq. [9] gives the gradient as

$$\left. \frac{\partial C}{\partial X} \right|_{X=L} = \frac{2C_0}{L} \sum_{n=1}^{\infty} (-1)^n e^{-\frac{n^2\pi^2 Dt}{L^2}} \quad [11]$$

The flux  $F$  (mol cm<sup>-2</sup> sec<sup>-1</sup>) of material diffusing across each surface is obtained from Eq. [10] and [11] with Fick's first law as

$$F = -D \frac{\partial C}{\partial X} \quad [12]$$

The total amount per unit area,  $Q_E$ , of hydrogen diffusing out at each surface is obtained by integrating the flux,  $F$ , over the entire range of time. Hence, the amount of hydrogen evolved at  $X = 0$  is

$$\begin{aligned} Q_E \Big|_{X=0} &= \int_0^{\infty} F_{(X=0)} dt \\ &= \frac{-2C_0 D}{L} \int_0^{\infty} \left( \sum_{n=1}^{\infty} e^{-\frac{n^2\pi^2 Dt}{L^2}} \right) dt \quad [13] \end{aligned}$$

Integrating in Eq. [13] term by term gives a well-known convergent series as

$$Q_E \Big|_{X=0} = -\frac{2C_0 L}{\pi^2} \sum_{n=1}^{\infty} \frac{1}{n^2} = \frac{-C_0 L}{3} \quad [14]$$

In a similar fashion, Eq. [11] and [12] give

$$Q_E \Big|_{X=L} = \frac{-2C_0 L}{\pi^2} \sum_{n=1}^{\infty} \frac{(-1)^n}{n^2} = \frac{C_0 L}{6} \quad [15]$$

The sign of  $Q_E$  in Eq. [14] and [15] reflects the vectorial character of the flux with respect to the coordinate system. It is thus appropriate to consider absolute values to obtain the total amount extracted,  $Q_{Tot}$ , as

$$Q_{Tot} = |Q_E|_{X=0} + |Q_E|_{X=L} = \frac{C_0 L}{2} \quad [16]$$

The amount stored in the membrane (per unit area) at steady state before current interruption ( $t < 0$ ) is readily determined by integration of Eq. [3] as

$C_0 L/2$  (mol cm<sup>-2</sup>), in agreement with Eq. [16]. Hence, the fraction of hydrogen diffusing out at  $X = 0$  is

$$\frac{|Q_E|_{X=0}}{Q_{Tot}} = \frac{2}{3} \quad [17]$$

and the fraction diffusing out at  $X = L$  is

$$\frac{|Q_E|_{X=L}}{Q_{Tot}} = \frac{1}{3} \quad [18]$$

*Solution by Laplace transforms.*—To check the results obtained as Eq. [17] and [18], Eq. [2], [3], [1], and [4] were solved using the method of Laplace transforms. The concentration of hydrogen within the membrane during fast decay is given by

$$\begin{aligned} C(x,t) &= C_0(1 - X/L) - C_0 \sum_{n=0}^{\infty} \operatorname{erfc} \left\{ \frac{2nL + X}{2\sqrt{Dt}} \right\} \\ &+ C_0 \sum_{n=0}^{\infty} \operatorname{erfc} \left\{ \frac{2L(n+1) - X}{2\sqrt{Dt}} \right\} \quad [19] \end{aligned}$$

Differentiating Eq. [19] with respect to  $X$ , and multiplying the slopes by  $-D$ , the flux (Eq. [12]) at  $X = 0$  is

$$\begin{aligned} F \Big|_{X=0} &= \frac{DC_0}{L} \left[ 1 - \frac{1}{\sqrt{\pi\tau}} \left( \sum_{n=0}^{\infty} e^{-\frac{n^2}{\tau}} \right) \right. \\ &\quad \left. + \sum_{n=0}^{\infty} e^{-\frac{(n+1)^2}{\tau}} \right] \quad [20] \end{aligned}$$

and the flux at  $X = L$  is

$$F \Big|_{X=L} = \frac{DC_0}{L} \left[ 1 - \frac{2}{\sqrt{\pi\tau}} \sum_{n=0}^{\infty} e^{-\frac{(2n+1)^2}{4\tau}} \right] \quad [21]$$

Equations [20] and [21] have to be integrated with respect to  $\tau$  over the range  $0 < \tau < \infty$  to get the total amounts of hydrogen diffusing out at the surfaces  $X = 0$  and  $X = L$ , respectively. Equations [20] and [21] both become infinite for  $\tau = 0$ . Also, for  $\tau = \infty$ , the integral of Eq. [20] and [21] becomes infinite because of the term of unity. Hence, with an analytic solution of the integrals not possible, a graphical integration was performed since the summations in Eq. [20] and [21] converge rapidly for numerical evaluation. The results are in good agreement (within 2%) of the values in Eq. [17] and [18]. Equations [19], [20], and [21] are useful in preparing tables and curves for short time, since Eq. [8], [10], and [11] are very slowly convergent for  $\tau < 0.05$ . The  $n = 0$  term of Eq. [21] is sufficient even up to  $\tau \leq 0.3$  and provides a simple form.

Thus, during fast decay, only one third of the total amount of hydrogen diffuses out through the potentiostated side ( $X = L$ ), and provides a lower bounding limit, while the upper limit [ $(Q_E|_{X=L})/(Q_{Tot}) = 1$ ] is obtained during the slow decay because of the condition imposed by Eq. [5]. Comparison of the extracted amount of hydrogen with the value predicted from the initial concentration profile (Eq. [3]) thus provides further insight as to the nature of the boundary condition existing at  $X = 0$  during decay, with Eq. [4] and [5] as limits.

### Experimental Results

Hydrogen permeation experiments were performed with the potentiostat circuit as essentially described by McBreen *et al.* (4). A constant current circuit was used for the cathode input side of the membrane. Build-up and decay transients were recorded for various charging current densities in 0.2N NaOH and 0.1N H<sub>2</sub>SO<sub>4</sub> catholytes for annealed Armco iron at 22°C. The anolyte was always 0.2N NaOH.

Table I. Analysis of decay transients

Annealed Armco iron; 22°C; catholyte: 0.1N H <sub>2</sub> SO <sub>4</sub> ; anolyte: 0.2N NaOH Average diffusivity, $D \times 10^6 \text{ cm}^2 \text{ sec}^{-1}$				
Charging current density, mA/cm <sup>2</sup>	From decay			
	From build-up*	Fit to Eq. (7) (fast)	Fit to Eq. (6) (slow)	$ Q_E _{X=L}/Q_{Tot}$
0.021	4.84	3.86	10.48	0.334
0.064	4.16	4.23	11.21	0.326
0.194	5.52	4.63	12.68	0.280
0.409	6.60	5.34	14.50	0.266
0.841	7.66	5.78	15.70	0.258
2.13	8.45	6.40	17.20	0.243
4.27	8.31	6.22	16.90	0.235

\* Numerical values for the build-up permeation-time curve may be computed by subtracting the right-hand side of Eq. (7) from unity.

By fitting the experimental build-up curves to theory (4), hydrogen diffusivity,  $D$ , and surface concentration,  $C_0$ , were evaluated. It should be noted that there is no total agreement between theory and data over the entire build-up time span. By minimizing the misfit at different time intervals, a corresponding best fitted diffusivity may be computed. The trend suggests that diffusivity increases with hydrogen concentration. This aspect will be fully explored in forthcoming publications.

In the present computations of  $C_0$  from the steady-state permeation current, the diffusivity value is that obtained by a best fit to the build-up theory for early time. This value of  $D$  may be seen to be the most appropriate choice since the hydrogen arriving at  $X = L$  at the time of breakthrough has traversed a region free of hydrogen. At steady state, the flux at  $X = L$  is given by Eq. [12] with, however, the implicit feature given in Eq. [1], namely that the local diffusivity (allowing for possible concentration dependence) corresponds to the zero concentration value. Based on this value of  $C_0$  and the steady-state concentration profile given by Eq. [3], the total amount of hydrogen,  $Q_{Tot}$ , held within the membrane was calculated to be

$$Q_{Tot} = \frac{1}{2} C_0 V \quad [22]$$

where  $V$  = volume of the charged section of the membrane.

An estimate of the amount of hydrogen extracted at the potentiostated side ( $X = L$ ) was obtained by measuring the area beneath the decay current-time traces and converting to equivalents of hydrogen. This value was then compared with  $Q_{Tot}$  to obtain the ratio  $|Q_E|_{X=L}/Q_{Tot}$ . Table I shows the results obtained for permeation from 0.1N H<sub>2</sub>SO<sub>4</sub>. Figure 1 shows the decay transients which were compared with the two theoretical decay curves (fast, Eq. [7], and slow, Eq. [6]) to yield average  $D$  values given in columns 3 and 4 of Table I. Also indicated in this table are the  $D$  values obtained from build-up transients, based on the best fit over all time. As mentioned previously, the diffusivity at small time was used for calculating  $Q_{Tot}$  in column 5. This value is  $4.0 \times 10^{-5} \text{ cm}^2 \text{ sec}^{-1}$ . Comparison of the two possible decay-fitted values with the build-up  $D$  indicates clearly that the boundary condition given by Eq. [4] is most likely. The ratio  $|Q_E|_{X=L}/Q_{Tot}$  in Table I varies from the theoretical limit of 0.33 for fast decay to even smaller values. Thus, the charging at 0.021 mA/cm<sup>2</sup> follows the expected behavior and also gives the best fit over-all in Fig. 1. However, charging at higher currents produces a shift of the decay curves to shorter times, indicating an increase in  $D$ , listed in Table I. The decrease in  $|Q_E|_{X=L}/Q_{Tot}$  from 0.334 to 0.235 as charging current increases brings these values into a region below the lower numerical limit calculated in Eq. [18]. This negative deviation from the

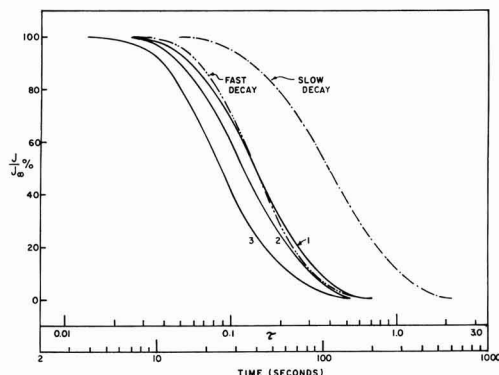


Fig. 1. Decay transients for Armco iron, 0.1N H<sub>2</sub>SO<sub>4</sub>. Catholyte, 22°C. Charging current densities (mA/cm<sup>2</sup>) are: curve 1, 0.021; curve 2, 0.194; and curve 3, 2.13.

limit based on constant diffusivity theory is in accord with a diffusivity which increases with increasing concentration. For such concentration dependence of  $D$ , the basic Eq. [2] and subsequent results are no longer applicable. Qualitatively, however, the concentrated region near  $X = 0$  should provide a more rapid flux and an amount  $|Q_E|_{X=0}$  greater than predicted by Eq. [14]. Thus, the flux and amount at  $X = L$  will be less than that predicted in Eq. [15], causing the values for  $|Q_E|_{X=L}/Q_{Tot}$  to be less than the theoretical constant  $D$  limit of 0.333.

During permeation experiments using 0.1N H<sub>2</sub>SO<sub>4</sub> as catholyte, a cathodic protection current of 0.0215 mA/cm<sup>2</sup> was always applied to prevent corrosion of the Armco iron membrane. Permeation build-up and decays were then recorded by applying a cathodic current from a separate circuit. The response of the cathode ( $X = 0$ ) to step current switching was sufficiently rapid so as to produce a virtually potentiostated surface when compared with the orders of magnitude greater diffusion-controlled hydrogen decay time. Thus, the boundary condition in Eq. [4] is assured.

When 0.2N NaOH catholyte was used, corrosion was not a severe problem, so that no cathodic protection was needed. Figure 2 shows decay transients observed for this case. Table II gives the  $D$  values and  $|Q_E|_{X=L}/Q_{Tot}$  ratios obtained from these data. Best over-all fitting in Fig. 2 was found for the short time region for the 0.86 mA/cm<sup>2</sup> study. For lesser and greater cathodic input current densities, no clear pattern of shifting was observed as found for 0.1N H<sub>2</sub>SO<sub>4</sub> (Fig. 1). In Table II, the build-up and decay determined  $D$  values

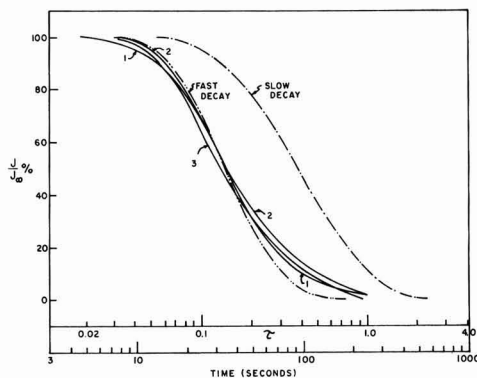


Fig. 2. Decay transients for Armco iron, 0.2N NaOH. Catholyte, 22°C. Charging current densities (mA/cm<sup>2</sup>) are: curve 1, 0.43; curve 2, 0.86; and curve 3, 4.30.



Table II. Analysis of decay transients

Annealed Armco iron; 22°C; 0.2N NaOH electrolyte				
Charging current density, mA/cm <sup>2</sup>	From build-up	Average diffusivity, $D \times 10^6 \text{ cm}^2 \text{ sec}^{-1}$		$ Q_E _{X=L}/Q_{Tot}$
		From decay		
		Fit to Eq. (7) (fast)	Fit to Eq. (6) (slow)	
0.43	5.27	4.53	12.20	0.356
0.86	5.46	4.53	12.20	0.372
2.15	5.16	—	—	0.338
4.30	5.25	4.96	12.95	0.326

do not change appreciably with charging current, in contrast with results for 0.1N H<sub>2</sub>SO<sub>4</sub> (Table I). The ratio  $|Q_E|_{X=L}/Q_{Tot}$  ranges from 0.326 to 0.372, in good agreement with the lower limit of 0.333 associated with fast decay.

### Discussion and Conclusions

Testing of the present decay mathematics shows unexpected lower than theoretical values for  $|Q_E|_{X=L}/Q_{Tot}$  for 0.1N H<sub>2</sub>SO<sub>4</sub>. In combination with the shift of the build-up transients to shorter time with increased current, the data provide strong evidence for a hitherto unsuspected concentration dependence of hydrogen diffusivity in iron. The evidence suggests that  $D$  increases with increasing concentration. For 0.2N NaOH and 0.1N H<sub>2</sub>SO<sub>4</sub>, the fit of the decay current-time curve in comparison with the build-up curve and also the  $|Q_E|_{X=L}/Q_{Tot}$  ratio values are best associated with a surface condition at  $X = 0$  which corresponds to zero hydrogen concentration. From the trend of  $|Q_E|_{X=L}/Q_{Tot}$  values below the constant  $D$  limit of 0.333, it is probable that, for similar charging current, the concen-

tration of hydrogen in iron is greater in the 0.1N H<sub>2</sub>SO<sub>4</sub> catholyte than in the 0.2N NaOH solution.

In testing the possibility that traps may be contributing to the nonconstant diffusivity, the phenomenological diffusivity discussed by Oriani (5) should always be less than the true lattice diffusivity. As predicted (5), the true lattice diffusivity is  $3.06 \times 10^{-5} \text{ cm}^2 \text{ sec}^{-1}$  at 22°C, in good agreement with the lowest values in Tables I and II, i.e.,  $5 \times 10^{-5} \text{ cm}^2 \text{ sec}^{-1}$ . As shown, the  $D$  values increase to about  $8 \times 10^{-5} \text{ cm}^2 \text{ sec}^{-1}$  with increasing current, so that trapping is an unlikely alternative to the presently suggested concentration dependence.

### Acknowledgments

The financial support of the Office of Naval Research (N00014-67-A-0216-0004, School of Chemical Engineering, University of Pennsylvania) is gratefully acknowledged. The opinions and assertions contained herein are the private ones of the authors and are not to be construed as official or reflecting the views of the Navy Department.

Manuscript submitted Nov. 1, 1971; revised manuscript received Jan. 18, 1972.

Any discussion of this paper will appear in a Discussion Section to be published in the December 1972 JOURNAL.

### REFERENCES

1. M. A. V. Devanathan and Z. O. J. Stachurski, *Proc. Roy. Soc.*, **A270**, 90 (1962).
2. W. Beck, J. O'M. Bockris, M. A. Genshaw, and P. K. Subramanian, *Met. Trans.*, **2**, 883 (1971).
3. C. D. Kim and A. W. Loginow, *Corrosion*, **24**, 313 (1968).
4. J. McBreen, L. Nanis, and W. Beck, *This Journal*, **113**, 1218 (1966).
5. R. A. Oriani, *Acta Met.*, **18**, 147 (1970).

## Standard Potentials of Ag-AgCl Electrode and Related Thermodynamic Quantities in Dimethyl Sulfoxide-Water Mixtures from 5° to 45°C

Rabindra N. Roy, William Vernon, Alfred Bothwell, and James Gibbons

Department of Chemistry, Drury College, Springfield, Missouri 65802

### ABSTRACT

EMF measurements were performed at 5°, 15°, 25°, 35°, and 45°C on the cell of the type Pt|H<sub>2</sub> (g, 1 atm)|HCl (m), DMSO (X), H<sub>2</sub>O (Y)|AgCl, Ag, where X = 5, 10, and 20 w/o (weight per cent) dimethyl sulfoxide (DMSO). The standard potentials were evaluated by means of a curve-fitting program. The mean molal activity coefficients of HCl have been determined for molalities from 0.001 to 0.1 mol kg<sup>-1</sup>. The cell has also been used to derive (i) the primary medium effect on HCl, (ii) the relative partial molal enthalpy ( $L_2$ ) of HCl, and (iii) the thermodynamic constants  $\Delta G^\circ$ ,  $\Delta H^\circ$ , and  $\Delta S^\circ$  for the transfer of HCl from water to the respective solvent compositions (X = 5, 10, and 20). The standard emf has been expressed as a function of temperature. The electrostatic contribution of the Gibbs free energy of transfer has been calculated, based on Born's model, and the results have been interpreted in terms of acid-base interactions, as well as the structure-breaking processes of the solvents.

The behavior of electrolytes in dipolar, aprotic solvent-water media such as tetrahydrofuran (THF)-water (1), 1, 2 dimethoxyethane (DME)-water (2, 3) are of interest in understanding acid-base interactions, ionic solvation, and association phenomena of solution chemistry. Mixtures of dipolar aprotic solvent (DMSO) with water (4, 5), have been found to strongly acceler-

ate the rates of many reactions involving nucleophiles or bases (6, 7). Although the chemistry of pure DMSO has been the subject of numerous investigations (8-10), no thermodynamic information for this electrolyte in DMSO-water mixtures (X = 5, 10, and 20), where X = weight per cent (w/o) of DMSO, has been reported to date. The present work is based on emf measurements on the cell, without liquid junction, Pt|H<sub>2</sub> (g, 1 atm)|HCl (m), DMSO (X), H<sub>2</sub>O (Y)|AgCl, Ag at 5°,

Key words: dimethyl sulfoxide, medium effect, activity coefficient, mixed solvents standard emf, thermodynamic.

15°, 25°, 35°, and 45°C. As a prerequisite to studies of acid-base equilibria, solvent effects on rates, instability constants, solubilities, and structures of solvents, we have reported the results on (i) the standard emf of the cell for  $X = 5, 10$ , and  $20$ , (ii) the activity coefficient of HCl, (iii) the primary medium effect, (iv) the relative partial molal enthalpy of HCl, and (v) the thermodynamic functions for the transfer of one mole of the acid from the aqueous standard state to the standard state in the mixed solvents.

### Experimental

DMSO (Fisher spectroanalyzed) was used without further purification, and the label indicated the water content to be 0.02%. The solvent had a dielectric constant of 46.7 at 25°C.

An aqueous stock solution of hydrochloric acid was prepared from twice-distilled, constant-boiling acid. Analytical reagent grade acid was used to make up the constant-boiling acid. The acid was standardized by a gravimetric determination of chloride as AgCl. The average difference among replicate determinations was less than  $\pm 0.03\%$ . The bromide content was found to be less than 0.002 m/o (mole per cent). The distilled water used in the preparation of the solutions had a conductance of  $0.7-0.8 \times 10^{-6} \text{ ohm}^{-1} \text{ cm}^{-1}$ . The mixed solvents were prepared by weighing DMSO, water, and hydrochloric acid. All solutions were freshly prepared before each run. The acid concentration was known to within  $\pm 0.02\%$ .

The silver-silver chloride electrodes were of the thermal electrolytic type (11) and were aged in 0.1M HCl, which was deoxygenated by bubbling hydrogen. Two days after preparation, the finished electrodes were intercompared and had bias potentials usually less than  $\pm 0.02 \text{ mV}$ . The hydrogen electrodes were lightly coated with platinum black, according to the recommendations of Hills and Ives (12).

The purification of the hydrogen gas and other experimental details have been described previously (13).

All measurements were made with two Ag-AgCl electrodes and two hydrogen electrodes. The equilibrium was reached in about 3-4 hr after the initiation of hydrogen bubbling. The potentials of the cell were measured at 5°, 15°, 25°, 35°, and 45°C by means of a K-3 Universal Type Potentiometer which was calibrated against an Eppley standard cell. A mirror-type galvanometer with a sensitivity of  $\pm 0.02 \text{ mV}$  per division was used. The thermostat maintained a temperature within  $\pm 0.01^\circ\text{C}$ .

The emf usually was measured at 25° at the beginning, in the middle, and at the end of each run. These three readings agreed within  $\pm 0.09 \text{ mV}$ . The average value is given in Table I. The criterion for the attainment of equilibrium was a steady reading to the nearest 0.1 mV for a period of about 1 hr. Each emf value recorded in Table I is the average of two pairs of electrodes in the same cell. Observed values of emf have been converted to a hydrogen partial pressure of 1 atm. The dielectric constant ( $D$ ) of the mixed solvent at each Celsius temperature,  $t$ , was calculated from the equations

$$\log D (X = 5) = 1.8938 - 0.00204(t - 25^\circ) \quad [1]$$

$$\log D (X = 10) = 1.8925 - 0.00204(t - 25^\circ) \quad [2]$$

$$\log D (X = 20) = 1.8888 - 0.00204(t - 25^\circ) \quad [3]$$

derived from the data of Tommila and Pajunen (15). The density,  $\rho_0$ , of each of these mixtures, at different temperatures, was obtained by an interpolation and extrapolation procedure from the literature (15).

DMSO has a very low vapor pressure. In order to correct the emf to a hydrogen partial pressure of 1 atm, vapor pressures of the solvent components were assumed to obey Raoult's law, and were so calculated.

Table I. Electromotive force (volts) of the cell  
Pt | H<sub>2</sub> (g, 1 atm) | HCl (m), DMSO (X), and H<sub>2</sub>O (Y) | AgCl, Ag  
at different temperatures

X and Y are weight percentages

$\frac{\text{mHCl},^a}{\text{moles/kg}}$	5°	15°	25°	35°	45°
X = 5					
0.00501	0.4900	0.4929	0.4945	0.4966	0.4994
0.01001	0.4577	0.4586	0.4605	0.4617	0.4635
0.0300	0.4071	0.4064	0.4073	0.4063	0.4058
0.0400	0.3932	0.3933	0.3946	0.3929	0.3905
0.0476	0.3861	0.3853	0.3866	0.3841	0.3819
0.0601	0.3755	0.3742	0.3743	0.3732	0.3710
0.0811	0.3609	0.3600	0.3604	0.3586	0.3558
0.0922	0.3560	0.3544	0.3535	0.3521	0.3486
X = 10					
0.00500	0.4893	0.4901	0.4922	0.4933	0.4951
0.01001	0.4566	0.4566	0.4580	0.4589	0.4582
0.0400	0.3937	0.3925	0.3899	0.3875	0.3852
0.0501	0.3849	0.3818	0.3789	0.3759	0.3745
0.0601	0.3769	0.3737	0.3701	0.3666	0.3632
0.0801	0.3632	0.3599	0.3557	0.3509	0.3480
0.1001	0.3523	0.3498	0.3448	0.3403	0.3372
0.1502	0.3345	0.3320	0.3255	0.3200	0.3140
X = 20					
0.00386	0.4995	0.5010	0.5037	0.5072	0.5092
0.01001	0.4546	0.4558	0.4575	0.4586	0.4590
0.03002	0.4059	0.4056	0.4054	0.4036	0.4015
0.0400	0.3940	0.3928	0.3924	0.3894	0.3867
0.0500	0.3843	0.3827	0.3826	0.3815	0.3742
0.0601	0.3736	0.3725	0.3731	0.3694	0.3646
0.0801	0.3618	0.3603	0.3579	0.3546	0.3489
0.1001	0.3510	0.3496	0.3483	0.3431	0.3373
0.1501	0.3331	0.3305	0.3275	0.3219	0.3152

<sup>a</sup> Accuracy of molality within 0.05%.

### Results

**Standard emf.**—The most common method used to evaluate the standard potential involves the graphical extrapolation of some linear plot of emf of the cell against the concentration of hydrochloric acid, as in the following equations (16)

$$E'' = E + 2k \log m - 2ksc^{1/2} / (1 + a_0 Bc^{1/2}) - 2k \log (1 + 0.002mM_{xy})$$

$$= E^\circ_m + f(m) \quad [4]$$

where  $E^\circ_m$  is the standard potential of the cell on the molal (m) scale,  $E$  is the observed electromotive force of the cell,  $c$  is the molarity of HCl,  $a_0$  is the ion-size parameter,  $M_{xy}$  is the mean molecular weight,  $k = 2.3026RT/F$ , and  $B$  and  $s_f$  are the Debye-Hückel constants. In this paper, we report the results of  $E^\circ_m$  determined by a theoretically justified polynomial curve-fitting program, which does not require the above information such as the ion-size parameter, the Debye-Hückel constants, the densities, and the dielectric constants of the mixed solvents. It is indeed attractive to contemplate the derivation of  $E^\circ_m$  without the information required in the Gronwall, LaMer, and Sandved (17) extension of the Debye-Hückel theory.

Sen, Johnson, and Roy (18) and our recent papers (19-21) have convincingly demonstrated that an equation of the form

$$E + (2RT/F) \ln m = E^\circ + A_1 m^{1/2} + A_2 m + A_3 m^{3/2} + \dots \quad [5]$$

is theoretically sound and accurately expresses the standard potential.

The activity coefficient (on molal scale) can be expressed by the equation (18)

$$\ln \gamma_{\pm} = A_1' m^{1/2} + A_2' m + A_3' m^{3/2} + \dots \quad [6]$$

where coefficients in Eq. [5] and [6] are not arbitrary adjustable parameters. The form of Eq. [6] has been shown to be consistent with the theory (22).

Table II summarizes the values of the standard potentials on three scales, namely the molal (m), molar (c), and mole fraction (N) scales in DMSO-water

Table II. Standard emf of the cell; Pt | H<sub>2</sub> (g, 1 atm) | HCl (m), DMSO (X), H<sub>2</sub>O (Y) | AgCl, Ag at different temperatures

X = w/o DMSO

t/°C	E° <sub>m</sub>	E° <sub>c</sub>	E° <sub>s</sub>
X = 5 (±0.0003V)			
5	0.2314	0.2310	0.0408
15	0.2255	0.2252	0.0280
25	0.2179	0.2178	0.0136
35	0.2102	0.2103	-0.0010
45	0.2036	0.2039	-0.0144
X = 10 (±0.0006V)			
5	0.2312	0.2306	0.0426
15	0.2210	0.2205	0.0274
25	0.2148	0.2145	0.0129
35	0.2093	0.2091	0.0003
45	0.2029	0.2028	-0.0130
X = 20 (±0.001V)			
5	0.2271	0.2257	0.0426
15	0.2186	0.2174	0.0274
25	0.2117	0.2096	0.0129
35	0.2076	0.2067	0.0032
45	0.1990	0.1983	-0.0120

mixtures. The values of E°<sub>m</sub> are expressed as a function of t(°C) by the equations

## 5% DMSO

$$E^{\circ}_m = 0.2179 - 7.085 \times 10^{-4} (t - 25^{\circ}) - 9.782 \times 10^{-7} (t - 25^{\circ})^2 \quad [7]$$

## 10% DMSO

$$E^{\circ}_m = 0.2147 - 6.840 \times 10^{-4} (t - 25^{\circ}) + 5.807 \times 10^{-6} (t - 25^{\circ})^2 \quad [8]$$

## 20% DMSO

$$E^{\circ}_m = 0.2119 - 6.704 \times 10^{-4} (t - 25^{\circ}) + 3.300 \times 10^{-6} (t - 25^{\circ})^2 \quad [9]$$

The standard potentials on the molar and mole fraction scale, E°<sub>c</sub> and E°<sub>N</sub>, respectively, have been calculated by means of the relationships

$$E^{\circ}_c = E^{\circ}_m + 2k \log \rho_0 \quad [10]$$

and

$$E^{\circ}_N = E^{\circ}_m - 2k \log (1000/M_{xy}) \quad [11]$$

where ρ<sub>0</sub> is the density of the mixed solvent at the particular temperature, and M<sub>xy</sub> is the mean molecular weight of the solvent.

The mean molal activity coefficients of hydrochloric acid, sγ<sub>±</sub>, in DMSO-water mixtures at 25°C were computed from the equation

$$\log s\gamma_{\pm} = [E^{\circ}_m - \{E + (2RT/F) \ln m\}] / (4.6052RT/F) \quad [12]$$

using the respective values of E°<sub>m</sub> listed in Table II. The smoothed values of {E + (2RT/F) ln m} at rounded molalities were obtained from the constants of Eq. [5] and the values of sγ<sub>±</sub> are presented in Table III.

The primary medium effect (ion-solvent interaction) is concentration-independent and measures the change in escaping tendency of HCl in the transfer from a standard state in one solvent to a standard state in another solvent. Thermodynamically, it can be represented as

$${}^wE^{\circ}_m - {}^sE^{\circ}_m = \lim_{m \rightarrow 0} (4.6052RT/F) \log {}^s_w\gamma_{\pm} \quad [13]$$

Table III. Mean activity coefficients (sγ<sub>±</sub>) of hydrochloric acid in 5, 10, and 20 w/o dimethyl sulfoxide at 25°C

m <sub>HCl</sub> , moles/kg	X = 5	X = 10	X = 20
0.001	0.957	0.950	0.927
0.002	0.942	0.933	0.902
0.005	0.917	0.905	0.857
0.01	0.892	0.879	0.817
0.02	0.859	0.852	0.772
0.05	0.824	0.820	0.718
0.1	0.801	0.797	0.692

Table IV. Primary medium effect (molal scale) of dimethyl sulfoxide-water mixtures on hydrochloric acid at 5°, 25°, and 45°C

X = w/o dimethyl sulfoxide

X	5°C	25°C	45°C
5	0.0244	0.0372	0.0373
10	0.0263	0.0631	0.0435
20	0.0637	0.0983	0.0737

where the value of <sup>s</sup>E°<sub>m</sub> is the same as E°<sub>m</sub>. The superscripts w and s on E°<sub>m</sub> represent water and the mixed solvent, respectively. The subscripts w and s on γ<sub>±</sub> mean that γ<sub>±</sub> is referred to unity at infinite dilution in water and in a mixed solvent, respectively. These values are presented in Table IV.

**Relative partial molal enthalpy.**—The relative partial molal enthalpies of HCl for 5 w/o DMSO at five different temperatures were computed with the following equations (23)

$$L_2 = \bar{H} - \bar{H}^{\circ} = \bar{H} - \bar{H}^{\circ} = -2RT^2(\ln s\gamma_{\pm})/\delta T \quad [14]$$

The (δ ln sγ<sub>±</sub>/δT) value required by Eq. [14] was obtained from the first derivative of the least square polynomial

$$-\log s\gamma_{\pm} = A + BT + CT^2 \quad [15]$$

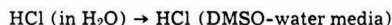
where T is the thermodynamic temperature. The constants of Eq. [15] are given in Table V, together with the standard error of the calculated values of log sγ<sub>±</sub>.

Combination of Eq. [14] and [15] yields

$$L_2 = (2RT^2 \ln 10) (B + 2CT) \quad [16]$$

The values of L<sub>2</sub> are given in Table VI.

**Standard Gibbs energy, entropy, and enthalpy of transfer of HCl from water to the mixed solvent.**—The standard thermodynamic functions for the transfer process (t)



in three DMSO-water mixtures were calculated from the standard emf of the cell in water (16) and in the mixed solvent together with the temperature coefficients of E°<sub>m</sub> in water and the respective mixed solvents. The Gibbs energy of transfer is defined by the equation

$$\Delta G^{\circ}_{t(\text{HCl})} = {}^s\bar{G}^{\circ}_{\text{HCl}} - {}^w\bar{G}^{\circ}_{\text{HCl}} = {}^s\Delta G^{\circ}_{\text{HCl}(\text{soln})} - {}^w\Delta G^{\circ}_{\text{HCl}(\text{soln})} \quad [17]$$

where  $\bar{G}^{\circ}_{\text{HCl}}$  represents the molar Gibbs energy in the

Table V. Constants of the equation -log sγ<sub>±</sub> (molal scale) = A + BT + CT<sup>2</sup>

X = 5

m <sub>HCl</sub> , moles/kg	A	B × 10 <sup>4</sup>	C × 10 <sup>7</sup>	Std. error
0.001	-0.02612	1.8949	-1.1646	0.0001
0.002	-0.01209	0.9731	-1.1688	0.0001
0.01	-0.01793	2.4595	-3.2742	0.0002
0.01	-0.01239	5.2685	-4.6751	0.0001
0.1	-0.15180	12.2221	-8.7866	0.0001

Table VI. Relative partial molal enthalpy (L<sub>2</sub>)<sup>a</sup> of hydrochloric acid in 5 w/o DMSO between 5° and 45°C

m <sub>HCl</sub> , moles/kg	5°	15°	25°	35°	45°
0.001	370	389	409	428	447
0.002	481	524	568	616	656
0.01	671	718	766	816	868
0.05	791	819	845	868	889
0.1	2173	2276	2377	2475	2570

<sup>a</sup> L<sub>2</sub> is expressed in j/mole. 1 thermochemical calorie = 4.1840 joules.

Table VII. Thermodynamic quantities<sup>a</sup> (mole fraction scale) for the transfer of HCl from water to dimethyl sulfoxide-water mixtures at 25°C

X = w/o DMSO

X	$\Delta G^\circ_t$	$\Delta G^\circ_{el}$	$\Delta G^\circ_{chem}$	$\Delta H^\circ_t$	$\Delta S^\circ_t$	D
5	231	6	225	-1630	-6.2	78.30
10	324	17	307	-829	-3.9	78.07
20	294	87	207	-471	-2.6	77.41

<sup>a</sup>  $\Delta G^\circ$  and  $\Delta H^\circ$  are expressed in joules mole<sup>-1</sup> and  $\Delta S^\circ$  in joules K<sup>-1</sup> mole<sup>-1</sup>.

mixed solvent (s) and water (w), respectively. The effect of the solvent on transfer Gibbs energy has been calculated on the mole fraction scale which does not contain the change of the number of solvent molecules by different solvents; therefore, it will eliminate Gibbs energy changes due to concentration changes. The pertinent relationship for the transfer Gibbs energy is given by

$$\Delta G^\circ_t = F(wE^\circ_N - sE^\circ_N) \quad [18]$$

The values of this quantity are given in Table VII

The transfer of charged particles, the hydrogen ion and chloride ion, from water to DMSO-water mixtures can be thought of in three stages: (i) desolvation of the ions in water, (ii) transfer of H<sup>+</sup> and Cl<sup>-</sup> to the mixed solvent (s), and (iii) resolution of the ions in the mixed solvent (s). The parameters that adequately describe the effect of this changing solvent composition on the transfer Gibbs energy are not yet well understood. It is convenient, however, to divide the transfer energy into two parts (24-26)

$$\Delta G^\circ_t = \Delta G^\circ_{el} + \Delta G^\circ_{chem} \quad [19]$$

The electrostatic term,  $\Delta G^\circ_{el}$ , represents the coulombic forces between the ionic charge and the charge distributions on the solvent molecules. All other effects, including the basicity and the difference in work required to create a cavity for the ions in the two media, contribute to the second term (24, 27). The electrostatic contributions to the transfer energy has been computed from the Born equation

$$\Delta G^\circ_{el} = (Ne^2/2)(D_s^{-1} - D_w^{-1})(r_+^{-1} + r_-^{-1}) \quad [20]$$

where  $D_s$  and  $D_w$  represent the dielectric constants of the mixed solvent and water, respectively. The radius of the "hydrogen ion" ( $r_+$ ) is taken as 2.76Å (28) and that of the chloride ion ( $r_-$ ) is taken as 1.81Å (29). The values of  $\Delta G^\circ_{chem}$  have been obtained by subtracting the electrostatic free energy from the total transfer quantity. Table VII summarizes the values of these quantities.

By the application of the usual thermodynamic relationship

$$\Delta S^\circ_t = -d(\Delta G^\circ_t)/dT \quad [21]$$

to the temperature variation of  $E^\circ_m$ , one obtains

$$\Delta S^\circ_t = F[(a + 2bT - 50b - k) - (d_w + 2b_wT - 50b_w - k_w)] \quad [22]$$

where  $a$  and  $b$  are the second and third coefficients of Eq. [7] to [9]. The values of  $a_w$  and  $b_w$  are given in the literature (16); the constant  $k = (2R/F)\ln(1000/M_{xy})$ , and  $k_w$  ( $a$  constant) is taken as  $6.92 \times 10^{-4}$ . The values of  $\Delta S^\circ_t$  are given in Table VII.

The values of the transfer enthalpy, shown in Table VII, were obtained from the relation

$$\Delta H^\circ_t = \Delta G^\circ_t + T\Delta S^\circ_t \quad [23]$$

The values of the electrostatic energy,  $\Delta G^\circ_{el}$ , may be accurate, but the experimental uncertainties in the values of  $\Delta H^\circ_{el}$  and  $\Delta S^\circ_{el}$  will be greater; hence, no attempts were made to calculate these quantities. The correct evaluation of the values of  $\Delta G^\circ_{el}$  is hampered

by the uncertainties of effective ionic radii and the variation of the dielectric constant with distance from the ionic surface (dielectric saturation). Nevertheless, the values of  $\Delta G^\circ_{el}$  (and hence  $\Delta G^\circ_{chem}$ ) can be considered sufficiently significant to draw some general conclusions which are qualitatively correct.

## Discussion

The values of the activity coefficient, Table III, for X = 5, 10, and 20 at 25°C decrease (at a given molality) with the increasing proportions of DMSO. The general pattern of this trend is similar to that found in our other investigations, such as glycerol-water (30), isopropyl alcohol-water mixtures (31). Hydrochloric acid shows the characteristic of a strong electrolyte in the experimental DMSO-water mixtures and its behavior is very similar to that in water. An error of  $\pm 0.09$  mV in emf value corresponds to an error of  $\pm 0.003$  in the values of  $s_{\pm}$ .

An examination of Table IV shows that the escaping tendency of HCl is greater in DMSO-water mixtures than in pure water, because the primary medium effect of DMSO-water mixtures on HCl becomes greater with gradual addition of DMSO.

The total transfer Gibbs energy appears to be positive for all experimental solvent compositions in the DMSO-water system. Hydrochloric acid thus appears to be in a higher Gibbs energy state in the mixed solvent than in water. The positive values of  $\Delta G^\circ_{chem}$  also suggest that, as far as the acid-base reaction or solvation is concerned, the transfer of HCl from water to DMSO-water mixtures is not favored. In other words, water is more basic than the mixed solvent. The values of  $\Delta G^\circ_t$  are accurate to within  $\pm 24$  joule mole<sup>-1</sup>.

The values of  $\Delta H^\circ_t$  and  $\Delta S^\circ_t$  reflect contributions from the effects of the ions on the structure of the solvents while the values of  $\Delta G^\circ_t$  provide information in regard to acid-base theory of ion solvation. The function,  $\Delta G^\circ_t$ , is a simpler one, and may not be affected by structural factors (32-34). It may also be regarded as the resultant of the other two, and more complex. Table VII shows that the values of  $\Delta H^\circ_t$  and  $\Delta S^\circ_t$  are negative, which suggests that, on the transfer process, the net amount of order created by HCl is more in the mixed solvent than in water. Hydrochloric acid thus breaks more structure in water than in DMSO-water mixtures. This is further supported with the view (35) that all structure-forming processes, including solvation of ions are exothermic and are accompanied by a decrease in entropy.

## SYMBOLS

$wE^\circ_N, sE^\circ_N$	standard electrode potential in water and in a mixed solvent (mole fraction scale), volts
$wE^\circ_m, sE^\circ_m$	standard electrode potential in water and in a mixed solvent (molal scale), volts
$a_0$	ion-size parameter, angstroms
X	w/o DMSO in a mixture with water
$s_{\pm}$	mean ionic activity coefficient of HCl (molal scale) in a mixed solvent relative to unit value at infinite dilution in a mixed solvent (subscript, s)
$D_s, D_w$	dielectric constant of the mixed solvent and water, respectively
$M_{xy}$	mean molecular weight of the solvent kg · mole <sup>-1</sup>
$r_+, r_-$	radius of the cation (H <sup>+</sup> ) and anion (Cl <sup>-</sup> ), respectively, angstroms
$L_2$	relative partial molal enthalpy, cal/mole
$E^\circ, A_1, \dots$	the constants of Eq. [5]
A, B, C	empirical constants of Eq. [15]

## Acknowledgments

The authors are indebted to Dr. J. Padron for providing the facility for this experimental work and Mr. G. Moore for his technical assistance.

Manuscript submitted May 4, 1971; revised manuscript received May 26, 1971.

Any discussion of this paper will appear in a Discussion Section to be published in the December 1972 JOURNAL.

## REFERENCES

1. R. N. Roy and B. Sen, *J. Chem. Eng. Data*, **13**, 79 (1968).
2. R. N. Roy, W. Vernon, and A. L. M. Bothwell, *ibid.*, **16**, 347 (1971).
3. D. A. Johnson and B. Sen, *ibid.*, **13**, 376 (1968).
4. E. Tommila and I. Palenius, *Acta Chem., Scand.*, **17**, 1980 (1968).
5. C. A. Kingsbury, *J. Am. Chem. Soc.*, **87**:23, 5409 (1965).
6. A. J. Parker, *Quart. Rev. (London)*, **16**, 163 (1962).
7. C. D. Ritchie in, "Solute-Solvent Interactions," J. F. Coetzee and C. D. Ritchie, Editors, Marcel Dekker, New York (1969).
8. H. L. Clever and E. F. Westrum, *J. Phys. Chem.*, **74**, 1309 (1970).
9. M. Salomon, *This Journal*, **118**, 1392 (1969).
10. G. Holleck, D. R. Cogley, and J. N. Butler, *ibid.*, **116**, 952 (1969).
11. R. G. Bates, "Determination of pH," p. 281, John Wiley & Sons, Inc., New York (1964).
12. G. J. Hills and D. J. G. Ives in, "Reference Electrode," p. 107, D. J. G. Ives and G. J. Janz, Editors, Academic Press, New York (1961).
13. R. N. Roy and B. Sen, *J. Chem. Eng. Data*, **12**, 584 (1967).
14. I. M. Kolthoff and T. B. Reddy, *This Journal*, **108**, 980 (1961).
15. E. Tommila and A. Pajunen, *Suomen Kemistilehti*, **B41**, 172 (1968).
16. H. S. Harned and B. B. Owen, "The Physical Chemistry of Electrolytic Solutions," 3rd ed., pp. 458, 715, Reinhold Publishing Corp., New York (1958).
17. T. H. Gronwall, V. K. LaMer, and K. Sandved, *Physik. Z.*, **29**, 358 (1928).
18. B. Sen, D. A. Johnson, and R. N. Roy, *J. Phys. Chem.*, **71**, 1523 (1967).
19. R. N. Roy, W. Vernon, and A. L. M. Bothwell, *This Journal*, **118**, 1303 (1971).
20. R. N. Roy, W. Vernon, and A. L. M. Bothwell, *J. Chem. Therm.*, **3**, 769 (1971).
21. R. N. Roy, W. Vernon, and A. L. M. Bothwell, *J. Chem. Soc., (A)*, 1242 (1971).
22. A. J. Dill, L. M. Itzkowitz, and O. Popovych, *J. Phys. Chem.*, **72**, 4580 (1968).
23. R. A. Robinson and R. H. Stokes, "Electrolyte Solutions," 2nd revised ed., p. 34, Butterworths, London (1965).
24. R. G. Bates and R. A. Robinson in, "Chemical Physics of Ionic Solutions," chap. 12, B. E. Conway and R. G. Barradas, Editors, John Wiley & Sons, Inc., New York (1966).
25. O. Popovych, *Crit. Rev. Anal. Chem.*, **1**, 73 (1970).
26. M. Alfenaar and C. L. deLigny, *Rec. Trav. Chim.*, **86**, 929 (1967).
27. S. Goldman, P. Sagner, and R. G. Bates, *J. Phys. Chem.*, **75**, 826 (1971).
28. M. Paabo, R. G. Bates, and R. A. Robinson, *ibid.*, **70**, 247 (1966).
29. L. Pauling, "The Nature of the Chemical Bond," 3rd ed., pp. 464, 521, Cornell Univ. Press, Ithaca, N. Y. (1960).
30. R. N. Roy, W. Vernon, and A. L. M. Bothwell, *J. Electroanal. Chem.*, **30**, 335 (1971).
31. R. N. Roy and A. Bothwell, *J. Chem. Eng. Data*, **15**, 548 (1970).
32. D. Feakins in, "Physico-Chemical Processes in Mixed Aqueous Solvents," p. 71, F. Franks, Editor, American Elsevier Publishing Co., New York (1967).
33. R. G. Bates in, "Hydrogen-Bonded Solvent Systems," p. 49, A. K. Covington and P. Jones, Editors, Taylor and Francis, London (1968).
34. F. Franks and D. J. G. Ives, *Quart. Rev. London*, **20**, 1 (1966).
35. H. S. Frank and M. G. Evans, *J. Chem. Phys.*, **13**, 507 (1945).

## Diffusion Kinetics at Microelectrodes

Chris R. Ito, S. Asakura, and Ken Nobe\*

School of Engineering and Applied Science, University of California, Los Angeles, California 90024

## ABSTRACT

The effect of the electrode size on the diffusion current of the cathodic reaction  $I_3^- + 2e = 3I^-$  was investigated under transient conditions. Plane circular surfaces of platinum electrodes with diameters,  $d$ , ranging from 1.27 to 0.0127 cm were used. The diffusion current under potentiostatic conditions could be expressed as

$$i = \frac{nFA\sqrt{DC}}{\sqrt{\pi}} \left( \frac{1}{\sqrt{t}} + \frac{2M\sqrt{\pi d}}{d} \right)$$

where  $M$  is an empirical parameter which is a function of  $d$ . For  $d < 0.1$  cm,  $M = 1$  and the diffusion mode was equivalent to semi-infinite spherical diffusion. On the other hand, for  $d > 0.3$  cm,  $M = 0$ , and semi-infinite linear diffusion was the controlling mode. The change in the diffusion mode occurred rather abruptly at about  $d = 0.2$  cm.

Diffusion kinetics at a microelectrode often plays an important role in electrochemical processes (e.g., electroanalytical chemistry methods, electrodeposition, and electropolishing). It is known that the mass transfer processes at microconfigurations differ to a great extent from those at macroconfigurations. However, comparatively few fundamental studies have been reported on the subject. By dimensional analysis, Agar (1) determined that the mass transfer mode under steady-state conditions changed from convection control to diffusion control as the electrode size decreased. Ibl (2) applied boundary layer theory in his investigation of

the mass transfer process at thin wire electrodes. He determined that the deviation of the diffusion current at plate electrodes increased as the diameter decreased. Jacquet (3) observed the thickness of the anodic diffusion layer during electropolishing and found that it was greater over valleys than over peaks. Beacom (4) studied the thickness of the diffusion layer over small notches by the Schlieren method. Wagner (5) examined theoretically the mass transfer process at a rough surface where the surface roughness was approximated by a sine wave.

A number of papers (6) have been published on electroanalytical studies using stationary microelectrodes. However, only a few of these studies have considered

\* Electrochemical Society Active Member.

Key words: chronoamperometry, tri-iodide, platinum.



the difference between diffusion kinetics at microelectrodes and macroelectrodes.

Under transient conditions, diffusion at planar electrodes has usually been approximated by semi-infinite linear diffusion, regardless of the electrode size. Cottrell (7), Laitinen and Kolthoff (8), and Laitinen (9) showed the constancy of the product of the current and the square root of the time under potentiostatic conditions. However, Vielstich and Delahay (10) pointed out the limitations of applying semi-infinite linear diffusion to small electrodes. Lorenz (11) reported that surface roughness on the order of the diffusion layer thickness increased the transition time during galvanostatic polarization. Although Laitinen and Kolthoff (8) attempted to verify the applicability of semi-infinite spherical diffusion to spherically shaped microelectrodes, convection effects precluded these experimental measurements. Bard (12) surmised that the increase in the chronopotentiometric transition time constant at long transition times is due to spherical diffusion and natural convection. In order to predict more accurately the current-time behavior of finite planar electrodes during chronoamperometric experiments, Lingane (13) expanded the chronoamperometric constant as a power series in terms of the reciprocal of the radius and neglected the second and higher order terms. This expression was almost identical to that obtained for semi-infinite spherical diffusion, the former differing only slightly from the latter in the numerical value of the coefficient of the first-order term. The separate contributions of spherical diffusion and convection could not be determined from Bard's (12) and Lingane's (13) results and, therefore, their dependence on the electrode size could not be ascertained.

As shown in this brief review, only a few studies have been reported on diffusion kinetics at microelectrodes under transient conditions in spite of the importance for transient studies of electrode processes. In this work, the effect of the electrode size on the diffusion kinetics has been studied under transient conditions where the time did not exceed 1 sec. In order to exclude the complication resulting from a slow charge transfer process, a highly reversible redox reaction,  $I_3^- + 2e = 3I^-$ , was examined.

### Experimental

The test cell was a 3 liter Pyrex kettle jar and a specially constructed cover with nine ground glass joints for the positioning of a thermometer, a gas bubbler for deaeration, an auxiliary electrode, a reference electrode, and five test electrodes.

The reference electrode was platinum wire. This wire was placed inside the Luggin capillary. The end of the capillary was placed as close as possible to the test electrode in order to minimize the ohmic potential drop within the electrolyte between the test and reference electrodes. The counterelectrode was a large platinum foil.

The test electrodes were of reference grade platinum and had a plane, circular surface with diameters ranging from 1.27 to 0.0127 cm. The electrodes of small diameter, 0.058, 0.0254, 0.0127 cm, were prepared by sealing the platinum wire in a glass tube of 0.6 cm diameter. The glass tubing was then sanded and polished so that only the cross section of the wire was exposed. For larger diameter wires of 0.206 and 0.129 cm, the platinum wire was sealed in glass tubing with Apiezon wax. The wire was held in the glass tubing and the melted wax was sucked up into the tubing. The electrode was sanded and polished as before. Mercury was used to make contact between the platinum and the copper lead wire. For the electrodes of 1.27 and 0.635 cm diameter, a circular piece of platinum foil was glued onto the polished cross section of an iron rod with conductive epoxy cement. Then, shrinkable Teflon was fitted around the electrode and only the platinum surface was exposed. A holder for these electrodes was

constructed of Teflon rod. Electrical contact was made by a pressure-fitted copper wire.

The electrolyte was 1N potassium iodide containing various amounts of iodine, ranging from 0.1 to 0.001M (molar). The added iodine reacted with  $I^-$  to produce  $I_3^-$  forming the  $I_3^-/I^-$  redox couple (14, 15). Before each run, the electrolyte was deaerated with pre-purified nitrogen for approximately 3 hr.

The potential was controlled and generated with a high speed potentiostat and a mercury relay. The rise time of the potential step imposed on the system was less than 10  $\mu$ sec. The current was recorded with a high speed oscillograph (frequency response of 500 Hz).

### Results

In this paper, the cathodic current is taken as a positive value. A decrease in current due to the diffusion of  $I_3^-$  after the imposition of a potential step was observed. Typical current variations with time are shown in Fig. 1. The current was the function of time ( $t$ ), applied potential ( $E$ ), and the concentration of  $I_3^-$  ( $C$ ). As can be seen in Fig. 1, the current-time curve does not shift when  $E$  is negative enough. In order to examine only the diffusion process, attention was focused on this limiting current,  $i$ . The limiting current thus obtained is plotted vs.  $1/\sqrt{t}$  in Fig. 2 and 3, for all electrode diameters at  $C = 0.02M$ . All plots show a linear relation in the range of 0.01-1 sec. While the plots intersect the origin,  $1/\sqrt{t} = 0$ ,  $i = 0$  for large diameter electrodes, they do not for the small diameter electrodes. The following relationship was obtained

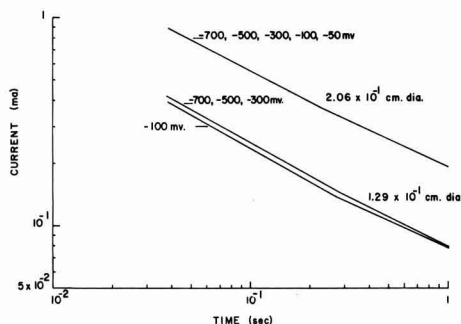


Fig. 1. Current variation with time

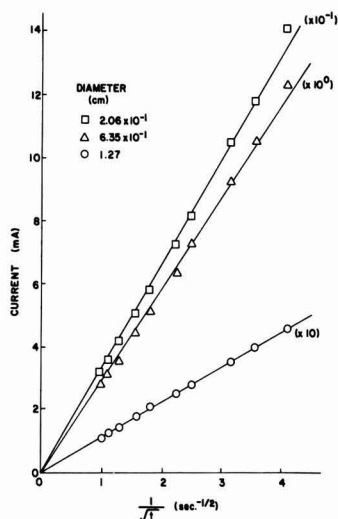
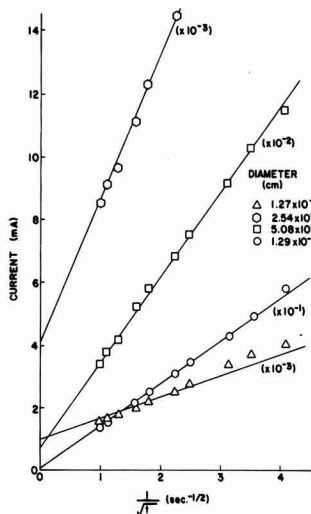


Fig. 2. Plots of current vs.  $1/\sqrt{t}$  for relatively large electrodes

Fig. 3. Plots of current vs.  $1/\sqrt{t}$  for relatively small electrodes

$$i = S(1/\sqrt{t} + f(d)) \quad [1]$$

where  $S$  is the slope of the plot and  $f(d)$  is some function of the diameter. For electrodes of large diameters,  $f(d)$  is zero. The slope,  $S$ , is plotted vs. the electrode diameter ( $d$ ) on a log-log plot in Fig. 4. A linear relation with a slope 2 was obtained, i.e.

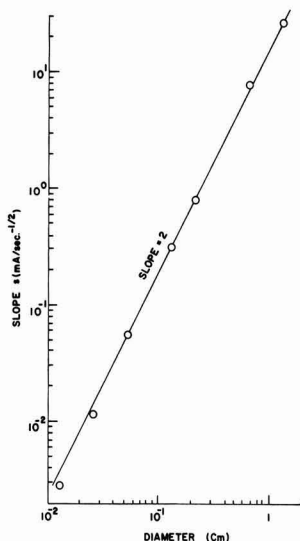
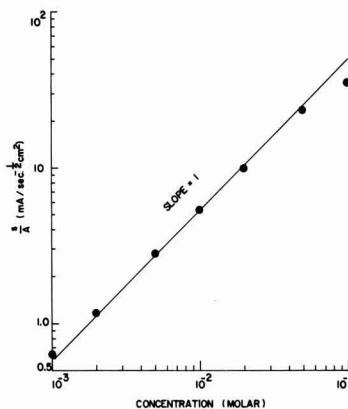
$$S = k_1 d^2 \quad [2a]$$

which can be rearranged to the form

$$S = k_1'(\pi/4)d^2 = k_1'A \quad [2b]$$

where  $A$  is the electrode area. The dependence of  $k_1'$  on  $C$  is shown in Fig. 5. The log of  $S/A$  is linearly related to the log of  $C$  with a slope of unity. Then,  $S$  can be expressed as

$$\frac{S}{A} = k_2 C \quad [3]$$

Fig. 4. Dependence of slope  $S$  on the electrode diameterFig. 5. Dependence of  $S/A$  on concentration

where  $k_2$  is a constant determined experimentally (534 A-cm-sec<sup>1/2</sup>/mole) and is independent of  $C$  and  $d$ .

The current ( $i$ ) can be extrapolated to  $1/\sqrt{t} = 0$  to determine  $f(d)$  as seen in Fig. 3. The extrapolated current ( $i_x$ ) gives the relation

$$f(d) = i_x/S \quad [4]$$

A linear relation was obtained between  $i_x$  and  $d$ , as shown in Fig. 6, when the diameter is less than 0.129 cm, i.e.

$$i_x = k_3 d, \text{ for } d \leq 0.129 \text{ cm} \quad [5]$$

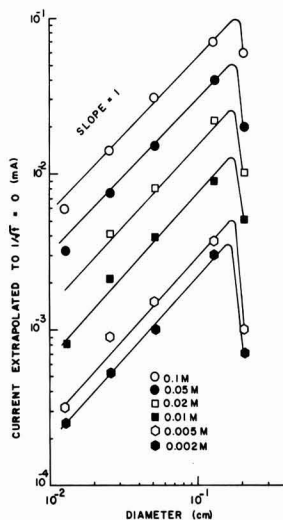
where  $k_3$  is a function of  $C$  and independent of  $d$ . To determine the dependence of  $k_3$  on  $C$ ,  $\log(i_x/d)$  is plotted vs.  $\log C$  in Fig. 7. This plot gives a linear relationship with a slope of unity. Thus, a proportionality between  $k_3$  and  $C$  was obtained and

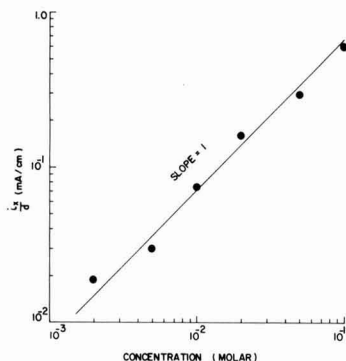
$$i_x = k_4 d C \quad [6]$$

Equations [4] and [6] give

$$f(d) = k_4 d C / S, \text{ for } d \leq 0.129 \text{ cm} \quad [7]$$

where  $k_4$  is a constant determined experimentally (7.15 A-cm<sup>2</sup>/mole) and is independent of  $d$  and  $C$ . Since  $f(d)$  is zero for large electrode diameters, the cur-

Fig. 6. Current extrapolated to  $1/\sqrt{t} = 0$ ,  $i_x$ , vs. electrode diameter.

Fig. 7. Plots of  $i_x/d$  vs. concentration

rent ( $i$ ) in Eq. [1] can be expressed empirically as

$$i = k_2 CA [1/\sqrt{t} + M(k_4/k_2)(d/A)] \quad [8]$$

where  $M$  is a function of the diameter and can have values between zero and one. The dependence of  $M$  on diameter is shown in Fig. 8. It was found that  $M$  decreased rather abruptly from unity to zero as the electrode diameter increased. This abrupt decrease occurred at about the electrode diameter of 0.2 cm.

### Discussion

It is known that when a circular plane electrode is large and the polarization duration is short, mass transport at the electrode is controlled by semi-infinite linear diffusion. However, when the electrode dimension is small, mass transfer is approximated by semi-infinite spherical diffusion. The limiting current for a potential step is given by Eq. [9] for semi-infinite linear diffusion and by Eq. [10] for semi-infinite spherical diffusion (16)

$$i_{lin} = \frac{nFA\sqrt{DC}}{\sqrt{\pi}\sqrt{t}} \quad [9]$$

$$i_{sph} = \frac{nFA\sqrt{DC}}{\sqrt{\pi}} \left( \frac{1}{\sqrt{t}} + \frac{2\sqrt{D\pi}}{d} \right) \quad [10]$$

where  $n$  and  $F$  have their usual significance and  $A$  and  $D$  are the electrode area and the diffusion coefficient of  $I_3^-$ , respectively.

The current can be expressed generally for all electrode diameters examined in this study by introducing an empirical parameter  $M$

$$i = \frac{nFA\sqrt{DC}}{\sqrt{\pi}} \left( \frac{1}{\sqrt{t}} + \frac{2M\sqrt{D\pi}}{d} \right) \quad [11]$$

In the case of  $d \leq 0.1$  cm, the diffusion mode is semi-infinite spherical diffusion and  $M = 1$ . For  $d > 0.3$  cm,  $M = 0$  and semi-infinite linear diffusion is the controlling mode. The change from semi-infinite spherical to semi-infinite linear diffusion occurs around  $d = 0.2$  cm. It is evident that when plane circular electrodes similar in size to those examined in this investigation are used, the change of the diffusion mode with the electrode dimensions is an important consideration.

### Acknowledgment

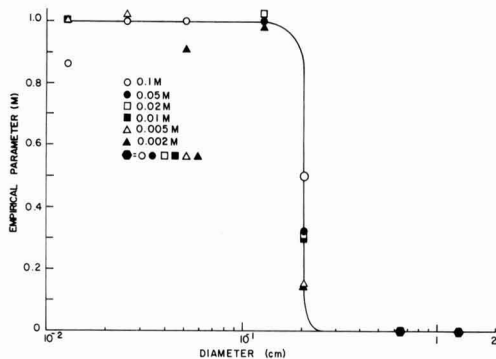
This work is part of the UCLA Engineering research program in Air Pollution.

Manuscript submitted Sept. 25, 1971; revised manuscript received Dec. 29, 1971.

Any discussion of this paper will appear in a Discussion Section to be published in the December 1972 JOURNAL.

### REFERENCES

1. J. N. Agar, *Discussions Faraday Soc.*, No. 1, 26 (1947).
2. N. Ibl, *Electrochim. Acta*, **1**, 3 (1959).
3. P. A. Jacquet, *Nature*, **135**, 1076 (1935).
4. S. E. Beacom, *Plating*, **46**, 814 (1959).
5. C. Wagner, *This Journal*, **101**, 225 (1954).
6. I. M. Kolthoff and J. J. Lingane, "Polarography," 2nd ed., Vol. 1, p. 399, Interscience, New York (1952).
7. F. Cottrell, *Z. Phys. Chem.*, **42**, 385 (1902).
8. H. Laitinen and I. Kolthoff, *J. Am. Chem. Soc.*, **61**, 3344 (1939).
9. H. Laitinen, *Trans. Electrochem. Soc.*, **82**, 289 (1942).
10. W. Vielstich and P. Delahay, *J. Am. Chem. Soc.*, **79**, 1874 (1957).
11. W. Lorenz, *Z. Elektrochem.*, **59**, 730 (1955).
12. A. J. Bard, *Anal. Chem.*, **33**, 11 (1961).
13. Z. G. Soos and P. J. Lingane, *J. Phys. Chem.*, **68**, 3821 (1964); P. J. Lingane, *Anal. Chem.*, **36**, 1723 (1964).
14. J. Mellor, "A Comprehensive Treatise on Inorganic and Theoretical Chemistry," Vol. 2, p. 815, Longmans and Green Co., New York (1922).
15. J. Lingane, "Electroanalytical Chemistry," p. 141, Interscience Publishers, Inc., New York (1958).
16. P. Delahay, "New Instrumental Methods in Electrochemistry," Interscience Publishers, Inc., New York (1954).

Fig. 8. Variation of the empirical parameter  $M$  with electrode diameter.

# Local Natural Convection Mass Transfer Measurements

J. R. Lloyd

University of Notre Dame, Notre Dame, Indiana 46556

and E. M. Sparrow and E. R. G. Eckert

University of Minnesota, Minneapolis, Minnesota 55455

## ABSTRACT

Apparatus and experimental technique for measurements of local natural convection mass transfer on vertical and upward-facing inclined surfaces are described, and corresponding results are presented and discussed. The experiments were performed using the electrochemical technique, with  $\text{Cu}^{++}$  as the transferred ions and sulfuric acid as the supporting electrolyte. The objective of the research was to obtain highly local information. Two types of mass transfer probes were employed, the smaller of which were about  $\frac{1}{4}$  mm in spanwise width, with a probe-to-probe spacing of  $1/20$  mm. These miniature probes were used in the measurement of spanwise mass transfer variations encountered in the laminar-turbulent transition regime on inclined surfaces. Local laminar mass transfer results and instability Rayleigh numbers for vertical and inclined plates were measured by means of a set of small circular probes. All data were collected for limiting current operation, and the requisite concentration levels of  $\text{Cu}^{++}$  ions were examined and documented. In addition, the influence of cathode-to-anode orientation was investigated, as were the edge effects associated with the lateral edges of the test surface.

Electrochemical techniques have been used by numerous investigators in recent years to study mass transfer between a surface and a liquid environment, as witnessed, for instance, by a recently published summary paper by Mizushima (1). One of the attractive features of these techniques is the capability of obtaining local mass transfer results, that is, mass transfer results for a small region of the over-all surface being studied. The present concern with local measurements is motivated by the nature of the phenomenon being investigated. It has been shown by flow visualization studies (2) that for natural convection adjacent to an inclined upward-facing surface, the breakdown of the laminar regime is marked by the presence of a secondary flow. That is, superposed on the main streamwise flow, there are alternate regions of inflow and outflow distributed more or less periodically across the horizontal span of the surface. It would be expected that such an inflow-outflow pattern would give rise to a spanwise variation of surface mass transfer. The typical spanwise dimension of the inflow-outflow cells observed in this investigation is 1 mm. Therefore, to resolve the spanwise mass transfer distribution within a cell, several local measurements must be made within a span of 1 mm. Thus, it is necessary that the mass transfer probes be very small and, also, that they be very close together.

The instrumentation and experimental technique for performing highly localized measurements of the type discussed above is described here in detail. Also, representative spanwise mass transfer distributions are presented for the laminar-to-turbulent transition regime in natural convection flow on inclined surfaces.

Quite apart from the just-mentioned spanwise distributions, another type of local measurements was made which is appropriate to either the laminar or turbulent regimes. The instrumentation and technique for this measurement is also described. Local mass transfer results are presented for laminar natural convection flow on vertical and inclined surfaces. From these results, the Rayleigh number marking the breakdown of the laminar regime is identified.

A survey of the available literature failed to disclose local electrochemical mass transfer measurements characterized by probe sizes and by probe-to-probe proximities as small as those of the present investiga-

tion. Only in connection with wall shear stress measurements, where electrodes are embedded in an inert wall, have comparably small electrodes been employed (3). Representative prior studies, where either local or quasi-local electrochemical mass transfer measurements are reported, may be found in Ref. (4-6) for natural convection flow and in Ref. (7, 8) for forced convection flow.

## Experimental Apparatus

An over-all schematic diagram of the experimental apparatus is pictured in Fig. 1. The electrochemical fluid, an aqueous solution of cupric sulfate and sulfuric acid, both reagent grade, was contained in a polyethylene tank ( $61 \times 45.6 \times 45.6$  cm, length  $\times$  width  $\times$  height). The cupric ions play the role of the transferred ion and plate out on the cathode, thereby giving rise to concentration and density gradients in the fluid adjacent to the cathode. In turn, the density gradient creates a buoyancy force which causes the natural convection flow.

As seen in the figure, the main components of the apparatus included the cathode (which is the test surface), anode, reference electrode, circuitry, instrumentation, power source, and voltage control. These several components will now be described, starting with the test surface.

A front-face schematic of the test surface is shown in Fig. 2. As pictured therein, the test surface con-

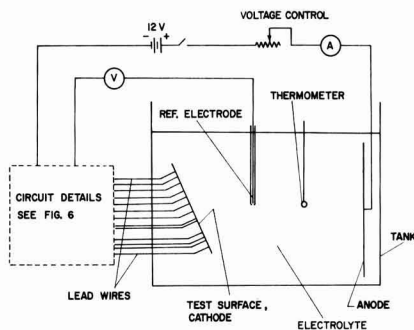


Fig. 1. Over-all schematic of the experimental apparatus

Key words: natural convection, inclined surface, mass transfer, limiting current.

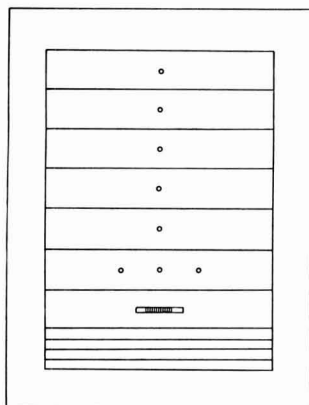


Fig. 2. Front-face view of the test surface

sisted of eleven individual segments set into an electrically passive framework. All segments were fabricated from nickel 200 and were 0.635 cm thick and 15.2 cm in spanwise width. The seven probe-bearing segments were 2.54 cm high, whereas the four uninstrumented segments, which served to vary the streamwise locations of the mass transfer probes, were 0.635 cm in height. The positions of the segments could be interchanged at will, so that their arrangement in Fig. 2 is only for illustration. The active surface had a streamwise height of 20.3 cm and a spanwise width of 15.2 cm. The width of the surrounding Teflon frame was 2.54 cm.

Six of the segments were instrumented with small circular electrodes (0.343 cm diameter) which served as local mass transfer probes for flow conditions characterized by spanwise uniformity (i.e., either laminar or turbulent flow). The circular probes were situated at the centers of the respective host segments and, in one case, two supplementary probes were installed 2.54 cm to either side of the center. The installation of the circular probes is illustrated in Fig. 3, which is a schematic view of the back face of one of the host bars. The probe was electrically insulated from the host bar by a 0.0127 cm annular gap filled with epoxy. The back side of the probe and the attached end of the current-carrying lead wire were embedded in epoxy. Glyptal insulating paint was applied to the epoxy and to the entire back face of the host bar.

The seventh instrumented segment contained an ensemble of 55 very small probes whose function was to measure the spanwise mass transfer distribution in the laminar-turbulent transition regime on inclined upward-facing surfaces. The probe ensemble consisted of successive sheets of nickel 200 and of polyethylene insulation. Each probe had a spanwise dimension of 0.0254 cm, with a spacing between probes (i.e., thickness of the polyethylene foil) of 0.0051 cm. In the streamwise direction, the probes were 0.318 cm in length. The end pieces of the ensemble were also of nickel 200, 0.635 cm thick, and cut in the same shape as the probes. The ensemble was held together by two nickel screws which were insulated from the probes by Teflon tubing. A photograph of the probe section is given in Fig. 4, wherein the active sensing surface is along the bottom-most edge.

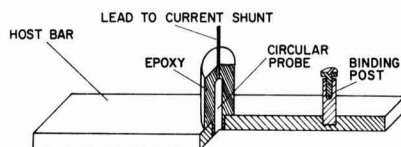


Fig. 3. Diagram showing installation of circular probes

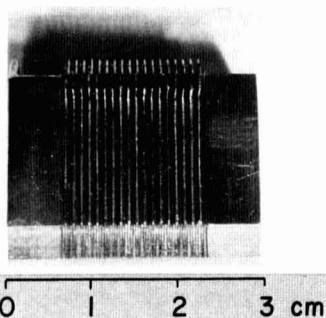


Fig. 4. Photograph of the ensemble of miniature probes

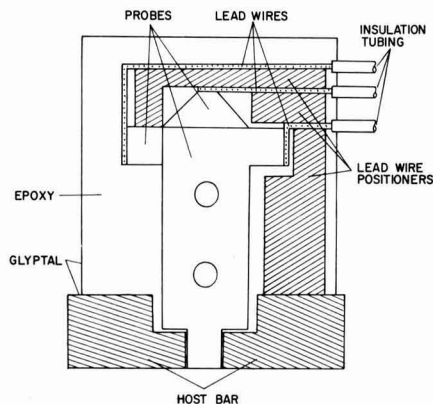


Fig. 5. Diagram showing installation of miniature probes

The assembly of the probe section and its installation in the host bar are illustrated in Fig. 5. A rectangular hole slightly larger than the face of the probe section was machined into the bar, with a clearance of about 0.02 cm being maintained. Glyptal insulating paint was poured into the gap and a coating of epoxy applied to the face of the probe section and on the hardened Glyptal filler. The hardened epoxy was carefully finished with grade 600 wet or dry Tri-M-ite paper and a fine hone, exposing the faces of all 55 probes. The probe section was held in place by a bracket mounted on the back of the host bar.

Lead wires were soldered to the probes and segregated from each other by positioners as shown in Fig. 5, the lead wires being affixed to the positioners with epoxy. The figure shows the different positions of lead wire attachment for three successive probes. The entire back side of the probe section, the positioners, and the ends of the lead wires were painted with Glyptal, embedded in epoxy, and painted again with Glyptal to ensure that no unaccounted areas were exposed to the electrolyte solution.

Each one of the eleven segments comprising the test surface was equipped with a binding post on its back face to facilitate connection to the external circuit. The posts and wire were of nickel 200. Glyptal insulating paint was applied to the binding posts, and plastic tape was wrapped around them to retard corrosion of the area of electrical contact.

The segmented test surface was housed in a Teflon frame which has already been mentioned in connection with Fig. 1. A groove was machined along the inner circumference of the frame to receive the segments, so that the exposed face of the test surface and of the frame were in the same plane. The segments themselves were carefully aligned to ensure that they presented a smooth, continuous surface to the flow, and



the alignment, once attained, was fixed by electrically isolated, thumb-tightened set screws. The Teflon frame was supported by a nickel-plated stand, which was painted with Glyptal to make it electrically and chemically neutral. The stand facilitated the positioning of the test surface at various angles of inclination. Typically, the test surface was situated about 4 cm above the floor of the tank, and its topmost edge was 15 to 20 cm beneath the surface of the electrochemical bath.

The anode was a 40-cm square copper sheet, 0.08 cm thick. For the data runs, the anode was positioned as indicated in Fig. 1. However, a number of preliminary runs were made to explore the influence of anode position on the mass transfer results, and the findings of these runs are reported in a later part of the paper.

A reference electrode was placed in the electrolyte solution to facilitate the measurement of the voltage between the fluid bulk and the test surface. The reference electrode was a 0.1 cm diameter copper wire housed in a Teflon tube. A small hole at the bottom of the tube permitted the electrolyte to contact the electrode. The reference electrode was typically positioned to the side of the test surface (about 5 cm away) and at its half-height.

### External Circuitry and Instrumentation

A schematic diagram of the electric circuitry is presented in Fig. 6. A 12V automotive storage battery, supplemented by a rheostat and a trimming pot, served as the power supply. The cathode voltage was measured with a 0-1.5V, 1%, d-c Simpson panel meter. A calibrated Weston Model 901 d-c ammeter served to measure the over-all current flow through the electrolyte.

The segments which make up the cathode were tied together electrically, so that they were all of the same potential. Adjacent segments were actually in contact, but gaps are indicated in the figure in order to delineate the separate segments. A current shunt was incorporated into the circuit for each of the probes. The current shunts for the eight circular probes were 15-ohm calibrated precision resistors. For the ensemble of 55 miniature probes, 55-1%, 174-ohm calibrated precision resistors served as the current shunts.

For the steady mass transfer rates encountered under laminar flow conditions, the voltage drops across the current shunts were measured with a Leeds and Northrup K-3 potentiometer, supplemented by a low contact resistance, 24-position thermocouple selector switch. For the unsteady mass transfer rates that are characteristic of nonlaminar flows, the shunt voltage drops were read with a Dymec Digital Voltmeter. This

instrument could be programmed to read repetitively the output of a single probe at preselected intervals of time. Alternatively, it could be programmed to read successively the outputs of as many as 24 probes, with the sweeping of the 24 probes being repeated as many times as desired. To accommodate the 55 probes of the ensemble to the Dymec, they were subdivided into two sets of 24 and one set of seven. About 45 sec were required to disconnect one set and to connect another.

### Experimental Technique

During the course of each data run, copper was plated out on the test surface. Removal of deposited copper and refinishing of the surface was a necessary aspect of the experimental procedure. The importance of removing the deposited copper is heightened when local mass transfer probes are used, as in the present experiments. If not removed, a build-up of deposited copper could eventually bridge over the insulation between a probe and its host bar or between adjacent probes. Such a bridging over would cause the local probe to become inoperative.

At the conclusion of each data run, the cathode and anode were water washed and carefully dried with soft paper towels, and the mass transfer probes were checked for shorts. Prior to the start of a new data run, the electrodes were painstakingly resurfaced. The resurfacing operations were performed in such a way as to ensure that the surfaces of the probes and the host bars were coplanar. First, the test surface was wiped clean of any airborne particles. Then, grade 600 wet or dry Tri-M-ite paper was used to refinish all parts of the test surface except for the ensemble of 55 miniature probes, for which a wet, very fine hone was used (to avoid shorts between adjacent probes). Immediately after the refinishing, methanol technical was freely applied to wash away small particles of copper sanding dust. Next, the epoxy insulation between the probes and their host bars was cleaned with a stiff bristle brush and methanol technical, after which all parts of the test surface were washed again with liberal amounts of methanol technical and wiped with paper gauze pads. Finally, all probes were checked to verify the absence of shorts.

The anode was also subjected to a sequence of resurfacing operations similar to those for the test surface, with grade 180 wet or dry paper being employed in the refinishing of both sides of the anode.

Prior to the initiation of the mass transfer process, the electrochemical solution was stirred to ensure uniformity of concentration and temperature, and a waiting period was allowed for the decay of motions due to stirring. No data were collected until the starting transient of the system had died away.

The data acquisition procedure for laminar and for nonlaminar conditions differed because the mass transfer rates were, respectively, steady and unsteady. Only the unsteady situation merits discussion here. The signal from any one of the circular probes was read by the Dymec Digital Voltmeter at intervals of 0.2 to 0.3 sec for a period of 3 min to determine timewise variations in the local rate of mass transfer. Alternatively, the outputs of the eight circular probes were read in succession, with the eight-probe sweep being repeated again and again. Local time averages were evaluated from instantaneous data collected from both of these measurement procedures. For the ensemble of miniature probes, the signals from the first 24 probes were read successively by the Dymec in a period of about 7 sec, and the scanning of this set of probes was repeated until about 1½ min had elapsed. Then, the second set of 24 probes was connected to the Dymec and readings were taken for 1½ min, and so forth.

The composition of the bulk solution was obtained by sampling. The concentrations of the copper ions and sulfuric acid were determined, respectively, by spectrometric and titration methods, described in Ref. (9) and (10), respectively. Vertical concentration

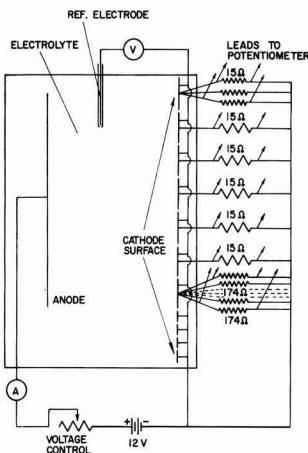


Fig. 6. Electric circuitry diagram

gradients were monitored, and data acquisition was restricted to cases where the gradient was less than 0.00007M (molar) concentration of copper ions per centimeter. No change in the mixed mean bulk concentration was detected during the course of a data run.

### Limiting Current Conditions

To facilitate the evaluation of mass transfer coefficients, all final data were taken for the limiting current operating condition. This condition corresponds to a zero concentration of transferred ion (i.e., copper) at the cathode, thereby eliminating the need for concentration measurements at the test surface. Limiting current operation can be identified by a plateau in a graph of cathode current vs. cathode voltage (measured with respect to the reference electrode).

The attainment of a limiting current plateau is favored by higher concentrations of copper ions in the fluid bulk. On the other hand, the rate at which copper plates out on the test surface is also increased with higher bulk concentrations. Such higher plating rates can lead to short circuiting of the mass transfer probes. Furthermore, high plating rates enhance the rapidity at which the surface of the plated copper may become roughened, thereby causing a change in the effective surface area (11). It is relevant, therefore, to perform the experiments at the lowest bulk copper ion concentrations which are compatible with the existence of a limiting current plateau.

Figures 7 and 8 show typical current-voltage curves. The bulk copper ion concentration ranged from 0.0066 to 0.0825M for these test conditions, while the sulfuric acid concentration was about 1.5M for all cases. It is evident that limiting current plateaus do not exist for the 0.0066 and 0.0113M concentrations. On the other hand, the curves for the 0.0375 and 0.0825M concentrations indicate limiting current operation. The absence of limiting current plateaus at low copper ion concentrations has already been noted by Fenech and

Tobias (5). The cause of this behavior is not completely understood at the present.

On the basis of Fig. 7 and 8 and of other such current-voltage curves, it was established that limiting current operation could be attained for bulk copper ion concentrations above 0.03M. To ensure that all final data actually corresponded to limiting current operation, a current voltage curve such as those of Fig. 7 and 8 was mapped out for each data run. A sequence of six or seven steps was taken to define limiting current conditions. At each step, the current was monitored with a strip chart recorder, and a steady reading was approached before advancing to the next step. The length of the data acquisition period under steady limiting-current conditions varied with the type of flow observed; for laminar flow approximately 1½ min, for turbulent flow approximately 3 min, and to monitor two sets of local spanwise readings about 4 min.

### Results and Discussion

Owing to the fact that all data were taken for limiting current operation and in the presence of excess supporting electrolyte, the local mass transfer coefficient  $k_x$  can be evaluated as

$$k_x = i/nF c_\infty \quad [1]$$

where  $i$  and  $c_\infty$ , respectively, denote the measured values of the current density and the concentration of copper ions in the fluid bulk. The quantities  $n$  and  $F$  are the valence of the copper ions and the Faraday number. A dimensionless representation for  $k_x$  is provided by the Sherwood number  $Sh_x$ , which is defined as

$$Sh_x = k_x x / D \quad [2]$$

in which  $x$  is the streamwise distance along the test surface, with  $x = 0$  corresponding to the leading edge of the active surface.

The other dimensionless grouping relevant to the natural convection process is the Rayleigh number. In constructing the Rayleigh number appropriate to an inclined test surface, we use the component of the body force parallel to the surface (i.e.,  $g \cos \theta$ ) and indicate the presence of the inclination angle  $\theta$  by the notation  $Ra_\theta$ . Then, the local Rayleigh number is given by

$$Ra_{\theta,x} = [\rho_f g \cos \theta (\rho_\infty - \rho_w) x^3 / \mu^2] Sc \quad [3]$$

where  $Sc$  denotes the Schmidt number  $\mu/\rho D$ , and  $\rho_\infty$  and  $\rho_w$  are the densities in the fluid bulk and at the surface. The quantities  $D$ ,  $\rho$ , and  $\mu$  appearing in Eq. [2] and [3] were evaluated at the average of the concentrations at the wall and in the bulk. Typically, the wall-to-bulk fluid property variations were on the order of 1%. Detailed information about the evaluation of the fluid properties is given in Ref. (12). The property evaluations were based on data given in Ref. (5) and in Ref. (19-24).

An initial set of experiments was performed to explore the effect of cathode-to-anode orientation. Another objective of this set of experiments was to examine the influence of edge effects associated with the lateral edges of the test surface. The experiments in question were performed for laminar flow conditions and with the test surface vertical. However, instead of the configuration pictured in Fig. 2, the test surface assembly was turned through 90 degrees, so that the main line of circular probes was situated along a horizontal, each probe being at the same distance from the leading edge. Five electrically active, instrumented segments were employed, each with a central circular probe, plus Plexiglas spacer bars which were used to segregate the active segments. The active segments and spacers were arranged so that, proceeding along the horizontal span of the test surface, one encounters the 2.54 cm Teflon frame, 10.16 cm of active surface, a 2.54 cm spacer, 2.54 cm of active surface, a 5.08 cm spacer, and the Teflon frame.

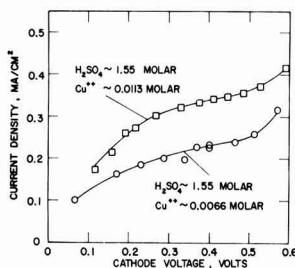


Fig. 7. Current-voltage curves at low  $Cu^{++}$  concentrations

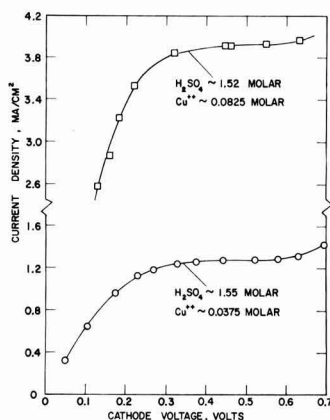


Fig. 8. Current-voltage curves showing limiting current plateaus

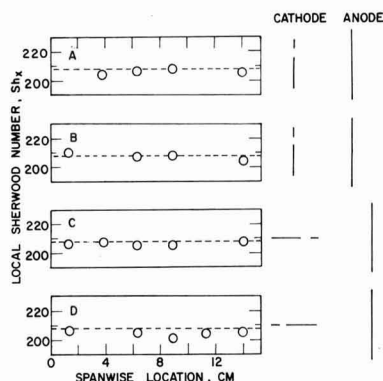


Fig. 9. Spanwise uniformity tests for laminar flow adjacent to a vertical plate.

Local Sherwood number results from four experimental runs, performed over a period of several days, are shown in Fig. 9. The dashed line appearing in each graph represents the prediction of laminar vertical plate theory corresponding to  $Sc = 2000$  (13)

$$Sh_x / 0.499 Ra_x^{1/4} = 1 \quad [4]$$

Adjacent to the graph for each run is a plan-view schematic indicating the positioning of the cathode and the anode. The line representing the cathode denotes the active portions of the surface, and the break in the line denotes a spacer. In runs A and B, the cathode and anode were parallel, whereas in runs C and D they were at right angles. Owing to the shorting out of a mass transfer probe, only four data points appear in the graphs for runs A and B.

Inspection of the figure indicates that the mass transfer results show no systematic variation with spanwise location, regardless of the position of the anode or of the proximity of a probe to the lateral edges of the test surface. Furthermore, the agreement of the data with laminar theory is excellent, the average deviation being about 1.6%. These findings indicate that for the conditions of the present experiments, cathode-to-anode orientation and edge effects have a negligible influence on the mass transfer results. Furthermore, the excellent agreement with theory lends confidence in the experimental technique, instrumentation, and thermophysical properties used in the data reduction.

For all subsequent experimental runs, the test surface was situated in its original configuration, and the anode was positioned parallel to the cathode and as far away as possible.

A second series of experiments was performed to determine local laminar mass transfer results for vertical and inclined surfaces and, in addition, to examine the conditions marking the breakdown of the laminar regime. The circular mass transfer probes were used in these experiments. The results are plotted in Fig. 10 with  $Sh_x / 0.499 Ra_x^{1/4}$  on the ordinate and  $Ra_{\theta,x}$  on the abscissa. The motivation for the form of the ordinate variable stems from the analytical prediction for laminar natural convection mass transfer on a vertical plate, Eq. [4], which, when generalized by replacing  $g$  with  $g \cos \theta$ , becomes

$$Sh_x / 0.499 Ra_{\theta,x}^{1/4} = 1 \quad [5]$$

Equation [5] corresponds to  $Sc = 2000$ , which is the typical Schmidt number of the experiments. In view of Eq. [5] and if laminar theory is obeyed, the data, when plotted using the coordinates of Fig. 10, should fall on a horizontal line having an ordinate value of unity. A particular advantage of such a presentation is that deviations from the laminar line are readily

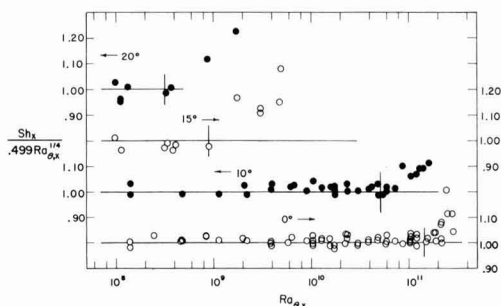


Fig. 10. Local laminar mass transfer results on vertical and inclined surfaces.

observable, thereby facilitating the identification of the onset of laminar-turbulent transition.

Results for surface inclination angles, relative to the vertical, of 0, 10, 15, and 20 degrees are plotted in Fig. 10. The data for each inclination angle are referred to a separate ordinate scale, as designated by the arrows. Results for inclination angles greater than 20 degrees are not shown in the figure since, for such angles, the flow at the lowermost probe was not laminar.

Inspection of Fig. 10 shows excellent agreement between the laminar data and the analytical prediction expressed by Eq. [5], adding further confidence in the experimental technique, instrumentation, and thermophysical properties. For the inclination angles of 0 and 10 degrees, the experimental results are generally within 3% of the prediction in the laminar range. At the 15 and 20 degree inclination angles, where there are fewer laminar data, the agreement is within 4%.

The present local mass transfer results for the vertical plate, when integrated over a streamwise length  $L$ , yield  $Sh_L = 0.665 Ra_L^{1/4}$ , which is in excellent agreement with the over-all measurements of Wilke, Tobias, and Eisenberg (14). On the other hand, the over-all measurements of Fouad and Ahmed (15) on vertical and inclined plates appear to lie outside the laminar regime, so that no comparisons are possible.

Next, attention may be turned to the onset of laminar-turbulent transition. One way of identifying the onset of transition is from the systematic upward departure of the data, as plotted in Fig. 10, from the horizontal lines which correspond to laminar flow. A second indication is given by the measurements of current flow. For strictly laminar conditions, the current readings were very steady. However, for Rayleigh numbers just below those at which data lift-off occurred, small fluctuations in the readings were observed. The Rayleigh numbers at which these fluctuations were first noted are indicated by short vertical lines for each angle of inclination. These Rayleigh numbers are regarded here as marking the onset of transition and are listed in Table I.

The table indicates that the transition Rayleigh number decreases with increasing angle of inclination. The drop-off is especially sharp between 10 and 20 degrees, and this might well be due to the change in the nature of the laminar instability as observed via flow visualization (16).

The transition Rayleigh numbers of Table I, which correspond to mass transfer at  $Sc = 2000$ , do not corre-

Table I. Rayleigh numbers at the onset of transition

$\theta$ (degrees)	$Ra_{\theta,x}$
0	$1.5 \times 10^{11}$
10	$5.0 \times 10^{10}$
15	$9.1 \times 10^9$
20	$3.5 \times 10^9$

late too well with those encountered in heat transfer experiments at Prandtl numbers in the range 0.7-5 (16). (The Schmidt and Prandtl numbers play analogous roles in the mass and heat transfer processes.) In particular, at inclination angles of 0 and 10 degrees, the  $Ra_{\theta,x}$  of Table I are substantially higher than the available transition values from heat transfer studies. Thus, the Rayleigh number might not, in itself, be a sufficient criterion for transition, and there might be a separate dependence on the Schmidt (or Prandtl) number. This possibility has already been suggested by Fouad and Ibl (17). Also, it is quite possible that the natural disturbances in the fluid environment may be smaller in the mass transfer case than in the heat transfer case, thereby favoring a later transition in the former.

The transition Rayleigh number of Table I for the vertical plate falls in the range encountered in other electrochemical mass transfer experiments; however, as noted in Ref. (18), there is a substantial spread in the results from different investigations.

The last set of experiments to be reported here are those in which the array of miniature probes was used to measure spanwise mass transfer distributions on inclined surfaces in the laminar-turbulent transition regime. Some preliminary experiments for laminar flow adjacent to a vertical surface gave data which agreed very well with the analytical predictions. The deviations were only a few per cent, and this might well have been due to uncertainties in the visual determination of the electrically active surface area of the miniature probes.

Representative transition regime results for inclined surfaces are pictured in Fig. 11, which is for an inclination angle of 30 degrees relative to the vertical. The figure shows instantaneous spanwise mass transfer distributions. The ordinate is the current density, which is directly proportional to the mass transfer rate. The abscissa is the spanwise location, measured relative to the first probe in the ensemble. Data from probes 1 through 24 are plotted in the left-hand part of the figure, while data from probes 25 through 48 are shown in the right-hand part. To provide a clearer picture, dashed lines have been faired through the points for a given instant of time.

The instantaneous distributions presented in Fig. 11 were constructed from cross plots of the data collected from the successive sweeps of the probe ensemble. The time lapses between the successive instantaneous distributions are indicated in the figure, as is the Rayleigh number.

From the figure, it is seen that the instantaneous mass transfer rate varies in an oscillatory manner across the span of the plate. The amplitude of the variation is a substantial fraction of the spanwise

average. The distance between adjacent peaks and valleys is on the order of 1 mm. Results similar to Fig. 11, but for other inclination angles, are available in Ref. (12).

### Concluding Remarks

The miniature probes employed in the present experiments appear to have been equal to the task of resolving the spanwise variations encountered in the transition regime on inclined surfaces. The spanwise dimensions of the probes and of the insulation between the probes were the smallest that could be fabricated consistent with the avoidance of short circuits in the probe assembly prior to its use in the electrochemical solution. During the course of the experiments, the sulfuric acid in the electrochemical solution attacked the epoxy insulation, ultimately causing short circuiting of adjacent probes.

It is clear from Fig. 11 that had larger probes and/or greater probe-to-probe separation distances been employed, an accurate picture of the spanwise variations would not have been obtained.

Manuscript submitted Aug. 13, 1971; revised manuscript received Jan. 11, 1972.

Any discussion of this paper will appear in a Discussion Section to be published in the December 1972 JOURNAL.

### REFERENCES

1. T. Mizushima in, "Advances in Heat Transfer," Vol. 7, T. F. Irvine and J. P. Hartnett, Editors, Academic Press, New York (1971).
2. E. M. Sparrow and R. B. Husar, *J. Fluid Mech.*, **37**, 251 (1969).
3. J. S. Son and T. J. Hanratty, *ibid.*, **35**, 353 (1969).
4. C. Wagner, *This Journal*, **95**, 161 (1949).
5. E. J. Fenech and C. W. Tobias, *Electrochim. Acta*, **2**, 311 (1960).
6. G. Schütz, *Int. J. Heat Mass Transfer*, **6**, 873 (1963).
7. A. Iribarne, A. O. Gosman, and D. B. Spalding, *ibid.*, **10**, 1661 (1967).
8. T. Mizushima, *op. cit.*, pp. 128-132 and 135-136.
9. E. B. Sandell, "Colorimetric Determination of Traces of Metals," Interscience Publishers, New York (1950).
10. I. M. Kolthoff and E. B. Sandell, "Textbook of Qualitative Inorganic Analysis," Macmillan, New York (1965).
11. N. Ibl and J. N. Schadeegg, *This Journal*, **114**, 54 (1967).
12. J. R. Lloyd, "Laminar, Transition, and Turbulent Natural Convection Adjacent to Vertical and Upward Facing Inclined Surfaces," Ph.D. Thesis, Department of Mechanical Engineering, University of Minnesota (1971).
13. A. J. Ede in, "Advances in Heat Transfer," Vol. 4, J. P. Hartnett and T. F. Irvine, Editors, Academic Press, New York (1967).
14. C. R. Wilke, C. W. Tobias, and M. Eisenberg, *Chem. Eng. Prog.*, **49**, 663 (1953).
15. M. G. Fouad and A. M. Ahmed, *Electrochim. Acta*, **14**, 651 (1969).
16. J. R. Lloyd and E. M. Sparrow, *J. Fluid Mech.*, **42**, 465 (1970).
17. M. G. Fouad and N. Ibl, *Electrochim. Acta*, **3**, 233 (1960).
18. J. Selman and J. Newman, *This Journal*, **118**, 1070 (1971).
19. M. Eisenberg, C. W. Tobias, and C. R. Wilke, *ibid.*, **103**, 413 (1956).
20. G. W. Vinal and D. N. Craig, *J. Res. Nat. Bur. Std.*, **10**, 781 (1933).
21. A. F. W. Cole and A. R. Gordon, *J. Phys. Chem.*, **40**, 733 (1935).
22. W. A. James, E. A. Hollingshead, and A. R. Gordon, *J. Chem. Phys.*, **7**, 89 (1939).
23. E. A. Hollingshead and A. R. Gordon, *ibid.*, **8**, 423 (1940).
24. Landolt-Bornstein, "Physikalisch-Chemische Tabellen," 5 Auflage, **1**, 248 and 397 (1936).

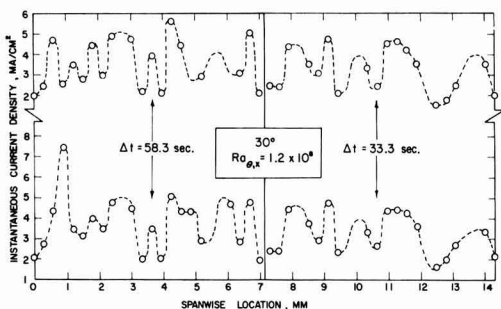


Fig. 11. Instantaneous spanwise mass transfer distributions in the laminar-turbulent transition regime.



# Throwing Power Measurements during High Rate Nickel Dissolution under Active and Transpassive Conditions

Dieter Landolt\*

Energy and Kinetics Department,  
School of Engineering and Applied Science, University of California, Los Angeles, California 90024

## ABSTRACT

Throwing power measurements for anodic dissolution of nickel under electrochemical machining conditions were performed in a flow channel apparatus. Acidified 1M NaCl and neutral 1M NaClO<sub>3</sub> solutions were chosen as examples of a nonpassivating and a passivating electrolyte. Anode and cathode potential measurements and current efficiency determinations were used for the interpretation of measured throwing power data. Current distribution at high current densities was little affected by passivation. The lower throwing power found for the passivating NaClO<sub>3</sub> electrolyte compared to the nonpassivating NaCl electrolyte was therefore solely due to a different dependency of dissolution efficiency on current density.

Throwing power is a concept used by electroplaters to describe the ability of a bath to yield macroscopically uniform deposits. Throwing power is usually determined experimentally in a Haring Blum cell (1) by measuring the weight change of two equipotential cathodes located at different distances from a central anode. Several empirical formulas are in use for calculating a numerical value of throwing power from such measurements. The concept of throwing power can also be applied to electrochemical machining (ECM) for characterizing the degree of "overcut" or "stray cutting" occurring during a machining operation with a given electrolyte. A low value of throwing power is desirable in ECM because "overcut" can be reduced by restricting anodic dissolution to the immediate vicinity of the cathodic tool. In analogy to the electroplating situation, the experimental determination of ECM throwing power may include the measurement of the weight loss of two equipotential anodes located at different distance from a central cathode. Such measurements have recently been reported by Brook and Iqbal (2), but their data have been criticized by Chin and Wallace (3). The latter authors propose a different experimental method based on the assumption that a logarithmic relationship between weight loss ratio and length ratio exists.

It has been mentioned in the literature that better dimensional accuracy can be obtained in ECM if passivating electrolytes such as sodium chlorate are employed (4, 5), but few pertinent data have been given so far to explain this behavior. The present study was undertaken with the aim to investigate the difference in ECM throwing power between a nonpassivating and a passivating electrolyte and to relate the measured throwing power to the more fundamental parameters, current distribution and dissolution efficiency. For this purpose weight loss determinations and electrode potential measurements for anodic dissolution of nickel were carried out with well-defined cell geometry under carefully controlled experimental conditions. Acidified sodium chloride and neutral sodium chlorate solutions were chosen as examples of a nonpassivating and a passivating electrolyte, respectively. The metal-electrolyte combinations were chosen because of their technological interest and because their electrochemical behavior had been studied previously in this laboratory. Separate experiments performed on a technical ECM machine suggested that general conclusions based on the behavior of nickel in these two electrolytes ought to be applicable to the machining of steel also (6).

## Experimental

**Apparatus and experimental method.**—In the present study it was necessary to measure dissolution rates, electrode potentials, and throwing power under identical, well-defined conditions. Because this is difficult to accomplish in a Haring Blum type cell involving the simultaneous dissolution of two anodes, it was considered more suitable to perform subsequent experiments with a single anode at varying gap width while keeping cell voltage and temperature constant. For that purpose a flow channel cell with fixed electrodes was used in which the distance between anode and cathode was given by the thickness of a Teflon spacer inserted between two PVC cell blocks. A detailed description of the cell and the apparatus which included a discontinuously driven piston pump and a 2 liter electrolyte storage flask has been given elsewhere (7). The flow channel employed was 0.317 cm wide and 0.0534, 0.140, or 0.267 cm high. The distance between fluid inlet and upper edge of the electrodes was 7 cm. At the smallest gap width of 0.0534 cm this corresponded to 77 hydraulic diameters, sufficient to establish fully developed velocity profiles at the electrodes. At larger gap width the velocity profiles at the electrodes were not fully developed, but the conclusions of the present study are not affected by this fact.

The 0.317 cm wide and 1.02 cm long electrodes were made of nickel 200 cast into a PVC holder. Before each measurement the anodes were ground to a 400 carborundum surface finish and washed with detergent. To maintain geometry, the duration of the experiments was kept short. The maximum amount of dissolved material in any experiment corresponded to an average depth of dissolution of  $69 \times 10^{-4}$  cm or 13% of the smallest gap width. Length ratios needed in throwing power calculations were not corrected for this small change. All experiments were conducted at a constant volume flow rate of 16.9 ml/sec. At the smallest gap width this corresponded to a linear velocity of 1000 cm/sec. Temperature in all experiments was  $25.5^\circ \pm 0.5^\circ\text{C}$ . Analytical grade chemicals and distilled water were used. Special care was taken to avoid the presence of chloride ion in the NaClO<sub>3</sub> solution. Tests with AgNO<sub>3</sub> indicated that the chloride ion concentration in these solutions was below the detection limit of  $10^{-4}$  moles/liter. The apparatus did not contain any metallic parts in contact with the solution, thus eliminating possible contamination of the solution during experiments. Effects of gas evolution and electrolyte heating on measured throwing power data were eliminated by restricting the current density to values below 15 A/cm<sup>2</sup> (8). This current den-

\* Electrochemical Society Active Member.

Key words: electrochemical machining, throwing power, transpassive dissolution, nickel, sodium chlorate.



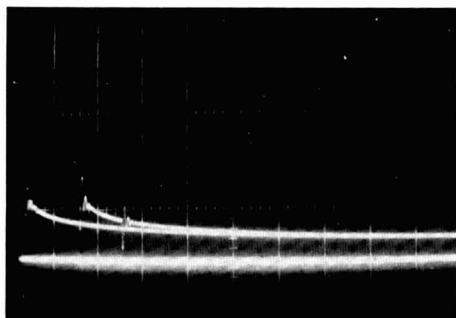


Fig. 1. Anodic potential decay transients measured in 0.9M NaCl + 0.1M HCl. Flow velocity 1000 cm/sec; potential scale 0.2 V/division; time scale 50  $\mu$ sec/division; current densities 3.6 A/cm<sup>2</sup> (left), 6.5 A/cm<sup>2</sup> (right). Horizontal line = open circuit potential.

sity is somewhat low for practical ECM, but is significantly higher than current densities used in conventional electrolysis. The experiments were therefore expected to provide a valid insight into the factors determining throwing power in high rate metal dissolution.

**Throwing power measurements.**—At first current vs. cell voltage curves were determined by applying a constant voltage to the cell from a constant voltage/constant current power supply<sup>1</sup> and recording the resulting current as a function of time on a strip chart recorder.<sup>2</sup> The same procedure was then used for throwing power measurements, except that in addition the time of the experiment was measured with a stopwatch and the total charge passed was calculated by integration of the current trace. In all experiments the anode was ground on 400 carborundum, rinsed, and dried. It was then weighed on an analytical balance to 0.1 mg accuracy and inserted into the cell. After the experiment it was quickly removed, rinsed, dried, and reweighed.

In order to compute throwing power data from separate weight loss measurements performed at different gap width voltage, temperature and time have to be identical. In the present experiments, the amount of material dissolved at the smallest gap width had to be small to preserve geometry (see above). Keeping the experimental time the same in all experiments would therefore have resulted in even smaller amounts being dissolved at the lower currents corresponding to larger gap width. To circumvent this problem, the experiments at larger gap were run for a longer time period than at the smaller gaps. A "reduced" weight loss corresponding to the time of the shortest experiment was then computed from the measured weight loss and current data.

**Current-voltage curves.**—When measuring potential-current curves at high current density, voltage drops between capillary tip and measuring electrode have to be eliminated. This was accomplished here in two different ways. On one hand, a constant current was applied to the cell using the power supply mentioned above. After 2 to 3 sec, the current was interrupted by means of a mercury relay and the nonohmic potential decay was monitored on an oscilloscope with a time scale of 50  $\mu$ sec/division (Fig. 1). A dynamic hydrogen reference electrode was used in these experiments. It consisted of two platinized platinum wires across which a constant current density of approximately 1 mA/cm<sup>2</sup> was applied. The potential of this electrode was periodically checked against a saturated calomel electrode.

In the second type of experiment, a constant potential was applied to the working electrode and the current was recorded as function of time. A multipurpose

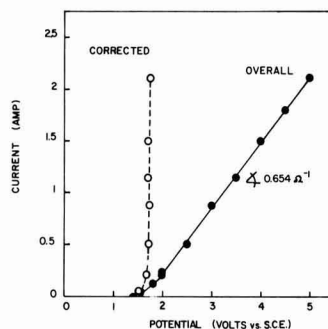


Fig. 2. Anodic current potential curve illustrating algebraic IR correction. Electrolyte 1M NaClO<sub>3</sub>; flow velocity 1000 cm/sec; electrode area 0.322 cm<sup>2</sup>.

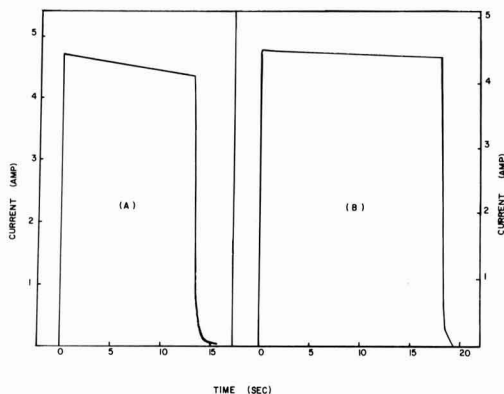


Fig. 3. Current time response to application of constant cell voltage: (A) 0.9M NaCl + 0.1M HCl, applied voltage = 9.55V; (B) 1M NaClO<sub>3</sub>, applied voltage = 14.2V, electrode area 0.322 cm<sup>2</sup>, gap 0.0534 cm, flow velocity 1000 cm/sec.

electrochemistry unit<sup>3</sup> including potentiostat, function generator, and recorder was employed. In this case anode potentials were measured vs. a saturated calomel reference electrode. From the measured current time traces, the over-all current potential curve was plotted as illustrated in Fig. 2. At high current densities these curves exhibited a linear behavior and the effective ohmic resistance could be estimated from the slope. Using this resistance value, the IR contribution to each measured point was evaluated and subtracted from the over-all potential. Although this procedure is not accurate enough for mechanistic studies, it was sufficient for the purposes of the present investigation. All current potential measurements were performed at the smallest gap width and a temperature of 25.5 $\pm$ 0.5°C.

## Results

Typical current transients measured on application of a constant cell voltage are given in Fig. 3. They exhibit a steady decrease with time which is due to the dissolution of the anode. Initial current values measured with freshly ground anodes are plotted vs. cell voltage in Fig. 4. Weight loss experiments were performed at the voltages indicated by the dotted line (Fig. 4). The results are summarized in Table I. Throwing power data derived from these measurements are given in the first five columns of Table II. The length ratio is obtained by dividing the larger by the smaller gap width, the weight loss ratio by dividing the "reduced" weight loss corresponding to the smaller gap by that corresponding to the larger gap.

<sup>1</sup> Harrison Laboratories Model 6267A, 0-36V, 0-10A.

<sup>2</sup> Honeywell Elektronik Model 194.

<sup>3</sup> Princeton Applied Research, Model 170.

Table I. Experimental weight loss determination

Electrolyte	Applied voltage (V)	Gap (cm)	Initial current density, A/cm <sup>2</sup>		Dissolution time (sec)	Measured weight loss (mg)	Current efficiency for dissolution* (%)	Reduced weight loss (mg)**	
			Measured	Average				Individual	Average
0.9M NaCl + 0.1M HCl	9.55	0.0534	4.7	4.72	13.5	18.7	100.2	18.7	18.9
			4.75		13.5	19.1	101.7	19.1	
		0.140	1.83	1.84	29.1	16.6	102.4	7.70	7.71
			1.85		34.5	19.7	103.6	7.71	
		0.267	1.07	1.05	50.5	16.3	97.4	4.36	4.27
1M NaClO <sub>3</sub>	14.2	0.0534	1.03	4.55	53.5	16.5	100.6	4.17	7.43
			4.55		18.0	7.3	30.2	7.3	
		0.140	4.54	1.79	18.7	7.9	31.4	7.56	
			1.80		45.0	5.7	24.0	2.28	
		0.267	1.00	1.00	45.0	5.7	24.0	2.28	
			1.00		61.0	2.8	15.0	0.83	
			1.00		61.2	3.2	17.1	0.94	0.88

\* Based on Ni<sup>2+</sup> formation.

\*\* Weight loss computed for the time of the shortest experiment, i.e. 13.5 sec in sodium chloride and 18.0 sec in sodium chlorate.

Numerical values of throwing power shown in the fifth column were computed by using an empirical formula which is commonly employed in the electroplating literature

$$TP = \frac{(L - M) 100}{L + M + 2} \quad [1]$$

Here  $L$  is the length ratio and  $M$  is the weight loss ratio.

For the chloride solution the calculated value of throwing power is nearly zero. This indicates that in this case the weight loss is almost inversely proportional to electrode distance (primary current distribution). In NaClO<sub>3</sub>, on the other hand, negative values of throwing power are obtained. This means that here the weight loss at larger gap width is even less than predicted for primary current distribution. The throwing power data of Table II are also represented in Fig. 5 in the form of a "linear throwing index" plot. The "linear throwing index" is defined as the slope of the best straight line resulting from plotting the weight loss ratio vs. the length ratio. The "linear throwing index" is 1 for primary current distribution and zero for secondary current distribution. In NaClO<sub>3</sub>, a throwing index larger than one is obtained, indicating again an even less uniform cutting rate than corresponding to primary current distribution.

Results of anode and cathode potential measurements in 0.9M NaCl + 0.1M HCl are given in Fig. 6. The black dots were derived from potential decay transients as illustrated by Fig. 1. All the other points were determined from measurements of the type illustrated in Fig. 2. The IR free potential values exhibit anodic Tafel behavior up to the highest current densities employed. Due to uncertainties in IR compensation, the points scatter considerably making an accurate determination of the Tafel slope difficult. The solid line indicated in Fig. 6 which reasonably well represents the data has a slope of 80 mV consistent with results of other nickel dissolution studies (9, 10). The cathodic data can be approximated by two logarithmic relationships with a slope of approximately 190 mV. The plateau separating the two cathodic Tafel regions is apparently due to a change in the mechanism of the hydrogen evolution reaction coinciding with the depletion of H<sup>+</sup> ions near the cathode. Conditions during weight loss experiments shown in Tables I and II corresponded to the upper cathodic Tafel region. It may be

noted that potential data given here include possible concentration polarization effects since they refer to

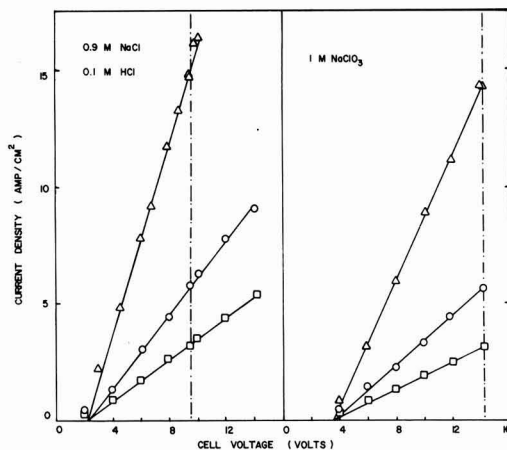


Fig. 4. Current vs. cell voltage curves for different gap width:  $\Delta$  = 0.0534 cm,  $\circ$  = 0.140 cm,  $\square$  = 0.267 cm, flow rate 16.9 ml/sec.

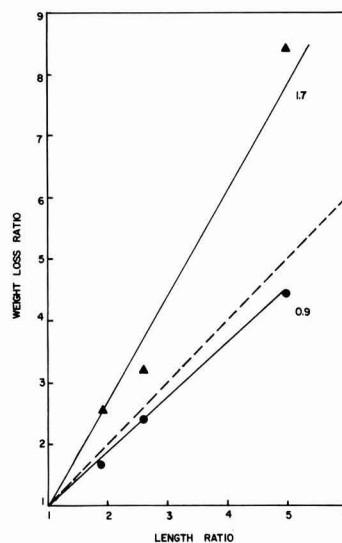


Fig. 5. Weight loss ratio as a function of length ratio for 1M NaClO<sub>3</sub> ( $\Delta$ ) and 0.9M NaCl + 0.1M HCl ( $\bullet$ ). Slopes indicated represent the "linear throwing index;" broken line with slope 1 corresponds to primary current distribution.

Table II. Throwing power data

Solution	Applied voltage (V)	Length ratio	Weight loss ratio	Throwing power	Current ratio	Calculated current ratio
0.9M NaCl + 0.1M HCl	9.55	5.0	4.42	0.077	4.49	4.87
		2.62	2.45	0.054	2.57	2.58
		1.91	1.81	0.058	1.75	1.89
1M NaClO <sub>3</sub>	14.2	5.0	8.45	-0.30	4.55	4.89
		2.62	3.26	-0.16	2.54	2.58
		1.91	2.59	-0.27	1.79	1.89

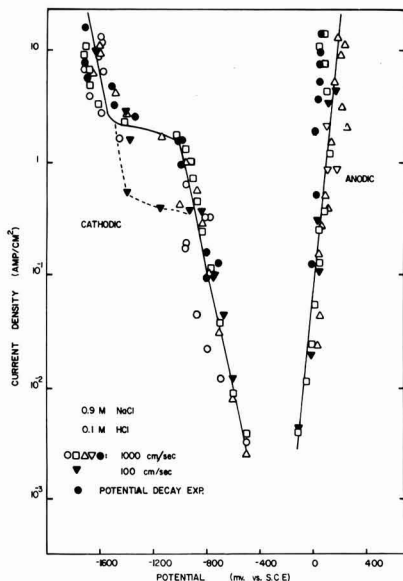


Fig. 6. Anodic and cathodic current potential curve (excluding IR drops) for nickel in 0.9M NaCl and 0.1M HCl at different flow velocity, gap = 0.0534 cm.

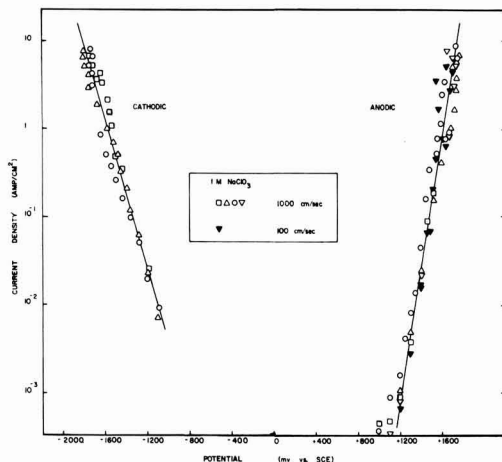


Fig. 7. Anodic and cathodic current potential curve (excluding IR drops) for nickel in 1M NaClO<sub>3</sub> at different flow velocity; gap = 0.0534 cm.

measurements taken at sufficiently long times to establish steady state with respect to mass transfer. This was done purposely because the aim of the measurements was not so much to establish detailed charge transfer kinetics, but to measure electrode potentials prevailing under conditions of throwing power determinations. From the data taken at different flow rate (Fig. 6) it appears, however, that anodically mass transfer did not substantially affect the polarization curve.<sup>4</sup> Potential data for 1M NaClO<sub>3</sub> are given in Fig. 7. Again Tafel behavior is observed, the anodic and cathodic slopes being approximately 150 and 240 mV, respectively. No significant effect of flow rate on mea-

<sup>4</sup> This statement holds true only within the range of measurements shown. Indeed it was observed that at a flow rate of 100 cm/sec increasing the current density above the maximum values given in Fig. 6 led to a change in the shape of the current transient and to brightening of the surface, both facts being indications of a change in dissolution mechanism.

sured anode potentials is observed. Compared to the data obtained in chloride solution, the anodic Tafel line is shifted to much higher potentials here. This is due to anodic passivation: nickel in acidified NaCl dissolves in the active mode, but it spontaneously passivates in neutral NaClO<sub>3</sub>. The anodic current voltage curve shown, therefore, refers to transpassive behavior. Previous studies in this laboratory (9) showed that vigorous oxygen evolution occurs in the transpassive potential region.

### Discussion

Numerical values of throwing power or throwing index such as given in Table II or Fig. 5 are useful for comparing different electrolytes, but they do not have much physical significance because for a given metal electrolyte combination they depend on cell dimensions and applied voltage (11, 12). In order to gain an insight into the physical parameters governing ECM throwing power, one has to consider separately current distribution and dissolution efficiency. Current distribution can be computed from a knowledge of the current-potential curve and the specific electrolyte resistance. For example, in the case of the present throwing power experiments it is possible to estimate the current ratios of Table II from measurements at a single gap width. Neglecting edge effects, the current density is given by

$$i \approx (U - \phi_t) / \rho_e l \quad [2]$$

with  $\rho_e$  = specific electrolyte resistance and  $\phi_t$  = sum of anode and cathode potentials,  $U$  = applied cell voltage,  $l$  = gap width. From Fig. 6 and 7,  $\phi_t$  can be approximated for NaCl and NaClO<sub>3</sub>, respectively by

$$\phi_t(\text{NaCl}) = 1.58 + 0.27 \log i \quad [3]$$

and

$$\phi_t(\text{NaClO}_3) = 3.22 + 0.37 \log i \quad [4]$$

The magnitude of  $\rho_e$  can be estimated from cell voltage and potential data as illustrated by Fig. 8. From Eq. [2], [3], and [4], the current density for a given cell voltage and gap width is obtained and current ratios for different gap widths can be computed. Results given in the last column of Table II show good agreement between calculated and measured current ratios. It is to be noted that in the present experiments current distribution is not affected by anodic passivation. This conclusion ought to apply in ECM whenever significant concentration polarization effects are absent and a logarithmic current-potential relationship exists.

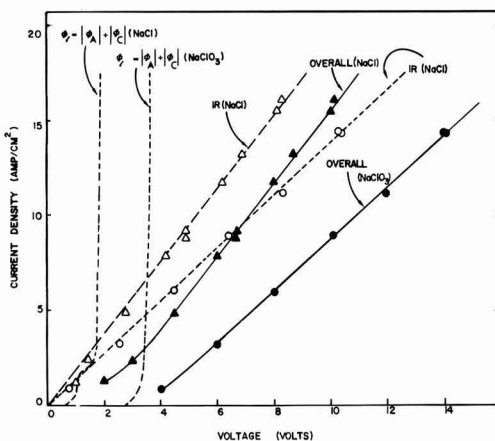


Fig. 8. Ohmic voltage drop in cell obtained by subtracting independently measured electrode potentials from cell voltage. Gap 0.0534 cm, flow velocity 1000 cm/sec;  $\Delta$  cell voltage,  $\triangle$  IR in 0.9M NaCl + 0.1M HCl,  $\bullet$  cell voltage,  $\circ$  IR in 1M NaClO<sub>3</sub>, . . . sum of anode + cathode potentials (from Fig. 6 and 7).

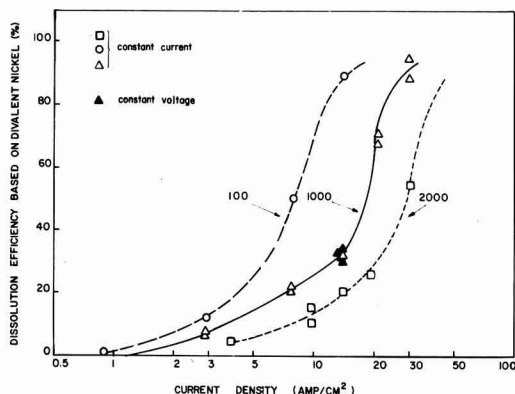


Fig. 9. Current efficiency for nickel dissolution in 1M  $\text{NaClO}_3$  (based on  $\text{Ni}^{2+}$  formation) as a function of current density; gap 0.0534 cm, flow velocity 100, 1000, 2000 cm/sec.

Current distribution on the work piece is then determined by the magnitude of a dimensionless parameter (13)

$$P = \frac{b}{2.3 \rho_e l i} \quad [5]$$

where  $b$  is the anodic Tafel slope,  $\rho_e$  the specific electrolyte resistance,  $l$  a characteristic length, and  $i$  the current density. Primary current distribution is approximated for  $P \ll 1$ . Because of the high current densities employed this condition usually ought to be satisfied in ECM. For example, using the measured  $b$  and  $\rho_e$  values for NaCl and  $\text{NaClO}_3$ , respectively, with the gap width  $l$  as characteristic length the value of  $P$  in the present experiments varied between 0.0046 to 0.0041 for NaCl and between 0.0057 and 0.0051 in  $\text{NaClO}_3$ . Upon application of higher current densities, the value of  $P$  would be even smaller. It is worth noting that  $P$  does not depend on the actual anodic potential values, but only on the slope of the current voltage curve. Therefore the width of the passive potential region in a conventional potentiostatic current-voltage curve should not significantly affect current distribution under ECM conditions, contrary to some statements found in the literature (15).

The data in Table II indicate that the reason for the observed difference in throwing power between the passivating  $\text{NaClO}_3$  and the nonpassivating NaCl lies in a different dependency of dissolution efficiency on current density. In the case of NaCl, the metal dissolution efficiency is constant, while in the case of  $\text{NaClO}_3$  it is a strong function of current density. This is further illustrated by the data of Fig. 9, which were obtained from weight loss determinations performed at constant current density at the smallest gap width of 0.0534 cm. For comparison the weight loss data of Table I, obtained at constant voltage, are also indicated. Because of oxygen evolution, very low metal dissolution efficiencies are obtained at low current densities, but with increasing current the dissolution efficiency sharply increases. The detailed shape of the curve depends on flow rate; the higher the flow rate, the lower the dissolution efficiency at a given current

density. A similar S shaped curve for dissolution efficiency of nickel in  $\text{NaClO}_3$  plotted vs. current density has been obtained previously in this laboratory in a different experimental cell (9). The numerical values obtained in that study were somewhat different, however, and no effect of stirring was observed. This was probably because hydrodynamic conditions were not as well defined as here. A more detailed investigation of the experimental factors affecting current efficiency for nickel dissolution in the transpassive potential region will have to be made before a mechanistic interpretation of the shape of the curves shown in Fig. 9 can be given.

The present results show clearly, however, that a discussion of how passivating electrolytes affect the dimensional control in ECM cannot be based on current potential measurements alone, but it has to include the study of reaction stoichiometry. Lower values of throwing power than theoretically possible with a nonpassivating electrolyte can indeed be obtained with a passivating electrolyte provided the current efficiency for metal dissolution is an increasing function of current density. The present study, therefore, supports and puts on a firm basis ideas advanced by other workers (6, 16, 17) who recognized the importance of the metal dissolution efficiency in obtaining good dimensional control with passivating ECM electrolytes.

### Acknowledgment

Financial support of this work by the Office of Naval Research under Contract No. N00014-69-A-0200 is greatly appreciated.

Manuscript submitted Dec. 1, 1971; revised manuscript received Jan. 15, 1972.

Any discussion of this paper will appear in a Discussion Section to be published in the December 1972 JOURNAL.

### REFERENCES

1. H. E. Haring and W. Blum, *Trans. Am. Electrochem. Soc.*, **44**, 313 (1923).
2. P. A. Brook and Q. Iqbal, *This Journal*, **116**, 1458 (1969).
3. D. T. Chin and A. J. Wallace, Jr., *ibid.*, **118**, 831 (1971).
4. M. A. LaBoda and M. L. McMillan, *Electrochem. Technol.*, **5**, 340 (1967).
5. J. P. Hoare, M. A. LaBoda, M. L. McMillan, and A. J. Wallace, Jr., *This Journal*, **116**, 199 (1969).
6. D. Landolt and J. Sutherland, *UCLA Engineering Report No. 7174*, October 1971.
7. D. Landolt, Submitted to *Rev. Sci. Instr.*
8. D. Landolt, R. H. Muller, and C. W. Tobias, *This Journal*, **117**, 839 (1970).
9. M. Datta and D. Landolt, *UCLA Engineering Report No. 7102*, January 1971; *Corrosion Sci.*, To be published.
10. M. L. Kronenberg, J. C. Bantor, E. Yeager, and F. Hovorka, *This Journal*, **110**, 1007 (1963).
11. J. N. Agar and T. P. Hoar, *Discussions Faraday Soc.*, **1**, 158 (1947).
12. T. P. Hoar and J. N. Agar, *ibid.*, **1**, 162 (1947).
13. C. Wagner, *Plating*, **48**, 988 (1961).
14. J. A. Klingert, S. Lynn, and C. W. Tobias, *Electrochim. Acta*, **9**, 297 (1964).
15. J. P. Hoare, *This Journal*, **117**, 142 (1970).
16. K. Chickamori and S. Ito, *Denki Kagaku*, **38**, 492 (1970).
17. W. König and H. Degenhardt, "Fundamentals of Electrochemical Machining," Charles L. Faust, Editor, Electrochemical Society Inc. (1971).



## Gallium Oxidation in Alkaline Solution

R. S. Perkins<sup>1</sup>

Department of Chemistry, University of Southwestern Louisiana, Lafayette, Louisiana 70501  
and

Rate Processes Institute, University of Utah, Salt Lake City, Utah 84112

The electrochemistry of gallium is important not only in practical applications, but also for theoretical considerations due to its existence as either a liquid or a solid in aqueous electrode systems.

Past studies of the anodic oxidation of Ga in alkaline solutions have been limited. It is the purpose of this study to investigate in somewhat more detail, using cyclic voltammetry, the first stages of anodic oxidation of Ga in aqueous NaOH solutions.

### Experimental

A three compartment Pyrex cell was used.

Carbonate free NaOH solutions were made of reagent grade materials. Solutions were made from water doubly distilled from a basic permanganate solution.

The reference, counter, and test electrodes were each in a separate cell compartment and each were in the same solution. A closed stopcock effectively separated the reference and working compartments. An open stopcock connected the counter and working compartments. A hydrogen reference electrode and a platinum counterelectrode were used. Test electrodes of several designs were used. All test electrodes were made from gallium of 99.999% purity. In some experiments the test electrode consisted of a gallium hemisphere of 0.06 cm<sup>2</sup> geometrical area formed in one end of a U-shaped glass tube. Another design consisted of gallium forced through a 0.051 cm diameter channel in a short length of Teflon tube. The emerging gallium formed a bead of area approximately 0.008 cm<sup>2</sup>. In one experiment this bead was removed and the electrode was planar with an area equal to the cross sectional area of the 0.051 cm diameter channel in the Teflon.

The gallium electrode used was prepared and installed in the cell in an atmosphere of nitrogen. After fabrication, the gallium electrode was solidified. Experiments were carried out at room temperature, approximately 25°C.

Except for the reference electrode compartment, the cell was deaerated with nitrogen.

A conventional cyclic voltammetry apparatus was used with an Exact Electronics function generator and a Wenking potentiostat. The resulting curves were displayed on an X-Y recorder.

In some experiments, current-potential curves were obtained as the gallium electrode was mechanically renewed by scraping. For this work an experimental arrangement similar to that described previously (1) was used. The Teflon mounted gallium electrode was used.

### Data

The data taken was in the form of potential-current plots over the potential region of hydrogen evolution to various points of anodic oxidation. Experiments in each solution were done at a number of sweep rates as will be noted in the discussion to follow. A typical curve obtained in 1M NaOH is given in Fig. 1. It is seen to consist of a region of hydrogen evolution, a region of anodic oxidation which is composed of sev-

eral smaller regions defined by shoulders and changes of slope, and a small region of cathodic reduction which obviously represents much less charge than the corresponding region of anodic oxidation. The qualitative features of this curve do not change greatly when the sweep rate is altered.

### Discussion

In these experiments the most striking feature of the data is the fact that with increasing anodic potential, the current increases without limit in the potential range studied, and this current is not due to oxygen evolution. Experiments were also performed in which the potential was adjusted to greater anodic values, and it was observed that although the current finally levelled out with increase of potential, no subsequent decrease was noted and oxygen evolution was never observed. It is reported that oxygen evolution in 1M KOH solutions does not occur until a potential of 10-30V vs. NHE is imposed on the electrode (2,3). The absence of passivation may be explained by assuming that the product of oxidation does not form a thick film on the electrode. In view of the large amount of product formed, it must be concluded that the product of oxidation is soluble in the solution used. In this region of pH, the reaction product predicted thermodynamically is Ga<sub>2</sub>O<sub>3</sub>. This substance is highly soluble and forms GaO<sub>3</sub><sup>3-</sup> in basic solution (4). Dissolution of the electrode was observed visually at high current densities. Formation of a soluble product also explains the small amount of cathodic charge observed.

It is seen from Table I that over a relatively wide range of sweep rate, the size of the cathodic charge is fairly constant. This would indicate that the sub-

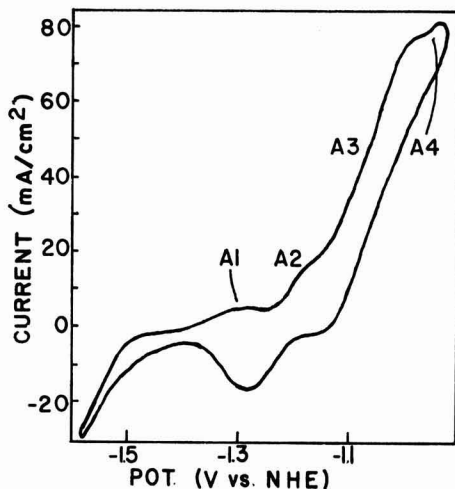


Fig. 1. Current-potential curve for spherical Ga electrode in 1M NaOH. Sweep rate = 0.47 V/sec.

<sup>1</sup> Present address: Department of Chemistry, University of Southwestern Louisiana, Lafayette, Louisiana 70501.

Key words: gallium, oxidation, anodic, oxide, dissolution, films.



Table I. Effect of sweep rate in 1M NaOH

Sweep rate, V/sec	Anodic charge, mcoulomb/cm <sup>2</sup>	Cathodic charge, mcoulomb/cm <sup>2</sup>
0.0255	123	*
0.0408	72.7	*
0.051	93.7	2.60
0.153	32.2	2.39
0.255	23.2	2.15
0.47	22.7	2.19 (Fig. 1)
0.51	20.9	2.22

\* Peak too small to determine area.

stance being reduced is a thin film of oxide on the electrode.

Further evidence of a thin film of oxide on the electrode is given by the scraping experiments in which it is indicated that the reaction is retarded and by exposing fresh electrode surface, additional product may be formed. In the scraping experiments, the Ga electrode was mechanically scraped with a sharpened sapphire rod rotating at 30,000 rpm. The scraping was done at various parts of both the anodic and cathodic sweeps but not in the region of hydrogen evolution. In all regions of oxidation (A1 through A4) the anodic current is increased by scraping. The scraping does not produce a smooth curve of higher current but rather a number of transients reflecting the violent scraping conditions at the electrode. The size of the transients was not reproducible although the general effect was. Most transients were larger than the prescrape current at a given voltage by a factor of between 2 and 10. In some instances, at lower current densities, scraping increased the current by as much as a factor of fifty. As well as can be determined, the current transient is not produced until the scraping drill touches the electrode. Contact with a nonrotating drill has no effect. The transient is definitely not due to stirring of bulk solution.

An idea of the thickness of the thin film can be obtained by assuming a roughness factor of one for the test electrode and further assuming that the cathodic peak is due only to reduction of the oxide film and not due at all to reduction of soluble product in solution near the electrode. With these assumptions, a value of approximately 3.4 monolayers of Ga<sub>2</sub>O<sub>3</sub>, as measured in terms of layers of Ga consumed, is calculated for film thickness at the time of reduction. This agrees well with film thickness obtained by constant current discharge of passivated Ga (5).

The amount of charge equal to this film thickness on the anodic sweep corresponds to the area under the curve making up the two first parts of the oxidation peak (A1 and A2). For calculating area, the anodic boundaries of A1 and A2 were taken as vertical lines drawn down to the potential axis from the current-potential curve at the points of slope changes defining A1 and A2. Experiments were done in which the sweep was reversed after A2. This reversal hardly affected the area of the cathodic peak. It appears then, that the cathodic peak is due to the reduction of an oxide film, the formation of which is represented by A1 and A2. The first part of the oxidation peak, A1, corresponds to approximately a monolayer of coverage on the electrode. It is likely that such a monolayer would alter the electrode enough to significantly change the kinetics of a reaction. Formation of such monolayers has been studied on mercury (6). The experiments done here do not allow us to state with certainty the composition of any films formed. The initial monolayer may be Ga<sub>2</sub>O<sub>3</sub>, or chemisorbed oxygen, or some oxide which has not been well characterized thermodynamically.

Oxidation of gallium in 1M NaOH would appear to proceed, therefore, by an initial formation of a monolayer of oxide or oxygen with subsequent thickening of this film to about three or four layers. At this point the properties of the film become such that the rate of dissolution increases and prevents further thickening.

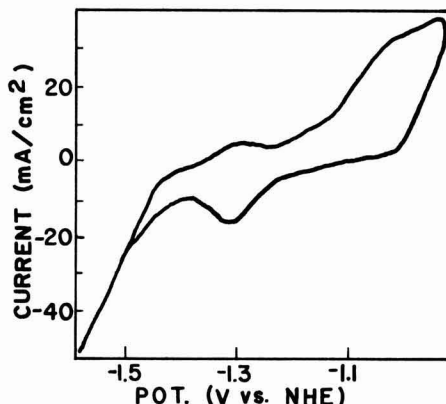


Fig. 2. Current-potential curve for planar Ga electrode in 1M NaOH. Sweep rate = 0.47 V/sec.

Further increase of potential should increase the rate of oxidation of gallium and such an increase of current is observed. As higher current densities are obtained, diffusion either through the oxide film or through the electrolyte should play a more important part in the reaction. Evidence that this is true is seen in Fig. 1 and 2. The two curves in these figures were obtained under experimental conditions which were identical except that the electrode area and shape differed. Curve 1 was obtained using a spherical electrode and curve 2 was obtained with a planar electrode. The two curves differ in that at high anodic potentials the current density obtained is higher for the spherical electrode. This is to be expected if diffusion is involved (7, 8). Evidence that the diffusion is taking place in solution is that stirring increases the anodic current as was also found by Popova and Simonova (9). The similarity of regions A1 for the two types of electrode is at variance, however, with the diffusion studies of Faizullin *et al.* (10).

Solutions of 0.1M NaOH give smaller anodic currents. Thus the limiting diffusion is that of OH<sup>-</sup> and not of product ions.

The current-potential curve has another change of slope very near the anodic end of the potential sweep. The current increases more slowly with change of potential. This is probably not due to a change in product as the A3 and A4 segments are so similar. It is possibly due to a change in the nature of the oxide film on the electrode. Perhaps diffusion in the oxide begins to play a part in the rate of oxidation at this point but the data here are not extensive enough to study this further.

#### Acknowledgment

I would like to thank Drs. T. N. Andersen and H. Eyring for their help and encouragement. The work was supported by a Petroleum Research Fund grant.

Manuscript submitted July 15, 1971; revised manuscript received Feb. 1, 1972.

Any discussion of this paper will appear in a Discussion Section to be published in the December 1972 JOURNAL.

#### REFERENCES

1. R. S. Perkins, R. C. Livingston, T. N. Andersen, and H. Eyring, *J. Phys. Chem.*, **69**, 3329 (1965).
2. F. F. Faizullin and E. V. Nikitin, *Elektrokhimiya*, **2**, 112 (1966).
3. E. V. Nikitin and F. F. Faizullin, *Aspir. Rab. Kazan. Gos. Univ. Khim. Geol.*, **1967**, 44.
4. Marcel Pourbaix, "Atlas of Electrochemical Equilibria in Aqueous Solutions," Pergamon Press Inc. (1966).
5. T. I. Popova, N. A. Simonova, Z. I. Moiseeva, and N. G. Bardina, *Elektrokhimiya*, **6**, 706 (1970).
6. R. D. Armstrong, W. P. Race, and H. R. Thirsk, *J. Electroanal. Chem.*, **19**, 233 (1968).



7. W. H. Reinmuth, *J. Am. Chem. Soc.*, **79**, 6358 (1957).  
 8. R. S. Nicholson and I. Shain, *Anal. Chem.*, **36**, 706 (1964).

9. T. I. Popova and N. A. Simonova, *Elektrokhimiya*, **6**, 1125 (1970).  
 10. F. F. Faizullin, E. V. Nikitin, and N. N. Guidina, *ibid.*, **3**, 120 (1967).

## A Rapid and Complete Method to Remove Plutonium Contamination from Aluminum

P. L. Wallace, J. C. Walden, and J. W. Magana

Lawrence Radiation Laboratory, University of California, Livermore, California 94550

### The Process

This process was first described in a German patent (1), and is used here to decontaminate aluminum parts of complex shapes. Its principal usage has been in decontaminating x-ray spectrographic cell holders. This contamination occurs when acid solutions of plutonium leak from standard liquid cells and attack the aluminum.

The process involves (i) degreasing the part in acetone, (ii) dipping it in a heated (90°C) bath for about 30 sec, (iii) rinsing the part in water, (iv) drying it, and, finally, (v) checking it for any residual contamination. All of these operations are carried out in an open front hood to prevent contamination spread.

The composition of the cleaning bath is given in Table I. It has been found important to not reuse the solution for large numbers of parts, because depletion of some components causes the reaction rate to lessen. Rinsing quickly after cleaning is mandatory, because the part will blacken rapidly otherwise. No electric current is necessary to augment the process.

### Results

Parts having fixed plutonium contamination of greater than 10,000 alpha counts/min have been decontaminated to no detectable counts with the 30 sec cleaning.

Table I. Cleaning bath composition

Component	Volume (%)
Phosphoric acid	50
Nitric acid	6.5
Acetic acid	6
Sulfuric acid	25
Water	12.5

Plus 3 g/cc of crystalline nickel nitrate,  $\text{Ni}(\text{NO}_3)_2 \cdot 6 \text{H}_2\text{O}$ .

Key words: plutonium, aluminum, decontamination.

The surface condition after cleaning is bright and somewhat shiny. However, the patent writeup indicates that a 3 min immersion would produce a mirror-like finish. While such a finish is desirable, it does entail more metal removal than is wanted to maintain the sample holder's close tolerances.

To get a feeling for the actual amount of metal removed during processing, aluminum tubes were tested as mockups for the cell holders. The weight loss for five 20g tubing sections (4 cm long by 2.0 cm ID; 2.6 cm OD) in 30 sec (bath temperature 90°C) varied from 50 to 100 mg, depending on the amount the bath was depleted by usage. The outside diameter change on these tubes was less than 0.03 mm in each case.

### Conclusions

A rapid method of decontaminating aluminum parts has been found. To date, it has made every sample holder that had been grossly contaminated available for reuse.

### Acknowledgment

Thanks are due to D. M. Cheney (Argonne National Laboratories, Idaho Reactor Site) who first brought this process to one author's (P. L. Wallace) attention about 1960. The adaptation for decontamination was discovered here some 10 years later.

This work was performed under the auspices of the U. S. Atomic Energy Commission.

Manuscript submitted Nov. 3, 1971.

Any discussion of this paper will appear in a Discussion Section to be published in the December 1972 JOURNAL.

### REFERENCE

1. A. Vernet, Process for Producing Shiny Surfaces on Objects Made of Aluminum and Aluminum Alloys, German Pat 804-054 (1948), UCRL-Trans. 10518 (1971).

## An Electrochemical Technique for Microsectioning Silver

Nghi Q. Lam, Steven J. Rothman, and L. J. Nowicki

Materials Science Division, Argonne National Laboratory, Argonne, Illinois 60439

The electrochemical technique for removing thin uniform sections from a metallic sample consists of forming an anodic oxide layer that can be either mechanically stripped or chemically dissolved without attack of the metal substrate. This method has not been applied to silver to date; the sectioning techniques that have been used have been based on the formation of dissolvable films of silver iodide or silver bromide and their dissolution in either a 1M sodium-

Key words: anodization, silver, sectioning, stripping, surface preparation.

thiosulfate solution (1) or a solution of 1.0 g/liter KCN in water (2). In our preliminary experiments, the former solvent stained the silver surface, probably due to the formation of colloidal silver on the surface (1), and the latter solvent attacked the silver substrate at an unacceptable rate. We have therefore developed an electrochemical method of removing thin sections of silver for the determination of very small diffusion coefficients. This method has also proved useful for preparing a good surface on silver diffusion samples.

### Experimental Methods and Results

**Surface preparation.**—Monocrystalline silver rods of 1.24 cm diam were grown from 99.999% purity silver by the Bridgman method and spark-cut into disks a few millimeters thick. After mechanical polishing through  $0.3\mu$   $\text{Al}_2\text{O}_3$ , the samples were chemically polished with a solution made up of 25 ml of saturated chromic acid and 3 ml of 10%  $\text{HCl}$  (3). The chemical polishing was performed by swabbing the silver surface with a cotton-tipped applicator saturated with the solution and rinsing the sample intermittently in running water. Chemical polishing in this manner for 10 min removes a layer  $\sim 15\mu$  thick, which was the approximate depth of the region deformed in polishing. At the end of this polishing step, the sample was washed with distilled water and then with alcohol in an ultrasonic vibrator, and dried in warm air. After chemical polishing, a few layers approximately 200 Å thick were removed from the silver surface by anodizing in an electrolyte of 0.5%  $\text{KOH}$  in water (with current density =  $1.0 \text{ mA/cm}^2$ , time = 22 sec) and then dissolving the silver oxide in an aqueous solution of  $\text{NH}_4\text{OH}$ . This procedure helped remove submicroscopic irregularities from the surface. The entire surface obtained was optically flat and free of pits.

**Sectioning.**—Most of the anodizing experiments were made on a (100) face of a silver single crystal that had been irradiated for 3 days in a flux of  $3 \times 10^{12}$  thermal neutrons/ $\text{cm}^2\text{-sec}$ . The specific activity of the crystal ( $^{110}\text{Ag}$ ) was measured as  $5.43 \times 10^3 \text{ cpm}/\mu\text{g}$ , thus allowing a conversion from counts/min to micrograms of silver. A simple anodizing cell was used. The platinum foil cathode was cleaned with  $\text{HNO}_3$  before use. Silver paint was used to fasten a copper wire to the back of the specimen for the electrical connection. The sample was masked with Tygon protective paint, so that only the preanodized surface was exposed to the electrolyte. The wire was also coated with Tygon. The electrolyte consisted of 5g  $\text{KOH}$  per liter of water. After anodizing, the silver oxide films, which, if thick enough, showed uniform interference colors, were dissolved in a solution of 1% (in volume)  $\text{NH}_4\text{OH}$  in water.

To determine whether this solvent attacks the silver, oxide layers of different thicknesses were formed on the irradiated silver crystal by anodizing with current densities of 0.17, 0.48, and  $0.85 \text{ mA/cm}^2$  for 30 sec. The sample was then immersed in the  $\text{NH}_4\text{OH}$  solution, and the activity of the solution was counted as a function of time. Figure 1 shows that the  $\text{NH}_4\text{OH}$  solution dissolved the oxide and attacked the silver to an insignificant extent. About 5 sec were sufficient to remove an oxide layer 1000 Å thick. Interference microscopy showed that the silver surface remained clean and flat after oxide removal.

The thickness of silver removed is plotted as a function of anodizing time in Fig. 2 for various current densities. The thickness removed in each anodizing-dissolution step was determined by counting the solvent for  $^{110}\text{Ag}$  content and using the measured value of specific activity to convert to micrograms of silver. The sample was also weighed on a microbalance before and after removal of 40 sections; the difference between amounts of material removed, as measured by the two techniques, was about 9%, which is within the experimental error. The step height on a nonradioactive silver crystal, part of which was masked by a spot of Tygon paint, was measured on an interference microscope after anodizing and removing 40 sections under the same current and time conditions. The step height agreed, within the experimental error, with the thickness removed from the radioactive sample. The amount of material removed per anodization under identical conditions was reproducible to  $\pm 8\%$ . Less than 3% of the removed activity was found in the anodizing solution and on the cathode.

The same anodizing treatments on silver crystals of random orientation yielded the same anodic film

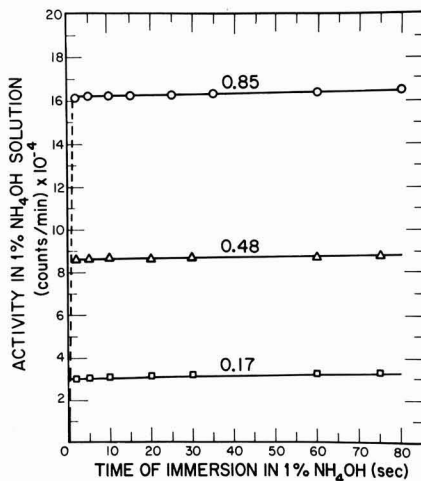


Fig. 1. Plot of  $^{110}\text{Ag}$  activity of 1%  $\text{NH}_4\text{OH}$  solution after immersing the anodized silver sample in the solvent for various times. The different thicknesses of silver oxide were formed by anodizing for 30 sec with current densities of ( $\square$ ) 0.17, ( $\triangle$ ) 0.48, and ( $\circ$ )  $0.85 \text{ mA/cm}^2$ .

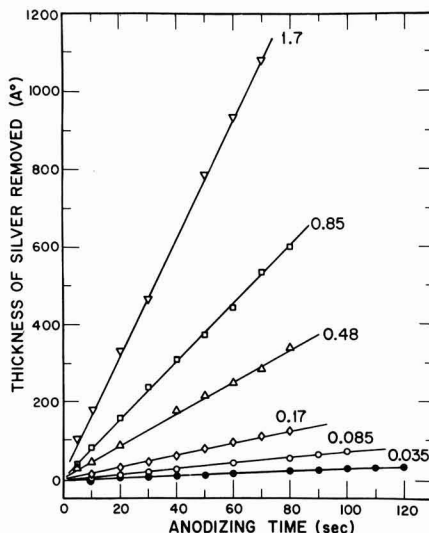


Fig. 2. Calibration of the anodizing of monocrystalline silver in an aqueous electrolyte containing 0.5%  $\text{KOH}$ . The numbers on the curves indicate the anodic current densities in units of  $\text{mA/cm}^2$ .

thickness, indicating that the rate of anodization is orientation independent, as was observed for gold (4). The thickness of the anodized layer was found to be independent of the  $\text{KOH}$  concentration in the electrolyte. The same observation was also made by Vermilyea (5) in a study of anodic oxidation of tantalum.

The thickness of silver that was anodically oxidized in 1 sec, deduced from the slopes of the curves in Fig. 2, is shown in Fig. 3 as a function of current density. An increase in current density from  $0.17 \text{ mA/cm}^2$  to  $1.7 \text{ mA/cm}^2$  led to a tenfold augmentation in the anodizing rate, similar to the case of anodizing gold (4). For high current densities ( $> 1 \text{ mA/cm}^2$ ), it was better to use current pulses of  $\frac{1}{2}$ -sec duration rather than constant current densities, because the oxygen evolution, which occurred shortly after establishing the current, could affect the uniformity and thickness of the oxide.

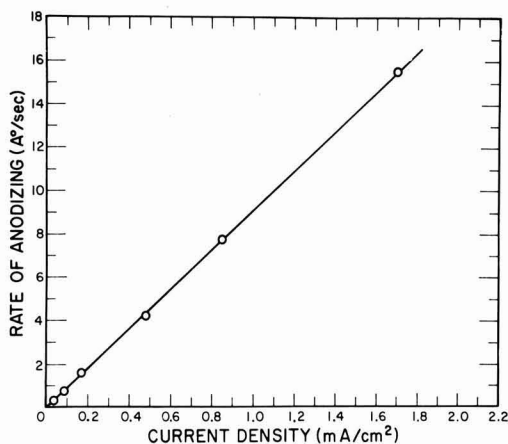


Fig. 3. Relationship between the rate of anodizing (in Å/sec) and the anodic current density (in mA/cm²). Anodizing rate =  $9.1 \times$  (current density).

### Conclusions

The anodic oxidation technique can be used for removing reproducible thin sections from silver. An

aqueous solution containing 1%  $\text{NH}_4\text{OH}$  appears to be the best solvent for removing the silver oxide, inasmuch as it does not attack the silver substrate and enables one to obtain a clean surface after the dissolution. A combination of chemical polishing and anodizing-dissolution techniques can be used instead of electropolishing to prepare a flat, strain-free silver surface prior to diffusion experiments.

### Acknowledgment

The authors wish to thank Dr. N. L. Peterson for his constant interest in this work.

This work was performed under the auspices of the U. S. Atomic Energy Commission.

Manuscript submitted Nov. 29, 1971; revised manuscript received Feb. 2, 1972.

Any discussion of this paper will appear in a Discussion Section to be published in the December 1972 JOURNAL.

### REFERENCES

1. T. Andersen and G. Sørensen, *Rad. Effects* 2, 111 (1969).
2. R. G. Vardiman and M. R. Achter, *ORNL Report 6869* (1968); and *Trans. AIME*, 245, 178 (1969).
3. H. J. Levinstein and W. H. Robinson, *J. Appl. Phys.*, 33, 3149 (1962).
4. J. L. Whitton and J. A. Davies, *This Journal*, 111, 1347 (1964).
5. D. A. Vermilyea, *Acta Met.*, 1, 282 (1953).

## Brief Communication



### Transport in Non-Newtonian Flow

R. Greif, R. Kappesser, and I. Cornet\*

Department of Mechanical Engineering, University of California, Berkeley, California 94720

Rendering a fluid non-Newtonian by the addition of a high molecular weight polymer alters the heat, mass, and momentum transport characteristics of the fluid (1-10). Electrochemists have long dealt with such non-Newtonian systems, for example, for achieving smoother and finer grained deposits in electrolytic metal deposition or in electrodeposition of rubber or related synthetic polymers from latices.

There have been several investigations that have dealt with the determination of the molecular diffusivity in non-Newtonian systems (3, 6, 7, 9, 10). These studies utilize mass flux measurements in conjunction with theoretical results for non-Newtonian systems to obtain the diffusivity. In these studies the relationship between the shear stress and the rate of strain is written in the form of a power-law, viz.

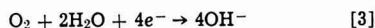
$$\tau_{xy} = -K \left( \frac{\partial V_x}{\partial y} \right)^n \quad (1)$$

although more complex relations are possible. In contrast, the corresponding expression for the molecular flux of mass or heat is assumed to be a linear function of the concentration, or temperature, gradient so that

$$J = -D \frac{\partial C}{\partial z} \text{ or } q = -\lambda \frac{\partial t}{\partial z} \quad (2)$$

In this study we experimentally demonstrate the validity of the assumption that  $J$  is a linear function of the concentration gradient.

In a previous investigation (10) we determined the molecular diffusivity of oxygen in aqueous 4% sodium chloride solutions which were rendered non-Newtonian by addition of various concentrations of Polyox WSR 301 (Union Carbide), a completely water soluble polymer of ethylene oxide. The system consisted of a rotating Monel disk, which was made cathodic while the anode was a platinized-titanium wire mesh cylinder. The mass flux of oxygen diffusing to the rotating disk was determined by measuring the mass transfer limiting current for the net reaction



The mass flux is dependent on the over-all oxygen concentration difference,  $\Delta C_0 = C_{0,x} - C_{0,w}$ . The concentration of oxygen far from the disk,  $C_{0,x}$ , was measured by Winkler analysis while the concentration at the disk surface,  $C_{0,w}$ , was taken to be zero. Equating the experimental and theoretical results for the mass flux yielded the results for the diffusivity.

A critical confirmation of the experiment and analysis was readily made by comparing the value obtained for the diffusion coefficient in the absence of Polyox with the value reported in the International Critical Tables (11). The results were in excellent agreement under this Newtonian flow condition (10).

\* Electrochemical Society Active Member.

Key words: transport, non-Newtonian theory, molecular flux, concentration gradient.

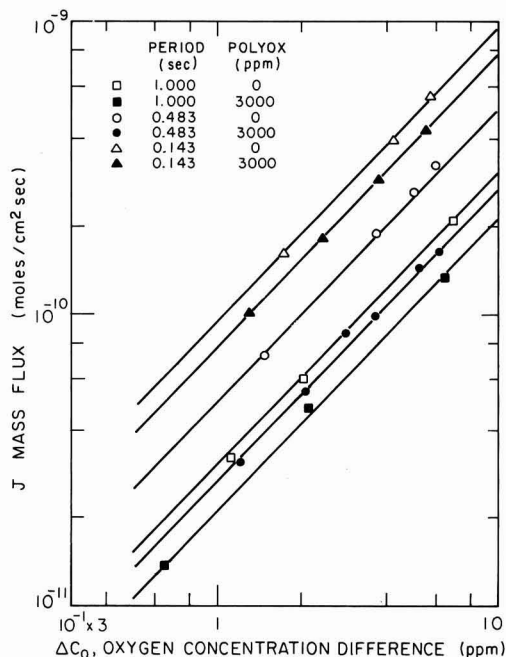


Fig. 1. Comparison of mass flux dependence on concentration gradient in Newtonian and non-Newtonian fluids.

In the analysis for the mass transport the molecular flux had been assumed to be linearly dependent on the concentration gradient (cf. Eq. [2]). We had thought that this assumption had been previously confirmed but apparently this is not so. Therefore, a series of tests was performed at different concentration differences, that is, for different values of  $\Delta C_0 = C_{0,\infty}$ . This was achieved by first bubbling nitrogen through the solution until the desired concentration of oxygen was achieved. We note that all our previous experiments had been performed at essentially a single value of  $C_{0,\infty}$ .

The experimental results are presented in Fig. 1 in terms of the mass flux vs. the oxygen concentration difference. Results are shown for the Newtonian fluid (0 ppm of Polyox) and for the non-Newtonian fluid (3000 ppm of Polyox) for three periods of rotation (Reynolds number). For a linear system, the mass flux would vary linearly with the concentration difference, and this is clearly the result shown. Note that the linear slope of 1.0 is observed for all the conditions tested, thereby demonstrating the validity of Eq. [2].

Although Eq. [1] is not required, as far as the above conclusion is concerned, the values of the coefficients,  $K$  and  $n$  are of interest. For shear stress in units of dynes/cm<sup>2</sup> and rate of strain in units of sec<sup>-1</sup>,  $n = 1.00$ ,  $K = 0.0094$  for 0 wppm of Polyox and  $n = 0.68$ ,  $K = 0.88$  for 3000 wppm of Polyox (temperature of 27°C). These values were obtained from measurements we performed with a Fann U-G, Model 35, rotating cylinder viscometer. Now, the theoretical result for the mass

flux to a rotating disk in laminar flow divided by the concentration difference, that is,  $J/\Delta C_0$ , varies with rpm according to  $(\text{rpm})^{1/n+1}$  (9, 10). Thus, an independent check is afforded by comparing the value of  $n$  obtained directly from the viscometer measurement and the value of  $n$  obtained directly from the mass flux measurement. The results are in excellent agreement (10).

Lastly it should be noted that the shear rates determined from the viscometer measurements varied from 150 to 1000 (sec<sup>-1</sup>) (10). In the present experiments with a 3.65 cm diam disk, the maximum shear rates may be calculated (12, 13) and the results vary from 40 to 1200 (sec<sup>-1</sup>).

### Acknowledgment

The authors acknowledge with appreciation the assistance of J. A. Paterson. We also acknowledge with appreciation the support of this research by the Office of Saline Water, the Office of Naval Research, and the Sea Water Conversion Laboratory.

Manuscript submitted Nov. 5, 1971; revised manuscript received Feb. 4, 1972.

Any discussion of this paper will appear in a Discussion Section to be published in the December 1972 JOURNAL.

### NOMENCLATURE

$C$	Concentration of diffusing species, moles/cm <sup>3</sup>
$C_0, C_{0,\infty}, C_{0,w}$	Concentration of O <sub>2</sub> in fluid, bulk, or at the wall, respectively, moles O <sub>2</sub> /cm <sup>3</sup> or ppm O <sub>2</sub>
$D$	Diffusion coefficient, cm <sup>2</sup> /sec
$J$	Mass flux, moles/cm <sup>2</sup> sec
$K, n$	Fluid constants as in Eq. [1]
$q$	Heat flux, calories/cm <sup>2</sup> sec
$t$	Temperature, °K
$V_x$	Fluid velocity in $x$ direction, cm/sec
$x, y, z$	Coordinates, cm
$\lambda$	Thermal conductivity, calories/cm sec °K
$\tau_{xy}$	Shear stress, dynes/cm <sup>2</sup>

### REFERENCES

1. A. H. P. Skelland, "Non-Newtonian Flow and Heat Transfer," John Wiley & Sons, New York (1967).
2. W. L. Wilkinson, "Non-Newtonian Fluids," Pergamon Press, New York (1960).
3. S. B. Clough, H. E. Read, A. B. Metzner, and V. C. Behn, *A.I.Ch.E. (Am. Inst. Chem. Engrs.) J.*, **8**, 346-350 (1962).
4. A. Metzner and D. Gluck, *Chem. Eng. Sci.*, **12**, 185-190 (1960).
5. A. Metzner, R. Vaughn, and G. Houghton, *A.I.Ch.E. (Am. Inst. Chem. Engrs.) J.*, **3**, 92-100 (1957).
6. G. Astarita, *Ind. Eng. Chem. Fundamentals*, **4**, 236-237 (1965).
7. G. Astarita, *ibid.*, **5**, 14-18 (1966).
8. G. Astarita, G. Marrucci, and G. Palumbo, *ibid.*, **3**, 333-339 (1964).
9. G. S. Hansford and M. Litt, *Chem. Eng. Sci.*, **23**, 849-864 (1968).
10. R. Greif, I. Cornet, and R. Kappesser, *Intern. J. Heat Mass Transfer*, To be published.
11. "International Critical Tables," McGraw-Hill Book Co., New York (1928).
12. P. Mitschka, *Collection Czech. Chem. Commun.*, **29**, 2892-2905 (1964).
13. P. Mitschka and J. Ulbrecht, *ibid.*, **30**, 2511-2526 (1965).

This Discussion Section includes discussion of papers appearing in the *Journal of The Electrochemical Society*, Vol. 118, No. 2, 4, 9, and 10; February, April, September, and October 1971.

### Investigation of the Direct Reduction of Zinc Oxide in Alkaline Electrolytes

D. Drazic and Z. Nagy (pp. 255-257, Vol. 118, No. 2)

**K. Schwabe, O. Hladik, and H. Oude<sup>1</sup>:** Drazic and Nagy have investigated the direct reduction of zinc oxide in alkaline electrolytes in the paper under discussion. From their experiments they conclude that our suggestion about the direct reduction of solid zinc oxide confirmed by our radiochemical investigations<sup>2</sup> and by the investigations of other authors is not true; the current efficiency of the direct reduction should be very small with respect to the reduction of the soluted zincate. We cannot agree with this opinion.

The conditions of the experiments are quite different. We have worked with a "paste electrode," that means under conditions which can be compared with a working alkaline zinc battery. The surface of the zinc oxide was very large with respect to the volume of the zincate solution. The conductivity of the zinc oxide was small compared with that of the ZnO single crystal applied by Drazic and Nagy. From the high electron conductivity of the single crystal, it is clear that it works as cathode under the conditions described by the authors, because the amount of zincate in the solution is much larger than that of ZnO in the single crystal. Up to 100 mA/cm<sup>2</sup>, we have not observed any hydrogen evolution with our paste electrode; reducing zincate solution without solid zinc oxide already at 10 mA/cm<sup>2</sup> the hydrogen evolution is visible. With our paste electrode we observe H<sub>2</sub> evolution only if the reduction of the paste of ZnO was reduced and the formed Zn came in direct contact with the solution. The difference

<sup>1</sup> Forschungsinstitutes Meinsberg, Meinsberg Post 7305 Waldheim, Dresden, Germany.

<sup>2</sup> O. Hladik and K. Schwabe, *Electrochim. Acta*, 15, 635 (1970).



Fig. 1. Electroplated dendrites from saturated solution of potassium zincate (100 mA/cm<sup>2</sup>).

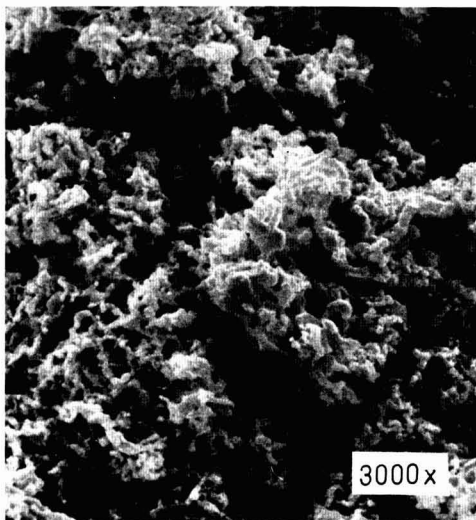


Fig. 2. Crystals electroplated from ZnO/KOH-paste (100 mA/cm<sup>2</sup>)

in the cathodic overvoltage, which the authors have found, is quite reasonable under their conditions, but not under our conditions. The structure of the zinc reduced from zincate solution is that of dendrites (Fig. 1) found also by Gerischer.<sup>3</sup> From ZnO-paste we receive a zinc powder without macrostructure (Fig. 2) because it is formed by destruction of the ZnO lattice. We are therefore convinced, that under our conditions, similar to that of an alkaline Zn-battery, mainly the solid ZnO is reduced because our results can only be explained by this mechanism.

**D. Drazic and Z. Nagy:** When referring to the paper of K. Schwabe and O. Hladik<sup>4</sup> we wanted to point out that the polarization curves obtained with the ZnO paste electrode in 1M and 11M hydroxide solutions can also be explained by a process other than the solid-state oxide reduction.

It is known that the polarization curves obtained with porous electrodes (ZnO paste is also a porous system) include a considerable IR voltage drop formed inside the pores, especially at higher current densities. The resulting linear current-voltage relation is particularly well pronounced in Fig. 5 of their paper.<sup>5</sup> Since no IR drop corrections were made, and the authors have not discussed this matter at all, we had reasons to believe (e.g., if the resistance of the pores in ZnO paste was only 0.5 ohm, the IR drop could be as high as 500 mV at 1000 mA/cm<sup>2</sup>) that the polarization curves obtained without IR drop corrections should be similar in solutions of similar conductivities, no matter what reaction was going on inside the electrode.

Further, the results of the radiotracer measurements to which the authors refer, seem very logical, but give information only about transfer processes taking place in the bulk of the solution and have nothing to do with the electrode reaction. The results would be the same whether zincate ion or a solid-state reaction path was

<sup>3</sup> H. Gerischer, *Surface Sci.*, 13, 265 (1969).

<sup>4</sup> O. Hladik and K. Schwabe, *Electrochim. Acta*, 15, 635 (1970).

<sup>5</sup> O. Hladik and K. Schwabe, *Electrochim. Acta*, 15, 635 (1970).



operative. Namely, if the zincate ion path was operative, it would be the zincate ions formed by dissolution of ZnO very close to the metallic zinc surface inside the pores which would be reacting, and not the zincate ions from the bulk of the solution.

The absence of hydrogen evolution from the paste electrode can also be explained by the dissolution-deposition mechanism: the zincate concentration within the pores is kept high by the continuous dissolution of the oxide.

Finally, referring to the question of morphology of zinc deposited within the porous electrode, we think that the nondendritic deposit cannot be considered as proof that zincate ions are not the reacting particles in the electrochemical step of the over-all deposition reaction. It has been shown<sup>6</sup> that one of the necessary preconditions for dendritic growth is diffusion control of the electrode process. This condition is not fulfilled within the pores because of ready availability of zincate through the dissolution of ZnO and, therefore, no dendrites can be expected until the zincate ions from the solution layer start taking part in deposition, i.e., very close to the end of the charging process.

Hence, we still do not have any reason to believe that our conclusion about the importance of zincate ion reaction path in the charging process cannot be applied to the real situation in batteries.

### The Thermodynamics and Electrode Kinetic Behavior of Nickel in Acid Solution in the Temperature Range 25° to 300°C

R. L. Cowan and R. W. Staehle (pp. 557-568, Vol. 118, No. 4)

**V. Ashworth<sup>7</sup> and P. J. Boden<sup>8</sup>:** The authors have shown that the data required to construct electrochemical equilibrium diagrams for any system at a temperature other than 298°K may be readily computed by means of the empirical "correspondence principle" technique due to Criss and Cobble. However, the subsequent interpretation of these diagrams is rarely so straightforward as it might appear at first even when their intrinsic limitations are fully appreciated.

In particular, it is important to recognize that the abscissa of the diagram properly refers to the negative logarithm of the hydrogen ion activity ( $-\log a_{H^+}$ ) which for a single solution will vary to a greater or lesser extent throughout the temperature range (i.e.,  $d \log a_{H^+}/dT \neq 0$ ). With the exception of solutions within a very limited range of hydrogen ion activity it is, therefore, invalid to use the solution pH measured at room temperature (298°K) as the reference point on the abscissa in connection with a diagram constructed for a higher or lower temperature. Fortunately it is possible to calculate the change in  $a_{H^+}$  of a solution with change in temperature and further, for a more limited number of cases, a second scale may be added to the diagram such that the use of the room temperature pH becomes permissible.

In the simplest case, as the temperature of an unbuffered aqueous solution is raised, chemically equivalent amounts of additional hydrogen and hydroxyl ions will be generated as a result of the increased dissociation of water. The ionic product of water, ( $K_w(T)$ ), at temperature  $T$  is given by

$$K_w(T) = (a_{H^+}(298^\circ K) + x)(a_{OH^-}(298^\circ K) + x)$$

where  $x$  is the additional ion activity as a result of the temperature change from 298°K to  $T$ K. At 298°K and pH  $n$

$$a_{H^+} = 10^{-n}$$

and

$$a_{OH^-} = 10^{-(14-n)}$$

<sup>6</sup> A. R. Despic, J. W. Diggle, and J. O'M. Bockris, *This Journal*, 115, 507 (1968).

<sup>7</sup> Department of Chemical Engineering, U. M. I. S. T., Manchester, England.

<sup>8</sup> Department of Metallurgy, Nottingham University, Nottingham, N97, 2RD, England.

thus at temperature,  $T$

$$K_w(T) = (10^{-n} + x)(10^{-(14-n)} + x) \quad [1]$$

and the negative logarithm of the hydrogen ion activity becomes  $-\log_{10}(10^{-n} + x)$ . Clearly, with a knowledge of the value of  $K_w(T)$ , the solution of Eq. [1] will yield the corresponding value of  $x$  for any given value of  $n$  and it becomes possible to refer the negative logarithm of the hydrogen ion activity at  $T$  to the room temperature pH. It is this former value which should be used as a reference point when employing the diagrams derived by the authors when considering unbuffered solutions. Alternatively, as shown in Fig. 1, a second scale may be added to the abscissa which conveniently relates pH (at 298°K) to the  $a_{H^+}$  at temperature. Since the room temperature pH is more commonly measured this second scale is the more convenient to use, but its asymmetry makes it imprecise for neutral and alkaline solutions. Under these circumstances its linearization, as shown in Fig. 2, becomes desirable. The asymmetry of the new abscissa derives from its logarithmic nature; briefly, although  $x$  varies symmetrically with  $n$ , reaching a maximum in the neutral pH region, the introduction of small amounts of hydrogen ion by dissociation makes a greater contribution to  $-\log a_{H^+}$  at high rather than low pH values.

When a solution has some buffer capacity, the hydrogen ion activity no longer varies as the dissociation constant of water; and, although in these circumstances the use of the second scale is incorrect, calculation of the new activity is possible. Thus an aqueous solution of a weak acid (HA) will contain  $H_2O$ , HA,  $H^+$ ,  $A^-$  and  $OH^-$ , to preserve electroneutrality

$$[H^+] = [OH^-] + [A^-] \quad [2]$$

where the square brackets represent concentrations and, further, neglecting activity coefficients

$$K_w = [H^+][OH^-]$$

Thus from Eq. [2]

$$[H^+]^2 = [H^+][OH^-] + [H^+][A^-]$$

and

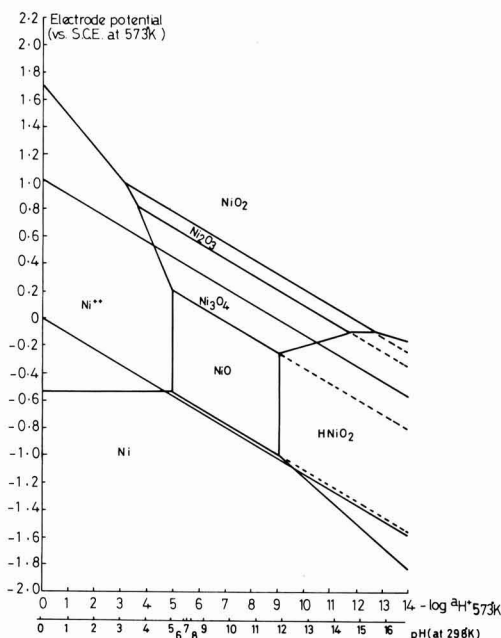


Fig. 1. Potential pH diagram calculated for nickel at 573°K



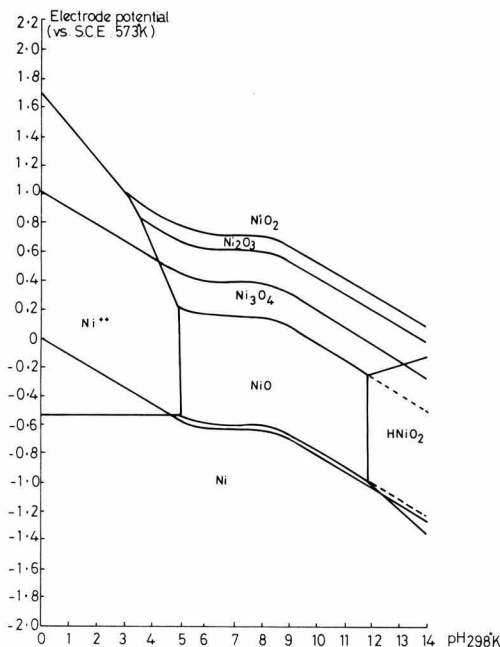


Fig. 2. Potential pH diagram calculated for nickel at 573°K with abscissa in pH units measured at 298°K.

$$2[H^+][d[H^+]] = dK_{w-} + [H^+][d[A^-]] + [A^-][d[H^+]]$$

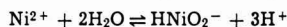
or

$$d[H^+] = \frac{dK_{w-} + [H^+][d[A^-]]}{2[H^+] - [A^-]} \quad [3]$$

That is, if some undissociated HA is present in the solution at 298°K, by raising the temperature the hydrogen ion activity will alter as a result of changes in both  $K_{w-}$  and  $K_{HA}$  (the acid dissociation constant). In the special case where  $[A^-]$  cannot change (unbuffered solutions of strong acids and in pure water),  $d[A^-]$  becomes zero for a temperature rise and the value of  $d[H^+]$  from Eq. [3] will coincide with the value of  $x$  given by Eq. [1]. The analogous equation to Eq. [3] for a solution containing a weak base (BOH) is given by

$$d[H^+] = \frac{dK_{w-} - [H^+][d[B^+]]}{2[H^+] + [B^+]}$$

To use the derived equilibrium diagrams correctly it becomes necessary to calculate the value of  $d[H^+]$  and, hence,  $a_{H^+}$  for the buffered solution at the temperature in question. A buffered condition which may be overlooked occurs when the metal-water system generates a self-buffering situation which controls the  $a_{H^+}$  by means of displacement of a hydrolytic equilibrium. For example, in the Ni/H<sub>2</sub>O system the equilibrium



may become important at very high temperatures and itself represent such a self-buffered system. Although the nickel ion activity ( $Ni^{2+} + HNiO_2^-$ ) is defined, when the diagram is calculated (say at  $10^{-6}$  kg ions/m<sup>3</sup>), the hydrogen ion activity will depend on the dissociation constant of the weak acid  $Ni^{2+}$ . Any combination of  $a_{Ni^{2+}}$  and  $a_{HNiO_2^-}$  which satisfies the requirement

$$a_{Ni^{2+}} + a_{HNiO_2^-} = 10^{-6} \text{ kg ions/m}^3$$

is permissible. Nevertheless, the use of Eq. [3] is equally applicable to such a system and requires only

a recognition that all solution species must be considered in calculating the variation in hydrogen ion activity.

Returning to the original paper the authors point out that, on the basis of their electrochemical equilibrium diagrams, "the range of stability of the nickel oxy-anion  $HNiO_2^-$ , increases greatly with increasing temperature." Superficially this suggests that, in mildly oxidizing alkaline solution, nickel metal will be in equilibrium with NiO at 298°K; whereas, in the same solution heated, say to 573°K, the metal will be in equilibrium with the oxy-anion. That is, in the former case the material may become passive and in the latter it may corrode. In fact such a highly alkaline solution (see the authors' Fig. 2 in the paper under discussion) will be, at best, only poorly buffered; the temperature rise will increase the  $a_{H^+}$ , and as our Fig. 2 shows, the probability is that the solution will be no more aggressive at 573°K than it was at 298°K, although both predictions may be overruled by kinetic factors. The implication of this calculation is that the temperature differential of the dissociation constant of the "acid" NiO is comparable with that for the ionic product of water. As a broad generalization it can be said that the equilibrium diagrams for the Ni/H<sub>2</sub>O system predict that an increase in temperature will lead to an over-all increase in the stability range of NiO (from pH 9-12 at 298°K to pH<sub>(298°K)</sub> 5-12 at 573°K), the metal being resistant, to a wider range of aqueous environments at the higher temperatures. It is interesting to speculate that had the region of stability of the oxy-anion advanced to values of  $-\log a_{H^+}$  approaching 7 at the higher temperature, then a test solution based on a temperature stable buffer system of pH ca. 7 at room temperature might prove to be more aggressive to Ni than an unbuffered solution of similar pH (at 298°K), the additional hydrogen ions generated in the latter case shifting the metal into a passive region.

The foregoing analysis of the change of  $a_{H^+}$  with temperature broadly confirms the observations of Greeley, reported by the authors, that for a closed hydrogen saturated acid solution only small changes in  $a_{H^+}$  occur with increase in temperature. Nevertheless, that small change has a significant effect on  $-\log a_{H^+}$  in weakly acid solutions (pH > 4 at 298°K). For example, we have calculated the activity of the hydrogen ion at various temperatures for the solutions used by the authors, assuming them to be effectively unbuffered (solutions of strong acids and the salts of strong acids and bases), with the results given in Table I.

Table I.

	298	323	Temperature (°K)				523	573
			363	423	473			
$-\log a_{H^+}$	1.30	1.30	1.30	1.30	1.30	1.30	1.30	1.30
	3.40	3.40	3.40	3.40	3.40	3.40	3.40	3.40
	6.30	6.24	6.04	5.75	5.60	5.55	5.55	5.55

The table shows that only in the case of the two most acid solutions does  $-\log a_{H^+}$  remain constant. This effect interacts not only with the interpretation of the equilibrium diagrams but also with the authors' correction to  $E_{corr}$ . This correction was used by the authors to allow for the thermal liquid junction potential in their system and, further, to transpose their potential measurements to the standard hydrogen scale at the test temperature. The correction is valid for the two most acid solutions but, as a result of the assumption that  $a_{H^+}$  remains constant throughout the temperature range, the authors' values for  $E_{corr}$  and the arrest potentials in the least acid solution are in error by up to 86 mV  $[(6.30 - 5.55) \times 2.3 RT/F]$ , that is, the potentials are not all on the "same thermodynamically meaningful scale." This does not invalidate the conclusions drawn from the potential decay experiments

Table II.

Temp. °K	$E_{\text{arrest}}$ (V)		$E_{\text{Ni/NiO}}$ vs. SHE (298°K)	$E_{\text{Ni/Ni}_3\text{O}_4}$ vs. SHE (298°K)
	vs. SHE (T°K)	vs. SHE (298°K)		
pH 1.3				
295	+0.240	+0.237	+0.041	+0.231
327	+0.213	+0.239	+0.036	+0.225
pH 3.4				
306	+0.078	+0.085	-0.089	+0.101
328	+0.048	+0.074	-0.102	+0.087
370	-0.075	-0.011	-0.126	+0.062
571	-0.205	+0.033	-0.241	-0.061
pH 6.3				
295	-0.204	-0.207	-0.251	-0.061
327	-0.261	-0.235	-0.289	-0.100
354	-0.335	-0.286	-0.320	-0.131
381	-0.350	-0.278	-0.350	-0.163
574	-0.500	-0.259	-0.574	-0.394

since the failure to allow for changes in  $a_{\text{H}^+}$  in correcting the arrest potentials is counteracted by the same omission in the calculation of the equilibrium potentials for the oxides.

Thermal temperature coefficients of standard electrode potential may be calculated from first principles by the method due to de Bethune *et al.*<sup>9</sup> which uses entropy data determined at 298°K. For the Ni/NiO and Ni/Ni<sub>3</sub>O<sub>4</sub> equilibria we have obtained coefficients of +0.097 and +0.062 mV/°K, respectively, using the entropy data given by Cowan and Staehle. In Table II we record the calculated thermal equilibrium potentials (i.e. with respect to a standard hydrogen electrode at 298°K) for these reactions at the pH levels investigated by the authors. In deriving these values no allowance has been made for changes in  $a_{\text{H}^+}$  with temperature in order that our calculations should be on the same basis as the reported results. The table also includes the values of the potential arrests obtained by the authors both as reported and also corrected to the standard hydrogen scale at 298°K (assuming  $dE^\circ/dT$  for the hydrogen electrode to be 0.871 mV/°K). The calculations appear to confirm the views of the authors that in the two most acid solutions and at the highest temperature in the least acid solution the bulk oxide, if not the passive film, is Ni<sub>3</sub>O<sub>4</sub>; whereas, at lower temperatures in this latter solution the bulk oxide is NiO although the near correspondence between the arrest and equilibrium potentials may well be fortuitous. While it is gratifying that the equilibrium potential calculated for elevated temperatures by two entirely independent methods give rise to the same conclusions, when compared with the present experimental data it is disappointing that these potentials do not coincide when transposed to the same reference scale. The accuracy of the method used by the authors for estimating  $C_p$  at temperature has been questioned recently<sup>10</sup> and it may be that the disagreement arises from this source although we have no reason to suppose that the entropy data used in our calculations is more accurate.

A serious limitation of the electrochemical equilibrium diagram has always been that it can only be as good as the data from which it is constructed. This restriction is magnified in the high temperature diagrams and a cautious approach to the interpretation of experimental data in terms of such diagrams seems appropriate.

**M. Kesten<sup>11</sup>:** In the paper under discussion, Cowan and Staehle found that the active-passive transition of the metal disappeared when the temperature of the electrolyte was raised above 90°C. For the interpretation and possible explanation of this phenomenon it is worthwhile to refer to the considerable number of

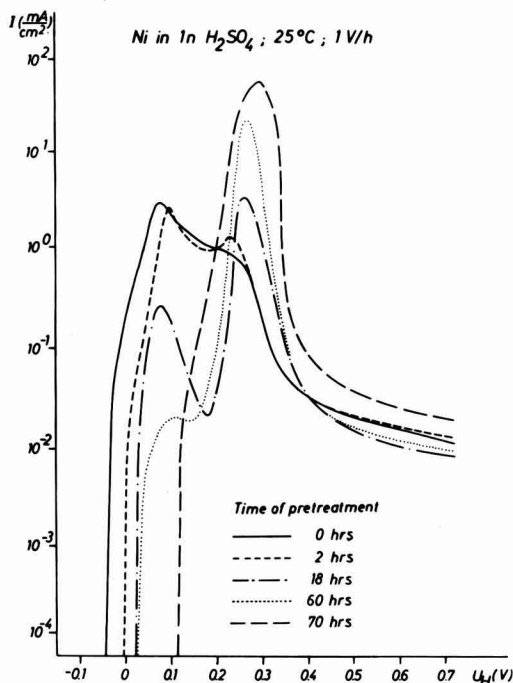


Fig. 1. Anodic polarization behavior of nickel (99.998%) in the active to noble scan mode. Before the experiment the samples have been kept in the electrolyte for different times.

recent investigations dealing with the specific influence of anions on the polarization characteristics of metals.<sup>12-22</sup> It has been proved in these studies that anions, which are adsorbed on the surface of the metal, are apt to participate in the dissolution mechanism. Their effectiveness on the reactions taking place at the interface depends on the bonding strength between them and the surface atoms of the metal. While weakly adsorbed ions inhibit the active metal dissolution by reducing the available free surface, strongly adsorbed ions are able to accelerate the dissolution of the metal whenever they undergo chemical reactions with the surface atoms.

This kind of behavior is not only restricted to the halide ions Cl<sup>-</sup>, Br<sup>-</sup> and J<sup>-</sup>. It has been found for sulfate ions as well, although, under similar conditions these ions are adsorbed to a much smaller degree.<sup>23</sup> Because of the necessary activation energy, the specific adsorption of anions from the electrolyte is a matter of time and temperature. According to Dreyer and Dreyer,<sup>24</sup> the time to reach a maximum coverage with sulfate ions on a Zr surface is about 10<sup>3</sup> min at 20°C, while at 80°C this process is completed in 20 min. Besides all this, the competitive adsorption of other particles of the electrolyte (e.g., OH<sup>-</sup> ions or chemisorbed oxygen) can also play an important

<sup>12</sup> Y. M. Kolotyrkin, *This Journal*, **108**, 207 (1961).

<sup>13</sup> K. E. Heusler and G. H. Cartledge, *This Journal*, **108**, 732 (1961).

<sup>14</sup> B. Y. Konyaev and V. A. Khitrov, *Zashchita Metal*, **2**, 745 (1966).

<sup>15</sup> Y. M. Kolotyrkin, *Zashchita Metal*, **3**, 131 (1967).

<sup>16</sup> N. Y. Buné, *Zashchita Metal*, **1**, 168 (1965).

<sup>17</sup> N. Y. Buné, *Zashchita Metal*, **3**, 50 (1967).

<sup>18</sup> G. Lopovok, Y. M. Kolotyrkin, and L. A. Medvedeva, *Zashchita Metal*, **2**, 527 (1966).

<sup>19</sup> W. J. Lorenz, *Corrosion Sci.*, **5**, 121 (1965).

<sup>20</sup> Z. A. Iofa, V. V. Batrakov, and Kho Ngok Ba, *Protection of Metals*, **1**, 44 (1965).

<sup>21</sup> Z. A. Iofa, *Zashchita Metal*, **6**, 49 (1970).

<sup>22</sup> M. Kesten and H. G. Feller, *Electrochim. Acta*, **16**, 763 (1971).

<sup>23</sup> T. Murakawa, Y. Kato, S. Nagaura, and N. Hackerman, *Corrosion Sci.*, **7**, 657 (1967).

<sup>24</sup> I. Dreyer and R. Dreyer, *Z. Physik. Chem.*, **236**, 107 (1967).

<sup>9</sup> A. J. de Bethune, T. S. Licht, and N. Swendeman, *This Journal*, **106**, 616 (1959).

<sup>10</sup> J. V. Dobson and H. R. Thirsk, *Electrochim. Acta*, **16**, 315 (1971).

<sup>11</sup> Institut für Metallphysik, Technische Universität Berlin, 1 Berlin 15, Germany.

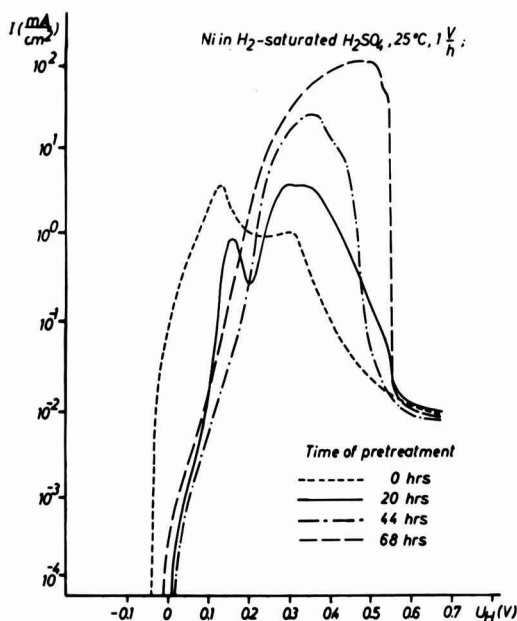


Fig. 2. Anodic polarization behavior of nickel (99.998%) in the active to noble scan mode. Consecutive runs measured with the same sample. Between the runs the sample has been kept unpolarized in the electrolyte for one day.

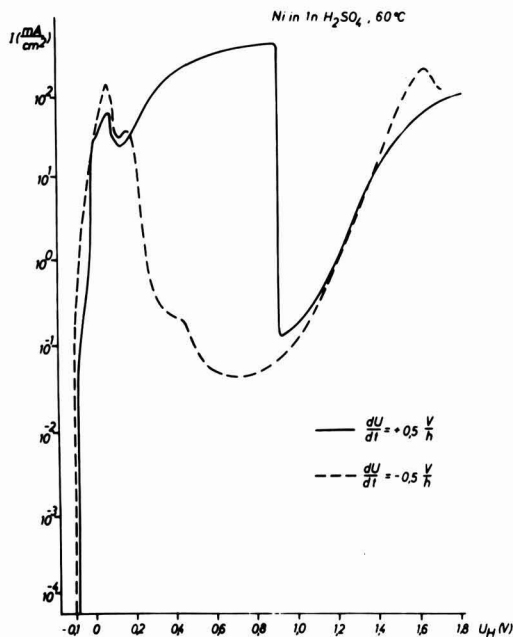


Fig. 3. Anodic polarization behavior of nickel (99.998%) in both scan modes at 60°C.

role.<sup>25,26</sup> Under these circumstances the question of a pretreatment of the sample before the experiment becomes a critical factor for the interpretation of any result.

<sup>25</sup> K. Schwabe, *Electrochim. Acta*, **6**, 223 (1962).

<sup>26</sup> K. Schwabe and C. Weissmantel, *Z. Physik. Chem.*, **215**, 48 (1960).

Our recent studies, about the influence of specifically adsorbed sulfate ions on the anodic behavior of nickel,<sup>27</sup> proved that one can get very similar results to those reported by Cowan and Staehle. But instead of increasing the temperature, the adsorption conditions for the sulfate ions were changed prior to the polarization experiment. Figure 1 shows the polarization curves obtained in 1N H<sub>2</sub>SO<sub>4</sub> with nickel samples pretreated differently. Before the polarization was started the samples were kept in the electrolyte at the open circuit potential for different times. With increasing time of pretreatment the amount of specifically adsorbed sulfate ions increases too. At the same time, the primary nickel dissolution is lowered considerably. On the other hand, a remarkable increase in metal dissolution is observed in a potential region where untreated samples already undergo the active-passive transition. It could be demonstrated that, in this range of second activation, the nickel dissolves because of the direct participation of the sulfate ions in the dissolution process.

The described effect increases, when hydrogen is bubbled through the solution (Fig. 2). With increasing metal dissolution the so-called passivation potential is shifted to higher values. Finally, Fig. 3 shows the polarization curve of an untreated sample measured in 1N H<sub>2</sub>SO<sub>4</sub> at 60°C. It indicates that the time for getting a sufficient coverage with sulfate ions can be minimized by increasing the test temperature.

The potential of the sudden passivation of the electrode is not reproducible. Polarization curves of that kind, reported also by Cowan and Staehle, are typical for dissolution processes proceeding with high current densities. In these cases the shape of the curve no longer reflects the true relationship between the current density and the electrode potential, because of the IR drop in the potential measuring system.<sup>28</sup> From those data alone it is not possible, therefore, to decide whether an electrode is in the active or passive condition corresponding to a certain measured potential.

On the basis of the cited literature and our own experimental results the vanishing of the active-passive transition in nickel, under the condition reported by Cowan and Staehle, is not unexpected. It is a consequence of the specific adsorption of sulfate ions favored by the temperature of the electrolyte.

### Polarization Behavior of Graphite in Sodium Chloride Solutions in the Presence and Absence of Ethylene

A. Bélanger, G. Bélanger, and A. K. Vijh  
(pp. 1543-1545, Vol. 118, No. 9)

N. Ibl and P. M. Robertson<sup>29</sup>: We are investigating, and have been for some time, the oxidation of olefins (mainly isobutylene) at various electrodes in H<sub>2</sub>SO<sub>4</sub> and HClO<sub>4</sub> solutions, with and without the addition of mercury salts. Our results are in agreement with those of the authors. No reaction was observed at graphite anodes. Substantial oxidation takes place only at gold electrodes.<sup>30</sup> The oxidation on gold of lower molecular weight olefins, such as ethylene, has been the subject of a few recent papers.<sup>31,32</sup> On the other hand, with the system of the authors, chlorhydrin (which is an intermediate in the production of the oxide) is easily formed. We obtained, with very high current efficiency (up to 97%), ethylene and propylene chlorhydrin at graphite anodes,<sup>33</sup> the pH being, however, somewhat more acid than that in the experiments of Bélanger et al.

<sup>27</sup> M. Kesten and H. G. Feller, *Electrochim. Acta*, **16**, 763 (1971).

<sup>28</sup> J. Osterwald, *Ber. Bunsenges. Physik. Chem.*, **66**, 401 (1962).

<sup>29</sup> Technisch-chemisches Laboratorium, Swiss Federal Institute of Technology, Zurich, Switzerland.

<sup>30</sup> P. M. Robertson, H. Isler, and N. Ibl, *Chem. Ing. Tech.*, In preparation.

<sup>31</sup> J. W. Johnson, S. C. Lai, and W. J. James, *Electrochim. Acta*, **15**, 1511 (1970).

<sup>32</sup> T. N. Hartley and D. Price, *This Journal*, **117**, 448 (1970).

<sup>33</sup> N. Ibl and A. Selvig, *Chem. Ing. Tech.*, **42**, 180 (1970).

A. Bélanger, G. Bélanger, and A. K. Vijh: We appreciate Ibl and Robertson's comments and are gratified that their results are in agreement with ours for the comparable system. The related work on gold cited by these authors also appears of interest although clear-cut explanation of different behavior at gold and other electrodes is still an open question, notwithstanding the interpretations put forward previously.<sup>34</sup>

In this context, it is perhaps relevant to point out that our recent attempts<sup>35</sup> to carry out partial anodic oxidation of methane and ethylene in liquid ammonia, with a view to prepare alkyl amines, have not been successful even when a variety of electrode material was examined.

### Energetics of Single Ion Solvation in Nonaqueous Solvents and the Effects on Electrode Kinetics

M. Salomon (pp. 1609-1614, Vol. 118, No. 10)

O. Popovych<sup>36</sup>: In this paper Salomon raises the known<sup>37</sup> valid objection to Izmailov's extrapolation methods of determining the solvation energies of single ions, but then proceeds to use what appears to be a slight modification of one of these methods. According to Salomon, Izmailov extrapolated as a function of reciprocal radius,  $r^{-1}$ , only the combinations  $(\Delta G^\circ_M - \Delta G^\circ_H)$  and  $-(\Delta G^\circ_H + \Delta G^\circ_X)$ , obtaining nonlinear plots with potentially two different intercepts. What he fails to mention, however, is that Izmailov was aware of these difficulties and, therefore, recommended plotting the average of the above functions,  $[(\Delta G^\circ_M - \Delta G^\circ_X)/2 - \Delta G^\circ_H]$ , which in mathematical form is identical with Salomon's own Eq. [1] in the paper under discussion. This average function also gives linear plots and unique values for the intercept. The only discrepancy between Izmailov's and Salomon's approaches is that the former used average reciprocal radii of isoelectronic ions, whereas the latter interpolated his data points for hypothetical anions and cations of equal radii. Unfortunately, neither the essence of this modification, nor the rationale for its supposed superiority over Izmailov's approach are brought out for the benefit of the reader.

In my opinion, the same objections pertain to Salomon's as to Izmailov's methods. In both approaches, long extrapolations to infinite radius are made from data points representing a narrow range of small ions, mostly those of alkali metals and the halides. None of the ions in Salomon's plots are as large as 4-5 Å (the point corresponding to  $r^{-1} = 0.2$ , in Fig. 1 of the paper being discussed, must be an extrapolation already). On the other hand, we found<sup>38,39</sup> that the  $\Delta G^\circ$ 's for the tetraalkyl and tetraaryl ions with radii in the 4-5 Å range are determined overwhelmingly by their non-electrostatic, or neutral components,  $\Delta G^\circ$  (neut), which are not functions of  $r^{-1}$ . Salomon dismisses the whole question of  $\Delta G^\circ$  (neut) too lightly, at the same time attributing, incorrectly, to Noyes<sup>40</sup> an endorsement of the isoelectronic inert-gas assumption for its estimation.

Salomon's rejection of the reference-electrolyte method for the estimation of solvation-energy changes for single ions is poorly founded. It is motivated mainly by the possibility of experimental errors in the determination of solubility products, rather than by any flaws in the method itself. Certainly no chemist would seriously accept the generalization that solubility products are unreliable because of possible complications due to ion pairs, crystal solvates, complexes, and

micelles. Of these obstacles, only a slight degree of ion pairing was encountered in our work with the reference electrolytes, and it was easily corrected with the aid of conductance data. Thus, the above experimental difficulties are neither generally encountered nor are they fundamental to the evaluation of the reference-electrolyte method.

The only genuine criticism directed at the basic assumption of the reference-electrolyte method, is that cited from the work of Coetzee and Sharpe<sup>41</sup> who deduced from NMR shifts the existence of specific solvation effects even with the large reference ions. We have shown,<sup>38</sup> however, that the differentiating effects of the several solvent pairs in question are, at the most, of the order of experimental error in the measured solvation-energy changes for the tetraphenylarsonium and the tetraphenylphosphonium reference ions. The experimental error of the  $\Delta pK_{sp}$  determinations is about 0.1 kcal/mole. To my knowledge, no extrapolation method is capable of that kind of precision.

M. Salomon: The relative merits between extrapolation and reference ion methods for obtaining individual ionic contributions to free energies and/or enthalpies is indeed a complex problem as indicated by Popovych above and elsewhere.<sup>42</sup> From a theoretical viewpoint there is much to be desired in either method, but there are instances in which one is to be preferred. This is true for the methanol-water systems as several inconsistencies appear in the use of solubility data (see below). In the case of careful solubility measurements, such as those reported by Cogley *et al.*<sup>43</sup> where oxygen and water were rigorously excluded from various propylene carbonate (PC) solutions, there is excellent agreement with those results obtained by the emf method (e.g., see footnote 44). For the salts NaCl and KCl, the solubility data of Cogley *et al.* give  $\Delta G^\circ_{soln}$  values of 10.7 and 9.5 kcal/mole<sup>-1</sup>, respectively: the emf data give 10.5 and 9.4 kcal/mole<sup>-1</sup>, respectively, for these salts. The split into  $\Delta G^\circ_i$  (ion) values by the solubility method<sup>43</sup> and the extrapolation method<sup>44</sup> are gratifyingly close so that it is difficult to choose between the two.

The methanol-water systems studied by various methods<sup>42,45-47</sup> are, however, not consistent as is shown in Table V of my original paper. In this table, it should be noted that for those cases<sup>45,47</sup> where the sum  $\Delta G^\circ_i(M^+) + \Delta G^\circ_i(X^-)$  are not equal to the observed<sup>46</sup>  $\Delta G^\circ_i(MX)$ , the results based on an extrapolation method<sup>47</sup> and a reference ion method<sup>45</sup> are similar. Both indicate that methanol is a weaker base than water. There is, however, contrary evidence<sup>46,48,49</sup> which indicates that methanol is the stronger base and this is suggested by negative values of  $\Delta G^\circ_i(M^+)$  for the transfer of small cations from water to pure methanol or methanol-water mixtures.

Let us consider first, Izmailov's method of extrapolation.<sup>47</sup> We have shown elsewhere,<sup>49</sup> and in my paper, that the values of  $\Delta G^\circ_{soln}(MX)$  used by Izmailov are in error and that this accounts for the nonlinearity of his cation plot. While it is true that Izmailov does plot the average function

$$\{(\Delta G^\circ_{M^+} - \Delta G^\circ_{X^-})/2 - \Delta G^\circ_H\} \text{ vs. } \frac{1}{2}(\Gamma_{M^+} + \Gamma_{X^-}) \quad [1]$$

Popovych's statement above indicates that this procedure is in fact identical with mine. This is not the

<sup>34</sup> J. W. Johnson, S. C. Lai, and W. J. James, *Electrochim. Acta*, 15, 1511 (1970).

<sup>35</sup> A. K. Vijh, *This Journal*, in preparation.

<sup>36</sup> Department of Chemistry, Brooklyn College of the City University of New York, Brooklyn, New York 11210.

<sup>37</sup> O. Popovych, *Critical Reviews in Analytical Chemistry*, 1, 73 (1970).

<sup>38</sup> O. Popovych, A. Gibofsky, and D. H. Berne, *Anal. Chem.*, in preparation.

<sup>39</sup> D. H. Berne and O. Popovych, *Anal. Chem.*, in preparation.

<sup>40</sup> R. M. Noyes, *J. Am. Chem. Soc.*, 84, 513 (1962).

<sup>41</sup> J. F. Coetzee and W. R. Sharp, *J. Phys. Chem.*, 75, 3141 (1971).

<sup>42</sup> O. Popovych, *Critical Reviews in Analytical Chemistry*, 1, 73 (1970).

<sup>43</sup> D. R. Cogley, J. N. Butler, and E. Grunwald, *J. Phys. Chem.*, 75, 1477 (1971).

<sup>44</sup> M. Salomon, *J. Phys. Chem.*, 74, 2519 (1970); *J. Electroanal. Chem.*, 26, 319 (1970).

<sup>45</sup> O. Popovych, *J. Phys. Chem.*, 70, 1671 (1966); *Anal. Chem.*, 38, 558 (1966).

<sup>46</sup> D. J. Peakins, "Physico-Chemical Processes in Mixed Aqueous Solvents," F. Franks, Editor, Elsevier, New York (1967).

<sup>47</sup> N. A. Izmailov, *Russ. J. Phys. Chem.*, 34, 1142 (1960).

<sup>48</sup> F. Franks and D. J. G. Ives, *Quart. Rev.*, 20, 1 (1966).

<sup>49</sup> C. M. Criss and M. Salomon, "Physical Chemistry of Organic Solvents," A. K. Covington and T. Dickinson, Editors, Chap. 2.4, Plenum Press, London (1972).

case as is exemplified in my paper and in the following quote from Izmailov: " $\Delta G^\circ_{\text{H}^+} + \Delta G^\circ_{\text{X}^-}$  can be plotted as a function of  $1/r$  for the corresponding halide ions and the quantity  $\Delta G^\circ_{\text{H}^+} - \Delta G^\circ_{\text{M}^+}$  as a function of  $1/r$  for the corresponding metal ions. Both these quantities will tend, as  $r$  increases, to one value  $\Delta G^\circ_{\text{H}^+} + \dots$ . Determination of the limit is not very reliable since it is necessary to extrapolate from distances remote from  $1/r = 0$ . Since, however, the two plots tend the same limit, and  $\Delta G^\circ_{\text{H}^+} + \Delta G^\circ_{\text{X}^-}$  is a linear function of  $1/r$ , it is nevertheless possible to find that limit. This is facilitated by plotting an auxiliary line, representing the means of the sums and differences, which tends to the same limit  $\Delta G^\circ_{\text{H}^+} + \dots$ ." Thus Izmailov does not report (as Popovych suggests) average values of the intercepts for the cation and anion plots but, rather, a single one. The values of  $\Delta G^\circ_{\text{H}^+}$ , which I and which Franks and co-workers (e.g., see footnotes 46 and 48) report, are averages of the cation and anion intercepts. The belief that not all components of the solvation energy vanish at  $1/r \rightarrow 0$ , which incidentally was discussed and considered to be negligible by Izmailov, is the essence of the difference between our two works. The statement by Popovych, that the essence or rationale for my method is not brought out for the reader, is not well founded as considerable discussion was presented. Since my method assumes that these nonvanishing components to  $\Delta G^\circ$  (ion) become equal for very large ions, there is then the question (which Popovych did not comment upon) of whether or not this is valid. The reference to Noyes' paper serves only to illustrate an alternate model which might invalidate my method and does not refer to any stand on the subject by this author.

The use of reference ions to calculate  $\Delta G^\circ_i$  (ion) values is not rejected in my paper as discussed above. There are, however, times when the use of some reference salts should be excluded as there are instances in which some extrapolations should also be excluded. In the methanol-water systems there is no data in the literature that I could find which might indicate that such salts as tetrabutylammonium tetraphenylboride ( $\text{Bu}_4\text{NBP}_4$ ) or triisooamylbutylammonium tetraphenylboride ( $\text{TAB}\cdot\text{BP}_4$ ) do not exhibit specific solvation or ion-ion interactions; however, there is the NMR data on similar salts studied by Coetzee and Sharp<sup>50</sup> which cautions one in the use of this method for the solvents under consideration here. I do not doubt that free energies based on solubility can be measured to within 0.1 kcal/mole. What I do doubt, in some cases, is the accuracy of some measurements. For example, based on the solubility of KCl in water and methanol, a value of  $\Delta G^\circ_i(\text{KCl})$  was obtained<sup>45</sup> which is  $\sim 1$  kcal/mole lower than that obtained by the emf method (e.g., see footnote 46). This exceeds Popovych's stated accuracy by a factor of ten. There is also the question regarding the solubilities of the salts of the large reference ion in water and methanol<sup>45</sup> because of their in-

stability in aqueous solutions, and because of the different standard states employed. Since the salts  $\text{Bu}_4\text{NBP}_4$  and  $\text{TAB}\cdot\text{BP}_4$  are unstable in water, an additivity method was used<sup>45</sup> to obtain  $\Delta G^\circ_i(\text{salt})$ : e.g.

$$\Delta G^\circ_i(\text{TAB}\cdot\text{BP}_4) = \Delta G^\circ_i(\text{TAB}\cdot\text{Pi}) + \Delta G^\circ_i(\text{KBP}_4) - \Delta G^\circ_i(\text{KPi}) \quad [2]$$

where  $\text{Pi}$  = picrate ion. Equation [2] is thermodynamically correct and the accuracy of the quantity on the LHS is dependent upon that of the RHS. Assuming that oxygen and water have been rigorously excluded from the methanol solutions, a problem of different standard states can arise using solubility data. For example, in methanolic  $\text{TAB}\cdot\text{Pi}$  solutions, the concentration of undissociated salt (or ion-pair?) is 0.125M compared to the free ion concentration of 0.267M. Similarly, for  $\text{Bu}_4\text{NPI}$  solutions in methanol the solvated salt (or ion-pair?) concentrations is 0.359M compared to 0.514M for the free ions.<sup>45</sup> Two points are of interest here: first, for solutions of such high concentrations,  $\gamma_{\pm}$  cannot be calculated from a simple Debye-Hückel equation<sup>51,52</sup> but rather from one of the extended relations; second, is the point that the calculation of  $\Delta G^\circ_{\text{slon}}$  (salt) for the above saturated solutions (from  $-2RT \ln [M_{\text{sat}} \gamma_{\pm}]$ ) refers to standard states of 0.125M and 0.359M of undissociated salt for  $\text{TAB}\cdot\text{Pi}$  and  $\text{Bu}_4\text{N}\cdot\text{Pi}$ , respectively. While a constant ionic strength media is as valid a standard state, as is the zero ionic strength media, one must be consistent in employing the same standard state throughout. Since a mixing of standard states does occur in this work,<sup>45</sup> another source of error is introduced into the solubility data. The fact that ion-pairing has been corrected for in this work is, therefore, irrelevant to accuracy of the  $\Delta pK_{\text{so}}$  results.

Finally, in answering Popovych's comments on ion-size relations, I think adequate discussion has been presented in my paper and elsewhere<sup>46,48,49,53</sup> where the basis of a linear  $1/r$  relation is attributed to enthalpy and entropy effects. Certainly linear relations exist; or is this being questioned? If on this matter Popovych is justifying his use of reference ions of equal Stokes radii, then I can only say again that the significance of these radii is unclear. The fact that Walden's rule holds (only) for the larger ions in many solvents is misleading since it suggests a causative relationship between  $\lambda^\circ$  and  $\eta$ ; the relevant value for  $\eta$  in Stokes' frictional factor  $6\pi\eta r_s$  is uncertain due to electrostriction, local structure-making or breaking effects, and dielectric relaxation effects which really requires the use of local rather than bulk values of  $\eta$  (cf. 52, 54).

<sup>51</sup> W. J. Hamer, National Bureau of Standards Publication No. NSRDS-NBS 24, Dec. (1968).

<sup>52</sup> B. E. Conway, "Physical Chemistry, An Advanced Treatise," E. Eyring, Editor, Vol. IXA, Chap. 1, Academic Press, New York (1970).

<sup>53</sup> M. Salomon, *J. Phys. Chem.*, **74**, 2519 (1970).

<sup>54</sup> G. J. Hills, "Chemical Physics of Ionic Solutions," B. E. Conway and R. G. Barradas, Editors, Chap. 23 (and following discussions), John Wiley & Sons, New York (1966).

<sup>50</sup> J. F. Coetzee and W. R. Sharp, *J. Phys. Chem.*, **75**, 3141 (1971).

## Erratum

In the paper "Electrolytic Determination of Porosity in Gold Electroplates, II. Controlled-Potential Techniques" by Ronald J. Morrissey which appeared on pp. 446-450 in the April 1972 JOURNAL, Vol. 119, No. 4, on p. 447 the term  $(\beta_a/\beta_a + \beta_c)$  in Eq. [2] and [4] should appear as an exponent rather than as a multiplier, so that the correct expressions should be

$$I_{\text{corr}} = C_1 A_a^{\frac{\beta_a}{\beta_a + \beta_c}} \quad [2]$$

and

$$\frac{\Delta I}{\Delta V} = C_1 C_2 A_a^{\frac{\beta_a}{\beta_a + \beta_c}} \quad [4]$$





## Oxidation of Beta-Phase Plutonium

J. W. Lindsay, K. Terada, and M. A. Thompson

Dow Chemical U. S. A., Rocky Flats Division, Golden, Colorado 80401

## ABSTRACT

Oxidation of  $\beta$ -phase plutonium was studied by hot-stage x-ray diffraction, microtopography, and thermogravimetry. The oxidation process was found initially to proceed by the formation of a protective sesquioxide film. Subsequently, the protective film was destroyed by blistering and the reaction rate accelerated.

Plutonium is very susceptible to oxidation. The mechanisms involved in this oxidation are complicated by the existence of six temperature-dependent allotropic modifications of the metal and a rather complex metal-oxygen relationship (1). Of the six metallic phases, the low-temperature  $\alpha$ -phase which is stable to 112°C, has received the most attention (2-8). Under conditions of low humidity, oxidation of the  $\alpha$ -phase appears to follow a parabolic rate law. Sackman (4) observed a series of successive parabolic weight gain curves when the reaction was allowed to proceed for extended periods of time. This behavior was thought to arise from the continued failure and regrowth of a protective sesquioxide film.

Few in-depth investigations of the reactions of higher temperature metallic phases with oxygen have been made. Schnizlein and Fischer (9), in investigating the oxidation process above 140°C reported parabolic kinetics through the  $\beta$  (112°-185°C),  $\gamma$  (185°-310°C), and  $\delta$  (310°-452°C) phases. The parabolic model involves the simultaneous production of a protective inner film and an outer porous layer. Thompson (10) observed two linear stages of oxidation in the  $\beta$ -phase with parabolic kinetics being followed only in the  $\gamma$ - and  $\delta$ -phases.

Both Thompson and Schnizlein observed a reduction in the rate of oxidation of  $\delta$ -phase metal at about 400°C. Thompson (10) and Vesterberg and Ekbohm (11) reported an additional rate reduction occurring in the  $\beta$ -phase at about 160°C.

The present study was designed to investigate reaction mechanisms and kinetics associated with the oxidation of  $\beta$ -phase plutonium. Special attention was given to the relationship between the reaction rate, types of oxides formed, and microtopography of the resulting oxide products. Kinetic data were obtained by thermogravimetry. The types of oxides produced and the exterior oxide surface characteristics were followed by hot-stage x-ray diffraction and microscopy using conditions duplicating those in the rate studies.

## Experimental Material and Procedures

**Material.**—Very pure electrorefined plutonium metal was used in the kinetic and mechanistic investigations. The electrorefined button was cast into an ingot and hot-rolled in the  $\beta$ -phase to a thickness of 0.018 in. Impurities in the resulting sheet are listed in Table I.

Key words: corrosion,  $\alpha$ -Pu<sub>2</sub>O<sub>3</sub>, PuO<sub>2</sub>.

**Procedures.**—Isothermal oxidation experiments were conducted with fresh polished samples. The samples were given a final finish with dry jeweler's rouge. The oxidation was followed thermogravimetrically on a Mettler I Thermoanalyzer enclosed in a glove box. The atmosphere used in the investigation was a 20% O<sub>2</sub>-80% Ar mixture. Moisture was removed to less than 10 ppm by volume by passing the gas over a molecular sieve desiccant. Moisture levels were determined with a Consolidated Engineering Corporation Model 26-303 hygrometer. All runs were made at 640 Torr.

Hot-stage x-ray diffraction patterns of the initial stages of oxidation were made at various isotherms with a Picker Nuclear diffractometer fitted with a hot-stage cell. Metal samples and atmospheres were kept as closely as possible to those employed in the kinetics investigations. Hot-stage optical microscopy investigations were made using a Unitron Model HHS metallograph. Conditions were again kept as closely as possible to those employed in the thermogravimetric runs.

## Results

**Thermogravimetry.**—Isothermal weight gain curves showing the rate of oxygen reaction with respect to time are shown in Fig. 1. The figure also shows that the over-all reaction rate increases with temperature between 120° and 175°C before decreasing to a minimum at about 190°C. Above 190°C, the rate resumes its increase with temperature. Each curve consists of two distinct stages of oxidation. This phenomenon oc-

Table I. Bulk metal impurities

Element	Impurity, ppm by weight	Element	Impurity, ppm by weight
Al	28.0	Li	0.05
As	0.7	Mg	2.0
B	0.09	Mn	9.0
Ba	0.8	N	3.0
Be	0.06	Na	2.0
C	10.0	Nd	8.0
Ca	0.9	Ni	0.6
Cd	0.8	Np	1.0
Cl	6.0	O	38.0
Co	0.04	P	0.1
Cr	2.0	Pb	0.2
Cu	0.7	Pr	4.0
F	0.2	S	0.7
Fe	7.0	Si	7.0
Gd	4.0	Ta	31.0
I	0.2	Ti	1.0
K	0.9	U	65.0
La	5.0	W	2.0
		Zn	2.0



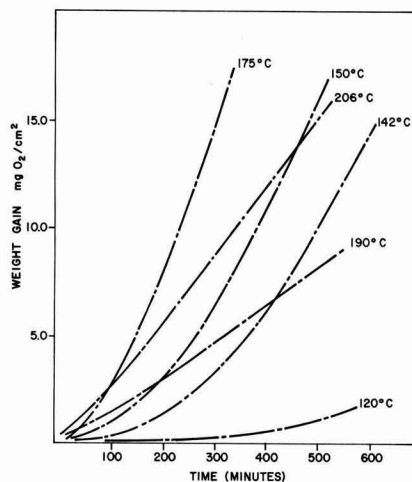


Fig. 1. Weight gain curves showing oxidation behavior from 120° to 206°C.

curves throughout the  $\beta$ -phase. The 206°C curve was included in Fig. 1 to show that two stages of oxidation also occur in the lower temperature region of the  $\gamma$ -phase. The two stages are shown more clearly in the plot of the natural logarithms of the weight change with respect to the logarithms of time for the isotherm at 142°C (Fig. 2).

The initial stage of oxidation (Fig. 3), whose duration shortens with increasing temperature, conforms reasonably well to a linear rate law. Effect of temperature on the rate of oxidation during the initial stage is shown in the Arrhenius plot in Fig. 4.

The parabolic rate preceding the linear rate, reported by Schnizlein and Fischer (9) and Larson and Cash (7) was not observed in the weight gain curves. However, weight change data at the beginning of the isothermal oxidation were lost because it required several minutes for the balance to reach equilibrium after the metal was exposed to the oxidizing gas. Figure 3 shows that when the linear rate is extrapolated to the weight gain axis, the intercepts steadily increase as the temperature rises above 150°C. This suggests that the observed linear rate is not in effect during the very early stages of reaction.

Following a brief transition period, which is best seen in Fig. 2, the reaction proceeds by an accelerating rate.

**Microscopy.**—Microtopographic examinations were made of the oxide surface during both the initial

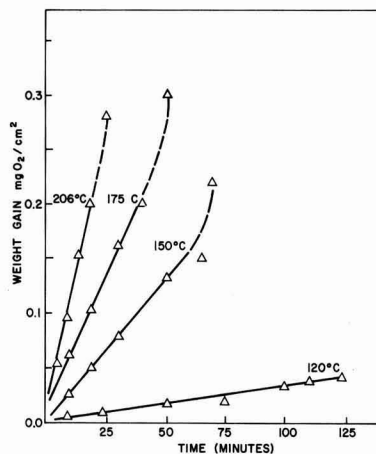


Fig. 3. Initial stage of oxidation

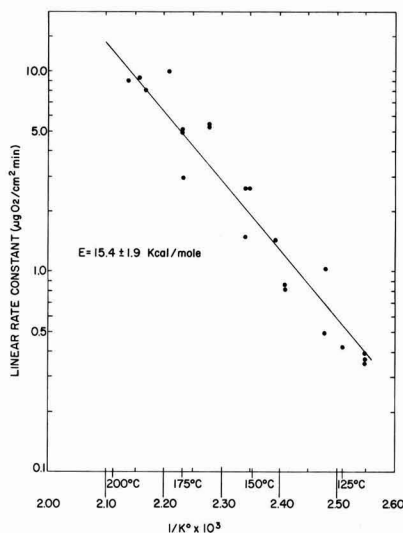


Fig. 4. Arrhenius plot of rate constants obtained from first stage of oxidation.

linear stages and the transition stages using the same conditions as those employed in the kinetic investigations. Several series of photomicrographs were taken of the surface at 750X magnification with direct and indirect illumination and at temperatures from 120° to 206°C.

During the linear stage of oxidation, an interesting pattern of oxide growth was observed. A compact, black oxide film was formed over most of the metal surface. The remaining areas consisted of dark, circular areas which formed early in the oxidation and grew larger in size and number with time. As these circular areas grew, it became apparent that they were blister-like features on the surfaces. These features eventually resulted in mounds of loose, brownish-green oxide which ultimately covered the entire surface.

Hot-stage photomicrographs taken of the oxidation process at 145°C and various time intervals are shown in Fig. 5. The photomicrographs are of representative areas of the surface and show the growth of the blister-like oxides. The light areas correspond to the compact, black oxide film, except for Fig. 5a where

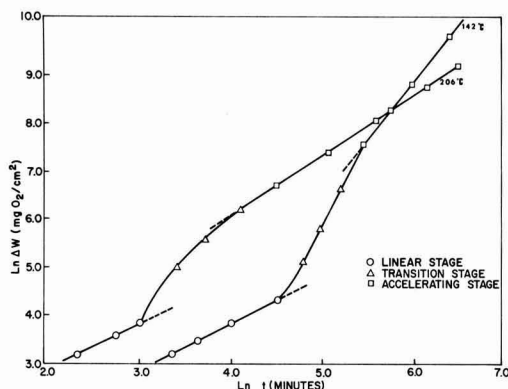


Fig. 2. Ln-Ln plot of weight gain with respect to time

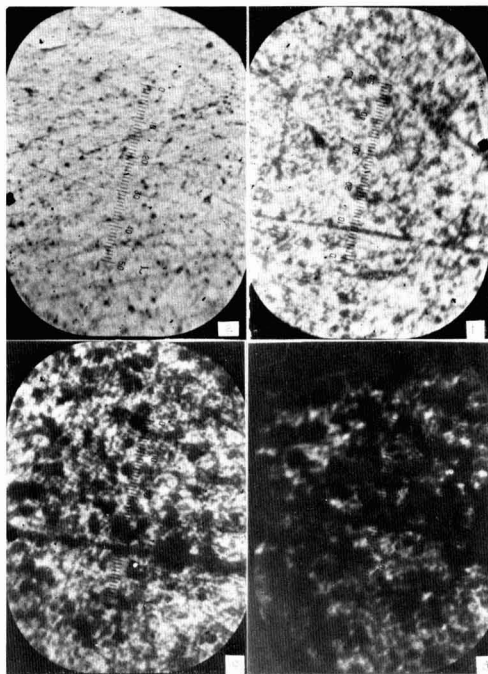


Fig. 5. Hot-stage photomicrographs (750X) of plutonium oxidation at 145°C. (a) Initial surface, (b) after 20 min, (c) after 40 min, (d) after 80 min.

the light area is the metal surface. There is no definite correlation between the spots on the initial metal surface and the dark, circular areas which develop during oxidation. Similar observations were made in other hot-stage microscopy experiments between 120° and 206°C. The rate of formation and growth of blisters increased with temperature.

**X-ray diffraction.**—Following several exploratory scans at each of several isotherms, it was determined that only  $\alpha$ -Pu<sub>2</sub>O<sub>3</sub> and PuO<sub>2</sub> were produced in the oxidation of  $\beta$ -phase plutonium. Progress of the formation of the two oxides was followed by scanning the  $\alpha$ -Pu<sub>2</sub>O<sub>3</sub> 2 $\theta$  peaks at 28.0° and 55.0°, and the PuO<sub>2</sub> 2 $\theta$  peaks at 28.1° and 56.5° (12). In addition, the strong  $\beta$  peak of the metal at 34.3° was periodically scanned since its presence was a good indication that loss of inner oxide layers from the diffraction scan was not due to a thicker outer film exceeding the penetration limit of the x-ray beam. Figure 6 shows the results of hot-stage x-ray diffraction and thermogravimetric experiments at 175°C. The relative areas under the 2 $\theta$  peaks of 55.0° and 56.5° for  $\alpha$ -Pu<sub>2</sub>O<sub>3</sub> and PuO<sub>2</sub>, respectively, are plotted against time to show the change in relative amounts of the oxides during a reaction. Also plotted on the same time coordinate is the thermogravimetric data of an experiment at the same temperature. The PuO<sub>2</sub> shown in the graph is slightly exaggerated due to a weak  $\alpha$ -Pu<sub>2</sub>O<sub>3</sub> diffraction peak at 56.4°, but it does not mask the trend.

Alpha-Pu<sub>2</sub>O<sub>3</sub> was the principal oxide formed during the early stages of reaction. The decrease in the amount of the sesquioxide occurred when the rates of PuO<sub>2</sub> formation and weight gain began to accelerate.

Observation of only a small change in the  $\beta$ -metal peak height indicated that the loss of diffraction intensity of the  $\alpha$ -Pu<sub>2</sub>O<sub>3</sub> was not due to its covering by a thick layer of PuO<sub>2</sub>. An initial decrease in PuO<sub>2</sub> was observed. This phenomenon is thought to be the result of the net reduction of the dioxide by the sub-

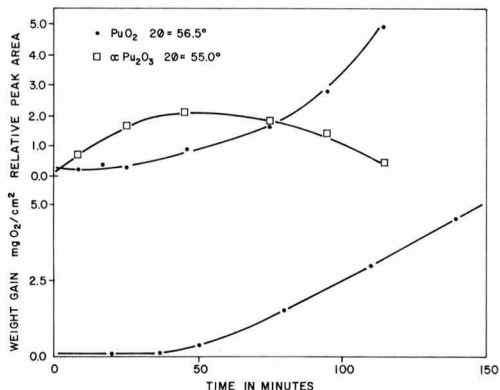


Fig. 6. Hot-stage x-ray diffraction and weight gain data for oxidation at 175°C.

strate metal to the sesquioxide (13). This reduction started at temperatures above 150°C. The same type of behavior described above was observed at other temperatures. The difference was only in the rates. X-ray diffraction analyses of samples removed from the thermogravimetric analyzer during the accelerated stage of oxidation were also made. Oxides readily removed from the sample surface with a camel's hair brush were analyzed separately from those that were more adherent to the metal. The loose oxide was all PuO<sub>2</sub>. The slightly more adherent oxide was practically all PuO<sub>2</sub>. These oxides were not as compact nor as adherent as the initially formed  $\alpha$ -Pu<sub>2</sub>O<sub>3</sub> film.

### Discussion

Isothermal weight gain curves obtained from the oxidation of  $\beta$ -phase plutonium have the general form shown in Fig. 7. The different stages of the oxidation discussed in this section are indicated in the figure.

Although experimental difficulties in this work prevented the detection of the parabolic stage (A), x-ray diffraction and TGA data point to its occurrence.

The first part of the reaction definable by TGA (stage B) conformed to a linear rate. X-ray diffraction analyses demonstrated that the compact oxide formed during the early part of this stage was principally  $\alpha$ -Pu<sub>2</sub>O<sub>3</sub>. The decrease of the amount of the sesquioxide as the greenish-brown PuO<sub>2</sub> covered the surface was the result of the reaction

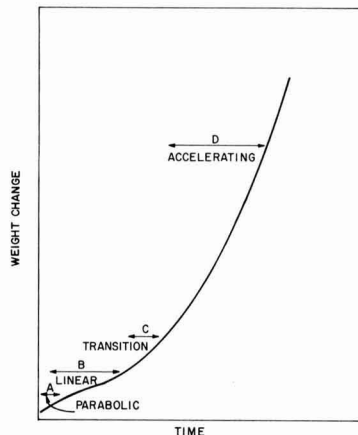
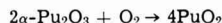


Fig. 7. Typical weight gain curve for isothermal oxidation of  $\beta$ -phase plutonium.

The acceleration of the oxidation rate as the sesquioxide was depleted indicated that the initial parabolic rate resulted from the formation of a protective film of  $\alpha$ -Pu<sub>2</sub>O<sub>3</sub>. Microscopic examination of the  $\alpha$ -Pu<sub>2</sub>O<sub>3</sub> film surface during its formation showed localized blistering of an otherwise compact oxide film. Appearance of the blisters was observed very early in the isothermal oxidation process. The apparent linear rate was the result of a combination of the decreasing rate of oxidation due to growth of a thicker, protective sesquioxide film and an increasing rate of oxidation due to loss of areas covered by the protective film. The protective sesquioxide film was progressively replaced by less coherent and consequently less protective PuO<sub>2</sub>.

The transition stage (C) began when the oxidation rate started to accelerate. The rate accelerated as the protective  $\alpha$ -Pu<sub>2</sub>O<sub>3</sub> was progressively depleted and replaced by nonprotective PuO<sub>2</sub>.

During the accelerated stage (D), the oxidation reached its maximum rate. The amount of sesquioxide on the metal became undetectable by x-ray diffraction and the entire surface was covered by the greenish-brown oxide. It is interesting that the  $\alpha$ -Pu<sub>2</sub>O<sub>3</sub> did not reform under the blisters as a protective film. One possible explanation is that the conditions under which the initial oxide layer and succeeding layers were formed were quite different. The initial oxide film was formed immediately following polishing of the metal in air. During this relatively slow oxidation, the oxide formed could become the nucleus for succeeding oxide growth which could withstand higher stresses before failure. This type of oxide is contrasted to that formed where bare metal is suddenly exposed to oxygen at elevated temperatures. Support for this mechanism was obtained in a series of experiments in which metal samples were exposed to air at room temperature for 24 hr prior to oxidation. In each case, a definite delay in the accelerated oxidation rate was exhibited with high concentrations of  $\alpha$ -Pu<sub>2</sub>O<sub>3</sub> remaining for as great as four times longer.

Figure 1 shows that above 175°C, there is a minimum rate in the later stages of reaction. Thompson (10) first reported this and more recently, Vesterberg and Ekblom (11) working with moist argon, made a similar observation. However, in these earlier reports, the rate minimum was found at about 160°C, while it was observed at 190°C in this work. According to Schnizlein and Fischer (9) the accelerated rate can be eliminated by oxidation with extremely dry oxygen. One may conclude from it that the rate minimum is the result of activity of moisture on the oxide film.

### Summary and Conclusions

Oxidation of  $\beta$ -phase plutonium metal involves several processes. Initially, there is a concurrent forma-

tion of protective  $\alpha$ -Pu<sub>2</sub>O<sub>3</sub> film and blisters in the oxide. At the beginning, the  $\alpha$ -Pu<sub>2</sub>O<sub>3</sub> grows relatively rapidly, and the blister formation and growth rate is low. With time, this is gradually reversed and eventually the entire surface is disrupted. The  $\alpha$ -Pu<sub>2</sub>O<sub>3</sub> is oxidized to PuO<sub>2</sub>. For the period of linear reaction rate, an activation energy of  $15.4 \pm 1.9$  kcal/mole was calculated.

As the protective sesquioxide is oxidized to a non-protective PuO<sub>2</sub>, the oxidation rate accelerates to a maximum. This maximum accelerated rate increased with temperature but began to decrease at about 175°C to minimum at 190°C.

### Acknowledgment

The authors gratefully acknowledge the assistance of H. L. Bramlet and R. L. Meisel in the x-ray diffraction work and R. W. Loser in the computer reduction of some data. This work was performed under United States Atomic Energy Commission Contract AT(29-1)-1106.

Manuscript submitted Sept. 13, 1971; revised manuscript received Jan. 17, 1972.

Any discussion of this paper will appear in a Discussion Section to be published in the December 1972 JOURNAL.

### REFERENCES

1. E. R. Gardner, T. L. Markin, and R. S. Street, *J. Inorg. Nucl. Chem.*, **27**, 541 (1965).
2. K. S. Covert and M. Kolodney, USAEC Report LA-314, June 1945.
3. E. Dempsey and A. E. Kay, *J. Inst. Metals*, **86**, 739 (1958).
4. J. F. Sackman, "Plutonium 1960," pp. 222-229, E. Grison, W. B. H. Lord, and R. D. Fowler, Editors, Cleaver-Hume, London (1961).
5. J. F. Sackman, AWE-O-4/62 (1962).
6. J. T. Waber and E. S. Wright, "The Metal Plutonium," pp. 194-204, A. S. Coffinberry and W. N. Miner, Editors, Univ. of Chicago Press, Chicago (1961).
7. D. T. Larson and D. L. Cash, *J. Phys. Chem.*, **73**, 2814 (1969).
8. A. Tanon and H. Bordes-Page's "Plutonium 1965," pp. 603-616, A. E. Kay and M. B. Waldron, Editors, Chapman and Hall, London (1967).
9. J. G. Schnizlein and D. F. Fischer, *This Journal*, **114**, 23 (1967).
10. M. A. Thompson, USAEC Report RFP-491 (1966).
11. V. Vesterberg and L. Ekblom, "Plutonium 1970," pp. 164-170, W. N. Miner, Editor, Met. Soc., AIME, New York (1970).
12. R. N. R. Mulford and C. E. Holley, Jr., USAEC Report LA-DC-8266 (1966).
13. K. Terada, R. L. Meisel, and M. R. Dringman, *J. Nucl. Mat.*, **30**, 340 (1969).

# Plutonium Oxidation in Moist Oxygen-Nitrogen Mixtures

J. L. Stakebake and L. M. Steward

Dow Chemical U. S. A., Rocky Flats Division, Golden, Colorado 80401

## ABSTRACT

Plutonium oxidation studies were conducted at 90°C in dry air and moist oxygen-nitrogen mixtures using both cast and rolled plutonium. Oxidation in dry air obeyed a linear rate law with average rate constants of 0.042 and 0.050 mg/cm<sup>2</sup>hr for the cast and rolled plutonium, respectively. Both metal samples were found to oxidize faster in the moist oxygen mixtures than in moist nitrogen. Linear oxidation rates were observed in moist oxygen-nitrogen mixtures with average rate constants of 0.68 and 0.34 mg/cm<sup>2</sup>hr for the cast and rolled plutonium. In moist nitrogen oxidation followed a parabolic rate law with average rate constants of 3.60 and 1.11 mg/cm<sup>2</sup>hr<sup>1/2</sup> for the cast and rolled samples, respectively. The reaction with water vapor observed during this investigation was greatly influenced by the purity of the metal as well as its metallurgical history. Samples of cast, electrorefined plutonium containing some microcracks reacted very rapidly, while for the relatively impure rolled material the reaction was somewhat slower. In all cases at this temperature, the reaction with water vapor was diffusion controlled and not reaction controlled as has been reported previously. The diffusing species is believed to be OH<sup>-</sup> ions formed by the dissociative adsorption of water on plutonium dioxide.

Plutonium metal is very reactive and highly susceptible to oxidation which destroys the integrity of the metal. Two methods are known to minimize the amount of oxidation. One is by reducing the reactivity of the metal by alloying with another metal such as gallium, aluminum, or zirconium. Another is to minimize the contact of plutonium with oxidizing gases. However, taking advantage of the second method of reducing oxidation requires some understanding of the oxidation characteristics of plutonium metal. For example, plutonium oxidation is greatly enhanced by the presence of water vapor. Thompson (1) observed that an increase in water content of an oxygen atmosphere from 1.5 to 35 ppm resulted in an oxidation rate increase of about 19-38.6  $\mu\text{g}/\text{cm}^2\text{hr}$  at 85°C. Raynor and Sackman (2) found that the rate of oxidation at 90°C increased with increased humidity up to about 2% relative humidity. Above 2% relative humidity, increasing the water vapor content had little effect on the reaction. This effect was not observed above 215°C but at 190°C as little as 180 ppm H<sub>2</sub>O caused the linear oxidation rate to accelerate an order of magnitude (3).

According to most of the earlier studies, the accelerating effect of water vapor on plutonium oxidation is more pronounced in inert gases than in air or oxygen. For example, Waber (4) stored two plutonium samples at 75°C and 50% relative humidity in helium and also air. After 26 hr, the extent of oxidation of the sample stored in helium was about 60 times greater than for the sample stored in air. Raynor and Sackman (5) have also studied the oxidation of plutonium in argon and air at 30°, 60°, and 90°C and 95% relative humidity. In all cases, the oxidation was faster in argon than in air. However, this difference was very small for unalloyed plutonium at 90°C. These early observations have led to the conclusion that it is better to store plutonium in "dry" air than in a "dry" inert gas in order to minimize corrosion. Under these conditions, the oxygen tends to inhibit the oxidation by water.

Unfortunately, storing plutonium in air presents a fire hazard since plutonium will burn in atmospheres containing more than 6% oxygen (6). Therefore, it is often preferable to store and handle plutonium in an inert atmosphere despite the increased susceptibility to oxidation. Since oxygen has been reported to inhibit water oxidation of plutonium, it is conceivable that low oxygen concentrations in an inert atmosphere would provide a significant amount of corrosion protection. However, almost no work has been done to evaluate

the effect of small oxygen concentrations on the oxidation rate of plutonium by water vapor in inert gases. Tanon *et al.* (7) performed some glove box oxidation experiments using various argon-oxygen mixtures. Their results showed that the rate of oxidation of plutonium in argon-oxygen mixtures was less than in argon but greater than in pure oxygen. This was true at 50° and 70°C, but no results were reported at 90°C. The scatter of the results did not permit any definite relationship to be established between the rate of oxidation and the oxygen concentration. To be able to minimize the oxidation of plutonium in semi-inert atmospheres, this relation must be established.

Experiments discussed in this paper provide information on the oxidation behavior of plutonium in reduced oxygen atmospheres at 90°C. These experiments also provide additional information on the effects of impurities on plutonium oxidation and the nature of the plutonium-water reaction.

## Experimental

**Apparatus.**—The experimental system used for the measurement of oxidation rates is shown in Fig. 1. The principal component is a Cahn® recording electro-microbalance. This balance has an accuracy of  $\pm 5 \mu\text{g}$ . With the vacuum system incorporated into the balance system, the working pressure can be varied from  $10^{-7}$  to 600 Torr. A resistance furnace controlled with a power proportioning programmer was used to heat the samples. The actual temperature of the sample was measured with a thermocouple located adjacent to the

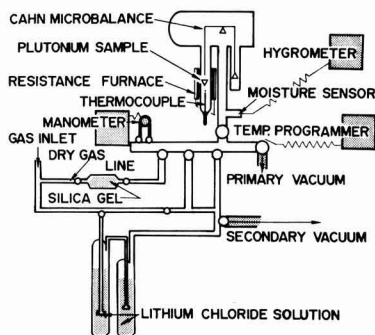


Fig. 1. Experimental apparatus

Key words: plutonium oxidation, moist oxygen-nitrogen.

Table I. Mass spectrometer analysis of two plutonium samples

Element	Rolled Pu, ppm by weight	Cast Pu, ppm by weight
Ag	3	3.0
Al	47	5.0
Am	1563	—
C	100	32.0
Cl	4	3.0
Co	2	—
Cr	86	0.5
Cu	23	0.5
F	2	0.7
Fe	430	9.0
Ga	31	5.0
In	2	—
Mg	2	0.4
Mn	17	0.6
Mo	2	—
N	5	0.5
Ni	69	2.0
Np	19	11.0
O	160	40.0
P	37	0.4
Pb	4	0.6
S	2	0.7
Si	94	5.0
Sn	2	2.0
Ta	27	7.0
Ti	2	—
U	230	25.0
W	15	270.0
Zn	26	5.0
Zr	2	—
Other	2	6.3
Total	3010	435.0

sample inside the hangdown tube. Gas mixtures were introduced into the system via a series of traps which conditioned the gas to the desired water content. Moisture levels were measured with a Panametrics® hygrometer during each run.

**Samples.**—Two different batches of plutonium were used for this study. One batch had been stored for about six years and was originally rolled from an electrorefined ingot. Thompson (8) used this same metal in his work and reported an average total impurity content of 870 ppm. During storage, the impurity content increased to about 3010 ppm with americium and iron being the major impurities (Table I).

Nearly all previous microbalance studies have been conducted with samples cut from rolled sheets. Recent developments, however, permitted the use of thin cast samples. The second batch of plutonium was vacuum cast from an electrorefined ingot into plates about 0.75 mm thick. Total impurities in this batch were 435 ppm (Table I).

Sample coupons were cut from bulk sheets about 0.75 mm thick so as to have a final surface area of about 0.50 cm<sup>2</sup>. Each coupon was mechanically polished using 600 grit silicon carbide paper. Other techniques, such as electropolishing and a metallographic polish with 1 $\mu$  diamond paste, were also tried. The mechanical polish, however, seemed to yield the most reproducible results.

**Procedure.**—Immediately after polishing the samples were loaded on the balance and the system evacuated. Samples which were to be oxidized in a dry atmosphere were outgassed for 2 hr at about  $1 \times 10^{-6}$  Torr. Those to be run in a moist atmosphere were evacuated to  $1 \times 10^{-5}$  Torr. After evacuation, the temperature of the sample was increased to 90°C and the system back-filled to a pressure to 500 Torr with the reacting gas. For this study, the reacting gases were mixtures of nitrogen and 0, 3, and 21 v/o (volume per cent) oxygen and also 100% oxygen. Two moisture contents, 5 and 12,000 ppm, were used during this experiment. The 12,000 ppm moisture level was generated by passing the gas through two traps containing a saturated solution of LiCl. Purified gases were passed through a silica gel trap to obtain the 5 ppm moisture level.

Data from the plutonium oxidation runs were processed using a digital computer curve fitting program (9) to determine the best equation for the data. In many cases, it is difficult to fit the rate data exactly to any one simple rate equation, because changes during

the oxidation run are frequent. For the data from this study, the single equation which best fits the data was chosen.

## Results and Discussion

**Oxidation of unalloyed plutonium.**—Results from this study of the oxidation of rolled and cast unalloyed plutonium are shown in Fig. 2 and 3. The pronounced effect water has on plutonium oxidation is quite evident from these runs. At 90°C oxidation was found to be faster in the moist oxygen containing atmospheres than in moist nitrogen. This observation is opposite that observed at lower temperatures where oxidation has been reported to be faster in the inert gas and any oxygen present apparently exerts an inhibiting effect on the oxidation process (5, 7).

**Oxidation in dry air.**—Compared to the rate observed with moisture present, plutonium oxidation in dry air was relatively slow and very reproducible. Curve A in Fig. 2 and 3 shows the results of oxidation in dry air for the rolled and the cast samples, respectively, after subtracting any inhibition time. The runs in dry air were all initially inhibited for periods up to about 200 hr. This inhibition was probably caused by the formation of a nonporous, adherent oxide film on the surface prior to the start of the experimental run. Although inhibition times for different samples varied from 32 to about 200 hr, the final oxidation rate was the same in all cases. The oxidation process in dry air followed the

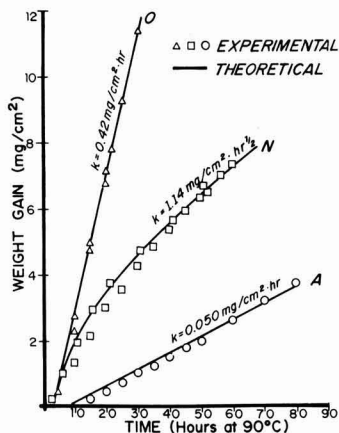


Fig. 2. Oxidation of rolled unalloyed plutonium at 90°C in dry air A, moist oxygen-nitrogen mixtures O, and moist nitrogen, N.

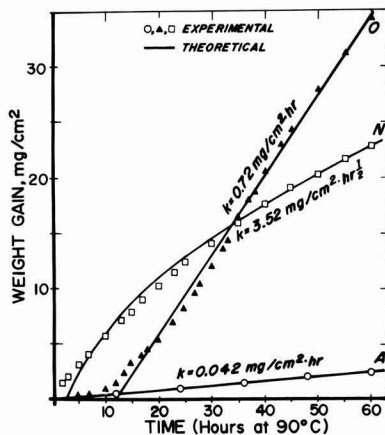


Fig. 3. Oxidation of cast electrorefined plutonium at 90°C in dry air A, moist oxygen-nitrogen mixtures O, and moist nitrogen, N.



linear rate law,  $x = kt + c$ . The rate constant,  $k$ , was determined to be 0.050 mg/cm<sup>2</sup>hr for the rolled plutonium and 0.042 mg/cm<sup>2</sup>hr for the cast plutonium.

Data from this study were compared to the results obtained earlier by Thompson (8) under the same conditions and with the same rolled metal. At 90°C, in dry air, Thompson reported a linear oxidation rate of about 0.048 mg/cm<sup>2</sup>hr. The average rate from all runs in this study was 0.046 mg/cm<sup>2</sup>hr. On the basis of these comparisons, it appears that storage and the accompanying increase in impurities (up to at least 3000 ppm) as well as radiation damage, has no effect on the metal oxidation rate in dry air. Furthermore, the method of metal preparation, either rolling or casting, did not influence the oxidation rate appreciably.

Linear oxidation kinetics can result from several possible rate-determining processes (10). These include: phase boundary processes involving metal/oxide or oxide/oxide interfaces; diffusion through an oxide film of constant thickness; and the adsorption of oxygen. Formation of a porous oxide, resulting in a reaction at the metal/oxide interface, is probably the most commonly used explanation for linear kinetics. However, in the present experiments the initial oxide formed was not porous as evidenced by the long inhibition times.

The observed results can be explained, however, by assuming the initial reaction with the nonporous oxide film was one which formed a porous oxide. This was a rearrangement process within the oxide structure and not further oxidation. Variations in the length of the inhibition time were due to differences in the thickness of the initial nonporous layer. After formation of the porous oxide, oxidation took place at the metal/oxide interface. Adsorption as the rate-controlling step was ruled out because the reaction rate was independent of oxygen pressure. The possible reaction at an oxide/oxide interface likewise was not considered to be the primary rate-determining step since only PuO<sub>2</sub> was detected by x-ray diffraction at this temperature. However, this interaction cannot be completely ruled out at this time.

**Oxidation in moist oxygen-nitrogen atmospheres.**—The primary objective of this study was to determine the effect of oxygen on the oxidation of plutonium by water vapor. Runs were made in moist nitrogen atmospheres containing 3 and 21% oxygen and also in 100% oxygen. In all cases, the oxidation rate was faster in the oxygen-containing atmospheres than in moist nitrogen. This is opposite all previously reported results (4, 5, 7). One possible explanation is the temperature at which these runs were carried out. The majority of the evidence for a protective oxide film has been found at room temperature and that work done at 90°C showed little difference between oxidation in moist oxygen and in moist argon (5). Furthermore, it should be noted that the experimental procedures used in earlier studies provided mostly qualitative and semi-quantitative information. Because of this, a definite explanation of the effect of oxygen on plutonium oxidation by water has not been reported.

Typical results from this study are shown as curve O in Fig. 2 and 3. It is obvious from these runs that water vapor greatly accelerates the oxidation of plutonium. The protective oxide layer normally formed by oxygen during oxidation in moist atmospheres was not observed with the possible exception of the first few hours on some runs. Run O in Fig. 3 is such an example. In this case, the oxidation proceeded along the curve obtained for dry air for about 7 hr indicating water vapor was not yet taking part in the reaction. After 7 hr, the rate began increasing until the final linear rate was reached. The final linear rates obtained for the oxygen runs shown in Fig. 2 and 3 (curve O) were 0.42 and 0.72 mg/cm<sup>2</sup>hr for the rolled and cast plutonium samples, respectively. All of the runs in oxygen-containing atmospheres followed a linear rate

law with an average rate of 0.34 mg/cm<sup>2</sup>hr for the rolled plutonium and 0.68 mg/cm<sup>2</sup>hr for the cast metal. The difference in rates between the two metal samples is attributed to the difference in purity as well as the metallurgical history. This is consistent with the results reported by Raynor and Sackman (5).

Rate constants obtained for the rolled metal were compared with the 0.18 mg/cm<sup>2</sup>hr rate obtained earlier by Thompson (8) using the same metal. The rate observed in this study was about twice as fast. This increased rate was probably due to differences in the moisture content for the two studies.

**Effect of oxygen partial pressure on plutonium oxidation.**—The relation between oxygen pressure and the plutonium oxidation rate has not been clearly established. There has been a fairly significant pressure effect reported at higher temperatures (8, 11). This ranges from a very positive effect at about 200°C (11) to an inverse effect at 400°C (8). However, the effect appears to be minimal at room temperature. Tanon *et al.* (7) reported an inverse oxygen pressure dependence for oxidation in moist atmospheres at 50° and 70°C. The exact relationship could not be defined from their data and no results were reported at temperatures greater than 70°C.

The results from this study show a very strong positive effect at low oxygen concentrations. This is evidenced by the difference between curves O and N in Fig. 2 and 3. The exact oxygen concentration required for this effect was not determined; however, it was less than 3 v/o or a partial pressure of 15 Torr. Oxygen concentrations greater than 3 v/o produced no effect on the oxidation rate at 90°C.

**Oxidation in moist nitrogen atmospheres.**—Typical results from the oxidation of unalloyed plutonium in moist nitrogen are shown in Fig. 2 and 3 (curve N). At 90°C plutonium oxidation by water vapor was found to be very fast and to obey a parabolic rate law, i.e.,  $x = kt^{1/2} + c$ , as shown in Fig. 4. The rate constants for the typical runs shown in Fig. 4 were 1.14 mg/cm<sup>2</sup>hr<sup>1/2</sup> for the rolled metal and 3.52 mg/cm<sup>2</sup>hr<sup>1/2</sup> for the cast sample. The average rate constants for all of the runs made with these two samples were 1.11 mg/cm<sup>2</sup>hr<sup>1/2</sup> for the rolled plutonium and 3.60 mg/cm<sup>2</sup>hr<sup>1/2</sup> for the cast plutonium.

The products from the reaction between water and plutonium were examined by x-ray diffraction and found to be PuO<sub>2</sub>. No PuH<sub>2</sub> was detected although this was not totally unexpected due to the similarity in crystal structure between PuO<sub>2</sub> and PuH<sub>2</sub>. The nitride, PuN, is not expected to form under 300°C and was not detected in the products. The color of the PuO<sub>2</sub> formed during oxidation of the rolled plutonium was yellow-green, while the oxide formed from oxidation of the cast metal was black. This difference in color may be indicative of two different mechanisms and is discussed in more detail later.

Because of the threefold difference in reaction rate for the two types of plutonium samples, the character

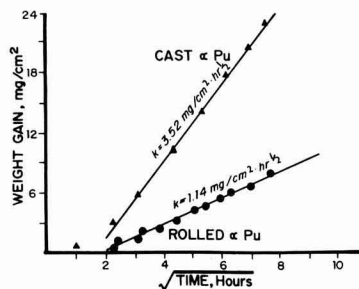


Fig. 4. Parabolic oxidation of cast and rolled plutonium at 90°C in moist nitrogen.

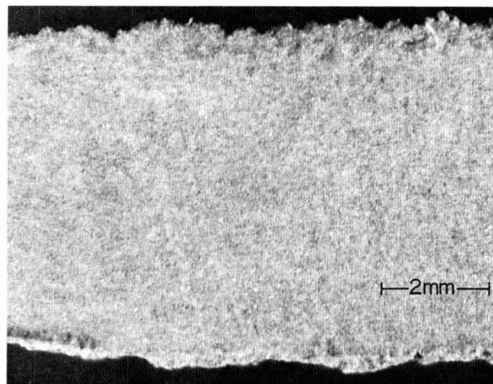


Fig. 5a. Surface of a rolled plutonium coupon following oxidation at 90°C in moist nitrogen.

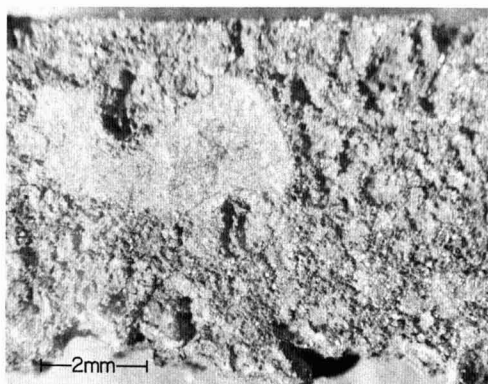


Fig. 6a. Surface of a cast plutonium coupon following oxidation at 90°C in moist nitrogen.

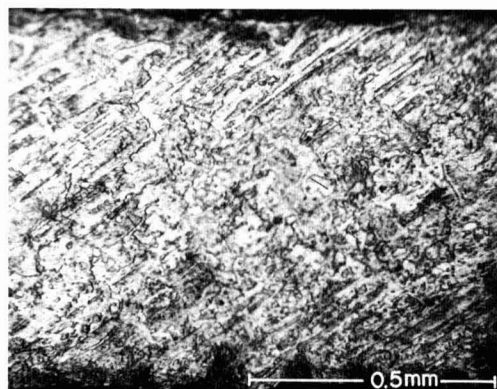


Fig. 5b. Cross section of a rolled plutonium coupon following oxidation at 90°C in moist nitrogen.

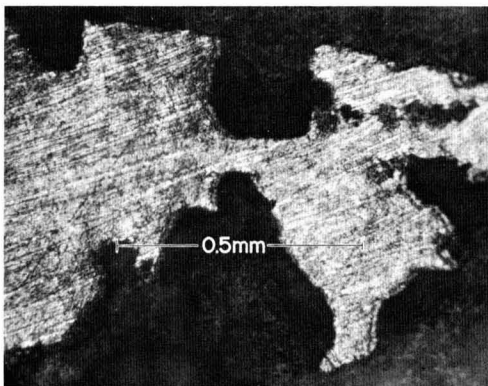


Fig. 6b. Cross section of a cast plutonium coupon following oxidation at 90°C in moist nitrogen.

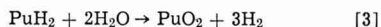
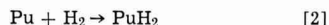
of the plutonium metal was examined in detail. Photomicrographs were taken of coupons from both the rolled and cast samples after about 25% of total oxidation in moist nitrogen. Figure 5a shows the surface of the rolled coupon after all loose oxide had been removed. The water vapor appeared to be nearly uniform with the major reaction occurring on the edges. Figure 5b is a cross-sectional view of the same coupon. Again, there was no serious pitting, indicating the reaction was fairly uniform. These surfaces are indicative of an atypical water reaction with plutonium which was probably caused by the high impurity content. Photomicrographs of the cast plutonium coupon are included as Fig. 6a and 6b. The water vapor attack on this sample was catastrophic. In Fig. 6a, severe pitting is shown on the surface and in Fig. 6b the cross-sectional view shows that some of these pits nearly penetrate the coupon. This type of attack is similar to the hydrogen reaction with plutonium and is identical to that normally expected with water vapor.

Initially, the difference in impurities appeared to be the primary reason for the different types of attack on the two samples. Further comparison of these two samples, however, provided additional reasons for the difference in rates. Metallographic examinations of the two metal samples showed the cast material to contain numerous microcracks (Fig. 7). These cracks were absent in the rolled material (Fig. 8). The microcracks in the cast specimens could account for the catastrophic type attack. In this case, moisture

could condense in the microcracks causing accelerated oxidation and subsequent breakaway.

The microcracks probably originate from internal stresses caused by cooling through the  $\beta$ - $\alpha$  phase transformation during casting. Since the rolled plutonium sample also was cooled from the  $\gamma$ -phase to the  $\alpha$ -phase it might also be expected to contain microcracks. However, it was essentially free from any cracks. One reason for the lack of cracks may be the relatively high impurity content. It has been shown that impurities reduce the incidence of microcracking (12). Iron, particularly, serves as a stress-relieving agent by precipitation as  $\text{Pu}_6\text{Fe}$  in the grain boundaries. Thus, somewhat indirectly, impurities may be the major contributing factor in the two different oxidation rates.

**Mechanism of water vapor attack.**—Several mechanisms (13) have been proposed to explain the oxidation of plutonium by water vapor. Draley (14) proposed a hydride mechanism for the interaction of hydrogen with metals. In the case of plutonium, water reacts to form plutonium hydride which further reacts to form the oxide. That is



Waber (15) suggested that the reaction between plutonium and water vapor is under anodic control. The cathodic reaction involves the dissociation of adsorbed

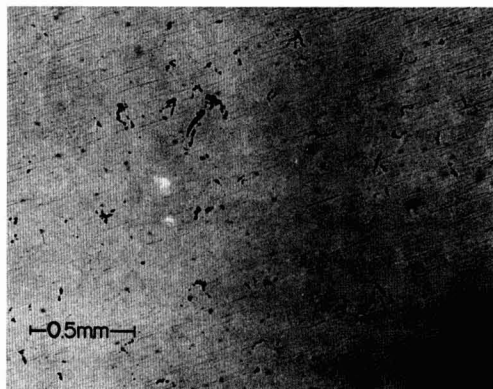
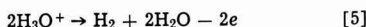


Fig. 7. Metallographic section of a cast plutonium sample

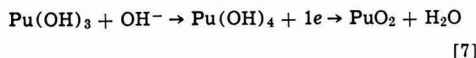


Fig. 8. Metallographic section of a rolled plutonium sample

water vapor on the oxide-covered plutonium metal. Therefore



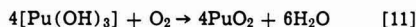
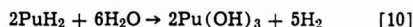
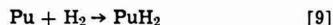
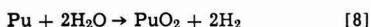
The anodic reaction takes place on the diffusion of  $\text{OH}^-$  anions to the metal/oxide interface and involves the reactions



which are said to be rate controlling. Hydrogen produced by dissociation of adsorbed water was thought to have only a minor effect on the over-all reaction rate. In this mechanism, it is assumed that the water produced at the metal/oxide interface in reaction [7] dissociates so that the reaction sequence [6] and [7] is again repeated. However, it is possible that water could react differently with the metal according to reactions [1]-[3] or that the hydrogen produced by the dissociation of the water could react directly with the metal thus producing some hydride.

Thompson (8) has proposed a compromise between the "hydride" and the "hydroxide" mechanisms. This hypothesis attempts to explain the importance of small amounts of moisture as well as the presence of hydride in the reaction products.

The reaction sequence is



with the rate-controlling step being the hydride-water reaction [10]. In the case of oxidation by water vapor in nitrogen, Eq. [11] would have to be modified to Eq. [7].

Results obtained in this study do not clearly support any of the previously proposed mechanisms. For example, the plutonium-water vapor reaction followed a parabolic rate law indicating a diffusion-controlled reaction. Previous reports, including those of Waber (15) and Thompson (8), indicated the reaction was linear and reaction controlled. The difference between these proposed mechanisms and the diffusion-controlled mechanism proposed from this work may be the temperature employed, but this has not been verified. The diffusion involved in this study was probably the diffusion of  $\text{OH}^-$  ions to the metal/oxide interface as suggested by Waber (15). This is supported by parallel studies of water adsorption on  $\text{PuO}_2$  (16). However, in this case the diffusion was rate controlling and not the  $\text{Pu} + \text{OH}^-$  reaction.

Two different plutonium dioxides appeared to be formed by reaction of the rolled and cast metal with water. Oxide resulting from oxidation of the rolled plutonium was a yellow-green while that from the cast metal was black. Black is the color which is normally observed when plutonium dioxide is formed from a hydroxide intermediate (17) or if plutonium hydride is present. Therefore, on the basis of the product formed, the reaction between the cast electrorefined plutonium and water vapor appears to follow a "hydroxide" type mechanism. Strictly on the basis of color, the reaction between the rolled plutonium and water vapor does not follow the proposed mechanism. However, color can be a function of purity and particle size so one of the mechanisms may still be applicable.

Hydrogen is a product of the plutonium-water reaction, regardless of the mechanism proposed. In these studies hydrogen has been detected in the gas phase following a reaction. Whether or not this hydrogen reacts with the plutonium is the difference between the "hydroxide" and various "hydride" mechanisms. Since hydrogen reacts so readily with plutonium, it is difficult to believe there is no hydride present. However, hydride is difficult to detect and was not found in this study. Additional work of an analytical nature is required to establish conclusively the mechanism for this reaction.

### Summary and Conclusions

The oxidation of both rolled and cast unalloyed plutonium at 90°C was investigated in nitrogen-oxygen mixtures containing 12,000 ppm water vapor and also in dry air. Plutonium was found to oxidize faster in the oxygen-containing mixtures than in pure moist nitrogen. Earlier studies by other workers have shown the oxidation rates in moist air and moist argon or helium to be nearly the same or slightly faster in moist nitrogen at 90°C. It appears from this work that at about 90°C water vapor begins to exert less of an accelerating effect on the oxidation rate and oxygen assumes more of a controlling role. Because of the rapid oxidation in oxygen atmospheres at 90°C, it is apparent that there is no inhibiting effect by oxygen on the water vapor reaction. Metal purity and metallurgical history had no effect on the oxidation rate in dry air but became more important with the addition of water vapor.

The oxygen pressure dependence of this reaction became very strong at some partial pressure less than 15 Torr. The exact pressure at which this occurred was not determined. For this study there was no oxy-

gen pressure dependence observed for partial pressures between 15 and 500 Torr.

The attack by water vapor observed during this study was greatly influenced by the purity of the metal as well as its metallurgical history. Samples of cast electrorefined plutonium containing some microcracks reacted very rapidly while for the impure rolled material the reaction was somewhat slower. In all cases at this temperature, the reaction with water vapor was diffusion controlled and not reaction controlled as previously reported. The diffusing species is believed to be  $\text{OH}^-$  ions formed by the dissociation of water vapor adsorbed on the plutonium dioxide.

#### Acknowledgment

This work was performed under United States Atomic Energy Commission Contract AT(29-1)-1106.

Manuscript submitted Nov. 22, 1971; revised manuscript received Jan. 7, 1972.

Any discussion of this paper will appear in a Discussion Section to be published in the December 1972 JOURNAL.

#### REFERENCES

1. M. A. Thompson in, "Plutonium Handbook", Vol. 1, p. 155, O. J. Wick, Editor, Gordon and Breach, Science Publishers, New York (1967).
2. J. B. Raynor and J. F. Sackman, *J. Nucl. Mater.*, **23**, 302 (1967).
3. J. G. Schnizlein and D. F. Fischer, *This Journal*, **114**, 23 (1967).
4. J. T. Waber in, "Plutonium Handbook", Vol. 1, p. 153, O. J. Wick, Editor, Gordon and Breach, Science Publishers, New York (1967).
5. J. B. Raynor and J. F. Sackman in, "Plutonium 1965," p. 575, A. E. Kay and M. B. Waldron, Editors, Chapman & Hall, London (1967).
6. L. E. Musgrave, "The Effect of Water Vapor, Reduced Oxygen Concentrations, and Solvent Vapors on Plutonium Ignition," USAEC Report RFP-1376, Rocky Flats Division, Dow Chemical U.S.A. (1970).
7. A. Tanon and H. Bordes-Pages in, "Plutonium 1965," p. 603, A. E. Kay and M. B. Waldron, Editors, Chapman & Hall, London (1967).
8. M. A. Thompson in, "Plutonium 1965," p. 592, A. E. Kay and M. B. Waldron, Editors, Chapman & Hall, London (1967).
9. R. W. Loser, Unpublished data, Rocky Flats Division, Dow Chemical U.S.A. (1971).
10. P. Kofstad, "High Temperature Oxidation of Metals," p. 233, John Wiley & Sons, Inc., New York (1966).
11. J. T. Waber in, "Plutonium Handbook," Vol. 1, p. 167, O. J. Wick, Editor, Gordon and Breach, Science Publishers, New York (1967).
12. H. R. Gardner, *Trans. AIME*, **224**, 358 (1962).
13. J. L. Stakebake, *J. Nucl. Mater.*, **38**, 247 (1971).
14. J. E. Draley, *This Journal*, **104**, 329 (1957).
15. J. T. Waber, Second U. N. Geneva Conference on the Peaceful Uses of Atomic Energy, p. 204, (1958).
16. J. L. Stakebake and L. M. Steward, *J. Colloid Interface Sci.*, In press.
17. J. L. Drummond and G. A. Welch, *J. Chem. Soc.*, **1957**, 4781.

## TiO<sub>2</sub> Film Properties as a Function of Processing Temperature

E. T. Fitzgibbons,\*<sup>1</sup> K. J. Sladek,\* and W. H. Hartwig

Departments of Electrical and Chemical Engineering, The University of Texas at Austin, Austin, Texas 78712

#### ABSTRACT

Thin film TiO<sub>2</sub> was produced at 150°C by chemical vapor deposition using hydrolysis of tetraisopropyl titanate. Films were amorphous as grown, but annealing in air caused crystallization, with anatase formed beginning at 350°C and rutile at 700°C. Density and index of refraction increased substantially with increasing anneal temperature, while etch susceptibility in HF and H<sub>2</sub>SO<sub>4</sub> decreased. Comparison with literature data showed two groups of processes. One group yields films having properties that gradually approach those of rutile with increasing process temperature. The other group gives rutile directly at moderate temperatures. Deposition of amorphous film followed by etching and annealing is suggested as a means for pattern definition.

Thin film TiO<sub>2</sub> has been produced by anodization and thermal oxidation of Ti, evaporation of TiO<sub>2</sub>, reactive sputtering of Ti, a variety of chemical vapor deposition (CVD) processes, and even by liquid deposition. The electrical, chemical, and physical properties of TiO<sub>2</sub> films exhibit considerable diversity, which arises from differences in stoichiometry and structure among films formed by different means. The present research began with the discovery of a unique low-temperature process for producing films of readily etchable amorphous TiO<sub>2</sub>. Annealing procedures were found to convert these films to the anatase and rutile forms of the material. Film properties could then be determined for a range of well-controlled structures. One purpose of this investigation was to provide a comprehensive set of structure-property data which might serve to explain discrepancies in reported values of density, refractive index, and etch susceptibility. Another purpose was to develop a means for produc-

ing thin film TiO<sub>2</sub> for applications requiring pattern definition.

Titanium dioxide exists in two tetragonal structures, anatase and rutile, plus orthorhombic brookite. Rutile is the thermodynamically stable form at all temperatures investigated so far, but anatase and brookite retain their structures until heated to fairly high temperatures, at which they transform irreversibly to rutile. Reported temperatures for significant rates of conversion to rutile are 800°-1100°C for anatase and 700°-1300°C for brookite (1, 2). Theoretical densities of anatase and rutile are calculated to be 3.94 and 4.27 g/cm<sup>3</sup>, respectively, using recent values of the unit cell dimensions (1). These agree reasonably well with measured values of 3.90 and 4.23 g/cm<sup>3</sup> (2). Average index of refraction (*n*) values at 0.55 μm are 2.57 for natural crystals of anatase and 2.74 for synthetic crystals of rutile (1).

While properties of bulk anatase and rutile are well established, little agreement has been reached regarding the properties of thin film TiO<sub>2</sub>. One of the most thorough studies is due to Hass (3), who produced films both by thermal oxidation of Ti and by a CVD

\* Electrochemical Society Active Member.

<sup>1</sup> Present address: North American Rockwell Microelectronics Company, Anaheim, California 92803.

Key words: thin films, chemical vapor deposition, titanium dioxide.



process. Evaporated Ti films were oxidized above 200°C and the resulting oxide was shown to be rutile by electron diffraction. The index of refraction of these films was 98-99% of that of bulk, single-crystal rutile for the whole range from 0.4 to 2.0  $\mu\text{m}$ . In contrast, hydrolysis of  $\text{TiCl}_4$  produced amorphous films below 280°, and anatase films above 300°C, with  $n$  values near 2.3.

Films of  $\text{TiO}_2$  have also been produced by anodization (4, 5), reactive sputtering (6), vacuum evaporation (7), and by drying substrates which had been dipped into a titanate solution. Drying at 180°-900°C gave films with  $n$  values of 1.95-2.45 (8).

CVD processes include the  $\text{TiCl}_4$ - $\text{H}_2\text{O}$  reaction near 300°C (3), at 150°C (9), and at 800°C (10). Pyrolysis of tetraisopropyl titanate (TPT) at 300°-700°C gave amorphous and anatase films exhibiting a range in density, refractive index, and etch susceptibility (11). Reaction of  $\text{TiCl}_4$  with  $\text{O}_2$  gave epitaxial rutile on some substrates above 700°C and polycrystalline rutile at lower temperatures (12). In the present work the TPT- $\text{H}_2\text{O}$  reaction was used, as described next.

### Deposition Phenomena

The CVD apparatus is illustrated in Fig. 1. The two liquid feeds are evaporated from heated flasks into metered carrier gas streams. The feed streams then issue from parallel nozzles at the ends of the delivery lines, intermingling with each other and with the room air, and are directed onto the substrate, which is heated from beneath. Film growth is controlled manually by moving the substrate around under the nozzles or by moving the nozzles. By observing the sharp interference colors, the operator can manually control the thickness uniformity of the film to within 100-200Å over a 1.25-in. diameter substrate wafer.

The best temperature range for the TPT evaporator is 75°-85°C. The water evaporator temperature is not critical and films can even be grown without using the  $\text{CO}_2$  carrier and water source; in that case, the water vapor in the ambient air is evidently sufficient to maintain the reaction. The growth dynamics appear to be the same with and without the water vapor stream and the structural, optical, and chemical properties are also the same in both cases. The only differences were observed in the reproducibility of electrical properties, and the water vapor source was used to stabilize these.

Under typical conditions, the helium flow rate was 1 l/min, the  $\text{CO}_2$  flow rate was  $\frac{1}{4}$  l/min, the TPT and water evaporators were at 75° and 90°C, respectively, and the substrate heater was at 150°C. With these parameters, a 1.25-in. substrate could be covered with a 2000Å film in 10 min.

These conditions were chosen after making a number of observations about the film quality obtained under various deposition conditions. When the TPT evaporator was too hot (90°-100°C) a milky film having diffuse interference colors resulted. Microscopic examination revealed that the film lacked coherence,

but rather was made up of tiny stacked spheres. The film had an odor of alcohol or TPT and was soft enough to be smeared with a cloth. Evidently, the TPT condensed after leaving the nozzle and the resulting film was made up of small droplets of TPT which had reacted at their outer surfaces only. Similar results were obtained with the TPT evaporator at 75°C when the He carrier flow exceeded 2 l/min, when the nozzle was closer than 1 in. from the substrate, or when the substrate temperature was below 100°C. Excessive  $\text{CO}_2$  carrier flows ( $> \frac{1}{2}$  l/min) caused a white powdery deposit, evidently due to premature hydrolysis of TPT, giving a powder product which rained down onto the substrate. The same effect occurred when the nozzle was held more than 3 in. from the substrate. In summary, the conditions chosen above were selected to avoid both incomplete and premature reaction which led to formation of films lacking coherence. Under the chosen conditions, the films were smooth and relatively hole free. No detail could be observed in the scanning electron microscopy at 20,000X, except for an occasional pinhole.

When film thicknesses of 4000-5000Å were reached during a normal deposition, cracks would appear and propagate over the film, reducing it to a field of small triangular pieces, each separated from the substrate with its points bending upward. This was observed with all the substrates described below at approximately the same film thickness. Several experiments with duplex films were performed. When a film was grown to several thousand angstroms and then later a new film was grown atop the previous one, fracture occurred when the sum of the two thicknesses fell into the 4000-5000Å range. However, when a film was grown and annealed above 350°C (to be described later) and then a new film was grown on the annealed one, fracture occurred when the second film reached 4000-5000Å. This behavior indicates that the film is deposited with an intrinsic tensile stress. Fracture may be associated with a failure of the film-substrate adhesive bond due to increased shear stress as the film thickens.

Films could be grown on any smooth object that could be heated. In the present work, different substrates were used for different experiments. Fused quartz was used for optical transmission measurements. Fused quartz covered with evaporated Pt and also polished Si were used as substrates in determining refractive index and thickness relationships by ellipsometry and interferometry. Soft glass microscope slides, as well as some of the other materials, were used in x-ray analysis. Before deposition, the fused quartz and the soft glass substrates were cleaned thoroughly in low residue detergent, were rinsed in deionized water, and were heated in air at 1000° and 350°C, respectively, to drive off surface contaminants. The Pt/quartz substrates were annealed in air at 1000°C to stabilize them, and no further cleaning was performed. The Si wafers had been commercially prepared using mechanical and electrochemical polishing and were used as supplied.

### Annealing and Crystallization

Films produced by the CVD method described above underwent dramatic changes in physical and chemical properties during annealing. The changes in crystal structure are described here.

Crystalline phases were identified using an x-ray diffractometer with copper  $K_{\alpha 1}$  radiation. Four types of samples were used. Powder samples were obtained by allowing the standard deposition process to continue for several hours until a thick white powdery deposit had built up; this was then scraped off and divided into samples for testing. The other three types of samples consisted of 3000-4000Å films grown on fused quartz, soft glass, and polished Si.

The powder in the as-grown condition showed no sign of crystallinity and was evidently amorphous. No

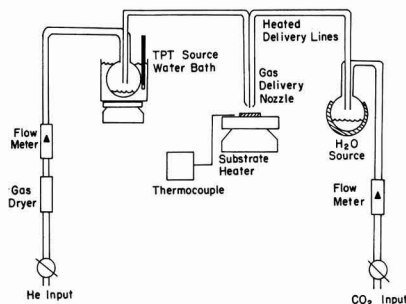


Fig. 1. Chemical vapor deposition system



Table I. Crystalline phase and anneal temperature for TiO<sub>2</sub> on several substrates

Anneal temperature, °C	Powder sample	Substrate <sup>b</sup>		
		Soft glass	Polished Si	Fused quartz
150 (as grown)	Amorphous	Amorphous	Amorphous	Amorphous
350	Amorphous + anatase	Amorphous + anatase	Amorphous + anatase	Amorphous + anatase
700	Rutile + anatase	Rutile + anatase	Rutile + anatase	Anatase
1000	Rutile	—	Rutile	Anatase

<sup>a</sup> All anneals carried out in air.

<sup>b</sup> Crystalline phases identified in all films showed no orientation.

crystallization occurred during aging at room temperature in air for one week. Annealing the powder for 10 min at 350°C resulted in the appearance of the two strongest diffraction peaks of the anatase form of TiO<sub>2</sub>. A sample annealed at 700°C for 2 hr showed the five strongest anatase peaks and the three strongest rutile peaks. A 20-hr anneal at 1000°C completely converted the powder to rutile; many rutile peaks were observed, and no anatase peaks were detectable.

Table I summarizes the data for all four types of samples. In every case the as-grown material is amorphous, and material annealed at 350°C shows some anatase. However, the weakness of the anatase patterns suggested that only partial crystallization occurred at 350°C. This temperature can be regarded roughly, as an amorphous-anatase transition temperature. Additional anneals at 300°–400°C indicate that the transition is not sharp, but rather occurs over a range of about 50°C in which the extent of crystallization gradually progresses. The temperature, 700°C, appears similarly to be characteristic of the anatase-rutile transition. This transition appears to be less sharp and progresses over a range of about 300°C. An important exception is the films on fused quartz which persist in the anatase form, even after annealing at 1000°C. Somehow, the quartz-TiO<sub>2</sub> interface stabilizes the anatase structure, perhaps by preventing nucleation of rutile.

The present data are in accord with some of the literature data described earlier. The anatase-rutile transition occurs in bulk samples at 800°–1100°C (1, 2). In films produced by CVD or liquid dipping, a change from amorphous to anatase structures was found at 280°–300°C (3), and at 250°–350° (8). An anatase-rutile transition was observed at 800°C (3), and several investigators produced rutile directly at 800°C or above (10, 13). In contrast, rutile films were produced as low as 400°C from Ti oxidation (3) and from the TiCl<sub>4</sub>-O<sub>2</sub> reaction (12).

### Thickness and Index of Refraction

Changes in interference colors occurred as a result of annealing, and these indicated a change in thickness, *d*, and/or index of refraction, *n*. If a standard color chart for SiO<sub>2</sub> was used, the changes indicated that annealing a 150°C film at 1000°C caused an increase in *d*. However, measurements using an ellipsometer indicated a substantial decrease in *d*, accompanied by an increase in *n*, indicating that a single color chart, based on fixed *n*, would be misleading. To obtain additional independent values of *d* and *n*, a multiple beam interferometric technique was used. Both the ellipsometer and the interferometer used the 5460 Å green line of Hg.

Coated and uncoated portions of a step were used to find both *d* and *nd* with the interference method (14). The ellipsometer yields separate values of *d* and *n* (15). A cross check was provided by a color chart, which gives *nd* (14).

Results obtained before and after annealing at 1000°C are shown in Table II. The several methods give good agreement, and it is clear that annealing

Table II. Change in thickness and index of refraction due to annealing at 1000°C

Sample condition	Thickness, Å (method) <sup>1</sup>	Index of refraction (method) <sup>1</sup>
As grown, 150°	3820(I), 3870(E)	1.98(I), 2.10(E)
Annealed, 1000°	2510(I)	2.49(I)
As grown, 150°	2400(E)	2.00(E), 1.95(C)
Annealed, 1000°	1580(E)	2.40(E), 2.47(C)
As grown, 150°	1900(E)	2.10(E), 2.06(C)
Annealed, 1000°	1220(E)	2.60(E), 2.50(C)

<sup>1</sup> I = interferometer; E = ellipsometer, C = color chart plus ellipsometer-determined thickness.

causes a substantial decrease in *d* and increase in *n*. To complete these measurements, a final series of data was obtained as a function of anneal temperature. A film was deposited on Pt/quartz and data were obtained by ellipsometry, using averages of two to four measurements. Figure 2 is a plot of resulting values of thickness and index of refraction.

The thickness shrinkage of 35% is quite remarkable in magnitude. Since the film is constrained to a fixed area, any density changes are evidently exhibited only in one dimension. One might suspect that such a violent dimensional change would set up stresses which might rupture the film. However, examination of a 1000°C annealed film in the scanning electron microscope at 20,000X showed no cracks, tears, or eruptions.

It was suspected that the shrinkage might be accompanied by a mass loss, as would be expected if the as-grown material were a hydroxide or hydrate. A hydroxide, Ti(OH)<sub>4</sub>, would lose 31% of its initial weight if complete dehydration occurred. Several experiments were carried out in an effort to detect a weight change on annealing. In the most sensitive experiment, a sample was weighed on a vacuum microbalance and annealed *in situ*. No weight change could be detected within the experimental uncertainty of ± 7% of the initial film weight. Although the sensitivity of this experiment was rather low, the result does rule out mass reduction as a primary cause of the volume shrinkage.

It is possible that the films are microporous and that shrinkage occurs by sintering. Swaroop (16) and Pliskin and Lehman (17) attributed densification of SiO<sub>2</sub> films to sintering. Sladek and Herron (18) investigated TiO<sub>2</sub> film growth by the TPT-H<sub>2</sub>O reaction at 25°C, and suggested that voids are incorporated when isopropyl groups are removed from the growing film during surface reaction.

The difference between a microporous material and a "homogeneous" one of abnormally low density is only in the size of the void spaces. Our observations using the scanning electron microscope detected no pores. Qualitatively, the optical transparency and sharp interference colors of our films indicate negligible scattering by void spaces. However, both of these

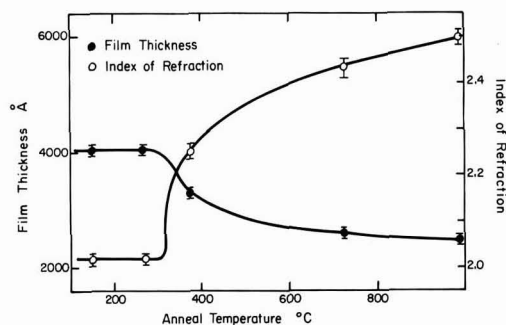


Fig. 2. Thickness and index of refraction as a function of anneal temperature. TiO<sub>2</sub> on Pt/quartz.

Table III. Chemical susceptibility to several etches

Anneal temperature, °C	0.5% HF	48% HF	Etch rate and behavior	100% H <sub>2</sub> SO <sub>4</sub>	85% H <sub>3</sub> PO <sub>4</sub>
150	50-75 Å/sec	Very rapid		Slow at 25°C	Leaves residue
350	On Pt: very slow On Si: undercutting	Slow and uneven		25-40 Å/sec at 50°C About 15 Å/sec at 50°-100°C	
700	No etching	On Pt: slow On Si: undercutting		Very slow	
1000	No etching	On Pt: slow On Si: undercutting		About 1000 Å/hr at 120°C	Very slow at 120°C

observations would be insensitive to voids of size below about 200Å. We attribute the abnormally low density of the present amorphous films to voids of size somewhere in the range between atomic dimensions and about 200Å.

### Susceptibility to Chemical Etch

Etch susceptibility is a prerequisite for electronic applications of TiO<sub>2</sub>. Some past work indicates that amorphous TiO<sub>2</sub> is readily etched while high-temperature and hence crystalline forms are quite impervious to chemical attack. Barksdale (19) observed in 1949 that, while bulk TiO<sub>2</sub> is known to be slightly soluble in H<sub>2</sub>SO<sub>4</sub>, HF, and a few strong alkalis, material annealed near 1000°C is almost completely inert chemically.

Etchability of TiO<sub>2</sub> as a function of anneal temperature was determined for films grown on Si and on Pt substrates. Results are summarized in Table III. Again there is a wide, controllable gradation in properties, with the low-temperature form showing high chemical susceptibility while the 1000°C material is nearly inert. Films on Si behaved the same as those on Pt except for the 48% HF case. This etch lifted the TiO<sub>2</sub> off the surface of Si, evidently by dissolving a thin interfacial layer of SiO<sub>2</sub> and undercutting the TiO<sub>2</sub>.

These results are in accord with data of Yokozawa *et al.* (11), who reported that their amorphous TiO<sub>2</sub> films etched in dilute HF at 4-60 Å/sec, while anatase films etched only slowly in concentrated HF. Feuer-sanger (9) reported that his films were easily etched in 10% HF; this suggests that they were amorphous, as would be expected for a 150°C process. His high index of refraction (discussed later) is then the only property that does not agree with the present results. Harbison and Taylor (10) reported an etch rate of 700 Å/min in 48% HF for material grown at 800°C. This is much higher than would be expected from our results.

### Optical Absorption

An optical transmission spectrum of a 350°C annealed film is shown in Fig. 3. This was obtained by measuring the difference between the transmission of the film on fused quartz and the transmission of the fused quartz alone. We attribute the maxima and min-

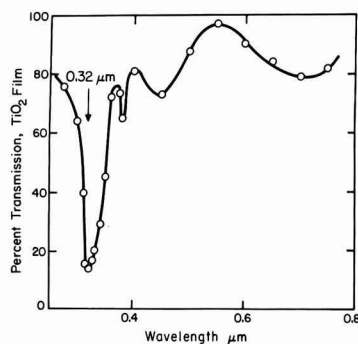


Fig. 3. Optical transmission spectrum, 2600Å film of TiO<sub>2</sub> annealed at 350°C.

ima above 0.35 μm to interference due to multiple internal reflection, and the strong absorption peak at 0.32 μm (3.9 eV) to an electronic transition. Transmission in an amorphous TiO<sub>2</sub> film was also measured and similar results were obtained, except that the strong absorption peak was much broader, although still centered at 0.32 μm. In agreement with these results, Maserjian (20) found an absorption peak at 0.32 μm with a rutile film. In contrast, however, single-crystal rutile exhibits an absorption edge (21) at 0.41 μm (3.0 eV). The cause of the discrepancy between bulk single-crystal and thin film TiO<sub>2</sub> is not known. However, in both this work and that of Maserjian (20) the 0.32 μm peak has been established.

### Discussion

Present data on density and index of refraction are compared with literature values in Fig. 4. Since absolute values of density were not obtained in this work, it was necessary to choose a value for one condition, and 2.5 g/cm<sup>3</sup> for the amorphous films was used, based on the results of Yokozawa *et al.* (11).

Results of two of the CVD studies (11, 13) and the liquid deposition (8) show good agreement with present data in both properties plotted. Results of Hass (3) on films formed by TiCl<sub>4</sub> hydrolysis and by oxidation of "TiO" (formed by evaporating Ti with O<sub>2</sub> present) show an increase in *n* with temperature similar to that observed here, although with somewhat higher values of *n*.

In contrast, Hass (3) obtained nearly the bulk rutile value of *n* with oxidized Ti, and Ghoshtagore and Noreika (12) found an even higher value with films formed from TiCl<sub>4</sub> + O<sub>2</sub> in the whole temperature range studied. (We have applied a small correction to their reported value of *n<sub>D</sub>* to obtain a value applicable at 0.55 μm.) The fact that their *n* exceeds the random-orientation average for bulk rutile could have been due to preferred orientation of their films.

In summary, one group of processes produces films which show a characteristic variation in physical and

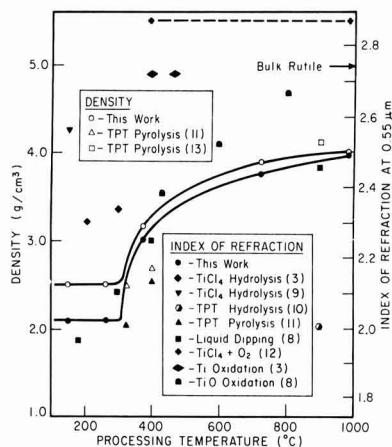


Fig. 4. Density and refractive index vs. processing temperature: a comparison with other work.

chemical properties with maximum processing temperature, whether this temperature is reached during deposition or during postdeposition anneal. These variations arise from densification and crystallization and ultimately yield material with properties approaching those of the equilibrium (rutile) bulk state. However, it is also possible to bypass these intermediate stages and obtain rutile directly at moderate temperatures.

We have found that, of the several forms produced, rutile or anatase-rutile mixtures have superior dielectric properties. The relative dielectric constant/dissipation factor at 1 kHz was about 100/0.04 for material annealed at 700°-1000°C. The sign of the surface charge of TiO<sub>2</sub> on Si was negative, and positive, negative and zero, values could be obtained by growing duplex TiO<sub>2</sub>/SiO<sub>2</sub> films. (Details of these electrical studies will be reported later.) These properties suggest a number of applications for rutile in integrated circuit technology.

Although it is possible to produce rutile films directly, they are almost impossible to etch (Table III). In contrast, the deposition-annealing process used here could lend itself readily to the various etch steps needed for integrated circuit production. Standard photomasking techniques could be used to define a desired pattern in the as-grown film, and a later anneal would convert the material to its stable form.

The fact that the TiO<sub>2</sub> itself changes chemical susceptibility suggests that patterns might be defined without photoresists, if a means were found for selective conversion in desired areas. This idea has led to some further work (to be reported later) in which an electron or photon beam is used to define positive patterns in amorphous TiO<sub>2</sub>.

In conclusion, it is possible to produce rutile films either directly or via a series of stages progressing in density, refractive index, and etch susceptibility. The present method of low-temperature deposition followed by annealing is promising for applications requiring pattern definition.

#### Acknowledgment

This work was supported in part by the National Aeronautics and Space Administration and in part by the Joint Services Electronics Program under Research Grant AFOSR-69-1792.

Manuscript submitted Aug. 20, 1971; revised manuscript received Jan. 20, 1972. This was Paper 10 and part of Paper 11 presented at the Washington, D.C., Meeting of the Society, May 9-13, 1971.

Any discussion of this paper will appear in a Discussion Section to be published in the December 1972 JOURNAL.

#### REFERENCES

1. "Kirk-Othmer Encyclopedia of Chemical Technology," Second ed.; Vol. 20, pp. 390-395 (1969).
2. G. Skinner, H. L. Johnston, and C. Beckett, "Titanium and Its Compounds," pp. 21-28, H. L. Johnston Enterprises, Columbus, Ohio (1940).
3. G. Hass, *Vacuum*, **2**, 331 (1952).
4. L. Young, "Anodic Oxide Films," Academic Press, New York (1961).
5. O. S. Heavens, Rept. *Progr. Phys.*, **23**, 1 (1960).
6. T. K. Lakshmanan, C. A. Wysocki, and W. J. Slegesky, *IEEE Comp. Parts*, **CP-11**(2), 14 (1964).
7. M. Shiojiri, *J. Phys. Soc. Japan*, **21**, 335 (1966).
8. T. N. Krylova and G. O. Bagdyk'yants, *Opt. Spectry. (USSR) (English Transl.)*, **9**, 339 (1960).
9. A. E. Feuersanger, *Proc. IEEE*, **52**(12), 1463 (1964).
10. D. R. Harbison and H. L. Taylor in "Thin Film Dielectrics," pp. 254-278, F. Vratney, Editor, Electrochem. Soc. (1969); also D. R. Harbison, Ph.D. Dissertation, Univ. of Texas at Austin (January 1969).
11. M. Yokozawa, H. Iwasa, and I. Teramoto, *J. Appl. Phys. (Japan)*, **7**, 96 (1968).
12. R. N. Ghoshtagore and A. J. Noreika, *This Journal*, **117**, 1311 (1970).
13. S. Sakurai and M. Watanabe, *Rev. Elec. Commun. Lab. (Tokyo)*, **11**, 178 (1963), as quoted by Yokozawa et al. (11).
14. R. M. Burger and R. P. Donovan, "Fundamentals of Silicon Integrated Device Technology," Vol. 1, pp. 78-100, Prentice-Hall, Englewood Cliffs, N. J. (1967).
15. R. J. Archer, "Manual on Ellipsometry," Gaertner Scientific Corp., Chicago (1968).
16. B. Swaroop, in "Thin Film Dielectrics," pp. 407-431, F. Vratney, Editor, Electrochem. Soc. (1969).
17. W. A. Pliskin and M. S. Lehman, *This Journal*, **112**, 1013 (1965).
18. K. J. Sladek and H. M. Herron, *I&EC Prod. Res. Dev.*, **11**, 92 (1972).
19. J. Barksdale, "Titanium. Its Occurrence, Chemistry, and Technology," Ronald Press, New York (1949).
20. J. Maserjian, "Conduction Through Thin Titanium Dioxide Films," N66-39934, Oct. 1, 1966.
21. D. C. Cronmeyer, *Phys. Rev.*, **87**, 876 (1952).

# Cathodoluminescence Characteristics of $\text{Mn}^{2+}$ -Activated Willemite ( $\text{Zn}_2\text{SiO}_4$ ) Single Crystals

R. J. R. S. B. Bhalla\*<sup>1</sup> and E. W. White

Materials Research Laboratory, Pennsylvania State University, University Park, Pennsylvania 16802

## ABSTRACT

Cathodoluminescence studies were made of  $\text{Mn}^{2+}$ -activated willemite single crystals using an electron microprobe and a simple interference-type spectrometer attachment. Use of the microprobe allows single-crystal cathodoluminescence measurements to be made on comparatively small ( $<0.01$  mm) crystals. Green cathodoluminescence emission from  $\text{Mn}^{2+}$ -activation was found to be partially polarized. The electric vector of emission was along a direction perpendicular to the  $c$ -axis of the crystals. Examination of the emission spectra in the two perpendicular polarization directions, corresponding to the analyzer direction parallel to the  $c$ -axis, and perpendicular to the  $c$ -axis, showed a difference of about 100 Å in the emission peak positions. Measurements of spectra and integrated intensity of emission were also made as a function of manganese concentration. The intensity of luminescence was maximum for Mn concentration of 2.9 w/o (weight per cent). The peak position of the  $\text{Mn}^{2+}$  band was found to shift from 5160 to 5300 Å as the manganese concentration increased from just a trace to about 12 w/o. The polarized cathodoluminescence emission can be explained on the basis of crystal-field theory and symmetry arguments. These arguments lead to the conclusion that the two  $\text{Zn}^{2+}$  sites in the willemite structure, which are occupied by the  $\text{Mn}^{2+}$  ions, have effective local symmetries of  $C_{3v}$  and  $C_1$ , respectively. The emission peak shift to longer wavelengths, as the manganese concentration is increased, cannot be explained by simple crystal-field theory. A model showing emission from  $\text{Mn}^{2+}$ - $\text{Mn}^{2+}$  pairs dominating at higher concentrations, in comparison to emission from isolated  $\text{Mn}^{2+}$  ions, is proposed to explain this shift of emission peak to longer wavelengths.

Emission spectra from oriented single crystals of impurity activated (or self-activated) phosphors can give very important clues to the site symmetry of the activator. In the past polarized emission from phosphor single crystals has been studied to determine nature and symmetry of the luminescence centers (1, 2). Thus, although the advantages of single-crystal studies were recognized for some time, such studies have been limited to very few well-known phosphors. The main reason for this is the general lack of large enough single crystals. Furthermore, almost no studies of these luminescence characteristics exist for cathode-ray excitation in single crystals. A recent communication (3) has described preliminary results for a cathodoluminescence study of oriented single crystals of  $\text{Mn}^{2+}$ -activated willemite. The main purpose of this paper is to give a detailed account of the polarized cathodoluminescence studies of  $\text{Mn}^{2+}$ -activated single crystals of willemite [ $\text{Zn}_2\text{SiO}_4(\text{Mn})$ ]. In addition, spectra and luminescence intensity, as a function of manganese concentration, are also measured on artificially doped single crystals of willemite.

## Experimental

An applied Research Laboratory Model EMX electron microprobe was used for cathode-ray excitation of the willemite luminescence from sample areas as small as 5  $\mu\text{m}$  diameter. The electron microprobe offers the additional advantage that the luminescence emission is observed from the surface of the sample excited by the electron beam rather than observing in transmission as is generally done in conventional cathodoluminescence apparatus. The electron beam is incident normal to the specimen surface and is coaxial with the light microscope objective. The broad band luminescence spectra were recorded using a simple light spectrometer and photomultiplier readout described by Greer and White (4). A Polaroid analyzing cap was

attached to the eye piece of the probe microscope making it possible to record the luminescence emission spectra in any polarization direction. Use of this arrangement made it possible to study, individually, very small ( $<0.01$  mm) single crystals, and micron scale inhomogeneities in larger grains with a sensitivity which is not possible with conventional cathodoluminescence apparatus.

Samples used in this study were natural willemite crystals from Franklin, New Jersey, and Tsumeb, South-West Africa. Franklin, New Jersey, specimens showed the strong green luminescence characteristic of  $\text{Mn}^{2+}$ -activated orthorhombic willemites and were found to contain 0.1-4.0% manganese in solid solution. Mn was rather uniformly distributed in the individual crystals. Other cationic impurities which have been reported in bulk chemical analyses of willemites are Fe, Mg, and Ca (5). However, probe analysis showed these impurities to be located in micron scale, highly oriented inclusions. No Fe, and only traces of Ca and Mg were detected in the willemite matrix. Absence of Fe in the willemite matrix is significant since it is known to act as a killer of luminescence in most materials. Willemite, which has only fourfold coordinated cationic sites, has a very low tolerance for Fe. In contrast to the Franklin, New Jersey, specimens, the South-West Africa willemite crystals do not luminesce green and have no detectable Mn or Fe impurities.  $\text{Mn}^{2+}$  was introduced in these crystals by solid-state diffusion at 1250°C. Selected samples were then set in Lakeside 70 and prepared as polished thin sections by grinding and polishing. Final sample surfaces were polished successively with 6, 3, 1, and  $\frac{1}{4}$   $\mu\text{m}$  diamond pastes and coated with a thin layer of carbon (200-400 Å) by vacuum evaporation to provide a conductive path for the electrons. This method of preparation yielded grains with many different crystallographic orientations. Grains having the desired orientations for study were selected using a polarizing light microscope and marked for convenient location in the microprobe.

\* Electrochemical Society Active Member.

<sup>1</sup> Present address: Central Research Laboratory, American Cyanamid Company, Stamford, Connecticut 06904.

Key words: cathodoluminescence, single crystal,  $\text{Mn}^{2+}$ -activated willemite, electron microprobe, polarized emission.

### Experimental Results

**Polarized cathodoluminescence.**—Willemite belongs to the rhombohedral crystal class and as such has two principle axes (*a* and *c*). Crystals with orientations such that the *c*-axis was perpendicular to the surface (*a* in the plane) did not show any polarization of the green  $\text{Mn}^{2+}$  emission. However, the crystals with orientations such that the surface contained the *c*-axis, showed partial polarization of  $\text{Mn}^{2+}$  emission. The degree of polarization, *p*, given by  $p = (I' - I'') / (I' + I'')$ , where *I'* and *I''* are maximum and minimum intensities as the analyzer is rotated around its axis, was found to be 0.25. The electric vector of the emitted radiation was along a direction perpendicular to the *c*-axis.

Emission spectra of  $\text{Mn}^{2+}$ -activated willemites were comparable to the commercially available willemite powders and consisted of a single broad band with peak position around 5250 Å (for 1% Mn). This peak shifted toward slightly longer wavelengths as the concentration of Mn increased. The peak position as well as the degree of polarization were not found to be current density dependent. Examination of the emission spectra in the two perpendicular polarization directions corresponding to the analyzer directions parallel and perpendicular to the *c*-axis showed a difference of about 100 Å in the peak positions. This is illustrated in Fig. 1. The peak intensities were matched by lowering the electron beam current while recording the spectrum in the maximum transmission direction. The more intense spectrum, obtained with the electric vector perpendicular to the *c*-axis, yielded the longer wavelength peak.

**Effect of  $\text{Mn}^{2+}$  concentration on cathodoluminescence.**—Measurement of the variation in the green emission spectral characteristics as a function of Mn concentration were made on South-West Africa willemite crystals into which  $\text{Mn}^{2+}$  was introduced by solid-state diffusion at 1250°C. The diffusion was carried out on small transparent prismatic crystals. Selected crystals were coated with very finely powdered  $\text{MnCO}_3$  and heated to 1250°C for 12 hr in a platinum crucible. Crystals treated in this way were then mounted for probe analysis as usual. Cross sections through such crystals gave a concentration gradient of Mn. The luminescence intensity and the emission spectra along with Mn, Zn, and Si concentrations were recorded at many points along the Mn gradient. These measurements established that the  $\text{Mn}^{2+}$  is introduced in the lattice at the expense of  $\text{Zn}^{2+}$ . Figure 2 shows a plot of integrated luminescence intensity as a function of Mn concentration. This measurement was made at 20 keV and sample current of  $2 \times 10^{-8}$  A. The spot size was about 2 μm in diameter. The intensity of luminescence is maximum for a Mn concentration of 2.9 w/o (weight per cent). This value is higher than the optimum of 1% reported

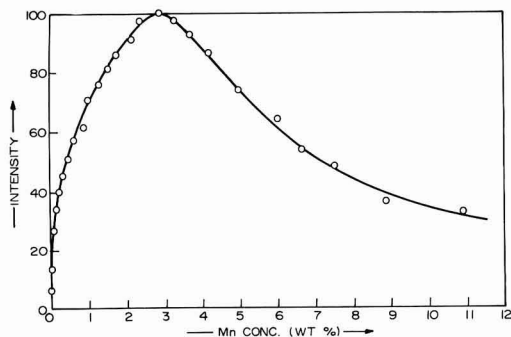


Fig. 2. Plot of integrated intensity vs. Mn concentration for a South-West Africa willemite crystal into which Mn was diffused by solid-state reaction with  $\text{MnCO}_3$  at 1250°C. Measurements were made at 20 keV and a sample current of  $2 \times 10^{-8}$  A. The spot size was about 2 μm diameter. No correction was made for the possible change in the photomultiplier response as the emission peak shifts to slightly longer wavelengths for higher Mn concentrations.

for powder phosphors (6). It may be pointed out that the optimum concentration is dependent on the electron beam energy which is not specified in Ref. (6). It was found that, as the Mn concentration increases, the luminescence peak position shifts toward longer wavelengths. As the concentration of Mn increases from just a trace to about 12% the peak position shifts from 5160 and 5300 Å. This observation compares well with similar results reported by Leverenz (6) on powder phosphors.

### Discussion of Results

For an explanation of the polarization of  $\text{Zn}_2\text{SiO}_4(\text{Mn}^{2+})$  luminescence, and the spectra in the two polarization directions, it is necessary to consider only the local symmetry of the activator site. The position of the  $\text{Mn}^{2+}$  energy levels involved in this luminescence emission, with respect to the position of valence and conduction bands of willemite, is not known. However, as is usual with  $\text{Mn}^{2+}$ -activated phosphors, it is fairly certain that the transition responsible for green emission of  $\text{Mn}^{2+}$ -activated willemites is localized within the 3d shell (7, 8). Although excitation by cathode-rays may be substantially through the conduction band, the final transition giving rise to the luminescence emission takes place within the  $\text{Mn}^{2+}$  activator without any involvement of valence or conduction bands.

$\text{Mn}^{2+}$  replaces  $\text{Zn}^{2+}$  in the crystal structure of willemite and  $\text{Zn}^{2+}$  is fourfold coordinated forming approximately a tetrahedral arrangement (9). Detailed refinement of the willemite structure has not been reported, thus the exact coordinates and distortions of the tetrahedral sites are not known. If there were no distortions in the tetrahedral  $\text{Zn}^{2+}$  sites then the symmetry of the site occupied by the activator  $\text{Mn}^{2+}$  would be  $T_d$ . The ground state of  $\text{Mn}^{2+}$ , which has  $3d^5$  configuration, is  $^6S$  with symmetry  $^6A_1$ . This state is changed very little in energy under the influence of a crystal field. The first excited term  $^4G$  in the free ion gets split up into branches  $^4A_1$ ,  $^4E$ ,  $^4T_2$ , and  $^4T_1$  in a tetrahedral field, with  $^4T_1$  level having the lowest energy. The transition responsible for  $\text{Mn}^{2+}$  emission is believed to be the one from  $^4T_1 \rightarrow ^6A_1$  (7). Group theoretical calculations show that if the symmetry of the emitting  $\text{Mn}^{2+}$  ion were perfectly tetrahedral there would be no polarization of the emitted radiation as the transitions in *x*, *y*, and *z* directions are equally allowed. In the crystal structure of willemite the Zn atoms, thus also the replacing Mn atoms, are reported at general positions and have a space group symmetry of  $C_1$  (9). Under such symmetry conditions the emitting  $^4T_1$  level would split up into three levels and again, according to group theory, transitions from these levels

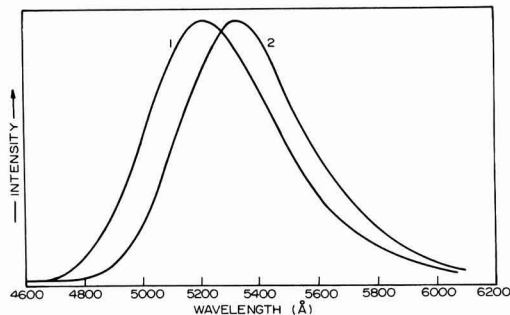


Fig. 1. Polarized cathodoluminescence spectra of  $\text{Mn}^{2+}$  in willemite. Curve 1 corresponds to the analyzer direction (electric vector) along the *c*-axis and curve 2 corresponds to the analyzer direction perpendicular to the *c*-axis. The peak intensities of the two curves are normalized to facilitate comparison of the spectra.



Table I. Estimated Zn-O bond lengths of the distorted tetrahedra around Zn(1) and Zn(2) positions

Bond type	Bond length (Å)
Zn(1)-O <sub>1</sub>	1.93
Zn(1)-O <sub>2</sub>	1.75
Zn(1)-O <sub>3</sub>	1.88
Zn(1)-O <sub>4</sub>	2.05
Zn(2)-O <sub>1</sub>	1.82
Zn(2)-O <sub>2</sub>	1.92
Zn(2)-O <sub>3</sub>	1.94
Zn(2)-O <sub>4</sub>	1.96

to the ground level are equally allowed in the x, y, and z directions giving no polarization. The fact that the emitted radiation is polarized leads to the conclusion (on the basis of crystal field theory arguments) that the emitting center has a local symmetry which is lower than  $T_d$  but higher than the space group symmetry  $C_1$ .

Any lowering of perfect  $T_d$  symmetry of the center would result in splitting of the triply degenerate  ${}^4T_1$  into two or three separate levels depending on the lowered symmetry of the center. Polarization properties under the reduced symmetry conditions can be understood easily on the basis of group theoretical arguments (10), if the local symmetry of the center is known. An attempt to find out the local symmetries of  $Mn^{2+}$  ions in the willemite structure was made by calculating bond lengths and the following explanation is attempted on that basis.

The willemite structure has two different distorted tetrahedral  $Zn^{2+}$  sites [herein called Zn(1) and Zn(2) sites] where  $Mn^{2+}$  can go (9, 10). Approximate distortions in these sites were determined by using the atomic coordinates given by Bragg and Zachariasen (9). Calculations of bond lengths for the two sites are tabulated in Table I. It can be seen that the Zn(1) sites are highly distorted and do not seem to have any symmetry. Thus, taking  $C_1$  as symmetry of this site,  $Mn^{2+}$  replacing  $Zn^{2+}$  on such sites would show no polarization. However, the Zn(2) sites have three bonds which are approximately equal, with an average bond length of 1.94 Å. The fourth bond has a bond length 1.82 Å which is appreciably shorter than the rest. It is very likely that this site has an effective pseudosymmetry of  $C_{3v}$ , with the threefold axis along the shorter bond.  $Mn^{2+}$  replacing  $Zn^{2+}$  on this site would have the emitting triply degenerate  ${}^4T_1$  level split into a doubly degenerate level,  ${}^4E$ , and a nondegenerate  ${}^4A_2$  level. Strictly group theoretical arguments show that the transition  ${}^4A_2 \rightarrow {}^6A_1$  is forbidden and the transition  ${}^4E \rightarrow {}^6A_1$  is allowed in (x, y) direction, i.e., a direction perpendicular to the shorter bond length. Since this direction makes smaller angles ( $\sim 35^\circ$ ) with the basal plane, the electric vector in the basal plane would be of greater magnitude than the component along the c-axis. This explains the observed partial polarization of emission along a direction perpendicular to the c-axis. The energy level diagrams for the emission of  $Mn^{2+}$  at the two  $Zn^{2+}$  sites are shown in Fig. 3. At Zn(1) sites ( $C_1$  symmetry, Fig. 3b) the  ${}^4T_1$  level splits into three  ${}^4A$  levels and these are equally allowed in x, y, and z directions, thus, contributions along the perpendicular to the c-axis are equal. The splitting is probably too small to show up in the broad band spectra. Figure 3c shows the splitting of  ${}^4T_1$  level at Zn(2) sites ( $C_{3v}$  symmetry). Level  ${}^4E$  is placed higher than  ${}^4A_2$  in the energy level diagram since the  ${}^4A_2$  level is connected with the shorter bond, thus, a greater crystal field. The small shift of peak to shorter wavelengths, for the spectra along the c-axis, can be explained if the peak of  $Mn^{2+}$  band for Zn(1) is at a comparatively shorter wavelength than the peak due to  $Mn^{2+}$  at Zn(2) position.

The above model explains the observed polarization satisfactorily (observed polarization,  $\phi = 0.25$ , in comparison to the calculated value of 0.21). However, the symmetries of the two Zn sites can be predicted with

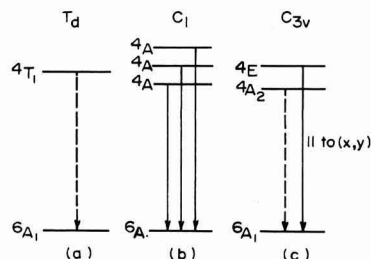


Fig. 3. Splitting of triply degenerate  ${}^4T_1$  (G) level of  $Mn^{2+}$  ion under the influence of lowered symmetries. All the transitions are forbidden by spin symmetries, and for  $T_d$  symmetry the transition  ${}^4T_1 \rightarrow {}^6A_1$  is also forbidden by orbital symmetry. Under  $C_1$  symmetry all transitions are allowed but under  $C_{3v}$  symmetry only the transition  ${}^4E \rightarrow {}^6A_1$  is allowed in (x, y) directions by the orbital symmetries.

more confidence only when precise atomic coordinates for willemite structure become available. All other theoretically possible lower symmetries, which can be formulated for Zn(2) sites, do not explain the observed polarization satisfactorily.

Recently Palumbo and Brown (12) have made absorption measurements on  $Zn_2SiO_4:Mn$  powders and have seen complete splitting of the  ${}^4T_1$  level. They did not study polarized absorption from single crystals and assignment of symmetries is not possible on the basis of their data. However, these measurements clearly show the symmetries (of one or both sites) lower than  $T_d$ . Another study of interest is that of Perkins and Sienko (11). They studied ESR spectra from  $Mn^{2+}$ -doped  $Zn_2SiO_4$  single crystals. Their data showed the location of  $Mn^{2+}$  at two crystallographically nonequivalent zinc positions in the willemite structure. They did not elaborate on the distortions of these sites but discounted any possibility of  $Mn^{2+}$  at six coordinated sites, which would produce an associated defect also.

It may be pointed out here that the selection rules given in Fig. 3 are for electric dipole type of interactions and are allowed (or forbidden) by the symmetry of purely electronic wave functions. These rules would be somewhat relaxed by vibronic coupling, however, the intensity contributions due to vibronic coupling are usually an order of magnitude smaller than those due to purely electronic transitions.

Simple crystal-field explanation of the observed peak shift toward longer wavelengths, as the concentration of  $Mn^{2+}$  in the lattice is increased, is not possible. Increased concentration of  $Mn^{2+}$  of ionic radius 0.80 Å, which replaces  $Zn^{2+}$  of ionic radius 0.74 Å, causes the lattice to expand slightly (13). Thus on the basis of simple crystal field theory it would be expected that this would result in emission peak shifts toward shorter wavelengths since the field strength at the activator has been reduced (14). However, at higher concentrations it is no longer justified to consider emission from isolated  $Mn^{2+}$  ions only. With an increase in concentration, the probability that two  $Mn^{2+}$  ions would occupy immediate neighboring positions increases rapidly and the emission from these ion pairs would be expected to show up increasingly with the increase in  $Mn^{2+}$  concentration. This type of pair absorption has been found to occur in  $Mn^{2+}$  activated cubic ZnS crystals (15). An explanation of the observed shift of the green band to longer wavelengths with increasing Mn concentration can be made on the basis of pair emission concept if the model shown in Fig. 4 is considered. For simplicity, splitting of the  ${}^4T_1$  level is ignored. The pair of two neighboring  $Mn^{2+}$  ions is shown to give rise to two levels, one of which is higher than the original  ${}^4T_1$  level and the second level lower. A shift toward the red is expected if all the emission peak is a mixture of contributions from single ions and ion pairs. As the concentration of  $Mn^{2+}$  increases the contribution to emission intensity from ion pairs increases

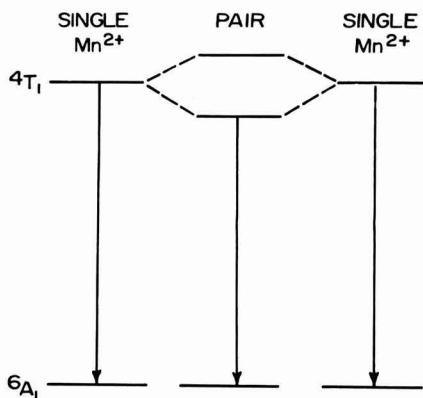


Fig. 4. Formation of ion pairs by two neighboring Mn<sup>2+</sup> ions, shown for perfect T<sub>d</sub> symmetry. The green emission peak would shift toward longer wavelengths if the emitting level for the pair is the lower level.

and the contribution from single ions decreases. This would give rise to the observed shift of emission peak wavelength.

#### Acknowledgment

The authors wish to thank Professors W. B. White, R. Roy, and H. K. Henisch for continued interest and many helpful discussions. Support for this work was provided by Advanced Research Projects Agency Contract No. DA-49-083-OSA-3140.

Manuscript submitted July 1, 1971; revised manuscript received Dec. 23, 1971. This was Paper 53 pre-

sented at the Los Angeles Meeting of the Society, May 10-15, 1970.

Any discussion of this paper will appear in a Discussion Section to be published in the December 1972 JOURNAL.

#### REFERENCES

1. P. P. Feofilov, "The Physical Basis of Polarized Emission," State Physico-Mathematical Press, Moscow (1959); Consultants Bureau, New York (1961).
2. S. Shionoya in, "Luminescence of Inorganic Solids," p. 206, P. Goldberg, Editor, Academic Press (1966).
3. R. J. R. S. B. Bhalla and E. W. White, *J. Appl. Phys.*, **41**, 2267 (1970).
4. R. T. Greer and E. W. White, *Trans. Second Nat. Conf. on Electron Probe Analysis*, Paper 51 (1967).
5. C. Palache, *U.S. Geol. Survey Prof. Paper* 180 (1937).
6. H. W. Leverenz, "Introduction to Luminescence of Solids," p. 223, John Wiley & Sons, Inc., New York (1950).
7. L. E. Orgel, *J. Chem. Phys.*, **23**, 1958 (1955).
8. M. A. Konstantinova-Shlezinger, *Bull. Acad. Sci., USSR-Phys. Ser.*, **30**, 729 (1966).
9. W. L. Bragg and W. H. Zachariasen, *Z. Krist.*, **72**, 518 (1930).
10. F. A. Cotton, "Chemical Applications of Group Theory," Interscience (1963).
11. H. K. Perkins and M. J. Sienko, *J. Chem. Phys.*, **46**, 2398 (1967).
12. D. T. Palumbo and J. J. Brown, *This Journal*, **117**, 1184 (1970).
13. H. G. Jenkins, A. H. McKeag, and H. P. Rooksby, *Nature*, **143**, 978 (1939).
14. See, for example, energy level diagrams, J. S. Berkes, Materials Research Laboratory Monograph No. 2, Pennsylvania State University (1968).
15. D. S. McClure, *J. Chem. Phys.*, **39**, 2850 (1963).

## Effect of Impurity Gas Additions on the Superconducting Critical Current of Vapor-Deposited Nb<sub>3</sub>Sn

R. E. Enstrom,\* J. J. Hanak, J. R. Appert,\* and K. Strater<sup>†</sup>

RCA Laboratories, Princeton, New Jersey 08540

#### ABSTRACT

The addition of various gaseous impurities into the process gases used in the chemical vapor deposition of superconducting Nb<sub>3</sub>Sn has been found to alter the grain size of Nb<sub>3</sub>Sn and thereby the critical current (*I<sub>c</sub>*). Increasing concentrations of CO<sub>2</sub>, CO, and N<sub>2</sub> cause a progressive decrease in the particle size and a concomitant increase of *I<sub>c</sub>* up to three times the value found for undoped specimens. In contrast, O<sub>2</sub> and CH<sub>4</sub> increase the particle size and reduce *I<sub>c</sub>*. *I<sub>c</sub>* is linearly dependent on the reciprocal of the grain size, 1/*D*, to values of *D* as small as 400 Å. The present work suggests that impurities serve to control the grain size, presumably by the formation of small second-phase precipitates which interfere with the growth of Nb<sub>3</sub>Sn grains.

One of the requirements of superconducting materials used in the construction of high-field solenoids is a high critical current, *I<sub>c</sub>*. Over the years it has been found that *I<sub>c</sub>* is proportional to the density of flux pinning centers, which can consist of a variety of defects such as second-phase impurities, dislocations, strain, radiation damage, etc.

In order to achieve a high, current-carrying capacity with ductile metallic alloy superconductors, such as Nb-Zr and Nb-Ti, the materials are extensively cold-

worked during fabrication and are also heat-treated according to prescribed schedules. However, these conventional methods cannot be utilized with Nb<sub>3</sub>Sn, since it is a nonductile, mechanically weak compound. In Nb<sub>3</sub>Sn prepared by diffusion of tin into niobium, a significant increase in *I<sub>c</sub>* has been achieved by the addition of small amounts (0.7%) of zirconium to the niobium (1). Zirconium presumably forms precipitates with impurities scavenged from the niobium, thereby increasing *I<sub>c</sub>*. For chemically, vapor-deposited Nb<sub>3</sub>Sn ribbon (2,3), we reported earlier a strong dependence of *I<sub>c</sub>* on the grain size (4). We have found, in turn, that the grain size can be influenced by impurities in the process gases (5). A study of the addition of various

\* Electrochemical Society Active Member.

<sup>†</sup> Present address: RCA Electronic Components, Somerville, New Jersey 08876.

Key words: Nb<sub>3</sub>Sn, doping impurities, particle size, critical current, superconductivity.

gases during vapor deposition has made it possible to control and obtain reproducibly high values of  $I_c$  as is described in detail in this paper.

### Experimental Procedure

The Nb<sub>3</sub>Sn-coated ribbons were prepared by the hydrogen reduction of tin and niobium chlorides using equipment and procedures previously described (3). Briefly, Nb and Sn metal sources are reacted with Cl<sub>2</sub> at 900° and 800°C, respectively, and the chlorides are fed along with a H<sub>2</sub> carrier gas into the growth zone where the Nb<sub>3</sub>Sn is synthesized. A continuous length of metal ribbon is passed through the growth zone and heated electrically to about 1000°C, while the growth furnace is maintained at about 700°C. This temperature profile keeps the incoming metal chlorides volatile and minimizes deposition of Nb<sub>3</sub>Sn on the walls of the quartz growth tube. To achieve a stoichiometric ratio in the vapor-grown Nb<sub>3</sub>Sn layer (75.0% Nb), the gas phase must have a Nb:Sn chloride ratio between 1:3 and 1:4.

Since this study focused on impurity gas additions, the process gases were purified where possible. Ultra-pure hydrogen<sup>2</sup> with a total impurity content of less than 10 ppm was passed through a platinum catalyst and any water of reaction absorbed with CaSO<sub>4</sub>. Helium was purified by passing the gas stream through Linde 5A and 13X molecular sieve held at 77°K. The hydrogen chloride gas used in the present study was not further purified. However, infrared analysis indicated no impurity bands to be present in the range 3-15  $\mu$ m, the region where CO<sub>2</sub> and phosgene would appear if present. Infrared analysis of the Cl<sub>2</sub> showed it also to be quite pure.

The impurity gas additions studied included CO<sub>2</sub>, CO, CH<sub>4</sub>, O<sub>2</sub>, and N<sub>2</sub> and these were injected either into the hydrogen or into the chlorine stream prior to entry into the growth apparatus. CO<sub>2</sub>, CO, and CH<sub>4</sub> additions ranged from 0.01 to 1 v/o (volume per cent) of the total Cl<sub>2</sub> flow of 140 ml/min, while the O<sub>2</sub> and N<sub>2</sub> additions ranged up to 36 v/o. The equipment was equilibrated for ½ hr prior to the preparation of the 30m length of ribbon used in the superconductivity tests.

The critical current was measured on 30m lengths of ribbon, silver plated to increase electrical stability (6), and wound onto a coil form to produce a small magnet. This small magnet was, in turn, placed into another superconducting magnet, at 4.2°K, and energized so that the two magnetic fields were additive and parallel to the coil axis. The current through the small sample magnet was increased to a value which quenched superconductivity, thereby causing a large increase in voltage across a pair of potential leads; this was taken as the critical current. This procedure was repeated at background fields from 0 to 40 kG to generate a curve of  $I_c$  as a function of H. Tests at higher fields were conducted at the facilities of NASA, in Cleveland, Ohio, and at the Francis Bitter Magnet Laboratory at M.I.T. Measurements of the transition temperature,  $T_c$ , for selected samples were performed as previously described (7).

The vapor-grown layers were also examined by optical and electron microscopy. In addition, the subgrain size was determined as a function of processing using an x-ray line broadening method and procedures described earlier (4). X-ray fluorescence analyses for Nb and Sn composition on the ribbon were performed using procedures already described (3) to monitor the stoichiometry of the deposit.

### Results and Discussion

**Effect of doping gases on  $I_c$ .**—The critical current increases by about a factor of three with the addition of CO<sub>2</sub> as shown in Fig. 1. Here, the undoped Nb<sub>3</sub>Sn ribbon carries 65A at 40 kG (curve 1) and the ribbon doped with 0.25% CO<sub>2</sub> carries 183A (curve 6). Since the thickness of the Nb<sub>3</sub>Sn is similar for most samples,

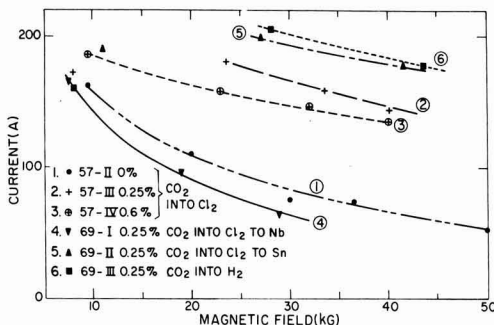


Fig. 1. Critical current as a function of total magnetic field for Nb<sub>3</sub>Sn ribbon samples doped with CO<sub>2</sub>.

this corresponds to current densities,  $J_c$ , of about  $2.5 \times 10^5$  and  $8.0 \times 10^5$  A/cm<sup>2</sup>, respectively. It may also be seen that  $I_c$  is a function of the CO<sub>2</sub> concentration and that the optimum value is around 0.25% for injection into the Cl<sub>2</sub> gas stream (curves 2 and 3).

Alternative doping gas injection sites were investigated and these results also are summarized in Fig. 1. The addition of 0.25% CO<sub>2</sub> to the Cl<sub>2</sub> stream leading to the Sn metal source (curve 5) results in an  $I_c$  (H) curve nearly equivalent to that observed for injection into the H<sub>2</sub> port (curve 6). However, the same concentration of CO<sub>2</sub> injected into the Cl<sub>2</sub> stream leading to the Nb metal source (curve 4) results in an  $I_c$  (H) curve somewhat below that observed for undoped Nb<sub>3</sub>Sn ribbon. This latter result probably can be explained by gettering of the CO<sub>2</sub> in the Cl<sub>2</sub> stream by the Nb metal to form NbC and Nb<sub>2</sub>O<sub>5</sub> so that the CO<sub>2</sub> is not available to the growing Nb<sub>3</sub>Sn layer. In contrast, CO<sub>2</sub> does not completely react with the Sn source at the 800°C chlorination temperature and therefore is available to the Nb<sub>3</sub>Sn being synthesized in the deposition chamber.

This hypothesis was confirmed by a thermodynamic analysis of the possible reactions of Sn with CO or CO<sub>2</sub>, which showed that the free energy change is zero at 800°C. Thus, any reaction between CO<sub>2</sub> and Sn would be near equilibrium, thereby allowing a substantial portion of the CO<sub>2</sub> to pass through unreacted. If kinetics limited the rate of reaction, an even greater fraction of CO<sub>2</sub> would pass through the Sn metal zone and into the Nb<sub>3</sub>Sn deposition chamber. If CO<sub>2</sub> is injected into the Cl<sub>2</sub> stream before it is split into portions going to the Nb source and to the Sn source, then the CO<sub>2</sub> is gettering from the Cl<sub>2</sub> exiting from the Nb chamber. Accordingly there is an apparent difference in the optimum values for the amount of CO<sub>2</sub> injected into the gas stream at the various locations.

This effect probably explains the dependence of the  $I_c$  (H) curve on CO concentration given in Fig. 2. In-

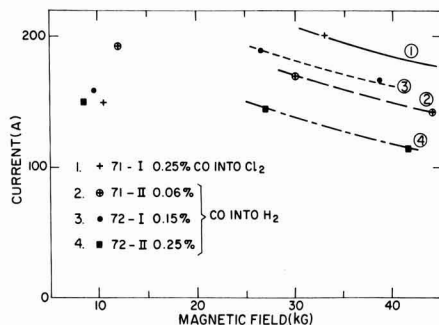


Fig. 2. Critical current as a function of total magnetic field for Nb<sub>3</sub>Sn ribbon samples doped with CO.

<sup>2</sup> Matheson Company, East Rutherford, New Jersey.

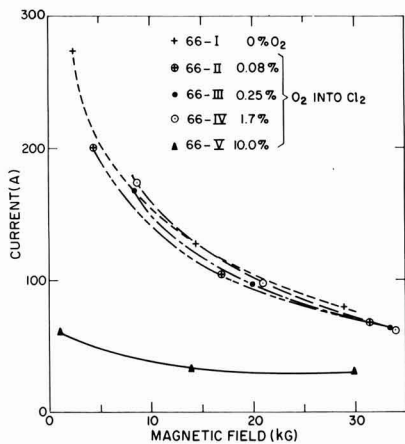


Fig. 3. Critical current as a function of total magnetic field for  $\text{Nb}_3\text{Sn}$  ribbon samples doped with  $\text{O}_2$ .

jection of the CO into the total  $\text{Cl}_2$  stream results in a portion of the CO being gettered by the Nb metal source and the remainder, perhaps 0.18%, enters the deposition chamber. This concentration is closer to an optimum value and accordingly produces the  $\text{Nb}_3\text{Sn}$  ribbon with the highest current-carrying capability.

Thus, we have seen that both  $\text{CO}_2$  and CO are effective in increasing  $I_c$ . In the next two series of runs, a hydrocarbon,  $\text{CH}_4$ , and  $\text{O}_2$  were used. The results for the introduction of  $\text{O}_2$  into the  $\text{Cl}_2$  stream are shown in Fig. 3. Here, the undoped  $\text{Nb}_3\text{Sn}$  ribbon has the highest  $I_c$ . Increasing concentrations of  $\text{O}_2$  result in successively lower  $I_c$  values and the value for 10%  $\text{O}_2$ , 29A at 30 kG, represents the lowest  $I_c$  observed at that magnetic field of all the various samples tested. It should be pointed out that all of the doped layers, except the 10%  $\text{O}_2$ -doped  $\text{Nb}_3\text{Sn}$ , had compositions within 1% of the correct stoichiometric ratio. The high  $\text{O}_2$ -doped sample was seriously deficient in Nb, presumably because of the formation of Nb oxides. Although these results indicate that large concentrations of  $\text{O}_2$  should be excluded from the reactant gas stream, it is also apparent that  $I_c$  is rather insensitive to small oxygen impurity concentrations.

The results for the  $\text{CH}_4$  doping demonstrate that  $\text{CH}_4$  in concentrations of 0.15-0.25% is not effective in increasing the critical current. But, other results (5) show that hydrocarbon gases with a molecular weight greater than 16 ( $\text{CH}_4$ ) are as effective as CO and  $\text{CO}_2$  in increasing the  $I_c$ , presumably because they are less stable than  $\text{CH}_4$ . Therefore, since both CO and  $\text{CO}_2$  and hydrocarbons such as ethane can successfully dope  $\text{Nb}_3\text{Sn}$  to high values of  $I_c$ , it is concluded that carbon is the principle atom responsible for the enhancement of  $I_c$  in these cases.

The next series of experiments performed with  $\text{N}_2$  gas additions is summarized in Fig. 4. In this case,  $\text{N}_2$  concentrations up to 36% were used to achieve values about twice as high as could be achieved with undoped  $\text{Nb}_3\text{Sn}$ . However,  $\text{N}_2$  concentrations from 0.1 to 5% produced  $\text{Nb}_3\text{Sn}$  with  $I_c$  values not very much higher than for undoped  $\text{Nb}_3\text{Sn}$ . It should be pointed out that 99.999% pure  $\text{N}_2$  containing less than 10 ppm hydrocarbon impurities had been used in these experiments which, when further diluted in the gas stream, should not influence  $I_c$  even at the highest flows of  $\text{N}_2$  used. Thus, it appears that  $\text{N}_2$  also can be used to enhance  $I_c$ . However, the use of  $\text{CO}_2$  in conjunction with  $\text{N}_2$  does not lead to a higher  $I_c$  than achieved with  $\text{CO}_2$  alone, implying that the modes of enhancement are not additive.

Next, the influence of the Sn/Nb chloride ratio in the gaseous ambient was examined to determine its effect

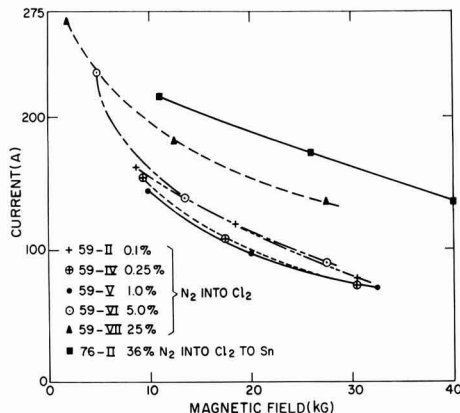


Fig. 4. Critical current as a function of total magnetic field for  $\text{Nb}_3\text{Sn}$  ribbon samples doped with  $\text{N}_2$ .

on  $I_c$ . As mentioned earlier, a Sn/Nb ratio greater than 3/1 must be used to achieve the correct stoichiometry in the vapor-grown  $\text{Nb}_3\text{Sn}$  layer; lower ratios result in  $\text{Nb}_3\text{Sn}$  with excess Nb and a lower  $T_c$ . Accordingly, ratios greater than 3/1 were examined both with and without  $\text{CO}_2$  additions, and it was found that higher ratios produce  $\text{Nb}_3\text{Sn}$  that is up to 2.5% richer in Sn.

In Fig. 5 it is seen, in turn, that the 3 Sn/1 Nb ratio has the highest  $I_c$  (H) curve for both doped and undoped ribbons. But,  $\text{CO}_2$  is effective in increasing the  $I_c$  at a given value of H for the three chloride ratios examined. It can be observed that the interval between the 3/1 and the 5/1 ratios is about the same for the doped and undoped series but that the 4/1 curve lies closer to the 5/1 curve for the undoped samples and closer to the 3/1 curve for the  $\text{CO}_2$ -doped  $\text{Nb}_3\text{Sn}$ . This latter result is fortunate since this allows some margin for error in the adjustment of the Sn/Nb chloride ratio while permitting a high  $I_c$  (H) relationship to be achieved.

In the standard growth process for the preparation of  $\text{Nb}_3\text{Sn}$  ribbon, the ribbon travels 15 m/hr counter-current to the gas stream and the total flow rate of chlorine to the Nb and Sn metal sources is 140 ml/min. The effect of several variations in the process on the  $I_c$  (H) curve are given in Fig. 6 and these may be compared with both  $\text{CO}_2$ - and CO-doped as well as undoped ribbon samples. It may be seen that concurrent travel of the gas and the stainless steel substrate leads to an  $I_c$  (H) curve that is about 50% lower than when a counter-current arrangement is used. The reason for this result is not clear.

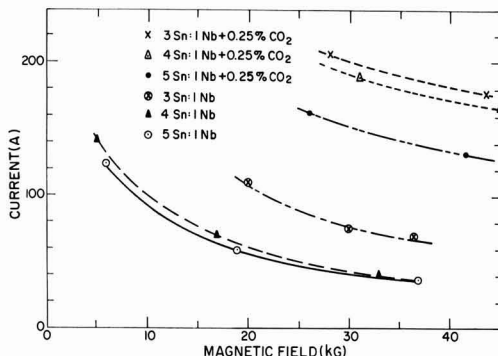


Fig. 5. Critical current as a function of total magnetic field for  $\text{Nb}_3\text{Sn}$  ribbon samples prepared with various Sn/Nb ratios in the vapor ambient.

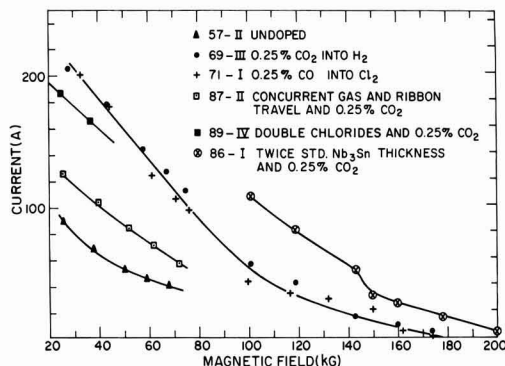


Fig. 6. Critical current as a function of total magnetic field for Nb<sub>3</sub>Sn ribbon samples prepared under various vapor-growth conditions.

Higher partial pressures of the metal chlorides were investigated to study the effect on  $I_c$  and to increase the growth rate so that a thicker layer and thus a higher  $I_c$  could be attained for a given ribbon speed. It was found that doubling the partial pressures of the Nb and Sn chlorides by doubling the Cl<sub>2</sub> flow rates to the metal sources degrades the  $I_c$  (H) curve somewhat, as shown in Fig. 6. Moreover, no significant increase in deposit thickness was observed. The deposit thickness was increased to twice the normal thickness, however, by decreasing the ribbon speed from 15 to 7 m/hr.  $I_c$  was thereby doubled as shown in Fig. 6, indicating that the deposit is homogeneously doped throughout its thickness. The factor-of-two higher  $I_c$  is very important, especially for the construction of magnets above about 120 kG where the  $I_c$  is dropping rapidly. In addition, the thicker Nb<sub>3</sub>Sn has a significantly higher critical field,  $H_{c2}$ , presumably because the extra Nb<sub>3</sub>Sn grown onto the ribbon is further removed from the metallic substrate and therefore less contaminated by diffusion of Fe, Mo, and Ni from the substrate. The nature of the interface between the Nb<sub>3</sub>Sn and the stainless steel will be examined in another publication (8).

Impurity doping of Nb<sub>3</sub>Sn deposits on ribbon substrates lowers the  $T_c$  onset from 17.0°K for undoped material to 15.0°K for optimally doped material. Part of this decrease is due to elastic strain built into the ribbon, as shown by an increase of  $T_c$  to 15.9°K when the substrate is etched away with nitric acid, and part is due to a large strain in the lattice introduced by the presence of the impurities. When the substrate-free deposit is annealed at 850°C for 2 hr, the  $T_c$  increases to 17.9°K which is probably due to relief of the internal strain.

**Effect of doping on grain size of Nb<sub>3</sub>Sn.**—A striking change in the appearance of the Nb<sub>3</sub>Sn from a dull, nonreflective surface to a very bright, reflective surface occurs with the introduction of CO, CO<sub>2</sub>, or N<sub>2</sub> into the gas stream. This change appeared to be associated with a reduction of the Nb<sub>3</sub>Sn crystallite size. Accordingly, grain size measurements were made by x-ray line broadening of all specimens using techniques described in our earlier paper (4). It was found that increasing concentrations of CO<sub>2</sub>, CO, and N<sub>2</sub> decrease the Nb<sub>3</sub>Sn grain size from ~1000 Å (100 nm) for an undoped sample to a minimum of ~370 Å (37 nm) for the most heavily doped samples. For O<sub>2</sub> and CH<sub>4</sub> doping, a tendency toward an increase of grain size is observed. The  $I_c$  data were converted to critical current density,  $J_c$ , and to  $\alpha = J_c H$  and were plotted in Fig. 7 as a function of the inverse of the grain size,  $1/D$ . A similar linear dependence of  $J_c$  vs.  $1/D$  was obtained up to  $1/D \approx 2.5 \times 10^5 \text{ cm}^{-1}$  [grain size  $\approx 400 \text{ Å}$  (40 nm)] as before (4), regardless of the doping gas

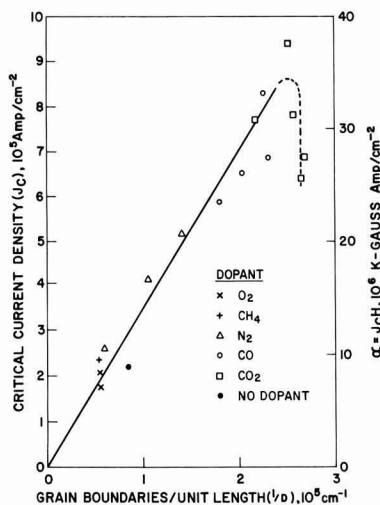


Fig. 7. Critical current density at 40 kG as a function of the reciprocal of the grain size.

used. The variable  $1/D$  represents the number of pinning sites per unit distance and  $J_c$  is linearly dependent on it. The doping gas thus appears merely to provide a control over the grain size of Nb<sub>3</sub>Sn, probably via the formation of submicroscopic precipitates such as carbides or nitrides of niobium which interfere with grain growth of Nb<sub>3</sub>Sn.

Attempts to identify the form which the impurities take in the deposit were only partially successful. Mass spectroscopic analyses of carbon in an undoped and a CO<sub>2</sub>-doped deposit (0.25% CO<sub>2</sub> in gas phase) show 50-100 ppm and 700-2400 ppm, respectively, indicating the incorporation of carbon. This amount of carbon would be sufficient to form a second phase. But, neither x-ray nor electron diffraction techniques were able to identify the presence of phases other than Nb<sub>3</sub>Sn. However, a transmission electron micrograph of a specimen thinned by etching showed a multitude of dark spots which could be interpreted as a fine precipitate of a second phase (9).

## Conclusions

The addition of various gaseous impurities into the process gases used in the chemical vapor deposition of superconducting Nb<sub>3</sub>Sn has been found to alter the grain size of Nb<sub>3</sub>Sn and thereby the critical current. Increasing concentrations of impurity gases including CO<sub>2</sub>, CO, and N<sub>2</sub> have been found to cause a progressive decrease in the Nb<sub>3</sub>Sn particle size and an increase in  $I_c$ . Additions of O<sub>2</sub> and CH<sub>4</sub>, on the other hand, tend to increase the particle size of Nb<sub>3</sub>Sn and lower  $I_c$ . Regarding the effectiveness of doping, CO<sub>2</sub> and CO have been found to be the most effective since about 0.25% impurity causes up to a threefold increase of  $I_c$  compared to undoped specimens. In contrast, 36% of N<sub>2</sub> impurity is required to increase  $I_c$  twofold. The process is rather insensitive to oxygen impurity as 1.7% O<sub>2</sub> decreases  $I_c$  only 6% and large amounts of O<sub>2</sub> (10%) are required to decrease  $I_c$  to less than 1/2 the value of undoped specimens. Since  $I_c$  scales up with deposit thickness at a given doping level, doping is a bulk effect. The increase of  $I_c$  and  $J_c$  has a similar linear dependence on the inverse of the grain size  $1/D$  as reported previously (4), regardless of the type of dopant used. It appears, therefore, that the impurities serve only as a means of controlling the grain size, presumably by the formation of small, second-phase precipitates which interfere with the growth of Nb<sub>3</sub>Sn grains.



### Acknowledgments

The authors are grateful to the staffs of the M.I.T. Francis Bitter Magnet Laboratory and NASA, Cleveland, for their cooperation during the high-field superconductivity tests.

Manuscript submitted June 24, 1971, revised manuscript received Oct. 20, 1971.

Any discussion of this paper will appear in a Discussion Section to be published in the December 1972 JOURNAL.

### REFERENCES

1. W. DeSorbo, *Cryogenics*, **4**, 218 (1964).
2. J. J. Hanak, "Metallurgy of Advanced Electronic Materials," p. 161, G. E. Brock, Editor, Interscience Publishers, New York (1963).

3. J. J. Hanak, K. Strater, and G. W. Cullen, *RCA Rev.*, **25**, 342 (1964).
4. J. J. Hanak and R. E. Enstrom, "Proc. Tenth International Conf. on Low Temperature Physics," Vol. IIB, p. 10, Moscow, U.S.S.R. (1967).
5. R. E. Enstrom, J. J. Hanak, F. R. Nyman, and K. Strater, U.S. Pat. No. 3,400,016, September 1968.
6. H. C. Schindler and F. R. Nyman, *RCA Rev.*, **25**, 570 (1964).
7. J. L. Cooper, *ibid.*, **25**, 405 (1964).
8. R. E. Enstrom and J. Appert, To be published.
9. M. C. Inman, "Phenomenon of Superconductivity" (Phase II), October 1966, prepared by RCA Laboratories, Princeton, N. J., for Air Force Materials Laboratory, Wright-Patterson Air Force Base, Ohio, p. 56.

## Hydrogen Chloride and Chlorine Gettering: An Effective Technique for Improving Performance of Silicon Devices

R. S. Ronen and P. H. Robinson\*

RCA Laboratories, Princeton, New Jersey 08540

### ABSTRACT

Moderate levels of lifetime killing impurities in silicon can be removed or neutralized by a high-temperature treatment in the presence of approximately 1% gaseous hydrogen chloride or chlorine in dry oxygen. Results using bulk silicon as well as thin-film silicon on sapphire (SOS) indicate a significant improvement in the effective minority carrier lifetime. Crystal quality, doping level, oxygen content of the silicon, and surface treatment are found to be important variables. The paper describes the effect of chlorine gettering on various bulk silicon and SOS devices.

It has been well documented that many high-temperature fabrication steps used in silicon device processing often result in the reduction of minority carrier lifetime (1-6), because of the redistribution of heavy metallic impurities, e.g., Au and Cu, or the precipitation of such impurities on dislocations. Thus these impurities become effective recombination centers (7, 8). Heavy metal impurities were found to have states near the center of the gap (2, 5, 6, 9). Oxidation, in particular, was very detrimental to lifetime (10). Contaminants can come from a number of sources, such as the bulk and surface of the wafer or the furnace tube.

Various gettering techniques to eliminate them or prevent them from generating effective traps have been reported (3, 4, 11, 12). One has been a phosphorus glass layer in contact with the Si at elevated temperatures (4, 11). A second technique uses KCN or sintered Ni in contact with the Si to prevent impurities from in-diffusing during processing (13). Oxides such as  $\text{P}_2\text{O}_5$ ,  $\text{B}_2\text{O}_5$ , and  $\text{V}_2\text{O}_5$  have also been used, as have been chlorides ( $\text{BCl}_3$  and  $\text{PCl}_5$ ), during high-temperature diffusion for the preservation of lifetime (3, 4). Transmission electron microscopy and infrared microscopy verified the elimination of Cu precipitates from dislocations after gettering treatment (14).

Recently, bulk Si as well as thin-film Si on insulators has shown a significant increase in minority carrier lifetime after heating in a dry  $\text{O}_2/\text{HCl}$  ambient (15, 18). At  $950^\circ\text{C}$ , the lowest temperature used for the HCl gettering process, the diffusion constants of the lifetime killing impurities (Cu, Fe, Au) in Si range from  $10^{-5}$  to  $10^{-8}$   $\text{cm}^2/\text{sec}$ . Since  $\text{Cl}_2$  is more reactive than HCl we

believe that it can more effectively improve lifetime; that is, gettering can be done at a lower temperature, and the magnitude of the improvement would be greater for the same time and temperature using  $\text{Cl}_2$  rather than HCl. This paper describes various results obtained with  $\text{Cl}_2$  gettering; a comparison of HCl and  $\text{Cl}_2$  is made.

### Experimental Procedure

Gettering was carried out in a dry  $\text{O}_2$  ambient either before device processing when films were being studied or after fabrication, just before metalization. A typical procedure consisted of the following steps:

1. Thorough cleaning of the wafer, to remove surface impurities.
2. Gettering in a mixture of 1%  $\text{Cl}_2$  in dry  $\text{O}_2$  at a temperature  $T_g$  of  $800^\circ$  to  $1150^\circ\text{C}$ .
3. Annealing in dry He for 15 min at  $T_g$  to remove  $\text{Cl}_2$  from the furnace and sample and to reduce positive oxide charge (16).
4. Hydrogen annealing for 15 min at  $500^\circ\text{C}$  to reduce density of interface states.

The effective minority carrier lifetime was then determined by C-V and C-t measurements (17). Gettering times range from 1 to 100 hr, and the gettering temperatures were either  $950^\circ$  or  $1050^\circ\text{C}$ . The lifetime improvement was found to be dependent on the time  $\times$  temperature product. When junction devices were being studied, a period of 2 hr at  $950^\circ\text{C}$  was used so as not to alter the diffusion profile in these devices significantly.

On several occasions, oxidation prior to the admission of HCl or  $\text{Cl}_2$  was necessary to prevent etching and pitting of the Si. The concentration of HCl or  $\text{Cl}_2$  was kept low ( $\sim 0.5$ -1%) because severe attack of the Si was observed at higher concentrations ( $\sim 5$ -10%).

\* Electrochemical Society Active Member.

Key words: gettering, minority carrier lifetime, SOS, silicon, HCl,  $\text{Cl}_2$ .

Water vapor was removed from the oxygen gas by a dry ice trap. For SOS devices C-V measurements were not always effective because of series resistance. C-V measurements at d.c. and high frequency were employed with SOS devices to determine lifetime.

We tried different annealing techniques which included only inert gases such as  $N_2$ , He, Ar,  $H_2$ , as well as oxygen but no HCl or  $Cl_2$ , at various temperatures and periods. The wafers and devices showed little or no improvement, and the  $O_2$  treatment was in fact detrimental to lifetime in most cases. These heat-treatments were carried out under conditions identical to those used for  $Cl_2$ .

### Measuring Technique

The effective minority carrier lifetime was determined from the transient response of a depletion capacitance structure (17). To facilitate the measurement a mercury probe made contact with the  $SiO_2$  in a circular pattern ( $\sim 35$  mil diam). A back contact was employed in the bulk Si measurements, and a circular contact around the dot for the SOS measurements. To minimize series resistance, particularly when measuring SOS, an interdigitated pattern was used, thus making the resistance smaller than the capacitive reactance.

Heiman (17) has shown that  $\tau_{eff} = (T/2) (N_i/N_a)$  is an approximate solution to the recovery from deep depletion of an MOS capacitor;  $\tau_{eff}$  = effective lifetime of minority carrier in depletion region,  $T$  = recovery time constant,  $N_i$  = intrinsic carrier concentration,  $N_a$  = carrier concentration of wafer under investigation. The three wave shapes shown in Fig. 1 represent recovery of an MOS capacitor with shallow surface states, with deep surface states, and with no surface states. If the transient response on the wafers is observed before and after gettering, and the response has the same shape, only one calculation of  $T$  is necessary. The second and third wave shapes were typically observed on SOS and good-quality Si, respectively.

The MOS capacitor structure used for C-t measurements is shown in Fig. 2. From the typical C-V curve shown in Fig. 3 one can calculate the doping density to within a few diffusion lengths of the surface, and effective oxide charge, and get an indication of the surface state density (19). A typical C-t curve is shown in Fig. 4. The effective minority carrier lifetime is obtained, following Heiman's method (17), without much processing; however, the results must be interpreted with care.

Comparative lifetime measurements, before and after gettering, are meaningful even though the technique assumes recombination centers at mid-gap. It was assumed that the majority carrier concentration does not change during gettering at  $950^\circ C$  for 2 hr. This was shown to be valid by Hall measurements, C-V curves, and 4-point probe measurements.

For very thin SOS devices (those with planar junctions such as epitaxial bipolar transistors), the C-V

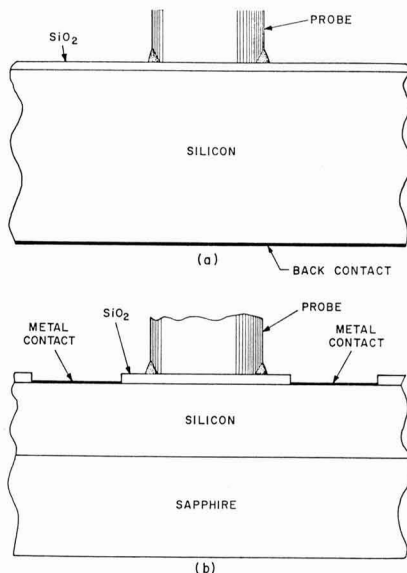


Fig. 2. Structure of MOS capacitor. a, Bulk; b, SOS

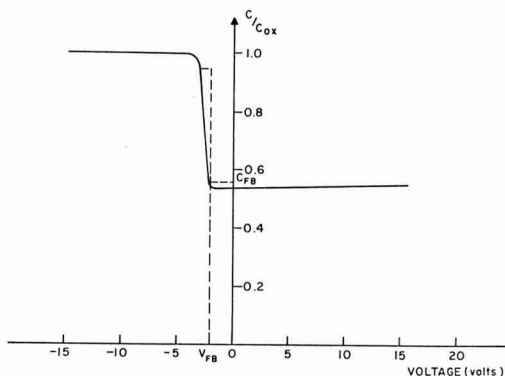


Fig. 3. Typical capacitance-voltage curve, p-type bulk silicon

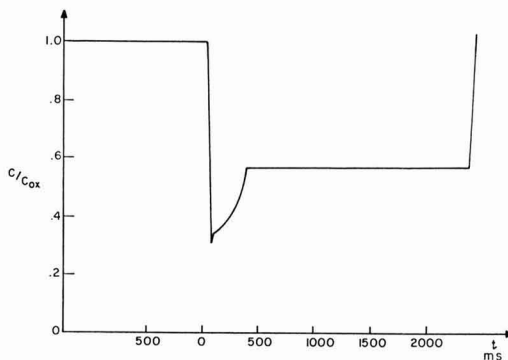


Fig. 4. Typical capacitance-time curve, bulk silicon

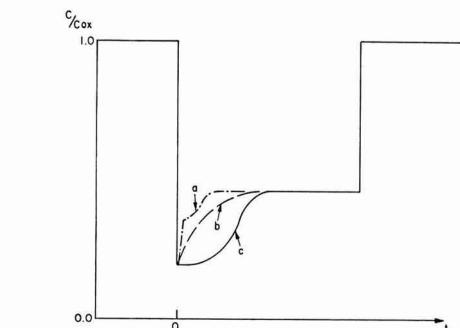


Fig. 1. Transient response of an MOS capacitor. a, Response in the presence of shallow surface states; b, response with deep surface states; c, response with no surface states.

and pulse-capacitance measurements are difficult to make or useless; hence, other methods were used. SOS devices were evaluated by extending the logarithmic plot of the forward I-V characteristics asymptotically, determining the slope, and evaluating the zero voltage

intercept. The effective minority lifetime is then obtained, and comparison of measurements taken before and after gettering becomes meaningful. An I-V logarithmic plot exhibits a good straight line to the point where series resistance effects obscure the real junction behavior. We assume a simple junction theory of the form  $I = I_0 \exp qV/nkt$  ( $1 \leq n \leq 2$ ), with  $n = 1$  for pure diffusion and  $n = 2$  when recombination in the transition region is dominant (9). The slope of the linear part of logarithmic plot yields  $n$  directly, giving information about the relative magnitude of diffusion vs. recombination in the material (surface and bulk effects). The zero voltage intercept of the I-V asymptote yields a measure of the minority carrier lifetime in the depletion region of a diode. The forward diffusion current (linear part) at  $V = 0$  is equated to the reverse leakage current (recombination), and the lifetime  $\tau$  is calculated. This is only an approximate method, but comparison of curves before and after gettering and the absolute value of the leakage current yield very useful results. In the case of multilevel planar junctions such as SOS epitaxial bipolar transistors, high-frequency measurements of  $f_T$  vs. current, give the base transit time. The linear part of the curve depicting  $[f_T]^{-1}$  vs.  $M$  is extrapolated to  $M \equiv (kT/q)/I_E = 0$  (corresponding to  $I_E \rightarrow \infty$ , i.e., zero emitter delay time) where  $f_T = D/\pi w^2$  and base transit time  $T_r = w^2/2D = 1/(2\pi f_T)$ . Knowing  $T_r$  and  $D$  yields the base width. The low-frequency common base current gain, when very close to unity, yields the minority carrier lifetime

$$\alpha_0 \approx 1 - \frac{1}{2} \frac{w^2}{L^2} = 1 - \frac{w^2}{2Dt} = 1 - \frac{T_r}{\tau}$$

when  $\beta_0 = \alpha_0/(1 - \alpha_0) \gg 1$ , we get  $\tau = \beta_0 T_r$ . The base width was also obtained by other techniques and found to be in close agreement with that obtained from UHF measurements.

### Experimental Results

**General observations.**—1. Gettering is more effective on good-quality bulk crystals and thin-film SOS layers with scratch-free surfaces. Impurities introduced during processing can be eliminated or their effect significantly reduced by gettering.

2. In wafers exhibiting low lifetime due to oxygen contamination even below the sensitivity of mass spectrography ( $10^{16}/\text{cc}$ ) improvement via gettering is marginal. The lifetime killing species is apparently bonded

to the Si differently in this case, or the  $\text{SiO}_2$  complexes introduce deep recombination centers. This was mainly observed in thin epitaxial layers grown on sapphire.

3. Using  $\text{Cl}_2$ , improvement was greater on n-type Si than on p-type material of comparable doping density. This indicates that the lifetime killing impurity may not reside near mid-gap in both types, an observation in agreement with Waldner and Sivo (4).

4. Up to a limit, the effectiveness of gettering increases with time and temperature. At gettering temperatures above  $1000^\circ\text{C}$  no further improvement was obtained after 30 hr.

5. If the Si is heavily contaminated with metal impurities or  $\text{O}_2$ , some impurities tend to concentrate in the  $\text{SiO}_2$  layer formed during oxidation, thus yielding large C-V shifts. Stripping the  $\text{SiO}_2$  and regetting still results in large C-V shifts as well as charge storage effects in the oxide; this prevents meaningful C-T measurements.

6. Gettering diode structures resulted in the reduction of reverse leakage currents by several orders of magnitude. The reverse and forward I-V characteristics were also found to improve significantly.

7. Gettering MOSFET's showed only better drain diode breakdown characteristics, with no other effect on device performance observed. Metalized MOSFET's, with Al or Cr-Au, could not be gettered at the proper temperatures.

8. Mass spectrographic analyses on bulk and thin-film SOS were below the sensitivity range needed to detect changes in the Au and Cu content before and after gettering. Analysis showed a concentration of  $\text{Cl}_2$  in the oxide after gettering  $10^8$ - $10^4$  higher than in the bulk material. This may be responsible for tying up the impurities in the oxide at the interface.

**Bulk silicon.**—A series of p- and n-type [100] and [111] bulk silicon wafers were obtained from Ventron and Monsanto and were gettered with  $\text{Cl}_2$  for different periods and temperatures, as shown in Table I. The effective lifetime after high-temperature oxidation was reduced to 100-300 nsec in most wafers and to 1-2  $\mu\text{sec}$  in material that had both surfaces polished and relatively free of work damage. The [111] Ventron material, least affected by gettering, had unpolished back surfaces. The [100] n-type wafers, with both surfaces chemically polished, showed the greatest improvement; less consistent results were obtained with the [111] oriented wafers. After 16 hr of gettering no

Table I. Silicon wafers gettered with  $\text{Cl}_2$

Manufacturer	Orientation	Type	Resistivity, ohm-cm	Process*	Original $\tau$ (if known), $\mu\text{sec}$	$\tau$ , $\mu\text{sec}$	Remarks
Ventron	[111]	P	8-11	A1	<2	0.05	Rough back
				B1		0.07	
				D1		0.07	
				E1		0	
				A1		0.1	
		N	8.5-11.5	B1	<2	0.3-0.5	Polished back (chemically)-relatively work-damage free
				D1		1.5-2.0	
				A1		1.0	
				B1		0.02	
				D1		0.05	
Monsanto	[100]	N	10	A1	5-10	0.05	Chemically polished back
				D1		0.6	
				A2		0.04	
				E2		9.0	
Ventron	[100]	N	10	A1	<10	0.02	Rough back
				B1		1.2	
				A1		0.02	
				B1		0.02	
Monsanto	[100]	P	10	A2	<10	1.0	Rough back
				B2		5.25	
				A2		0.3	
				B2		0.75	
		N	10	C2		0.1	Relatively smooth back
				C2		45.0	
				A2		0.5	
				B2		4.5	
Monsanto	[100]	N	10	A2	<10	2.2	Chemically polished back
				B2		5.5	

\* Symbols: A, 5 min steam  $\text{SiO}_2$  at  $1050^\circ\text{C}$ ; B, process "A" followed by 2 hr  $\text{Cl}_2$  gettering; C, process "A" followed by 4 hr  $\text{Cl}_2$  gettering; D, process "A" followed by 16 hr  $\text{Cl}_2$  gettering; E, process "A" followed by 100 hr  $\text{Cl}_2$  gettering; 1, gettering temperature =  $950^\circ\text{C}$ ; 2, gettering temperature =  $1050^\circ\text{C}$ .

further improvement was observed in any of the wafers.

HCl gettering was studied and at 950°C was found to be slightly less effective than chlorine at the same temperature, while at high temperatures,  $\sim 1100^\circ\text{C}$ , HCl was more effective by a factor of 2-5. Typical lifetimes were 1  $\mu\text{sec}$  for an n-type  $\text{Cl}_2$ -gettered silicon wafer, as compared with 4  $\mu\text{sec}$  for the HCl gettered one, with  $T_g = 1150^\circ\text{C}$ .

Cooling the bulk silicon wafers and the SOS films at  $100^\circ\text{C}/\text{min}$  in He or quenching them in He produced no significant difference in the results.

**Results on thin-film silicon on sapphire.**—The minority carrier lifetime of thin-film SOS layers as grown is typically 1-2 nsec. After high-temperature processing it is usually reduced to 0.1 nsec or less. The lifetime was found to increase to 4 nsec in 2- $\mu\text{m}$ -thick p-type layers after gettering in  $\text{Cl}_2$  at  $950^\circ\text{C}$  for 2 hr. Increasing the gettering temperature to  $1050^\circ\text{C}$  increased the lifetime to the 10-40 nsec range. The n-type films showed a slight improvement over these p-type results, i.e., 20-50 nsec. The C-V measurements on these layers had high series-resistance contacts; to overcome this problem interdigitated geometries were used. Films  $\geq 2 \mu\text{m}$  with doping densities  $> 10^{16}$  were needed, since, with higher resistivity Si, the maximum depletion width can be equal to or greater than the film thickness, rendering deep-depletion measurements invalid. Typical C-V and C-t wave forms are shown in Fig. 5.

**Silicon-on-sapphire epitaxial bipolar transistors.**—Mesa-type epitaxial SOS bipolar transistors were gettered using either HCl or  $\text{Cl}_2$  at  $950^\circ\text{C}$  for 2 hr just prior to the metalization step. Interdiffusion effects are insignificant, and measurements of the base width before and after gettering showed no change in thickness. The effect of this treatment on device performance, however, was quite dramatic. Figure 6 shows the transistor characteristics of a typical device before gettering, Fig. 7 after gettering. Low-frequency gain,  $\beta$ , increased by a factor of 2-10 after this treatment, and many devices with  $\beta \approx 20$  were obtained (Fig. 8). A few devices with  $\beta = 60$  were obtained. These most probably had very thin base regions and, hence, should make very good high-frequency transistors. A large reduction in the leakage current of emitter-base and base-collector diodes, along with an increase in the breakdown voltage, was observed. This is shown in the I-V characteristics of Fig. 9, before and after gettering. Note the different current scales on the two parts. The linear part of the forward I-V characteristics,  $I = \exp$

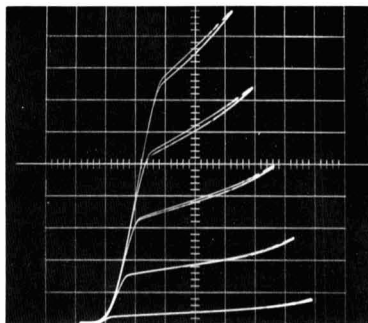


Fig. 6. Bipolar transistor before gettering.  $\beta = 2$ , Vertical, 1 mA/cm; horizontal, 2 V/cm, base current, 1 mA/step.

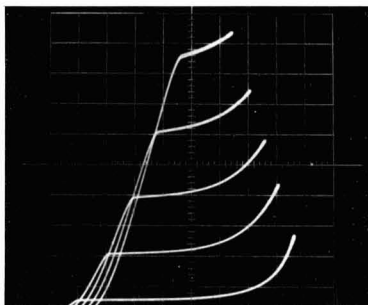


Fig. 7. Bipolar transistor after gettering.  $\beta = 8$ . Vertical, 2 mA/cm; horizontal, 2 V/cm; base current, 0.5 mA/step.

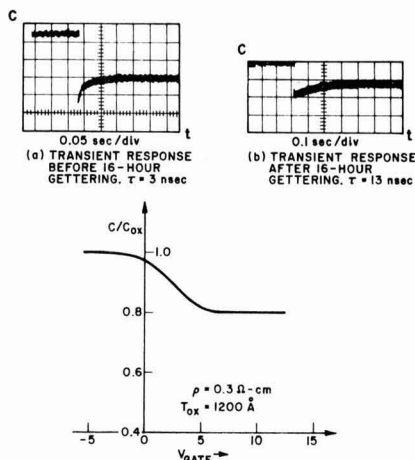


Fig. 5. Capacitance-time curves for an SOS capacitor before and after gettering; capacitance-voltage curve after gettering.

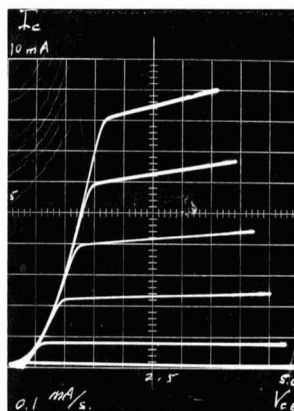


Fig. 8. Typical SOS bipolar characteristics.  $\beta = 20$

$(qv/nkt)$ , exhibited  $\eta < 1.4$  as compared with  $\eta > 1.6$  before gettering. This result is indicative of a change in the recombination mechanism in the space charge region of the diodes (see Fig. 10).

Another measurement, that of  $[f_c]^{-1}$  vs.  $[I_E]^{-1}$ , showed that the base transit time and the minority carrier lifetime in the base region had increased to 325 and 16 nsec, from values less than 2 and 0.1 nsec, respectively. This is shown in Fig. 11. Effective minority carrier lifetimes in SOS devices and films measured by the three different methods agree rather well.

The gettering process has significantly improved the SOS bipolar transistor.

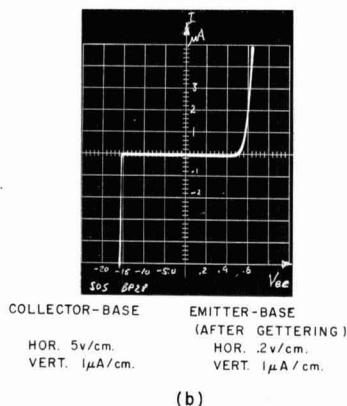
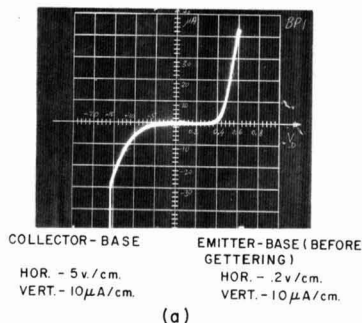


Fig. 9. Effect of gettering on the I-V characteristics of the two junctions in an SOS bipolar transistor.

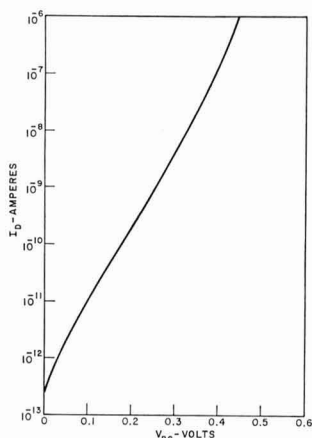


Fig. 10. Forward current voltage characteristic of base-collector junction.

### Conclusions

A small amount of gaseous HCl or Cl<sub>2</sub> introduced during oxidation in dry oxygen significantly reduced recombination rate in both bulk Si and SOS films and devices. The mechanism whereby the lifetime is increased is still open to speculation. One possibility is the formation of volatile metallic impurity chlorides. Other mechanisms, such as Cl<sub>2</sub> diffusing into the Si and somehow tying up heavy or light ions, thereby neutralizing them or reducing their effectiveness as recombination centers, are also possible, as is some cleaning of the furnace. The gettering mechanism appears

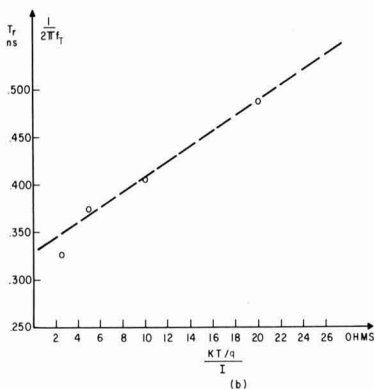
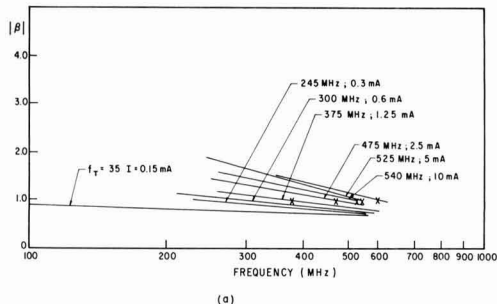


Fig. 11. High frequency behavior of SOS bipolar. (a)  $\beta$  vs. frequency; (b)  $[f_T]^{-1}$  vs.  $[I_E]^{-1}$ .

to be related to the O<sub>2</sub> content of the starting material.

Low-temperature Cl<sub>2</sub> is somewhat more effective than HCl, and improvements in the electrical characteristics of both diodes and bipolar transistors fabricated in SOS resulted from the gettering treatment. Because of the increase in the minority carrier lifetime due to Cl<sub>2</sub> and HCl gettering, bipolar transistors with average current gains of 20 have been produced.

### Acknowledgments

The research reported herein was supported in part by the Air Force Avionics Laboratory, Air Force Systems Command, Wright-Patterson Air Force Base, Ohio, under Contract No. F33615-70-C-1100 and RCA Laboratories, Princeton, New Jersey. The authors would like to thank C. W. Mueller and D. Dumin for interesting discussions; also C. F. Arasim and R. O. Wance for their assistance in this study, and to S. Dierk for editorial assistance. The encouragement of both H. Steenbergen and D. Peacock of the Air Force Avionics Laboratory is highly appreciated.

Manuscript submitted March 31, 1971; revised manuscript received Dec. 8, 1971.

Any discussion of this paper will appear in a Discussion Section to be published in the December 1972 JOURNAL.

### REFERENCES

1. L. M. Nijland and L. J. Van Der Pauw, *J. Elec. Control*, **3**, 391 (1957).
2. A. Goetzberger and W. Shockley, *J. Appl. Phys.*, **31**, 1821 (1960).
3. L. A. Murray and H. Lressel, *Electrochem. Technol.*, **5**, 406 (1967).
4. M. Waldner and L. Sivo, *This Journal*, **112**, 298 (1960).
5. R. N. Hall and J. H. Rocette, *J. Appl. Phys.*, **35**, 379 (1964).
6. J. E. Lawrence, *This Journal*, **112**, 796 (1965).
7. J. D. Struthers, *J. Appl. Phys.*, **27**, 1560 (1956).



8. B. I. Boltaks and I. J. Sosinov, *Z. Tekh. Fiz.*, **28**, 679 (1958).
9. C. T. Sah, R. N. Noyce, and W. Shockley, *Proc. IRE*, **45**, 1228 (1957).
10. K. D. King, Final Report, AF19 (628-303) (1963).
11. S. W. Ing, R. E. Morrison, L. L. Alt, and R. W. Alldrich, *This Journal*, **110**, 533 (1963).
12. E. J. Mets, *ibid.*, **112**, 420 (1965).
13. Y. Tokumaru, *Japan. J. Appl. Phys.*, **2**, 542 (1963).
14. J. E. Lawrence, *Trans. Met. Soc. AIME*, **242**, 484 (1968).
15. F. P. Heiman and P. H. Robinson, *This Journal*, **118**, 141 (1971).
16. B. E. Deal, A. S. Grove, and E. H. Snow, *ibid.*, **114**, 266 (1967).
17. F. P. Heiman, *IEEE Trans.*, **ED-14**, 781 (1967).
18. D. J. Dumin and W. N. Henry, *Met. Trans.*, **2**, 677 (1971).
19. K. H. Zaininger and F. P. Heiman, *Solid State Technol.*, **13**, 49 (1970).
20. D. J. Dumin, *Solid State Electron.*, **13**, 415 (1970).

## Sputtered Cadmium Oxide and Indium Oxide/Tin Oxide Films as Transparent Electrodes to Cadmium Sulfide

R. R. Mehta and S. F. Vogel

International Business Machines Corporation, SDD, San Jose, California 95114

### ABSTRACT

Thin films of cadmium oxide (CdO) and indium oxide/tin oxide ( $\text{In}_2\text{O}_3/\text{SnO}_2$ ) were reactively sputtered from their respective metal or alloy targets. CdO films combine sheet resistances of less than 100 ohms/square with optical transmission greater than 45% for wavelengths greater than 5000Å, and make ohmic contacts with high-resistivity CdS films. Indium oxide/tin oxide films show optical transmission greater than 45% for wavelengths greater than 4000Å and sheet resistances of 100 to 200 ohms/square. Indium oxide/tin oxide also makes useful contacts to CdS films, but reduces the resistivity of the CdS films. A band diagram is proposed which qualitatively explains the ohmic nature of the contacts between two wide bandgap materials.

Recent interest in optoelectronic devices has led to the development of electrode materials which are transparent to light. One application of such materials is the use of transparent electrodes in a ferroelectric/photoconductor storage device (1, 2). Another application is in high-sensitivity photodetectors. There, maximum photocurrents (3, 4) are obtained when the photoconductor is sandwiched between the electrodes and the radiation is incident in the direction of the applied field, and when the thickness of the photoconductor equals the absorption length.

To be useful in high-sensitivity photodevices, the transparent electrode should have sheet resistances no larger than a few hundred ohms/square and maximum possible optical transmission. Also, the transparent electrode must make ohmic contact with the photoconductors.

In the past, thin metal films (e.g., gold, indium), have been used as the transparent electrodes. However, they have the disadvantage of lower transparency for reasonable values of sheet resistance. Some attempts have been made to use metal oxides (e.g., cadmium oxide and indium oxide) as transparent electrodes to photoconductors.

Only limited information about the basic properties of cadmium oxide is available. This is due to the unavailability of large single crystals (5). However, several papers have appeared during the past few years on studies of powdered material, sintered blocks, compressed tablets, or sputtered films (6). Some basic properties are given in the International Tables of Constants and Numerical Data (7). The effects of doping CdO by In and Cu and the effect of reduced oxygen in the reactively sputtered films have been studied by Lakshmanan (8). Electrical transport properties in single-crystal  $\text{In}_2\text{O}_3$  have been discussed by Weiher (9). From high-temperature conductivity measurements, Weiher deduced the bandgap of indium oxide to be 3.1 eV, close to the value of 3.5 eV reported by Rupprecht (10). Recently, Fraser and Cook (11)

reported some measurements on films of indium oxide/tin oxide sputtered from oxide targets.

The first use of  $\text{In}_2\text{O}_3/\text{SnO}_2$  as a transparent electrical contact with a photoconductor (CdS) was reported by Shivonen and Boyd (12). They used 82% indium/18% tin alloy sputtered in oxygen to give a transparent contact on a CdS crystal. Their films were about 200Å thick, had a resistance of 100 to 150 ohms/square, and showed very good transmittance characteristics, i.e., > 80% for  $\lambda > 5000\text{Å}$ . Williams (13) used thin films of  $\text{In}_2\text{O}_3$  as transparent contacts to ZnS crystals. He also prepared  $\text{In}_2\text{O}_3/\text{SnO}_2$  films by sputtering indium/tin alloy (4:1) in oxygen. However, he found that films so deposited had a high concentration of free metal and were opaque. These films had to be further heated in air at 300°-400°C to obtain transparency. The V-I curve measurements by Williams (13) indicated that the  $\text{In}_2\text{O}_3/\text{SnO}_2$  films made ohmic contacts to ZnS crystals.

Our paper deals with the properties of CdO and  $\text{In}_2\text{O}_3/\text{SnO}_2$  films deposited by reactive sputtering. Deposition conditions, such as the gas, the pressure, and the substrate temperature, are varied. Optical and electrical properties of these films are studied as a function of the deposition conditions. The quality of the contact to high resistivity ( $> 10^7$  ohm-cm) thin polycrystalline films of CdS is investigated. Substrate and post-heat-treatment temperatures are kept below approximately 350°C to avoid diffusion of Cd or In from the oxide films into CdS.

### Deposition of the CdO and $\text{In}_2\text{O}_3/\text{SnO}_2$

Two kinds of transparent electrodes were deposited by reactive sputtering of two metal targets: cadmium (14) and 82 In/18 Sn (12, 13).

The sputtering system was a diode-type MRC<sup>1</sup> Model SM8500 sputtering module mounted on a Norton-NRC<sup>2</sup> diffusion-pumped vacuum system Model 3116.

<sup>1</sup> MRC-Materials Research Corporation, Orangeburg, New York 10962.

<sup>2</sup> Norton-NRC: Now a division of Varian Associates, Palo Alto, California 94304.

Key words: transparent electrodes, cadmium oxide films, indium oxide/tin oxide films, cadmium sulfide films, reactive sputtering.

With a circular target (cathode) 5 in. in diameter, a cathode-substrate distance between 1 and  $1\frac{1}{2}$  in. was chosen. A magnetic field of 100 gauss produced by coils around the cathode and anode concentrated the discharge and caused relatively high deposition rates with an rf power of 200W. Substrates of Pyrex glass and tin oxide coated glass (NESA, Corning 9753) with a thin photoconductive film of CdS were placed on the heated anode. The substrate temperature was an important parameter in determining the resistivity of the films; therefore, temperature was measured directly with a fine-wire thermocouple on the surface of the substrate.

Naturally, the metal targets can be sputtered with d-c power; most indium oxide/tin oxide films were deposited with a d-c voltage of around 1.5 kV and a discharge current around 70 mA. However, sputtering with radio-frequency power (13.56 MHz) was preferred, because it allowed the use of lower gas pressures in the development stages of the work. When rf power of 200W was applied, the target assumed a self-bias of typically 1000V.

A pure oxygen atmosphere ranging in pressure from 6 to 200  $\mu$  was initially used for the sputtering of CdO. Later, an improvement in the optical transparency was obtained when an oxygen/nitrogen mixture was used. As little as 2% oxygen in nitrogen at a total gas pressure of 100  $\mu$  caused completely reactive sputtering and led to the best results with CdO. However, the  $\text{In}_2\text{O}_3/\text{SnO}_2$  films were finally sputtered only in pure oxygen; 50/50 oxygen/nitrogen and oxygen/argon mixtures caused higher electrical resistances in the films.

CdO and  $\text{In}_2\text{O}_3/\text{SnO}_2$  films differed appreciably in their deposition rates at otherwise equal conditions. CdO showed a rate of about 200 Å/min when sputtered in pure oxygen and 130 Å/min when sputtered in the oxygen/nitrogen mixture. Deposition times of 10 min (pure oxygen sputtering) were required to form films of satisfactory sheet resistances. The deposition rate of the  $\text{In}_2\text{O}_3/\text{SnO}_2$  films was six times lower. Correspondingly, the deposition times were 1 hr.

After the deposition, some films were heat-treated at approximately 340°C on a hot plate for 1 hr in air. Such treatment not only reduced the electrical resistivity but also increased the optical transmission of the oxide films.

### Experimental Results

**Optical and electrical properties of CdO films.**—Table I gives thickness, optical transmission, electrical sheet resistance, resistivity, and estimated electron density of CdO films prepared under various deposition conditions. Curves 1 and 2 in Fig. 1 show transmission as a function of wavelength for two representative films, one sputtered in 100%  $\text{O}_2$  atmosphere and the second prepared with 2.5%  $\text{O}_2$  in  $\text{N}_2$  atmosphere.

These data were measured on a Cary 14 spectrophotometer. As previously reported (15), the films sput-

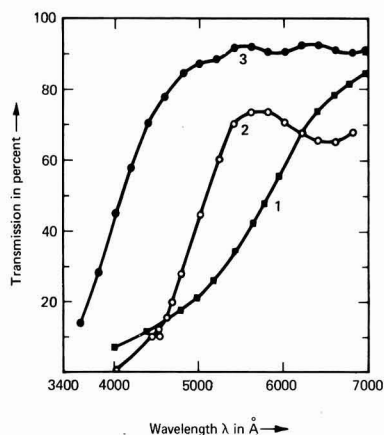


Fig. 1. Spectral transmittance of CdO and  $\text{In}_2\text{O}_3/\text{SnO}_2$  films. Curve 1 is for CdO film No. 91 sputtered in 100%  $\text{O}_2$  ambient; curve 2 is for CdO film No. 144 sputtered in 2.5%  $\text{O}_2$  in  $\text{N}_2$  ambient; curve 3 is for  $\text{In}_2\text{O}_3/\text{SnO}_2$  film No. 214 C-1. Details of preparation are in Tables I and II.

tered in 2%  $\text{O}_2$  in  $\text{N}_2$  have higher transmission for shorter wavelengths. The thickness measurements on these films were made with a Sloan<sup>3</sup> angstrometer which works on the principle of multiple beam interferometry. Sheet resistance measurements were made with a four-point probe. The mobility of electrons is assumed to be 120  $\text{cm}^2/\text{V}\cdot\text{sec}$  (7), and the calculated value of electron concentration is listed in Table I. These values are very close to the values given by Lakshmanan.

**Contact properties of CdO to CdS films.**—A cadmium sulfide (CdS) film is deposited by a chemical spray process (16). In this process, a solution of cadmium acetate is mixed with a solution of thiourea to form a soluble complex. This soluble complex is directed in the form of a finely atomized spray to the surface of a heated substrate where it is decomposed to form a film of cadmium sulfide.

The substrate was a tin oxide (NESA) coated glass slide. The conducting coating of tin-oxide acted as a base (or bottom) electrode. CdO spots having an area  $\sim 10^{-2} \text{ cm}^2$  were deposited on the CdS film. Deposition conditions were the same as for sample 144 listed in Table I, except deposition time was half that for sample 144. Indium metal spots of the same size area were deposited near the CdO spots, so that their contact quality could be compared. The V-I characteristics are always measured between the top electrode (CdO or In) and bottom tin-oxide (NESA) electrode. The measured V-I curves when the sample is illuminated

<sup>3</sup> Sloan Instrument Corporation, Santa Barbara, California.

Table I. Details of preparation, optical and electrical properties of cadmium oxide films

Sample Number	Conditions of film deposition and subsequent heat-treatment	Thickness of films, Å	Optical transmission in % at wavelength			Sheet resistance of films, ohms per square	Resistivity of films, ohm-cm	Electron concentration in films assuming (7) $\mu = 120 \text{ cm}^2/\text{V}\cdot\text{sec}$
			4000Å	5000Å	6000Å			
91	60 $\mu$ $\text{O}_2$ pressure; sputtering time of 10 min; heat-treated at 340° and 400°C for 1 hr each	2260	6.8	25.2	71.9	62.0	$1.40 \times 10^{-3}$	$3.72 \times 10^{19}$
98	100 $\mu$ $\text{O}_2$ pressure; sputtering time of 10 min; heat-treated at 100°C for 1 hr in air	1740	2.5	10.8	59.0	26.0	$4.52 \times 10^{-4}$	$1.15 \times 10^{20}$
102	100 $\mu$ $\text{O}_2$ pressure; sputtering time of 10 min; substrate temp 205°C; heat-treated in air for 1 hr at 340° and 400°C	1770	13.6	44.4	74.0	82.0	$1.45 \times 10^{-3}$	$3.60 \times 10^{19}$
140	100 $\mu$ $\text{O}_2$ in $\text{N}_2$ pressure; sputtering time of 10 min; max substrate temp 270°C	1220	1.2	40.0	66.0	43.0	$5.75 \times 10^{-4}$	$9.90 \times 10^{19}$
144	100 $\mu$ $\text{O}_2$ in $\text{N}_2$ pressure; sputtering time of 10 min; max temp 240°C	1275	1.2	44.4	70.8	29.0	$3.7 \times 10^{-4}$	$1.41 \times 10^{20}$

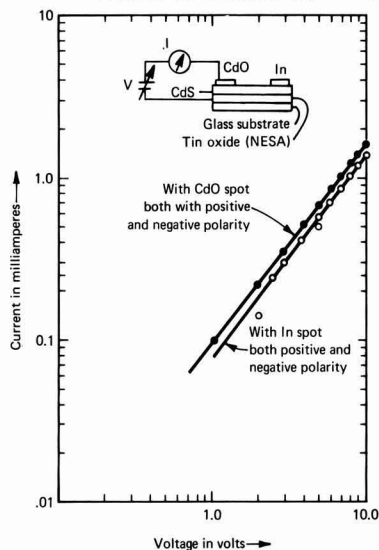


Fig. 2. Current-voltage characteristics under illumination for CdO and In spots on CdS film which is on tin oxide-coated glass substrate (NESA). Sample is illuminated through the glass substrate. Measurement configuration is also indicated.

through the glass substrate for the CdO and In spots for both polarities are shown in Fig. 2. The slope of these curves is practically constant for both polarities and both CdO and In spots. This suggests that contact quality is equally good for CdO and In, and the linearity of the curves suggests that the contacts are ohmic under the examination conditions.

A further test on this sample was carried out with the measurement of the spectral response of the photoconductor, with light incident through the NESA-coated glass substrate and through the CdO electrode. The results are depicted in Fig. 3. As expected for  $\lambda < 5000\text{\AA}$ , the photocurrent is about a factor of 2 smaller for light incident through the CdO spot. For  $\lambda > 5000\text{\AA}$ , the photocurrent is smaller by only a factor of 1.7. In this wavelength region, CdO serves as a reasonable contact to the CdS film. In the dark, there does not seem to be any change in the film resistivity as a result of CdO deposition and postdeposition heat-treatment.

**Optical and electrical properties of  $\text{In}_2\text{O}_3/\text{SnO}_2$  films.**—Table II gives the conditions of film deposition and subsequent heat-treatment, thickness, optical transmission, sheet resistance, and resistivity of  $\text{In}_2\text{O}_3/\text{SnO}_2$  films. From the table it is clear that films deposited at  $300^\circ\text{--}350^\circ\text{C}$  and subsequently heat-treated at  $340^\circ\text{C}$  in air combine low resistivity with high optical transmittance. There does not seem to be a dramatic difference in films produced by either d-c or rf sputtering. In general, higher substrate temperatures favor the lower sheet resistance and higher transmission. Curve 3 in Fig. 1 shows a transmission of film 214 C-1 as a function of wavelength.

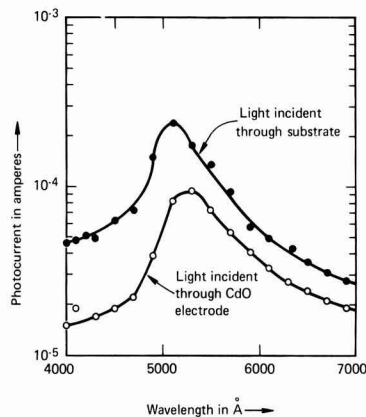


Fig. 3. Photoconductivities (constant intensity) of CdO spots on chemically sprayed CdS film, one with light incident through the contact and the other with light through the glass substrate with NESA coating. The applied voltage is 5V in both cases. Incident photon flux is about  $10^{15}$  photons/cm<sup>2</sup> sec.

**Contact properties of  $\text{In}_2\text{O}_3/\text{SnO}_2$  on CdS films.**—Again, the contact properties of  $\text{In}_2\text{O}_3/\text{SnO}_2$  films were evaluated in conjunction with the CdS film. Electrodes of  $10^{-2}$  cm<sup>2</sup> area were sputtered through a mask on the same kind of chemically sprayed CdS film mentioned before, which was an a NESA-coated glass substrate; NESA formed the bottom electrode for photoconductivity measurements. On the same films, In metal electrodes of the same area were evaporated between the  $\text{In}_2\text{O}_3/\text{SnO}_2$  electrodes. This electrode arrangement permitted a direct comparison of contact quality of  $\text{In}_2\text{O}_3/\text{SnO}_2$  and In to CdS film. The V-I characteristics are always measured between the top electrode ( $\text{In}_2\text{O}_3/\text{SnO}_2$  or In) and the bottom tin oxide (NESA) electrode.

Figure 4 shows the V-I plot for this film under a photon flux density of  $10^{15}/\text{cm}^2$  sec. Curves 1 and 2 show the current through the sample as a function of voltage with light incident through the  $\text{In}_2\text{O}_3/\text{SnO}_2$  electrode for positive and negative applied voltages, respectively. Curves 3 and 4 show the current through the sample vs. voltage when the light is shining through the NESA for both polarities of voltage. The difference in currents for curves 1-2 and 3-4 is due to a difference in light absorption (and reflection) in the indium oxide/tin oxide films on one side and in the tin-oxide coated glass substrate in the other side of the photoconductor. These curves have a constant slope reasonably close to unity, suggesting that current is proportional to voltage. The difference between the current in positive and negative polarities for curves 1-4 is small; the reason for this difference is not understood at the present time. Curve 5 shows current through the CdS film as a function of voltage for an In metal electrode when light is shining through the tin-oxide coated glass substrate. The higher current for curves 3 and 4 compared to 5 can be interpreted

Table II. Details of preparation, optical and electrical properties of indium oxide/tin oxide films

Sample Number	Conditions of film deposition and subsequent heat-treatment	Thick-ness, Å	% Transmission at $\lambda$		Sheet resist-ance, ohms per square	Resistivity of films, ohm-cm
			5000Å	7000Å		
181 A-1	60 $\mu$ , O <sub>2</sub> ; d-c 1.6 kV; 95 mA; 1:09 hr; 370°C substrate temp; 340°C for 1 hr in air	—	95	89	72	—
181 B	Same conditions as 181 A-1 except no heat-treatment	1880	98	91	150	2.82 $\times 10^{-3}$
191 A	100 $\mu$ O <sub>2</sub> rf; 150W (indicated); 290°C substrate temp; no heat-treatment	4600	81	91	210	9.66 $\times 10^{-3}$
191 B-1	Same conditions as 191 A; heat-treated in air at 340°C for 1 hr	3720	83	98	93	3.46 $\times 10^{-3}$
213 E	60 $\mu$ , O <sub>2</sub> ; 400W; 1:30 hr dep. time; max substrate temp 371°C	—	86	90	195	—
213 C-1	Same as 213 E; heat-treated in air for 1 hr at 343°C	—	91	94	110	—
214 E	60 $\mu$ O <sub>2</sub> ; 400W; 1:30 hr dep. time; max temp 377°C	—	85	90	80	—
214 C-1	Same as 214 E; heat-treated in air for 1 hr at 343°C	—	93	54	88	—

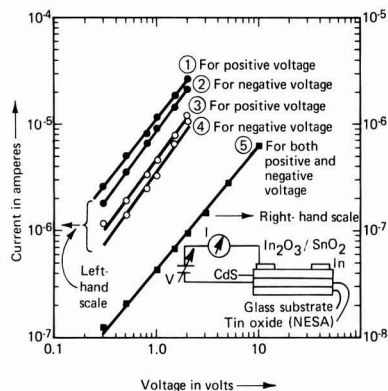


Fig. 4. Current-voltage characteristics under illumination for a CdS film which is on NESA-coated glass substrate and having both  $\text{In}_2\text{O}_3/\text{SnO}_2$  (sample No. 214 C-1) and In as top electrodes. Incident flux for all three sets of curves is  $10^{15}$  photons/cm<sup>2</sup>/sec. Curves 1 and 2 are for an  $\text{In}_2\text{O}_3/\text{SnO}_2$  spot with light incident through the top electrode. Curves 3 and 4 are for the  $\text{In}_2\text{O}_3/\text{SnO}_2$  spot with light incident through bottom electrode of NESA. Curve 5 is for In spot with light incident through NESA. For curves 1-4 refer to the current scale on the left. For curve 5 refer to the current scale on the right.

possibly in terms of a sensitization effect resulting from doping of the CdS by In during the sputtering and heat-treatment of indium oxide/tin oxide. This effect is similar to that reported by Shivanon and Boyd (12).

This hypothesis of sensitization is further confirmed by measuring the dark current for both  $\text{In}_2\text{O}_3/\text{SnO}_2$  and In electrodes (Fig. 5). For  $\text{In}_2\text{O}_3/\text{SnO}_2$  the dark currents are almost an order of magnitude larger than those obtained for In electrodes, suggesting doping by In and consequently a reduction in resistivity of the film. The In doping for  $\text{In}_2\text{O}_3$  electrodes results from heat-treatment performed during and after deposition to obtain desired optical transmittance and sheet resistance. However, in the case of In electrodes, no heat-treatment is performed during or after evaporation of In. As a result, the film resistivity is unchanged. The difference between V-I curves for positive and negative polarities in the case of  $\text{In}_2\text{O}_3/\text{SnO}_2$  suggests

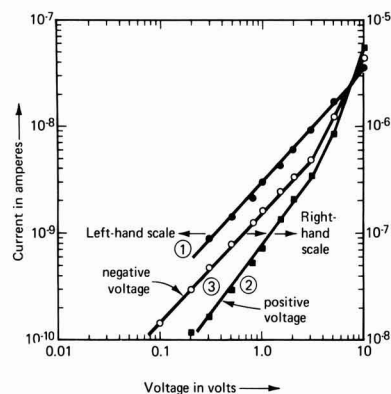


Fig. 5. Current-voltage characteristics in the dark for CdS films having electrodes of both  $\text{In}_2\text{O}_3/\text{SnO}_2$  and In. Curve 1 is for both positive and negative voltages with In electrode. Curve 2 is for  $\text{In}_2\text{O}_3/\text{SnO}_2$  electrode for positive applied voltages and also for  $\text{In}_2\text{O}_3/\text{SnO}_2$  electrode for negative applied voltages. For curve 1 refer to current scale on the left, and for curves 2 and 3 refer to the scale on the right.

a barrier at the interface when no illumination is incident.

To summarize,  $\text{In}_2\text{O}_3/\text{SnO}_2$  gives ohmic contact to CdS under illumination. However, for these  $1\mu$  thick CdS films, deposition of the transparent electrodes results in some In doping of the CdS films. This causes the CdS films to have lower dark resistivity.

### Discussion—Band Model

From the above-illustrated measurements it is clear that CdO and  $\text{In}_2\text{O}_3/\text{SnO}_2$  produce ohmic contact with CdS under present conditions of measurement. Little is known about the interface between wide bandgap materials like  $\text{In}_2\text{O}_3/\text{SnO}_2$  and CdS. The junction between these two materials is a heterojunction. As a simple extension of the Kroger *et al.* (17) model for ohmic contact of a metal to a semiconductor, we propose a model for ohmic contact of heavily doped, wide bandgap material to an undoped, narrower bandgap material. This model is illustrated in Fig. 6. An ohmic contact is brought about by a rather thin layer (region III) of highly conducting (strongly n-type) material in the photoconductor adjacent to the electrode (region IV). This heavily doped n-type layer in the case of the CdO contact is produced by diffusion of Cd into CdS. For the  $\text{In}_2\text{O}_3/\text{SnO}_2$ , the heavily doped n-type layer is produced by the diffusion of In into CdS. Between the highly conducting part of CdS and the electrode, there may exist an exhaustion barrier (layer II) which, due to the presence of such a strongly conducting layer, is so thin that electrons may easily tunnel through it. The region of strongly conducting CdS acts as a supply of electrons for the highly resistive bulk (region IV), and the whole system acts ohmic when an electric field is applied.

### Conclusions

The transparent electrode material for an electro-optic device can have a sheet resistance as high as a few hundred ohms per square. From the measurements reported here, it appears that resistances in this range can be readily achieved in sputtered cadmium or indium oxide/tin oxide films. CdO is a better material for making ohmic contact than  $\text{In}_2\text{O}_3/\text{SnO}_2$  because it does not reduce the resistivity of the thin CdS film.

However, the optical transmission properties of CdO on CdS are less desirable compared to those of  $\text{In}_2\text{O}_3/\text{SnO}_2$ . Since CdO has an optical transmittance greater than 70% for wavelengths of 6000Å, it may form a better transparent contact to Cd(S, Se) or CdSe, with absorption edges at wavelengths longer than 6000Å. In general, the transparent electrode requirements for an electrooptic device may be met by films of either cadmium oxide or indium oxide/tin oxide.

### Acknowledgments

The authors wish to thank D. E. Hill who assisted with the sputtering runs, and J. L. Wolf for making

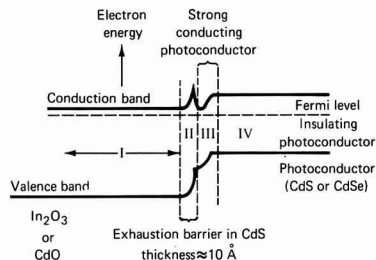


Fig. 6. Proposed band model of an ohmic contact between highly resistive n-type bulk material IV and a highly conducting transparent metal oxide electrode I. Region III is a thin layer of strongly n-type semiconductor, and region II is an exhaustion barrier due to the difference in work function between electrode I and material III.

the thickness, optical, and electrical measurements. The authors are indebted to Mr. D. W. Chapman for his encouragement throughout this work and for giving helpful suggestions on the manuscript.

Manuscript submitted Aug. 3, 1971; revised manuscript received Dec. 6, 1971.

Any discussion of this paper will appear in a Discussion Section to be published in the December 1972 JOURNAL.

#### REFERENCES

1. A. H. Meitzler, J. R. Maldonado, and D. B. Fraser, *Bell System Tech. J.*, July/August, p. 953 (1970).
2. S. A. Keneman, G. W. Taylor, A. Miller, and W. H. Fonger, *Appl. Phys. Letters*, **17**, No. 4, 173 (1970).
3. G. W. White, *Phil. Mag.*, **27**, 370 (1974).
4. Y. T. Shvonen and D. R. Boyd, *Bull. Am. Phys. Soc.*, **5**, 105 (1960).
5. R. Haul and D. Lust, *J. Appl. Phys. Suppl.*, **33**, No. 1, 487 (1962).
6. J. S. Preston, *Proc. Roy. Soc.*, **449** (1950); C. Helwig, *Z. Physik*, **132**, 621 (1952); L. Holland and G. Siddal, *Vacuum*, **11**, No. 4, 375 (1953); V. K. Miloslavskii and A. I. Ranyuk, *Soviet Optics and Spectroscopy*, **536** (1960); F. Lappe, *Z. Physik*, **137**, 380 (1954); R. W. Wright, *Proc. Phys. Soc.*, **64A**, 350 (1951); R. W. Wright and J. A. Bastin, *This Journal*, **71**, 109 (1958).
7. "International Tables of Constants and Numerical Data," **12**, Pergamon Press (1961).
8. T. K. Lakshmanan, *This Journal*, **110**, 548 (1963).
9. R. L. Weiher, *J. Appl. Phys.*, **33**, 2834 (1962).
10. G. Rupprecht, *Z. Physik*, **139**, 504 (1954).
11. D. B. Fraser and H. D. Cook, Paper 29 presented to Electrochemical Soc. Meeting, May 1971.
12. Y. T. Shvonen and D. R. Boyd, *Rev. Sci. Instr.*, **31**, 992 (1960).
13. V. A. Williams, *This Journal*, **113**, 234 (1966).
14. L. Holland, "Vacuum Deposition of Thin Films," Chapman and Hall (1961).
15. J. Stuke, *Z. Physik*, **137**, 401 (1954).
16. R. R. Chamberlin and J. S. Skarman, *This Journal*, **113**, 86 (1966).
17. F. A. Kroger, G. Diemer, and H. A. Glassens, *Phys. Rev.*, **105**, 297 (1956).

## Coprecipitation of $\text{Ga}_2\text{O}_3$ in the Liquid-Phase Epitaxial Growth of GaP

M. Kowalchik, A. S. Jordan, and Mildred H. Read

Bell Telephone Laboratories, Incorporated, Murray Hill, New Jersey 07974

#### ABSTRACT

Coprecipitation of  $\beta\text{-Ga}_2\text{O}_3$  has been observed in O-doped GaP epitaxial films grown by liquid-phase epitaxy under isothermal conditions at an average growth temperature of  $\sim 1040^\circ\text{C}$ . The coprecipitation seems to be independent of cooling rate and of the source of O [ $\text{Ga}_2\text{O}_3$  powder, bulk  $\text{Ga}_2\text{O}_3$ , or glassy  $\text{Zn}(\text{PO}_3)_2$ ]. The coprecipitation of  $\beta\text{-Ga}_2\text{O}_3$  could be prevented either by imposing a temperature gradient over the ampoule (to enhance vapor transport via  $\text{Ga}_2\text{O}$ ) or by reducing the amount of O added to the Ga-rich solution in an isothermal system to  $\sim 2.5 \times 10^{-2}$  a/o (atom per cent). The latter result is interpreted as giving the solubility at  $\sim 1040^\circ\text{C}$  of  $\text{Ga}_2\text{O}_3$  in Ga saturated with GaP and is used to obtain an estimate of the eutectic valley in the ternary Ga-P- $\text{Ga}_2\text{O}_3$  system.

GaP red light-emitting diodes (LED's) have become devices of technological importance in the last decade. The early work of Starkiewicz and Allen (1) demonstrated that the presence of both Zn and O as dopants in the GaP crystals is needed for the generation of red light at room temperature. In the case of solution growth (SG) (2, 3) and sealed-tube liquid-phase epitaxy (LPE) (4, 5), the concentration of Zn added to the Ga-P solutions by different investigators to maximize the electroluminescent or photoluminescent efficiency varies from 0.03 (5) to 0.14 a/o (atom per cent) (4). Because of vaporization losses the Zn additions in open-tube LPE (6, 7) are higher [0.15 (7) to 0.20 a/o (6)]. At these Zn concentrations in the Ga-P solutions the resulting crystals are expected to contain (8) Zn at concentrations less than  $10^{18} \text{ cm}^{-3}$  (at a typical growth temperature of  $\sim 1040^\circ\text{C}$ ); hence, the deleterious effect of Auger recombination (9) on efficiency is avoided.

However, the doping requirements for maximizing the efficiency by means of O additions (in the form of  $\text{Ga}_2\text{O}_3$ ) are less well understood. In particular, in open-tube LPE "best" devices have been reported for 0.15 (7) and 0.4 a/o O (6). In sealed-tube growth (SG or LPE) maximum efficiencies have been found over a surprisingly wide range of O additions, specifically between 0.03 (2) and 1.05 a/o O (5). The solubility of  $\text{Ga}_2\text{O}_3$  in liquid Ga (10) is only  $\sim 0.03$  a/o O at

$\sim 1040^\circ\text{C}$ ; hence, the reasons for much exceeding this solubility limit in closed-tube LPE systems were not immediately obvious.

The initial objective of this study is to explain the disparate results on the O-doping of GaP. In the next section it is shown that in a nonisothermal, closed-tube LPE system the loss of O from the tipping solution via the vaporization of  $\text{Ga}_2\text{O}$  is responsible for the high optimum O concentration (5), exceeding the solubility limit (10). Our experiments demonstrate that when more than  $\sim 0.025$  a/o O is added to the Ga-P solution in an isothermal, sealed-tube LPE growth system at  $\sim 1040^\circ\text{C}$ , coprecipitation of  $\text{Ga}_2\text{O}_3$  takes place along with the GaP epitaxial growth. The major objective of this study is to identify, characterize, and explain these precipitates. In particular, the coprecipitation of  $\text{Ga}_2\text{O}_3$  with GaP (or its absence in a nonisothermal system) is shown to be consistent with thermodynamic information for the Ga- $\text{Ga}_2\text{O}_3$  binary system. Moreover, by interpreting the coprecipitation results by means of a ternary phase diagram, the oxygen concentration along the eutectic valley in the Ga-P- $\text{Ga}_2\text{O}_3$  system is estimated.

#### Experimental Procedure and Results

The usual LPE growth of GaP by Nelson's method (11) involves a cooling rate of approximately  $10^\circ\text{C}/\text{min}$ . To achieve such a relatively large cooling rate many LPE systems utilize furnaces with a small thermal mass which do not possess an isothermal zone



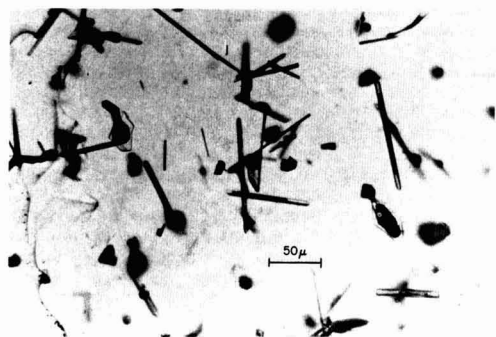
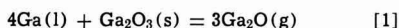


Fig. 1. Transmission photomicrograph of needle-shaped  $\beta\text{-Ga}_2\text{O}_3$  precipitates in the GaP matrix grown from a solution containing 1.05 a/o O (added as  $\text{Ga}_2\text{O}_3$ ) and 0.05 a/o Zn. The solution was cooled from  $\sim 1050^\circ\text{C}$  to  $\sim 600^\circ\text{C}$  at a rate of  $\sim 10^\circ\text{C}/\text{min}$ .

over the entire length of the ampoule used for crystal growth. It has been found (12) for a small thermal mass furnace with a viewing port (typical of those used to make efficient LEDs) that there may be a decrease in temperature of about  $25^\circ\text{C}$  between the Ga-rich melt and the seal-off area (4) at a nominal LPE growth temperature of  $\sim 1040^\circ\text{C}$ . Because of the reversible reaction of Ga and  $\text{Ga}_2\text{O}_3$  to produce  $\text{Ga}_2\text{O(g)}$  according to



a temperature difference causes a drop in the equilibrium partial pressure of  $\text{Ga}_2\text{O(g)}$  (20 Torr for a temperature difference of  $25^\circ\text{C}$  at  $\sim 1040^\circ\text{C}$ ) (13, 14). The reversible nature of this reaction is demonstrated by the observed condensation of  $\text{Ga}_2\text{O}_3$  and Ga at the cool (seal) end of the capsule during an LPE run.

In order to minimize the loss of  $\text{Ga}_2\text{O}_3$  via this vapor transport, all the experiments reported herein have been conducted in nearly isothermal furnaces. In the initial phase of this study a furnace (without a viewing port) with a  $\sim 4^\circ\text{C}$  difference along the sealed capsule was used. The 10 cm long quartz capsule, similar in construction to capsules described by previous workers (4, 5), enclosed a quartz boat which contained the GaP substrate at one end, near the seal-off plug, and the solution of Ga-GaP-dopants<sup>1</sup> at the other end. The plug serving as the seal was placed tightly against the boat, after evacuation to  $10^{-6}$  Torr, to minimize the capsule volume.

In a typical run the sealed ampoule, containing the substrate and solution doped with 1.05 a/o O added as  $\text{Ga}_2\text{O}_3$  and 0.05 a/o Zn [serving as a reference dopant concentration in comparison with published values (5)], was heated to  $1065^\circ\text{C}$  and held for 30 min to achieve saturation. An LPE layer was then grown by tipping the furnace and capsule assembly at  $1050^\circ\text{C}$  and cooling at a rate of  $\sim 10^\circ\text{C}/\text{min}$  to  $600^\circ\text{C}$ . By monitoring thermocouples attached to either end of the capsule, it was determined that the temperature difference was minimal (less than  $4^\circ\text{C}$  in this series of experiments) throughout the LPE cycle. After completing a run, excess  $\text{Ga}_2\text{O}_3$  was found only on the top of the solution, indicating negligible vapor transport. Examination of the typically  $\sim 50\ \mu\text{m}$  thick epitaxial layer by optical reflection and transmission microscopy disclosed the presence of a needle-like second phase embedded in the GaP matrix. In Fig. 1 we show a transmission photomicrograph of this second phase in the LPE layer. Note that the thin needles are found at all levels between surface and growth interface and

are occasionally as long as  $100\ \mu\text{m}$ . That the needles are not an etching artifact due to reaction of the GaP with  $\text{HNO}_3$ , frequently used to digest the Ga, is shown by the fact that they are also seen without etching. Additional experiments have shown that an undoped or a Zn-doped solution did not result in needles in the LPE layer but a solution doped with  $\text{Ga}_2\text{O}_3$  alone (1.05 a/o O) did. Moreover, when a sharp temperature gradient was imposed along the capsule, by extending the length of the ampoule with a quartz spacer placed between the end of the boat and the seal and cooling with a stream of  $\text{N}_2$ , no needles were observed in the LPE layer, even at 1.05 a/o O additions. Not unexpectedly, after this run a mixture of Ga droplets and  $\text{Ga}_2\text{O}_3$  was found on the seal and no excess  $\text{Ga}_2\text{O}_3$  appeared on the surface of the Ga solution.

Microscopic examination of the as-received  $\text{Ga}_2\text{O}_3$  powder at 800X showed a few needles, 5-10  $\mu\text{m}$  long. These needles were similar in shape although not in size to the ones found in the LPE layers. This similarity strongly suggested that precipitation of the monoclinic, high-temperature  $\beta$  form of  $\text{Ga}_2\text{O}_3$  had occurred in the epitaxial films. The precipitates were conclusively identified by a wide-film, modified, Debye-Scherrer x-ray diffraction method (15). With the flat LPE layer and substrate stationary at  $16^\circ$  to the beam, an x-ray photograph of the epitaxial film was generated. A typical photograph (Fig. 2) for a run with 1.05 a/o O addition shows the curved lines of polycrystalline  $\beta\text{-Ga}_2\text{O}_3$  superimposed on the single-crystal GaP pattern. In addition, an examination of the  $\beta\text{-Ga}_2\text{O}_3$  precipitate-rich layer by the Direct Image Mass Analyzer (DIMA) (16) exhibits a strong O-signal when sputtered in an oxygen beam. As viewed by the DIMA, a  $\beta\text{-Ga}_2\text{O}_3$  needle is represented by a bright elongated image which is much more intense than the background O signal detected from the GaP matrix.

After this positive identification of  $\beta\text{-Ga}_2\text{O}_3$  precipitates, a number of changes were made in the experimental apparatus and procedure. In place of the conventional quartz tipping boat, we utilized a slider (17) assembly, fabricated from  $\text{Al}_2\text{O}_3$  (G.E.-Lucalox). It was anticipated that the use of  $\text{Al}_2\text{O}_3$  would eliminate the observed reaction between Ga and quartz to form  $\text{Ga}_2\text{O(g)}$  (13). In addition, a new furnace with a variation of only  $1^\circ\text{C}$  over the capsule was introduced. Figure 3 is a schematic of the quartz sealed assembly, located in the isothermal zone of the furnace. As in the earlier experiments, the Ga-rich solution, here contained in an opening cut through the moving slider, was tipped onto the GaP substrate. With the slider, however, growth could be terminated at will at any temperature by tipping the slider to its



Fig. 2. X-ray photograph of precipitates and matrix. Note the spotty curved lines of polycrystalline  $\beta\text{-Ga}_2\text{O}_3$  superimposed on the monocrystalline GaP pattern.

<sup>1</sup> The source materials used for these experiments were phosphine-grown polycrystalline GaP (Monsanto),  $\text{Ga}_2\text{O}_3$  powder (Alusuisse), and Zn (United Minerals), all with 99.999% nominal purity. The n-type GaP substrates, cut from liquid encapsulation Czochralski (LEC) grown ingots, were mechanically polished on the phosphorus (B) face.

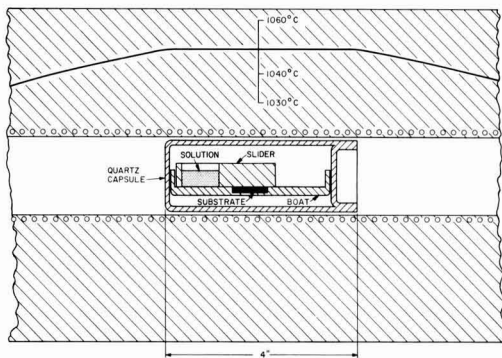


Fig. 3. Slider assembly and its relation to the temperature profile of the furnace (schematic). The slider and boat are made of  $\text{Al}_2\text{O}_3$  (G.E.-Lucalox).

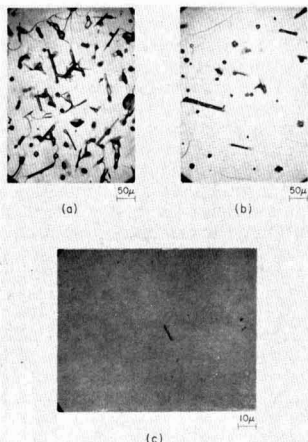


Fig. 4. Effect of decreasing  $\text{Ga}_2\text{O}_3$  additions to the solution on the density of  $\beta\text{-Ga}_2\text{O}_3$  precipitates. The transmission photomicrographs (a), (b), and (c) correspond to 0.45, 0.075, and 0.03 a/o O additions, respectively. All three crystals were grown by cooling the solution from  $\sim 1050^\circ$  to  $1035^\circ\text{C}$  at a rate of  $1^\circ\text{C}/\text{min}$ .

initial position, resulting in the removal of the excess solution from the substrate.

In this manner GaP LPE layers were grown, with 0.45, 0.075, and 0.03 a/o O additions as  $\text{Ga}_2\text{O}_3$  to the solution, between  $1050^\circ$  and  $1035^\circ\text{C}$  at a cooling rate of  $1^\circ\text{C}/\text{min}$ . Transmission micrographs of these crystals (Fig. 4) show a strong reduction in the concentration of  $\beta\text{-Ga}_2\text{O}_3$  precipitates with decreasing  $\text{Ga}_2\text{O}_3$  additions to the solution. The precipitates completely disappear, as viewed at  $800\times$ , between 0.027 and 0.021 a/o O additions to the solution.

Experiments performed by cooling from  $1050^\circ$  to  $1020^\circ\text{C}$  at a rate of  $2^\circ\text{C}/\text{min}$  also resulted in  $\text{Ga}_2\text{O}_3$  precipitation, demonstrating that the precipitation is apparently unaffected by cooling rate between  $1^\circ$  and  $10^\circ\text{C}/\text{min}$ . It should be noted that when the solution was cooled to  $1020^\circ\text{C}$  even an O addition of only 0.025 a/o gave rise to a few precipitates. Finally, we changed the source of O from  $\text{Ga}_2\text{O}_3$  powder to bulk  $\text{Ga}_2\text{O}_3$  or glassy  $\text{Zn}(\text{PO}_3)_2$  (18). Both of these additions to the Ga-GaP solution yielded precipitates.

### Discussion

The presence of precipitates in GaP is not unique among III-V compounds. For example, Eckhardt (19)

has observed precipitates of  $\alpha\text{-Ga}_2\text{O}_3$  [the low-temperature form (20)] less than  $3\text{ }\mu\text{m}$  in size in Czochralski- and Bridgman-grown GaAs. Recently, Kressel *et al.* (21) have identified by electron diffraction  $\text{Ga}_2\text{Te}_3$  precipitates in GaAs which they attributed to precipitation from solid solution. However, several observations indicate that the  $\beta\text{-Ga}_2\text{O}_3$  second phase in the GaP LPE layers is not the result of solid-state precipitation. First, as seen in Fig. 1, there is no distinct orientation relationship between the precipitates and the matrix. Second, the precipitates are obviously too large to originate from a supersaturated solid solution. Third, precipitates were observed in epitaxial layers grown by relatively slow cooling rates in the narrow temperature range tipping experiments ( $1^\circ\text{C}/\text{min}$ ,  $1050^\circ\text{-}1035^\circ\text{C}$ ;  $2^\circ\text{C}/\text{min}$ ,  $1050^\circ\text{-}1020^\circ\text{C}$ ), wherein the excess Ga solution was removed from the film prior to withdrawal from the furnace. It is unlikely that the rate of solid-solution precipitation is rapid enough to account for the formation of precipitates in these experiments, since precipitation would have to take place during the short time required to cool the crystal to room temperature.

Therefore, it is concluded that the  $\beta\text{-Ga}_2\text{O}_3$  precipitates are the consequence of the coprecipitation of  $\text{Ga}_2\text{O}_3$  with GaP from a Ga-rich solution supersaturated with respect to both  $\text{Ga}_2\text{O}_3$  and GaP. Thus, the tipping experiments conducted between  $1050^\circ$  and  $1035^\circ\text{C}$ , showing that the precipitates completely disappear between 0.027 and 0.021 a/o O additions, can be interpreted as giving the solubility of O in liquid Ga also saturated with GaP to be  $\sim 0.025$  a/o O at  $\sim 1040^\circ\text{C}$ . Hence, when O is added to the tipping solution in excess of  $\sim 0.025$  a/o in a sealed isothermal system at a mean growth temperature of  $\sim 1040^\circ\text{C}$ , the presence of precipitates in the epitaxial film results from supersaturation with respect to two solid phases. Conversely, the absence of precipitates in GaP grown in a nonisothermal system indicates that the solution became unsaturated due to the loss of excess oxide via  $\text{Ga}_2\text{O}_3(\text{g})$  transport according to Eq. [1].

The coprecipitation can be more readily discussed in terms of a schematic ternary liquidus isotherm at  $\sim 1040^\circ\text{C}$  for the Ga-P- $\text{Ga}_2\text{O}_3$  system, shown in Fig. 5, which was drawn in analogy with the Ga-As-Si system (22, 23). The work of Foster and Scardefield (10) gives the solubility of  $\text{Ga}_2\text{O}_3$  (or O) in Ga between  $1000^\circ$  and  $1200^\circ\text{C}$ . The present tipping experiments show a small ( $\sim 20\%$ ) reduction in the O solubility at

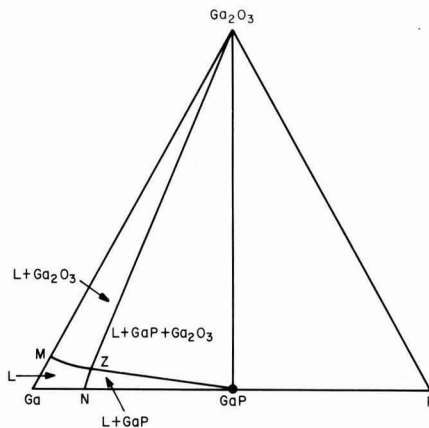


Fig. 5. Schematic  $1040^\circ\text{C}$  liquidus isotherm for the Ga-P- $\text{Ga}_2\text{O}_3$  system. Points M, N, and Z are the  $1040^\circ\text{C}$  solubilities of  $\text{Ga}_2\text{O}_3$  in Ga ( $\sim 0.01$  m/o) (10), P in Ga (2.5 a/o) (24), and the ternary eutectic point of  $\text{Ga}_2\text{O}_3$  ( $\sim 0.008$  m/o), respectively. The compositions within the triangle are not drawn to scale; the mole fraction of  $\text{Ga}_2\text{O}_3$  dissolved in Ga is more than two orders of magnitude smaller than the atom fraction of P saturating Ga.

<sup>2</sup> Bulk polycrystalline  $\text{Ga}_2\text{O}_3$  was pulled by W. Grodkiewicz of Bell Laboratories by the Czochralski method under  $\sim 3$  atm of argon pressure.

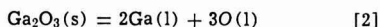
$\sim 1040^\circ\text{C}$  when the solution is also saturated in GaP. In Fig. 5 points M and N, respectively, represent the binary solubilities of  $\text{Ga}_2\text{O}_3$  ( $\sim 0.01$  m/o) (10) and P ( $\sim 2.5$  a/o) (24) in Ga at  $\sim 1040^\circ\text{C}$ , and point Z is the ternary eutectic point at which the solution, saturated with  $\text{Ga}_2\text{O}_3$  ( $\sim 0.008$  m/o  $\text{Ga}_2\text{O}_3$  or  $\sim 0.025$  a/o O) and P, is in equilibrium with GaP and  $\beta\text{-Ga}_2\text{O}_3$ . According to the schematic liquidus isotherm, as long as the  $\text{Ga}_2\text{O}_3$  additions to the solution vary along the curve  $N-Z$ , O-doped GaP but not  $\beta\text{-Ga}_2\text{O}_3$  will precipitate. However, over-all solution compositions which are located within the Z-GaP- $\text{Ga}_2\text{O}_3$  tie triangle yield a liquid of composition Z in equilibrium with both solid phases, permitting their coprecipitation.

There are two phenomena, consistent with Fig. 5, which may lead to precipitation. The first one is mechanical in nature, due to the closeness in density between Ga and  $\text{Ga}_2\text{O}_3$  at the tipping temperature. Accordingly, at  $\sim 1040^\circ\text{C}$  the  $\text{Ga}_2\text{O}_3$  powder is either suspended in the liquid solution or it sinks to the vicinity of the substrate. However, the possibility that most of the observed precipitates originate directly from suspended particles which have never dissolved is discounted because only 5% of the as-received powder consists of needles, and even these are about a factor of 10 shorter than the precipitates. Therefore, we suggest that the small excess oxide particles,<sup>4</sup> suspended in the O- and GaP-saturated solution, may serve as nucleation sites for the growth of the observed  $\beta\text{-Ga}_2\text{O}_3$  needles during the second phenomenon (coprecipitation) which is of chemical origin. During LPE growth, as the temperature decreases, the ternary eutectic point (point Z in Fig. 5) moves toward the Ga corner of the phase diagram, corresponding to an increasing supersaturation of the liquid with respect to GaP and  $\text{Ga}_2\text{O}_3$  which results in the coprecipitation of both solid phases.

Since we would expect the number of nucleation sites to be proportional to the amount of excess oxide added to the solution (above point Z), the preceding interpretation is consistent with Fig. 4, showing an increasing amount of precipitates with increasing  $\text{Ga}_2\text{O}_3$  additions in LPE layers grown under otherwise identical conditions. It should be noted that the presence of oxide nuclei is not a prerequisite for coprecipitation, especially when an LPE layer is grown over a wider temperature range. For example, when a solution of composition Z (0.025 a/o O) was cooled to  $1020^\circ\text{C}$  instead of  $1035^\circ\text{C}$ , the resulting epitaxial film contained a few precipitates.

Although at  $\sim 1040^\circ\text{C}$  the solubility of  $\text{Ga}_2\text{O}_3$  in Ga saturated with GaP is only a little less than the reported solubility of  $\text{Ga}_2\text{O}_3$  in liquid Ga alone, it is by no means assured that at higher temperatures, corresponding to larger phosphorus concentrations in the solution, the difference between binary and ternary solubilities will remain small. An approximate thermodynamic calculation can be performed to yield the variation of the O solubility in the ternary system as a function of temperature. Here we consider ternary solubility at the ternary eutectic point Z, illustrated in Fig. 5, which is an invariant point at a set temperature, T. The variation of Z with T gives the ternary eutectic valley.

The dissolution of  $\text{Ga}_2\text{O}_3$  in Ga or in Ga saturated with P can be represented by the reaction



where O represents the oxygen dissolved in the liquid. Under the conditions of Foster and Scardefield's binary

<sup>3</sup> At  $\sim 30^\circ\text{C}$  the density of liquid Ga (25) (6.09 g/cc) is greater than that of  $\beta\text{-Ga}_2\text{O}_3$  (20) (5.88 g/cc). However, at  $1040^\circ\text{C}$  the measured density of Ga (25) (5.48 g/cc) is smaller than the estimated density of  $\beta\text{-Ga}_2\text{O}_3$  ( $\sim 5.65$  g/cc) which is based on an extrapolation of the linear expansion coefficients of  $\text{Al}_2\text{O}_3\text{-Ga}_2\text{O}_3$  solid solutions (26) to pure  $\text{Ga}_2\text{O}_3$ .

<sup>4</sup> Because of the brittleness of bulk  $\text{Ga}_2\text{O}_3$  and the reaction of  $\text{Zn}(\text{PO}_3)_2$  with Ga to form  $\text{Ga}_2\text{O}_3$ , the presence of oxide particles suspended in the melt cannot be excluded even when O was added in one of these forms.

solubility measurements (10), the binary activities,  $a_{i,b}$ , of the designated species in the liquid are given by  $a_{\text{Ga},b} = x_{\text{Ga},b}\gamma_{\text{Ga},b} \approx 1$  and  $a_{\text{O},b} = x_{\text{O},b}\gamma_{\text{O},b}$ , where  $x_{i,b}$  and  $\gamma_{i,b}$  are the atom fraction and activity coefficient of species i, and b refers to the binary system. However, a comparison of the Ga- $\text{Ga}_2\text{O}_3$  (10) and Ga-P (24) binary data shows that the mole fraction of  $\text{Ga}_2\text{O}_3$  dissolved in Ga is more than two orders of magnitude smaller than the atom fraction of P saturating Ga, indicating that the activity of Ga in the ternary system cannot be taken as unity. As the activity of  $\text{Ga}_2\text{O}_3$  is unity, the equilibrium constant, K, for Eq. [2] becomes

$$K = a_{\text{Ga},t}^2(x_{\text{O},t})^3(\gamma_{\text{O},t})^3 \approx (x_{\text{O},t})^3(\gamma_{\text{O},t})^3 \quad [3]$$

where the subscript t refers to the ternary system. Rearranging Eq. [3] gives

$$\ln \frac{x_{\text{O},b}}{x_{\text{O},t}} = \ln \gamma_{\text{O},t} - \ln \gamma_{\text{O},b} + 2/3 \ln (x_{\text{Ga},t}\gamma_{\text{Ga},t}) \quad [4]$$

As there are no thermodynamic data for the liquid phase, we assume regular binary and ternary solution behavior (27). Assuming in addition to  $x_{\text{Ga},b} \approx 1$  that  $x_{\text{O},t} \ll x_{\text{P},t}$  and  $x_{\text{Ga},t} + x_{\text{P},t} \approx 1$ , we find approximate expressions for the activity coefficients<sup>5</sup> which when substituted into Eq. [4] yield

$$\ln \frac{x_{\text{O},b}}{x_{\text{O},t}} \approx \left( \frac{1 - x_{\text{Ga},t}}{RT} \right) \left[ -\omega_{\text{Ga-O}} + \omega_{\text{P-O}} + \frac{\omega_{\text{Ga-P}}}{3} (2 - 5x_{\text{Ga},t}) \right] + 2/3 \ln x_{\text{Ga},t} \quad [5]$$

where the  $\omega_{ij}$ 's are the ternary interchange energies.

To evaluate Eq. [5] we take  $\omega_{\text{Ga-P}}$  from the work of Thurmond (24) and since  $x_{\text{P},t} + x_{\text{Ga},t} \approx 1$ ,  $x_{\text{Ga},t}$  can be approximated by its value along the Ga-P liquidus curve (24). However,  $\omega_{\text{Ga-O}}$  and  $\omega_{\text{P-O}}$  are both unknown. The simplest assumption is to set  $\omega_{\text{P-O}} = 0$  (ideal solution), since at the high temperatures of interest P-O liquids do not exist. By substituting the ratio  $x_{\text{O},b}/x_{\text{O},t}$  ( $3 \times 10^{-2}/2.5 \times 10^{-2}$ ) in units of atom per cent at  $\sim 1040^\circ\text{C}$  into Eq. [5], we obtain  $\omega_{\text{Ga-O}} \approx -25$  kcal/mole. The negative deviation from Raoult's law implied by this value is considered reasonable in comparison, for instance, with the Cu(l)-O system. Recent thermodynamic measurements (28) yield  $\omega_{\text{Cu-O}} \approx -6.3$  kcal/mole at  $1100^\circ\text{C}$ . By using the estimated value of  $\omega_{\text{Ga-O}}$  and keeping  $\omega_{\text{P-O}} = 0$ ,  $\ln(x_{\text{O},b}/x_{\text{O},t})$  can be readily calculated from Eq. [5] up to the melting point of GaP. A combination of this ratio with the Ga- $\text{Ga}_2\text{O}_3$  solubility curve of Foster and Scardefield (10) gives the variation of  $x_{\text{O},t}$  along the Ga-P- $\text{Ga}_2\text{O}_3$  eutectic valley, shown in Fig. 6.

Although in Fig. 6 the departure of  $x_{\text{O},t}$  from  $x_{\text{O},b}$  becomes pronounced at higher temperatures, below about  $1100^\circ\text{C}$  only a small error is made by using the binary solubility curve (10) instead of the ternary eutectic valley. Because of the calculated maximum there is only about a factor of 2 increase in the ternary oxygen solubility between  $\sim 1100^\circ\text{C}$  and the melting point of GaP. The sections of the eutectic valley at high and low temperatures are shown as dashed lines because they are based on portions of the binary solubility curve which were found by extrapolating the published curve. Moreover, if  $\omega_{\text{P-O}} \neq 0$ , according to Eq. [5] this would influence  $x_{\text{O},t}$  only at high  $x_{\text{P},t}$  corresponding to high temperatures.

The estimate shown in Fig. 6 does not eliminate the need for further experimental work to establish the eutectic valley of the system Ga-P- $\text{Ga}_2\text{O}_3$ . Such information in conjunction with thermodynamic analysis of the type presented here would greatly aid the understanding of this technologically important ternary system. Unfortunately, even if the Ga-P- $\text{Ga}_2\text{O}_3$  eutectic

<sup>5</sup> The expressions are:  $RT \ln \gamma_{\text{O},b} \approx \omega_{\text{Ga-O}}$ ,  $RT \ln \gamma_{\text{O},t} \approx x_{\text{Ga},t}\omega_{\text{Ga-O}} + (1 - x_{\text{Ga},t})\omega_{\text{P-O}} - x_{\text{Ga},t}(1 - x_{\text{Ga},t})\omega_{\text{Ga-P}}$ , and  $RT \ln \gamma_{\text{Ga},t} \approx (1 - x_{\text{Ga},t})^2\omega_{\text{Ga-P}}$ .

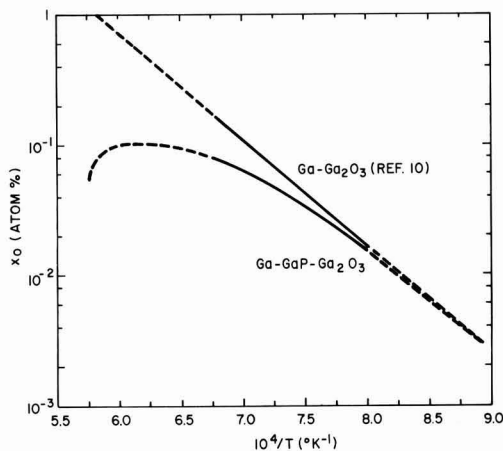


Fig. 6. Estimated eutectic valley for the Ga-P-Ga<sub>2</sub>O<sub>3</sub> ternary system and its relation to the solubility of Ga<sub>2</sub>O<sub>3</sub> in Ga (10). The plot is given in terms of a/o O vs. reciprocal temperature. Note that Ga<sub>2</sub>O<sub>3</sub> can only coprecipitate with GaP at O concentrations above the loop.

valley were known, independent experimental work would be required to give the equilibrium concentration of O dissolved in GaP crystals. However, one can predict on thermodynamic grounds that GaP in equilibrium with liquid compositions along the eutectic valley (Fig. 5, point Z; Fig. 6) contains the maximum amount of oxygen which can be dissolved at each temperature. Liquid compositions above Z result in precipitation of a second phase,  $\beta$ -Ga<sub>2</sub>O<sub>3</sub>, without an increase in the equilibrium oxygen concentration in the GaP crystal.

Of course, GaP epitaxial films which are free of precipitates may be grown in a nonisothermal LPE system even when a large excess of Ga<sub>2</sub>O<sub>3</sub> is added to the solution, initially moving the over-all liquid far above Z. The loss of O from the growth solution via the vaporization and transport of Ga<sub>2</sub>O according to Eq. [1] explains not only the absence of  $\beta$ -Ga<sub>2</sub>O<sub>3</sub> needles in LPE layers grown in a nonisothermal system but also the disparity in reported optimum O additions [0.03 (2) and 1.05 a/o O (5) for SG and LPE, respectively]. Our preliminary experiments demonstrate that efficient diodes can be fabricated in an isothermal LPE system without excessive O additions to the solution. Using the slider (Fig. 3), a nearly precipitate-free p-type layer was grown at ~1040°C onto an n-type LPE and LEC structure from a solution containing 0.03 a/o O in the form of Zn(PO<sub>3</sub>)<sub>2</sub> and 0.045 a/o Zn. The annealed and encapsulated diodes exhibited red electroluminescent (EL) efficiencies as high as 2.7%, which we consider promising since the dopant concentrations have not yet been optimized. This figure is within about a factor of two of the best reported values of 4.5% (29) and 6% (30) for similar structures which were grown from solutions containing a large excess of Ga<sub>2</sub>O<sub>3</sub> but presumably under nonisothermal conditions [tipping in a small thermal mass furnace (29) and dipping, (30) respectively].

The effect of the concentration of  $\beta$ -Ga<sub>2</sub>O<sub>3</sub> precipitates on EL efficiency of devices has not been examined in detail. However, point contact EL efficiency measurements were made on mesa diodes taken from a relatively precipitate-free and from a heavily precipitated area (such as shown in Fig. 2) of a p-type LPE film grown on a 2.5 cm long n-type LEC substrate from a solution containing 1.05 a/o O added as Ga<sub>2</sub>O<sub>3</sub> and 0.05 a/o Zn. The EL efficiencies were as much as 15 times higher for the diodes prepared from the clean segment than for the ones made from the heavily precipitated area. We think that the reduction in effi-

ciency is very likely due to the difficulty of achieving suitable contact with a heavily precipitated p-type layer. But a small concentration of precipitates may not have any significant effect on the EL efficiency. Indeed, we speculate that such small concentrations of precipitates may be present in the LED's reported in the literature but have been overlooked because of their negligible effect on diode performance. Finally, recent measurements of Glorizova *et al.* (31) show that the 100°K hole mobility of Zn, O-doped SG GaP drops precipitously when more than 0.03 a/o O is added to the melt as Ga<sub>2</sub>O<sub>3</sub>. Since we have also seen Ga<sub>2</sub>O<sub>3</sub> precipitates in SG platelets, the results of Glorizova *et al.* (31) may be related to scattering by a second phase.

### Acknowledgments

We would like to express our appreciation to F. A. Trumbore for many helpful discussions and suggestions in the course of this work. We are also grateful to C. D. Thurmond for several discussions and advice. Useful discussions with R. H. Saul, M. E. Weiner, and S. Wagner are also acknowledged. We thank L. R. Dawson for the DIMA work.

Manuscript submitted Aug. 9, 1971; revised manuscript received Dec. 13, 1971. This was RNP 250 presented at the Atlantic City Meeting of the Society, Oct. 4-8, 1970.

Any discussion of this paper will appear in a Discussion Section to be published in the December 1972 JOURNAL.

### REFERENCES

1. J. Starkiewicz and J. W. Allen, *J. Phys. Chem. Solids*, **23**, 881 (1962).
2. M. Gershenzon, F. A. Trumbore, R. M. Mikulyak, and M. Kowalchik, *J. Appl. Phys.*, **36**, 1528 (1965).
3. R. A. Logan, H. G. White, and F. A. Trumbore, *Appl. Phys. Letters*, **10**, 206 (1967).
4. K. K. Shih, M. R. Lorenz, and L. M. Foster, *J. Appl. Phys.*, **39**, 2747 (1968).
5. R. H. Saul, J. Armstrong, and W. H. Hackett, Jr., *Appl. Phys. Letters*, **15**, 229 (1969).
6. I. Ladany, *This Journal*, **116**, 993 (1969).
7. F. A. Trumbore, M. Kowalchik, and H. G. White, *J. Appl. Phys.*, **38**, 1987 (1967).
8. A. S. Jordan, *This Journal*, **118**, 781 (1971).
9. See, for example, K. P. Sinha and M. DiDomenico, Jr., *Phys. Rev.*, **B1**, 2623 (1970).
10. L. M. Foster and J. Scardefield, *This Journal*, **116**, 494 (1969).
11. H. Nelson, *RCA Rev.*, **24**, 603 (1963).
12. L. Derick, Personal communication.
13. C. N. Cochran and L. M. Foster, *This Journal*, **109**, 144 (1962).
14. C. D. Thurmond and C. J. Frosch, *This Journal*, **111**, 184 (1964).
15. Mildred H. Read, 27th Annual Diffraction Conference, Pittsburgh, November 1964.
16. J. V. DiLorenzo, R. B. Marcus, and R. Lewis, *J. Appl. Phys.*, **42**, 729 (1971); J. V. DiLorenzo, *This Journal*, **118**, 1645 (1971).
17. M. B. Panish and S. Sumski, *J. Appl. Phys.*, **41**, 3195 (1970).
18. A. S. Jordan, L. Derick, R. Caruso, and M. Kowalchik, Paper 49 presented at Electrochem. Soc. Meeting, Houston, Texas, May 7-11, 1972.
19. G. Eckhardt, *J. Appl. Phys.*, **33**, 1016 (1962).
20. I. A. Sheka, I. S. Chaus, and T. T. Mityureva, "The Chemistry of Gallium," p. 32, Elsevier Publishing Co., Inc., New York (1966).
21. H. Kressel, F. Z. Hawrylo, M. S. Abrahams, and C. J. Buicocchi, *J. Appl. Phys.*, **39**, 5139 (1968).
22. M. B. Panish, *This Journal*, **113**, 1226 (1966).
23. F. E. Rosztochy, "Proceedings of the International Conference on the Physics and Chemistry of Semiconductor Heterojunctions and Layer Structures," Vol. 1, p. 333, Akademiai Kiado, Budapest (1971).
24. C. D. Thurmond, *J. Phys. Chem. Solids*, **26**, 785 (1965).
25. K. E. Spills, *Proc. Phys. Soc.*, **48**, 299 (1936).
26. H. P. Kirschnner, *J. Am. Ceram. Soc.*, **52**, 379 (1969).
27. I. Prigogine and R. Defay, "Chemical Thermodynamics," p. 257, Longmans Green and Co., London (1954).



28. C. R. Nanda and G. H. Geiger, *Met. Trans.*, **1**, 1235 (1970).  
 29. W. H. Hackett, Jr. and R. H. Saul, Abstract 81, Extended Abstracts of the Los Angeles Meeting of the Electrochemical Society, May 10-15, 1970.

30. B. P. Johnson and R. M. Potter, *Bull. Am. Phys. Soc., Ser. II*, **16**, 433 (1971).  
 31. R. I. Glorizova, V. M. Grachev, L. I. Kolesnik, and L. I. Marina, *Sov. Phys., Semicond.*, **4**, 1363 (1971).

# Mass Spectrometric Studies of Vapor-Phase Crystal Growth

## II. GaN

Vladimir S. Ban

RCA Laboratories, Princeton, New Jersey 08540

### ABSTRACT

A mass spectrometer has been coupled to an open-tube, vapor-phase, crystal growth apparatus in order to study vapor-phase processes leading to the deposition of GaN crystals. Studies of the  $\text{HCl}$  and  $\text{Cl}_2$  reactions with gallium showed that  $\text{GaCl}_{(g)}$  is the only gallium chloride formed. Studies of  $\text{NH}_3$  decomposition showed that very little  $\text{NH}_3$  decomposes under given experimental conditions, but this can be changed by the presence of W and Pt. Thermochemical data were collected or calculated for all species detected in the system. The reaction mechanisms leading to the deposition of GaN are discussed. It is concluded that the reaction controlling the deposition of GaN can be written as



Comparison of the experimentally determined vapor composition with one predicted from the available thermochemical data showed that important deviations from the thermochemical equilibrium occur in our system.

Gallium nitride has a direct energy bandgap of 3.39 eV (1) and is therefore an interesting material for electronic applications. Recently, single-crystalline epitaxial films of GaN were successfully prepared by means of the open-tube, vapor-transport method (1). The apparatus and technique used were very similar to those used previously in the preparation of other III-V compounds (2).

The chemistry of vapor-phase processes leading to the deposition of GaN was not completely understood. For this reason, we undertook studies of some fundamental aspects of the GaN deposition. In particular, the following processes were studied: (a) the transport of Ga with  $\text{HCl}$  and  $\text{Cl}_2$  in the temperature range of  $700^\circ\text{--}900^\circ\text{C}$ ; (b) the thermal decomposition of  $\text{NH}_3$  in the same temperature range as affected by various catalysts; and (c) the reactions leading to the deposition of GaN and the influence of temperature on the rate of this reaction. The influence of the replacement of  $\text{H}_2$  by He as a carrier gas was also studied. Furthermore, the thermochemistry of the deposition system is discussed and the experimentally determined composition of the vapor phase is compared with the composition predicted from the chemical equilibrium calculations.

In order to determine the composition of the vapor phase under a variety of experimental conditions, we coupled a time-of-flight mass spectrometer to the vapor-growth tube. With the mass spectrometer, we could directly identify species present in the vapor phase and determine their relative abundances.

### Experimental Procedure and Results

The mass spectrometer-vapor growth tube system is shown schematically at the top of Fig. 1. Details of this system and the sampling technique have been described in Part I of this series (3), which reports a study of the  $\text{GaAs}_{2-x}\text{P}_{1-x}$  system. The present experiments were done in a similar fashion to those described in Part I. However, the temperature gradients, concentrations of reacting gases, and flow rates were

chosen to be similar to those employed (1) in growth of GaN epitaxial layers. GaN was also deposited on the walls of the reactor in the course of our experiments.

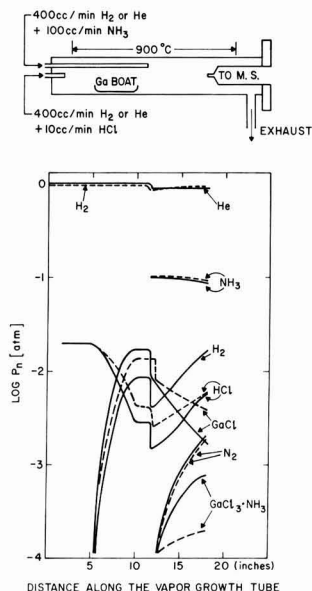


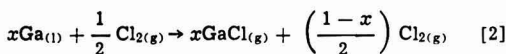
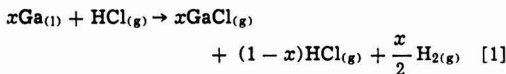
Fig. 1. Mass spectrometric determination of the variation of partial pressures of species along the growth tube during epitaxial growth of GaN. The apparatus and experimental conditions are schematically represented in the upper part of the drawing. (Dotted lines give pressures when  $\text{H}_2$  is the carrier, solid lines when He is the carrier. Kinks in the pressure curves at 12 in. are caused by the additional volume of gas introduced at that point by the  $\text{NH}_3$  inlet tube. These curves are drawn from the determination of initial and final partial pressures of vapor species.)

Key words: mass spectrometry, vapor-phase deposition, GaN crystals, epitaxial growth, chemical kinetics, thermodynamics.



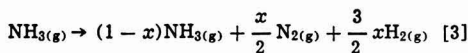
Occasionally, even the sampling capillary became clogged with GaN deposit.

**Halogen transport of Ga.**—The HCl transport of Ga in the temperature range of 400°–800°C was discussed in Part I (3). This time we also examined the Cl<sub>2</sub> transport of Ga as well as the influence of the carrier gas (H<sub>2</sub> vs. He) on the HCl transport efficiency. The boat containing gallium was 12.5 cm long; 25 cm<sup>2</sup> of the liquid gallium surface was exposed to the gas phase. With the chosen flow rates (500 cm<sup>3</sup>/min H<sub>2</sub> or He + 10 cm<sup>3</sup>/min HCl or Cl<sub>2</sub>), the gas stream velocity was about 3.5 cm/sec. It was found that HCl and Cl<sub>2</sub> react with Ga according to the following reactions



where  $x$  = mole fraction of HCl or Cl<sub>2</sub> reacting. Values of  $x$  for various experimental conditions are given in Table I. These values were obtained by changing the position of the HCl or Cl<sub>2</sub> inlet, which could be placed either upstream or downstream from the boat containing Ga. The mass spectrometer signal due to HCl (or Cl<sub>2</sub>) was first measured with the inlet placed downstream, so that the halogen species could not react with Ga. A second measurement was made with the inlet placed upstream, so that a portion of the halogen did react. Since the second signal was due to the unreacted HCl (or Cl<sub>2</sub>), its ratio to the first signal was equal to  $(1-x)$ . The mass spectra also showed that the monochloride (GaCl) was the only gallium chloride species resulting from the halogen-gallium interaction.

**Decomposition of NH<sub>3</sub>.**—It is important to know to what extent ammonia is decomposed into nitrogen and hydrogen, because GaN cannot be deposited by direct reaction between GaCl and N<sub>2</sub>. Ammonia is a thermodynamically unstable gas (4) at temperatures usually employed in the growth of GaN crystals, and over 99.5% of incoming NH<sub>3</sub> would decompose if equilibrium were achieved under our experimental conditions. However, it is known that thermal decomposition of NH<sub>3</sub> is a sluggish reaction. It can be accelerated with various catalysts, e.g., Pt and W (5). Normally, the walls of the growth tube are made of quartz, but sometimes, in order to prevent the deposition of a permanent layer of the insoluble GaN on the reactor wall, a removable tungsten or graphite liner is placed in the tube. This could change the composition of the gaseous phase. We therefore studied the influence of various materials on the decomposition of NH<sub>3</sub>, which can be described by the following equation



where  $x$  = mole fraction of NH<sub>3</sub> decomposing. A foil of Pt, W, or graphite (25 cm<sup>2</sup> in each case) could be placed in and removed from the growth tube. Mass spectrometer signals due to NH<sub>3</sub> and N<sub>2</sub> were measured with and without the foil in the system. The values of

Table I. Mole fractions of HCl<sub>(g)</sub> or Cl<sub>2(g)</sub> reacting with Ga<sub>(l)</sub> according to Eq. [1] and [2], respectively

$P_{\text{HCl}}$  or  $P_{\text{Cl}_2} = 2.0 \times 10^{-3}$  atm, total flow rate = 510 cm<sup>3</sup>/min, Ga surface area = 25 cm<sup>2</sup>

T, °C	Mole fraction ( $x$ ) of Cl <sub>2</sub> or HCl		
	Cl <sub>2</sub> in He	HCl in He	HCl in H <sub>2</sub>
700	0.78	0.79	0.70
800	0.78	0.83	0.72
900	—	0.86	—

Table II. Mole fraction of NH<sub>3(g)</sub> decomposing according to Reaction [3]

$P_{\text{NH}_3} = 2.0 \times 10^{-1}$  atm, total flow rate = 500 cm<sup>3</sup>/min, catalyst surface area = 25 cm<sup>2</sup>

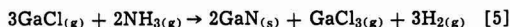
Catalyst and carrier gas	Mole fraction ( $x$ ) of NH <sub>3</sub>				
	700°C	800°C	850°C	900°C	950°C
Quartz, H <sub>2</sub>	0	—	0.02	—	0.03
Quartz, He	0	—	0.02	—	0.04
Graphite, H <sub>2</sub>	0	0.02	—	0.02	—
Graphite, He	0	0.03	—	0.04	—
Pt, H <sub>2</sub>	0	0.02	—	0.02	0.02
Pt, He	0	0.10	—	0.23	0.35
W, H <sub>2</sub>	0	0.04	0.10	0.22	0.47
W, He	0	0.11	0.25	0.40	0.54

$x$  computed from these measurements in the temperature range of 700°–950°C are given in Table II. In these experiments, a mixture of 100 cm<sup>3</sup>/min of NH<sub>3</sub> with 400 cm<sup>3</sup>/min of He or H<sub>2</sub> was passed through the tube. The influence of the carrier gas on the extent of decomposition is also depicted in Table II. When no catalyst was present, no more than about 4% of the NH<sub>3</sub> was decomposed at temperatures as high as 950°C. This was estimated from the increase in the N<sub>2</sub> signal at the elevated temperatures in comparison with N<sub>2</sub> background signal at room temperature.

**Deposition reactions.**—In analogy with the deposition of other III-V compounds, one can postulate two thermodynamically feasible reactions which might lead to the deposition of GaN



and



In order to test for the occurrence of these reactions, we monitored mass spectrometrically the pressures of GaCl, HCl, and GaCl<sub>3</sub> in the system before and after the introduction of NH<sub>3</sub>. In these experiments Ga was transported with HCl. A decrease in the GaCl signal and an increase in the HCl signal after the introduction of NH<sub>3</sub> indicated that Reaction [4] does indeed occur. No GaCl<sub>3</sub> was detected, but we discovered a [GaCl<sub>2</sub> · NH<sub>3</sub>]<sup>+</sup> ion in the mass spectra. The most probable parent molecule is GaCl<sub>3</sub> · NH<sub>3</sub>, whose existence at reasonably high temperatures has been reported (6). It is known that metal trihalides lose a halogen atom when ionized by the electron beam, giving a MX<sub>2</sub><sup>+</sup> ion as the most prominent peak in the mass spectrum (7). From the intensity of the peak we estimate that the partial pressure of GaCl<sub>3</sub> · NH<sub>3</sub> was between 1 and  $5 \times 10^{-4}$  atm. From these results we concluded that Reaction [5] also occurs in our system, producing GaCl<sub>3(g)</sub>, which then reacts with NH<sub>3</sub> to form the observed ammonia complex.

The increase in  $P_{\text{HCl}}$  and the decrease in  $P_{\text{GaCl}}$  due to the reaction of GaCl with NH<sub>3</sub> at 900°C are listed in Table III. Values of  $P_{\text{GaCl}}$  and  $P_{\text{HCl}}$  after the reaction between HCl and gallium were known from the gallium transport experiments, initial  $P_{\text{NH}_3}$  was  $1.0 \times 10^{-1}$  atm and the total flow in the system was 1.0 l/min. The carrier gas was either H<sub>2</sub> or He. Values of  $P_{\text{GaCl}}$  and  $P_{\text{HCl}}$  after the reaction with NH<sub>3</sub> were calculated from the respective changes in mass spectrometric intensities of these species.

We used the same procedure to measure the consumption of GaCl as a function of temperature be-

Table III. Changes in  $P_{\text{GaCl}}$  and  $P_{\text{HCl}}$  due to reactions with NH<sub>3</sub>

$P_{\text{NH}_3} = 1.0 \times 10^{-1}$  atm, total flow rate = 1.0 l/min,  $T = 900^\circ\text{C}$

	He carrier	H <sub>2</sub> carrier
Initial $P_{\text{GaCl}}$ (atm)	$8.5 \times 10^{-3}$	$7.5 \times 10^{-3}$
Final $P_{\text{GaCl}}$ (atm)	$1.7 \times 10^{-3}$	$3.8 \times 10^{-3}$
Initial $P_{\text{HCl}}$ (atm)	$1.5 \times 10^{-3}$	$2.5 \times 10^{-3}$
Final $P_{\text{HCl}}$ (atm)	$5.8 \times 10^{-3}$	$5.7 \times 10^{-3}$

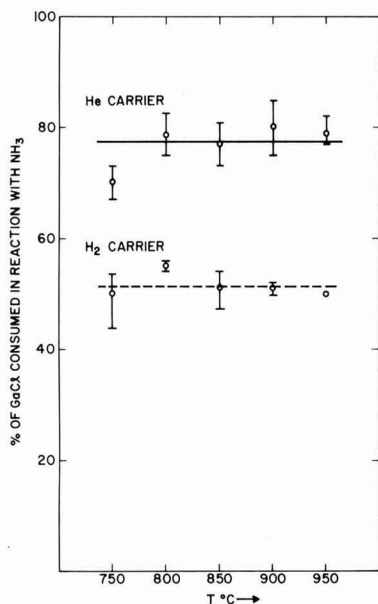


Fig. 2. Percentage of incoming  $\text{GaCl}_{3(g)}$  consumed in reaction with  $\text{NH}_{3(g)}$  at various temperatures. Initial partial pressures (in atm):  $P_{\text{H}_2}$  or  $P_{\text{He}} = 9 \times 10^{-1}$ ,  $P_{\text{NH}_3} = 1 \times 10^{-1}$ ,  $P_{\text{GaCl}} = 8 \times 10^{-3}$ . Total flow = 1 l/min, reaction time = 4 sec.

tween 750° and 950°C. The results are presented in Fig. 2. The extent of GaCl consumption was not markedly temperature dependent, but it was significantly greater for He as the carrier gas than for  $\text{H}_2$ . In these experiments the reactor walls were graphite lined.

### Thermochemical Data

By means of our mass spectrometric measurements, we determined qualitatively and quantitatively the species present in the vapor phase and also specified the reactions occurring in the system. These results combined with reliable thermochemical data for all species in the system make possible a meaningful discussion of the chemistry of the vapor-phase deposition.

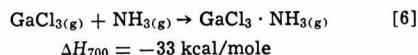
For this purpose the most useful data are the standard free energies of formation  $\Delta F^\circ_f$  of all species in the temperature interval of interest. Knowledge of  $\Delta F^\circ_f$  permits one to calculate the standard free energies of reaction  $\Delta F^\circ_r$  for reactions occurring in the system, and from these to find values of equilibrium constants  $K_p$  and values of equilibrium partial pressures for the vapor species.

In Table IV we list values of  $\Delta F^\circ_f$  for species in the system at  $T = 1173^\circ\text{K}$ , the temperature at which epitaxial layers of GaN are usually grown. Data for  $\text{GaCl}_{(g)}$  and  $\text{GaCl}_{3(g)}$  were taken from a recent paper by Kirwan (8).  $\text{GaCl}_{3(g)}$  is not present in the system as such, but data for it are necessary to compute the  $\Delta F^\circ_f$  for  $\text{GaCl}_3 \cdot \text{NH}_{3(g)}$ . Data for  $\text{HCl}_{(g)}$  and  $\text{NH}_{3(g)}$  were taken from JANAF Tables (4).

Table IV. Values of  $\Delta F^\circ_f$  (free energy of formation) at  $T = 1173^\circ\text{K}$  for species present in the GaN deposition system

Species	$\Delta F^\circ_f$ (kcal/mole)	Reference
$\text{HCl}_{(g)}$	-24.3	(4)
$\text{GaCl}_{(g)}$	-28.9	(8)
$\text{GaCl}_{3(g)}$	-71.5	(8)
$\text{NH}_{3(g)}$	+19.9	(4)
$\text{GaCl}_3 \cdot \text{NH}_{3(g)}$	-55.6	Calculated from data in (7) and (9)
$\text{GaN}_{(s)}$	+6.2	Calculated from data in (10) and (11)

The value for  $\Delta F^\circ_f$  of  $\text{GaCl}_3 \cdot \text{NH}_{3(g)}$  was determined from  $\Delta H$  data given by Friedman and Taube (6)



The  $\Delta S$  for reactions of this type (i.e.,  $M_{(g)} + X_{(g)} \rightarrow MX_{(g)}$ ) is usually around  $-22 \text{ eu}$  (9). Using the expression  $\Delta F^\circ_r = \Delta H^\circ_r - T\Delta S^\circ_r$ , one finds for the above reaction  $\Delta F^\circ_r = -4 \text{ kcal/mole}$  at  $T = 1173^\circ\text{K}$ . Since

$$\Delta F^\circ_r = \Delta F^\circ_f \text{GaCl}_3 \cdot \text{NH}_{3(g)} - (\Delta F^\circ_f \text{NH}_{3(g)} + \Delta F^\circ_f \text{GaCl}_{3(g)})$$

one finds  $\Delta F^\circ_f \text{GaCl}_3 \cdot \text{NH}_{3(g)} = -55.6 \text{ kcal/mole}$  at  $T = 1173^\circ\text{K}$ .

Marina and Nashel'skii (10) estimate  $\Delta S^\circ_f$  and  $C_p$  of  $\text{GaN}_{(s)}$ . Their values are based on the corresponding thermochemical data for the elemental Group IV semiconductors which are well known. The  $\Delta H^\circ_f$  of GaN at  $298^\circ\text{K}$  is  $-26.4 \text{ kcal}$  (11). This value is based on experimental work done by Hahn and Juza (12), and applied to the reaction



The above data permit one to calculate  $\Delta F^\circ_f$  for  $\text{GaN}_{(s)}$ ; at  $1173^\circ\text{K}$   $\Delta F^\circ_f = 6.2 \text{ kcal/mole}$ .

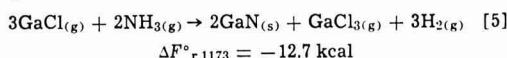
### Discussion

Our studies of Ga transport, which are summarized in Table I, showed that between 70 and 80% of the introduced HCl participates in the transport reaction, in good agreement with the values determined in Part I (3). Replacement of  $\text{H}_2$  with He as a carrier gas improved the efficiency of the HCl transport, and the HCl/He mixture was more efficient than the  $\text{Cl}_2/\text{He}$  mixture, but the differences in values were not very significant. More important, in all cases chemical equilibrium was not established, since according to the thermochemical data in Ref. (8), practically all the HCl and  $\text{Cl}_2$  introduced should have reacted with Ga. It was shown in Part I (3) that the relatively high flow rates employed in our growth systems are responsible for the observed deviations from equilibrium in the transport reaction.

Table II shows the influence of various catalysts on the thermal decomposition of  $\text{NH}_3$ . The metals tungsten and platinum are significantly more efficient catalysts than the nonmetals graphite and quartz (reactor walls). However, below  $700^\circ\text{C}$  very little decomposition occurred, regardless of the catalyst. Furthermore, the influence of the carrier gas was quite pronounced. The decomposition proceeded more readily in the presence of He than in the presence of  $\text{H}_2$ , particularly in the case of platinum; in the presence of He significant amounts of  $\text{NH}_3$  decomposed on platinum, while virtually no decomposition occurred in the presence of  $\text{H}_2$ . This is possibly due to some interaction of  $\text{H}_2$  with platinum which changes the catalytic activity of Pt and therefore inhibits the decomposition of  $\text{NH}_3$ .

Studies of  $\text{NH}_3$  decomposition, as summarized in Table II, indicated that the reactor wall materials and the carrier gas are factors with a significant influence on the composition of the gas phase in the growth system. Frequently, only the vapor species directly participating in the reactions in a system are considered in predicting the vapor-phase composition. Secondary factors, such as those mentioned, are often neglected. Such neglect can lead to serious errors in estimates of the vapor-phase composition.

Combining thermochemical data and the mass spectrometric results one can now discuss the chemistry of the deposition system. Besides the direct reaction of GaCl with  $\text{NH}_3$  (Reaction [4]), there are other routes leading to the deposition of GaN. One possible sequence of reactions is

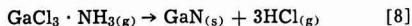


The resultant  $\text{GaCl}_{3(g)}$  then reacts with  $\text{NH}_{3(g)}$  to form the observed  $\text{GaCl}_3 \cdot \text{NH}_{3(g)}$  complex



$$\Delta F^\circ_{r, 1173} = -4.0 \text{ kcal}$$

This complex is thermodynamically unstable with respect to the following reaction

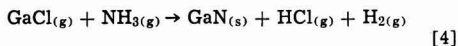


$$\Delta F^\circ_{r, 1173} = -11.2 \text{ kcal}$$

Indeed,  $\text{AlN}_{(s)}$  has been deposited by decomposing the analogous complex  $\text{AlCl}_3 \cdot \text{NH}_{3(g)}$  (13). Recently, the thermal decomposition of a  $\text{GaBr}_3 \cdot 4\text{NH}_3$  complex has been used for the deposition of GaN films (14).

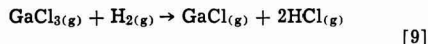
Our results also permit us to say something about the kinetics of the above reactions. Reactions [4] and [5] are fairly fast; e.g., 80% of introduced  $\text{GaCl}_{3(g)}$  reacts with  $\text{NH}_{3(g)}$  in 4 sec<sup>1</sup> when He is used as the carrier gas, 50% when  $\text{H}_2$  is the carrier. Reaction [6] must be fast also, because no unreacted  $\text{GaCl}_{3(g)}$  was detected. On the other hand, Reaction [8] is slower than [6], because an appreciable amount of  $\text{GaCl}_3 \cdot \text{NH}_{3(g)}$  exists in the vapor phase.

Summation of Eq. [5], [6], and [8] yields the overall controlling equilibrium for the deposition of  $\text{GaN}_{(s)}$



$$\Delta F^\circ_{r, 1173} = -9.3 \text{ kcal}$$

An alternative reaction path is also thermodynamically feasible. The resultant  $\text{GaCl}_{3(g)}$  (Reaction [5]) can undergo reduction by  $\text{H}_{2(g)}$



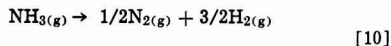
$$\Delta F^\circ_{r, 1173} = -6.0 \text{ kcal}$$

The  $\text{GaCl}_{(g)}$  then reacts with  $\text{NH}_{3(g)}$  according to Reaction [5] and contributes to the deposition of  $\text{GaN}_{(s)}$ .

Summation of Reactions [5] and [9] leads again to Eq. [4] which therefore establishes the controlling equilibrium for both complex reaction paths as well as for the direct  $\text{GaCl}-\text{NH}_3$  reaction. Most likely, the direct Reaction [4] is the biggest contributor to the deposition of GaN, because partial pressures of reactants GaCl and  $\text{NH}_3$  are much higher than partial pressures of either  $\text{GaCl}_3$  or  $\text{GaCl}_3 \cdot \text{NH}_3$ .

From the value of  $\Delta F^\circ_r = -9.3$  kcal for Reaction [4] the corresponding value of the equilibrium constant  $K_{(4)} = 55$ . This value of  $K_{(4)}$  suggests that in the case of the  $\text{H}_2$  carrier the partial pressure  $P_{\text{H}_2} = 9 \times 10^{-1}$  atm is sufficiently high to prevent all  $\text{GaCl}_{(g)}$  from reacting with  $\text{NH}_{3(g)}$  ( $P_{\text{NH}_3} = 1 \times 10^{-1}$  atm). When He is used as the carrier gas (i.e.,  $P_{\text{H}_2} \approx 10^{-3}$  atm) more  $\text{GaCl}_{(g)}$  reacts (Fig. 2). However, in neither case was the equilibrium reached.

Figure 1 shows the partial pressures of various gaseous species along the tube for the cases of  $\text{H}_2$  and He as the carrier gas. The pressure curves were drawn from the determination of the initial and final partial pressures of vapor species; no experimental data were obtained for the intervening points. It is usually assumed that in vapor-phase deposition apparatus thermochemical equilibrium is established throughout the system. Our results show that this is not the case in the GaN deposition system. From the thermochemical data in Table IV it is obvious that the following reactions would occur readily if equilibrium were achieved under our experimental conditions



$$\Delta F^\circ_{r, 1173} = -19.9 \text{ kcal/mole}$$

and

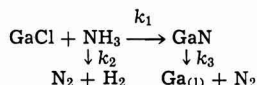
<sup>1</sup> Value of the reaction time (4 sec) was determined from the known gas stream velocity and the known distance between the  $\text{NH}_3$  inlet tube and the mass spectrometer sampling capillary.



$$\Delta F^\circ_{f, 1173} = -6.2 \text{ kcal/mole}$$

The decomposition of  $\text{NH}_{3(g)}$  has already been discussed. Lorenz and Binkowski have shown (16) that while the decomposition of  $\text{GaN}_{(s)}$  does occur at temperatures over 600°C, the rate of this reaction is very slow. Therefore, due to the kinetic limitations, the above reactions do not proceed in this system and the thermochemical equilibrium is not established. On the other hand, the deposition of  $\text{GaN}_{(s)}$  is a fast process.

Indeed, the very fact that  $\text{GaN}_{(s)}$  can be deposited under our experimental conditions is the result of the fortuitous kinetics. The deposition and the deposition-opposing processes can be represented by the following scheme



where  $k_1$ ,  $k_2$ , and  $k_3$  are rate constants of corresponding processes. One succeeds in depositing  $\text{GaN}_{(s)}$  only because the fact that  $k_1 \gg k_2, k_3$  leads to the favorable deviations from the thermochemical equilibrium. Due to these deviations the reacting  $\text{NH}_3$  is present in sufficiently high concentrations and the decomposition of the deposited  $\text{GaN}_{(s)}$  is practically negligible.

Significant deviations from the equilibrium situation were also detected in our earlier work on the  $\text{GaAs}_{x-1}\text{P}_x$  system (3).

### Conclusions

The main results of mass spectroscopic studies of the GaN deposition system are:

1. Both  $\text{Cl}_2$  and HCl react readily with  $\text{Ga}_{(l)}$  in the temperature interval 700°-900°C.  $\text{GaCl}_{(g)}$  was the only gallium chloride produced in these reactions.

2.  $\text{NH}_3$  does not undergo significant decomposition under the experimental conditions present in our deposition system. The influence of various catalysts and the carrier gas (He vs.  $\text{H}_2$ ) on the decomposition of  $\text{NH}_3$  was studied and reported.

3. On the basis of mass spectrometric results and collected thermochemical data we discussed the feasibility of various reaction mechanisms which lead to the deposition of GaN. The over-all reaction-controlling equilibrium can be written as



4. The ability to deposit GaN under our experimental conditions rests on the fact that reactions of decomposition of  $\text{NH}_3$  and GaN are much slower than the GaN deposition reaction. The resulting favorable deviation from the thermochemical equilibrium leads to the net accumulation of GaN, although it is actually a metastable phase at the temperatures employed.

### Acknowledgments

The author would like to thank T. Zrebiec for technical assistance. Enlightening discussions with D. Richman, R. Enstrom, M. Ettenberg, and J. Tietjen are gratefully acknowledged.

Manuscript submitted Aug. 11, 1971; revised manuscript received Dec. 15, 1971.

Any discussion of this paper will appear in a Discussion Section to be published in the December 1972 JOURNAL.

### REFERENCES

- H. P. Maruska and J. J. Tietjen, *Appl. Phys. Letters*, **15**, 327 (1969).
- J. J. Tietjen and J. A. Amick, *This Journal*, **113**, 724 (1966).
- V. S. Ban, *ibid.*, **118**, 1473 (1971).
- JANAF Tables of Thermochemical Data, D. R. Stull, Editor, Dow Chemical Co., Midland, Mich. (1965), and quarterly supplements; now available as PB-168370 from the Clearinghouse for Federal Scientific and Technical Information, Springfield, Va.

5. C. N. Hinshelwood, "The Kinetics of Chemical Change," The Clarendon Press, Oxford (1940).
6. H. L. Friedman and H. Taube, *J. Am. Chem. Soc.*, **72**, 2236 (1950).
7. J. W. Hastie and J. L. Margrave, *High Temp. Sci.*, **1**, 481 (1969).
8. D. J. Kirwan, *This Journal*, **117**, 1572 (1970).
9. L. Brewer *et al.*, "The Chemistry and Metallurgy of Miscellaneous Materials," p. 185, L. L. Quill, Editor, McGraw-Hill Co., New York (1950).
10. L. I. Marina and A. Ya. Nashelskii, *Russ. J. Phys. Chem. (English Transl.)*, **43**, 963 (1969).
11. D. D. Wagman, W. H. Evans, V. B. Parker, I. Halow, S. M. Bailey, and R. H. Schumm, *Nat. Bur. Std. Tech. Note* 270-3 (1968).
12. H. Hahn and R. Juza, *Z. Anorg. Allgem. Chem.*, **244**, 111 (1940).
13. A. J. Noreika and D. W. Ing, *J. Appl. Phys.*, **39**, 5578 (1968).
14. T. L. Chu, *This Journal*, **118**, 1200 (1971).
15. M. R. Lorenz and B. B. Binkowski, *This Journal*, **109**, 24 (1962).

## Thermodynamic Analysis of the III-V Alloy Semiconductor Phase Diagrams

### III. The Solidus Boundary in the $\text{Ga}_{1-x}\text{Al}_x\text{As}$ Pseudobinary System

L. M. Foster,\* J. E. Scardefield, and J. F. Woods

IBM T. J. Watson Research Center, Yorktown Heights, New York 10598

#### ABSTRACT

The solidus boundary in the  $\text{Ga}_{1-x}\text{Al}_x\text{As}$  pseudobinary system was determined by a technique which employs the electron microprobe to analyze the primary phase of compositions equilibrated in the two-phase field. The solid solutions in this system appear to be essentially ideal over the entire composition range, since the experimental solidus boundary is in good agreement with that calculated with the assumption of ideal solid and liquid solutions. This is consistent with the hypothesis that an alloy whose two components have the same lattice parameter will obey Raoult's law of mixing.

Of all the III-V compound semiconductors, alloys between GaAs and AlAs offer some of the most attractive features. Direct radiative transitions with high quantum efficiencies are permitted up to about 40 m $\mu$  (mole per cent) AlAs, corresponding to red (ca. 6800Å) light emission. The alloys are particularly amenable to preparation by liquid-phase epitaxy from gallium-rich solutions (1), and high quality, single-crystal GaAs substrates are readily available. A primary consideration in the early choice of  $\text{Ga}_{1-x}\text{Al}_x\text{As}$  for exploitation was the almost perfect lattice parameter match between GaAs and AlAs ( $a_{\text{GaAs}} = 5.653\text{Å}$ ;  $a_{\text{AlAs}} = 5.662\text{Å}$ ) (2). Because of this lattice match, strain-free layers of  $\text{Ga}_{1-x}\text{Al}_x\text{As}$  of high metallurgical quality could be deposited by epitaxial techniques onto GaAs substrates. Moreover, the lattice parameter match avoids the introduction of carrier trapping states at the interface between the epitaxial layer and the GaAs.

The authors recently suggested (3) that the degree of match between the lattice parameters of the two III-V compounds forming an alloy might also determine in part the homogeneity and general "quality" of bulk crystals of the alloy. This is a consequence of the absence of lattice strain that would otherwise be introduced when alloys are formed from components of different sizes. This strain makes a contribution to the excess free energy of mixing, which causes a departure of the phase boundaries in the  $T-x$  phase diagram from their positions for ideal solutions.

In the earlier investigation, Foster and Woods (3) determined the degree of nonideality of the three homologous alloy systems,  $\text{Ga}_x\text{In}_{1-x}\text{Sb}$ ,  $\text{Ga}_x\text{In}_{1-x}\text{As}$ , and  $\text{Ga}_x\text{In}_{1-x}\text{P}$ , in which the lattice parameters of the two components differ by 6.10, 6.92, and 7.38%, respectively. The excess free energy of mixing found for the three solid alloys correlated with the lattice parameter

mismatch, increasing from the antimonide to the arsenide to the phosphide.

In a separate study (4) it was shown that in the  $\text{GaSb}_{1-x}\text{As}_x$  system, where the lattice mismatch is still greater (7.52%), the excess free energy of mixing is also greater than for the other systems.

Although the relationship between the lattice parameter mismatch and the nonideality of a system is not known in detail, and probably cannot be simply described in terms of elastic strain, it was predicted that a vanishing mismatch would be accompanied by a vanishing excess free energy of mixing. The assumption that the  $\text{Ga}_{1-x}\text{Al}_x\text{As}$  system was ideal, because of the very good parameter match, had been made by others (5, 6), and this was largely supported by calculation of the Ga-Al interaction parameter from solubility data in the gallium-rich corner of the Ga-Al-As ternary. The liquidus data at low temperatures could be fit quite well using an interaction parameter of zero. The fit was poorer at the highest temperature (1100°C), however.

The present investigation to determine the solidus boundary in the  $\text{Ga}_{1-x}\text{Al}_x\text{As}$  system was undertaken in order to test the hypothesis that this pseudobinary system is ideal, with data obtained in the same manner as for the earlier systems (3).

#### Experimental

The procedure employed to obtain the solidus boundary has been described by Foster and Scardefield (7). In brief, referring to Fig. 1, a finely ground (to pass 200 mesh) mixture of the two components is pressed into a pellet and held at a constant temperature  $T$  within the two-phase region of the pseudobinary diagram for a sufficient time to become equilibrated. It will then consist of solid solution particles whose composition is given by the solidus at  $T$ , suspended in a liquid whose composition is given by the liquidus at this temperature. After the equilibrated sample is quenched, the solid solution particles can be readily

\* Electrochemical Society Active Member.

Key words: phase diagrams, compound semiconductors, solution theory.

Table I. Solidus data in the  $\text{Ga}_{1-x}\text{Al}_x\text{As}$  system

Temp, °C	$x_{\text{AlAs}}$ , mole fraction
1273	0.200
1313	0.368
1350	0.480
1435	0.680
1490	0.748
1563	0.835
1602	0.879
1653	0.926

identified visually and are analyzed with an electron microprobe. The entire solidus curve is generated by equilibrating a sufficient number of samples in the two-phase region over the temperature range between the melting points of the pure components.

The method of encapsulating the pressed sample pellets for equilibration at high temperatures is shown in Fig. 1 of Ref. (7). For the present experiments, a pyrolytic boron nitride crucible was preferred over the alumina one shown there because of the greater ease of removal of the sintered pellet after quenching. It was determined that 48 hr at temperature was sufficient for equilibration, as indicated by flat plateaus in the composition vs. distance plots of the microprobe data [see Ref. (7)].

For samples of high AlAs content it was necessary to maintain a film of kerosene over the polished surface until just before insertion into the microprobe vacuum in order to prevent reaction with air or moisture.

### Results and Discussion

Eight experimental points were determined. The data are given in Table I and plotted in Fig. 1. The samples for the four highest temperature points were equilibrated in a different furnace from that used for the lower four. The displacement of one set relative to the other probably reflects a small error in temperature measurement in one of the furnaces and is not considered significant. The melting point of GaAs (1240°C) was taken from Lichter and Sommelet (8). The melting point of AlAs (1770°C) was determined in this laboratory by R. J. Chicotka.

The continuous curves of Fig. 1 are the ideal liquidus and solidus boundaries calculated from [1] and [2] below (Eq. 13 and 14, Ref. 3).

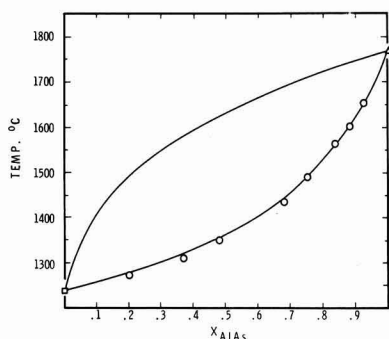


Fig. 1. GaAs-AlAs pseudobinary system. ○ This work; □ Ref. (8); △ R. J. Chicotka, personal communication. — Ideal boundaries calculated from [1] and [2] (see text).

$$x_{\text{Id}}^1 = \{1 - \exp[-L_1(T - T_1)/RTT_1]\} / \{\exp[-L_2(T - T_2)/RTT_2] - \exp[-L_1(T - T_1)/RTT_1]\} \quad [1]$$

$$x_{\text{Id}}^2 = \{1 - \exp[L_1(T - T_1)/RTT_1]\} / \{\exp[L_2(T - T_2)/RTT_2] - \exp[L_1(T - T_1)/RTT_1]\} \quad [2]$$

where the heat of fusion of GaAs,  $L_1$ , is taken to be 25.18 kcal/mole, as measured by Lichter and Sommelet (8). There are no experimental heat of fusion data for AlAs. The ideal curves were calculated with the entropy of fusion of AlAs assumed equal to that of GaAs; i.e.,  $S_f = L_f/T_f = 16.64$  eu, and  $L_2 = 16.64 \times 2043 = 34.0$  kcal/mole. This, of course, is very approximate; however, plots with the entropy of fusion of AlAs taken 0.5 eu higher or lower were essentially indistinguishable from those of Fig. 1.  $x_{\text{Id}}^1$  and  $x_{\text{Id}}^2$  in [1] and [2] are the mole fractions of AlAs in the liquid and solid, respectively.  $T_1$  and  $T_2$  are the melting temperatures of pure GaAs and AlAs.

It appears from Fig. 1 that the solidus in this system is very nearly ideal. This cannot be established unequivocally in the absence of data for the liquidus, since deviations from Raoult's law in the liquid would affect the solidus curve as well as the liquidus curve. [The liquidus data that are available (5, 6) are not at sufficiently high temperature for extrapolation onto the GaAs-AlAs tie line to give the liquidus in the pseudobinary.] According to our calculations, however, in order for such deviations to shift the solidus for a nonideal solid to the position calculated for an ideal solid, the liquid would have to be even less ideal than the solid. In the four systems studied previously (3, 4) the liquids were all more ideal than the solids. If this character is assumed for the  $\text{Ga}_{1-x}\text{Al}_x\text{As}$  system, it can be concluded that both liquid and solid phases in this system are ideal. This strengthens the hypothesis (3) that, in a III-V semiconductor alloy, departure from Raoult's law of mixing is closely associated with the degree of lattice mismatch between the two components of the alloy.

### Acknowledgment

The authors wish to thank R. J. Chicotka for supplying the AlAs and J. D. Kupis for performing the electron microprobe analyses.

Manuscript submitted Dec. 2, 1971; revised manuscript received Jan. 31, 1972.

Any discussion of this paper will appear in a Discussion Section to be published in the December 1972 JOURNAL.

### REFERENCES

1. J. M. Woodall, H. Rupprecht, and W. Reuter, *This Journal*, **116**, 899 (1969).
2. S. M. Ku and J. F. Black, *J. Appl. Phys.*, **37**, 3733 (1966).
3. L. M. Foster and J. F. Woods, *This Journal*, **118**, 1175 (1971).
4. L. M. Foster and J. F. Woods, *ibid.*, **119**, 504 (1972).
5. M. Ilegems and G. L. Pearson, "Gallium Arsenide," p. 3, C. I. Pearson, Editor, Inst. of Phy. and the Physical Soc., London (1969).
6. M. B. Panish and S. Sumski, *J. Phys. Chem. Solids*, **30**, 129 (1969).
7. L. M. Foster and J. E. Scardefield, *This Journal*, **117**, 534 (1970).
8. B. D. Lichter and P. Sommelet, *Trans. AIME*, **245**, 1021 (1969).



# The Effect of Mask Edges on Dopant Diffusion into Semiconductors

C. F. Gibbon, E. I. Povelonis, and D. R. Ketchow

Bell Telephone Laboratories, Incorporated, Murray Hill, New Jersey 07974

## ABSTRACT

A series of masked diffusions of Sn into GaAs and B into Si has been made through masks having stripe openings ranging in width from 20 mils (508  $\mu\text{m}$ ) down to 0.1 mils (2.5  $\mu\text{m}$ ). For Sn diffusion into GaAs from a pyrolytically deposited, doped  $\text{SiO}_2$  source the junction depth depends strongly on mask opening width. It increases with decreasing mask opening size, passes through a maximum as large as 3 times the unmasked value and then decreases slightly at the smallest opening widths. These results are shown to be consistent with the presence of an accelerated diffusion at the mask edge. This "pull-down" of the junction at the mask edge overlaps at narrow mask openings and produces the increase in junction depth. Diffusion of boron through an  $\text{SiO}_2$  mask opening also results sporadically in the production of a junction profile which suggests that diffusion is accelerated at the mask edge with an accompanying change in junction depth with mask opening size. It is shown that the effect appears in a variety of diffusion source systems. Three possible mechanisms by which mask edges could affect diffusion of dopants into semiconductor substrates are described. Some tentative explanations of the observed effects have been made on the basis of these mechanisms.

Although diffusion into semiconductors is often studied on unmasked slices, in practice most diffusions for device applications are masked to produce a planar pattern. In carrying out diffusions of Sn into GaAs the authors have observed that the junction depth obtained with a diffusion done through a mask opening is frequently much deeper than that obtained under identical circumstances in an unmasked slice. It is clear, therefore, that diffusions through mask openings are not necessarily identical to diffusions into unmasked slices done under the same conditions. At least three factors could cause enhanced penetration in the case of the masked diffusions; they are strain effects, source film edge effects, and indiffusion of impurities from the mask. These three factors are discussed below.

**Strain effects.**—In many cases, as for instance when using  $\text{SiO}_2$  masks on Si, the mask has a significantly different coefficient of expansion than the substrate. Stresses are then present at the mask/substrate interface at any temperature different from the temperature of formation or deposition of the mask. When a strip of the mask is removed for diffusion, it is conceivable that the elastic strain in the vicinity of the mask edge could be relieved by the generation of a dislocation network along the mask edge. This generation might not occur until later when the slice is heated for diffusion and the yield stress diminished by the increase in temperature. It has been shown (1) that mechanical deformation can accelerate or retard diffusion in silicon depending on the dopant type. Thus one might expect to find some enhancement or retardation of diffusion along the mask edge in a semiconductor substrate due to thermal strain effects.

**Source film edge effects.**—If the diffusion is done by driving the dopant into the substrate from a finite, predeposited, thin film source, then the effective source film thickness can change considerably near the mask edge. (See Fig. 1; the walls of the mask opening are shown as vertical in this illustration although they are generally at some angle to the surface due to undercutting.) At the mask edge the thickness of the film will increase due to the deposition of the film source on the side walls of the mask opening and also due to filleting of the corner if the source viscosity is low enough that it will flow under the influence of the source film surface tension. This effect will be im-

portant only in those cases where the source film is sufficiently thin or the diffusivity of dopant in the film sufficiently high that the finite thickness of the source becomes important in the diffusion kinetics.

**In-diffusion from mask.**—The mask itself can operate as a source of impurities during diffusion. This is particularly true for diffusions of certain dopants into compound semiconductors such as GaAs where pyrolytically deposited  $\text{SiO}_2$  films intentionally doped with phosphorus are used as masks (2). The phosphorus is needed to decrease the diffusivity of dopants in the mask medium but, of course, it could diffuse into the substrate itself. Therefore, along the mask edge the diffusion of the dopant could be altered by the presence of the in-diffusing impurity which has the mask as its source. If the impurity is electrically active it can produce a field which may either retard or accelerate the dopant depending on the relative charge and the difference in size of the diffusion coefficients of the two species (3). If the ions are substitutional and of considerably different size then strain effects might also produce an interaction between them, and an alteration of their diffusion coefficients. Thus again some variation in diffusion properties near the mask edge might be expected.

In this work it is shown that the differences in diffused junction depths between masked and unmasked substrates is related to an apparent dopant diffusion acceleration effect associated with mask edges. Several features of this mask enhanced diffusion effect make it of interest. First as noted below, in the case of boron diffusion into silicon from certain sources it is sporadic,

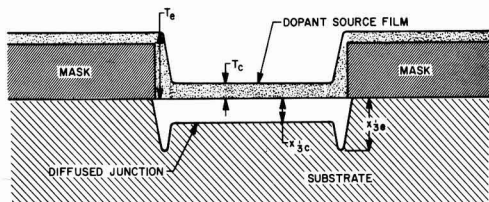


Fig. 1. Hypothetical diagram of diffusion source distribution around a mask opening and resulting junction profile;  $T_c$  and  $T_e$  are the center and edge thicknesses of the source film; and  $x_{jc}$  and  $x_{je}$  are the center and edge junction depths.

\* Key words: diffusion, silicon, gallium arsenide, masking.

occurring unpredictably for silicon substrates processed with nominally identical procedures in the same or different facilities. It thus represents a possible source of diminished control over diffused elements. Second, the effect gives a variation in the junction depth with mask opening size which makes monitoring diffused layer properties with separate test chips difficult. And third, the mask edge effect, when present, creates a junction profile with a point under the mask edge (see Fig. 1) which could be a source of altered reverse bias breakdown in diodes. [The overlapping effects of the mask edges for small ( $\leq 10 \mu\text{m}$ ) mask openings produces what appears to be simply a deeper junction than would be produced on an unmasked slice without the edge-associated pull-down.]

### Experimental

In order to investigate the existence and magnitude of mask opening effects on diffusion, a mask having openings from 20 mils ( $508 \mu\text{m}$ ) to 0.1 mil ( $2.5 \mu\text{m}$ ) wide was made and a series of diffusions was done into slices having this configuration etched into their masks. Diffusions were done with Sn through phosphorus-doped  $\text{SiO}_2$  masks into GaAs and with B through thermally grown  $\text{SiO}_2$  into Si.

The gallium arsenide substrates into which Sn diffusions were done were p-type boat-grown ingots having a base doping  $p = 5 \times 10^{16}/\text{cm}^3$ . The polished and etched slices were cleaned and phosphorus-doped  $\text{SiO}_2$  masks deposited on them. After application of photoresist, exposure through the mask and etching, approximately 3000 Å of tin-doped  $\text{SiO}_2$  was deposited as a diffusion source from a forming gas stream passed through a solution of ethylorthosilicate plus 2 volume per cent (v/o) tetramethyl tin. The dopant was then driven-in for 1 hr in forming gas at  $1050^\circ\text{C}$ . This tin diffusion system has been discussed in detail by Gibbon and Ketchow (4). The specimens were angle lapped, stained, and photographed after diffusion.

The boron diffusions were done into silicon wafers, 8 mils thick, cut from a 10-12 ohm-cm, n-type, phosphorus-doped,  $\langle 111 \rangle$  oriented silicon ingots, 0.850 in. in diameter. Three of these were float zone ingots and one Czochralski. These wafers had one side silica-sol polished, and it is into this side that the diffusions were performed.

Both sides of the substrate were either wet or dry oxidized to 10,000 Å (the oxide on the back side is retained throughout processing). The dry oxidations were done at  $1200^\circ\text{C}$  and the wet oxygen oxidations at  $1050^\circ\text{C}$ . A boron diffusion is then performed into the substrate wafer through the mask openings. Diffusion sources utilized included boron nitride, boron tribromide, boron-doped oxide films, and low energy boron ion implantations.

Several different BN source systems were used, but in each case a 10-20 min predeposition in an inert gas ambient at  $870^\circ\text{--}900^\circ\text{C}$  was followed by a 60-70 min drive-in in 10%  $\text{O}_2$  in  $\text{N}_2$  at  $1135^\circ\text{--}1150^\circ\text{C}$ . (These parameters were constant for each system, the ranges refer to all systems utilized.) The  $\text{BBr}_3$  source diffusion included a predeposition in 0.2%  $\text{O}_2$  in  $\text{N}_2$  at  $875^\circ$  or  $1140^\circ\text{C}$  and a drive-in in 10%  $\text{O}_2$  in  $\text{N}_2$  at  $1135^\circ\text{--}1140^\circ\text{C}$ . A control wafer, without any oxide mask, was usually diffused simultaneously with the oxide-masked substrate wafer. The sheet resistance of the diffused layer on the control wafer was measured with a 4-point-probe. Both the control wafer and the substrate wafer were angle-lapped, stained, and the junction depths of the diffusion measured and photographed with an interferometer. In studying the photomicrographs of the angle laps one should keep in mind that the diffused region is distorted by the magnification of distances perpendicular to the surface by a factor of 20 over those parallel to the surface. Surface concentrations were determined from sheet resistance and junction depth data using Irvin's curves (5).

## Tin Diffusion into GaAs

### Results

Figures 2 and 3 show the junction depths obtained after diffusion of Sn in GaAs as a function of mask opening size. The data are given for two different mask thicknesses: 1600 and 4800 Å. The junction depth in an unmasked slice given the same treatment was  $0.9 \mu\text{m}$ . The diffusion depth starts near this value for the center of the widest mask opening and increases with decreasing mask opening. It reaches a maximum of nearly three times the unmasked depth in the neighborhood of 20-50  $\mu\text{m}$  mask opening width. It then decreases slightly. The thickness of the mask seems to have little effect. Near the edge of the phosphorus-doped  $\text{SiO}_2$  mask the junction depths are deeper than at the center when the mask opening is larger than 50  $\mu\text{m}$ . This mask edge "pull-down" effect is clearly visible in Fig. 4, which shows photomicrographs of four diffused stripes of various widths in a specimen with a 1600 Å phosphorus-doped  $\text{SiO}_2$  mask. The junction outline is given a peculiar dish-like appearance by this mask edge effect. It can be seen that the apparent increase in center junction depth with decreasing opening width is due to the overlapping of the two-edge effects.

### Discussion

The first of the mechanisms postulated in the beginning of this paper by which diffusion might be altered by the presence of the mask edge is the presence of a deformed region due to the difference in the thermal expansion coefficient of the oxide and GaAs substrate.

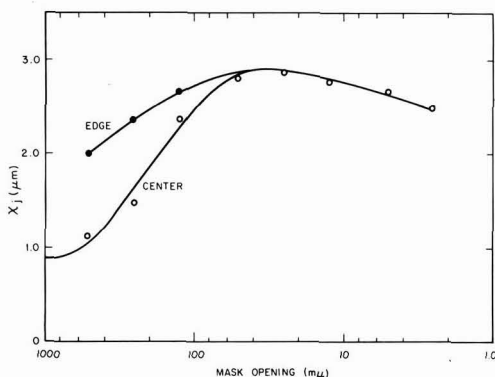


Fig. 2. The junction depth as a function of mask opening size for tin diffusion into GaAs with a 1600 Å P-doped  $\text{SiO}_2$  mask. Measurements from both the center and near the mask edge are shown.

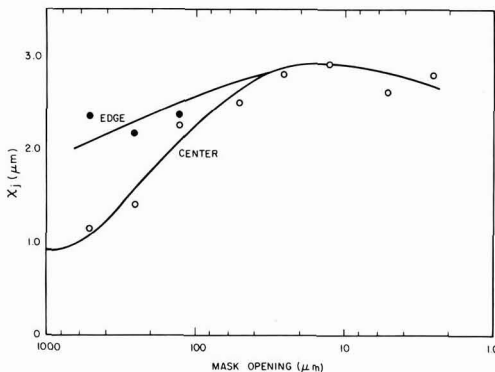


Fig. 3. The junction depth as a function of mask opening size for a 4800 Å mask.

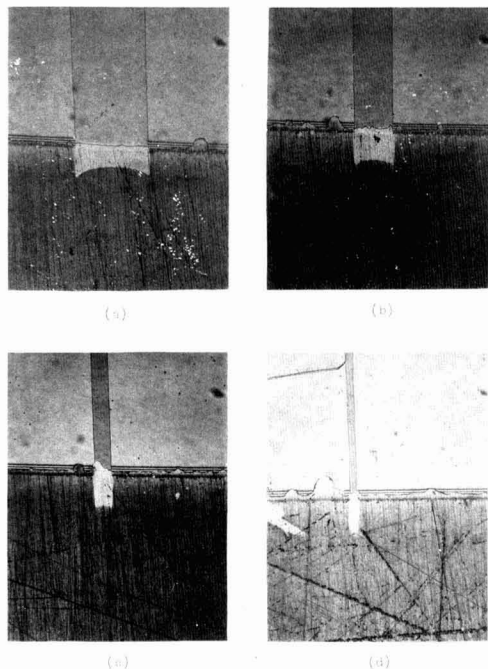


Fig. 4. Photomicrographs of angle-lapped slices of GaAs showing pull-down of diffusion near the phosphorus-doped  $\text{SiO}_2$  mask edge; mask opening width (a) 10 mils, (b) 5 mils, (c) 1 mil, and (d) 0.5 mils.

The thermal expansion coefficient of the phosphorus-doped  $\text{SiO}_2$  mask is not known; however, the expansivity of pure  $\text{SiO}_2$  is low, about  $6 \times 10^{-7}/^\circ\text{C}$ , while that of GaAs is nearly  $60 \times 10^{-7}/^\circ\text{C}$ . The general tendency is for a marked increase, up to an order of magnitude, in the thermal coefficient of expansion of silicate glasses as other compounds are added to  $\text{SiO}_2$ . For instance, borosilicate glasses have an expansivity around  $40 \times 10^{-7}/^\circ\text{C}$ . Thus the expansion coefficient of the mask is probably, but not certainly, less than GaAs, and interface stresses may develop when the masked substrate is heated above the deposition temperature. This stress could conceivably alter the diffusivity of the tin in the substrate and produce the observed pull-down at the mask edge.

The second effect postulated was variations in the source film thickness due to the presence of the mask walls (see Fig. 1). The possible extent of this effect can be estimated from Eq. [A4], which is developed in the Appendix, that is

$$R^2 = \left( \frac{x_{je}}{x_{jc}} \right)^2 = \frac{4Dt}{(x_{jc})^2} \ln \frac{T_e}{T_c} + 1 \quad [\text{A-4}]$$

In this case  $x_{je}$  for a wide mask opening is about  $1.0 \times 10^{-4}$  cm,  $D$  is approximately  $5 \times 10^{-13}$  cm<sup>2</sup>/sec (4),  $t$  is  $3.6 \times 10^3$  sec and it seems reasonable to assume that the largest difference one could postulate between  $T_e$  and  $T_c$  is about the thickness of the mask, so  $T_c$  is  $3 \times 10^{-5}$  cm and  $T_e$  is about  $8 \times 10^{-5}$  cm. If these values are used to find  $R$  from Eq. [A4], one finds

$$R = 1.2$$

This is less than the value of 2.0-2.5 which can be seen from Fig. 2 and 3 to hold for  $R$  at large mask openings. The difference of about 0.2  $\mu\text{m}$  between center and edge junction depth predicted is one-fifth the observed difference of 1.0-1.5  $\mu\text{m}$ . Thus source thickness variations appear unlikely to be the major source of the mask edge junction pull-down.

The third possibility for the origin of this effect is the coupling of the Sn diffusion flux to a flux of some impurity which diffuses in from the mask. In these experiments, the mask is doped with phosphorus, and thus it is possible that there is some in-diffusion of P. Very little is published on the subject of phosphorus diffusion in GaAs, but it is known from the work of Stone (6) that a surface concentration of P around  $10^{20}/\text{cm}^3$  can be produced from 1 atm of phosphorus pressure at  $1000^\circ\text{C}$ . Stone estimates the diffusion coefficient of phosphorus in GaAs to be  $10^{-12}$  to  $10^{-13}$  cm<sup>2</sup>/sec at  $700^\circ$ - $800^\circ\text{C}$ . Thus phosphorus may be present in the GaAs under the mask at  $1050^\circ\text{C}$ , the drive-in temperature utilized in the present work. The mechanism by which the phosphorus might couple with the tin diffusion to accelerate it is not clear. The phosphorus probably substitutes isoelectronically for arsenic on the arsenic sublattice, and thus it appears that the electronic effects would be small. Phosphorus with a tetrahedral covalent radius of 1.10 Å (7) is smaller than the arsenic it replaces which has a corresponding value of 1.18 Å. Since the covalent radius of Sn is larger than Ga, 1.40 Å as compared to 1.26 Å, if tin diffuses substitutionally it could be accelerated by a gradient in strain energy since the strain field associated with it would be opposite in sign to that associated with the phosphorus impurity.

In summary the junction depth variation with mask opening size is a result of junction pull-down along the mask edge. It appears that this acceleration of diffusion at the mask edge is due either to strain effects related to differences in the thermal coefficient of expansion of the substrate (GaAs) and the mask (P-doped  $\text{SiO}_2$ ), or to in-diffusion of phosphorus. A more definitive understanding of this effect will require further investigation.

## Boron Diffusion into Silicon

### Results

Figure 5 shows the variation in junction depth with mask opening size for a silicon slice diffused with the BN system (note the suppressed zero in this figure). Assuming the diffusion to be approximately Gaussian, calculation of the surface concentration from the sheet resistance and junction depth of an unmasked test slice gives  $C_s = 3 \times 10^{19}/\text{cm}^3$ .

Here, as in the case of Sn diffusion into GaAs, the junction depth varies with mask opening size and this effect is seen in the inset angle lap photographs in Fig. 5 to be associated with a junction pull-down at the mask edge. The enhancement in junction depth

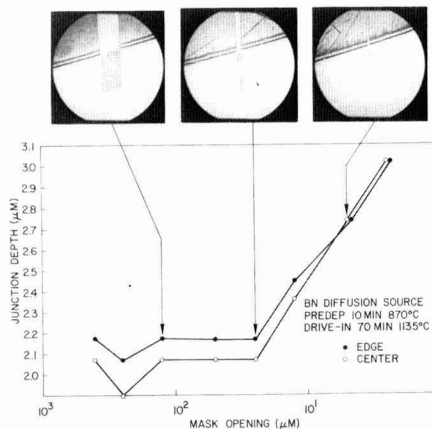


Fig. 5. Typical enhancement in junction depth vs. mask opening size for boron diffused into silicon using a source layer predeposited from oxidized BN disks.

for the smallest mask opening size is considerably greater than the individual enhancement along either edge which suggests that the effect combines superlinearly when the mask edges come in close proximity. It might be suggested that the general increase in junction depth is due to a nonuniform diffusion across the slice, however no such effect was seen on accompanying unmasked test slices, and it occurred in the same way on a number of identical masked slices.

It should be noted though that silicon slices were diffused which had none of the mask edge effect or junction depth dependence on mask opening size seen here. The occurrence, or nonoccurrence, was always uniform across a slice: the slice either showed the mask-edge pull-down or it did not. Identical slices were diffused in similar BN source systems by different operators with similar results: very roughly half the time the mask edge acceleration was seen in four different systems.

A number of variables were examined in detail to try to locate the origin of the sporadic appearance of the mask-edge effect. These included the orientation of the mask opening channels on the (111) slice surface, and the growth ambient and temperature of oxidation of the mask oxide. These variables were selected because it was felt they might influence the strain distribution around the mask edge. None of these variables detectably influenced occurrence of the mask-edge effect.

Another variable examined was the ingot source of the substrate. The slices utilized in this work were cut from four nominally identical ingots. Most of the experiments (86 slices) were carried out on slices from two ingots, one float zone and one Czochralski, in which the mask-edge effect occurred; in the other two (float-zone ingots from which 17 wafers were processed) no mask-edge pull-down was observed. Thus the occurrence of the effect may be contingent on the value of some property in the substrate; however, it was not possible to determine what this feature was. There was no clear relationship, for instance, between ingot growth type and the presence of the enhanced mask-edge diffusion.

For a single system, slices were diffused with a series of predeposition times in order to vary the final surface concentration. Table I lists the results of this experiment. The mask-edge acceleration appears to occur more frequently at higher concentrations. The sporadic nature of the mask-edge effect thus appears to be related to variations in the surface concentration between individual diffusions and to some differences in substrate properties. Although the list of variables examined seems reasonably exhaustive, other undefined variations from slice to slice may influence the appearance of this effect.

The effect appeared much less frequently and with a much smaller influence on junction depth in the case of diffusions from a source glass deposited from  $\text{BBr}_3$ . Figure 6 shows a typical case where some mask-edge

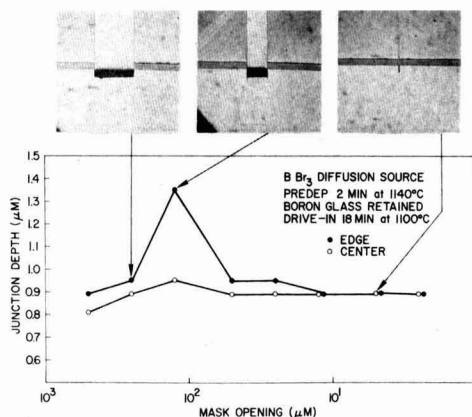


Fig. 6. Junction depth vs. mask opening size for diffusion source predeposited from  $\text{BBr}_3$ .

effect was apparent. In this system, the mask-edge effect did not appear uniformly across the slice, also other irregularities away from the mask edge occasionally appeared. Table II lists results of a series of diffusions done with different conditions to produce different surface concentrations. There is in this case little evidence of dependence on surface concentration.

Several other sources of boron were used for boron diffusion in this study. Diffusions from these sources also show the mask-edge acceleration effect. It was called to the authors' attention that an apparent mask-edge acceleration of diffusion is occasionally observed in integrated circuits in which a p-layer is diffused from a boron ion-implantation (8). In an effort to independently reproduce this effect,  $5 \times 10^{12}/\text{cm}^2$  and  $5 \times 10^{13}/\text{cm}^2$  implantations of boron were made at room temperature at 30 keV. The boron was then diffused in a 10%  $\text{O}_2$  in  $\text{N}_2$  ambient for 1 hr and 5 hr at  $1150^\circ\text{C}$ . Evidence of mask-edge acceleration could be detected in the 5 hr but not the 1 hr diffusions (see Fig. 7). The fact that such an effect is observed in these diffusions strongly suggests that filleting of a chemical source film is not the origin of the mask-edge effect.

Another experiment performed which indicated that the influence of mask-edge filleting is not the source of mask-edge acceleration was the diffusion of boron from channels of boron-doped  $\text{SiO}_2$  pyrolytically deposited from silane, diborane, and oxygen at  $350^\circ\text{C}$ . No oxide mask, as such, is present in this case. Boron-doped  $\text{SiO}_2$  was deposited uniformly over the slice and then all of it was removed except for stripes which were parallel bars forming a pattern just the negative of the mask pattern previously used. The slice was driven-in in  $\text{N}_2$  at  $1100^\circ\text{C}$ . As seen in Fig. 8 a channel edge acceleration appeared among these slices. (Some lateral diffusion along the unprotected surface also occurred.) Again, this result points away from source

Table I. Diffusions from a BN source

Time (min)	Predep. Temp. ( $^\circ\text{C}$ )	Time (min)	Drive-in Temp. ( $^\circ\text{C}$ )	Mask-edge effect	Surface conc. ( $\text{No./cm}^2$ )
1	870	60	1135	No	$1 \times 10^{10}$
1	870	60	1135	No	$1 \times 10^{10}$
1	870	60	1135	No	$1 \times 10^{10}$
5	870	60	1135	No	$6 \times 10^{10}$
5	870	60	1135	No	$6 \times 10^{10}$
5	870	60	1135	No	$6 \times 10^{10}$
10	870	60	1135	No	$1 \times 10^{11}$
10	870	60	1135	Yes	$1 \times 10^{11}$
10	870	60	1135	Yes	$1 \times 10^{11}$
20	870	60	1135	Yes	$3 \times 10^{11}$
20	870	60	1135	Yes	$3 \times 10^{11}$
20	870	60	1135	Yes	$3 \times 10^{11}$
100	870	60	1135	No	$9 \times 10^{11}$
100	870	60	1135	No	$9 \times 10^{11}$
100	870	60	1135	Yes	$9 \times 10^{11}$

Table II. Diffusions from a  $\text{BBr}_3$  source

Time (min)	Predep. Temp. ( $^\circ\text{C}$ )	Time (min)	Drive-in Temp. ( $^\circ\text{C}$ )	Evidence of mask-edge effect	Surface conc. ( $\text{No./cm}^2$ )
20	875	30	1135	Yes	$6 \times 10^{10}$
20	875	30	1135	No	$6 \times 10^{10}$
20	875	60	1135	No	$7 \times 10^{10}$
20	875	60	1135	No	$7 \times 10^{10}$
20	875	60	1135	No	$7 \times 10^{10}$
20	875	60	1135	No	$7 \times 10^{10}$
1	875	60	1135	Yes	$9 \times 10^{10}$
10	875	60	1135	No	$3 \times 10^{10}$
10	875	60	1135	No	$3 \times 10^{10}$
100	875	60	1140	No	$1 \times 10^{10}$
100	875	60	1140	No	$1 \times 10^{10}$
10	1140	10	1135	Yes	$4 \times 10^{10}$
10	1140	10	1135	No	$4 \times 10^{10}$



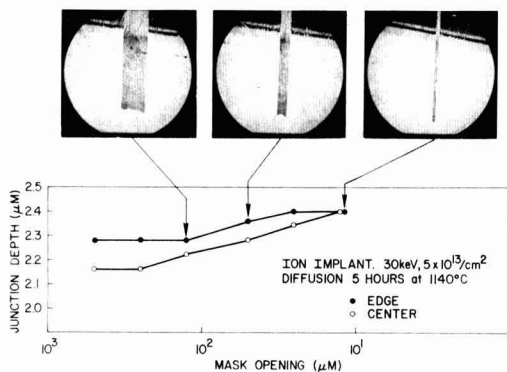


Fig. 7. Junction depth vs. mask opening size for a diffusion from an ion implanted source (Total dose =  $5 \times 10^{12}/\text{cm}^2$ ; implantation energy = 30 keV; diffusion 5 hr at  $1140^\circ\text{C}$ ).

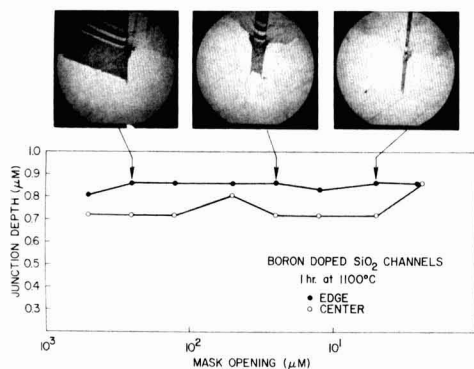


Fig. 8. Junction depth vs. channel width for boron diffusion from an unmasked stripe of deposited B-doped  $\text{SiO}_2$ .

accumulation at the mask edge as the origin of the apparent acceleration.

In summary, this study reveals the presence of a sporadic mask-edge diffusion phenomenon for boron diffusion into silicon. It does not depend on the type or thickness of the masking silica film used nor does it appear to be related to the facility in which the oxide film is formed. No consistent pattern has occurred regarding the mask-edge effect with any of the variations of the many parameters of predeposition and drive-in of the boron impurity which were studied, although there is some suggestion that the pull-down occurs more frequently for higher surface concentrations in the BN system. The possibility of a dependence on silicon ingot source from which the various substrate wafers were cut was found. No influence of the orientation of the channel patterns on the slice surfaces was discerned.

#### Discussion

The mask-edge effect as has just been seen has a very elusive origin. Its presence in slices diffused from ion implanted sources and B-doped  $\text{SiO}_2$  channels eliminates source filletting as a primary cause of it. As noted before some diffusion masks used on compound semiconductors are heavily doped to decrease the permeability of the mask material to the dopant and this may influence in-diffusion near the mask edge. However, the diffusion masks used on silicon are thermally grown  $\text{SiO}_2$  which is generally very lightly doped (by accumulation of base doping from the substrate), and, therefore, the influence of impurities in-diffusing from the mask seems unlikely to have a

strong influence on subsequent diffusion through openings made in the mask. (The fact that oxidation conditions do not have a critical influence on the appearance of the mask-edge effect supports this conclusion.)

Thus the presence of strain at the mask edge, due to the thermal expansivity mismatch seems the most prominent potential cause of the mask-edge effect. It should be pointed out, however, that x-ray topography has failed to reveal dislocations associated with mask edges in any of the boron diffused slices studied (9). (Dislocations have been observed to be generated at a mask edge (10); however, this appears to be associated with diffusions in which the surface is nearly saturated with the dopant, a condition not generally fulfilled in the present work.) This indicates that any strain effects which are active must be related to elastic strain fields with no influence of plastic deformation. This is a rather surprising observation since mechanical strain effects on diffusion in silicon are generally associated with the generation of dislocations (1). The random appearance of the pull-down strongly suggests that the conjunction of several factors may be required to precipitate its occurrence. The magnitude of the strain field surrounding the mask edge could be a very sensitive function of a number of factors (oxidation temperature, orientation, oxidation ambient, diffusion ambient, and substrate preparation); thus a strain field of appropriate sign and magnitude may be present only in a limited number of cases even where the procedure is nominally the same.

Elastic strain effects if present at the mask edge can influence diffusion in two ways. First there can be the direct influence of the strain field on the diffusion flux itself (11). Second the strain field can alter the equilibrium concentration of point defects and thus potentially influence the diffusion coefficient. Other somewhat more subtle effects of the presence of the mask may be the source of the diffusion acceleration, however. Perhaps, for instance, the transient flow of vacancies of the slice during cooling of the slice from the diffusion furnace may be influential.

#### Summary and Conclusions

1. An effect of mask opening size on diffusion into semiconductor substrates could arise from a number of sources: (i) strain effects at the mask edge; (ii) source film filletting at the mask edge; and (iii) in-diffusion of impurities from the mask.

2. It has been found that, in the diffusion of GaAs with Sn from Sn-doped  $\text{SiO}_2$  through openings in P-doped  $\text{SiO}_2$  masks, the junction depth depends strongly on the mask opening size. Examination of the photomicrographs of angle laps of the junctions suggests that the observed variation was due to a diffusion acceleration associated with the mask edge. An approximate calculation shows that this pull-down is probably not due to the presence of a thicker source film along the mask edge. Thus enhancement in the diffusion flux at the mask edge due either to mask-edge strain effects or to the simultaneous in-diffusion of phosphorus from the mask appears to be the origin of the effect.

3. In diffusions of boron into silicon the apparent mask edge associated diffusion acceleration is not associated exclusively with any particular diffusion source system; it appears sporadically in all systems examined including BN,  $\text{BBr}_3$ , B-doped predeposited  $\text{SiO}_2$  channels, and ion-implanted sources.

4. The effect appears in diffusion systems where mask-edge source filletting could not be its origin. Thus mask-edge strain is indicated as a likely source of the apparent diffusion acceleration.

5. Since no dislocations can be associated with the mask edges in x-ray topographic studies of these slices it appears that the effect might be related to elastic strain. However exact delineation of the mechanism of enhanced diffusion will require further study.



### Acknowledgments

J. V. Dalton, T. E. Saunders, P. N. Pappas, and K. R. Gardener each prepared several diffused slices for us. The ion-implanted diffusion sources were produced for us under the supervision of R. A. Moline. G. R. Weber deposited the B-doped oxide films.

We are grateful to G. A. Rozgonyi who took and interpreted several x-ray topographs for us.

Manuscript submitted July 26, 1971; revised manuscript received Feb. 7, 1972.

Any discussion of this paper will appear in a Discussion Section to be published in the December 1972 JOURNAL.

### APPENDIX

The only case considered is that where the diffusion is sufficiently long that the source film has begun to deplete. In that case we will approximate the source film as an instantaneous source having a surface concentration of  $C_0T$  (atoms/cm<sup>2</sup>) where  $C_0$  is the dopant concentration in the source film and  $T$  its thickness. For an instantaneous source

$$C = \frac{Q}{\sqrt{\pi Dt}} e^{-\frac{x^2}{4Dt}} \quad [A-1]$$

where  $C$  is the concentration at position  $x$  and time  $t$ .  $Q$  is the source surface concentration and  $D$  is the dopant diffusion coefficient. Then, if  $Q$  is associated with  $C_0T$ , the junction depth,  $x_j$ , is related to  $T$  by

$$\ln \left( \frac{C_s \sqrt{\pi Dt}}{C_0} \right) = \ln T - \frac{(x_j)^2}{4Dt} \quad [A-2]$$

where  $C_s$  is the concentration of dopant in the substrate. If the film thickness at the mask edge is  $T_e$  and at the mask center is  $T_c$ , then the junction depth at the edge ( $x_{je}$ ) and center ( $x_{jc}$ ) should be related by

$$(x_{je})^2 - (x_{jc})^2 = 4Dt \ln \frac{T_e}{T_c} \quad [A-3]$$

or, dividing by  $(x_{jc})^2$

$$(R)^2 - 1 = \frac{4Dt}{(x_{jc})^2} \ln \frac{T_e}{T_c} \quad [A-4]$$

where  $R$  is the ratio between the junction depth at the edge and the center. Since

$$(x_{jc})^2 = 4Dt \ln \frac{C_0 T_c}{C_s \sqrt{\pi Dt}} \quad [A-5]$$

we have

$$(R)^2 - 1 = \frac{1}{\ln (C_0 T_c / C_s \sqrt{\pi Dt})} \ln \frac{T_e}{T_c} \quad [A-6]$$

Thus the center to edge ratio should increase with increasing background doping in the substrate, diffusion coefficient, and time. It should decrease with increasing doping concentration in the source film and increasing source film thickness.

### REFERENCES

1. J. E. Lawrence, *Brit. J. Appl. Phys.*, **18**, 405 (1967).
2. D. Flatley, N. Goldsmith, and J. Scott, Paper 69 presented at Electrochem. Soc. Meeting, Toronto, May 3-7, 1964.
3. R. J. Jaccodine, *Appl. Phys. Letters*, **11**, 370 (1967).
4. C. F. Gibbon and D. R. Ketchow, *This Journal*, **118**, 975 (1971).
5. J. C. Irvin, *Bell System Tech. J.*, **41**, 387 (1962).
6. L. E. Stone, *J. Appl. Phys.*, **33**, 2795 (1962).
7. L. Pauling, "The Nature of Chemical Bond," Cornell University Press (1960).
8. K. Gardner, Private communication.
9. G. Rozgonyi, Private communication.
10. G. H. Schwuttke and J. M. Fairfield, *J. Appl. Phys.*, **37**, 4394 (1966); J. M. Fairfield and G. H. Schwuttke, *This Journal*, **115**, 415 (1968).
11. P. G. Shewmon, "Diffusion in Solids," p. 23, McGraw-Hill Book Co., New York (1963).

## Silicon Cleaning with Hydrogen Peroxide Solutions: A High Energy Electron Diffraction and Auger Electron Spectroscopy Study

R. C. Henderson\*

Bell Telephone Laboratories, Incorporated, Murray Hill, New Jersey 07974

### ABSTRACT

HEED and Auger electron spectroscopy have been used to evaluate silicon cleaning by sequential immersions in basic and acidic peroxide solutions. It was determined that an oxide film 13-15Å thick was left after the cleaning. This film contained boron at a surface concentration estimated at  $10^{13}$ - $10^{14}$  B/cm<sup>2</sup>. The carbide contamination that results upon heating to 800°C in ultrahigh vacuum was dramatically reduced when compared to wafers cleaned with other techniques. Wafers cleaned with the same process except for a final HF etch had no detectable boron in the surface oxide, formed relatively large amounts of surface silicon carbide at 800°C, and suffered extensive surface roughening with 1100°C heating in vacuum. The protective mechanism of the peroxide cleaning is thought to be due to formation of a thin nearly carbon free oxide layer that volatilizes when the wafers are heated in ultrahigh vacuum. It is recommended that experiments requiring a solvent type cleaning and the heating of Si in ultrahigh vacuum should use this cleaning method.

When a silicon wafer is heated to 800°C in ultrahigh vacuum, the silicon decomposes carbon-containing adsorbates to form  $\beta$ -SiC particle protuberances (1-2). These particles can play a significant role as evident

by their effect on silicon epitaxy experiments (3, 4). A thorough chemical precleaning is desirable since it is thought that this step is the dominating source of the carbon contamination (2).

A recent study has appeared evaluating the use of basic and acidic peroxide solutions in sequential steps

\* Electrochemical Society Active Member.

Key words: silicon cleaning, Auger electron spectroscopy, HEED.

for silicon cleaning (5). The work to be reported here presents the results of high-energy electron diffraction (HEED) and Auger electron spectroscopy experiments on wafers cleaned by this method and heated in ultra-high vacuum. Particular emphasis in this study has been placed on the desirability of HF as a final processing step. This emphasis was motivated by results indicating HF (i) enhances the carbon contamination (6), (ii) is a source of metal contamination (5), and (iii) is associated with the creation of stacking faults on (100) surfaces following oxidation (7).

The wafers used in these experiments were "Syton" polished (111) samples. The HEED optics and vacuum apparatus have been described previously (2). The Auger electron spectra were obtained using a coaxial cylindrical analyzer manufactured by the PHI Electronics Company. The detailed wafer processing, referred to here as peroxide cleaning, is presented in the Appendix. After loading, pump-down, and bakeout wafers were subjected to various heat-treatments in pressures not greater than  $1 \times 10^{-9}$  Torr. HEED diffraction patterns and Auger electron spectra were recorded after the samples had cooled to room temperature.

Some samples were examined by ellipsometry before being loaded in the vacuum station. In all cases the surface film found after cleaning was 13-15Å thick. A 1 min etch in concentrated HF reduced this thickness to 8-9Å.

Auger electron spectra obtained from a boron-doped wafer ( $10^{15}/\text{cm}^3$ ) cleaned with the peroxide method and before any heat-treatment are presented in Fig. 1. In addition to the carbon, SiO, and O peaks, there is a peak at 180 eV. According to tabulated values this peak could be due to the chlorine  $L_{3M_{23}M_{23}}$  or the boron  $KL_{2L_2}$  Auger transitions (8). No peaks were observed in the region 2200-2400 eV where the KLL chlorine peaks would be expected. Accordingly, the 180 eV peak is ascribed to boron. (From the peak size one would estimate the surface concentration to be  $10^{13}$ - $10^{14}/\text{cm}^2$ .)

Figure 2 shows the data obtained from the same wafer described above after heating at 500°C for  $10^3$  sec, heating at 900°C for  $10^3$  sec, and then rapid cooling to room temperature. No significant data changes were observed after the 500°C heat-treatment. However, it is evident that after the 900°C treatment the peaks due to Si have changed dramatically in a manner described before (8) and that the O and B have been reduced to values below their detection limits (which is expected to be  $10^{12}$ - $10^{13}/\text{cm}^2$ ). A small quantity of carbon remains. Confirming these observations, it is easy to calculate from SiO vapor pressure data (9) and the density of  $\text{SiO}_2$  that at 900°C in vacuum the

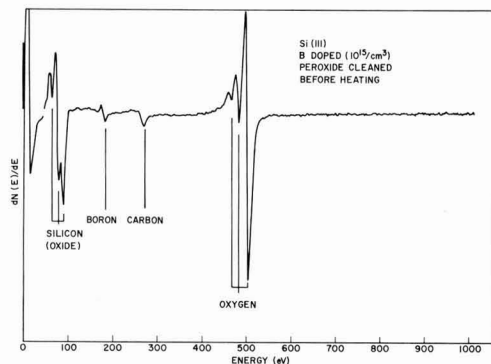


Fig. 1. Auger electron spectra from a wafer cleaned as detailed in Appendix and before any heat-treatment of the sample.

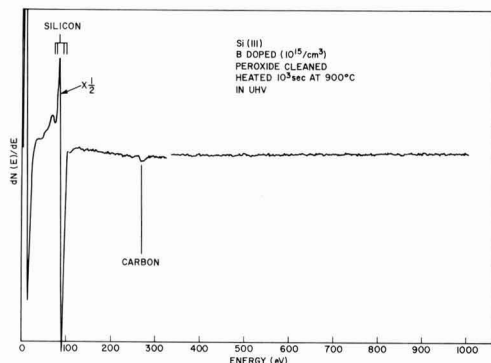


Fig. 2. Auger electron spectra from the wafer in Fig. 1, but after heating at 500°C for  $10^3$  sec, heating at 900°C for  $10^3$  sec and then cooling to room temperature.

observed 15Å of oxide would have evaporated in less than  $10^3$  sec.

The HEED diffraction pattern obtained from the same wafer after heating to 900°C is shown in Fig. 3A. The notable feature here is the extremely weak diffraction spots due to  $\beta$ -SiC. (The small streaks distributed on semicircular arcs are the Si(111)-7 surface structure described previously) (2). By way of contrast, note the plentiful amount of carbide evident in the pattern in Fig. 3B. The sample had been treated

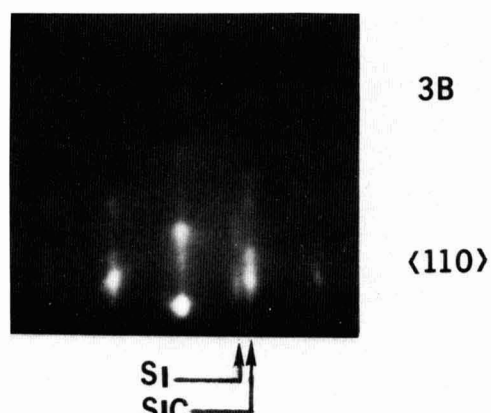
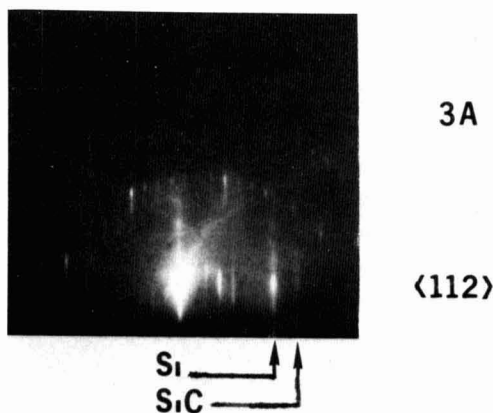


Fig. 3. A. HEED diffraction pattern from the wafer described in Fig. 2. B. HEED diffraction pattern from a wafer cleaned and heated as in Fig. 2 except for a final HF etch.

in the same manner as that of Fig. 3A, except that after the peroxide cleaning the wafer was dipped for 1 min in concentrated HF.

The experiments described above were repeated with phosphorus-doped ( $\sim 10^{16}/\text{cm}^3$ ) and antimony-doped ( $\sim 10^{15}/\text{cm}^3$ ) wafers. The results were identical.

In all these experiments there was no observable difference in the HEED or Auger data if the final wafer heating was in the range  $900^\circ\text{--}1100^\circ\text{C}$ . Lower temperatures, however, did not rid the surface of oxide within the  $10^3$  sec. Higher temperatures ( $\geq 1150^\circ\text{C}$ ) leave no observable carbide (2).

To confirm that the 180 eV peak was indeed boron, a peroxide cleaned wafer was heated to  $1100^\circ\text{C}$  for  $1 \times 10^3$  sec. Subsequently, the surface concentration was obtained by a capacitance inverse doping technique (10). The data showed  $3 \times 10^{17}$  B atoms/ $\text{cm}^3$  within  $0.1\mu$  of the surface. This number is to be expected based on the diffusion solution from a thin film source using the diffusion constant of boron at  $1000^\circ\text{C}$  ( $4 \times 10^{-13}$   $\text{cm}^2/\text{sec}$ ) and a surface concentration of  $1 \times 10^{13}$  B atoms/ $\text{cm}^2$ . The excellent agreement supports the conclusion of boron contamination.

The boron concentration was the one particular uncontrolled variable noted with this cleaning technique. With some wafers no boron was detected at all. On the other hand, consistency was observed for a given batch of samples, all cleaned at the same time although of varying dopant types or crystal faces. This fact implies that the contamination arises from the Pyrex glassware utilized or possibly the cleaning solutions themselves.

Wafers given a final HF etch after being peroxide cleaned differed in several respects from the data presented above. In the first place, no boron Auger peak was detected with these samples. Secondly, as evident from Fig. 3B, significantly greater amounts of carbide were formed when the wafer was heated. Finally, HF-etched wafers unaccountably often exhibit a matte-type finish due to surface roughening after being heated to  $\sim 1100^\circ\text{C}$ . For the most part, this effect does not occur with the peroxide cleaned wafers.

These latter results confirm earlier HEED experiments that demonstrate HF enhanced carbon contamination (6). In the early work wafers were cleaned by heating to  $1200^\circ\text{C}$  in vacuum until the surface was carbide free (presumably by solid-state diffusion of the carbon). A comparison was made between those wafers that were subsequently exposed to atmosphere and etched in HF and those that were just exposed to atmosphere. After heating to  $800^\circ\text{C}$  in vacuum the resulting diffraction patterns were quite similar to Fig. 3B and 3A, respectively.

Another comparison may be made to wafers cleaned by vapor etching in HCl gas at a substrate temperature of  $1100^\circ\text{C}$  until  $10\mu$  of Si has been removed. After loading the wafer into the vacuum station no carbon is detectable with the Auger electron spectrometer and only a faint trace of carbide is detectable with HEED after heating to  $900^\circ\text{C}$  (11). This latter technique is the most successful approach observed to date with respect to carbon. However, as a method the elevated temperature and the relatively large amount of Si removal required for successful cleaning, limit its applicability.

It is thought that the peroxide cleaning process produces a relatively small amount of carbide contamination by the following mechanism: After processing the 15Å of film remaining is silicon oxide that is relatively free of carbon-containing compounds. The oxide acts as a passivating and protective layer with respect to carbon adsorbates. At  $900^\circ\text{C}$  the oxide becomes relatively volatile. Since the majority of the adsorbates are physisorbed to the oxide, they are carried away during the sublimation process when the wafer is heated.

In contrast the surface that emerges from HF etch is particularly reactive. In addition to oxygen, the surface will also take up carbon compounds either from the HF directly or from the atmosphere. The resulting oxide film has relatively large amounts of carbon in contact with native silicon. When heated, the silicon attacks these compounds and yields copious amounts of SiC. Moreover, it is seen that carbon codeposited within this oxide phase is the major source of contamination rather than from the background gases of the vacuum station as had been previously supposed (1).

Previous HEED experiments have examined wafers cleaned by iodine passivation (12) or other etchants. Judging the amount of carbide from the intensity of the SiC diffraction spots, these experiments all show that the peroxide method is the most successful solvent type precleaning approach observed to date with respect to carbon. On the other hand, based on the discussion above, any method that would leave  $\sim 15\text{Å}$  of carbon-free oxide should serve equally as well.

Preferential local thermal etching is thought to be the mechanism that causes the surface roughening with high-temperature vacuum heating. The results obtained above suggest that this roughening is associated with the amount of silicon carbide contamination.

The boron incorporation is not surprising due to the known strong affinity of boron for the oxide phase (13). As noted above, this surface boron acts as a thin film diffusion source when these wafers are heated, and the Pyrex cleaning glassware is suspected to be the boron source. Although the boron can be eliminated by HF etching, this has undesirable effects with regard to carbon or metallic contamination. Consequently, it is recommended that the peroxide method described here be used, but modified by using quartz ware for the cleaning solutions.

It is also evident that the peroxide method does not completely eliminate the carbide resulting from heating the wafers. Moreover, vacuum ambient exposures of  $10^{-4}$  Torr · sec are sufficient that heat-treated "clean" silicon surfaces became carbon contaminated (2). Hence, some sort of *in situ* cleaning (e.g., argon sputtering) is desirable to obtain a rigorously clean surface or to rejuvenate one that has been treated in vacuum. In any case, since it is difficult to get rid of the carbide, the relatively small amount formed with the peroxide cleaning is advantageous.

A summary of the HEED and Auger electron spectroscopy results regarding the peroxide process are:

1. An oxide film 15Å thick is left after the cleaning. This film can contain appreciable amounts of boron presumably due to the use of Pyrex glassware.
2. Wafers heated in vacuum after this processing are considerably reduced in the carbide contamination when compared to other cleaning methods.
3. Etching with HF as a final processing step enhances the carbon contamination.
4. Surface roughening that occurs with  $1100^\circ\text{C}$  vacuum heating is largely reduced.
5. The protective mechanism of the cleaning process is thought to be due to the formation of a thin carbon-free oxide layer that volatilizes when the wafers are heated in ultrahigh vacuum.

In light of the desirability of reducing the carbide contamination, the peroxide cleaning method is recommended for experiments that require heating of Si in vacuum and where the high temperature and large amount of surface removal by the HCl vapor etching method cannot be tolerated. Etching with HF as a final step should be avoided. Quartz ware for containing the cleaning solutions should be used to avoid the boron contamination. Although these recommendations are particularly directed to Si vacuum experiments the information contained in this report should be useful for IC processing as well.

### Acknowledgments

The author wishes to thank Rohe Helm who assisted in setting up the Auger electron spectrometer and obtaining some of the data. Thanks are also due to R. Kaiser who obtained the ellipsometry data and M. Hanes who obtained the doping profile. Miss B. Kerns provided the detailed peroxide cleaning specifications.

Manuscript submitted Nov. 4, 1971; revised manuscript received Jan. 13, 1972. This was Paper 188 presented at the Cleveland, Ohio, Meeting of the Society, Oct. 3-7, 1971.

Any discussion of this paper will appear in a Discussion Section to be published in the December 1972 JOURNAL.

### APPENDIX

#### Peroxide Cleaning Specifications

1. Scrub polished wafer with acetone and then with 0.2% Triton X-100 solution. Rinse with filtered deionized water. Flush wet surface with absolute ethyl alcohol. Keeping slice surfaces wet transfer to a quartz holder in methyl alcohol.
2. Place holder and slices in a solution of  $\text{NH}_4\text{OH}$ - $\text{H}_2\text{O}_2$ - $\text{H}_2\text{O}$  maintained at  $80^\circ\text{C}$  for 10 min, insuring that the holder is beneath the liquid surface at all times. Agitate during this period. (The solution is to be made up fresh prior to use and is to have the following composition:
  - 1 part  $\text{NH}_4\text{OH}$ —reagent grade
  - 1 part  $\text{H}_2\text{O}_2$ —Superoxol, unstabilized
  - 4 parts  $\text{H}_2\text{O}$ —18 megohm, 0.2  $\mu\text{m}$  filtered
 Mix  $\text{NH}_4\text{OH}$  and  $\text{H}_2\text{O}$  and bring to temperature. Three minutes prior to use add  $\text{H}_2\text{O}_2$ .)
3. Overflow rinse with grade O or better deionized water for 2 min.
4. Rinse in cascade, 30 sec in each compartment. Agitate.

5. Place holder in a suitable container of fresh 49% HF for 2 min with agitation.
6. Rinse as in steps 3 and 4.
7. Place holder in a beaker of freshly prepared 4 to 1 to 1  $\text{HCl}$ - $\text{H}_2\text{O}_2$ - $\text{H}_2\text{O}$  at  $80^\circ\text{C}$  for 10 min. Agitate by hand. (Mix  $\text{HCl}$  and  $\text{H}_2\text{O}$  and bring to temperature. Three minutes before use add  $\text{H}_2\text{O}_2$ .)
8. Rinse as in steps 3 and 4.
9. Blow dry with filtered  $\text{N}_2$ .

### REFERENCES

1. I. H. Khan and R. N. Summergrad, *Appl. Phys. Letters*, **11**, 12 (1967).
2. R. C. Henderson, R. B. Marcus, and W. J. Polito, *J. Appl. Phys.*, **42**, 1208 (1971).
3. B. A. Joyce, J. H. Neave, and B. E. Watts, *Surface Sci.*, **15**, 1 (1969).
4. D. J. D. Thomas, *Phys. Status Solidi*, **13**, 359 (1966).
5. W. Kern and D. A. Puotinea, *RCA Rev.*, **31**, 187 (1970).
6. R. C. Henderson and W. J. Polito, Unpublished results.
7. C. M. Drum and W. Van Gelder, Paper 234RNP presented at Electrochem. Soc. Meeting, Atlantic City, N. J., October 4-8, 1970.
8. C. C. Chang, in "Modern Methods of Surface Analysis," Peter Mark and Jules D. Levine, Editors, p. 53, North-Holland Publishing Company, Amsterdam (1971).
9. J. J. Lander and J. Morrison, *J. Appl. Phys.*, **33**, 2089 (1962).
10. J. A. Copeland, *IEEE Trans. Electron Devices*, **ED-16**, May 1969.
11. R. C. Henderson and Rohe F. Helm, *Surface Sci.*, To be published.
12. R. Lieberman and D. Klein, *This Journal*, **113**, 956 (1966).
13. A. S. Grove, "Physics and Technology of Semiconductor Devices," p. 74, John Wiley & Sons, Inc. New York (1967).

## Thermodynamic Calculations of the Ge-H-Cl System

V. J. Silvestri\*

IBM Thomas J. Watson Research Center, Yorktown Heights, New York 10598

### ABSTRACT

The partial pressures of the gas species  $\text{GeCl}_4$ ,  $\text{GeCl}_2$ ,  $\text{GeHCl}_3$ ,  $\text{HCl}$ , and  $\text{H}_2$  in equilibrium with Ge solid have been calculated in the temperature range  $400^\circ$ - $1223^\circ\text{K}$  at chlorine to hydrogen ratios ranging from  $10^{-4}$  to 10. The theoretical efficiency for the deposition of germanium as applied to an open tube epitaxial system is discussed. Comparisons are made to the Si-H-Cl system.

In conjunction with growth rate and surface morphology studies in the  $\text{GeCl}_4$ - $\text{H}_2$  system, thermodynamic calculations giving theoretical maximum Ge deposition rates were made and compared with specific experimental Ge growth rate data (1). The purpose of this report is to separately, but more extensively describe the calculations and to display the pertinent features of the Ge-H-Cl equilibrium in a more general way. Comparable calculations have been reported by Lever (2) for the analogous Si-H-Cl system.

Equilibrium considerations in an open tube vapor growth system are useful (i) to determine a maximum yield for the system, (ii) for certain mass transport limited systems (3, 1) to predict deposition rates, and (iii) as a general guide for optimizing a process.

**Assumptions.**—The present analysis considered the gas species  $\text{GeCl}_4$ ,  $\text{GeCl}_2$ ,  $\text{GeHCl}_3$ ,  $\text{HCl}$ , and  $\text{H}_2$  in equilibrium with Ge solid.<sup>1</sup> The important assumptions

which were made for the calculations were:

1. The above gas species are the pertinent species.
2. All chlorine containing species are confined to the gas phase in equilibrium with solid Ge.
3. It was assumed that all gas species obey ideally Dalton's and the Ideal gas law.
4. Certain assumptions were also made with regard to the constancy of  $\Delta H^\circ_T$  and  $\Delta S^\circ_T$  for specific equilibria and these shall be cited appropriately below.

**Variables.**—The phase rule requires that a system having three components (Ge, H, and Cl), and consisting of two phases will have three degrees of freedom. Since these calculations were made specifically with reference to an open tube epitaxial deposition system, practical considerations lead to the following choice of independent variables: (i) total pressure, where for these calculations  $P_T = 1$  atm, since in most open tube systems this approximation is valid, (ii) temperature  $T$ , and (iii) the chlorine to hydrogen ratio,  $\text{Cl}/\text{H}$ , which is a conserved quantity in the gas phase.

**Equilibrium.**—For a given temperature the reaction chamber would contain the five gas species in equilib-

\* Electrochemical Society Active Member.

Key words: thermodynamics, germanium-hydrogen-chlorine system.

<sup>1</sup> Gas species such as  $\text{GeH}_2\text{Cl}_2$ ,  $\text{GeH}_2\text{Cl}$ ,  $\text{GeH}$ , and  $\text{GeCl}$  were not considered in the calculations, since it has been shown by Lever (2) that in the analogous Si-H-Cl system that the corresponding Si species were minor constituents.

rium with Ge solid. Among the five species considered to be present in the system, three independent equilibria may be written with their associated equilibrium constants,  $K$ , where  $P_x$  is the partial pressure of the species  $x$ .



$$K_1 = \frac{(P_{\text{GeCl}_4})(P_{\text{H}_2})^2}{(P_{\text{HCl}})^4} \quad [1]$$



$$K_2 = \frac{(P_{\text{GeCl}_2})(P_{\text{H}_2})}{(P_{\text{HCl}})^2} \quad [2]$$



$$K_3 = \frac{(P_{\text{GeHCl}_3})(P_{\text{H}_2})}{(P_{\text{HCl}})^3} \quad [3]$$

**Thermodynamic data.**—The calculations made use of the above equations along with the appropriate van't Hoff expressions of the form

$$\log K = -\frac{\Delta H}{2.303 RT} + \frac{\Delta S}{2.303 R} \quad (R \text{ is the gas constant})$$

relating the equilibrium constant with temperature  $T$  written below

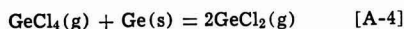
$$\log K_1 = \frac{6730}{T} - 8.02 \quad [1a]$$

$$\log K_2 = \frac{-465}{T} + 1.12 \quad [2a]$$

$$\log K_3 = \frac{7580}{T} - 7.45 \quad [3a]$$

The linear relationship for  $\log K_1$  (Eq. [1a]) is the best fit of  $K_1$  values for a number of temperatures in the temperature interval 400°–1100°K. The  $K_1$  values were calculated from room temperature enthalpy and entropy of formation data for Ge(s), H<sub>2</sub>(g), HCl(g) (4), and GeCl<sub>4</sub>(g) (5) corrected for higher temperatures using the tables of Kelley (6).

Sedgwick's (7) equilibrium data, Eq. [4a], for the reaction



$$\log K_4 = \frac{-7660}{T} + 10.25 \quad [4a]$$

was used along with Eq. [1a] to obtain Eq. [2a]. The reported  $K_4$  data for reaction, Eq. [A-4], was extrapolated to include the entire range of the calculations.

Thermodynamic data for GeHCl<sub>3</sub> is not known, and the room temperature enthalpy and entropy of formation were estimated by linear interpolation for the series GeH<sub>4</sub>, GeH<sub>3</sub>Cl, GeH<sub>2</sub>Cl<sub>2</sub>, GeHCl<sub>3</sub>, and GeCl<sub>4</sub>. This procedure is based on the assumption that bond energies are additive in generating the above series. Approximations of this type have been found to be valid in the analogous carbon series, and were used in estimating heats for the Si series (2). Using this method,  $\Delta H^\circ_{298}$  for GeHCl<sub>3</sub> was estimated at  $-90 \text{ kcal} \pm 10 \text{ kcal}$  from the room temperature enthalpy of GeCl<sub>4</sub> and the reported enthalpy of 21.6 kcal for GeH<sub>4</sub> (8). An interpolated room temperature entropy of 75.6 eu was used for GeHCl<sub>3</sub>, since the linear assumption was found to hold well for the above series for calculated values of GeH<sub>4</sub>, GeHCl<sub>3</sub>, and GeCl<sub>4</sub> as reported by Kelley (9). Equation [3a] was obtained assuming that  $\Delta H^\circ_{298}$  and  $\Delta S^\circ_{298}$  for reaction, [A-3], is constant over the temperature range of the calculations.

Because of the large uncertainty in the thermodynamic constants for GeHCl<sub>3</sub> the enthalpy of formation was varied in the calculations using values of  $-100$  and  $-85 \text{ kcal}$ . The effect of these enthalpy value

changes on the calculations shall be discussed later. Equation [3a] has been written using a  $-100 \text{ kcal}$  enthalpy value for GeHCl<sub>3</sub>(g). Dalton's law and Ideal gas law—from Dalton's law we have that the total pressure

$$P_T = P_{\text{GeCl}_4} + P_{\text{GeCl}_2} + P_{\text{GeHCl}_3} + P_{\text{H}} + P_{\text{HCl}} = 1 \text{ atm} \quad [5]$$

**Conservation of Cl, H, Ge in the system.**—The following conservation equations have been written in terms of partial pressures which are convenient to the calculations, since it has been assumed that the partial pressures of each species is related to its molar density in the system by the Ideal gas law  $PV = nRT$ . The following summations may be written

$$P_{\text{Cl}} = 4P_{\text{GeCl}_4} + 2P_{\text{GeCl}_2} + 3P_{\text{GeHCl}_3} + P_{\text{HCl}} \quad [6]$$

$$P_{\text{H}} = 2P_{\text{H}_2} + P_{\text{GeHCl}_3} + P_{\text{HCl}} \quad [7]$$

$$P_{\text{Ge}} = P_{\text{GeCl}_4} + P_{\text{GeCl}_2} + P_{\text{GeHCl}_3} \quad [8]$$

From Eq. [6-8] we can readily evaluate the various component ratios, such as

$$\text{Cl/H} = \frac{P_{\text{Cl}}}{P_{\text{H}}}, \quad \frac{\text{Ge}}{\text{Cl}} = \frac{P_{\text{Ge}}}{P_{\text{Cl}}}, \quad \text{and} \quad \frac{\text{Ge}}{\text{H}} = \frac{P_{\text{Ge}}}{P_{\text{H}}}$$

A convenient ratio to consider in this case is the Cl/H ratio. This ratio is an independent variable controlled experimentally, and is conserved in the gas phase. Thus the chlorine to hydrogen ratio at equilibrium, Cl(e)/H(e), is equal to the chlorine to hydrogen ratio at input, Cl(i)/H(i), and

$$\frac{4P_{\text{GeCl}_4}}{2(1 \text{ atm} - P_{\text{GeCl}_4})} = \frac{\text{Cl(i)}}{\text{H(i)}} = \frac{\text{Cl(e)}}{\text{H(e)}} \quad [9]$$

where  $P_{\text{GeCl}_4}$  is the partial pressure of the GeCl<sub>4</sub> in the gas stream, and  $(1 \text{ atm} - P_{\text{GeCl}_4}) = P_{\text{H}_2}$ .

Since we are interested in evaluating an efficiency for the system which describes the amount of dissolution of Ge in the gas phase or deposition of Ge from the gas at equilibrium, the Ge(e)/Cl(e), the Ge to chlorine ratio at equilibrium corresponding to a particular Cl(i)/H(i) must also be evaluated. The change in the Ge/Cl ratio from the input value can then be written in terms of an efficiency factor,  $\alpha$ , as defined by Sedgwick (9) where

$$\alpha = \frac{\frac{\text{Ge(i)}}{\text{Cl(i)}} - \frac{\text{Ge(e)}}{\text{Cl(e)}}}{\frac{\text{Ge(i)}}{\text{Cl(i)}}} \quad [10]$$

The  $\frac{\text{Ge(i)}}{\text{Cl(i)}}$  at input refers to the input gas consisting of GeCl<sub>4</sub> and hydrogen, and is therefore 0.25.

The factor,  $\alpha$ , which is a function of  $T$ , and Cl/H, where total pressure is assumed constant may change from 1 through 0 to negative values. Thus a positive value of  $\alpha$  predicts germanium deposition ( $\alpha = 1$  indicating 100% Ge deposition from the gas phase);  $\alpha = 0$  to no net deposition, since  $\frac{\text{Ge(i)}}{\text{Cl(i)}} = \frac{\text{Ge(e)}}{\text{Cl(e)}}$ ; and negative values of  $\alpha$  to various degrees of etching.

**Method of calculation.**—The calculations described below for the Ge-H-Cl employed a parametric approach which has been described in detail by Darken (10) and Lever (2). In such an approach one specifies a partial pressure ratio at equilibrium which allows one to calculate many sets of numerical values of the equilibrium partial pressures which are consistent with the values of the equilibrium constants and the

total pressure. By evaluating  $\frac{\text{Cl(e)}}{\text{H(e)}}$  and using Eq. [9] one can relate these solutions to a particular  $\frac{\text{Cl(i)}}{\text{H(i)}}$ .



For these calculations the quantity  $P_{\text{HCl}}/P_{\text{H}_2} = X$  was chosen.

By substituting for the partial pressures in Eq. [5] in terms of the appropriate  $K$ ,  $X$ , and  $P_{\text{HCl}}$  from Eq. [1-3] one obtains

$$(P_{\text{HCl}})^2 [K_1 X^2 + K_3 X] + P_{\text{HCl}} \left[ K_2 X + 1 + \frac{1}{X} \right] - 1 = 0$$

This quadratic equation can be readily solved for  $P_{\text{HCl}}$  by specifying a value for  $X$  for a given temperature, and employing Eq. [1a-3a]. The other partial pressures and component ratios of interest may then be readily evaluated.

### Results and Discussion

Calculations of partial pressures of all species, the  $\text{Ge(e)}/\text{Cl(e)}$  and  $\text{Cl}/\text{H}$  ratios, and  $\alpha$  were made in the temperature range  $400^\circ\text{--}1223^\circ\text{K}$  for a total pressure of 1 atm. The computer calculations were made using an APL program on IBM System 360.

The results are graphically displayed in Fig. 1-9. In Fig. 1-4, the partial pressures of the different species together with the  $\text{Ge(e)}/\text{Cl(e)}$  ratio have been plotted as a function of temperature for specific  $\text{Cl}/\text{H}$  ratios. For increasing  $\text{Cl}/\text{H}$  it is noted that in general the formation of  $\text{GeHCl}_3$ ,  $\text{GeCl}_2$ , and  $\text{GeCl}_4$  is favored, hence we note an increase in the equilibrium  $\text{Ge(e)}/\text{Cl(e)}$  ratio. Exclusive of  $\text{H}_2$  which is nearly always at an atmosphere,  $\text{HCl}$  is consistently the major vapor species. Normal operating conditions for epitaxial deposition systems are generally at inputs using  $\text{Cl}/\text{H}$  ratios in the 0.001 range and at temperatures of  $759^\circ\text{C}$  or higher (Fig. 2). It will be noted that the major chlorine containing species under these conditions are  $\text{HCl}$  and  $\text{GeCl}_2$ . For any given  $\text{Cl}/\text{H}$  condition (Fig. 1-4) we note that increasing temperature causes

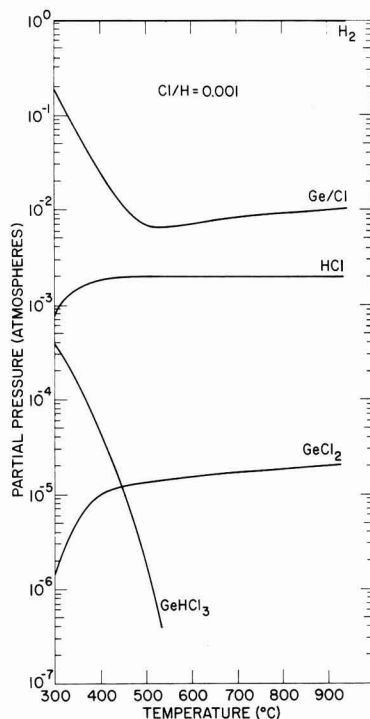


Fig. 2. Partial pressures of the various gas species vs. temperature at a total pressure of 1 atm at a chlorine/hydrogen ratio of 0.001.

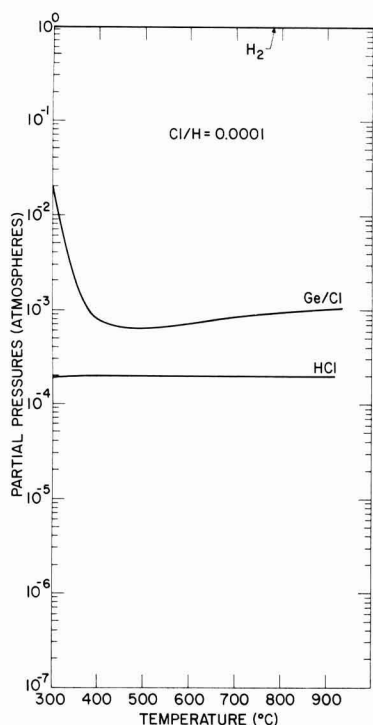


Fig. 1. Partial pressures of the various gas species vs. temperature at a total pressure of 1 atm at a chlorine/hydrogen ratio of 0.0001.

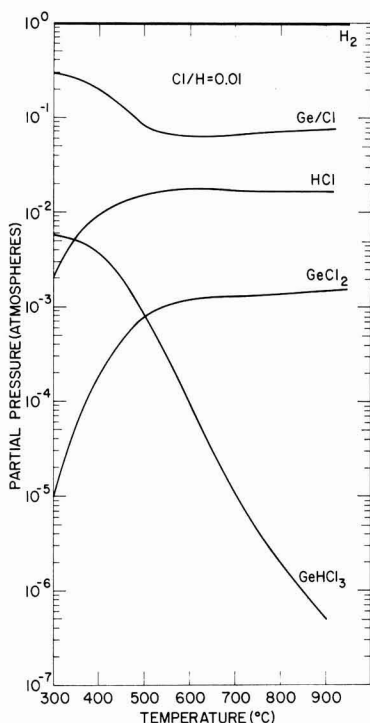


Fig. 3. Partial pressures of the various gas species vs. temperature at a total pressure of 1 atm at a chlorine/hydrogen ratio of 0.01.

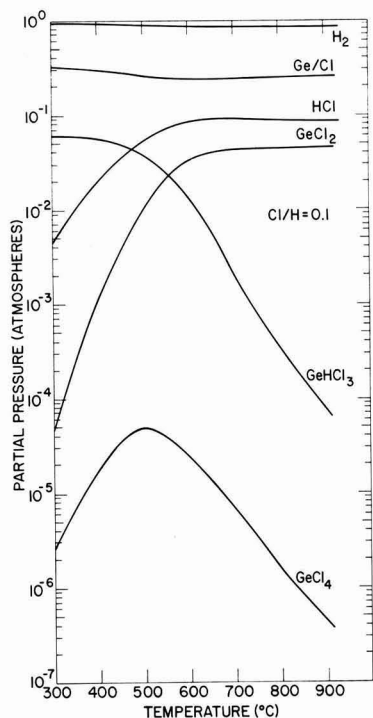


Fig. 4. Partial pressures of the various gas species vs. temperature at a total pressure of 1 atm at a chlorine/hydrogen ratio of 0.1.

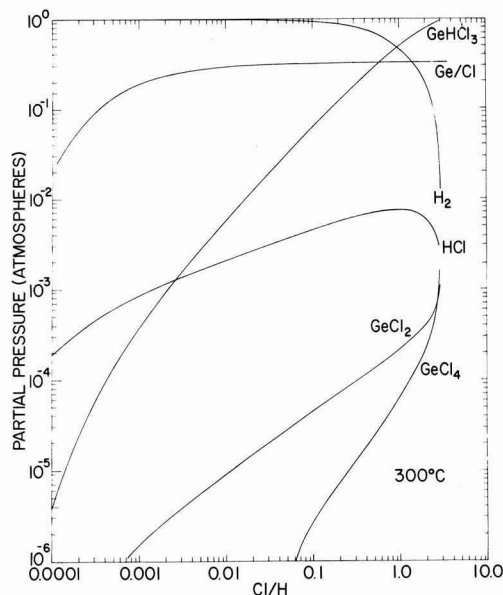


Fig. 5. Partial pressures of the various gas species vs.  $Cl/H$  ratio at a temperature of 300°C. Total pressure = 1 atm.

a reduction of  $GeHCl_3$  pressure and an increase in  $GeCl_2$  and  $HCl$  pressure.

In Fig. 5 and 6 the composition of the gas phase, in terms of partial pressure, is plotted for two temperatures, 300° and 800°C, respectively as a function of  $Cl/H$  ratio. For the lower temperature (Fig. 5) it can

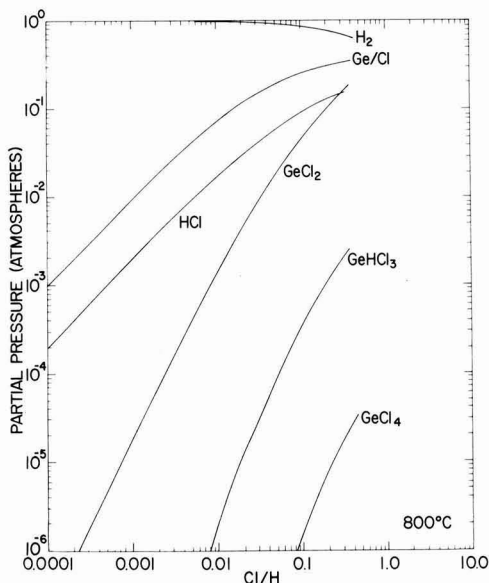


Fig. 6. Partial pressures of the various gas species vs.  $Cl/H$  ratio at a temperature of 800°C. Total pressure = 1 atm.

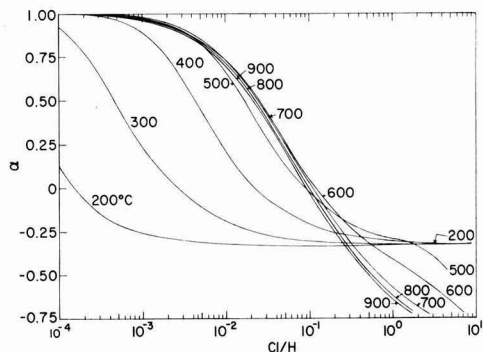


Fig. 7. Efficiency factor,  $\alpha$  vs.  $Cl/H$  ratio for different temperatures at a total pressure of 1 atm.

be clearly seen that  $GeHCl_3$  dominates the system as the major Ge bearing gas species, while at the higher temperature (Fig. 6)  $GeCl_2$  is dominant. Since the formation of any Ge bearing species leads to etching, one can consider the etching to be primarily due to the formation of  $GeHCl_3$  at lower temperatures and at higher temperatures to the formation of  $GeCl_2$ .

In Fig. 7 the efficiency factor,  $\alpha$ , has been plotted vs. the  $Cl/H$  ratio for specific temperatures. As might be expected from the previous figures, etching is favored ( $\alpha < 0$ ) for all temperatures at high  $Cl/H$  input ratios. The trend of all curves toward 100% efficiency,  $\alpha = 1.0$ , at low  $Cl/H$  ratios correspond to a complete reduction of all Ge bearing species ( $Ge(e)/Cl(e) = 0$ ), to form  $HCl$  and  $H_2$ . For  $Cl/H$  values  $< 0.1$  one observes that for the temperature interval 500°-900°C there is little change in  $\alpha$  resulting from temperature variation. This is more clearly seen in Fig. 8 where  $\alpha$  is plotted as a function of temperature for specific  $Cl/H$  inputs. The convergence of curves to a value of  $-0.33$  is the result of the dominant trend for  $GeHCl_3$  to form at low temperatures and high  $Cl/H$  ratios.

The effect of varying the enthalpy value of  $GeHCl_3$  from  $-100$  kcal to  $-85$  kcal in the calculation as discussed earlier, are summarized in Fig. 9. In Fig. 9 the

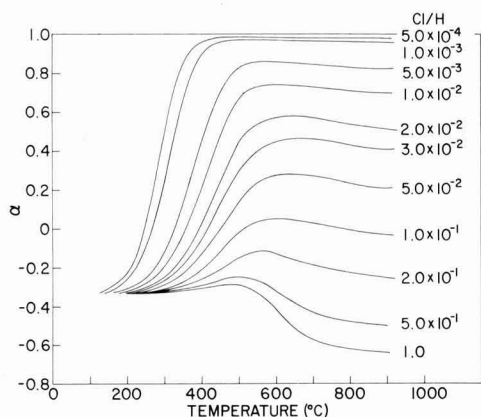


Fig. 8. Efficiency factor,  $\alpha$  vs. temperature at different Cl/H ratios at a total pressure of 1 atm.

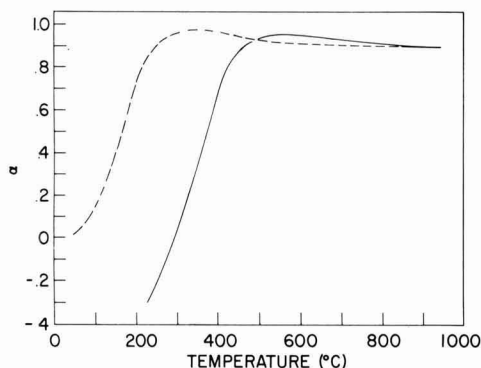


Fig. 9. Efficiency factor,  $\alpha$  vs. temperature calculated using two room temperature enthalpy values for  $\text{GeHCl}_3$ . Cl/H =  $2.2 \times 10^{-3}$ ; ---, (-85 kcal); —, (-100 kcal).

efficiency factor,  $\alpha$ , is plotted vs. temperature for a Cl/H ratio of  $2.2 \times 10^{-3}$  using the indicated enthalpy values for  $\text{GeHCl}_3$ . It will be noted that at temperatures  $< 500^\circ\text{C}$ ,  $\alpha$  becomes highly sensitive to the en-

thalpy value chosen. For the general calculations the more negative enthalpy value was used.

The Ge-H-Cl system is analogous to the Si-H-Cl system (2) with respect to the role that the corresponding gas species  $\text{SiHCl}_3$  and  $\text{GeHCl}_3$ , and  $\text{SiCl}_2$  and  $\text{GeCl}_2$  have on the dissolution or deposition rate. The general trends in both systems are:

1. That increased concentration of Ge or Si bearing vapor species reduces efficiency.
2. That in certain temperature intervals there is little variation of the Ge/Cl or Si/Cl ratios and hence efficiency. This results from increased formation of (M)Cl<sub>2</sub> vapor species being balanced by the reduction of (M)HCl<sub>3</sub> species where M can be either Ge or Si.
3. In the temperature intervals where significant variations of Ge/Cl or Si/Cl ratios occur, they are associated with the increased concentration of either (M)HCl<sub>3</sub> or (M)Cl<sub>2</sub>.

### Acknowledgments

The author wishes to gratefully acknowledge the helpful discussions with R. F. Lever, S. A. Papazian, and T. O. Sedgwick, and the programming assistance of W. J. Mesimer, M. E. Cowher, and S. A. Chan.

Manuscript submitted Nov. 15, 1971; revised manuscript received Jan. 10, 1972.

Any discussion of this paper will appear in a Discussion Section to be published in the December 1972 JOURNAL.

### REFERENCES

1. V. J. Silvestri, *This Journal*, **116**, 81 (1969).
2. R. F. Lever, *IBM J. Res. Develop.*, **8**, 460 (1964).
3. T. O. Sedgwick, *This Journal*, **111**, 1381 (1964).
4. O. Kubaschewski and E. Evans, "Metallurgical Thermochemistry," Pergamon Press, New York (1968).
5. D. F. Evans and R. E. Richards, *J. Chem. Soc.*, **1952**, 1292-4.
6. K. K. Kelley, Bureau of Mines Bulletin, 584, U.S. Government Printing Office, Washington, D.C. (1961).
7. T. O. Sedgwick, *This Journal*, **112**, 496 (1965).
8. S. R. Gunn and L. G. Green, *J. Phys. Chem.*, **65**, 779 (1961).
9. K. K. Kelly and E. G. King, Bureau of Mines Bulletin, 592, U.S. Government Printing Office, Washington, D.C. (1961).
10. L. S. Darken and R. W. Gurry, "Physical Chemistry of Metals," p. 218, McGraw-Hill Book Co., New York (1953).

# Some Properties of Vapor Deposited $\text{Ge}_3\text{N}_4$ Films and the $\text{Ge}_3\text{N}_4$ -Ge Interface

Takehisa Yashiro

Musashino Electrical Communication Laboratory,  
Nippon Telegraph and Telephone Public Corporation, Musashino-shi, Tokyo, Japan

## ABSTRACT

Germanium nitride films were deposited on germanium substrates heated to 400°–600°C by vapor phase reactions of germanium tetrachloride and ammonia. The properties of these films, such as the dissolution rate and the dielectric constant, were determined as a function of deposition temperature. The masking against Sb and As was also investigated. The films exhibited an instability related to trapping at room temperature but  $\text{Na}^+$  ion migration was not observed under bias-temperature stress. A hysteresis of the C-V curves for metal-nitride-semiconductor structures was noted. The amount of the hysteresis depended on deposition temperatures; a deposition temperature of 550°C resulted in the smallest hysteresis. By heat-treatment in  $\text{NH}_3$ , the magnitude of the hysteresis of the samples deposited at low temperature could be diminished while the interface state densities increased.

A method for depositing  $\text{Ge}_3\text{N}_4$  films by vapor phase reaction of germanium tetrachloride and ammonia has been reported by Nagai and Niimi (1). They investigated the physical and chemical properties of the films formed at temperatures between 400° and 600°C and reported that the films deposited at these temperatures were amorphous. When the films were kept at or above 600°C in  $\text{H}_2$ , Ar, or  $\text{N}_2$ , they were reduced or decomposed. They were crystallized by heat-treatment above 700°C in  $\text{NH}_3$  (2).

In this study, the physical properties of the nitride films and the electrical properties of the  $\text{Ge}_3\text{N}_4$ -Ge interface were investigated as a function of deposition temperature of the nitride films. It has been found that the electrical characteristics of the  $\text{Ge}_3\text{N}_4$ -Ge interface vary with deposition temperature. It became clear that germanium nitride can be utilized as a diffusion mask for Sb and As into germanium.

## Experimental

Germanium wafers used for these studies were (111) surface oriented, p-type, in the range of 0.2–3 ohm-cm. The wafers were etched in an acid containing 25 parts by volume of HF, 25 of  $\text{HNO}_3$ , and 0.75 of acetic acid with 0.2  $\text{Br}_2$  dissolved, and washed in distilled water. Germanium nitride was formed by reacting germanium tetrachloride and ammonia in a horizontal quartz tube with an inside diameter of 4.5 cm. The germanium tetrachloride vapor was transported to the rf-heated substrates by bubbling hydrogen through the saturator at 0°C. This gas was mixed with pure hydrogen and then with ammonia near the rf-heated substrates, as reported by Nagai and Niimi (1). Ammonia was dried by passing it through a cold trap kept at –30°C. The relative flow rates were as follows:  $\text{H}_2$  600 mliter/min;  $\text{NH}_3$  200 mliter/min;  $\text{H}_2$  through germanium tetrachloride 200 mliter/min. Depositions were carried out at 400°–600°C.

Metal-nitride-germanium (MNS) capacitor structures for electrical measurements were formed by vacuum evaporation of either aluminum or gold on the surface of the nitride film through the mask. The area of the electrodes ranged from  $3.0 \times 10^{-4}$  to  $4.5 \times 10^{-4} \text{ cm}^2$ .

## Results and Discussion

### Physical Properties

**Dielectric constant and etch rate.**—The thickness of the nitride films used for this experiment was 1540–1620 Å and was measured by multiple beam interfer-

ometry on mechanically polished test slices. The field plates of circular dots 200  $\mu$  in diameter were formed by photolithography. The capacitance of germanium nitride films was measured at 1 MHz by applying a large negative d-c bias to the field plates so that the p-type germanium surface was accumulated. From these values, the dielectric constant of germanium nitride films was calculated. The results, shown in Table I, indicate that the dielectric constant is almost independent of deposition temperature.

Since the etch rate is sensitive to the structural properties of the films, the value in  $\text{H}_3\text{PO}_4$  at 110°C was measured as a function of deposition temperatures. The results are also shown in Table I. It is noted that at lower substrate temperatures the etch rate increases. The increase in the etch rate for the lower deposition temperatures is thought to be due to the increase of unsaturated bonds of germanium in the germanium nitride (3–5).

**Diffusion masking.**—When the germanium nitride film was kept at or above 600°C in  $\text{H}_2$ , Ar, or  $\text{N}_2$ , the film was reduced or decomposed (1). However, since the film was stable to 650°C in  $\text{NH}_3$ , the masking properties of the germanium nitride film on germanium were investigated in  $\text{NH}_3$ . The diffusion was carried out in an open tube system. The source material was metallic Sb kept at 525°C or As at 350°C. Because of the low diffusion constant of acceptor elements (Ga, In, B) in germanium, they were excluded from this experiment.

Nitride films 1200 Å thick were deposited at 500°–550°C on the surface of chemically etched 0.2–3 ohm-cm p-type wafers in which circular dots 100  $\mu$  in diameter or rings 160  $\mu$  in outside diameter and 80  $\mu$  in inside diameter were opened for diodes. During the diffusion process, the germanium wafers were kept at 600°C for 1–5 hr.

The results were determined by two methods: (i) the diode characteristic measurement and (ii) the hot probe method after removing the nitride film. A typical diode curve obtained by As diffusion is shown in Fig. 1. From these results, it is concluded that ger-

Table I. Dielectric constant and etch rate of  $\text{Ge}_3\text{N}_4$

Deposition temperature (°C)	Dielectric constant	Etch rate in $\text{H}_3\text{PO}_4$ at 110°C (Å/sec)
600	7.8	23
550	8.0	38
500	8.0	44
450	7.9	75

Key words: germanium, germanium nitride, passivation.

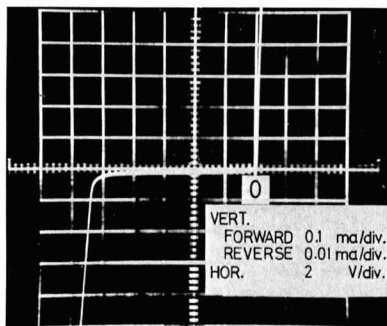


Fig. 1. Current-voltage characteristics of the germanium diode of the ring type. The substrate is  $0.3 \text{ ohm}\cdot\text{cm}$  and the masking film was deposited at  $500^\circ\text{C}$ . The diffusion depth and surface concentration are  $2.1\mu$  and  $2 \times 10^{19} \text{ cm}^{-3}$ , respectively.

manium nitride films  $1200\text{\AA}$  thick can be used as masks against the diffusion of Sb and As into germanium.

#### Electrical Properties

**Interface properties.**—The C-V curves of as-deposited  $\text{Ge}_3\text{N}_4$ -Ge structures were obtained at room temperature and 1 MHz. Typical examples are shown in Fig. 2. The scanning speed of the bias was 4 V/sec. The theoretical curve in the absence of surface charge and interface state (6) is also shown in the figure. Hysteresis was observed for all samples investigated and its extent depended on the deposition temperature. The deposition below  $500^\circ\text{C}$  resulted in large hysteresis. The smallest hysteresis was obtained on the sample deposited at  $550^\circ\text{C}$ . The shape of the C-V curves deposited below  $500^\circ\text{C}$  depended on the scanning speed of the bias. The low scanning speed showed that the curve becomes flatter. On the other hand, the deposition at  $600^\circ\text{C}$  showed a distortion as compared to the theoretical curve, i.e., the very gradual decrease of capacitance with the bias voltages. This phenomenon would indicate a continuous distribution of states in the forbidden gap of germanium (7). The "knee" (8) or "plateau" (9) observed in the  $\text{SiO}_2$ -Ge systems were not observed on as-deposited samples.

The direction of the hysteresis in this experiment is opposite to that which is caused by the polarization of insulators in metal-insulator-semiconductor structures (10, 11). Such a phenomenon can be explained if charges move across the  $\text{Ge}_3\text{N}_4$ -Ge interface and are trapped (12). Since the hysteresis is thought to be related to the bulk properties of the nitride film near the

$\text{Ge}_3\text{N}_4$ -Ge interface, the nitride film deposited at lower temperatures may be incompletely nitrified (13-15), i.e., there will be unsaturated bonds or vacancies in germanium nitride as suggested by the fast etching rates in  $\text{H}_3\text{PO}_4$ . On the other hand, as the origin of the interface states could be due to unsaturated bonds very near the semiconductor-insulator interface (16, 17), the high-temperature deposition is thought to make unsaturated bonds at the interface.

**Heat-treatment.**—It was observed that heat-treatment in  $\text{NH}_3$  affects the shape of C-V curves, i.e., the magnitude of the hysteresis and slope variation. In this investigation, three wafers on which germanium nitride was deposited at  $400^\circ$  or  $450^\circ\text{C}$  showing the large hysteresis and two wafers on which germanium nitride was deposited at  $550^\circ\text{C}$  showing the smallest hysteresis, were divided into many pieces and each piece was treated at a given temperature in  $\text{NH}_3$ . Then, gold electrodes were evaporated through the metal mask.

Typical C-V curves measured at room temperature are shown in Fig. 3. The samples were cut from the same wafer deposited at  $450^\circ\text{C}$  and then heat-treated at various temperatures for 30 min. The measuring frequency of 1 MHz was affected slightly by the frequency response of the interface states, so that the curves were obtained at 50 MHz to prevent the interface states from following the a-c signal. The voltages were applied from left to right. A feature of the  $\text{Ge}_3\text{N}_4$ -Ge interface after annealing is that increasing the treatment temperature causes the curves to become flatter because the interface states continuously distribute energy throughout the bandgap (7). Sedgwick (8) and Sedgwick *et al.* (18, 19) reported the appearance of a "plateau" or "knee" in the C-V curves in the  $\text{SiO}_2$ -Ge systems after annealing in  $\text{H}_2$  or  $\text{N}_2$  containing  $\text{H}_2$  above  $600^\circ\text{C}$  due to monoenergetic acceptor states at the interface. They reported that the acceptor states are located at the center of the Ge energy gap. However, since the samples of Fig. 3 were heat-treated in  $\text{NH}_3$  between  $500^\circ$  and  $650^\circ\text{C}$ , the plateau related to hydrogen was not observed. The other feature of the shape of C-V curves after annealing is the decrease in the extent of hysteresis. The polarization-type hysteresis observed by Iwauchi *et al.* (20) in the  $\text{Al}_2\text{O}_3$ -Ge structure after annealing in  $\text{N}_2$  was not observed in the  $\text{Ge}_3\text{N}_4$ -Ge structure.

In Fig. 4, the interface state density  $N_{\text{SS}}$  at zero surface potential and the extent of hysteresis  $\Delta N_{\text{FB}}$  are shown. The samples in the figure were obtained from the same wafer deposited at  $450^\circ$  or  $550^\circ\text{C}$  and heat-treated at various temperatures.  $N_{\text{SS}}$  was calculated

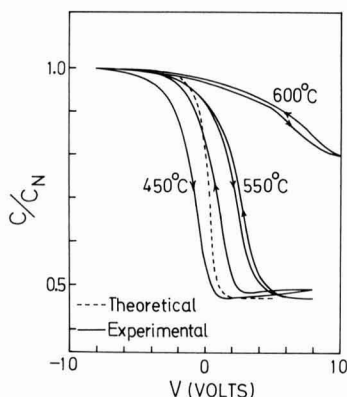


Fig. 2. C-V curves for MNS structures measured at 1 MHz showing the effect of deposition temperatures of the nitride. (p-type,  $0.45 \text{ ohm}\cdot\text{cm}$ ; film thickness  $1300\text{\AA}$ ; electrode Al.)

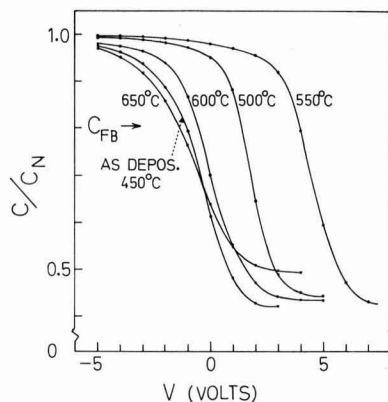


Fig. 3. C-V curves measured point by point and at 50 MHz for the samples after heat-treatment at various temperatures in  $\text{NH}_3$  for 30 min. (p-type,  $0.45 \text{ ohm}\cdot\text{cm}$ ; film thickness  $1150\text{\AA}$ ; electrode Au.)



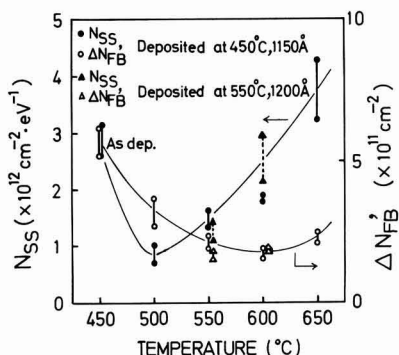


Fig. 4. Change of  $N_{SS}$  and  $\Delta N_{FB}'$  after annealing at various temperatures for 30 min. The sample deposited at 450°C was the same as that in Fig. 3. The sample deposited at 550°C was 0.7 ohm-cm, 1200 Å.  $N_{SS}$  and  $\Delta N_{FB}'$  after annealing at 550°C for the sample deposited at 550°C were about the same.

from the C-V curves measured at 50 MHz by the following equation (21, 22)

$$N_{SS} = \frac{C_N}{q} \frac{d\Delta V(\psi_s)}{d\psi_s}$$

where  $C_N$  is the capacitance of the nitride film,  $\Delta V(\psi_s)$  is the difference between the measured and ideal C-V curves, and  $\psi_s$  is the germanium surface potential.  $\Delta N_{FB}'$  was calculated by  $\Delta N_{FB}' = C_N \cdot \Delta V_{FB}/q$  and  $\Delta V_{FB}$  was obtained as the difference of  $V$  at the theoretical flat-band capacitance when  $V$  was swept from positive to negative and from negative to positive values by a constant applied field swing of about  $-8 \times 10^5$  to  $+8 \times 10^5$  V/cm. The C-V curves used to obtain  $\Delta N_{FB}'$  were measured at 1 MHz and automatically plotted on an X-Y recorder by the voltage sweep of 4 V/sec. The reason for the primed  $\Delta N_{FB}'$  is that the capacitance does not correspond to a true flat band condition because of the capacitive contribution of the interface state charges as stated above. The experimental results shown by bars are the upper and the lower limits of more than three measurements on the same piece.

As seen in the figure,  $N_{SS}$  and  $\Delta N_{FB}'$  are reduced by heat-treatment at 500°C for the samples deposited at 450°C. Above 550°C,  $\Delta N_{FB}'$  was found to decrease with increasing treatment temperature to 600°C, while  $N_{SS}$  increased uniformly. On the other hand, the reduction of  $\Delta N_{FB}'$  was not clearly observed on the samples deposited at 550°C in the temperature range investigated.  $N_{SS}$  does not change at 550°C but increases at 600°C. The increasing trend of  $N_{SS}$  at 600°C is the same as that of 450°C deposited samples. These trends of  $N_{SS}$  and  $\Delta N_{FB}'$  after annealing were reproducible. Only one of an anomalous curve shape observed is shown in Fig. 5. The C-V curve in this figure is similar to that of the other heat-treated samples with

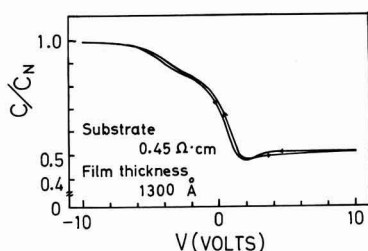


Fig. 5. C-V curve measured at 1 MHz showing a "break" after annealing at 600°C for 1 hr in  $NH_3$ . Germanium nitride was deposited at 400°C.

regard to the increase of the interface states and the decrease of the extent of hysteresis, but a "break" appears in the curve. This result was not reproducible. The reason for the appearance of the break is not clear at the present time.

To investigate the reason for the change of  $N_{SS}$  or  $\Delta N_{FB}'$ , the sample deposited at 450°C was annealed at 350°C in  $H_2$  or at 530°C in Ar for 30 min. Annealing in  $H_2$  at high temperature was excluded because of the reduction of germanium nitride. It was found that annealing in  $H_2$  or Ar did not reduce  $N_{SS}$  or  $\Delta N_{FB}'$  compared to as-deposited structures. Therefore, the effect of annealing in  $NH_3$  appears to be that nitrogen atoms fill unsaturated bonds in germanium nitride and reduce the hysteresis. At the same time, the reaction of germanium and nitrogen proceeds at the interface and the increase of  $N_{SS}$  results. This reaction at the interface between germanium nitride and germanium was also observed by Nagai (2).

**Ion migration.**—An instability related to metal-silicon dioxide-silicon structures is alkali ion migration within silicon dioxide as reported by Snow *et al.* (23). It is observed as a displacement of C-V curves along the voltage axis when the voltages are applied to the metal electrode above 150°C. The direction of the displacement is opposite to the applied voltages and the extent is a function of applied voltage, temperature, and time.

In this investigation, germanium wafers covered with 1300 Å of germanium nitride were first rinsed in a solution of NaCl (0.1%) and then aluminum electrodes 200 μ in diameter were deposited. The contamination of NaCl was confirmed by the microscopic observation prior to the deposition of the electrodes.

Initially, C-V curves were obtained at room temperature. The samples were then treated at 200°C, +2V on the field plate for 10 min and were cooled rapidly to room temperature with the voltage applied. Thereafter, C-V curves were traced again. The applied field during this treatment was smaller than the threshold field required for trapping of electrons ( $8.5 \times 10^5$  V/cm). The result of these bias-temperature treatments is shown in Fig. 6. A displacement of about 0.5V in the positive direction was observed. However, since this displacement is opposite to that of ion migration, we concluded that  $Na^+$  ions do not migrate appreciably within the germanium nitride films.

**Trapping.**—When positive or negative voltages exceeding some critical values are applied to the field plate at room temperature, the shift of C-V curves in the positive or negative direction, respectively, has been observed by many investigators (12, 14, 24-27). The direction of this displacement is opposite to that caused by ion migration. The reason for this displace-

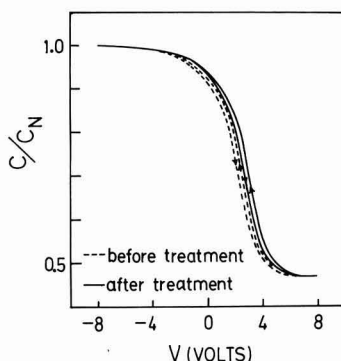


Fig. 6. Bias-temperature treatment for intentionally NaCl-contaminated Al- $Ge_3N_4$ -Ge structures.

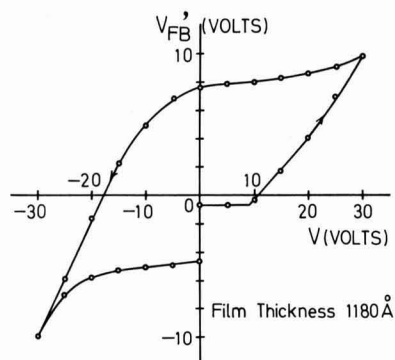


Fig. 7. Shift of  $V_{FB}'$  (see text) as a function of applied bias for 30 sec.

ment is thought to be due to trapping or releasing of carriers in the insulator.

It was found that the trapping occurs in the metal-germanium nitride-germanium system. A measurement of  $V_{FB}'$  vs. applied voltage is shown in Fig. 7. The meaning of the primed  $V_{FB}$  is the same as that given in the section on Heat-treatment. From these results, it was determined that the threshold field of the displacement is  $8.5 \times 10^5$  V/cm for the positive bias.

By a combination of photon radiation and C-V measurement, trap levels in germanium nitride were investigated. It was found that there are deep and shallow electron traps in germanium nitride (28). Therefore, the positive shifts in this investigation would be caused by trapping of electrons.

### Conclusion

Physical and electrical properties of germanium nitride and the germanium nitride-germanium interface were investigated. It became clear that germanium nitride can be used as a mask against the diffusion of Sb and As at  $600^\circ\text{C}$  in  $\text{NH}_3$ .  $\text{Na}^+$  ion migration was not observed by bias-temperature treatments at  $200^\circ\text{C}$ . The dielectric constant of germanium nitride was about 8.0 and was not significantly affected by the deposition temperatures. The etch rate depended on deposition temperature and is in the range of 23-75 Å/sec in  $\text{H}_3\text{PO}_4$  at  $110^\circ\text{C}$ . The hysteresis of C-V curves was observed for all the samples and was a function of the deposition temperature. A small hysteresis in the C-V curves was obtained on samples deposited at  $550^\circ\text{C}$ . At lower deposition temperature the hysteresis was larger. The magnitude of the hysteresis could be reduced by heat-treatment in  $\text{NH}_3$  while interface state density increased. The extent of the hysteresis and the interface state density for as-deposited samples at  $550^\circ\text{C}$  and for samples deposited below  $500^\circ\text{C}$  and then heat-treated at  $550^\circ\text{C}$  were about the same. An instability in germanium nitride due to trapping

of electrons was observed. Germanium nitride is unstable as compared with silicon nitride and is reduced or decomposed above  $600^\circ\text{C}$  in  $\text{H}_2$ , Ar, or  $\text{N}_2$ . However, the reverse characteristics of the germanium diodes that utilized germanium nitride as a diffusion mask and as passivation film were good.

### Acknowledgments

The author wishes to thank Professor T. Niimi of Keio University and Mr. Igarashi for helpful suggestions throughout the work. He is also grateful to Mr. Nagai and Mr. Shibata for their discussions and Mr. Yano for his preparation of germanium nitride films.

Manuscript submitted July 20, 1971; revised manuscript received ca. Dec. 7, 1971.

Any discussion of this paper will appear in a Discussion Section to be published in the December 1972 JOURNAL.

### REFERENCES

1. H. Nagai and T. Niimi, *This Journal*, **115**, 671 (1968).
2. H. Nagai, *Electrical Communication Laboratory Tech. J.*, **20**, 929 (1971) (in Japanese).
3. T. L. Chu, C. H. Lee, and G. A. Gruber, *This Journal*, **114**, 717 (1967).
4. K. E. Bean, P. S. Gleim, and R. L. Yeakley, *ibid.*, **114**, 733 (1967).
5. V. Y. Doo, D. R. Kerr, and D. R. Nichols, *ibid.*, **115**, 61 (1968).
6. R. Lindner, *Bell System Tech. J.*, **41**, 803 (1962).
7. B. E. Deal, E. L. MacKenna, and P. L. Castro, *This Journal*, **116**, 997 (1969).
8. T. O. Sedgwick, *J. Appl. Phys.*, **39**, 5066 (1968).
9. T. Yashiro, *Japan. J. Appl. Phys.*, **8**, 740 (1970).
10. E. H. Snow and B. E. Deal, *This Journal*, **113**, 263 (1966).
11. Y. Haneta and Y. Matsukura, *Japan. J. Appl. Phys.*, **6**, 1176 (1967).
12. S. M. Hu, D. R. Kerr, and L. V. Gregor, *Appl. Phys. Letters*, **10**, 97 (1967).
13. T. Sugano, K. Hirai, K. Kuroiwa, and K. Hoh, *Japan. J. Appl. Phys.*, **7**, 122 (1968).
14. D. M. Brown *et al.*, *This Journal*, **115**, 311 (1968).
15. M. T. Duffy and A. G. Revesz, *ibid.*, **117**, 372 (1970).
16. B. E. Deal, M. Sklar, A. S. Grove, and E. H. Snow, *ibid.*, **114**, 266 (1967).
17. P. V. Gray and D. M. Brown, *Appl. Phys. Letters*, **8**, 31 (1966).
18. T. O. Sedgwick and J. A. Aboaf, *IEEE Trans. Electron. Devices*, **ED-15**, 1015 (1968).
19. T. O. Sedgwick, J. A. Aboaf, and S. Krongelb, *IBM J. Res. and Develop.*, **14**, 2 (1970).
20. S. Iwauchi and T. Tanaka, *Japan. J. Appl. Phys.*, **10**, 260 (1971).
21. A. G. Revesz and K. H. Zaininger, *RCA Rev.*, **29**, 22 (1968).
22. Y. Haneta, *Japan. J. Appl. Phys.*, **8**, 929 (1969).
23. E. H. Snow, A. S. Grove, B. E. Deal, and C. T. Sah, *J. Appl. Phys.*, **36**, 1664 (1965).
24. S. M. Hu, *This Journal*, **113**, 693 (1966).
25. T. L. Chu, T. R. Szedon, and C. H. Lee, *Solid-State Electron.*, **10**, 897 (1967).
26. B. E. Deal, P. J. Fleming, and P. L. Castro, *This Journal*, **115**, 300 (1968).
27. C. A. T. Salama, *ibid.*, **117**, 913 (1970).
28. T. Yashiro, *Japan. J. Appl. Phys.*, **10**, 1691 (1971).

# Crystal Growth and Isothermal Annealing of $\text{Pb}_{1-x}\text{Sn}_x\text{Te}$ Alloys

G. Dionne

Hydro-Québec Institute of Research, Varennes, Quebec, Canada

and J. C. Woolley

University of Ottawa, Ottawa, Ontario, Canada

## ABSTRACT

Single crystal ingots of  $\text{Pb}_{1-x}\text{Sn}_x\text{Te}$  alloys have been grown using the Bridgman technique. A study of the crystal perfection revealed that in most cases the bulk of each ingot consists of a highly perfect single crystal with no detectable grain boundaries. In addition, the "as-grown" material is highly homogeneous in both alloy composition and carrier concentration, and is free from metal precipitates. A simplified isothermal annealing technique has been used to obtain various carrier concentrations in  $\text{Pb}_{1-x}\text{Sn}_x\text{Te}$  alloy samples with  $x = 0.06, 0.13, \text{ and } 0.21$ . The carrier concentration in these alloys, equilibrated at the liquid + solid/solid solution boundary, has been determined for several annealing temperatures.

The alloys  $\text{Pb}_{1-x}\text{Sn}_x\text{Te}$  and several other IV-VI compounds and alloys have much in common in that they have the same cubic rocksalt structure, have similar phase diagrams, can be prepared by similar methods, and their carrier concentrations can be controlled in a similar manner. These systems are often represented by the symbol MN to generalize the discussion (1), M representing the group IV elements and N the group VI elements. The use of the stoichiometric formulas MN (i.e., with the number of M atoms exactly equal to the number of N atoms) to represent these compounds and alloys is only approximate. At finite temperatures, the free energy of the crystal may be lowered by the introduction of atomic point defects, such as vacancies, and in general the compound is stable over a range of composition, called the homogeneity range, which sometimes does not include the stoichiometric composition. In undoped PbTe, SnTe, and their alloys the carrier concentration is a direct measure of the deviation from stoichiometry because the point defects, responsible for this deviation, supply practically all extrinsic carriers. While intrinsic effects and ionized impurities may also contribute to the total carrier concentration, for materials prepared from pure elements and not deliberately doped, these contributions are usually very small at low temperatures (1). In the present work, the lowest carrier concentration investigated was about  $10^{17} \text{ cm}^{-3}$ . At the temperature of the Hall measurements (77°K), the intrinsic carrier concentration will not exceed  $2.2 \times 10^{13} \text{ cm}^{-3}$  for any of the three alloy compositions investigated here (2). The alloys were prepared from elements of high semiconductor purity. While the impurity content was not directly determined, as will be shown in Fig. 3 the present alloys had higher mobilities than similar alloys prepared elsewhere (3), and the latter had total p-type impurities of approximately  $1 \times 10^{17} \text{ cm}^{-3}$  as found by mass spectrometry. Thus in the present work, it is reasonable to assume that the carrier concentration is a direct measure of the nonstoichiometry of the alloy except perhaps at the lowest carrier concentration values. It has been found for SnTe that each tin vacancy produces 2 holes (4-6). Brebrick (6) indicates that the hole to vacancy ratio  $c$  varies smoothly with  $x$  in these alloys and is closer to unity in the Pb-rich alloys. Thus in the present work, the value of  $c$  has been assumed to lie between 1 and 2.

**Key words:** nonstoichiometry, carrier concentration, IV-VI alloys, single crystals, semiconductors.

## Growth and Characterization

The furnace used to grow all the crystals is shown schematically in Fig. 1, together with a typical temperature profile. The furnace consisted of a high and a low temperature section which were independently controlled. The two sections were separated by a water-cooled jacket which permitted the establishment of a steep temperature gradient. The quartz ampoule, containing the melt, was held in a mullite tube which was driven slowly in the direction of the low temperature zone. The driving mechanism was built to provide three speeds: 1.1, 3.4, and 10.4 cm/day. In addition, the furnace could be tilted as shown in Fig. 1. The temperature gradient, at the temperature of freezing, was always greater than  $50^\circ\text{C}/\text{cm}$ .

The melts were prepared by mixing the elements in stoichiometric proportion. Lead, tin, and tellurium, all six 9's grade, were obtained from Cominco Ltd., Montreal. Lead and tin were available in the form of rods,

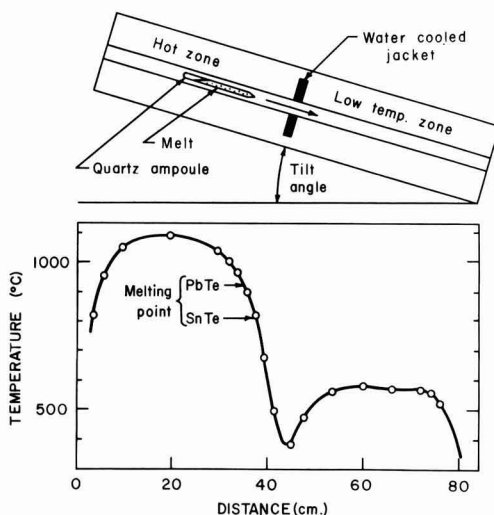


Fig. 1. Schematic of the furnace used for crystal growth and its temperature profile.

Table I. Starting composition, weight, 1st to freeze composition, and carrier concentration of  $Pb_{1-x}Sn_xTe$  alloys grown by the step-freeze technique

Ingot No.	Starting $x$	Weight, g	1st to Freeze $x$	Hole carrier concentration at 77°K, $cm^{-3}$
2	0.2	50	0.12	$2.4 \times 10^{19}$
3	0.4	50	0.27	$7.15 \times 10^{19}$
4	0.6	50	0.45	$2.4 \times 10^{20}$
5	0.8	75		$5 \times 10^{20}$
6	0.1	100	0.05	$1.2 \times 10^{19}$
7	0	67	0	$7 \times 10^{18}$
8	0.3	100	0.18	$4 \times 10^{19}$

approximately 12 mm in diameter, from which sections were cut and the oxide skin removed, with a steel blade, just before use. The elements were sealed under vacuum in a 13 mm inside diameter quartz ampoule, one end of which was made conical. The ampoule was then introduced in the hot zone of the step-freeze furnace and left there, at a temperature higher than 1000°C, for at least 1 day for complete mixing. The melt was driven through the steep temperature gradient at a speed of 3.4 cm/day, the conical tip being the first to freeze.

Table I lists the  $Pb_{1-x}Sn_xTe$  ingots grown using the above procedure. Ingots 2 to 4 were grown with the furnace in the horizontal position, while ingots 5 to 8 were grown with a tilt angle of 45° (Fig. 1). The main advantages of the tilted position are the following: (i) since the melt completely fills the ampoule, as shown in Fig. 1, large cross sections of crystal are obtained; (ii) there is no transport of material, through the vapor phase, over already grown material as there is in the horizontal set-up; (iii) there is no need to seal the quartz ampoules close to the material, thus oxidation during the sealing operation can be avoided.

The alloy compositions were determined using the results of Bis and Dixon (7) which showed that the lattice parameter  $a_0$  depends upon both composition  $x$  and carrier concentration  $p$  (i.e., nonstoichiometry), but that for a fixed value of  $p$ ,  $a_0$  varies linearly with  $x$ . Thus the composition of each sample was found by measuring the carrier concentration and the lattice parameter for the sample and then using the data in Fig. 2 of Bis and Dixon (7). Composition values determined in this way were accurate to better than 1%.

The lattice parameters were determined from Debye-Scherrer powder photographs taken with  $CuK\alpha$  radiation and using a standard 114.6 mm diameter camera. The  $\left( \frac{\cos^2\theta}{\sin\theta} + \frac{\cos^2\theta}{\theta} \right)$  extrapolation method was used to determine  $a_0$ . To remove any internal stress, produced during the grinding operation, the alloy powder samples to be used for the x-ray work were annealed for about 10 hr at a temperature no higher than 250°C. The accuracy of the lattice parameter so determined was  $\pm 0.0005\text{\AA}$ .

The starting compositions and the first-to-freeze compositions, listed in Table I, are consistent with the phase diagrams for  $Pb_{1-x}Sn_xTe$  determined by Wagner and Woolley (8). As expected from this phase diagram, the growing material is always richer in PbTe than the melt. As growth slowly proceeds, the melt becomes more and more depleted of PbTe and hence a composition gradient exists along the length of the ingot. However, the composition gradient is very small in the first quarter to freeze due to the relatively small separation between the liquidus and solidus curves at a given temperature. In ingot No. 2, for example, the composition varied by less than 2% in the first quarter of the ingot to freeze.

Table I also lists the range of carrier concentrations measured in these ingots. The higher the SnTe content of the alloys, the higher are the carrier concentrations. This is due to an increasing deviation from stoichiometry as we go from PbTe to SnTe. When grown from stoichiometric melts,  $Pb_{1-x}Sn_xTe$  alloys are always

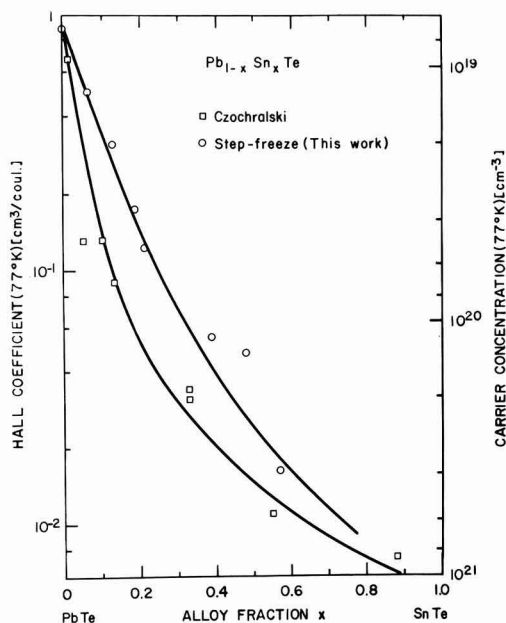


Fig. 2. Hall coefficient as a function of alloy composition in the "as-grown"  $Pb_{1-x}Sn_xTe$  alloys.

tellurium rich, and this excess tellurium is accommodated in the lattice by lead and/or tin vacancies, which ionize to produce p-type carriers. That the alloys grown from stoichiometric melt are tellurium rich is clearly seen in SnTe rich ingots, for which the last to freeze is always a small amount of pure tin. Brebrick (4) showed that the point defects in SnTe were tin vacancies and that the carrier-to-vacancy ratio was approximately 3. But Brebrick calculated the carrier concentration using  $p = 1/R_0e$ , in which  $R_0$  is the low field Hall constant and  $e$  is the electronic charge. When using the correct expression for the carrier concentration,  $p = r/R_0e$ , with the values for  $r$  given by Tsu *et al.* (9), the carrier-to-vacancy ratio becomes 2. This agrees with the intuitive notion that an ionized divalent ( $Sn^{2+}$ ) vacancy produces exactly 2 carriers. The increase of carrier concentrations from PbTe to SnTe is almost a hundredfold for ingots grown from stoichiometric melts (see Table I), suggesting that tin vacancies are more easily generated than lead vacancies.

Several circular disks cut from ingots No. 6 and No. 8 were lapped with coarse powder to produce microcleavages over the surface of the disks. By using a distant source of light, any small angle grain boundaries could be detected with a high degree of accuracy by observing the reflection from the numerous {100} microcleavage planes. A detailed examination revealed that the ingots were single crystal over their whole length with small grain boundaries predominantly in a small first-to-freeze region and near the surface of the ingots. With each circular disk so treated, the examination showed that more than 50% of its volume was single crystal with no detectable grain boundary, while the remaining volume had small angle grain boundaries present, the angles varying from about 2° to 5°. With ingots No. 6 and No. 8, x-ray back reflection photographs were taken at 3 mm intervals across a diameter of a face cut parallel to the long axis of the ingot with normal incidence of the x-ray beam. These x-ray photographs confirmed some of the above observations concerning the single crystal character and the crystal perfection of the material.

The "as-grown" material was homogeneous. First, metallographic examination showed no voids, no cracks,

and no sign of metal precipitation. We believe that the small growth rate (3.4 cm/day) and the steep temperature gradient at the freezing interface ( $> 50^\circ\text{C}/\text{cm}$ ) were responsible for the absence of metal precipitation and cellular substructure frequently observed in  $\text{Pb}_{1-x}\text{Sn}_x\text{Te}$  ingots (10). Second, x-ray diffraction (Debye-Scherrer powder photographs) indicated that the alloys were single phase and of good alloy homogeneity, in all cases the  $\alpha_1$ ,  $\alpha_2$  doublet being resolved in the high angle lines. Third, resistivity measurements taken at two different positions along the samples, indicated that the "as-grown" material was homogeneous in carrier concentration. Several samples were measured in this way at temperatures between 4.2°K and room, and, in all cases, the two resistivity measurements agreed to better than 1% at every temperature.

Values of Hall coefficient and Hall mobility are plotted in Fig. 3 and 4. For comparison, the results of Czochralski-grown (3) single crystals are also shown. It is seen that the alloys grown by the Bridgman method in this laboratory have fewer carriers and higher mobilities. The higher mobility for a given alloy composition is probably due to the corresponding lower carrier concentration.

### Isothermal Annealing

For the heat treatments, a constant temperature furnace was needed. In order to satisfy this requirement for several temperatures, an annealing furnace was constructed with two concentric furnace tubes, each with a particular type of winding. The outer heater consisted of a wire element very closely wound near each end of the furnace, and gradually more spaced towards the center of the furnace. The temperature profile of this outer heater alone thus peaked at each end and showed a minimum at the center. The inner heater was wound with a constant spacing between the turns and hence its temperature profile showed a broad maximum at the center of the furnace. For all temperatures at which the furnace was used, it was possible to find current settings on the two heaters which gave a resultant temperature variation with position of less than  $\pm 1^\circ\text{C}$  over at least 15 cm. The

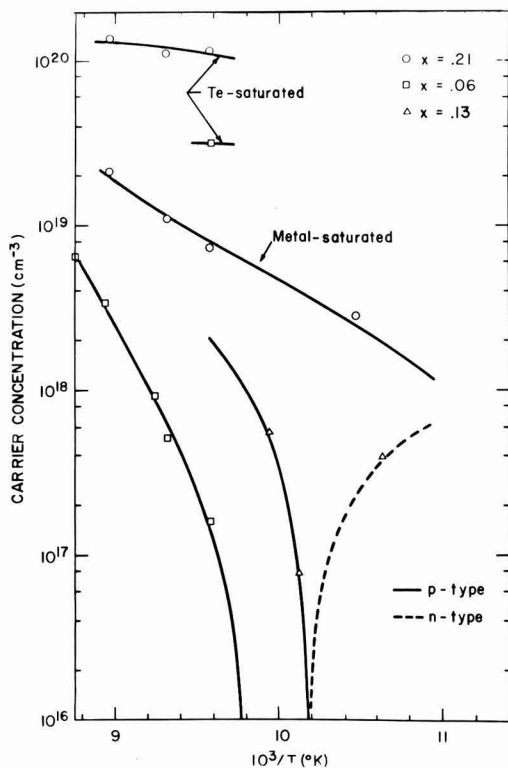


Fig. 4. Carrier concentration ( $1/R_0e$ ) at 77°K as a function of isothermal annealing temperature for  $\text{Pb}_{1-x}\text{Sn}_x\text{Te}$  alloys.

furnace temperature was maintained constant with time by a proportional control acting on the outer heater. For each annealing temperature, the appropriate value of the current in the inner heater was found by trial and error. The stability of the temperature over long periods of time was  $\pm 2^\circ\text{C}$ .

The explanation of the method used to control the deviation from stoichiometry in  $\text{Pb}_{1-x}\text{Sn}_x\text{Te}$  requires a knowledge of the various phase diagrams used to describe nonstoichiometry in MN systems. A general review of this information has been given by Strauss and Brebrick (1). These diagrams suggest several methods by which nonstoichiometry (or carrier concentration) can be controlled. For example, the carrier concentration can be controlled by fixing the temperature and the partial vapor pressure  $P_{\text{N}_2}$  over solid MN. However, this is a technique that requires special furnaces to control the two variables  $P_{\text{N}_2}$  and  $T$ . Another more practical method was first used by Brebrick and Allgaier in PbTe (11). The technique involved the equilibration under isothermal conditions of a relatively large Pb-rich PbTe charge with a sample of PbTe. The charge and the sample were enclosed in a sealed quartz ampoule, the volume of which was made small enough to prevent any change of composition of the sample by volatilization. When equilibrium is reached, the PbTe sample lies on the Pb-rich solidus line and is made to retain that phase by fast quenching to room temperature. For alloys of the system  $\text{Pb}_{1-x}\text{Sn}_x\text{Te}$ , this technique would require the preparation of metal rich charges having the same Pb-Sn ratios as those of the samples to be annealed. Here a simplified annealing technique has been used.

This technique is based on the same principle as that of Brebrick and Allgaier (1, 11). If the MN system is closed and contains all three phases (liquid, solid, and vapor), it has only one degree of freedom, and hence fixing the temperature fixes the equilibrium

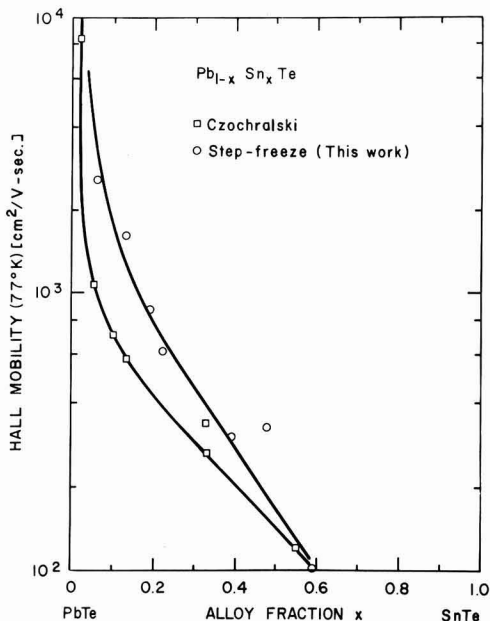


Fig. 3. Hall mobility as a function of alloy composition in the "as-grown"  $\text{Pb}_{1-x}\text{Sn}_x\text{Te}$  alloys.



composition of each phase. Thus, if the composition of the charge and sample combined lies in the liquid-solid region, the solid composition and the liquid composition are fixed by the values of the solidus and liquidus lines at the annealing temperature, and the partial pressure  $P_{N_2}$  in equilibrium with the system is fixed by that temperature. When the above condition is satisfied, the composition of the sample changes by solid-state diffusion until, at equilibrium, it reaches the M-saturated or N-saturated solidus line depending on whether the charge is M-rich or N-rich. By varying the annealing temperature, solid specimens can be equilibrated to various nonstoichiometry values, corresponding to various carrier concentrations or compositions.

The simplification of the present annealing technique over those used elsewhere (11, 12) is in the use of minute charges of pure N or pure M only. Since the only requirement is that the composition of the sample and charge combined lie between the solidus and the liquidus curve at the annealing temperature, the amount of M or N needed is given by

atoms of M or N  $> \{p \text{ (sample)}$

$$-p \text{ (at the solidus line)}\} V/c \quad [1]$$

in which  $p$  is the carrier concentration,  $V$  the volume of the sample, and  $c$  is the number of carriers per vacancy,  $c$  lying between 1 and 2. For example, consider a PbTe sample, with  $2 \times 10^{19}$  holes  $\text{cm}^{-3}$  and of dimensions  $0.1 \times 0.3 \times 1.0 \text{ cm}^3$ , which is to be equilibrated at a temperature for which the Pb-saturated solidus line is at the stoichiometric composition. The number of atoms of pure Pb required is given by Eq. [1] and is  $> 6/c \times 10^{17}$ . Thus only a little over 0.2/c mg of pure lead, introduced in the quartz ampoule with the PbTe sample, is necessary to equilibrate the sample to the stoichiometric composition. The exact amount is not critical and in general more than the amount calculated from Eq. [1] can be used to allow for the uncertainty in the exact value of  $c$  and to ensure that the composition of the charge and the sample together is well into the liquid-solid region. At the start of the annealing, the Pb charge is liquid. The excess tellurium in the sample is transferred (via vapor phase) to the charge until the charge has collected enough Te to cross the liquidus line. Then, the charge will be partly liquid and partly solid until equilibrium is reached. At equilibrium, the sample is lead saturated and lies on the solidus line. If the amount of pure lead used is so large as to prevent the charge from reaching the liquidus line before the sample reaches the solidus line, then surface melting of the sample will occur to provide the extra Te needed by the charge to reach the liquidus line. Thus, in order to prevent melting of the sample, an upper limit to the amount of pure Pb used as a charge is determined by the position of the liquidus line in the T-x projection [Fig. 1 of Ref. (1)]. This limit is given by

$$\text{atoms of M} < \frac{\Delta pV}{c} \left( \frac{1-x}{x} \right) \quad [2]$$

$$\text{atoms of N} < \frac{\Delta pV}{c} \left( \frac{x}{1-x} \right) \quad [3]$$

in which  $\Delta pV/c$  is the right hand side of Eq. [1] and  $x$  is the composition of the appropriate liquidus at the annealing temperature. For example, in PbTe  $x = 0.1$  at  $700^\circ\text{C}$  for the Pb-rich liquidus. From Eq. [2], we find  $9(\Delta pV/c)$  as the upper limit to the number of atoms in the Pb charge.

For the  $\text{Pb}_{1-x}\text{Sn}_x\text{Te}$  alloy samples, the charges used for N- and M-saturation were pure tellurium and a mixture of lead with tin respectively. The mixtures of lead with tin, at 5 atomic per cent (a/o) intervals, were prepared by melting the elements together at a high temperature and then quenching rapidly. For M-

saturation, the mixture having the closest Pb-Sn ratio to that of the  $\text{Pb}_{1-x}\text{Sn}_x\text{Te}$  sample to be equilibrated was used. It was not necessary to have exactly the same Pb-Sn ratio in both the charge and the sample because the charge was minute and could not produce an appreciable change in composition  $x$  of the much larger  $\text{Pb}_{1-x}\text{Sn}_x\text{Te}$  sample. The charges were weighed using a precision balance, and ranged in weight from 0.1 to 1.3 mg. Each sample and its charge were encapsulated in a small quartz ampoule, which was evacuated and backfilled with 1/3 atmosphere of argon to minimize thermal etching of the specimens (12). After the specimens had been equilibrated, the quartz ampoules containing the samples were rapidly quenched in water.

The main advantage of the present annealing technique are: (i) the preparation of the charge is simple and the equality of its Pb-Sn ratio to that of the sample is not as critical a requirement as it was in previous techniques (11, 12); (ii) the sample and the small charge can easily be separated inside the quartz ampoule and hence no complications such as a "tube within a tube" (12) are necessary to keep them separated; (iii) owing to the small size of the quartz ampoules, it is easier to have the whole ampoule in a region of constant temperature in the furnace. This is desirable to prevent transport of the sample, through the vapor phase, to colder regions of the ampoule; (iv) the small size of the quartz ampoule permits higher quenching rates. Fast quenching is desirable to prevent internal precipitation (1).

The results of the annealing experiments using the above technique are given in Table II for several compositions of  $\text{Pb}_{1-x}\text{Sn}_x\text{Te}$  alloys. The first column gives the sample number. The second column indicates the nature of the charge (M for Pb-Sn mixture, and Te for tellurium), the amount of which was determined using Eq. [1-3] assuming a suitable value for  $c$ , and which varied from 0.1 to 1.3 mg for a typical sample volume of  $0.15 \times 0.3 \times 1.0 \text{ cm}^3$ . The third, fourth, and fifth column give the thickness in mm, the annealing temperature in degrees centigrade, and the annealing time in days, respectively.

The annealing times chosen should be sufficiently long for equilibration. The values of interdiffusion coefficients necessary for the calculation of equilibration times are not available for the various carrier concentrations, alloy compositions, and temperatures used in the present work. However, if the smallest of the two interdiffusion coefficients determined for PbTe

Table II. Results of isothermal saturation annealing experiments obtained from  $\text{Pb}_{1-x}\text{Sn}_x\text{Te}$  alloys grown by the step-freeze technique. All carrier concentrations are p-type unless indicated (n) for n-type

Sample No.	Charge	Thickness, mm	Temp. ( $^\circ\text{C}$ )	Annealing time (days)	Hole carrier concentration at $77^\circ\text{K}$ , $\text{cm}^{-3}$	Carrier mobility at $77^\circ\text{K}$ $\text{cm}^2/\text{V-sec}$
(a) Composition $x = 0.06$						
6-0	None	As grown	771	4	$1.25 \times 10^{19}$	2,560
6-1	Te	1.02	771	4	$3.20 \times 10^{19}$	860
6-6	M	1.56	869	4	$6.41 \times 10^{18}$	4,670
6-5	M	1.3	845	8	$3.33 \times 10^{18}$	7,370
6-4	M	1.1	810	4	$9.00 \times 10^{17}$	12,870
6-3	M	1.4	800	6	$5.06 \times 10^{17}$	14,300
6-2	M	1.42	771	4	$1.56 \times 10^{17}$	14,920
(b) Composition $x = 0.21$						
8-1	None	As grown			$5.10 \times 10^{19}$	612
8-3	Te	1.6	842	2 1/2	$1.32 \times 10^{20}$	164
8-5	Te	1.34	771	4	$1.17 \times 10^{20}$	188
8-6	Te	1.34	800	6	$1.10 \times 10^{20}$	211
8-2	M	1.76	842	2 1/2	$2.14 \times 10^{19}$	1,680
8-7	M	1.43	800	6	$1.08 \times 10^{19}$	3,270
8-4	M	1.68	771	4	$7.11 \times 10^{18}$	4,750
8-8	M	1.5	680	30	$2.88 \times 10^{18}$	9,550
(c) Composition $x = 0.13$						
2-2	None	As grown			$2.00 \times 10^{19}$	1,600
2-2.1	M	1.0	734	2	$5.65 \times 10^{17}$	15,000
2-2.4	M	1.0	712	3	$7.9 \times 10^{16}$	16,000
2-2.3	M	1.0	667	7	$3.9 \times 10^{17(n)}$	40,600

(13) is assumed to apply for the alloys, the annealing times used here were more than sufficient for equilibrium to be reached in all cases. For example, the interdiffusion coefficient for the annealing temperature of sample 8-8 is  $5 \times 10^{-8}$  so that it would be equilibrated after 1.1 day which is about 25 times less than the annealing time used for that sample.

As with the "as-grown" material, the homogeneity of the annealed samples were checked by measurement of electrical resistivity and Hall effect. Since during the finite quenching time following the annealing, some diffusion may take place near the surface and produce a change in carrier concentration in a thin surface layer, the annealed samples were lapped on all 6 faces to remove about  $100\mu$  of material before the Hall and conductivity measurements were made. The homogeneity in carrier concentration, which indicates whether or not equilibration was attained during annealing, was checked by measuring the resistivity at two positions along each specimen. All samples with 21% SnTe and 6% SnTe were measured in this way at temperatures from 77°K to room and in every case the agreement between the two measurements was better than 1%. However at temperatures lower than 77°K, samples No. 6-3 and No. 6-2 showed drastic changes in resistivity and Hall coefficient. It should be pointed out that for these samples with low carrier concentration and high mobility, large surface effects are not unlikely and hence the observed resistivity anomalies need not be due to bulk material inhomogeneities. For all the annealed samples, including No. 6-2, and No. 6-3, metallographic examination revealed no sign of precipitation, supporting the assumption that during quenching either no retrograde solidus line was crossed, or, if such a line were crossed, it was at too low a temperature for precipitation to occur.

Values of carrier concentration ( $p = 1/R_0e$ ) and Hall mobility ( $R_0\sigma$ ) determined at 77°K are given in the sixth and seventh columns of Table II. The variation of  $p$  with annealing temperature is also shown in Fig. 4. Similar curves were obtained by Calawa *et al.*

(12) in  $Pb_{1-x}Sn_xTe$  and the general agreement between the two sets of results is good. However, our 13% SnTe curve shows a crossover temperature (from p-type to n-type) significantly higher than that reported by Calawa *et al.* (12) for the same composition. This difference could be due to the presence of ionized impurities, in addition to ionized vacancies, which would be n-type in our material or p-type in the material of Calawa *et al.*

### Acknowledgment

This work constitutes part of a thesis submitted to the University of Ottawa by G. Dionne in partial fulfillment of the requirements of the Ph.D. degree in Physics.

Manuscript submitted Nov. 3, 1971; revised manuscript received Jan. 24, 1972.

Any discussion of this paper will appear in a Discussion Section to be published in the December 1972 JOURNAL.

### REFERENCES

1. A. J. Strauss and R. F. Brebrick, *J. Phys. Colloque C-4*, suppl. 29, 21 (1968).
2. I. Melngailis, *ibid.*, 29, 84 (1968).
3. J. W. Wagner and R. K. Willardson, *Trans. TMS-AIME*, 242, 366 (1968).
4. R. F. Brebrick, *J. Phys. Chem. Solids*, 24, 27 (1963).
5. B. B. Houston, R. S. Allgaier, J. Babiskin, and P. G. Siebenmann, *Bull. Am. Phys. Soc.*, 9, 60 (1964).
6. R. F. Brebrick, *J. Phys. Chem. Solids*, 32, 551 (1971).
7. R. F. Bis and J. R. Dixon, *J. Appl. Phys.*, 40, 1918 (1969).
8. J. W. Wagner and J. C. Woolley, *Mater. Res. Bull.*, 2, 1055 (1967).
9. R. Tsu, W. E. Howard, and W. Esaki, *Phys. Rev.*, 172, 779 (1968).
10. J. F. Butler and T. C. Harmon, *This Journal*, 115, 67C (1968).
11. R. F. Brebrick and R. S. Allgaier, *J. Chem. Phys.*, 32, 1826 (1960).
12. A. R. Calawa, T. C. Harman, M. Finn, and P. Youtz, *Trans. TMS-AIME*, 242, 374 (1968).
13. L. Goldstein, *Compt. Rend. Acad. Sci., Paris*, 268, 686 (1969).

## Technical Notes



### Preparation and Properties of Hexaferrite Films

R. C. Taylor\* and V. Sadagopan\*

IBM Thomas J. Watson Research Center, Yorktown Heights, New York 10598

Polycrystalline hexaferrite films have been prepared both by RF sputtering and chemical vapor deposition (CVD) techniques for possible semi-transparent photomask (STP) applications. Among the three hexaferrite compositions investigated, the  $PbFe_{12}O_{19}$  films prepared by the CVD technique appear particularly interesting for STP applications in view of their satisfactory combination of hardness, optical transmission characteristics, and etchability. Hexaferrite films also have a potential application in the area of magnetic bubble domain devices.

The fabrication and utilization of masks is a significant aspect of the manufacture of integrated cir-

cuits. It is recognized that the quality of the circuits is largely dependent on the quality of the masks. The lack of transparency of current materials used for contact mask fabrication, such as chromium and photographic emulsions, makes it very difficult to visually align the mask with the structures underneath it, especially when the ratio of opaque to clear area is large. Recently, a number of new materials that are transparent in the visible region and opaque in the ultraviolet around 4000Å have been suggested for STP applications (1, 2, 3). The favorable optical characteristics of these materials permit the accurate visual alignment of the mask and make it possible to use much finer structures for contact printing. The general material requirements for STP applications are: (a)

\* Electrochemical Society Active Member.

Key words: chemical vapor deposition, magnetoplumbite, optical transmission spectra.

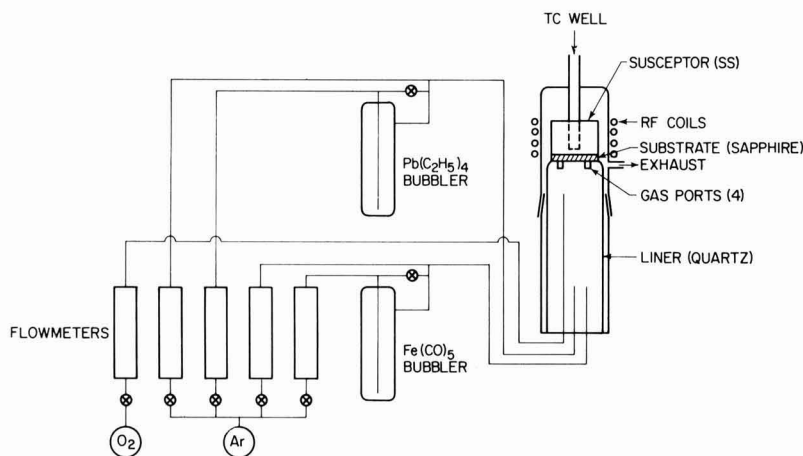


Fig. 1. Apparatus for the deposition of  $\text{PbFe}_{12}\text{O}_{19}$  films by the chemical vapor deposition technique.

zero transmission in the region below 3500Å to facilitate masking; (b) transmission of greater than 30% at 5890Å to permit visual alignment; (c) easy etchability in solvents compatible with photoresist processing; and (d) reasonable hardness to provide durability. In the light of the above requirements, we have examined a variety of transition metal oxides in addition to those screened by Sinclair *et al.* (1). Among these, thin films of  $\text{GaFeO}_3$ , prepared by sputtering techniques, and hexaferrite of the composition  $\text{PbFe}_{12}\text{O}_{19}$  (magnetoplumbite), prepared by the CVD method, appear to be promising for STP applications. We present here the details of the CVD method of preparation of  $\text{PbFe}_{12}\text{O}_{19}$  and its optical transmission characteristics and compare the optical properties of the latter with those of other hexaferrite films with compositions such as  $\text{BaFe}_8\text{Ga}_4\text{O}_{19}$  and  $\text{BaFe}_{8.5}\text{Al}_{3.5}\text{O}_{19}$ .

Polycrystalline films of magnetoplumbite have been vapor deposited onto single crystal sapphire substrates by pyrolysis of iron pentacarbonyl and tetraethyl lead in the presence of oxygen. The structure of the films was examined by standard x-ray diffraction techniques.

The apparatus for the chemical vapor deposition of magnetoplumbite is shown schematically in Fig. 1. The reactants, tetraethyl lead and iron pentacarbonyl, are contained in two quartz bubblers which are painted black to prevent photodecomposition of the reactants into free organic radicals and  $\text{Fe}(\text{CO})_5$ . Each source bubbler is connected to two flowmeters, one for metering the transport argon flow and one for the argon diluent flow. The reactant and oxygen vapors feed into a vertical quartz reactor. The quartz liner inside of the reactor is tapered at the top to support the substrate and contains four slits below the substrate which serve as gas exhaust ports. A stainless steel susceptor is in contact with the upper surface of the substrate and is RF heated. The thermocouple well goes almost to the bottom of the susceptor to monitor the substrate temperature. The substrate is mounted at the top of the reactor to prevent wall deposits from falling onto it. In a typical deposition of  $\text{PbFe}_{12}\text{O}_{19}$  onto a C-axis sapphire substrate, the reactant bubblers are kept at room temperature and the substrate is heated to 400°C. Argon flow is regulated to 50  $\text{cm}^3/\text{min}$  through the tetraethyl lead bubbler, and 7  $\text{cm}^3/\text{min}$  through the iron pentacarbonyl bubbler, resulting in transport rates of  $6 \times 10^{-5}$  moles/hr  $\text{Pb}(\text{C}_2\text{H}_5)_4$  and  $7 \times 10^{-4}$  moles/hr  $\text{Fe}(\text{CO})_5$ . The oxygen flow rate is 50  $\text{cm}^3/\text{min}$ . Under these conditions, a film of approximately 1000Å thickness is deposited in 3-4 hr. The films are polycrystalline with the standard hexaferrite structure. Attempts at film orientation by post-deposition annealing at 1000°C resulted in decomposition with the loss of PbO and a residual deposit of  $\text{Fe}_2\text{O}_3$  on the substrate.

The effect of substrate temperature on the rate of PbO deposition by the oxidation of  $\text{Pb}(\text{C}_2\text{H}_5)_4$  has been studied. The results are shown in Fig. 2. The shape of the curve shows the usual effects of kinetic control at low temperature, diffusion limitation at intermediate temperature, and gas-phase reactant depletion at higher temperature. These results were combined with those of MacChesney (2) and Carlton (4) for  $\text{Fe}(\text{CO})_5$  to arrive at the approximate deposition conditions.

Thin films of other hexaferrite compositions ( $\text{BaFe}_8\text{Ga}_4\text{O}_{19}$  and  $\text{BaFe}_{8.5}\text{Al}_{3.5}\text{O}_{19}$ ) for possible STP applications have been prepared by standard RF sputtering techniques starting from either a powder target or a bulk pressed disk. The films were prepared both in argon and in oxygen atmospheres. The details of the sputtering parameters and their effect on the structure, orientation, deposition rate, and composition of the films will be presented elsewhere.

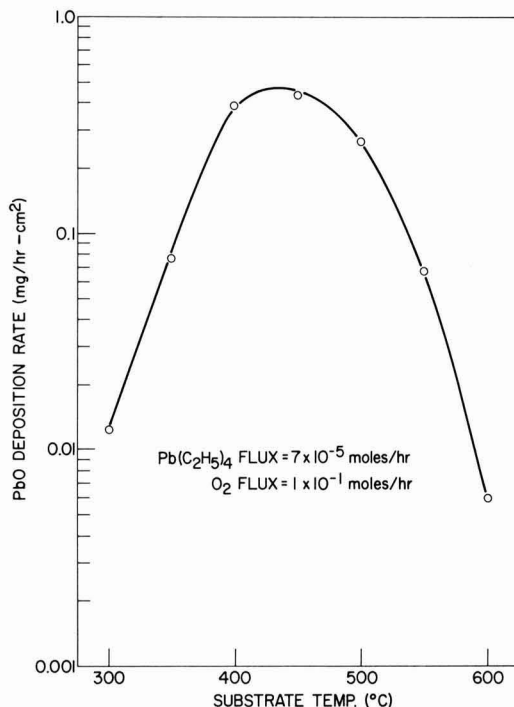


Fig. 2. Deposition rate of PbO vs. substrate temperature (°C)

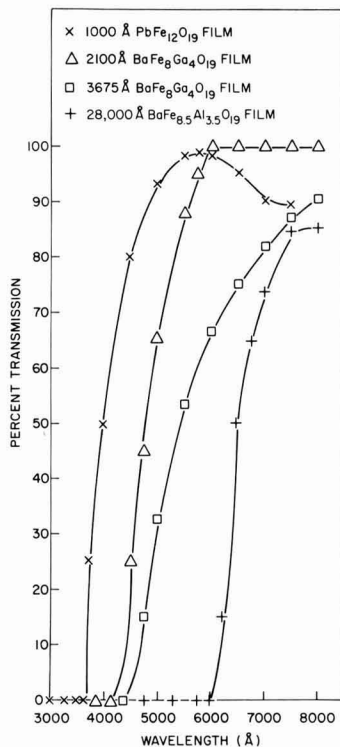


Fig. 3. Optical transmission vs. wave length of selected hexaferrite compositions; 1000Å  $\text{PbFe}_{12}\text{O}_{19}$  film was prepared by CVD method; 3675Å  $\text{BaFe}_8\text{Ga}_4\text{O}_{19}$  and 28,000Å  $\text{BaFe}_{8.5}\text{Al}_{3.5}\text{O}_{19}$  films were prepared in argon atmosphere in contrast to the 2100Å  $\text{BaFe}_8\text{Ga}_4\text{O}_{19}$  film which was prepared in oxygen atmosphere. A 2800Å argon-sputtered  $\text{BaFe}_{8.5}\text{Al}_{3.5}\text{O}_{19}$  film had transmission features similar to the data presented in this figure.

All the deposited films adhered well to the substrates and could not be scratched by a stainless steel needle. Their durability is thus satisfactory although no quantitative measurement of their abrasion resistance was made. The films with thickness greater than 2000Å were free from pinholes. The optical transmission characteristics of the different hexaferrite compositions are presented in Fig. 3. The data shows that the hexaferrite films sputtered in argon ambient have a broad absorption edge in contrast to the sharp absorption edge exhibited by films sputtered in oxygen ambient. The broad absorption edge of argon-sputtered films is interpreted to arise from oxygen nonstoichiometry in such films. Among the three hexaferrite compositions investigated,  $\text{BaFe}_{8.5}\text{Al}_{3.5}\text{O}_{19}$  films are not trans-

parent in the 5890Å (see-through) region (Fig. 3) and, hence, are not considered useful for STP applications. On basis of their favorable optical spectra, the vapor deposited  $\text{PbFe}_{12}\text{O}_{19}$  and sputtered  $\text{BaFe}_8\text{Ga}_4\text{O}_{19}$  films qualify for use in STP technology. The sputtered films, however, are remarkably resistant to chemical attack by acids that are compatible with photolithographic processing. On the other hand, vapor deposited  $\text{PbFe}_{12}\text{O}_{19}$  films are readily and uniformly etched by dilute HCl (9%) at room temperature at the rate of 300 Å/min. The observed differences in the etching behavior of sputtered and vapor deposited hexaferrite films are attributed to differences in morphology of the deposits unique to the individual film fabrication techniques (2). The ease with which vapor deposited  $\text{PbFe}_{12}\text{O}_{19}$  films dissolve in dilute HCl is, however, not an adequate criterion for its selection as a STP mask. An etched pattern could still be ragged if the rate of etching were distinctly different in different crystallographic directions. Etched test patterns have been obtained with satisfactory resolution. It is believed that the slow rate of deposition of  $\text{PbFe}_{12}\text{O}_{19}$  is partially responsible for the uniform etching. Thus, slow deposition might be an advantage rather than a handicap for this material.

In summary, on the basis of their adequate hardness, favorable optical absorption characteristics, satisfactory etchability, and ease of fabrication, the vapor deposited films of  $\text{PbFe}_{12}\text{O}_{19}$  are considered to be of particular interest for STP applications in the manufacture of semiconductor integrated circuits. Further, the optical and etching characteristics of  $\text{PbFe}_{12}\text{O}_{19}$  films compare favorably with those of vapor deposited films of  $\text{Fe}_2\text{O}_3$ , the only other material that, so far, has met the stringent criteria for masks capable of real time visual alignment. In addition to their potential usefulness for STP applications, the hexaferrites would be of considerable interest in the area of magnetic bubble domain devices if deposition conditions and substrate materials were modified in order to give single crystal films.

#### Acknowledgments

The authors are indebted to W. J. Haag for technical assistance in film growth and to E. A. Giess for fabrication of hexaferrite targets used in the sputtering part of the study.

Manuscript submitted Sept. 21, 1971; revised manuscript received Feb. 14, 1972.

Any discussion of this paper will appear in a Discussion Section to be published in the December 1972 JOURNAL.

#### REFERENCES

1. W. R. Sinclair, M. V. Sullivan, and R. A. Fastnacht, *This Journal*, **118**, 341 (1971).
2. J. B. MacChesney, P. B. O'Connor, and M. V. Sullivan, *ibid.*, **118**, 776 (1971).
3. V. Sadagopan *et al.*, Unpublished results.
4. H. E. Carlton and W. M. Goldberger, *J. Metals*, **17**, 611 (1965).

# The Detection of Silicon-Oxynitride Layers on the Surfaces of Silicon-Nitride Films by Auger Electron Emission

H. G. Maguire and P. D. Augustus

Allen Clark Research Centre, The Plessey Company Limited, Caswell, Towcester, Northants., England

Considerable attention has been paid recently to the properties of silicon nitride films as the diffusion mask and gate dielectric since the advent of the insulated-gate field-effect transistor, and a great amount of effort directed toward the investigation of these films for semiconductor device applications. There are many purposes for which dielectric films may be used in devices but for most practical device applications it is normally desirable to achieve a single-phase film in order to avoid possible inhomogeneous properties associated with mixtures. In order to possess uniform properties, these films should be amorphous in structure, impervious to contaminants to reduce instability effects, and be compatible with the substrate for acceptable mechanical and electrical characteristics. Previous work (1) concerning films intermediate in composition between silicon nitride and silicon dioxide has not been clear in distinguishing between the solid solution and mixture possibilities. Recent work, however, using electron diffraction (2) indicates that the silicon nitride and silicon dioxide end members form a continuous series of solid solutions rather than mixtures. Generally, a variation in the gas composition during deposition (3, 4) influences the stoichiometry of the nitride layers which will cause the electrical and optical properties to vary.

Apart from the electron diffraction work mentioned above, there does not appear to have been any investigation using microscopic techniques on these films. However, recently, backscattering and channeling effect measurements with MeV  $^4\text{He}$  ions have been used to analyze the composition as a function of depth of oxide and nitride layers on silicon (5). The composition was determined to be stoichiometric for high ratios of  $\text{NH}_3$  to  $\text{SiH}_4$  used in the deposition reaction but, for lower ratios, departures from this were found. Previously these techniques had been used to analyze ion implanted layers (6-8) and surface contamination (9), and  $\alpha$ -particle backscattering from a radioactive source such as  $^{242}\text{Cm}$  has also been used in chemical analyses of surfaces (10).

In view of the importance of nitride films in MNS and MNOS device fabrication, the present investigation of the surfaces onto which metal electrodes, normally aluminum, are to be deposited was undertaken using the techniques of Auger emission spectroscopy and low-energy electron diffraction. Using Auger electron emission, the surface of the sample to be studied is bombarded by primary electrons of several keV of energy while the energy distribution of the secondary and backscattered electrons is observed. Within this energy distribution, Auger electrons are observed with energies characteristic of the atoms from which they arise (11, 12). The low energies of the Auger electrons (below 1 keV) ensure that the observed effects arise from atoms very near the surface and the Auger method is particularly sensitive for the detection of the lighter elements on solid surfaces.

## Experimental

The variables of importance which affect the deposition rate of  $\text{Si}_3\text{N}_4$  and its subsequent properties are the composition and flow rate of the reactant mixture and the substrate temperature. In this work all deposi-

tions were carried out on Si substrates at a temperature of  $900^\circ\text{C}$  with ammonia as the major constituent in the reaction mixture. The flow rate of silane was 5 ml/min, while that of ammonia was 500 ml/min. The flow rate of the nitrogen carrier gas was 30 liter/min. Using these mixtures, the reaction kinetics taking place during the pyrolytic formation of  $\text{Si}_3\text{N}_4$  films is quite complicated and the possible reactions that may occur have already been considered in some detail (1).

Of the many films of varying thicknesses that were grown under identical conditions, two were selected, one having a growth time of 1.5 min and the other 2.5 min, giving films of thicknesses 610 and 1010 Å, and refractive indices of 1.88 and 1.95, respectively. These quantities were determined using ellipsometry.

The Auger spectrometer used, which was modified from a LEED system (13-15), consisted of three-grid electron optics constructed in these laboratories, with the electron gun producing a beam current of about 1  $\mu\text{A}$  at normal incidence to the specimen. The specimens used were typically 1 cm  $\times$  5 mm  $\times$  0.2 mm thick and were resistively heated while held in tantalum clips. A modulating frequency of 2 kHz was used throughout, and detection of the Auger signal was carried out by recording the second harmonic which yielded the derivative of the energy distribution,  $dN(E)/dE$ . Peak-to-peak modulation varied from 15V for detection in the higher energy range down to 3V in the lower energy range. All the observations described here were made using incident beam energies of not more than 1.5 keV.

After initial pumpdown from atmospheric pressure and overnight bakeout, a working pressure of  $5 \times 10^{-10}$  Torr was achieved which never exceeded  $2 \times 10^{-8}$  Torr during initial outgassing of the specimen. Temperatures were measured using an optical pyrometer with appropriate corrections made for emissivity and transmission through the viewport.

Both sides of the specimen were subjected to examination, and for comparison the first derivative of the energy distribution of secondary electrons from  $\text{Si}_3\text{N}_4$  and Si is shown in Fig. 1. The peaks at 522 and 495 eV are due to oxygen and are attributed to the  $\text{KL}_{2,3}\text{L}_{2,3}$  and  $\text{KL}_{1}\text{L}_{1}$  transitions, respectively (16). The peaks occurring at 389 and at 362 eV are the  $\text{KL}_{2,3}\text{L}_{2,3}$  transition of nitrogen and its associated plasmon. The peak at 270 eV is the  $\text{KL}_{2,3}\text{L}_{2,3}$  transition of carbon which is found on most samples freshly inserted into the UHV chamber and is increased by contamination from residual hydrocarbons during bakeout.

The remaining peaks below 100 eV from both sides of the specimen are due to silicon and reflect the effect of chemical binding. The spectrum from clean silicon which has been adequately discussed elsewhere (17-19) and will not be considered further, is shown in the upper trace of Fig. 2.

Heating the specimen at  $1140^\circ\text{C}$  for 5 min was sufficient to remove the oxygen from the silicon side of the specimen, but only a slight reduction in the oxygen peak was detectable on the nitride side from which practically all the carbon had desorbed. The same heat treatment for a further 20 min followed by argon ion bombardment (1  $\mu\text{A}$  at 500V for 30 min) removed the nitrogen and remaining carbon from the silicon side,

Key words: Auger, LEED, plasmon, ellipsometry.



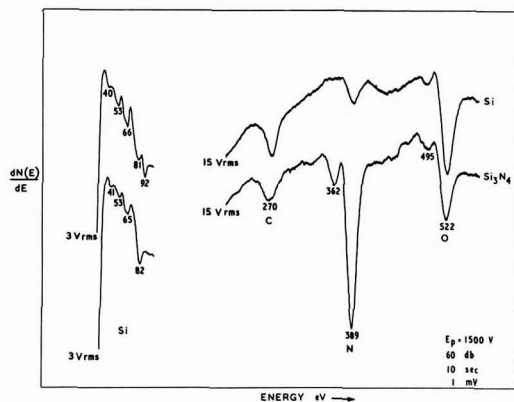


Fig. 1. The first derivative of the energy distribution of secondary electrons from Si (upper trace) and  $\text{Si}_3\text{N}_4$  (lower trace) for the as-inserted specimen showing the presence of C and O on both sides of the specimen, together with the degraded spectrum of silicon.

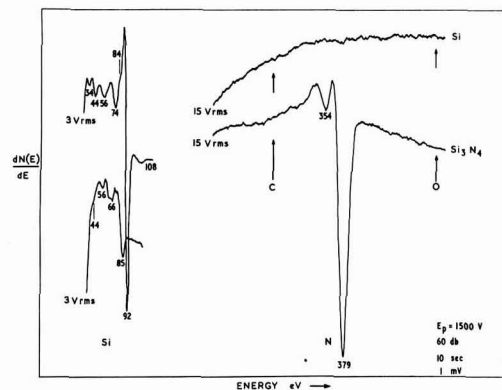


Fig. 2. The same specimen as in Fig. 1 but showing clearly the effect of the desorption of C and O from both sides of the specimen.

and was accompanied on the nitride side by an increase in the nitrogen peak.

Further heating for up to 2 hr was necessary in order to dislodge the remaining oxygen with an increase in the magnitude of the nitrogen peak to a final steady value. The silicon spectrum from the silicon side (Fig. 2) now has the character normally associated with "clean" silicon while that from the nitride has changed with the desorption of carbon and oxygen, and reflects the effect of chemical binding in the nitride.

Measurements of the thickness of the layers by ellipsometry after removal from the UHV chamber showed that they had decreased by about 30 Å, and that the refractive index had increased to just over 2.0. This may be compared to a value of about 1.99 obtained with a reactant molar ratio  $\text{O}_2/\text{SiH}_4 = 0$  (4).

Both specimens were scanned on a Perkin-Elmer 337 infrared spectrometer at room temperature, before and after the above-mentioned heat-treatment in UHV. No shift was found for either of the samples in the broad absorption band characteristic of the stretching of the Si-N bond. However, the absorption peaks differed for the two films; that for the thinner film occurring at about  $870\text{ cm}^{-1}$  and that of the thicker film at about  $840\text{ cm}^{-1}$ . Evidently the small amount of oxygen we are dealing with here limits severely any useful comparison using infrared techniques.

We have at all stages monitored the surfaces for LEED patterns and after the initial heat-treatment ob-

tained a good, clear ( $7 \times 7$ ) pattern on the silicon side. No patterns were obtained at any time from the nitride layer.

### Summary and Conclusions

Amorphous layers of silicon nitride of varying thickness have been deposited on silicon substrates by the pyrolysis of silane with ammonia. Care was taken to exclude likely sources of oxygen contamination. Using Auger emission spectroscopy, we have examined the surface of these layers and of silicon on the reverse side for comparison.

Initial heating of the specimen at  $1080^\circ\text{C}$  for about 40 sec was sufficient to desorb the oxygen from the silicon surface but only produced a slight reduction in the size of the oxygen peak from the nitride. Further heating at  $1140^\circ\text{C}$  did not result in a decrease in the oxygen signal. This then would suggest that on top of the silicon nitride layer is another layer consisting of silicon oxynitride,  $\text{Si}_2\text{O}_3\text{N}_2$ , and further that it is about 30 Å thick, as deduced by ellipsometry. It is possible that this film is more common than had been previously realized in which case one would not have a strictly metal-nitride interface but a metal ( $\text{Si}_2\text{O}_3\text{N}_2$ -nitride) interface. The effect of this on film characteristics is noticeable. One notices immediately a rise in the refractive index once all the oxynitride layer has been removed by prolonged heating in ultrahigh vacuum. The differing values reported in the literature for the refractive index for zero oxygen to silane ratios may in fact be due to the presence of just such a layer. It is expected that the presence of an oxynitride layer on the nitride will influence the value of the dielectric constant but it would appear that here it is the ratio of ammonia to silane in the formation of the nitride layer that is more important. It would also be of interest to investigate the effect of these films on the I-V and C-V characteristics bearing in mind the stronger polarity dependence of the oxynitride over the nitride.

Though every precaution was taken to ensure an oxygen free system, the only plausible explanation for the presence of oxygen is as an impurity in one of the reactor gases. The fact that oxygen occurs only in the top 30 Å would suggest possible contamination of the nitrogen carrier gas with water and/or oxygen, remembering, of course, that after the flow of the silane and ammonia is stopped, the specimen is left to cool with the nitrogen still on, during which time the surface of the layer remains at a sufficiently elevated temperature to react with the oxygen to form an oxynitride. Under these circumstances it would be difficult to avoid formation of such a layer at all.

In conclusion we may consider the mechanism by which the oxygen is desorbed. Assuming that oxygen on the surface from the interior is not an important factor since oxygen exchange between the surface and the bulk at temperatures below  $1000^\circ\text{C}$  is an exceedingly slow process (20), then removal of oxygen from the silicon is facilitated by evaporation of silicon monoxide which does not form associated molecules (21). As far as removal of oxygen from the nitride by total depletion of the oxynitride is concerned, we would tentatively suggest that silicon released from the rapid pyrolysis of silane results in a nitride layer containing excess silicon. Formation of the oxynitride then proceeds as suggested above, with the subsequent removal of oxygen by evaporation of silicon monoxide formed by the reaction of this excess silicon with the oxygen in the oxynitride layer. This process would require diffusion of the excess silicon from the nitride to react with oxygen to form volatile silicon monoxide but at a much slower rate than happens on the reverse side where silicon is readily available; hence the extended period of heating necessary to bring about removal of oxygen.

### Acknowledgments

Thanks are due to The Plessey Company Limited for permission to publish these findings and to R. Oakley who prepared the specimens and carried out the ellipsometric measurements.

Manuscript submitted March 29, 1971; revised manuscript received Oct. 25, 1971.

Any discussion of this paper will appear in a Discussion Section to be published in the December 1972 JOURNAL.

### REFERENCES

1. D. M. Brown, P. V. Gray, F. K. Jeumann, H. R. Philipp, and E. A. Taft, *This Journal*, **115**, 311 (1968).
2. N. C. Tombs, F. A. Sewell, and J. J. Cromer, *ibid.*, **116**, 862 (1969).
3. G. A. Brown, W. C. Robinette, and H. G. Carlson, *ibid.*, **115**, 949 (1968).
4. T. L. Chu, J. R. Szidon, and C. H. Lee, *This Journal*, **115**, 318 (1968).
5. J. Gyulai, O. Meyer, J. W. Mayer, and V. Rodriguez, *Appl. Phys. Letters*, **16**, 232 (1969).
6. L. Erikson, J. A. Davies, N. G. Johansson, and R. W.

- Mayer, *J. Appl. Phys.*, **842** (1969).
7. J. W. Mayer and O. J. March, "Applied Solid State Science," Vol. 1, p. 239, Academic Press Inc., New York (1969).
8. E. Bøgh, *Can. J. Phys.*, **46**, 653 (1968).
9. D. A. Thompson, H. D. Barber, and W. D. MacIntosh, *Appl. Phys. Letters*, **14**, 102 (1969).
10. J. H. Patterson, A. L. Turkevich, and E. Franzgrote, *J. Geophys. Res.*, **70**, 1311 (1965).
11. J. J. Lander, *Phys. Rev.*, **91**, 1382 (1953).
12. L. A. Harris, *J. Appl. Phys.*, **39**, 1419 (1968).
13. R. E. Weber and W. T. Peria, *ibid.*, **39**, 2425 (1968).
14. P. W. Palmberg and T. N. Rhodin, *ibid.*, **39**, 2425 (1968).
15. E. J. Scheibner and L. N. Tharp, *Surface Sci.*, **8**, 247 (1967).
16. J. A. Beardon and A. F. Burr, *Rev. Mod. Phys.*, **39**, 125 (1967).
17. N. J. Taylor, *Surface Sci.*, **15**, 169 (1969).
18. H. E. Bishop and J. C. Riviere, *ibid.*, **17**, 462 (1969).
19. H. G. Maguire and P. D. Augustus, *J. Phys. C. Solid State Phys.*, **4**, 174 (1971).
20. J. J. Lander and J. Morrison, *J. Appl. Phys.*, **33**, 2089 (1962).
21. W. Brewer and F. T. Greene, *J. Phys. Chem. Solids*, **2**, 286 (1957).

## DISCUSSION SECTION



This Discussion Section includes discussion of papers appearing in the *Journal of The Electrochemical Society*, Vol. 118, No. 2, 9, and 12; February, September, and December 1971.

### Observation of Mixed Thermoelectric Power in ThO<sub>2</sub>

N. M. Tallan and I. Bransky (pp. 345-349, Vol. 118, No. 2)

**D. S. Tannhauser<sup>1</sup>:** In the paper by Tallan and Bransky, and in a previous one by Ruka, Bauerle, and Dykstra,<sup>2</sup> the change of thermoelectric power of an ionically conducting oxide is measured when the atmosphere surrounding the sample is changed. The materials are ThO<sub>2</sub> in the paper being discussed, and (ZrO<sub>2</sub>)<sub>0.85</sub>(CaO)<sub>0.15</sub> in the paper by Ruka *et al.*<sup>2</sup> The atmosphere varies from pure oxygen through mechanically diluted oxygen to mixtures of CO<sub>2</sub>/CO and H<sub>2</sub>O/H<sub>2</sub>. The change of thermoelectric power, referred to that measured in an arbitrary standard atmosphere, is then plotted against the difference between physical quantities, which are called in these papers the partial molar entropies of oxygen, and which are calculated for the atmospheres involved. Agreement between experiment and theory is good.

It is the purpose of this note to point out that the use of the term "partial molar entropy" in these papers is wrong. This does not affect the validity of the papers but we believe it is worthwhile to point this out since the use of thermodynamic concepts in an incorrect way can be misleading and has often led to the wrong results.

According to Darken and Gurry<sup>3</sup> the definition of the partial molar entropy of component *j* in a multi-component mixture is

$$\bar{S}_j = \left( \frac{\partial S'}{\partial n_j} \right)_{T,P,n_{i \neq j}} \quad [1]$$

Here *S'* is the total entropy of the mixture, *n<sub>j</sub>* is the

<sup>1</sup> Department of Physics, Technion—Israel Institute of Technology, Haifa, Israel.

<sup>2</sup> R. J. Ruka, J. E. Bauerle, and L. Dykstra, *This Journal*, **115**, 497 (1968).

<sup>3</sup> L. S. Darken and R. W. Gurry, "Physical Chemistry of Metals," p. 238, McGraw Hill Book Co., New York (1953).

molar fraction of component *j*, and *T* and *P* are temperature and pressure of the mixture.

Darken and Gurry<sup>3</sup> then derive the following relation (their Eq. [10-23]) between the chemical potential and the partial molar entropy

$$\left( \frac{\partial \mu_j}{\partial T} \right)_{P,n_i} = -\bar{S}_j \quad [2]$$

In Eq. [2] the derivative with respect to temperature is calculated with all *n<sub>i</sub>* as well as *P* constant. This derivative has a real physical meaning for a mechanical mixture of components, i.e., components which do not react with each other, since there one can actually vary the temperature while keeping *P* and all *n<sub>i</sub>* constant.

For a chemical mixture in equilibrium this derivative does not have a physical meaning. It implies clamping of the composition of the mixture (e.g., CO<sub>2</sub>, CO, and O<sub>2</sub>) while the temperature is varied at constant pressure; and this clamping is not compatible with chemical equilibrium. However, the definition of Eq. [1] as well as the relation given in Eq. [2] still holds.

Tallan and Bransky show that the heterogeneous part  $\alpha_{het}$  of the thermoelectric power  $\alpha = \alpha_{het} + \alpha_{hom}$  of an oxide conducting by O<sup>2-</sup> ion diffusion can be expressed as

$$\alpha_{het} = -\frac{1}{q} \left[ \frac{1}{2} \frac{\partial \mu(O_2^{=})_{oxide}}{\partial T} - \frac{1}{4} \frac{\partial \mu(O_2)_{gas}}{\partial T} - \frac{\partial \mu(e^-)_{Pt}}{\partial T} \right] \quad [3]$$

They then calculate the change with oxygen partial pressure of  $\alpha$ , after assuming that  $\alpha_{hom}$  is independent of oxygen partial pressure and that the only term in  $\alpha_{het}$  that depends on oxygen partial pressure is the second term on the right of Eq. [3]. This gives the equation

$$\alpha_{gas 1} - \alpha_{gas 2} = \frac{1}{49} \frac{\partial \mu(O_2)_{gas 1}}{\partial T} - \frac{1}{49} \frac{\partial \mu(O_2)_{gas 2}}{\partial T} \quad [4]$$

Equation [4] is verified by plotting experimental values for  $\Delta\alpha$  against calculated values of  $\Delta\mu(\text{O}_2)_{\text{gas}}/\partial T$ . The latter are calculated by the use of the equation

$$-\frac{\partial\mu(\text{O}_2)}{\partial T} = 2 \left[ \bar{S}^\circ(\text{CO}_2) - \bar{S}^\circ(\text{CO}) - R \ln \frac{P(\text{CO}_2)}{P(\text{CO})} \right] \quad [5]$$

which is valid for a chemical gas mixture in which the ratio  $P(\text{CO}_2)/P(\text{CO})$  is independent of temperature.

Tallan and Bransky as well as Ruka, who apparently did the same calculation, call the derivative in Eq. [5] the partial molar entropy and denote it by  $\bar{S}(\text{O}_2)_{\text{gas}}$ . This, as stated above, is not correct, since the derivative is calculated for conditions in which the partial pressure, and, therefore, the molar fraction of oxygen, is a function of temperature.

The original theory of the thermopower of chemical cells was developed by Holtan, Mazur and de Groot.<sup>4</sup> After Eq. [38] of their paper, they introduce  $\Delta S$  as the change of entropy due to the heterogeneous electrode reaction, but they do not call this term the partial molar entropy. We repeat again that the calculations in the paper discussed here and in the paper by Ruka *et al.*<sup>2</sup> are correct, but the use of the expression "partial molar entropy" is misleading.

Equation [4] can, incidentally, be interpreted in a manner which is more familiar to electrochemists: we can write

$$\alpha_{\text{gas}} - \frac{1}{4} \frac{\partial\mu(\text{O}_2)_{\text{gas}}}{\partial T} = \text{constant}$$

and after multiplying by  $dT$  this equation gives

$$V_a - V_b = \frac{1}{4} [\mu(\text{O}_2)_a - \mu(\text{O}_2)_b] + \text{constant}$$

which, except for the constant term, is the equation of an electrochemical cell with different oxygen activity on its two sides  $a$  and  $b$ . The constant nonzero term, generated by the temperature gradient, comes from the entropies of transport of ions in the electrolyte and electrons in the platinum electrode which are assumed in Tallan and Bransky's paper and in the paper by Ruka *et al.*<sup>2</sup> to be independent of oxygen pressure.

### Phosphorescence Decay of Calcium Oxide Activated by Yttrium

L. M. Schwarz, J. M. Voutay-Poncet, and J. Janin  
(pp. 1512-1514, Vol. 118, No. 9)

**W. Lehmann<sup>5</sup>:** This paper is misleading as it implies luminescence in calcium oxide due to "activation" by yttrium, i.e., to traces of yttrium dissolved in the CaO lattice. We have looked into this system as well as into many other combinations of CaO with various other impurities. To set the matter clear, neither we nor the authors of this paper<sup>6</sup> have observed any luminescence in CaO clearly attributable to yttrium. Yttrium may possibly have an influence on the trap distribution in CaO and, thus, on the decay characteristic of phosphorescence of CaO activated by whatever else it might be. However, yttrium is no activator of luminescence in calcium oxide in the commonly used sense.

**L. M. Schwarz:** Dr. Lehmann's comment is right. The choice of the word "activated" is wrong. The system CaO(Y) has no fluorescence. Nevertheless the CaO samples we have examined are very phosphorescent and thermoluminescent at all temperatures. The addition of small quantities of certain elements like Ga, Y, Hf, etc., increases the phosphorescence and then

allows the study of its decay during a very long period. That is the only purpose of this paper.

### Dielectric Breakdown in Electrolytic Capacitors

F. J. Burger and J. C. Wu (pp. 2039-2042, Vol. 118, No. 12)

**S. E. Libby<sup>7</sup>:** Determination of the breakdown voltage of tantalum samples, when anodized in simple aqueous electrolytes at room temperature, was carried out. Several series of electrolytes were used. In each electrolyte series, the anion and its concentration was held constant and the cation species was varied, thereby varying the resistivity of the electrolyte solutions.

Tantalum samples were  $2 \times 2$  cm flags with an integral tab  $0.5 \times 2$  cm. The samples were cut from capacitor grade foil 0.001 in. thick. The samples were prepared for anodization by vapor degreasing trichloroethylene, washing in warm detergent solution, and rinsing in deionized water. Anodization was carried out using a constant current of  $0.005 \text{ A/cm}^2$ . The electrolyte was controlled at  $25^\circ \pm 1^\circ \text{C}$  and strongly stirred to avoid local heating effects.

Breakdown voltage was defined as the voltage at which the first observable deviation from linearity occurred in the voltage-time plot as recorded by a chart recorder with 10 V/in. scale factor. A VTVM with 11 megohm input impedance was used as a preamplifier to reduce loading effects. The measured breakdown voltage was corrected for IR drop in essentially the same manner as that used by Burger and Wu.

The following summary of an electrolyte series using acetate as the anion (Table I) serves to indicate the nature of the results obtained. Each electrolyte in the series was prepared in such a manner that the concentration of the acetate ion was 0.010M. Seven to ten determinations of breakdown voltage were carried out in each electrolyte.

Other series having different anions ( $\text{Cl}^-$  and  $\text{NO}_3^-$ ) and different anion concentrations (0.01 to 0.5M) were also used and the results were consistent: for a given anion and anion concentration, the breakdown voltage was constant and not dependent on the electrolyte resistivities.

It is obvious that these results do not remotely resemble those reported by Messrs. Burger and Wu. I can in no way account for the disagreement unless it is due to my use of electrolytes which are simple compared to those which they employed.

**F. J. Burger and J. C. Wu:** There are major differences in experimental technique which may account for discrepancies between our results and those of S. E. Libby. For example, he uses a current density ten times our own which was  $0.5 \text{ mA/cm}^2$ , also his temperature is  $25^\circ \text{C}$ , compared to our  $85^\circ \text{C}$ , his choice of acetate as the electrolyte bears a likely responsibility. Not all of our electrolytes are complicated, indeed electrolytes K, M, and O, as described in our paper, are quite simply dilute aqueous solutions containing 0.1, 0.03, and 0.01 parts by weight of phosphoric acid, respectively.

The conclusion at this stage must, therefore, be that some anomalies occurred in Mr. Libby's formation experiments which prevented the full potential of breakdown voltages from being attained. His voltages are from about 120 to 160V below what might have

<sup>7</sup> Pownall Center, Vermont 05261.

Table I.

Electrolyte	Resistivity at $25^\circ \text{C}$	Mean breakdown voltage	Standard deviation
$\text{HC}_2\text{H}_3\text{O}_2$	705 ohm-cm	343V	7.0V
$\text{KC}_2\text{H}_3\text{O}_2$	1020 ohm-cm	350V	4.2V
$\text{Cu}(\text{C}_2\text{H}_3\text{O}_2)_2$	1900 ohm-cm	345V	5.5V

<sup>4</sup> H. Holtan, Jr., P. Mazur, and S. R. De Groot, *Physica*, **19**, 1109 (1953).

<sup>5</sup> Westinghouse Research Laboratories, Pittsburgh, Pennsylvania 15235.

<sup>6</sup> Personal communication by L. M. Schwarz.

been predicted from electrolyte resistivities as supplied by him, in accordance with our experience.

The empirical linear relationship between breakdown voltage and log of electrolyte resistivity, as described by us, should be looked upon as a limiting relationship in the sense that the observed breakdown voltages have been found to be the highest attainable, provided no side reactions occur that interfere with the formation process. In the case of aluminum, we have singled out certain corrosion reactions as exam-

ples of the interference mechanisms. Anomalies of a different kind are known to occur in the tantalum system, *e.g.*, characterized by the production of the so called "gray" oxide. Whereas in the case of tantalum it has been found relatively easy to develop electrolyte systems and discover conditions that ensure trouble free anodization, this has been much less successful in the case of metals such as Nb and Zr; this latter point was briefly mentioned in our paper.



# Instructions to Authors of Papers

Revised October 7, 1971

## JOURNAL OF THE ELECTROCHEMICAL SOCIETY

is the official journal of the Society and contains three sections totaling some 2500 editorial pages annually: Electrochemical Science and Technology, Solid-State Science and Technology, and Reviews and News.

**Manuscripts** submitted to the Journal should be sent in **triplicate** (one original and two clear copies, preferably Xeroxed), to the Editorial Office, P.O. Box 2071, Princeton, New Jersey 08540.

**GENERAL** They must be typewritten, double-spaced, on one side only of white bond 8½ x 11 in. paper, 2½-4 cm (1-1½ in.) margins. Illustrations should also be sent in triplicate, with one original and two copies that are clear enough for easy review.

**Titles** should be brief and properly descriptive, followed by the author's name, professional connection and complete address, including city, state, and zip code. **Text** should be as brief as is consistent with clarity and should omit introductory or explanatory material which may be regarded as familiar to specialists in the particular field. Papers should be written in concise and good English and authors are urged to ensure they have been carefully edited and proofread before they are submitted. Suitable headings and subheadings should be included but sections should not be numbered. For current form and style, papers in recent issues should be consulted. Proprietary and trade names should be generally avoided; if used with discretion, they should be capitalized to protect the owners' rights.

If a paper was presented at a meeting of the Electrochemical Society, it should be mentioned in the covering letter sent with the original manuscript.

Under present Society policy, the review procedure is handled by the various Divisional Editors, with final acceptance or rejection by the Editor. Manuscripts are usually reviewed in several weeks and those returned to the author for revision should be resubmitted promptly to the appropriate Divisional Editor. This generally allows publication in five months or less from date of original receipt.

Authors are encouraged to suggest qualified reviewers for their manuscripts, with the editors reserving the right to final choice. It is helpful if the author tells which ECS division (listed in the front of each issue of the Journal) would be most interested in his paper. Inquiries concerning submitted manuscripts should be addressed to the Editor, President's Office, Rice University, Houston, Texas 77001.

Articles of wide diversity of interest are acceptable, but subjects primarily covered in the other specialized journals (e.g., analytical or nuclear chemistry) are not considered appropriate.

### TYPES OF ARTICLES

**Technical Papers** are divided into two categories: fundamental and applied. The former describes original research of basic nature and must have scientific depth. The latter may deal with any practical aspect of the fields of interest to the Society, e.g., plant design or operation, production and control methods, economics. Each paper should be introduced by an abstract stating the scope of the paper and summarizing fully its results and contents.

**Review Papers** furnish a current and critical analysis of the subject with citation only of truly pertinent references, and normally should not exceed 20 manuscript pages. An abstract is required.

**Technical Notes** are used for reporting brief research, developmental work, process technology, new or improved devices, materials, techniques, processes which do not involve more extensive basic scientific study. No abstract is required.

**Brief Communications** are used to report information of scientific or technological importance which warrants rapid dissemination, even though not necessarily a completed research. Length should be limited to 1000 words or less, with no more than two illustrations. No abstract is required. Publishing time is normally less than three months.

Authors are responsible for supplying a list of from three to five single key words to facilitate information retrieval. No paper will be published without them. Generic terms generally are to be avoided as are terms already contained in the title. Key words acceptable to **Chemical Abstracts** are also generally acceptable in Society publications. List key words at the bottom of the first page of the manuscript.

### KEY WORDS

Mathematical equations should be written on a single line if possible, and parentheses, brackets, the solidus (/), negative exponents, etc., may be used freely for this purpose. Authors are urged to consult Chapter VI of the "Style Manual" of the American Institute of Physics (available for \$2.50 at the American Institute of Physics, 335 East 45 Street, New York, N. Y. 10017) and to follow the patterns described there.

### EQUATIONS

Authors are encouraged to use symbols extensively. These should be defined in a list at the end of the paper, with units given. For example:

### SYMBOLS

$a, b, \dots$  = empirical constants of Brown equation  
 $f_i$  = fugacity of pure  $i$ th component, atm  
 $D_v$  = volume diffusion coefficient, cm<sup>2</sup>/sec

The AIP "Style Manual" referred to here gives a suitable list of common **Abbreviations**. Units usually will be abbreviated without periods throughout the text, as sec, min, hr, cm, mm, etc. **Metric Units** should be used throughout, unless English units are clearly more appropriate in the area of discussion.

### ABBREVIATIONS UNITS

**Electrode potentials:** Authors are urged to state and make use of the polarity of test electrodes with respect to the reference electrode used, i.e., Zn is normally negative, Cu normally positive with respect to the standard hydrogen electrode.

### POTENTIAL SIGNS

The sign for the emf of a cell should conform to the free energy change of the chemical reaction as written or implied, in accordance with the definition  $\Delta G = -nFE$ . These suggestions agree with the IUPAC conventions adopted in 1953.

**Literature References** should be listed on a separate sheet at the end of the paper in the order in which they are cited in the text. Authors' initials must be given, and the style and abbreviations adopted by **Chemical Abstracts** should be used. Any recent issue of Society journals may be consulted. Literature cited should be readily available; consequently personal communications, Department of Defense (DOD), and Office of Technical Services (OTS) citations should be minimized. When references are not readily accessible, **Chemical Abstracts** citation numbers must be supplied.

### REFERENCES

**Tables** should be typed on separate sheets.

### TABLES

**Photographs** should be used sparingly, must be glossy prints, and should be mailed with protection against folding. **Micrographs** should have a labeled length unit drawn or pasted on the picture. On both, label "top" where any uncertainty might arise. **Captions** for figures (including photographs) must be included on a separate sheet. Figure numbers must not appear in the body of the figure; they will be removed if they do. **Numerical Data** should not be duplicated in tables and figures.

### ILLUSTRATIONS

**Drawings and Graphs** ordinarily will be reduced to 8.3 cm (3¼ in.) column width, and after such reduction should have lettering no less than 0.15 cm high. Lettering must be of letter-guide quality. India ink on tracing cloth or paper is preferred, but India ink on coordinate paper with blue ruling is acceptable. Line weight 2 is used for borders and zero lines. When several curves are shown, each may be numbered and described in the caption. Lettering shown is approximately ¼ in. In plotting current or potential as ordinate, increasing negative values should go down.

To cover part of the cost of publication a page charge of \$40.00 per printed page is requested for the publication of technical material. A 10% reduction is allowed if at least one author of an article is an ECS member or an employee of a Patron or Sustaining Member firm. However, acceptance of a manuscript is on the basis of merit and is in no way dependent on such payment. The charge may be waived in individual cases.

### PUBLICATION CHARGE

Printed in U.S.A.





## Abstracts of "Recent News" Papers

Presented at the Electronics Division Semiconductors and Luminescence Sessions, the Electronics & Metallurgy Division 5th International Conference on Electron and Ion Beam Science and Technology, and the Dielectrics and Insulation Division Session, Houston, Texas, May 7-11, 1972

### 213RNP Influence of $\text{AsH}_3$ , $\text{PH}_3$ , and $\text{B}_2\text{H}_6$ on the Growth Rate and Resistivity of Polycrystalline Silicon Films Deposited from a $\text{SiH}_4\text{-H}_2$ Mixture

F. C. Eversteijn and B. H. Put, Philips Research Laboratories, Eindhoven, Netherlands

The deposition rate of polycrystalline silicon from a  $\text{SiH}_4\text{-H}_2$  mixture is substantially influenced by the addition of  $\text{AsH}_3$ ,  $\text{PH}_3$ , and  $\text{B}_2\text{H}_6$ . At a deposition temperature of  $580^\circ\text{C}$   $\text{AsH}_3$  causes a decrease by a factor of 7,  $\text{PH}_3$  a decrease by a factor of 2.5, while a two times higher deposition rate is obtained with  $\text{B}_2\text{H}_6$  addition.  $\text{B}_2\text{H}_6$  also affects the activation energy of the deposition reaction. The resistivity of the doped polycrystalline silicon films can be explained in terms of solid solubility and carrier mobility. Electron micrographs of the mirror-like silicon surfaces, obtained with and without dopant addition during growth, show a characteristic surface texture for each dopant.

### 214RNP An Indirect Method for Determining the Metallurgical Layer Thickness of Epitaxially Deposited Silicon from $\text{SiH}_4$

F. C. Eversteijn and G. J. P. M. v.d. Heuvel, Philips Research Laboratories, Eindhoven, Netherlands

The metallurgical layer thickness of epitaxially deposited silicon ( $d_{\text{met Si}}$ ) from  $\text{SiH}_4$  corresponds to the thickness of polycrystalline silicon ( $d_{\text{poly-Si}}$ ) simultaneously deposited on silicon covered with silicon nitride ( $\text{Si}_3\text{N}_4$ ) by means of the simple experimental relation:  $d_{\text{met Si}} = d_{\text{poly-Si}} - 0.10 \mu\text{m}$ . The experimental error amounts to  $\pm 0.02 \mu\text{m}$  for epitaxial layers up to  $4 \mu\text{m}$  and  $\pm 0.5\%$  in the thickness region of  $4 \mu\text{m}$  and higher. This method can be used down to  $0.5 \mu\text{m}$ .

### 215RNP Whisker-Free Growth of Polycrystalline Silicon

F. C. Eversteijn and B. H. Put, Philips Research Laboratories, Eindhoven, Netherlands

The growth of whiskers on silicon and silicon oxide, during deposition of polycrystalline silicon from a  $\text{SiH}_4\text{-H}_2$  mixture at temperatures below  $700^\circ\text{C}$ , is highly affected by the surface quality of the substrate. It has been found that heating the substrates prior to deposition in a hydrogen chloride-hydrogen mixture, at  $750^\circ\text{C}$  for 15 min, com-

pletely prevents the formation of whiskers during subsequent film growth. Details on substrate cleaning and on the mechanism of both formation and prevention of whiskers are presented.

### 216RNP Silicon Schottky Barrier FET's Prepared by Ion Implant-Diffusion

A. E. Feuersanger, GTE Laboratories, Bayside Research Center, Bayside, N. Y.

Enhancement- and depletion-type Schottky barrier FET's have been fabricated on high resistivity silicon. The n-type channel was formed by implantation of phosphorus ions followed by diffusion. This technique provides the required degree of control over the channel dimensions and doping level. The fabrication process includes oxide growth during diffusion, n<sup>+</sup> source-drain implantation, and a single self-aligned aluminum deposition. The characteristics of both enhancement and depletion devices fabricated by this process agree with JFET theory. Device parameters and low power switching circuit applications are discussed.

### 217RNP Silicon Lattice Constant Precision Measurements after High-Energy Ion Bombardment

C. F. Pihl and G. H. Schwuttke, IBM Corporation, East Fishkill Facility, Hopewell Junction, N. Y.

Precision lattice parameter measurements on silicon crystals, after 1 MeV N<sup>+</sup> bombardment, are reported. The measurements are based on Bond's method using an automated Apex diffractometer. Up to one million digital count data are taken at each position in the reflection curve, collected on magnetic tape, and computer analyzed. Thus a precision of  $1$  in  $10^6$  is obtained. Measurements are made at a number of positions across the wafer surface to include reference regions not subjected to ion implantation. Results confirm the previously proposed model of radiation damage in silicon after high-energy ion implantation.

### 218RNP Basic Distortion and Noise Mechanisms in Charge-Coupled Devices

D. F. Barbe, U. S. Naval Research Laboratory, Washington, D. C.

An analysis of the basic mechanisms causing distortion and noise in charge-

coupled devices is presented. The imaging application of charge coupling is emphasized. The fundamental sources of distortion are transfer inefficiency and leakage current. The fundamental sources of noise are interface-state noise, shot noise in the leakage current, and thermal noise during the formation of the potential wells. The over-all noise-equivalent-irradiance for a 100 element charge-coupled imager is presented.

### 219RNP Effects of Natural Convection and Forced Convection in Vapor Phase Growth Systems

J. P. Dismukes, RCA Laboratories, Princeton, N. J. and B. J. Curtis, RCA Laboratories Ltd., Zurich, Switzerland

The occurrence and possible effects of natural convection, in vapor phase crystal growth other than mixing, have largely been overlooked up to this time, although the phenomenon is known to introduce inhomogeneities in melt-grown crystals. Natural convection has become relatively well understood for air at room temperature. However, effects in gases at elevated temperatures have received little study. Convection in gases is reviewed in systems, with either a vertical or a horizontal temperature gradient, with emphasis on the effects of mixing motion and temperature oscillations on the grown crystal. Convection in gases is determined by the Rayleigh number, Prandtl

Abstracts of "Recent News" Papers	165C-167C
Section News	168C
People	167C-168C
New Members	168C
News Items	168C
Book Reviews	168C-169C, 171C-172C
ECS Financial Statements	170C
Call for Recent News Papers—	
Miami Beach Meeting	172C
Position Available	172C
Positions Wanted	172C

number, boundary conditions, and the molecular weight and size of the gas. Our calculations indicate that the Rayleigh number for gases varies as  $R \propto T^{-1}$ , where  $n = 4.6 \pm 4$  for an open flow system at constant pressure, and  $n = 2.6 \pm 4$  for a closed system. For fixed temperature difference and geometry, the Rayleigh number increases in the series of gases, He, H<sub>2</sub>, N<sub>2</sub>, Ar, O<sub>2</sub>, Br<sub>2</sub> and I<sub>2</sub>.

Literature on vapor phase crystal growth is reviewed; and it is found that, based on calculations, convection is present in some systems while absent in others. Only small convective mixing effects occur in resistance-heated vapor growth systems employing H<sub>2</sub> or He. However, pronounced temperature oscillations can occur in rf heated systems with cold walls. Temperature oscillation can occur in closed tube chemical transport employing halogens even for temperature differences as small as 10°C. New measurements are reported on horizontal and vertical flow-through vapor growth systems for both resistance heating and simulated rf heating using Ar, He, and Ar-He mixtures. In the resistance heated case the effects are small, but large convective effects and regular sinusoidal temperature oscillations have been observed in simulated rf heated systems.

220RNP

### Operating Conditions for the Use of Dichlorosilane to Deposit Silicon Nitride Films

D. J. Delong, A. E. Ozias, and W. C. Benzing, Union Carbide Corporation, Sistersville, W. Va.

A developmental study was made of the use of dichlorosilane to produce silicon nitride films. This paper summarizes the operating techniques and optimum conditions for the preparation of high quality silicon nitride. The major advantages of dichlorosilane are improved reproducibility and lower capital investment compared to silicon tetrachloride, higher operating temperatures, and reduced operating costs compared to the use of silane.

221RNP

### Gas Phase Etching of Sapphire: III. Chlorotrifluoromethane

H. M. Manasevit, North American Rockwell Electronics Group, Anaheim, Calif.

The ever increasing interest in the use of sapphire ( $\alpha$ -Al<sub>2</sub>O<sub>3</sub>) as a substrate for the heteroepitaxial growth of various materials has prompted a reexamination of gas-phase etching as an effective means for improving the surface of Al<sub>2</sub>O<sub>3</sub>. Based on a previous investigation, in which several fluorinated hydrocarbons were found effective as etchants for Al<sub>2</sub>O<sub>3</sub>, chlorotrifluoromethane was selected for further study as an etch-polishing agent for several Al<sub>2</sub>O<sub>3</sub> orientations. The results of these studies are presented.

222RNP

### Lead Salt Double Heterostructure Laser

K. J. Slegler and G. F. McLane, Naval Research Laboratory, Washington, D. C.

A PbS-PbS<sub>1-x</sub>Se<sub>x</sub>-PbS double heterostructure laser capable of emitting in the 4-8  $\mu$  wavelength range has been considered. In this wavelength range the PbS:Se alloy system should be inherently more attractive for a double heterostructure laser device than

would be a III-V alloy such as In As<sub>1-x</sub>Sb<sub>x</sub>. The results of some preliminary theoretical studies for the PbS-PbS<sub>1-x</sub>Se<sub>x</sub>-PbS structure are discussed.

223RNP

### Annealing of Beta Thin Film Silicon Carbide

I. Berman, Air Force Cambridge Research Laboratories, L. G. Hanscom Field, Bedford, Mass.

The stability of some of the silicon carbide polytypes has been examined by various people. The phase transitions and habit change investigations were made by observing the influence of annealing time and temperature from 1400°C to 2830°C on whiskers or needles of silicon carbide.

In this experiment thin films of beta silicon carbide were subjected to annealing temperatures from 1400°C to 2000°C. Unlike needles or whiskers, no transformation to 6H  $\alpha$  was observed. Electron diffraction patterns of the thin film surface were used to show the stability of 3C silicon carbide after each four-hour annealing step.

224RNP

### The Use of an Ionic Microprobe Analyzer for SiC Film Studies

J. B. Quoirin, B. Blanchard, and J. Mercier, C.N.R.S. Laboratoire de Magnetisme, Grenoble-Gare, France

An ionic microprobe analyzer allows the qualitative determination of the carbon and silicon distribution along the depth of thin SiC films grown either on or from silicon substrates. The secondary negative ions currents are measured with a good sensitivity. However, the resolution in depth is bad due to the shape of the craters. On the contrary, the secondary positive ions current (C<sup>+</sup>) is weak; but it corresponds to a well defined depth, at each instant, because the bottom of the crater is flat. In this case, the current-sensitivity is increased, sputtering the sample under oxygen. Noticeable differences concerning the distribution and the stoichiometry are observed with various fabrication procedures.

225RNP

### Efficient Mn(IV) Emission in Fluorine Coordination

A. G. Paulusz, Osram (GEC) Research Laboratories, The General Electric Company Ltd., Hirst Research Centre, Wembley, England

The efficiency and temperature characteristics of Mn<sup>2+</sup> activated phosphors are discussed in terms of the chemical bonding at the manganese center. The excitation and emission spectra of MnF<sub>6</sub><sup>2-</sup> groups in silico-fluorides are presented and compared with data for some other new Mn<sup>2+</sup> activated phosphors.

226RNP

### Efficiencies of Anti-Stokes Phosphors

S. Nathansohn, General Telephone and Electronics Laboratories, Bayside, N. Y.

There was a round table discussion of the efficiencies of anti-Stokes phosphors, for in-

frared  $\rightarrow$  visible conversion, measured at a number of cooperating laboratories.

227RNP

### A Telefocus Ion Gun with Variable Beam Profile

K. Wittmaack and F. Schulz, Gesellschaft für Strahlen- und Umweltforschung mbH München, Physikalisch-Technische Abteilung, 8042 Neuherberg, Germany

The influence of extraction geometry, extraction potential, and beam current on the shape of the beam profile has been studied in a telefocus ion gun of triode type. The gun consists of hot cathode PIG ion source, a moveable extraction cup electrode of variable length, and an acceleration tube electrode (up to 50 kV). The beam profile was monitored far outside the acceleration field with a thin wire which could be moved perpendicular behind a slit mask. Several modifications of the extraction geometry were investigated by varying the extraction gap, the shape of the ion source front plate, and the diameter of the circular aperture in the extraction electrode. The extraction potential could be changed through more than one order of magnitude at a fixed final acceleration potential by slightly varying the length of the extraction electrode.

Beam formation and focusing at a given target position was found to be possible in nearly all cases. Distortion-free beam profiles, however, could only be obtained by suitably adjusting the relevant gun parameters. Under very well-defined conditions, it was possible to produce ion beams with constant current density over more than 50% of the total beam diameter. The ion gun has been used successfully for large area sputtering and ion implantation.

228RNP

### Fabrication of Micron-Sized Permalloy Circuit Elements Suitable for Magnetic "Bubble" Propagation Using Electron Beam Lithography

R. C. Henderson, W. B. Suiter, and T. A. Weber, Bell Telephone Laboratories, Murray Hill, N. J.

The propagation of 2-4  $\mu$ m cylindrical magnetic domains ("bubbles") in garnet plattens requires correspondingly sized permalloy circuit elements such as T-bars or chevrons. An electron beam lithography technique termed "lift-off" has been used to make these circuits with permalloy elements 1-1.2  $\mu$ m in width, separated by 0.7-1  $\mu$ m, and with an 8-10  $\mu$ m periodicity. These structures have shown successful bubble propagation up to 100 kHz at threshold fields of 30 Oe.

While the desired patterns were, in fact, successfully made, it became clear during the work that the lift-off technique, which has been extensively used in the past, has a number of drawbacks. Poor adherence of the resulting metallization was frequently encountered, as well as remaining pieces of excess metal.

229RNP

### Electron Irradiation of MIS Capacitors—Annealing and Bias-Temperature Stress Studies

K. A. Pickar and L. R. Thibault, Bell Telephone Laboratories, Murray Hill, N. J.

When fabricating microelectronic circuit patterns, using electron beam lithography, damage to MIS systems from incident ener-

getic electrons can be expected. We examine here the annealing behavior and bias-temperature stress stability of the flatband voltage ( $V_{FB}$ ) and surface-state density ( $N_{SS}$ ) of irradiated capacitors using quasi-static high frequency C-V techniques. The results indicate that, in all cases, the large increases in  $N_{SS}$  seen after irradiation can be annealed with low temperature ( $< 450^\circ\text{C}$ )

heat treatments. Bias-temperature stressing with negative-field-plate bias produces only negligible differences in surface-state density between irradiated and unirradiated capacitors. Latent damage is revealed by the  $V_{FB}$  shift in  $\text{Al}_2\text{O}_3\text{-SiO}_2$  double-insulator capacitors. The flatband voltages of single oxide samples are stable under B-T stress. Samples made using lift-off techniques (metal evaporation on developed e-beam resist patterns) were comparable in B-T stress behavior with conventionally fabricated capacitors.

230RNP

### Current Voltage Characteristics of $\text{Al-SiO}_2\text{-Si}$ Structures

M. Av-Ron and M. Shatzkes,  
IBM Corporation, East Fishkill  
Facility, Hopewell Junction, N. Y.

Experimental results are presented concerning conduction, breakdown, and switching in  $\text{Al-SiO}_2\text{-Si}$  MOS dots. Transitions from the low conduction state are found to terminate in self-healing breakdowns. There also exists a higher conduction state in which destructive breakdowns do not occur.

## PEOPLE

**Theodore R. Beck**, new Society Vice-President, joined Flow Research, Inc., Kent, Washington, on May 1, 1972. Flow Research, founded and incorporated in 1970, is expanding experimental and theoretical contract research activities in fluid mechanics and related interdisciplinary areas. Dr. Beck will conduct electrochemical and corrosion research, and consult and collaborate on a corporate development of a high-pressure water-jet rock cutter. He has a contract with the Air Force Office of Scientific Research to study reactions and electrochemical kinetics of newly generated metal surfaces.

Dr. Beck has also been appointed Affiliate Professor, Department of Chemical Engineering, University of Washington, Seattle, where he will conduct studies on measurement and interpretation of surface stress of solid metal electrodes on a grant from NSF.

**James M. Booe**, director of the Chemical Laboratories of the Mallory Capacitor Company, a division of P. R. Mallory and Company, Inc., has retired from the organization after 42 years of service.

A nationally recognized research scientist, Mr. Booe is a member of sev-

# FROM ELECTROCATALYSIS TO FUEL CELLS

Edited by G. SANDSTEDT

## CONTENTS

Metal Catalysts for Fuel Cells

Inorganic and Organic Substances as Catalysts for Fuel Cells

Fuel Cells with Alkaline Electrolyte

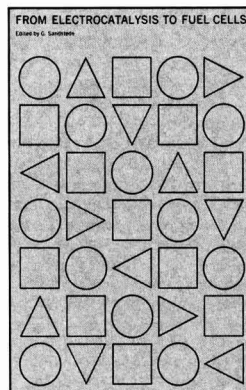
Fuel Cells with Acid Electrolyte

High Temperature Fuel Cells

Implantable Fuel Cells

Digression on Primary and Secondary Batteries

Developmental Goals and Prospects



FROM ELECTROCATALYSIS TO FUEL CELLS surveys the entire field of fuel cells with special emphasis on the results of research on electrocatalysts. Reports on new theories of electrocatalysis are included, as well as discussions of the state of the art of fuel cell technology as it applies to a multitude of systems. There are also papers on new secondary battery systems. This makes it possible to compare the properties and applications of the different electrochemical energy conversion devices in the light of the latest findings and to discuss in what way and to what extent fuel cells and secondary batteries can supplement each other.

This volume contains the proceedings of an international seminar held at the Battelle Seattle Research Center. In addition to reports on new research now being done at the European branches of Battelle, the book offers enough introductory material for people in related disciplines—chemical engineers, chemists, space engineers, bio-engineers, and physiologists—to become familiar with this special field.

G. Sandstedt is head of the Chemistry Department of the Battelle-Institut, e.V., Frankfurt/Main, Germany

441 pages, illus., tables. \$12.50

Published for Battelle Seattle Research Center by

UNIVERSITY OF WASHINGTON PRESS • Seattle, Washington 98195

ORDER FORM / UNIVERSITY OF WASHINGTON PRESS • Seattle 98195

Send \_\_\_\_\_ copy/ies of FROM ELECTROCATALYSIS TO FUEL CELLS (\$12.50 each).

\$ \_\_\_\_\_ enclosed. (In Washington State add 5% sales tax.)

NAME \_\_\_\_\_

ADDRESS \_\_\_\_\_

CITY/STATE/ZIP \_\_\_\_\_

## (People Cont.)

eral professional societies including The Electrochemical Society. He is a fellow in the American Institute of Chemists and holds the B.S. degree from Butler University. Mr. Booe holds more than 30 U.S. patents and more than 100 foreign patents, mostly in the field of electrochemistry.

## SECTION NEWS

### Detroit Section

The Detroit Section held its monthly meeting on April 13, 1972, at Greenfield's Northland Restaurant. Mr. Stanford R. Ovshinsky, founder and chairman of the board of Energy Conversion Devices, Inc., was the speaker.

Mr. Ovshinsky described some of the properties and demonstrated a few useful devices that could be made using amorphous semiconductors. Structural changes between a disordered and a more ordered state with the concomitant large change in many material properties are the basis for amorphous semiconductor operation. The structural changes can be initiated by various forms of energy such as an electrical pulse, light pulse, or light exposure. Many materials show good structural reversibility.

Amorphous semiconductor devices demonstrating high speed switching, high density information storage, and high resolution display were demonstrated.

### NEWS ITEMS

#### Characterization of Corrosion Products 1973 Symposium

A symposium on the Characterization of Corrosion Products is scheduled for the 1973 annual meeting of the National Association of Corrosion Engineers in Anaheim, California, during the week of March 19-23, 1973. The symposium is sponsored by the NACE Unit Committee T-3B on Corrosion Products.

Papers concerned with all phases of the collection, handling, and characterization of corrosion products are solicited. For example, areas of interest include: the techniques for analysis and identification of corrosion prod-

ucts; and the contribution of corrosion product characterization to the solution of corrosion problems with specific metals and alloys. It is anticipated that accepted papers, along with invited papers, could be the basis for a proceedings volume.

Offers of papers, with a title and some indication of the content, should be submitted prior to June 15, 1972 to the Symposium Chairman. An abstract will be required by September 1, 1972, with the final manuscript due on December 1, 1972. For further information contact the Symposium Chairman: Dr. W. D. France, Jr., General Motors Research Laboratories, General Motors Technical Center, Warren, Mich. 48090.

### Electrochemical Machining Conference

An international conference on electrochemical machining will be held for two days, Easter 1973, at the University of Leicester, Leicester, England. The conference will be organized under the joint cooperation of the (UK) Society for Electrochemistry and the (UK) ECM Coordinating Committee. A high standard is expected and topics will center around new industrial applications and developments. Contributions from industry will be particularly welcome, although a balance will be preserved with an appropriate representation of theoretical and research aspects.

The two-day meeting will cost about £10 (\$24.00-\$30.00). Those who propose to present a paper please enclose title and abstract. All those interested in taking part should contact Dr. David G. Lovering, the City University, Department of Chemistry, St. John Street, London EC1V 4PB, England.

## NEW MEMBERS

It is a pleasure to announce the following new members of The Electrochemical Society as recommended by the Admissions Committee and approved by the Board of Directors in April 1972.

#### Active Members

Casey, H. C., Jr., Murray Hill, N. J.  
Cliborn, J. H., Woodland Hills, Ca.  
Kienholz, P. J., Pittsburgh, Pa.  
Kuwana, T., Columbus, Oh.  
Levinson, I. R., Chicago, Ill.  
Palz, W., Paris, France  
Sato, K., Tokyo, Japan  
Stoneham, T. A., Cold Spring, N. Y.  
Tsai, K.-C., Santa Clara, Ca.  
Voss, E., Liederbach, Germany

#### Student

Choi, C. Y., New York, N. Y.  
Huang, J. C.-J., Cleveland, Oh.  
Morrow, A. J., Cambridge, Ma.

#### Reinstatement

Patrie, J., Voreppe, France

## BOOK REVIEWS

"Physics of Electronic Ceramics," Part A, edited by L. L. Hench and D. B. Dove. Published by Marcel Dekker, Inc., New York, N. Y. (1971). 564 pages; \$29.50.

"Physics of Electronic Ceramics, Part A" is the poorly edited and prolix proceedings of a conference that was held at the University of Florida in 1969 to assess the current status of understanding of electronic ceramics and to discuss applications of these materials. Semiconducting ceramic compounds, glasses, and amorphous thin films, as well as ceramic dielectrics and insulators, are treated in a series of review articles in this volume. A second volume (Part B, not reviewed) is to treat magnetic and electro-optic applications of ceramic materials.

Many of the articles are thorough and carefully written summaries that offer good introductions to various aspects of the field. For example, the papers by Chopra and by Davis on electrical properties of amorphous semiconductors, and the works by Adler and by Patterson on crystalline ceramics, are well worth reading. The two-year delay between the conference and the publication of the proceedings has outdated some of this material, although several authors have conscientiously supplied notes in proof directing the reader to more recent information.

An unfortunate proportion of the papers in this volume are irrelevant to the subject of the conference, technically inadequate, or are of limited intelligibility. There is, for example, a straightforward discussion of various applications of insulating films to silicon integrated circuits, e.g., as diffusion masks, MISFET gates, etc. It is not at all clear why this paper appears in a section otherwise devoted to the structural and electrical characterization of amorphous semiconducting films. In a review of methods of studying surface defects, two authors mention several techniques in passing and then devote the bulk of their article to a discussion of the application of field-ion microscopy to the observation of surface defects in refractory metals. It is not clear why this paper appeared in a book on ceramics. There are also several papers that are so poorly structured and so badly written as to be virtually unintelligible. It is not clear why these papers appeared.

The editors' contention that this volume is suitable for use as a text in a graduate level course does not bear scrutiny. The only step that appears to have been taken in this direction is the inclusion of somewhat more material in the introduction sections of many papers than one would normally expect

to find in review articles. In addition to the inclusion of irrelevant and inadequate material, the presentation is redundant, incomplete, and of an uneven level of sophistication. There are, for example, at least seven different, overlapping introductions to the transport properties of ceramics. Certainly one comprehensive treatment would have been preferable for a textbook.

Many of the shortcomings of this book are traceable to poor editing. This is surprising in view of the long list of editors associated with the work. Two men are directly responsible for this volume, but it is only one of a series of monographs ("Ceramics and Glass: Science and Technology", M. Dekker, Inc.) which is nominally supervised by a series editor and a fourteen-member editorial board.

Had this book appeared more promptly at a third its present length and price, and had it been presented simply as the proceedings of a review conference, it might have been a worthwhile addition to a scientific library's holdings. As it is, I would advise no one to buy this book.

D. A. Kiewit  
Hughes Research Laboratories  
Malibu, Calif. 90265

**"Modern Aspects of Electrochemistry No. 6,"** edited by J. O'M. Bockris and B. E. Conway. Published by Plenum Press, New York (1971). 373 pages; \$19.50.

This volume is the sixth in the excellent series on "Modern Aspects of Electrochemistry". The emphasis is on "modern" and the influence of the senior editor is evident throughout the series with the unmistakable emphasis, quite justifiable in this reviewer's opinion, on electrochemistry as opposed to ionics. The contributors represent an international selection of electrochemistry laboratories: Universidad Nacional de La Plata, Argentina (A. J. Arvia and S. L. Marchiano); University of Pennsylvania (Bockris); State University of New York at Stony Brook (H. L. Friedman); The University of Liverpool (A. Hickling); Instituto de Química Física "Rocasolano", Madrid, Spain (J. Llopis); and Union Carbide, Australia (D. B. Matthews). The book is divided into five chapters.

In the chapter entitled Computed Thermodynamic Properties and Distribution Functions for Simple Models of Ionic Solutions, Friedman reviews the advances in the theory of the equilibrium properties of electrolytes which have occurred subsequent to a similar review by Falkenhagen and Kelbg in Volume 2 of this series (1959). Llopis discusses the experimental determination of interface potentials in Surface Potentials at Liquid Interfaces. Arvia and Marchiano review Transport Phenomena in Electrochemical Kinetics

(an area which has been dominated by the Russians) in chapter 3. [The classic text in the field is Levich's "Physicochemical Hydrodynamics" (1962)]. Their chapter serves as an excellent introduction to the hydrodynamical behavior near a variety of electrodes and discusses quite lucidly the possible applications to kinetic studies.

## 1973 Palladium Medal Award, ECS

The eleventh Palladium Medal of The Electrochemical Society will be awarded at the Fall Meeting of the Society to be held in Boston, Massachusetts, October 7-11, 1973. The medal was established in 1951 by the Corrosion Division.

The recipient shall be distinguished for contributions to the field of Electrochemical Science and Corrosion. The recipient need not be a member of the Society, nor shall there be any restrictions or reservations regarding age, sex, race, citizenship, or place of origin or residence.

The award consists of a Palladium medal and a nickel replica thereof, both bearing the recipient's name, and the sum of one thousand five hundred dollars.

The recipient shall receive the award in person at the designated meeting of the Society and shall at that meeting deliver a general address to the Society on a subject related to the contributions for which the award is being presented. Expenses involved in the acceptance of the award shall be assumed by the recipient.

In addition to the above, with regard to the selection, the rules have the following provisions:

1. The selection of the recipient is the responsibility of the Palladium Medal Award Subcommittee of the Honors and Awards Committee consisting of six members of the Society who shall be knowledgeable in the field of the award and, ex officio, the Chairman of the Honors and Awards Committee. After due deliberations the Subcommittee shall determine whether the list of nominees includes any suitably qualified candidates for the award and, from those so qualified, shall select one candidate to be recommended to the Honors and Awards Committee as the award recipient. The Honors and Awards Committee will then make its recommendation to the Board of Directors. On approval of the recommendation for the granting of the award by the Board of Directors, the President of the Society shall inform the intended recipient of the action and shall determine whether the requirements governing acceptance of the award will be met. If there is agreement by the intended recipient with the requirements governing acceptance, the recipient of the award shall be announced in the *Journal*.

2. Nominations for the award shall be solicited by the Chairman of the Award Subcommittee by announcement in the *Journal of The Electrochemical Society* and communications to the Officers, and Division and Local Section Chairmen of the Society. Nominations shall be considered closed at the beginning of the Fall Meeting of the Society (Miami Beach, Florida, 1972) but nominations once made, shall be considered in effect for two consecutive award periods.

3. All nominations, whether made by a member of the Subcommittee or by any other member of the Society, must be accompanied by a full record of qualifications of the nominee for the award.

4. The nominator must assume the responsibility of providing the Chairman with six copies of the supporting documents. If the nominator does not have facilities to readily provide the Chairman with the six copies, the material shall be supplied to the National Office of the Society, which shall then prepare the necessary six copies for the Chairman. These copies must be in the hands of the Chairman no later than October 6, 1972.

Previous medalists have been:

Carl Wagner—1951  
Nathaniel H. Furman—1953  
Ulick R. Evans—1955  
Karl F. Bonhoeffer—1957  
Aleksandr N. Frumkin—1959

Herbert H. Uhlig—1961  
Norman Hackerman—1965  
Paul Delahay—1967  
Thomas P. Hoar—1969  
Leo Brewer—1971

Please address all nominations to the Chairman of the Palladium Medal Award Subcommittee, Dr. Manfred Breiter, General Electric R & D Center, P.O. Box 8, Schenectady, New York 12301.

Perhaps the most interesting section of this volume is chapter 4, The Mechanism of Charge Transfer from Metal Electrodes to Ions in Solution, by Matthews and Bockris. As they point out, "no process demands a more exclusively quantal discussion than does electron transfer." Three quantum approaches to charge transfer have been developed, which originate with Gurney, Libby, Topley, and Eyring (ab-



# The Electrochemical Society, Inc., Financial Statements

## as of December 31, 1971

### BALANCE SHEET—ALL FUNDS December 31, 1971

#### ASSETS

<b>General Fund</b>		
Cash in bank and on hand—allocated ..	\$ 93,163	
Chemical Bank Certificate of Deposit, 4 3/4% due 3/20/72 .....	50,000	
Accounts Receivable:		
Publications .....	\$16,638	
Divisions and other .....	6,328	22,966
Inventory of Society publications .....		6,720
Prepaid expenses .....		3,415
Furniture, fixtures and equipment .....	\$24,820	
Less: Accumulated depreciation .....	9,364	15,456
	<u>\$191,720</u>	
<b>Consolidated Special Funds</b>		
Cash—allocated (includes \$1,841 in sav- ings accounts) .....	\$ 13,868	
Marketable securities—at cost or mar- ket at date of gift (market value as of December 31, 1971—\$516,345) .....	435,473	
	<u>\$449,341</u>	
<b>Other Funds</b>		
Cash—allocated (includes \$8,022 in sav- ings accounts) .....	\$ 11,161	
	<u>\$ 11,161</u>	
<b>Total Assets—All Funds .....</b>	<b>\$652,222</b>	

#### LIABILITIES, DEFERRED INCOME and FUND BALANCES

<b>General Fund</b>		
Accounts payable .....	\$ 16,944	
Deferred income .....	121,136	
Reserve for Employee Pension .....	27,179	
General Fund Balance .....	26,461	
	<u>\$191,720</u>	
<b>Consolidated Special Funds</b>		
Consolidated Special Fund Balances ..	\$449,341	
	<u>\$449,341</u>	
<b>Other Funds</b>		
Funds held by the Society as Custodian ..	\$ 8,022	
Other Funds Balances .....	3,139	
	<u>\$ 11,161</u>	
<b>Total Liabilities, Deferred Income and Fund Balances—All Funds .....</b>	<b>\$652,222</b>	

### STATEMENT of GENERAL FUND INCOME, EXPENDITURES and FUND BALANCE For the Year Ended December 31, 1971

<b>Income</b>		
Memberships including journal sub- scriptions:		
Active, associate, and student .....	\$ 87,543	
Patron and sustaining .....	20,390	
	<u>\$107,933</u>	
Publications excluding members' jour- nal subscriptions .....	258,493	
National meetings .....	22,311	
Monograph royalties .....	5,865	
Dividends and interest .....	9,737 (A)	
Interest on General Fund Investments ..	4,772	
<b>Total Income .....</b>	<b>\$409,111</b>	
<b>Expenditures</b>		
Publications—printing and mailing .....	\$192,345	
National meetings .....	15,545	
Salaries and fringe benefits .....	143,412	
Office rental .....	21,415	
Postage and office supplies .....	15,180	
Young authors' prizes .....	300	
Depreciation .....	1,937	
Insurance .....	659	
Telephone .....	5,969	
Local sections support .....	2,247	
Investment management services .....	1,166	
Other .....	8,028	
<b>Total Expenditures .....</b>	<b>\$408,203</b>	
<b>Excess of Income Over Expenditures .....</b>	<b>\$ 908</b>	
Other Deductions:		
Princeton, N.J., relocation expenditures ..	\$ 41,933	
Reserve for employee pension .....	27,179 (B)	69,112
<b>Balance—December 31, 1970 .....</b>	<b>\$ 94,665</b>	
<b>Balance—December 31, 1971 .....</b>	<b>\$ 26,461</b>	
(A)—Consists of dividends and interest on the Society's portion of the Consolidated Special Funds.		
(B)—On January 31, 1972 the Society entered into an agreement with the Equitable Life Assurance So- ciety of the United States to in- itiate an employee pension plan. The above amount is the actu- aries computation of prior years costs involved.		
[ ] denotes red figures		

### STATEMENT of CONSOLIDATED SPECIAL FUNDS For the Year Ended December 31, 1971

	Total	Edward Goodrich Acheson Fund	F. M. Becket Memorial Award Fund	Consoli- dated Fellow- ship Fund	Colin Garfield Fink Fellowship Fund	Edward G. Weston Fellow- ship Fund	Society Reserve Fund	Corrosion Division	Electro- deposition Division	Electro- thermics and Metallurgy Division	Electro- ronics Division
<b>Balances—December 31, 1970 .....</b>	<b>\$409,951</b>	<b>\$52,697</b>	<b>\$15,814</b>	<b>\$65,489</b>	<b>\$13,382</b>	<b>\$13,807</b>	<b>\$200,992</b>	<b>\$33,246</b>	<b>\$7,234</b>	<b>\$7,290</b>	<b>\$ —</b>
<b>Additions</b>											
Dividends and interest .....	\$ 5,997	\$ 1,937	\$ 838	\$ 2,131	\$ 426	\$ 665		\$ 1,177	\$ 411	\$ 232	
Monograph royalties ..	1,820										
Capital gain dividends reinvested .....	30,013	3,583	1,593	4,091	818	1,276	\$ 16,117	1,921	277	381	[ 44]
Transfer from other funds .....	9,306										9,306
<b>Total Additions .....</b>	<b>\$ 47,136</b>	<b>\$ 5,520</b>	<b>\$ 2,431</b>	<b>\$ 6,222</b>	<b>\$ 1,244</b>	<b>\$ 1,941</b>	<b>\$ 16,117</b>	<b>\$ 3,098</b>	<b>\$ 688</b>	<b>\$ 613</b>	<b>\$9,262</b>
<b>Deductions</b>											
Award and expenses ..	\$ 1,049	\$ 78	\$ 212	\$ 102				\$ 657			
Fellowships .....	4,501		1,500	2,040	375	588					
Management services ..	706	224	99	255	51	77					
Other expense .....	1,490							990	500		
<b>Total Deductions ..</b>	<b>\$ 7,746</b>	<b>\$ 302</b>	<b>\$ 1,811</b>	<b>\$ 2,397</b>	<b>\$ 426</b>	<b>\$ 663</b>	<b>\$ —</b>	<b>\$ 1,647</b>	<b>\$ 500</b>	<b>\$ —</b>	<b>\$ —</b>
<b>Excess of Additions Over Deductions .....</b>	<b>\$ 39,390</b>	<b>\$ 5,218</b>	<b>\$ 620</b>	<b>\$ 3,825</b>	<b>\$ 818</b>	<b>\$ 1,278</b>	<b>\$ 16,117</b>	<b>\$ 1,451</b>	<b>\$ 188</b>	<b>\$ 613</b>	<b>\$9,262</b>
<b>Balances—December 31, 1971 .....</b>	<b>\$449,341</b>	<b>\$57,915</b>	<b>\$16,434</b>	<b>\$69,314</b>	<b>\$14,200</b>	<b>\$15,085</b>	<b>\$217,109</b>	<b>\$34,697</b>	<b>\$7,422</b>	<b>\$7,903</b>	<b>\$9,262</b>

[ ] denotes red figures

### STATEMENT of FUNDS HELD by the SOCIETY as CUSTODIAN and OTHER FUNDS

For the Year Ended December 31, 1971

#### FUNDS HELD BY THE SOCIETY as CUSTODIAN

	Electronics Division	Physical Electrochem- istry Division	Dielectrics and Insula- tion Division	Total	OTHER FUNDS		
<b>Balances—December 31, 1970 .....</b>	<b>\$8,019</b>	<b>\$2,315</b>	<b>\$3,817</b>	<b>\$14,151</b>	<b>Physical Electrochemistry Monograph Fund</b>	<b>Battery Divi- sion Mono- graph Fund</b>	<b>Total</b>
<b>Additions</b>					<u>\$1,429</u>	<u>\$ —</u>	
Interest on savings accounts .....	\$ 355	\$ 108	\$ 190	\$ 653			
Monograph royalties .....	983	341		1,324	\$ 44	\$1,916	\$1,960
Transfer of funds .....			1,200	1,200			
<b>Total Additions .....</b>	<b>\$1,338</b>	<b>\$ 449</b>	<b>\$1,390</b>	<b>\$ 3,177</b>	<b>\$ 44</b>	<b>\$1,916</b>	<b>\$1,960</b>
<b>Deductions</b>							
Transfer to Consolidated Special Funds ..	\$9,306			\$ 9,306			
Awards .....					250		250
<b>Excess of Additions Over Deductions ..</b>	<b>(\$7,968)</b>	<b>\$ 449</b>	<b>\$1,390</b>	<b>(\$ 6,129)</b>	<b>(\$ 206)</b>	<b>\$1,916</b>	<b>\$1,710</b>
<b>Balances—December 31, 1971 .....</b>	<b>\$ 51</b>	<b>\$2,764</b>	<b>\$5,207</b>	<b>\$ 8,022</b>	<b>\$1,223</b>	<b>\$1,916</b>	<b>\$3,139</b>

[ ] denotes red figures  
To the Board of Directors of  
The Electrochemical Society, Inc.

We have examined the accompanying financial statements of The Electrochemical Society, Inc., for the year ended December 31, 1971. Our examination was made in accordance with generally accepted auditing standards and, accordingly, included such tests of the accounting records and such other auditing procedures as we considered necessary in the circumstances.

In our opinion, the accompanying financial statements present fairly the financial position of The Electrochemical Society, Inc., at December 31, 1971 and the results of its operations for the year then ended, in conformity with generally accepted accounting principles applied on a consistent basis.

*Loeb & Prosser*

CERTIFIED PUBLIC ACCOUNTANTS

## ELECTROCHEMICAL AND BATTERY TECHNOLOGY

- • • Consultants
- • • Engineers
- • • Marketing Specialists

For further information  
contact:



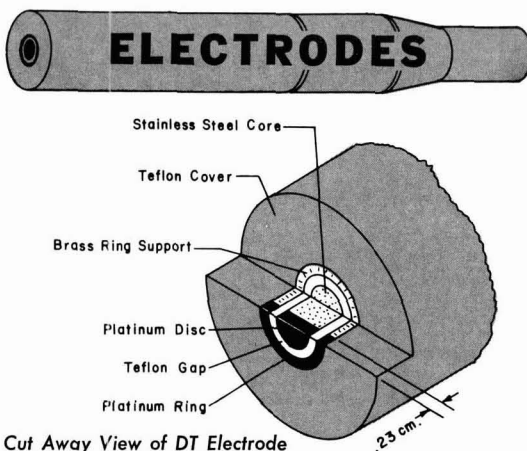
**POWER Applications, Inc.**  
41-06 Bell Blvd.  
(P. O. Box 305j)  
Bayside, New York 11361  
212-631-7784

### (Book Reviews Cont.)

solute rate theory). Matthews and Bockris present, with considerable insight, the similarities and differences in the treatments, review the most recent work, and indicate the fruitful directions for further study. Future results should be of particular interest to semiconductor electrochemistry and heterogeneous catalysis. This appears to be a subject ripe for considerable expansion; and we may expect, and hope, to soon see entire volumes devoted to the quantum theory aspects of charge transfer processes. The book concludes with a chapter entitled Electrochemical Processes in Glow Discharges at the Gas-Solution Interface, by Hickling.

In all, this volume would be a valuable addition to the library of any serious electrochemist and should be of interest to many in related fields.

Ronald L. Meek  
Bell Laboratories  
Murray Hill, N. J. 07974



**DISC AND RING DISC ELECTRODES  
FOR  
GENERAL AND CUSTOM APPLICATIONS  
ROTATORS AND POTENTIOSTATS**

**Pine Instrument Company**  
P. O. Box 429, Grove City, Pa. 16127  
Telephone 412/458-6391

"Separation Processes," by C. Judson King. Published by McGraw-Hill Book Co., New York, N. Y. (1971). 809 & xviii pages; \$19.50.

One of the less welcome by-products of the intrusion of engineering science into chemical engineering curricula has been the falling out of favor of macrosystem or process-oriented approaches in chemical engineering courses. Analysis, both engineering and mathematical, is but a tool for the engineer, an elegant and indispensable tool, but a tool nevertheless, to enable him to synthesize individual operations and functional units into a total process which produces something useful. Happily, Dr. King's book is one more signal of the return of perspective to the teaching of engineering. That is, chapters are devoted to the discussion of topics such as factors influencing product purities, capacity and efficiency of contacting devices, and energy requirements of separation processes, as well as the more traditional ones of multistage separation and various computation methods.

Although the author states that the book is intended to complement one

on transport phenomena, the treatment is quantitative where appropriate. There are a sufficient number of worked-out examples in the text, and problems for student exercises are available at the end of each chapter. Although almost all topics are treated quantitatively, there is an extensive descriptive treatment of topics such as mass or energy separating agents, "Patterns of Change and Computational Approaches" (a discussion of phase flows, concentration, and temperature profiles in processing equipment and general conceptual approaches to their mathematical calculation), "Selection of Separation Processes", and so on.

Principles of the hydrodynamic and mechanical design and evaluation of contacting equipment are treated in a chapter entitled Capacity and Efficiency of Contacting Devices. Dynamics, control schemes, and optimal operation and design are also discussed although mostly qualitatively. There are a large number of photographs of process plants, equipment, and constructional details of equipment throughout the book; there are also graphs, diagrams, a number of tables, and good bibliographies (after each chapter).

### Call for Recent News Papers Miami Beach, Florida Meeting October 8-13, 1972

Triplicate copies of a 75-word abstract of Recent News Papers must be received by the Symposium Chairman (as indicated below) not later than September 1, 1972, to be considered for inclusion in the Recent News Papers Session.

## Electronics Division

### Semiconductor General Session

Recent News Papers for the Semiconductor General Session are invited in the following areas:

1. Elemental, Compound, and Alloy Semiconductors
2. Device Technology
3. Thin Film Technology; Metals and Dielectrics
4. Passivation and Packaging Technology
5. Radiation Effects
6. Reliability Physics

The abstracts should be sent for receipt before September 1, 1972, to the Recent News Papers Session Chairman: Elliott Philofsky, Motorola Inc., Semiconductor Products Division, 5005 E. McDowell Road, Phoenix, Arizona 85008.

### (Book Reviews Cont.)

To point out some minor deficiencies of the book, this reviewer finds some chapter and topical headings less than descriptive of the material contained therein. For example, the chapter, Group Methods, deals with the simultaneous solution of multistage conservation equations in contrast to the stage-to-stage computation; the chapter entitled Additional Factors Influencing Product Purities includes the discussion of Rayleigh distillation, the definition of single phase and interphase mass transfer coefficients, and the breakthrough analysis of fixed-bed processes. The symbol  $(f_A)_D$  is used to denote the recovery fraction for component A in the distillate, a usage in variance with the convention of using Latin or Greek letters, especially letters descriptive of the concept or term in question. The book is, perhaps, too long and some topics are too fragmented for easy reference. All these considerations, however, are secondary to the clear writing and the sound and lucid exposition of separation processes to be found in the book.

"Separation Processes" is suitable as an advanced textbook or as a fundamental and comprehensive treatment of the principles and processes of separation of mixtures.

Arvo Lannus  
The Cooper Union  
New York, N. Y. 10003

## POSITION AVAILABLE

Please address replies to the box number shown, c/o The Electrochemical Society, Inc., P. O. Box 2071, Princeton, N. J. 08540.

**Electrochemists/Physical Chemists**—Applications are invited for post-doctoral appointments in the area of electrode kinetics/corrosion. Candidates should possess both training and experience in electrode kinetics with special emphasis on modern experimental techniques and applications to corrosion and other metal surface reactions.

Salary, depending upon qualifications and experience, starts at \$10,000/year. Contact: Professor Norbert D. Greene, Institute of Materials Science U-136, University of Connecticut, Storrs, Conn. 06268.

### Positions Wanted

Society members of any class may, at no cost and for the purposes of professional employment, place not more than three identical insertions per calendar year, not to exceed 8 lines each. Count 43 characters per line, including box number, which the Society will assign.

### Certificates, Pins, and Keys Now Available

The Society announces the availability of the following items:

Membership Certificates \$ 5.00  
Gold Membership Pin \$ 7.50  
Gold Membership Key \$15.00

Those interested should send their order accompanied by check to The Electrochemical Society, Inc., P.O. Box 2071, Princeton, N. J. 08540

## ADVERTISER'S INDEX

The Kendall Company	163C
Pine Instrument Company	171C
POWER Applications, Inc.	171C
Princeton Applied Research Corp.	159C
University of Washington Press	167C

## POSITIONS WANTED

Please address replies to the box number shown, c/o The Electrochemical Society, Inc., P. O. Box 2071, Princeton, N. J. 08540.

**Staff Technologist**—Ph.D. Inorganic chemist with industrial experience in electrochemistry, electrodeposition, metal reduction, alloy formation, coatings, and refractory materials synthesis. Highly competent in technical communications, both written and oral. Seeking industrial R&D position. Some liaison with production, marketing, and management desired. Reply Box C-98.

**Materials Engineer**—B.Sc. Experience in design and development of electrochemical equipment and instrumentation used in synthesis and evaluation of novel electronic materials such as phosphors, liquid crystals, and other electro-optic materials. Performed growth of single crystals. Familiar with high temperature and vacuum technology of refractory metals and ceramics. Interested in R&D or production. Reply Box C-99.

**Inorganic Chemist**—M.S. Research in lead-acid battery production has lead to improved understanding of plate composition and battery life. Also background in areas of electroanalysis and instrumentation. Productive, enterprising, and communicative. Seek responsible position in Engineering or R&D related to inorganic and electrochemistry. No agencies. Reply Box C-100.

**Electrochemist**—B.S. and M.A. Chemistry. Twelve years electrochemical experience. Research on battery technology and plating processes. Process control continuous plating line. Two years adjunct college instructor. Seeking challenging and rewarding position with industrial firm or educational institution. Reply Box C-101.

**Solid-State Chemist**—Ph.D. 1971, M.S. 1952. 19 yrs. exp. all aspects solid-state; R&D, pilot plant, & prod. background; inorganic, analytical & phys. chem. Synthesis of materials & phosphors my specialty. 36 new products and processes developed for light industry, 41 patents issued, 38 papers. Supervisory, management exp. Economic evaluation from conception to plant construction. Reply Box C-102.

**Electrochemist**—Ph.D. 1944. Seeks challenging industrial research or development position or academic position. R&D background includes electrode kinetics, batteries, electrodeposition, corrosion, and stress corrosion. 47 publications, administrative experience. Location open. Reply Box C-103.

**Physical Chemist**—Ph.D. 1961. 9 years experience in industrial R&D. Surface chemistry, electrochemistry, corrosion, electroplating. Instrument development and applications for process control. Publications and patents. Some teaching experience. Seeks industrial or academic opportunity. Will relocate. Reply Box C-104.

**Materials Science/Corrosion**—Ph.D., '57 (inorg. chem.). Extensive experience in industrial research, govt. science administration, and university teaching (met. engr.). Desires position in xtal growth, ceramics, corrosion, or related areas involving administrative responsibilities. Honors incl. Fellow, Washington Acad. Sci.; Amer. Inst. Chemists; and Research Award, NACE. Reply Box C-105.

## APPLICATION FOR ADMISSION

to

**The Electrochemical Society, Inc.**

Return completed application to:

Secretary

The Electrochemical Society, Inc.

Post Office Box 2071 • Princeton, New Jersey 08540

Do not write in this space	
No. _____	Checked: _____
Info. Req. _____ Rec'd _____	Approved: _____
Notice of Ackn. _____ Accep. _____	Elected: _____
_____ \$ _____	Adv. Date _____
recap	

**To the Board of Directors of The Electrochemical Society, Inc.:**Full Name \_\_\_\_\_  
(please print)residing at \_\_\_\_\_  
(please print)

and at present associated with \_\_\_\_\_

as \_\_\_\_\_

hereby makes application for admission to The Electrochemical Society, Inc., as a \_\_\_\_\_ member,  
and encloses check in amount of \$ \_\_\_\_\_ covering first year's dues. (See reverse side for proper class of membership  
and dues applying thereto.)

1. Date, and Place of Birth: \_\_\_\_\_ 2. Citizen or Subject of: \_\_\_\_\_

3. Education: Institution	Dates Attended	Major Subject	Degree Earned
_____	_____	_____	_____
_____	_____	_____	_____
_____	_____	_____	_____

4. Employment Record: Name of Employer	Dates	Position
_____	_____	_____
_____	_____	_____
_____	_____	_____

5. Please indicate your primary DIVISIONAL interest by writing the number 1 in front of that Division name.

If you have other divisional interests, indicate by placing succeeding numbers in front of Division names.

..... Battery	..... Electrodeposition	..... Electro-Organic
..... Corrosion	..... Electronics	..... Electrothermics and Metallurgy
..... Dielectrics and Insulation	<input type="checkbox"/> Semiconductors	..... Industrial Electrolytic
	<input type="checkbox"/> Luminescence	..... Physical Electrochemistry

6. Please check Local Section with which you wish to affiliate:

..... Boston	..... Detroit	..... Niagara Falls	..... Pittsburgh	..... South Texas
..... Chicago	..... Indianapolis	..... Ontario-Quebec	..... San Francisco	..... Natl. Capital Area
..... Cleveland	..... Midland (Mich.)	..... Pacific Northwest	..... So. Calif.-Nevada	..... None
..... Columbus	..... Metropolitan N.Y.	..... Philadelphia	..... North Texas	

7. Our Constitution provides that two Active Members of the Society (who can substantiate the above record) must recommend you for admission to membership. It would facilitate the handling of your application if you are able to have your references sign this application form; if not convenient, please list their names and addresses.

Name (please print) \_\_\_\_\_ Signature \_\_\_\_\_ Address \_\_\_\_\_

Name (please print) \_\_\_\_\_ Signature \_\_\_\_\_ Address \_\_\_\_\_

The undersigned certifies that the above statements are correct and agrees, if elected to the Society, that he will be governed by its Constitution and Bylaws. He furthermore agrees to promote the objects of the Society as far as shall be in his power.

SIGNATURE AND  
ADDRESS TO WHICH  
PUBLICATIONS AND  
COMMUNICATIONS  
SHOULD BE SENT.

(Signature)

(Street Address)

Date \_\_\_\_\_ 19 \_\_\_\_\_

(City, State, Zip Code)

(over)

**CONSTITUTION – Article II***Membership*

Section 1. The individual membership shall consist of Active, Honorary, and Emeritus Members. The Board of Directors may from time to time authorize other classifications of membership as defined in the By-laws of the Society.

(Active Member – Annual Dues \$25.00)

Section 2. An active Member shall: be interested in electrochemistry or allied subjects; possess a Bachelor's degree, or its equivalent; and have three or more years of post-graduate experience in the natural sciences. The degree of Master of Science (or of Engineering) shall be equivalent to one year of experience, and the Doctor's degree in Science (or in Engineering) shall be equivalent to three years of experience. In lieu of a scholastic degree, ten years of responsible professional experience in electrochemistry or allied subjects shall be required. One year of college work in natural science shall be deemed the equivalent of one year of experience. Election to Active Membership shall require the recommendation of two Active Members in good standing.

**BYLAWS – Article II***Non-Voting Memberships*

(Student Member – Annual Dues \$3.00)

Section 1. Student Member. A Student Member shall be a full-time undergraduate or graduate student registered for a degree in natural science or engineering. The applicant for Student Membership shall be recommended by two Active Members of the Society in good standing, and by a member of the senior staff of the college of his attendance. The Student Member shall submit suitable evidence of graduation to the Executive Secretary's office upon request. Upon graduation from college, unless he enters graduate school, the Student Member shall automatically become an Associate Member at the beginning of the next calendar year. He shall remain an Associate Member for three years and then automatically become an Active Member. If he enters graduate school as a full-time student he shall remain a Student Member as long as he remains in school. When he discontinues graduate studies, if he has completed three years of full-time graduate study he shall automatically become an Active Member at the beginning of the next calendar year. If he has completed less than three years of graduate study, he shall automatically become an Associate Member at the beginning of the next calendar year; then an Active Member after the equivalent of three years as Associate Member, each year of graduate study as a Student Member being credited as a substitute for one year as an Associate Member.

(Associate Member – Annual Dues \$18.00)

Section 2. Associate Member. An Associate Member shall have received an Engineering or Bachelor's degree with a major in natural science, but not yet have completed the requirement of three years of experience for Active Membership. In lieu of a scholastic degree, seven years of responsible professional experience in electrochemistry or allied subjects shall be required. An Associate Member shall automatically become an Active Member at the beginning of the next calendar year after he shall have acquired three years of professional experience in electrochemistry, or allied subjects. The applicant for Associate Membership shall be recommended by two Active Members of the Society in good standing.

**BYLAWS – Article XX***Dues*

Section 1. The annual dues for Active Members shall be twenty-five dollars. The annual dues for Student Members shall be three dollars, and for Associate Members, eighteen dollars. Each member shall receive the JOURNAL OF THE ELECTROCHEMICAL SOCIETY.

Section 2. When individuals are elected to membership, they must elect to initiate their membership as of January 1 or July 1 of the year of election; or, if elected during the last quarter, January 1, of the year following election.

In the case of a July 1 election for starting membership, dues will be prorated.

Section 3. Any Active Member who shall pay in one lump sum the amount indicated in the following table in accordance with his or her age at the time of payment shall be exempt from the payment of any further dues and shall be considered an Active Member during the remainder of his or her life.

Age	Amount
Through Age 35	\$400
36-40	350
41-45	300
46-50	250
51-55	200
56-60	150
Above 60	100

Section 5. Emeritus Members shall be exempt from the payment of annual dues and shall have all the rights and privileges of an Active Member.

**CONSTITUTION – Article III***Admission and Dismissal of Members*

Section 2. Application for individual membership shall be in writing on a form adopted by the Board of Directors.

Section 3. The Admissions Committee shall be a rotating committee consisting of three members. One member shall be appointed each year by the President with the approval of the Board of Directors for a term of three years to replace the outgoing member. This Committee shall receive from the Secretary all properly executed and properly recommended applications for admission which he has received from persons desirous of becoming members of the Society. It shall be the duty of this Committee, after examining the credentials of applicants, to make appropriate recommendation to the Board as to approval or rejection of the applications. Unanimous approval of an applicant by this Committee shall be required before the candidate's name may be submitted to the Board of Directors for election. The election to membership shall be by a mail vote of the Board of Directors. The candidate shall be considered elected two weeks after the date the proposed membership list is mailed to the Board if no negative votes have been received by the Secretary. If a candidate receives one negative vote, his application shall then be considered and voted upon at the next meeting of the Board of Directors. Two negative votes cast at this meeting shall exclude a candidate. The Board of Directors may refuse to elect a candidate who, in its opinion, is not qualified for membership. The names of those elected shall be announced to the Society. Duly elected candidates shall have all the rights and privileges of membership as soon as their entrance fee, if any, and dues for the current year have been paid.

Section 4. A member desiring to resign shall send a written resignation to the Office of the Society.

Section 5. Upon the written request of ten or more Active Members that, for cause stated therein, a member be dismissed, the Board of Directors shall consider the matter and, if there appears to be sufficient reason, shall advise the accused of the charges against him. He shall then have the right to present a written defense, and to appear in person before a meeting of the Board of Directors, of which meeting he shall receive notice at least twenty days in advance. Not less than two months after such meeting the Board of Directors shall finally consider the case and, if in the opinion of the majority of the Board of Directors a satisfactory defense has not been made and the accused member has not in the meantime tendered his resignation he shall be dismissed from the Society.

Section 9. Any member delinquent in dues after April 1 shall not receive the Society's publications and will not be allowed to vote in any Society election until such dues are paid. All members in arrears for one year after April 1 shall lose their membership status and can be reinstated only by action of the Board of Directors.





# NEW SYMPOSIA VOLUMES

## **ELECTROCHEMICAL CONTRIBUTIONS TO ENVIRONMENTAL PROTECTION**

The New Technology Committee with the Electrothermics and Metallurgy, Industrial Electrolytic, and Physical Electrochemistry Divisions of The Electrochemical Society, sponsored a symposium on Electrochemical Contributions to Environmental Protection during the Houston, Texas Meeting of the Society, May 7-11, 1972.

With emphasis on a timely and relevant new technology area, and electrochemical and solid-state processes and devices for solving pollution problems, papers on the following subjects were presented: Electrochemical Devices and Techniques for Pollution Monitoring; Solid-State and Optical Pollution Monitoring Devices; Electrochemical Processes for Pollution Control; Industrial Requirements for Effective Pollution Control.

The edited papers will be published in a soft bound volume in 1972. To obtain your copy, use the appropriate order form on the next page; please include payment.

## **FIFTH INTERNATIONAL CONFERENCE ON ELECTRON AND ION BEAM SCIENCE AND TECHNOLOGY**

The Electrothermics and Metallurgy Division of The Electrochemical Society sponsored the 5th International Conference on Electron and Ion Beam Science and Technology at the Houston, Texas Meeting of the Society, May 7-11, 1972.

The following topics were among those covered at the symposium: Physics of Electron and Ion Beams—advances in theory and interaction with materials, particularly in terms of mechanism; Advanced Electron and Ion Beam Processing Systems; Electron Beam Welding, Machining, and Cutting; Electron Beam Smelting, Refining, and Evaporation; Application of Electron Beams in Polymerization and Information Storage and Retrieval; Ion Implantation Sources and their Application in Solid-State Devices as well as Utilization of Electron and Ion Beams in Manufacturing, Monitoring and Failure Analysis of Integrated Circuitry.

The edited papers will be published in a soft bound volume in 1972. To obtain your copy, use the appropriate order form on the next page; please include payment.

# NEW SYMPOSIA ORDER FORMS

## Electrochemical Contributions to Environmental Protection

CONTENTS  
BOOKS

Return Postage  
Guaranteed

From -

The Electrochemical Society, Inc.  
P.O. Box 2071  
Princeton, N.J. 08540

### Electrochemical Contributions to Environmental Protection

I Wish To Order The Following Copies

	No. of Copies	Total Cost
Copies @ \$8		

Payment in U.S. funds must accompany order.

Name \_\_\_\_\_  
Address \_\_\_\_\_  
City \_\_\_\_\_ State \_\_\_\_\_  
Zip Code \_\_\_\_\_ Country \_\_\_\_\_

Name \_\_\_\_\_  
Address \_\_\_\_\_  
City \_\_\_\_\_ State \_\_\_\_\_  
Zip Code \_\_\_\_\_ Country \_\_\_\_\_

Do Not Use

EP

Insert Your Order No. Here

Forward this order form with full payment to  
THE ELECTROCHEMICAL SOCIETY, INC.  
P.O. Box 2071, Princeton, N.J. 08540

P.O. #

CK. #

RECAP

## 5th International Conference on Electron and Ion Beam Science and Technology

CONTENTS  
BOOKS

Return Postage  
Guaranteed

From -

The Electrochemical Society, Inc.  
P.O. Box 2071  
Princeton, N.J. 08540

### Electron and Ion Beam Science and Technology - 5th

I Wish To Order The Following Copies

	No. of Copies	Total Cost
Copies @ \$11		

Payment in U.S. funds must accompany order.

Name \_\_\_\_\_  
Address \_\_\_\_\_  
City \_\_\_\_\_ State \_\_\_\_\_  
Zip Code \_\_\_\_\_ Country \_\_\_\_\_

Name \_\_\_\_\_  
Address \_\_\_\_\_  
City \_\_\_\_\_ State \_\_\_\_\_  
Zip Code \_\_\_\_\_ Country \_\_\_\_\_

Do Not Use

EI5

Insert Your Order No. Here

Forward this order form with full payment to  
THE ELECTROCHEMICAL SOCIETY, INC.  
P.O. Box 2071, Princeton, N.J. 08540

P.O. #

CK. #

RECAP

## THE ELECTROCHEMICAL SOCIETY PATRON MEMBERS

### Dow Chemical Co.

Inorganic Chemicals Dept., Midland, Mich.

### General Electric Co.

Battery Business Section, Gainesville, Fla.

Chemical Laboratory, Knolls Atomic Power Laboratory,  
Schenectady, N. Y.

Electronic Capacitor & Battery Dept., Irmo, S. C.

Lamp Div., Cleveland, Ohio

Materials & Process Laboratory, Large Steam  
Turbine-Generator Dept., Schenectady, N.Y.

Nucleonics Laboratory, Pleasanton, Calif.

Research and Development Center,  
Physical Chemistry Laboratory,  
Solid State Physics Laboratory,  
Schenectady, N.Y.

The International Nickel Co., Inc., New York, N. Y.

### Olin Corporation

Chemicals Div., Research Dept.,  
New Haven, Conn.

### Westinghouse Electric Corp.

Electronic Tube Div., Elmira, N.Y.

Lamp Div., Bloomfield, N.J.

Semiconductor Div., Youngwood, Pa.

Research Laboratories, Pittsburgh, Pa.

K. W. Battery Co., Westinghouse Subsidiary,  
Skokie, Ill.

## THE ELECTROCHEMICAL SOCIETY SUSTAINING MEMBERS

Airco Speer Carbon-Graphite  
St. Marys, Pa.

Allen-Bradley Co.,  
Milwaukee, Wis.

Allied Chemical Corp.,  
Industrial Chemicals Division,  
Solvay, N. Y.

Aluminum Co. of America,  
New Kensington, Pa.

Aluminum Co. of Canada, Ltd.  
Montreal, Que., Canada

American Cyanamid Co.,  
Stamford Research Laboratories,  
Stamford, Conn.

American Gas & Chemicals, Inc.,  
New York, N. Y.

American Metal Climax, Inc.,  
New York, N. Y.

American Smelting and Refining Co.,  
South Plainfield, N. J.

The M. Ames Chemical Works, Inc.,  
Glens Falls, N. Y.

Ampex Corp.,  
Redwood City, Calif.

Analog Devices, Inc.  
Norwood, Mass.

Applied Electrochemistry Inc.  
Sunnyvale, California

BASF Wyandotte Corporation,  
Wyandotte, Mich.

Beckman Instruments, Inc.,  
Fullerton, Calif.

Bell Telephone Laboratories, Inc.,  
Murray Hill, N. J. (2 memberships)

Boeing Co.,  
Seattle, Wash.

Canadian Industries Ltd.,  
Montreal, Que., Canada

Carborundum Co.,  
Niagara Falls, N. Y.

Chrysler Corp.,  
Detroit, Mich.

Cominco Ltd.,  
Trail, B. C., Canada

The Detroit Edison Co.,  
Detroit, Mich.

Diamond Shamrock Corp.,  
Painesville, Ohio

E. I. du Pont de Nemours & Co., Inc.,  
Wilmington, Del.

Eastman Kodak Co.,  
Rochester, N. Y.

Electrode Corporation  
Chardon, Ohio

Eltra Corp.,  
Prestolite Div., Toledo, Ohio  
C&D Batteries, Conshohocken, Pa.

Engelhard Industries, Inc.,  
Newark, N. J.

The Eppley Laboratory, Inc.,  
Newport, R. I.

ESB Inc.,  
Philadelphia, Pa. (2 memberships)

Esso Research and Engineering Co.,  
Engineering Technology Div.,  
Florham Park, N. J.

## SUSTAINING MEMBERS (CONTINUED)

**Fairchild Camera & Instrument Corp.,**  
Research and Development Laboratory,  
Palo Alto, Calif.

**Falconbridge Nickel Mines Ltd.,**  
Thornhill, Ont., Canada

**FMC Corp.,**  
Inorganic Chemicals Div.  
Buffalo, N. Y.

**Foot Mineral Co.,**  
Exton, Pa.

**Ford Motor Co.,**  
Dearborn, Mich.

**General Motors Corp.,**  
AC Electronics Div., Milwaukee, Wis.  
Allison Div., Indianapolis, Ind.  
Delco-Remy Div., Anderson, Ind.  
Research Laboratories Div., Warren,  
Mich.

**General Telephone & Electronics Labora-  
tories, Inc.,** Bayside, N. Y.

**Globe-Union, Inc.,**  
Milwaukee, Wis.

**B. F. Goodrich Chemical Co.,**  
Cleveland, Ohio

**Gould, Inc.,**  
Energy Technology Laboratories  
St. Paul, Minn.

**Great Lakes Carbon Corp.,**  
New York, N. Y.

**Gulf Oil Canada Limited**  
Shawinigan Chemicals Div.,  
Montreal, Que., Canada

**Harshaw Chemical Co.,**  
Cleveland, Ohio (2 memberships)

**Hill Cross Co., Inc.,**  
West New York, N. J.

**Hooker Chemical Corp.,**  
Niagara Falls, N. Y. (2 memberships)

**HP Associates,**  
Palo Alto, Calif.

**Hughes Research Laboratories, Div. of  
Hughes Aircraft Co.,** Malibu, Calif.

**International Business Machines Corp.,**  
New York, N. Y.

**Jones & Laughlin Steel Corp.,**  
Pittsburgh, Pa.

**K. W. Battery Co.,**  
Skokie, Ill.

**Kawecki Berylo Industries, Inc.,**  
Boyertown, Pa.

**Kennecott Copper Corp.,**  
New York, N. Y.

**Kerr-McGee Corporation,**  
Technical Center,  
Oklahoma City, Okla.

**Arthur D. Little, Inc.,**  
Cambridge, Mass.

**Mallory Battery Company**  
Tarrytown, N. Y. (2 memberships)

**Marathon Battery Co.,**  
Cold Spring, N. Y.

**Molybdenum Corporation of America,**  
New York, N. Y.

**Monsanto Company**  
St. Louis, Mo.

**Motorola Inc.,**  
Phoenix, Ariz.

**M&T Chemicals Inc.,**  
Detroit, Mich.

**National Cash Register Co.,**  
Dayton, Ohio

**National Lead Co.,**  
New York, N. Y.

**National Steel Corp.,**  
Weirton, W. Va.

**Nortec Electronics Corp.,**  
Santa Clara, Calif.

**North American Rockwell Corp.,**  
El Segundo, Calif.

**Northern Electric Co.,**  
Montreal, Que., Canada

**Owens-Illinois Glass Co.,**  
Toledo, Ohio

**Park Electrochemical Corp.,**  
Great Neck, N. Y.

**Phelps Dodge Refining Corp.,**  
Maspeth, N. Y.

**Philips Laboratories, Inc.,**  
Briarcliff Manor, N. Y.

**PPG Industries, Inc.,**  
Chemical Div.,  
Pittsburgh, Pa.

**Radio Corp. of America,**  
Electronic Components and Devices,  
Lancaster, Pa

**Republic Foil  
National Aluminum  
A Unit of  
National Steel Corp.**  
Danbury, Conn.

**Sobin Chlor-Alkali, Inc.,**  
Orrington, Maine

**Sprague Electric Co.,**  
North Adams, Mass.

**Stackpole Carbon Co.,**  
St. Marys, Pa.

**Stauffer Chemical Co.,**  
Dobbs Ferry, N. Y.

**Teletype Corp.**  
Skokie, Ill.

**Texas Instruments Inc.,**  
Dallas, Texas

**3 M Company**  
St. Paul, Minn.

**Udylite Corp.,**  
Detroit, Mich. (4 memberships)

**Union Carbide Corporation,**  
Consumer Products Division,  
New York, N. Y. (3 memberships)

**United States Steel Corp.,**  
Pittsburgh, Pa.

**Varian Associates,**  
Palo Alto, Calif.

**Western Electric Co., Inc.,**  
Greensboro, N. C.

**Yardney Electric Division**  
Pawcatuck, Conn.

**Zenith Radio Corp.,**  
Chicago, Ill.

